Tritium Retention in Nuclear Graphite, System-Level Transport, and Management Strategies for the Fluoride-Salt-Cooled High-Temperature Reactor

Kieran Patrick Dolan

B.S./M.S. Nuclear Engineering
University of Wisconsin – Madison, 2015

S.M. Nuclear Science and Engineering, 2018
Massachusetts Institute of Technology

Submitted to the Department of Nuclear Science and Engineering in partial fulfillment of the requirements for the degree of

Doctor of Philosophy in Nuclear Science and Engineering
at the

MASSACHUSETTS INSTITUTE OF TECHNOLOGY

February 2021

Signature of Author: _____
Department of Nuclear Science and Engineering
October 26, 2020

Certified by: _____
Lin-wen Hu
Director of Research and Services, Senior Research Scientist, Nuclear Reactor Laboratory
Thesis Supervisor

Certified by: _____
Koroush Shirvan
John Clark Hardwick Career Development Professor, Nuclear Science and Engineering
Thesis Reader

Certified by: _____
Charles W. Forsberg
Principal Research Scientist, Nuclear Science and Engineering
Thesis Committee Member

Accepted by: _____
Professor Ju Li
Battelle Energy Alliance Professor of Nuclear Science and Engineering
Professor of Materials Science and Engineering
Chair, Department Committee on Graduate Students

This page intentionally left blank

Tritium Retention in Nuclear Graphite, System-Level Transport, and Management Strategies for the Fluoride-Salt-Cooled High-Temperature Reactor

By

Kieran Patrick Dolan

Submitted to the Department of Nuclear Science and Engineering
On October 26, 2020 in Partial Fulfillment of the Requirements for the Degree of Doctor of Philosophy in Nuclear Science and Engineering

Abstract

Advanced reactor concepts which use a lithium- or beryllium-bearing primary salt coolant will require technical solutions to mitigate the environmental release of tritium. One such design is the Fluoride-Salt-Cooled High-Temperature Reactor (FHR), which combines a molten Flibe ($2LiF\text{-}BeF_2$) salt coolant and tri-structural isotropic coated-particle fuel to produce power or process heat. Compared to current water-cooled reactors, managing tritium release from a FHR is further complicated by the mobility of tritium at high temperatures and limited knowledge of interactions between tritium and nuclear graphite in the molten fluoride salt environment.

The total activity, chemical forms, and retention mechanisms for tritium in nuclear graphite were studied through thermal desorption analysis of sample materials from three in-core Flibe salt irradiations (denoted FS-1, FS-2, and FS-3) at the MIT Reactor (MITR). Tritium desorption rates as a function of temperature were observed in distinct peak structures which are indicative of distinct trapping sites in graphite. The tritium content measurements led to estimations of overall retention in nuclear graphite of 19.6±1.9% from FS-1, 34±10% from FS-2, and 27.1±1.9% from FS-3 relative to the total calculated tritium generation in each experiment. Thermal desorption measurements of the MITR samples were consistent with previously proposed mechanisms for retention of gaseous hydrogen in graphite based on the chemical form of desorbed tritium, the activation energy of the desorption process, and the effect of excess H_2 on the desorption rate as a function of temperature. Therefore, a methodology based on gaseous retention mechanisms was proposed and developed to model the uptake of tritium into graphite from Flibe in a FHR.

A tritium retention model based on a bulk-diffusivity in graphite was developed as well as a model based on differential transport in graphite pores and grains. Using a system-level tritium transport model, the overall retention on graphite pebbles in a FHR was calculated to be 20.3% and 26.3% of the equilibrium generation rate for the bulk-diffusivity and pore and grain methods, respectively. In each case, modeling the transport and trapping of tritium inside graphite significantly reduced the retention rates compared to a retention process solely limited by mass transport in Flibe. According to the results of a sensitivity analysis, the level of tritium retention in core graphite has the largest uncertainty in the FHR tritium distribution because of relatively high standard deviations in literature measurements of tritium solubility and diffusivity in graphite.

Tritium management technology options were then examined in the system-level transport model based on permeation barrier coatings and tritium extraction systems. Permeation barrier coatings of a specified performance level applied to Flibe-facing surfaces were found to be more effective than exterior-surface coatings, while extraction systems with design constraints were able to significantly reduce overall tritium releases. A combination of the interior-surface barriers and extraction systems applied to various regions of the plant was shown to reduce tritium release into the FHR reactor building to levels below that of current light water reactors.

Thesis Supervisor: Lin-wen Hu
Title: Director of Research and Services, Senior Research Scientist, Nuclear Reactor Laboratory

Acknowledgements

This research project was a great experience for me, both professionally and personally, and would not have been possible without the contributions of others. I would like to thank my thesis advisor, Dr. Lin-wen Hu, for enabling this research opportunity and for the years of assistance in guiding my research progress. I would also like to thank Professor Koroush Shirvan for serving as my thesis reader and Dr. Charles Forsberg for participating in the thesis committee.

One great benefit to this project was having highly engaged stakeholders who helped keep my research focused on important technical questions. I would like to extend my thanks to Dr. Micah Hackett and Dr. Steven Huang from Kairos Power for the advice and research suggestions they have offered throughout my doctoral studies. I would also like to thank Kairos Power for supporting our research project.

Being involved in irradiation experiments and post-irradiation testing of samples at the MIT Nuclear Reactor Laboratory (NRL) gave me unique insights into technical aspects of my thesis. Thank you Dr. David Carpenter for facilitating the setup of the tritium desorption experiment, and thank you Dr. Guiqiu (Tony) Zheng for helping me prepare graphite samples. Thanks to Dr. Gordon Kohse, Dr. Michael Ames, Dr. Kaichao Sun, Yakov Ostrovsky, and others who were involved in the design and testing of the NRL Flibe experiments. Lastly, thank you Dr. Bill McCarthy and Matt Mahowald for managing tritium safety aspects of the desorption experiments.

My research efforts were helped significantly by previous students who have investigated FHR and tritium related topics. In particular, Dr. John Stempien's PhD thesis provided a thorough overview of tritium transport in FHRs and helped to build my understanding of the field. Professor Stephen Lam also frequently answered my technical questions and provided feedback on my experimental and modeling plans. Robert Patrick White was a useful resource in helping me understand tritium regulations. Thanks to you all.

Aside from research, I would like to thank those that have made my experience at MIT and elsewhere more enjoyable over the past years. Thanks to my family, who have always supported me in academic and career plans. Thank you Elizabeth and Clifford for being excellent roommates. Thank you NW12 officemates, ski trip friends, Atom Smasher intramural teammates, the trivia groups, and all others who make MIT Nuclear Science and Engineering a fun and interesting community.

Contents

Table of Figures

List of Tables

1. Introduction

The Fluoride-Salt-Cooled High-Temperature Reactor (FHR) is an emerging design for future advanced nuclear reactors. Key design features of the FHR are graphite-matrix coated-particle fuel originally established for High Temperature Gas-Cooled Reactors (HTGRs) and the molten fluoride salt coolant developed for Molten Salt Reactors (MSRs) [1]. The combination of coated-particle fuel and molten salt coolant enables potential economic benefits through high-temperature and low-pressure operating conditions while maintaining uniquely high safety margins to thermal limits [1]. Furthermore, relying on technologies demonstrated in previous reactor designs, rather than new technological breakthroughs, simplifies the basis for FHR commercialization. While several FHR design features have a high level of technological readiness relative to liquid-fueled MSRs, significant technical challenges remain which require further investigation. One FHR technical challenge – mitigating the environmental release of tritium – is the focus on this thesis.

1.1. Fluoride-Salt-Cooled High Temperature Reactor Technology Overview

Fluoride-Salt-Cooled High-Temperature Reactors encompass a range of possible design options. For example, fuel forms can exist in spherical or prismatic elements and several molten fluoride mixtures have been proposed as coolants. Several references are available which discuss considerations for FHR salt selection [2], the history and evolution of the FHR concept [3, 4], design details for a particular FHR [5, 6], and projected ecomonics [6, 7, 8]. Therefore, this section is intended to only provide an introduction to the main features of a FHR nuclear design.

One unifying feature among FHR designs is the use of tristuctural isotropic (TRISO) coated-particle fuel, which provides robust fission product retention at high temperatures through a multi-layered structure [3]. TRISO fuel refers to spherical particles which are typically less than 1mm in diameter and contain a central fuel kernel surrounded by a porous carbon buffer layer. The buffer layer porosity provides a volume for gaseous fission products to accumulate without significantly increasing the pressure inside the particle [9]. The main fission product barrier in TRISO particles is provided by a silicon carbide layer, which is further protected by an outer pyrolytic carbon barrier and an inner pyrolytic carbon layer between the SiC and porous carbon buffer [9]. Several thousand TRISO particles are contained in a carbon-based matrix material to comprise a fuel element. For the Mark-1 Pebble Bed FHR design, 4370 TRISO particles are

arranged into an annular ring in a 3cm diameter spherical fuel element, as shown in Figure 1.1 [6]. The annular fuel ring reduces the peak temperature in fuel kernels and provides a central region where low density graphite can be used to increase the buoyancy of fuel pebbles in the molten salt coolant [5].

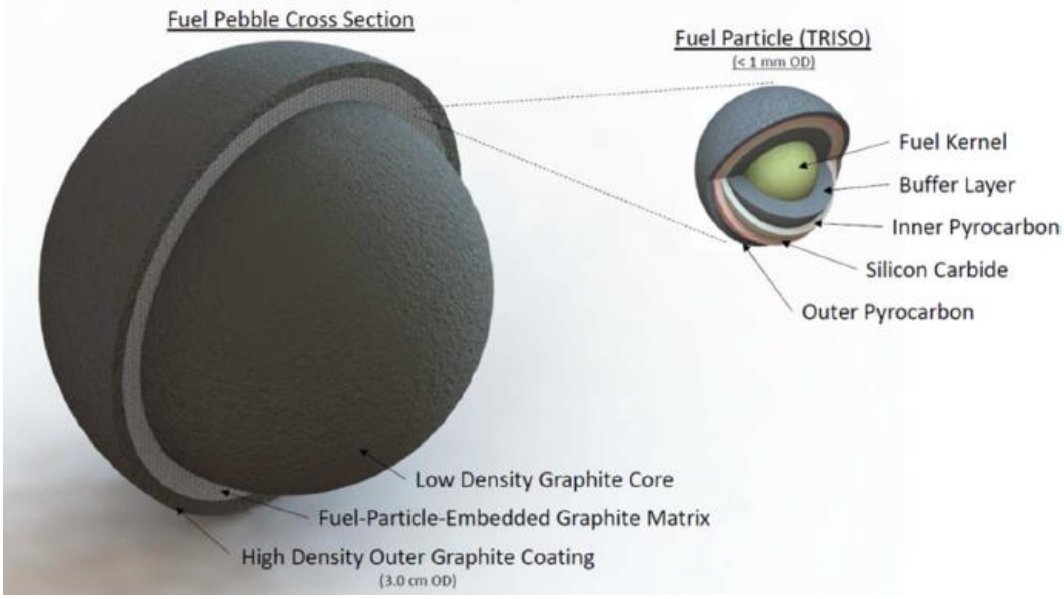

Figure 1.1. Mark-1 PB-FHR fuel element consisting of TRISO coated-particle fuel contained in an annular ring of a spherical fuel pebble. From [6].

Another commonality to all FHR concepts is the use of a molten fluoride salt as the primary coolant, which enables high-temperature and atmospheric pressure operation of the reactor. Atmospheric pressure operation can, in principle, be achieved for FHRs at any operating temperatures in between the coolant salt melting point and boiling point, which are compiled for several candidate fluoride salt mixtures in Table 1.1. Another notable observation in Table 1.1 is the high boiling point of candidate fluorides compared to proposed FHR operating temperatures of 600ºC-700ºC. A high margin of operating temperatures to salt boiling points implies that the FHR coolant will remain in a liquid phase during postulated accident scenarios where temperatures are increased. However, the elevated melting points of proposed fluoride salt mixtures creates a need for reactor external heating provisions to initially melt the salt when starting from a frozen state. Similarly, reactor transient conditions that produce reduced coolant temperatures must be evaluated to ensure that salt freezing does not disturb reactor safety functions. The impact of salt freezing can also be mitigated with active or passive systems that keep the fluoride coolants above melting temperatures [10].

Table 1.1. Composition of constituents, melting temperatures, and boiling points for candidate fluoride salt coolants. Starred boiling points are extrapolated from lower-temperature data [2].

Salt Constituents	Composition [mol%]	Melting Point [ºC]	Boiling Point [ºC]
$NaF\text{-}BeF_2$	57-43	340	1400*
$RbF\text{-}ZrF_4$	58-42	410	1450*
LiF-NaF-KF	46.5-11.5-42	454	1570
$LiF\text{-}BeF_2$	66.6-33.4	458	1400*
$NaF\text{-}ZrF_4$	59.5-40.5	500	1350*

A thorough review of candidate fluoride salt coolant properties and performance metrics is available elsewhere [2]. The selection of the most suitable fluoride salt depends somewhat on the particular characteristics and goals of a given reactor design. However, one attractive fluoride mixture with a relatively low melting point, low vapor pressure, suitable heat transfer properties, and beneficial neutronic characteristics is the 2:1 mixture of lithium fluoride and beryllium fluoride referred to as Flibe [2]. As an example of one factor, neutronic performance among fluoride salts is compared in Table 1.2 [2]. One particular advantage for Flibe is the ability to create a negative density reactivity coefficient, meaning that reactivity of a FHR core will decrease when Flibe is heated or coolant inventory is replaced by a void volume. The reactivity coefficients in Table 1.2 were calculated using a pin-cell model with a 238-group cross section set determined for a prismatic TRISO fueled geometry [2]. A negative void coefficient improves the safety of a FHR during transient scenarios and simplifies the requirements for licensing the reactor.

Table 1.2. Relative neutron capture ratio compared to graphite and density reactivity coefficients of selected fluoride salt mixtures [2]. All lithium-bearing salts were evaluated at 99.995% Li-7.

Salt Coolant	Neutron Capture per Volume vs. Graphite	Density Reactivity Coefficient ($/100K)
$LiF\text{-}BeF_2$	8	-0.01
$NaF\text{-}BeF_2$	28	0.06
$LiF\text{-}NaF\text{-}ZrF_4$	20	0.09
$NaF\text{-}ZrF_4$	24	0.11
$RbF\text{-}ZrF_4$	14	0.18
$KF\text{-}ZrF_4$	67	0.27

The combination of a molten fluoride salt coolant and TRISO fuel in a FHR enables a compact, high power density core which maintains capabilities of passive safety features. As one example, a design schematic of the Mk1 FHR core is shown in Figure 1.2 [11]. Reactor decay heat is removed passively with three direct reactor auxiliary cooling system (DRACS) loops each capable of removing 1% of reactor power through natural circulation of Flibe [6], which are accessed through the DHX flow paths labeled in Figure 1.2. Ambient air is the ultimate heat sink for the Mk1 FHR design, and thus there is no reliance on the availability of emergency core cooling water.

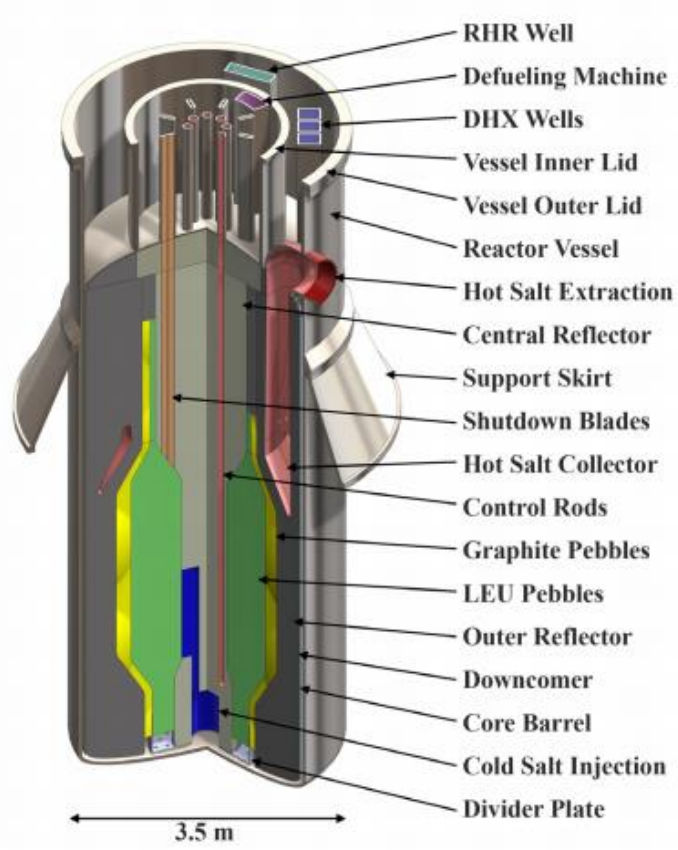

Figure 1.2. Mark-1 FHR core layout diagram. From [11].

While no FHR has ever been built or operated, the technological readiness of the FHR is partially supported by previous experience from other reactor designs and research programs. For example, seven helium-cooled reactors have previously operated with coated-particle fuel, which has produced a broad understanding of the fabrication and operational performance of TRISO fuel elements [12]. Similar experience was gained from the Molten Salt Reactor Experiment (MSRE), where uranium fluoride dissolved in a LiF-BeF_2 fuel salt was used in an 8 MWt test reactor

operational from 1965 to 1969 at Oak Ridge National Laboratory (ORNL) [13]. Renewed interest and recent research progress has also supported FHR development efforts [1, 14], such as through the refinement of the previously discussed Mk1 FHR concept [6], demonstration of acceptable Flibe corrosion rates with code-qualified alloys [15], and reestablishment of Flibe purification and irradiation capabilities [16, 17]. While significant progress has been made, specific strategies to address technical challenges for the FHR remain undecided in candidate reactor designs. One design challenge, and the central topic of this study, is the mitigation of tritium release from FHR power plants.

1.2. Tritium Management as a Key Technical Challenge

Neutronic and thermal hydraulic analysis of candidate fluoride salts reveals that the top performing salts all contain lithium fluoride or beryllium fluoride [2, 18]. The next best top candidate is $NaF\text{-}ZrF_4$, which presents added design challenges because of its relatively high melting point of 500ºC, high vapor pressure, and the difficulty in achieving a negative coolant void reactivity coefficient [2]. To optimize for coolant performance characteristics, as well as draw parallels from the experience base of the $LiF\text{-}BeF_2$-based MSRE, several current FHR designs under development have selected Flibe as their baseline coolant. For example, Flibe is used as the coolant in the University of California, Berkeley Mk1 FHR design [6], the TMSR-SF design from the Shanghai Institute of Applied Physics [19], and the KP-FHR design from the commercial reactor designer Kairos Power [20].

The use of Flibe salt results in improved heat transfer and neutron economy compared to other candidate fluorides, but creates the notable disadvantage of tritium production by neutron reactions with lithium and beryllium. Tritium is a radioactive isotope of hydrogen containing a nucleus of one proton and two neutrons. The decay of tritium has a half-life of 12.32 years and produces helium-3 along with an electron of 18.6 keV maximum energy and 5.7 keV average energy [21, 22]. Tritium has the second-lowest beta decay ground-state to ground-state energy release among all observed isotopes [23], and thus the energy of beta particles emitted by tritium decay is not a central issue in tritium release. However, tritium management is a unique challenge because of the mobility of tritium chemical forms and potential reactions with the biosphere. The possible release pathways in which tritium can result in radioactive dose to the public are described conceptually in Figure 1.3. The dose-consequence of tritium depends on the chemical

characteristics of different potential forms. For tritiated hydrogen gas, HT, inhalation results in about 0.01% absorption of tritium into the body with the remaining HT is exhaled and thus resulting doses are less than that of other tritium chemical forms [24]. For example, the effective dose produced from a given amount of tritium activity during inhalation is 10,000 times greater for tritiated water vapor (HTO) than for HT gas [25]. The chemical form of tritium affects the amount of dose received based on the various residence times for each chemical form in the body. Tritiated water will remain in the body with a biological half-life of 10 days and organically bound tritium (OBT) - tritium in carbon-based molecules - will exist with a biological half-life of roughly 40 days [24].

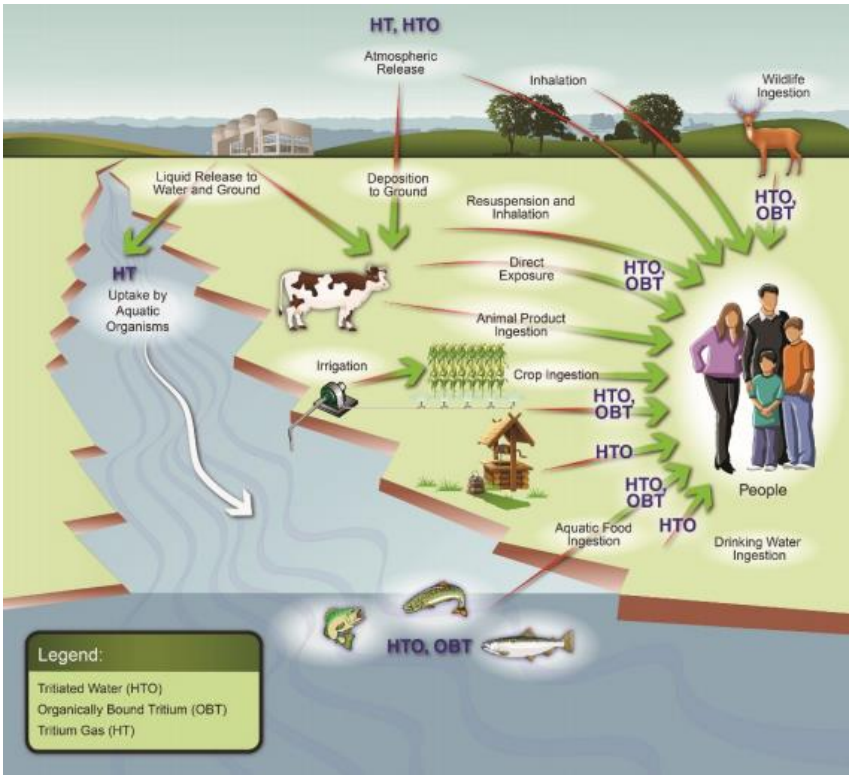

Figure 1.3. Conceptual model of tritium pathways for environmental release. From [24].

Because of the potential for tritium to interact with the environment, become incorporated with water and organic material, and cause internal doses in humans, tritium releases from nuclear power plants are tightly controlled. Selected regulations for tritium release limits in air and water effluents from nuclear plants are shown in Table 1.3. The effluent concentration limits are given in units of micro-Curies of tritium per milliliter of water or air, where one Curie is equal to $3.7 \cdot 10^{10}$ tritium decays per second. Allowable concentrations are calculated based on a certain allowable

annual dose to a member of the public, shown in Table 1.3 in units of millirem [26]. Based on past experience, typical tritium releases from current power plants are only a small portion of the allowable 10 Code of Federal Regulations (CFR) 20.1301 limits [27]. Therefore, additional criteria for ALARA, or "as low as reasonably achievable," limits are also shown in Table 1.3 based on 10 CFR 50. In this case, the ALARA limits allow for consideration of available technologies for release mitigation and economic cost analysis compared to realizable public health benefits [27].

Table 1.3. Relevant regulations for annual dose for radioactive releases and corresponding effluent concentrations for tritium release. From [26].

Type	Regulation	Annual Dose [mrem]	Effluent Concentration [μCi/ml]	
			Air	Water
Limit	10 CFR 20.1301 a1	100	-	-
	10 CFR 20 Appendix B Table 2	50	$1 \cdot 10^{-7}$	$1 \cdot 10^{-3}$
Standard	10 CFR 20.1301e / 40 CFR Pt 190.10a	25	$5 \cdot 10^{-8}$	$5 \cdot 10^{-4}$
ALARA	10 CFR 50 Appendix I Sec II. B.1	20	$4 \cdot 10^{-8}$	-
	10 CFR 50 Appendix I Sec II. B.2b	15	$3 \cdot 10^{-8}$	-
	10 CFR 50 Appendix I Sec II. A	3	-	$6 \cdot 10^{-5}$

One reason why tritium releases from current power plants are typically well below 10 CFR 20.1301 limits is the relatively low tritium production rate of the Boiling Water Reactors (BWRs) and Pressurized Water Reactors (PWRs) which comprise the current U.S. commercial nuclear fleet. All fission reactors create some tritium directly as a fission product [28], and PWRs and BWRs have additional sources of tritium created through neutron interactions with boron in control rods (BWRs) or boric acid dissolved in the primary coolant (PWRs) [29]. The PWR generation rate is also slightly higher than the BWR rate because of lithium hydroxide added to the coolant to balance the pH from the addition of boric acid [30]. Tritium production rates for various reactor types are compared in Table 1.4 [3, 29], where FHR values have a beginning of life (BOL) rate as well as an equilibrium rate (EQ) due to changing lithium-6 concentrations in the Flibe coolant over time [3]. Based on Table 1.4 values, FHRs are expected to exceed the tritium production of BWRs and PWRs as well as HTGRs and Heavy Water-cooled Reactors (HWRs) in terms of daily tritium production normalized to reactor thermal power. Therefore, FHRs will require additional attention towards managing and controlling tritium releases compared to other reactor designs.

Table 1.4. Comparison of tritium production rates among different reactor designs. From [3].

Reactor Class	Normalized Tritium Production Rate [Ci/GWt-day]
BWR	12.3
PWR	13.9
HTGR	18.0
HWR	1,176
FHR	BOL: 10,129 EQ:2,931

Even at low tritium production rates, the buildup of tritium inventory and release of tritiated sources from a nuclear plant can lead to violation of regulatory limits. For example, a leak of the advance off gas line in the Vermont Yankee BWR plant created from pipe tunnel design modifications in 1978 resulted in a tritium groundwater concentration measured in 2010 that exceeded the US Environmental Protection Agency's drinking water limit of $2 \cdot 10^{-5}$ μCi/ml [31]. While there were no health risks attributed to the leak of tritiated water, the incident contributed to the Vermont Senate's decision to vote in favor of closing the plant prior to the expiration of its operating license [32]. The Vermont Yankee experience highlights the need to consider all tritium-relevant regulations during operation of nuclear plants, rather than only the effluent concentration restrictions shown in Table 1.3.

Safe operation of reactors with elevated tritium production rates is achievable, as demonstrated by decades of experience with heavy water reactors [33]. Industrial solutions have been previously developed to monitor tritium activity around the plant, capture tritium prior to environmental release, and safely store tritium in compact waste forms [34]. However, technical challenges exist for FHR designers in predicting the tritium distribution among reactor systems, accounting for release rates to various plant regions, planning for various levels of tritium inventory in reactor components, and designing tritium capture and storage systems with adequate efficiencies to minimize tritium release to the environment.

1.3. Thesis Objectives and Outlines

The elevated production rate and mobility of tritium in high-temperature molten Flibe salt motivates the need to evaluate tritium control solutions as part of the FHR design process. A central goal of this study is to improve system-level tritium transport models, both by expanding the level of detail in the reactor model and by representing additional important tritium transport phenomena. Furthermore, Tritium distribution predictions from a system-level transport model can then be used to quantitatively asses to advantages and limitations of proposed tritium management strategies. Using the updated model, example tritium management strategies for the FHR are then proposed based on tritium extraction systems and permeation barrier coatings. Thesis objectives and how they are addressed in each section are discussed below.

Section 2 - Tritium Transport in Fluoride-Salt-Cooled High-Temperature Reactors

Objective: Identify key tritium transport phenomena and evaluate current available data and knowledge gaps.

Tritium transport phenomena are divided into the categories of generation, speciation, transport in Flibe, permeation through metals, and retention in graphite. Aspects of each process are discussed in detail to provide a useful technical background for interpreting the results of later sections. Measurements from previous studies of each experimentally-derived parameter used in the system-level tritium transport model are shown in plots and complied and tables in Section 2 to show the spread in literature data and identify the most suitable data sources.

Section 3 - Tritium Distribution in MITR Fluoride Salt Irradiations

Objective: Summarize lessons learned from MITR Flibe irradiations and how the results can be used to assist in development of a method to simulate tritium retention in FHR graphite.

Graphite samples from three in-core Flibe experiments at the MIT Reactor were analyzed for tritium content, chemical form, and retention mechanisms through thermal desorption testing. The desorption tests help to understand the percentage of tritium retained in graphite and its prototypical value in Flibe-graphite environment. Furthermore, details from the desorption experiments are compared to literature studies to draw parallels to the previously proposed mechanisms for retention of gaseous hydrogen in graphite.

Section 4 - Modeling Tritium Transport in Graphite under FHR Conditions

Objective: Describe methods to calculate tritium retention in graphite at FHR conditions and compare against experimental data.

Based on similarities observed in the MITR graphite desorption experiments, mechanisms for gaseous hydrogen in graphite were applied to determine the uptake, transport, and trapping of tritium from molten Flibe. A method based on a bulk-diffusivity of hydrogen in graphite is proposed along with another model using separate diffusivities and concentration terms to track tritium in graphite pores and filler grains. Results from each model were compared to previous absorption and desorption experiments of deuterium gas in nuclear graphite.

Section 5 - System-Level Tritium Transport Model Development

Objective: Outline the calculation process in a system-level tritium transport model, interpret the baseline results, and describe potential uncertainties which influence model predictions.

The implementation of the graphite retention model and other transport phenomena are described for the TRIDENT Mod1 code developed in Matlab Simulink. Outputs from the model under a set of baseline conditions are shown in order to describe the expected tritium release behavior in a standard FHR. Possible ways in which model results could deviate from the baseline are shown through an input parameter sensitivity analysis. Additionally, the impact of modeling assumptions on tritium chemical forms and pebble recirculation conditions were evaluated.

Section 6 - Overview of Tritium Management Strategies for the FHR

Objective: Evaluate FHR tritium management strategies using the TRIDENT Mod1 results.

Potential tritium release pathways in the FHR plant are first evaluated for the relative difficulty in capturing tritium from each region with commercially available materials. Tritium management strategies are then implemented into the TRIDENT Mod1 code and performance of each strategy is ranked on the degree to which tritium release is minimized in undesirable reactor regions where tritium capture is most difficult. Overall releases are compared to typical values from current operating light water and heavy water reactors.

Section 7 - Conclusions and Future Research Needs

Objective: Summarize tritium management simulation results and recommend topics for future work to improve tritium transport modeling efforts.

The results from system-level tritium transport models can help to quantitatively evaluate potential tritium management strategies in a FHR, and guide a path forward in developing effective tritium controls for future designs. However, the emphasis made on model results should be weighed against potential uncertainties in the calculation process. Specific parameters in need of additional investigation are highlighted based on the results of the sensitivity study. The impact of unresolved tritium transport phenomena on the tritium distribution is also hyposethesized. Further refinement of tritium transport models can strengthen the conclusions drawn from model outputs, and better guide the development of tritium management strategies for the FHR.

2. Tritium Transport in Fluoride-Salt-Cooled High-Temperature Reactors

An initial understanding of how and where tritium will be released from a FHR creates the technical basis for engineering controls and design decisions implemented as part of a tritium management strategy. Predicting the tritium distribution in a FHR is possible when relevant phenomena are sufficiently understood and accounted for. In this section, important technical considerations are summarized according to a rough chronological life-cycle of tritium atoms in a FHR – where tritium is first generated through neutron reactions, speciated into chemical forms in Flibe, and then transported to interfaces where it can dissosciate from the salt phase.

2.1. Tritium Generation

Flibe is the primary source of tritium in FHRs and thus focus of this work. Tritium generated from other sources in the reactor will most likely have less mobility than that of tritium present in the salt. For example, tritium generated by ternary fission in fuel kernels is not significantly released from TRISO fuel particles because of tritium retention in the pyrolytic carbon layer as well as the low tritium permeability of the silicon carbide layer [35]. Within Flibe, each salt constituent has a contribution to total tritium generation, with the dominant source from Li isotopes. The relevant reactions are shown in equations 2.1 through 2.7. As shown in the cross sections plotted in Figure 2.1, the lithium-6 reaction is the only Flibe source which can produce tritium at low neutron energies. The lithium-6 cross section is also quite large with a value of 938 barns at 300K [36]. Therefore, a Flibe-cooled FHR must use a salt enriched in lithium-7 to avoid the significant tritium production and neutronic penalty caused by lithium-6. However, it is not possible to completely eliminate lithium-6 in the reactor since it is continuously added through the reaction with beryllium in equation 2.6 to produce helium-6, and the decay of helium-6 to lithium-6 shown in equation 2.7. The breeding and burnup of lithium-6 results in a tritium production rate that changes over time and reaches equilibrium once the lithium-6 concentration is steady. The next highest tritium-producing reaction is from lithium-7 shown in equation 2.2, which is an inelastic scattering reaction that brings the nucleus to the continuum level with a threshold energy of 2.47 MeV and releases an alpha particle, a tritium atom, and the scattered neutron [37].

Eq. 2.1 $$^{6}Li + n \rightarrow {}^{4}He + {}^{3}H$$

Eq. 2.2 $$^{7}Li + n \rightarrow {}^{4}He + {}^{3}H + n'$$

Eq. 2.3 $$^{9}Be + n \rightarrow {}^{7}Li + {}^{3}H$$

Eq.2.4 $$^{19}F + n \rightarrow {}^{17}O + {}^{3}H$$

Eq.2.5 $$^{6}Li + n \rightarrow {}^{4}He + {}^{3}H$$

Eq.2.6 $$^{9}Be + n \rightarrow {}^{6}He + {}^{4}He$$

Eq.2.7 $$^{6}He \rightarrow {}^{6}Li + \beta + \bar{\nu}_e \quad (t_{1/2} = 0.8\ s)$$

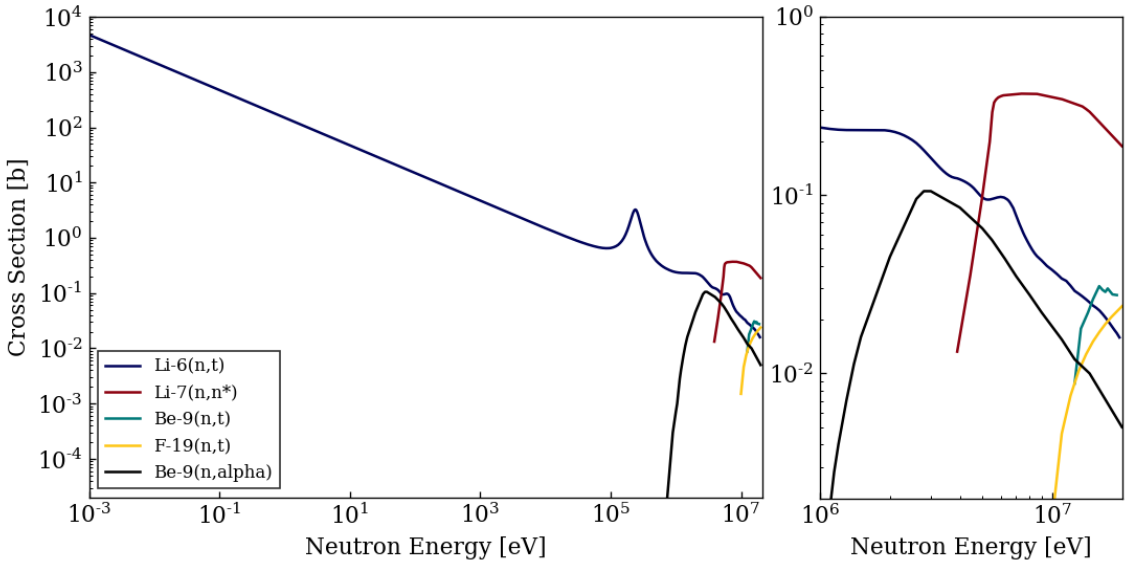

Figure 2.1. Neutron microscopic cross sections relevant to tritium production in Flibe salt (left) and focused plot of reactions at neutron energies above 1 MeV (right). From [36].

At high lithium-7 enrichments (>99.99%), the share of tritium generated by lithium-6 still becomes comparable to that of lithium-7. Tritium sources evaluated for the Molten Salt Breeder Reactor, the 2250 MW commercial-scale design envisioned to follow the Molten Salt Reactor Experiment (MSRE) [38], are shown in Table 2.1. It is not stated whether the production rates are the equilibrium or initial values, and the lithium-7 enrichment is only listed as 99.99+% [38]. However, it is clear that the lithium-7 reaction makes a significant contribution to total tritium generation. There is also a noticeable source of tritium from ternary fission, which creates roughly one tritium fission product per 10^4-20^4 fissions of uranium [28]. For a liquid-fueled reactor like the MSBR, ternary fission would result in a direct source of tritium into the fuel salt.

Table 2.1. Tritium sources and production rates calculated for a 2250 MWt MSBR. From [38].

Tritium Source	Production Rate [Ci/day]
Ternary Fission	31
^{6}Li(n,t)^{3}H	1210
^{7}Li(n,n*)^{3}H	1170
^{19}F(n,^{17}O)^{3}H	9
Total:	2420

The isotopic contributions to tritium generation were also calculated for the FS-3 irradiation at the MIT Reactor (MITR). In the irradiation, 101.5 grams of Flibe were irradiated inside of a capsule in a high flux region of the reactor core. The Flibe was supplied from ORNL, where it was originally used in the intermediate heat transfer loop of the MSRE. Based on measurements taken during the salt's production, the lithium-7 enrichment was between 99.990 and 99.991 wt% [39]. Reaction rates in the FS-3 Flibe were calculated based on a full-core model of the MITR including the experimental capsule [40], which are plotted as a function of neutron energy in Figure 2.2. The percent contributions of each reaction are shown in Table 2.2. Understanding the different contributions is important in determining how the tritium generation rate will evolve with time. The total tritium generation rate will also vary in a commercial-scale FHR based on the neutron flux and neutron energy spectrum seen by the salt.

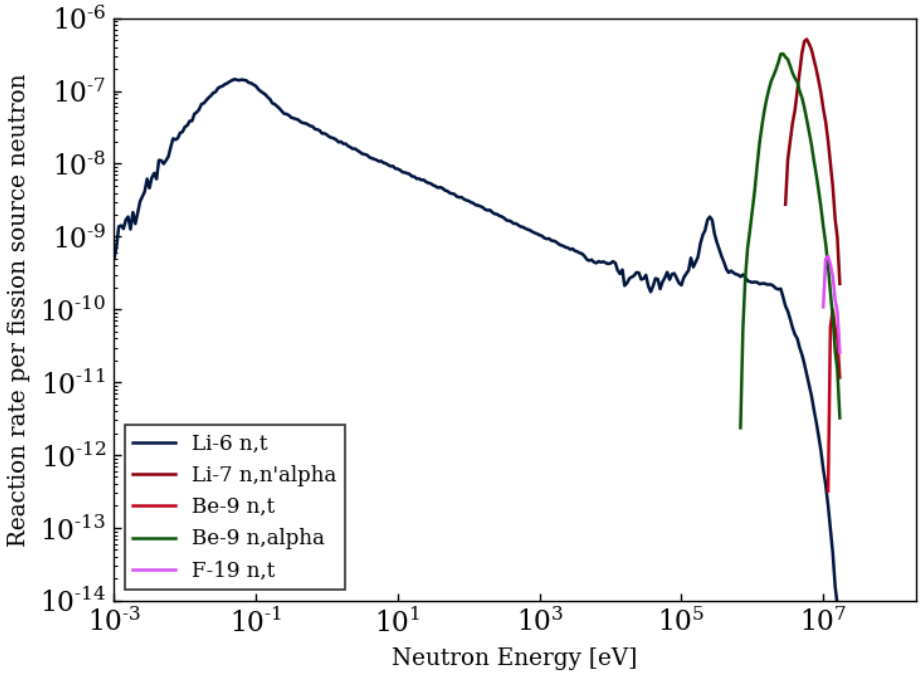

Figure 2.2. Reaction rates for tritium relevant reactions calculated in MCNP for the FS-3 irradiation at the MIT Reactor. From [41].

Table 2.2. Flibe constituent contributions to total tritium generation in the FS-3 irradiation experiment calculated by MCNP. From [41].

Reaction	Tritium Generation
$^{6}Li(n,t)^{3}H$	65.2%
$^{7}Li(n,n^{*})^{3}H$	34.8%
$^{9}Be(n,t)^{3}H$	0.003%
$^{19}F(n,^{17}O)^{3}H$	0.025%

Generation of tritium in a FHR from sources other than the Flibe coolant can be roughly estimated by assuming the reactor core design and neutron energy spectrum will be similar to that of a HTGR, although in practice there could be notable differences in neutron spectrum based on the ratio of carbon moderator to nuclear fuel in each reactor. The tritium source term for the high temperature gas-cooled reactor pebble-bed module (HTR-PM) reactor has been calculated based on a 40 year lifespan [42]. In the HTR-PM design, two 250 MWt modules are used to produce a total of 200 MWe. Production rates converted to a daily basis are shown in Table 2.3. The major sources are ternary fission as well as activation of boron in the B_4C control rods, along with activation of lithium and boron impurities in the graphite [42].

Table 2.3. Tritium production from various sources in a 250 MWt HTR-PM module. From [42].

Tritium Source	Generation Rate [Ci/day]	Proportion
Ternary fission	3.64	23.20%
He-3 in primary coolant	8.60E-1	5.46%
Li-6 in fuel elements	1.17	7.43%
Li-7 in fuel elements	1.75E-3	0.01%
Li-6 in graphite reflectors	2.72E-1	1.73%
Li-7 in graphite reflectors	2.59E-3	0.02%
Li-6 in carbon bricks	7.75E-3	0.05%
Li-7 in carbon bricks	1.89E-7	< 0.01%
B-10 in carbon bricks	3.51E-2	0.22%
B-10 in control rods	9.73	61.88%
B-10 in absorber balls	9.15E-05	< 0.01%
Total:	15.7	

If a FHR design also includes boron carbide control rods and graphite with similar impurity levels, then the non-Flibe tritium sources can be approximated by scaling the HTR-PM rates to the FHR power level. Production from helium-3 can be neglected since this originates from the HTR-PM coolant. The proportion of tritium sources for a 320MWt FHR are shown in Table 2.4, along with the equilibrium Flibe tritium production rate based on the Mk-1 FHR design [43]. All fuel element, reflector, and carbon bricks are combined into one category. In a rigorous analysis, the total generation should be calculated directly in a full-core model using the as-designed dimensions, material compositions, and neutron spectrum and flux of the reactor. However, this first-order approximation provides justification for focusing on Flibe in regards to tritium management in the FHR design since it is the source of 98% of tritium generation.

Table 2.4. Estimation of tritium sources in a 320MWt FHR using scaled non-Flibe sources from the HTR-PM tritium source term analysis [42]. The FHR values assume a core Flibe volume of 7.2 m^3 and total Flibe volume of 46.82 m^3 [3].

Tritium Source	Generation Rate [Ci/day]	Proportion
Ternary fission	4.66	0.5%
Impurities in graphite	1.86	0.2%
B-10 in control rods	12.5	1.3%
Flibe total (equilibrium)	938	98.0%
Total:	957	

2.2. Tritium Speciation

After generation, tritium will exist in the salt in either its chemically reduced form, T_2, or its oxidized form of TF [3]. The presence of a hydrogen partial pressure above the salt can also convert tritium of either form into HT [44, 45]. Assuming that the salt is a fully dissociated mixture of ions, TF is also written as T^+ [44]. Other oxidized forms such as HTO or T_2O are possible, although molten salt systems are typically purged of oxygen and moisture and Flibe chemistry would favor the formation of BeO with any remaining oxygen or water instead [46, 47]. Predicting and tracking the chemical form of tritium in the salt is important since transport properties and solubilities of each species are significantly different. Furthermore, the chemical form of tritium has a strong influence on mechanisms of tritium release. For example, both TF and T_2 can evolve from the salt to off-gas [44], but only T_2/HT is observed to permeate through metals [48, 49].

While different chemical forms can eventually exist in the salt, it is generally agreed that tritium is initially born into the oxidized form, TF [3, 44]. Assuming that tritium fluoride dissociates into ions in the salt, then TF can also be writted as T^+ [44]. The initial generation as TF can be inferred from the irradiation experiments from Suzuki et al, where the H_2 partial pressure in a helium sweep gas above Flibe was varied while the salt was irradiated. The chemical form of tritium released from the salt was monitored and as the H_2 decreased, the percentage of TF release was elevated. At the lowest used H_2 partial pressure of 1 Pa, TF accounted for 99% of the release [44]. Therefore, in the absence of other effects, like interactions with the H_2 cover gas, tritium was generated and eventually released from the salt as TF. The chemical form of tritium was also monitored during irradiations of frozen Flibe at room temperature and in contact with dry ice [50]. Irradiation of frozen Flibe led to roughly 15% production of T^-, likely as LiT, less than 1% T_2, and the remaining balance as TF. The fraction of TF slightly increased for the room temperature salt

compared to the irradiation with dry ice. When the salt was heated to 873K, there was no T^- measured in tritium released from the salt [50]. The preference for T^+ generation in molten Flibe can also be explained by a charge balance of reactants and products from the transmutation, as shown in equations 2.8 through 2.10 below. In all cases, tritium must exist as T^+ in order to balance the charges of the other elements in their typical redox states.

Eq.2.8 $$Li^+ + n \rightarrow He^o + T^+$$

Eq.2.9 $$Be^{2+} + n \rightarrow Li^+ + T^+$$

Eq.2.10 $$F^- + n \rightarrow O^{2-} + T^+$$

2.2.1. Speciation Based on Equilibrium Conditions

After generation as TF, tritium will distribute into different chemical forms based on conditions in the FHR. Determining the chemical speciation of tritium is a fundamental step towards understanding the transport and distribution of tritium in the reactor. Ultimately, the driving force of speciation is the redox potential, or chemical potential energy of the salt. A reducing chemical environment in molten fluoride salts is required to prevent excessive corrosion of structural alloys [51, 52]. Therefore, the production of tritium fluoride raises the salt chemical potential since TF is significantly more oxidizing than the salt constituents LiF and BeF_2 as well as likely impurities CrF_2, FeF_2, and NiF_2 produced by corrosion of candidate FHR structural alloys such as Hastelloy-N or 316 stainless steel [53, 3]. A FHR will operate within a set redox potential window, and a designated chemical control strategy will be employed in order to convert TF to T_2 to limit corrosion [3]. Once the generated tritium comes to chemical equilibrium in the salt, the amount of TF and T_2 can be calculated according to the designed redox potential.

One method for characterizing salt chemical behavior is based on the 'fluorine potential,' or partial pressure of free fluorine gas in the salt [54]. Fluorine potential, $\Delta\bar{G}_{F2}$, is defined in equation 2.11, where R is the universal gas constant, T is temperature in Kelvin, and p_{F2} is the partial pressure of F_2 gas in atmospheres. Because of its extreme reactivity, free fluorine gas should not exist in the salt in any reasonable quantity. Fluorine can be generated in nuclear applications from radiolysis, but the recombination rate of F_2 with displaced active metals increases with temperature and is sufficiently rapid such that no F_2 release from fluoride salts was observed in experimental measurements with salt temperatures above 150ºC [55]. While F_2 partial pressures are not expected to be significant in Flibe, defining a fluorine potential based on p_{F2} is a useful

closure for solving equilibrium chemical reactions relevant for molten fluoride salts. The fluorine potential can be related to the TF:T_2 ratio as shown in equation 2.12, where and p_{T2} are p_{TF} are the partial pressures of tritium fluoride and diatomic tritium, and ΔG^o_{TF} is the standard free energy of formation of TF gas [54].

Eq.2.11 $$\Delta\bar{G}_{F_2} \equiv RTln\left(p_{F_2}\right)$$

Eq.2.12 $$\Delta\bar{G}_{F_2} = 2RTln\left(p_{TF}/\sqrt{p_{T_2}}\right) + 2\Delta G^0_{TF}$$

The fluorine potential is set by the initial salt purification procedure and by chemical adjustments made during reactor operation. The upper bound for fluorine potential can be considered as the most oxidizing step during the purification process, typically where a gas sparge of 1:10 HF:H_2 is used which results in a $\Delta\bar{G}_{F2}$ of -590 kJ/mol F_2 according to equation 2.12 [54]. Chemical purification steps after the HF:H_2 sparge, such as pure H_2 sparging or beryllium additions will move the salt to a more reducing state [56]. After the final purification steps, salt chemistry will still be monitored and controlled during reactor operation. For the MSRE, it was determined that maintaining a 100:1 ratio of UF_4 to UF_3 in the fuel salt would result in sufficiently reducing conditions to prevent corrosion [57]. Instead of TF or T_2 partial pressures, the redox potential in this case is set by the activities of UF_4 and UF_3 in the salt (a_{UF4} and a_{UF3}), as shown in equation 2.13. The ΔG^o_{34} term refers to the standard free energy change of the UF_3 reaction with F_2 gas to produce UF_4 [54]. According to equation 2.13, the fluorine potential corresponding to a 100:1 UF_4 to UF_3 condition is -700.5 kJ/mol F_2 at 650°C [3].

Eq.2.13 $$\Delta\bar{G}_{F_2} = 2RTln\left(a_{UF_4}/a_{UF_3}\right) + 2\Delta G^0_{34}$$

For Flibe salts without uranium, a practical lower limit for fluorine potential is when Flibe is fully reduced and in chemical equilibrium with beryllium metal, which occurs at -902.5 kJ/mol F_2 [54]. The fluorine potential calculation for control by beryllium is shown in equation 2.14, which depends only on the activity of beryllium fluoride in the salt since the beryllium metal is assumed to have an activity of 1 [54]. Tritium fluoride to T_2 ratios are plotted in Figure 2.3 for a T_2 partial pressure of 1 atmosphere along with the three redox conditions described previously. Figure 2.3 shows a significant variation in tritium speciation between TF and T_2 over the range of FHR redox potentials.

Eq.2.14 $$\Delta\bar{G}_{F_2} = 2RTln\left(a_{BeF_2}\right) + \Delta G^0_{BeF_2}$$

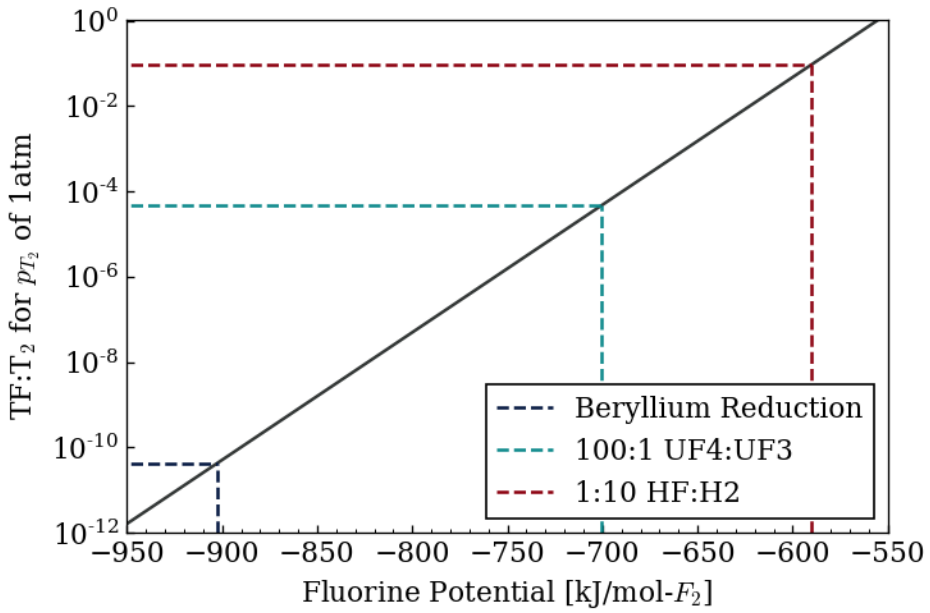

Figure 2.3. TF to T_2 ratios for a T_2 partial pressure of 1 atm calculated for various redox potentials. Dotted lines show the FHR lower bound at full Be reduction, upper bound from purification, and MSRE target redox potential [43, 54].

In practice, it is difficult to observe partial pressure of free fluorine in molten salt and electrochemical measurements are used to characterize redox potential instead. Fluorine potential can be converted into a voltage according to equation 2.15 below, where E_{salt} is the redox potential of the salt, F is Faraday's constant and E^{o}_{F2} is the standard potential for reduction of F_2 gas [56]. Standard electrode potentials for several half-cell reactions in Flibe have been tabulated by Baes [53], and are plotted as a function of temperature in Figure 2.4. The reaction potentials are defined in reference to $HF|H_2$ = 0 volts [53]. As discussed previously, the lowest feasible redox potential in Flibe would be where beryllium is used as a reducing agent, and all other electroactive species in the salts are reduced to the point where the redox potential is set by the $Be|BeF_2$ reaction. If a stronger reducing agent were used, then beryllium fluoride would also be reduced and the composition of the coolant would change. Without any redox control, corrosion of structural alloys will occur and corrosion products will exist as metal fluoride impurities in the salt. Since chromium forms the most stable fluoride of common alloying elements [58], chromium fluoride will preferentially leech into the salt and thereby control the redox potential according to $Cr|CrF_2$. Therefore, a redox potential window in the salt can be defined as the region below the $Cr|CrF_2$ voltage and above the $Be|BeF_2$ reaction [3].

Eq.2.15

$$E_{salt} = \frac{\Delta \bar{G}_{F_2}}{2F} + E^o_{F_2}$$

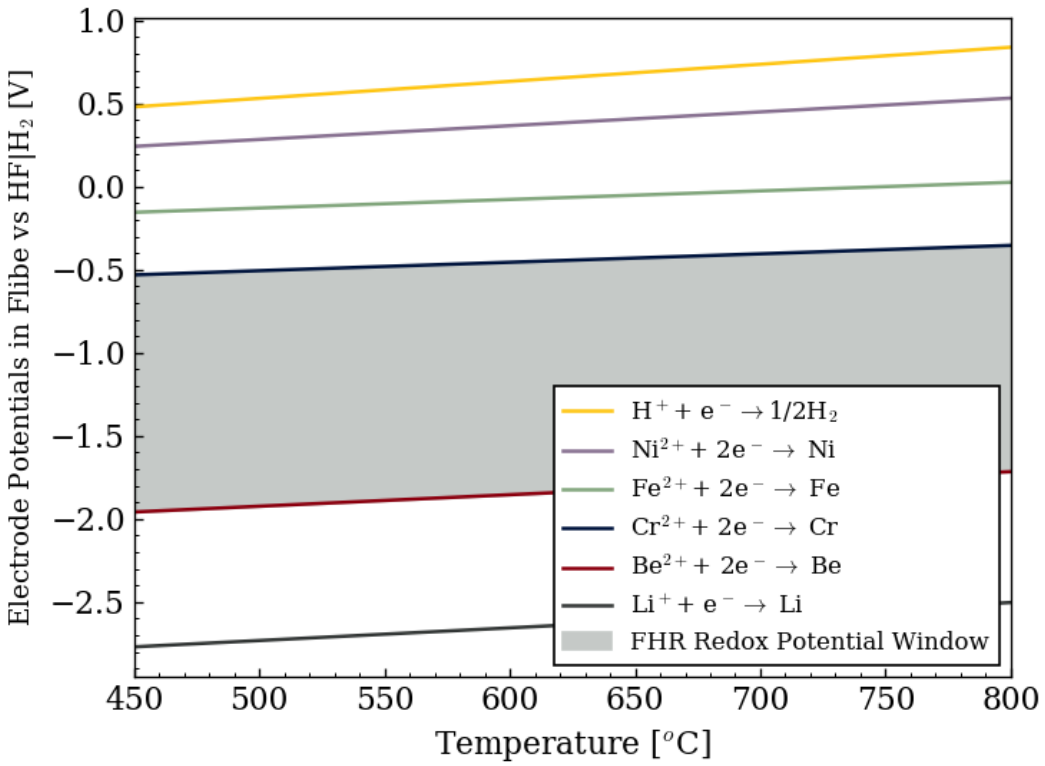

Figure 2.4. Electrode potentials vs. $HF|H_2$ for relevant half-cell reactions in Flibe. The FHR redox potential window refers to the salt potential range in which the reactor could operate [3].

Examples of redox potential measurements in molten fluoride systems help demonstrate what chemical conditions can be expected in future reactors. In the MSRE, the redox potential was assessed by electrochemically monitoring the UF_4:UF_3 ratio in the salt periodically [59]. The UF_4:UF_3 measurements over the reactor's operating history are shown in Figure 2.5 [57, 60]. There was a gradual oxidation occurring over time since the average stable valence state of fission products was slightly less than that of uranium fluoride in the salt [57], and therefore free fluorine was continuously liberated. The sharp decreases in UF_4:UF_3 occurred when beryllium metal was added to the primary salt to control chemical potential [57]. As shown in Figure 2.5, the MSRE was above the target ratio of 100:1 UF_4:UF_3 for roughly the first half of the period where potential was actively monitored.

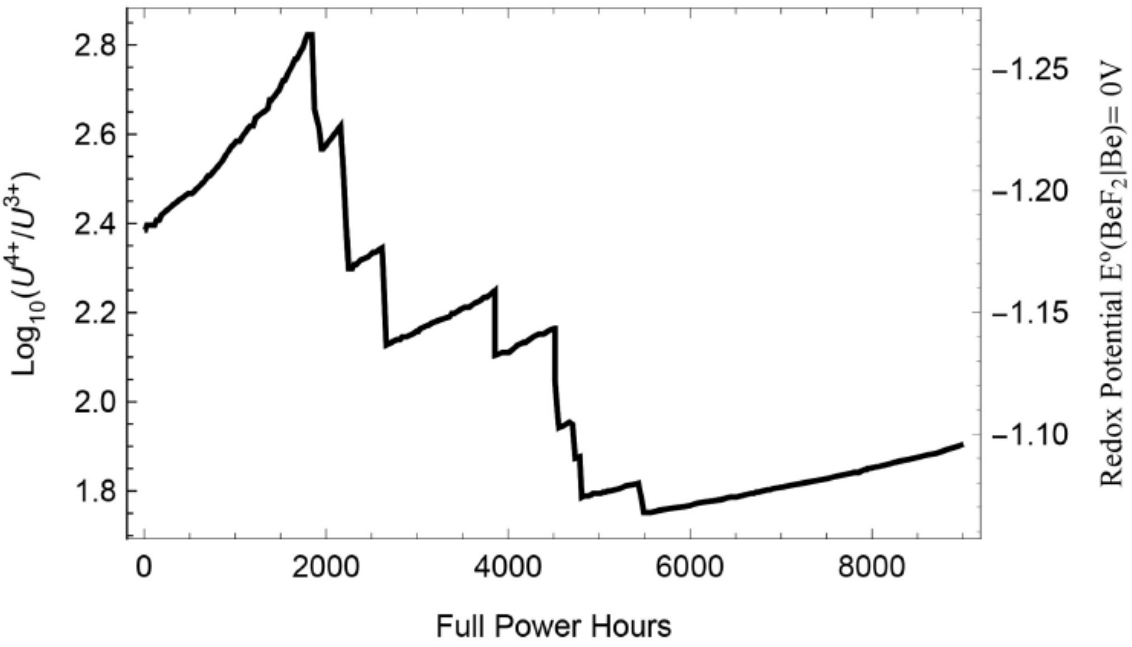

Figure 2.5. Measured UF4 to UF3 ratio in the primary salt during operation of the MSRE. Data compiled and converted in [60], and sourced from [57].

For coolant salts without uranium, a reference voltage signal can be created from the reduction of beryllium in the salt itself [56, 61, 62]. In this case, the redox potential of the salt can be calculated from difference of the standard potential of the beryllium reference reaction, $E^{o}_{Be|BeF2}$, and the measured voltage, E_{cell}, as shown in equation 2.16. Redox potential from three beryllium-referenced experiments are plotted with the standard electrode potentials of H^{+}, Ni, Fe, Cr, Be, and Li in Figure 2.6. The point at 500ºC refers to the measured redox potential of purified Flibe produced at the University of Wisconsin – Madison (UW) [56]. The next measurement at 600ºC was of Flinabe salt (15%LiF-58%NaF-27%BeF_2) in a thermal convection loop [61]. Lastly, the 650ºC point references measurements taken in another thermal convention loop with Flibe salt produced at ORNL [62]. Figure 2.6 also shows the MSRE operating redox range based on the highest and lowest values of UF_4:UF_3 in Figure 2.5. In all three experiments, the measured redox potentials are closer to Cr|CrF_2 than to Be|BeF_2. For the UW, ORNL, and MSRE salts, beryllium was also added to the salt in order to reduce the potential. Therefore, unless an aggressive reduction strategy is enforced in a reactor, the redox potential is likely to be elevated from corrosion products or other impurities in the salt. While these redox potentials may be acceptable for corrosion control, any significant deviations need to be accounted for in order to correctly predict tritium speciation.

Eq.2.16 $$E_{salt} = E^{o}_{Be|BeF_2} - E_{cell}$$

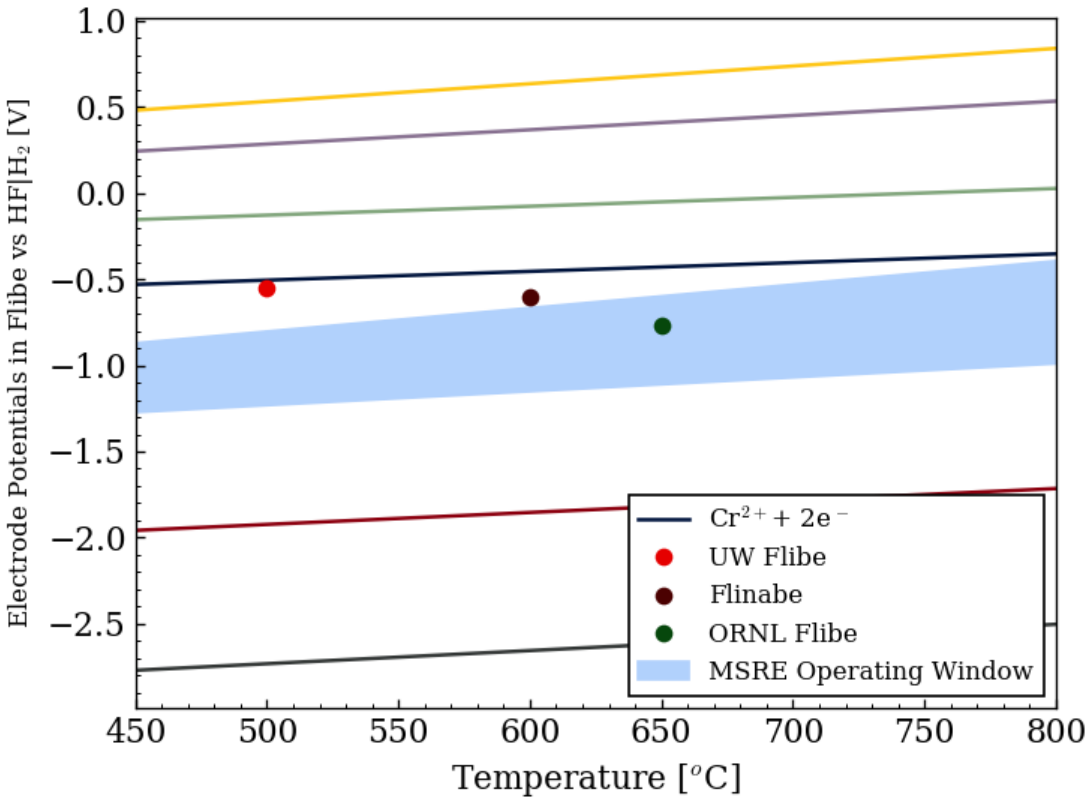

Figure 2.6. Electrode potentials from Figure 2.4 along with measured salt redox potential from three experiments and the observed upper and lower limits of the MSRE [56, 57, 61, 62]

2.2.2. Kinetic Factors in Tritium Speciation

The calculation for tritium speciation based on fluorine potential provides a simple way to determine the relative amounts of TF and T_2 in Flibe for a given chemical condition. However, a clear disadvantage is that the results are only valid for a chemical equilibrium in the salt, whereas tritium will be born far from the equilibrium condition if generated as TF. While chemical control systems will be implemented in a FHR set a reducing redox potential [5], if the time required for tritium to reach a reducing chemical equilibrium potential is similar to or less than the average residence time of tritium in the FHR primary loop, then there will be significantly higher concentrations of TF in the salt than that predicted by the fluorine potential model. This process is demonstrated in the irradiation experiments by Suzuki et al, where roughly 200g of Flibe was irradiated in the IntrexFlibe facility of the YAYOI fast neutron source reactor, shown in Figure 2.7 [44]. Tritium generated in the salt crucible had an average residence time on the order of hours

before evolving to the sweep gas, which was continuously monitored for tritium activity [63]. When beryllium metal with a surface area of roughly 20 cm^2 was added to the salt, there was still over 90% of tritium released from the salt as TF. As shown in Figure 2.7, the pure helium sweep gas with beryllium addition had a similar ability to convert TF to HT/T_2 as the sweep gas stream with 0.01%H_2 [64]. The authors speculate that the reaction of TF with beryllium was only able to occur at the surface of the added beryllium metal. Therefore, the transport of TF to the salt surface and evolution out of the salt was overall more likely than transport to, and reaction with, the beryllium metal.

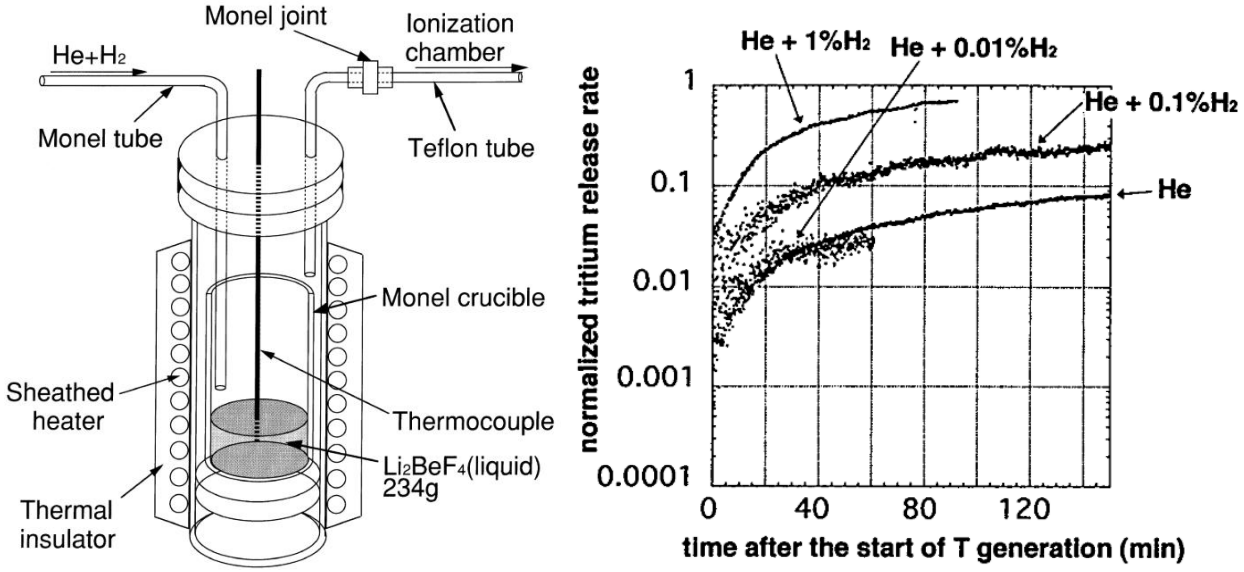

Figure 2.7. Experimental layout for tritium generation and sampling in the IntrexFlibe facility (left) [44]. Normalized release of non-condensable tritium (HT/T_2) during the irradiations in the case of helium with varying H_2 partial pressure [64]. Beryllium metal was added to the salt in the run which used pure helium (labeled He).

Other studies show that the dissolution of beryllium metal into Flibe is possible, which would then allow for TF reduction throughout the salt volume instead of only at the surface of added beryllium metal particles. The saturated concentration of Be^0 in Flibe was estimated to be 21 mol/m^3 based on immersion of a beryllium rod for 210 hours at 803K [65]. Beryllium dissolution can also be qualitatively observed in Figure 2.8, where Be metal flakes transitioned from discrete particles to liquid pools after several hours at 600ºC [60]. However, even when dissolution occurs, kinetic effects in reactions with beryllium are still observed. The reduction of tritium fluoride into T_2 by beryllium metal is shown in equation 2.17. Fukada et al were able to

calculate the reaction rate constant by monitoring the HF concentration in an off-gas stream after bubbling He+H_2+HF through Flibe during and after the immersion of a beryllium rod [66]. The beryllium dissolution was correlated with the immersion time beforehand so the Be^0 concentration could be predicted during the HF tests. Their results show a reaction rate constant, k_{BeF2}^*, of $1.5 \cdot 10^6$ mol/m^3-s as defined in equation 2.18. Since the product BeF_2 is significantly more stable than the reactant HF [66], the rate of the reverse reaction is neglected and the overall reaction depends only on the forward rate constant and the salt molar fractions of Be and HF, x_{Be} and x_{HF}, respectively.

Eq. 2.17 $$2TF + Be \rightarrow T_2 + BeF_2$$

Eq. 2.18 $$R_{HF \rightarrow H_2} = k^*_{BeF_2} x_{Be} x_{HF}$$

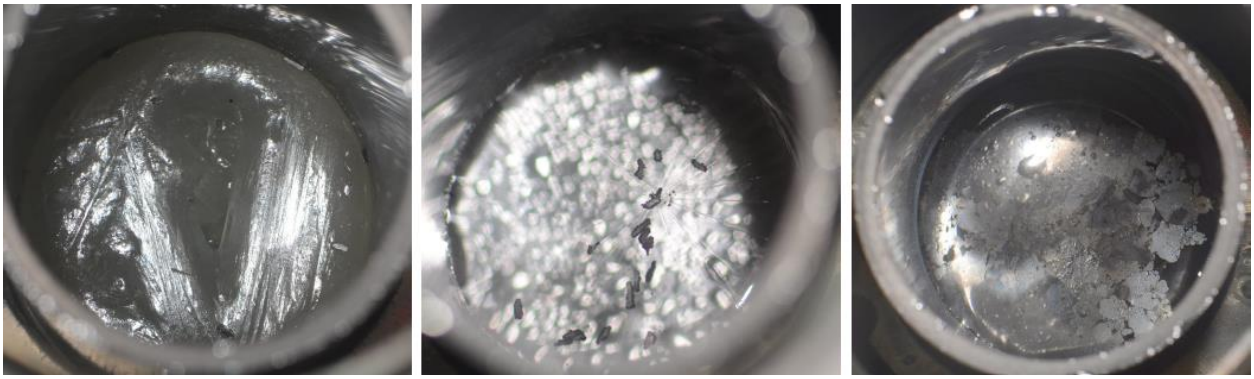

Figure 2.8. 60g of frozen Flibe in a glassy carbon crucible (left). Beryllium metal flakes with a 5mg total mass suspended by surface tension on the molten Flibe surface at 500ºC (center). Dissolution of flakes observed after 330 minutes at 600ºC (right). From [56, 60].

Reaction with added beryllium is just one way in which tritium chemical forms can be altered in Flibe. Because of the oxidizing nature of TF, the nickel, iron, and chromium in structural alloys can also be converted to metal fluorides. However, the oxidation of carbon to carbon tetrafluoride by HF is still not an energetically favorable reaction [53]. The oxidation of a generic metal 'M' by TF to produce T_2 is shown in equation 2.19. Equation 2.19 is balanced with 2 TF molecules since the dominant valence state of Ni, Fe, and Cr in Flibe is +2 [2]. If TF and HF impurities are both present in the salt, then equation 2.20 could occur and produce HT as a product instead of T_2. Any HF impurities will also convert to hydrogen through equation 2.21 below. However, additional HF can be created if moisture ingress occurs in the FHR primary loop systems, particularly through the reaction of beryllium fluoride to beryllium oxide [67]. These chemical reaction pathways for tritium conversion are illustrated in Figure 2.9.

Eq. 2.19 $$2TF + M \rightarrow T_2 + MF_2$$ *Rxn. 1*

Eq. 2.20 $$TF + HF + M \rightarrow HT + MF_2$$ *Rxn. 2*

Eq. 2.21 $$2HF + M \rightarrow H_2 + MF_2$$ *Rxn. 3*

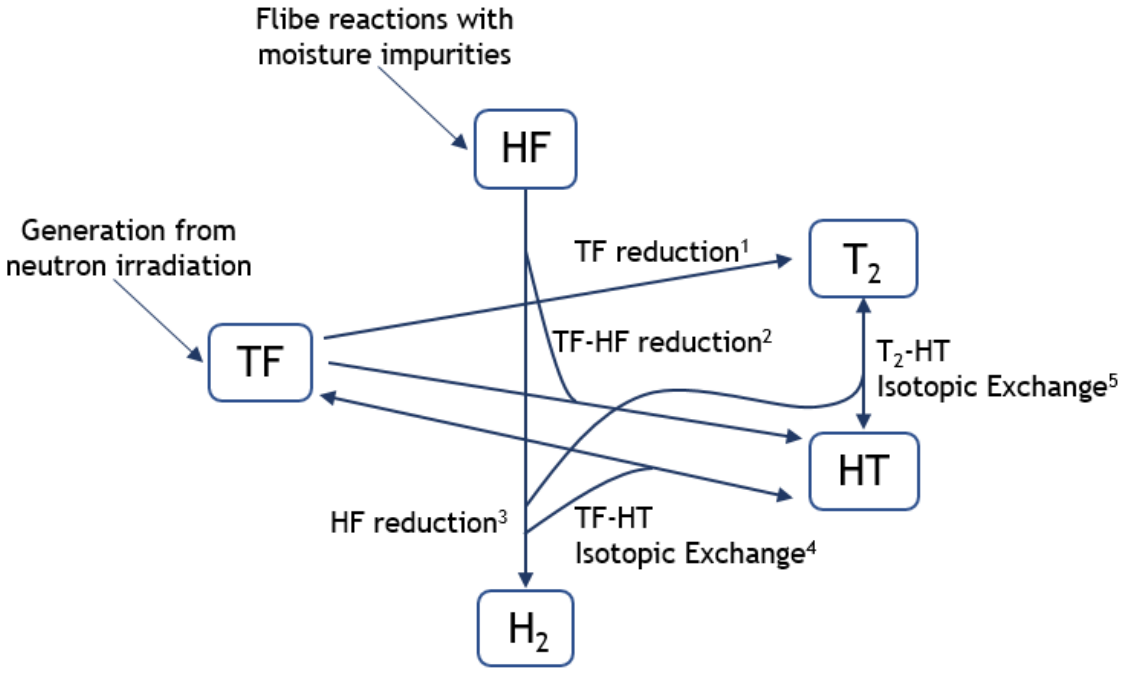

Figure 2.9. Conceptual network of pathways in which tritium chemical forms TF, T2 and HT can be altered in Flibe salt.

Predicting the chemical form of tritium in Flibe is further complicated by isotopic exchange reactions if H_2 is present – isotopic exchange reactions are noted with the superscripts 4 and 5 in Figure 2.9. The Suzuki et al Flibe irradiations clearly demonstrate that H_2 gas can convert TF in the salt to HT through the reaction in equation 2.22 [44, 48]. Through varying the H_2 pressure and fitting HT release data to a kinetic model, the reaction rate constant for the isotopic exchange reaction, k_{IE}, was estimated to be 100 m^3/mol-s [47]. The rate of isotopic exchange in units of mol/m^3-s can be calculated as shown in equation 2.23, where the bracketed species refers to a concentration in mol/m^3. To simplify the reaction model, it was assumed that both the forward and reverse isotopic exchange reactions have the same rate constant [47]. Lastly, isotopic exchange can mix a portion of T_2 and H_2 gases into HT [68]. Partial pressures of HT, H_2, and T_2 in a gas mixture can be determined based on equation 2.25 and the equilibrium constant for the reaction, K_{HT}, measured by Jones et al [69]. The influence of each species in hydrogen-tritium systems is important to consider for calculations of permeation and solubility in materials [45].

Eq. 2.22 $$TF + H_2 \leftrightarrow HT + HF$$ *Rxn. 4*

Eq. 2.23 $$R_{IE} = k_{IE}[TF][H_2] - k_{IE}[HT][HF]$$

Eq. 2.24 $$T_2 + H_2 \leftrightarrow 2HT$$ *Rxn. 5*

Eq. 2.25 $$(p_{HT})^2 = p_{H_2} p_{T_2} K_{HT}$$

Interrelationships between hydrogen and tritium-containing chemical species shown in Figure 2.9 create a significant challenge towards the implementation and validation of a kinetic speciation model. In certain scenarios, reaction pathways become one-directional and some species can be neglected. For example, if the FHR were flooded with excess H_2 to produce dissolved H_2 gas in the salt, then the reactions in equations 2.22 and 2.24 would become heavily product favored and HT would be the dominant form of tritium in Flibe. However, hydrogen injection may not be desirable because it will increase the fraction of tritium released by permeation [48], and potentially cause embrittlement of structural metals [70]. If no hydrogen is added, it is still difficult to neglect completely due to the production of H_2 from corrosion of HF impurities. Therefore, due to the lack of information on the concentration and production of the species listed in Figure 2.9 as well as the limited information on the kinetics of some reaction pathways, the equilibrium calculation based on redox potential is used for the modeling tritium transport results in this work. If the equilibrium method is later found to be inadequate, then a model which explicitly tracks the TF, HF, H_2, T_2, and HT in the salt should be investigated.

2.3. Tritium Transport in Molten Fluoride Salt

2.3.1. Transport in Static Flibe

One important implication of tritium speciation is the difference in transport properties of TF and T_2 in Flibe. Properties such as tritium diffusivity and solubility in Flibe govern the concentration, mobility, and release path of tritium from the salt, which ultimately can influence the optimal tritium management strategy for the reactor. Unfortunately, large discrepancies have been reported in literature for relevant transport data in Flibe as well as other fluoride salts. The results and interpretations from a set of experimental measurements are discussed in this section.

An apparatus for the direct measurement of gas solubility in molten salt is shown in Figure 2.10. Key components of the system are the saturator vessel, transfer tube, and stripping section. In the saturator section, gases are bubbled through the salt to ensure sufficient mixing and uptake

of the gas into solution. For the measurement of H_2 solubility in salt, a 2 hour vigorous bubbling period followed by 2 hours of slight overpressure caused sufficient saturation of Flibe [71]. After saturation, the salt is moved through the transfer tube to the stripping section. Salt in the transfer tube is quickly frozen after the transfer in order to isolate the stripping section from the saturator. Therefore, the gas released from the salt in the stripping section can be used to calculate the solubility if the amount of salt in the stripping vessel is known [71]. A similar setup was also used for measurement of HF solubility in Flibe [72].

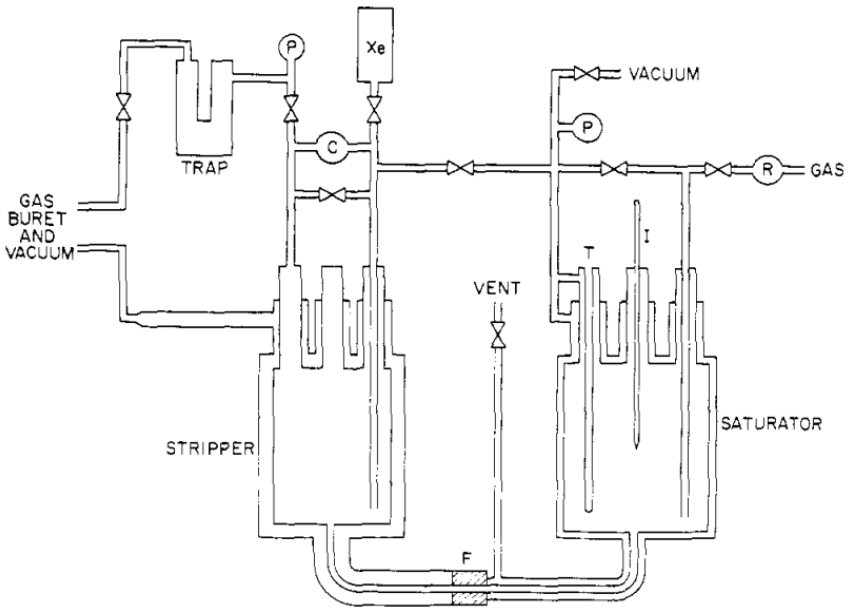

Figure 2.10. Experimental system for measuring gas solubility in molten salts consisting of a saturation section, stripping section, and transfer tube with a freeze valve [71].

Results from the solubility studies show that the concentration of hydrogen and hydrogen fluoride in molten Flibe is proportional to the partial pressure of charging gas above the salt [71, 72]. An example of results from the saturation and stripping apparatus are shown in Figure 2.11 for hydrogen and helium in Flibe [71]. A linear relationship between dissolved gas concentration and pressure is defined as Henry's law [73], which is shown in equations 2.26 and 2.27 for HF and H_2. In equation 2.26 with HF, for example, c_{HF} is the dissolved concentration of HF in mol-HF/m^3-salt, p_{HF} is the partial pressure in Pa, and thus the $K_{H,HF}$ is the slope of the concentration-pressure line in mol/m^3-Pa. The slope K_H is referred to as the Henry's law constant or just the solubility, which depends on the particular gas species as well as temperature. However, since HF and H_2 are dissolved as gases in the salt, the meaning of solubility via Henry's law has a very different interpretation than the solubility of a dissolved solid, for example.

Eq.2.26 $$c_{HF} = K_{H,HF} p_{HF}$$

Eq.2.27 $$c_{H_2} = K_{H,H_2} p_{H_2}$$

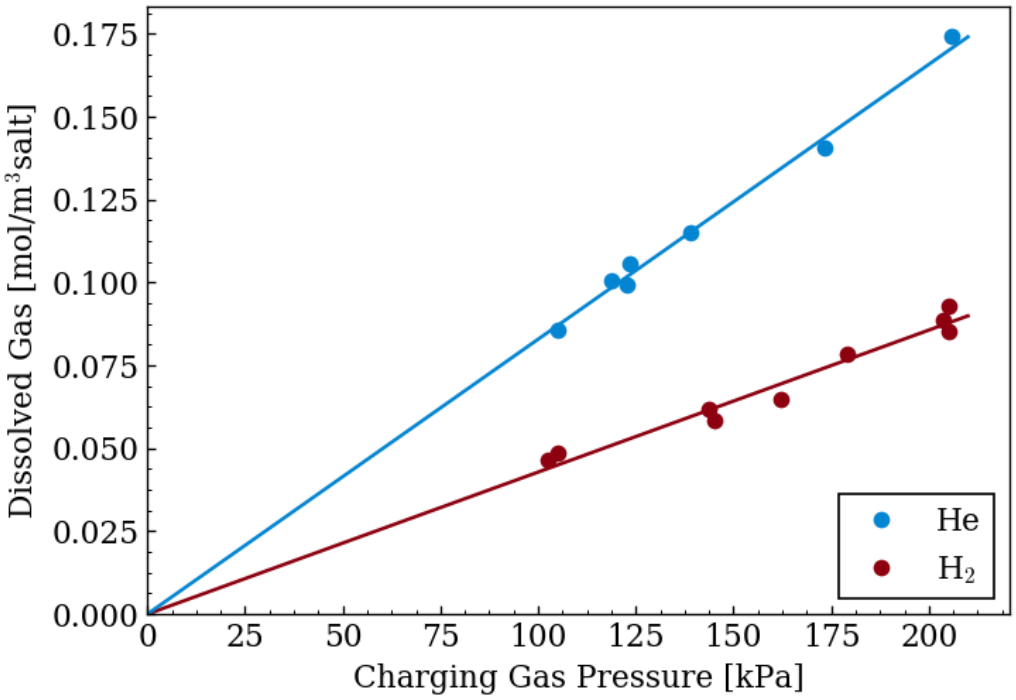

Figure 2.11. Dissolved gas concentration in Flibe verses partial pressure of the charging gas. Slope of linear fits results in Henry's law coefficients of $8.29 \cdot 10^{-7}$ and $4.28 \cdot 10^{-7}$ mol/m^3-Pa for helium and hydrogen, respectively [71].

Permeability and diffusivity are other properties which can be measured in a static salt experiment. A common technique involves creating an approximately one-dimensional salt geometry where an analytical solution to the diffusion equation can be obtained. One example of a typical apparatus is shown below in Figure 2.12, as used by Fukada et al and Calderoni et al. [74, 75]. In this system, the hydrogen isotope of interest is concentrated to a desired partial pressure in the gas space under the salt. A thin nickel permeation barrier separates the gas mixture and the salt, while the walls of the container are made of stainless steel. It is assumed that the thin nickel barrier provides a negligible permeation resistance, while the stainless steel is a very strong barrier. Therefore, the steady state flux of tritium through the salt depends only on the salt thickness (L_{Salt}), salt hydrogen permeability (Φ_{Salt}), and hydrogen differential pressure, as shown in equation 2.28. The salt permeability is a quantity defined as the product of the diffusivity of solubility of a species in the salt, which is shown for H_2 in equation 2.29.

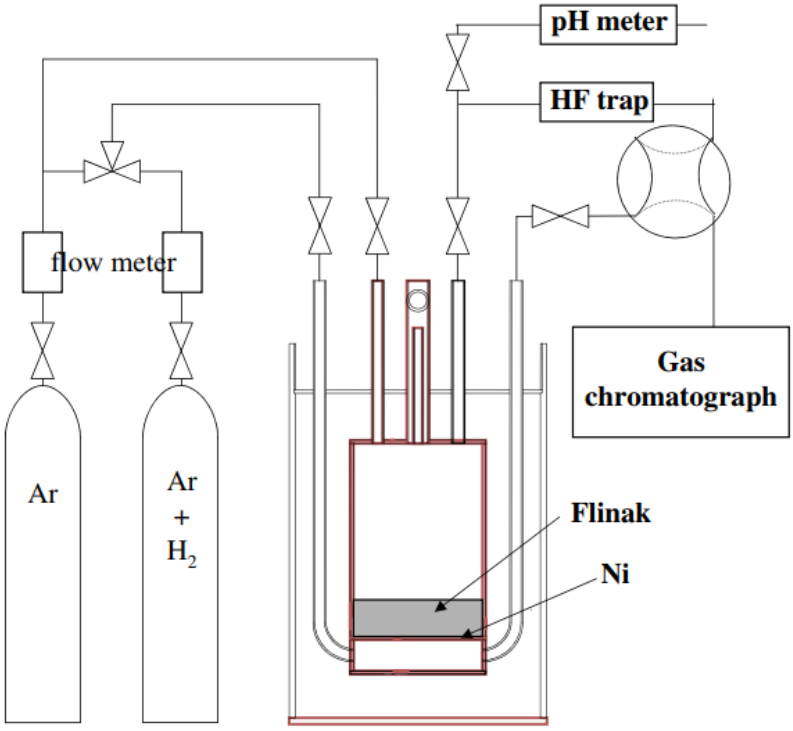

Figure 2.12. An experimental system used to measure permeability, diffusivity and solubility of hydrogen in Flinak salt. From [74].

Eq.2.28 $$j_{H_2,Steady} = \frac{\Phi_{Salt}}{L_{Salt}}\left(p_{H_2,Up} - p_{H_2,Down}\right)$$

Eq.2.29 $$\Phi_{Salt} = D_{H_2} K_{H,H_2}$$

Once the permeability is measured from the steady state flux, the diffusivity can be obtained by monitoring the time-dependent permeation rate through the salt. In the apparatus shown in Figure 2.12, the downstream permeation section is continuously swept by an inert off-gas which carries away the diffusing hydrogen. Therefore, it can be assumed that the partial pressure and concentration of hydrogen at the salt-gas downstream interface is zero ($p_{H2,Down} \approx 0$) [75]. If there is indeed no permeation resistance added by the nickel permeation membrane, then the input H_2 partial pressure on the upstream section of the membrane is equal to the partial pressure at the salt-nickel interface. In this case, the upstream boundary condition for hydrogen concentration in the salt would be set by the gas partial pressure and Henry's law in the salt. The time-dependent concentration profile of H_2 in the salt can be solved according to Fick's second law of diffusion along with the boundary conditions shown in equation 2.30 [75]. The one-

dimensional analytical solution for time-dependent H_2 flux, $j_{H2}(t)$, through the downstream surface of salt slab with length L is shown in equation 2.31 [74]. An example of permeation data and an analytical data fit is shown in Figure 2.13 for H_2 diffusion through Flinak salt. The steady state flux was also observed to follow a linear relationship to the charging pressure, as predicted by equation 2.28 [74]. When both the permeability and diffusivity have been determined, the solubility can also be calculated for each experiment through equation 2.29.

Eq.2.30 $$\frac{\partial c_{H_2}}{\partial t} = D\frac{\partial^2 c_{H_2}}{\partial x^2} \;\; ; \;\; c_{H_2}^{x=0} = K_{H,H_2} p_{H_2,Up} \;\; ; \;\; c_{H_2}^{x=L} = 0$$

Eq.2.31 $$j_{H_2}(t) = 2L\Phi_{Salt} p_{H_2,Up}\sqrt{\frac{L^2}{\pi D_{H_2} t}}\sum_{n=1}^{\infty}\left(-\frac{(2n-1)^2 L^2}{4D_{H_2} t}\right)$$

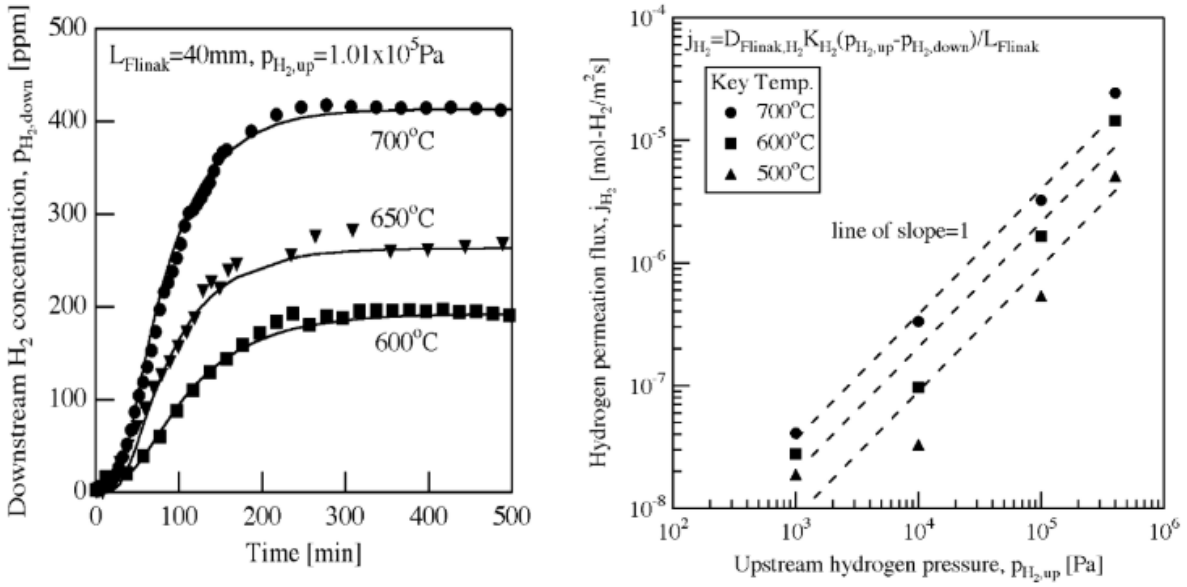

Figure 2.13 Hydrogen permeation through a 4cm ingot of molten Flinak at various temperatures (left). The steady state permeation flux was linearly proportional with the H_2 charging pressure over multiple orders of magnitude (right) [66].

Measurements for the diffusivity of hydrogen isotopes in fluoride salts are compiled and shown in Figure 2.14. Since the results involve measurements with tritium as well as hydrogen and deuterium, the diffusivity values are scaled to represent the isotopic effects of tritium. In contrast, there is assumed to be a negligible isotopic effect on the solubility of hydrogen and tritium in various materials [76]. For diffusion occurring as a pure random walk, diffusivities of isotopes would scale in an inverse square root ratio of masses according to Graham's law [4], as shown for

T_2 and H_2 in equation 2.32. Using the inverse square root mass ratio is a good approximation at higher temperatures, but is known to significantly deviate from true behavior at room temperature or below [76]. Results in Figure 2.14 also vary based on the method for hydrogen isotope introduction into the salt. The results from Fukada, Calderoni, and Zeng use the setup shown in Figure 2.12 with hydrogen introduction through permeation membrane [74, 75, 77]. The Nakamura and Anderl studies also introduced hydrogen through permeation, but Nakamura et al used a concentric tube within a salt annulus and Anderl et al used a nickel probe [78, 79]. Two evaluations of TF diffusivity in Flibe are also provided for comparison – TF introduced from neutron irradiation of frozen Flibe by Oishi et al and atomistic simulation of TF in Flibe by Lam [80, 81].

Eq. 2.32
$$\frac{D_{T_2}}{D_{H_2}} = \sqrt{\frac{m_{H_2}}{m_{T_2}}}$$

Table 2.5. Compiled diffusivity measurements for T_2 in Flibe. All values are converted to tritium diffusivities with equation 2.32.

Data Source	T_2 Diffusivity [m^2/s]	D_{T2} at 600°C [m^2/s]	Ref.
Calderoni et al	9.3e-7 exp(-42/RT)	2.86e-9	[75]
Lam	9.349e-7 exp(-40/RT)	3.78e-9	[81]
Nakamura et al	$(2/6)^{1/2}$ 2.09e-8 exp(-28/RT)	5.20e-10	[78]
Anderl et al	--	6.53e-10	[79]

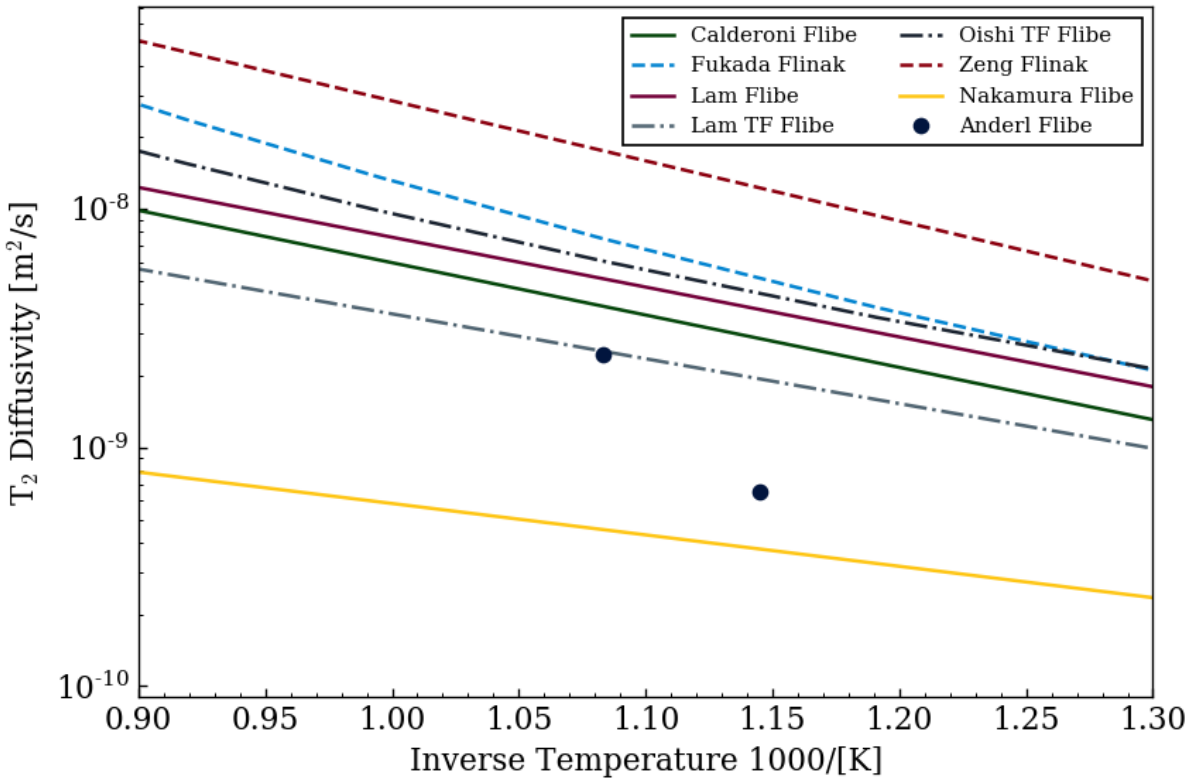

Figure 2.14. Compiled diffusivities – solid lines represent measurements in Flibe while the dashed lines were in Flinak [74, 75, 77, 78, 79]. Two TF diffusivities are provided for reference with dash-dot lines [80, 81].

Due to its position near the center of several measurements, the diffusivity provided by Calderoni et al has been considered as the baseline T_2 diffusivity in Flibe for previous tritium transport modeling efforts [3]. While the Calderoni experiment has several benefits, such as the use of Flibe instead of Flinak and T_2 instead of H_2/D_2, one issue was that the equilibrium permeation rate varied according to the square root of input T_2 pressure [75]. A square root dependence would indicate a process where hydrogen is dissociating and diffusion is not occurring as a H_2 diatomic molecule. One possible explanation is interference caused by the nickel permeation membrane. Hydrogen first needs to dissociate into monatomic H in order to permeate through metals, but can also recombine into H_2 at the downstream permeation surface [76]. If a square root dependence with pressure is observed instead of a linear dependence, then either the tritium source was not recombining into T_2 at the salt-nickel interface, or the nickel permeation window was actually the dominant permeation resistance and governed the pressure dependence of the experiment. It is not likely that the nickel membrane was a significant source of permeation

resistance, since Caleroni et al state that their permeation cell was provided by Professor Fukada, and in the Fukada et al study permeation results were equivalent with H_2 charging above the salt along with charging below the permeation membrane [74]. In contrast, Zeng at all measured a significant decrease in permeation rate for hydrogen charged under a permeation membrane and sampled in sweep gas above the salt [77].

Because of the square root dependence of permeation flux with T_2 partial pressure. Calderoni et al postulate that the tritium may have been diffusing as T^+ ions bonded to BeF_4^{2-} complexes [75]. Another possibility is that the 5 vol% H_2 in the sweep gas converted all tritium to HT in the salt, and therefore the diffusion appeared to occur in a dissociative process. In this case, the steady state permeation flux can be written for HT as in equation 2.33 below. Assuming an isotopic exchange equilibrium between H_2 and T_2, the partial pressure of HT in the salt can be written in terms of known variables by substituting in equation 2.25. As shown on the right of equation 2.33, the permeation flux of HT follows the square root of T_2 charging pressure after isotopic exchange is considered.

Eq.2.33
$$j_{HT} = \frac{D_{HT} K_{H,H_2}}{L} p_{HT,Up} = \frac{D_{HT} K_{H,H_2}}{L} \sqrt{p_{H_2} p_{T_2} K_{HT}}$$

Discrepancies between the intended and actual chemical forms of tritium in Flibe are one source of uncertainty in the diffusivity measurements discussed previously. Direct measurements of solubility are shown in Figure 2.15 for HF and H_2 based on the saturation and stripping technique [72, 82]. The solubility of HF is roughly two orders of magnitude higher than H_2, and both values change in a similar magnitude with temperature but in different directions. Here, the exponential fits of the Henry's law coefficients provided by Stempien are used [3]. The other solubility values in Figure 2.15 come from indirect measurements through permeation experiments. Since, the solubility measured by permeation was closer to the HF direct measurement than H_2, researchers suggested that H_2 was actually diffusing in the Flibe as T^+ [75, 79]. As previously discussed, the influence of H_2 present could have influenced the Calderoni et al T_2 solubility measurement. In Figure 2.15, a line is shown that attempts to correct the solubility measurement based on the missing factors in equation 2.33. The solubility of T_2 was converted to a solubility of HT by dividing the original values by the square root of the product $p_{H2}\, p_{T2}\, K_{HT}$. Assuming the sweep gas was at atmospheric pressure, the partial pressure of H_2 at 5 vol% would be 5,066 Pa.

The partial pressure of tritium varied in the experiments, but only the average pressure of roughly 550 Pa was used for the p_{T2} factor [75]. Values for K_{HT} are also readily available in literature [45]. After adjusting for the presence of H_2, the solubility for HT from the Calderoni experiment (labeled 'Calderoni Adjusted' in Figure 2.15) is less than the solubility from the direct measurement in Flibe. The solubilities are shown in Table 2.6 along with computed results at 600ºC. Since there is assumed to be a negligible isotopic effect in solubility [76], the values in Table 2.6 are listed as T_2 solubilities for simplicity. Overall, there is a higher spread observed in the solubility measurements compared to diffusivity of T_2 in Flibe.

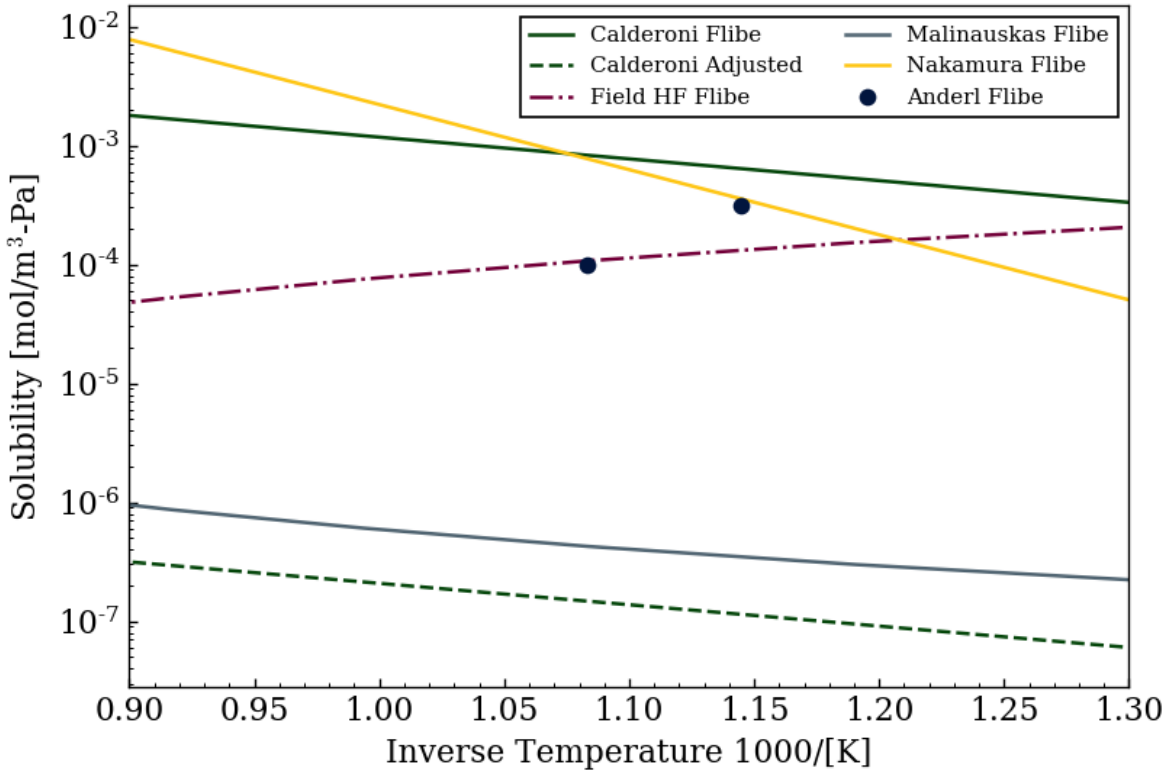

Figure 2.15. Compiled Henry's law coefficients for solubility of hydrogen isotopes in Flibe [75, 78, 79, 82]. A direct measurement of HF solubility in Flibe is shown with a dot-dash line [72].

Table 2.6. Solubility data for hydrogen isotopes in Flibe and calculated vales at 600ºC.

Data Source	T_2 Solubility [mol/m³-Pa]	$K_{H,T2}$ at 600ºC	Ref.
Calderoni et al	7.9e-2 exp(-35/RT)	6.37e-4	[75]
Malinauskas et al '74	2.714e-8exp(4.235e-3(T-273.15))	3.44e-7	[82, 3]
Malinauskas et al '72	--	4.28e-7	[71]
Nakamura et al	6.57e2 exp(-104.8/RT)	3.53e-4	[78]
Anderl et al	--	3.1e-4	[79]

2.3.2. Transport in Flowing Flibe

While diffusion governs the transport of tritium in static Flibe, the flow of bulk fluid also has a significant role in the tritium distribution of a FHR. The influence of advective verses diffusive transport of tritium can be examined through the Schmidt number (Sc), as defined in equation 2.34 for T_2 where μ and ρ are the viscosity and density of Flibe, respectively. A Schmidt number is conceptually similar to a Prandtl number, but in regards to mass transfer instead of heat transfer [3]. Since Flibe at FHR temperatures will have Schmidt numbers of 800 or above [5], the transport of tritium through fluid motion is actually the dominant mechanism for mass transfer in FHR systems.

Eq.2.34 $$Sc = \mu/(\rho D_{T_2})$$

The influence of fluid flow on mass transfer can be represented through the use of a mass transfer coefficient. A coefficient with units of meters per second can be defined based on the fluid's Sherwood number (Eq. 2.36), species diffusivity, and characteristic length, as shown in equation 2.35 [83]. Since the diffusivity of T_2 in Flibe is an input, the calculated mass transfer coefficient is specific to T_2 in the salt – there would be a separate mass transfer coefficient for TF, for example. The characteristic length, d, in a FHR would either be the pebble diameter in the core, diameter of tubing in the hot leg, cold leg, or heat exchanger, or hydraulic diameter of the downcomer annulus.

Eq.2.35 $$k_{T_2} = ShD_{T_2}/d$$

The Sherwood number, Sh, is a dimensionless parameter which can be thought of as the mass transfer analogy to the Nusselt number [3]. Sherwood numbers can be measured directly in mass transfer experiments in order to create correlations with other dimensionless numbers. For example, the mass transfer coefficient in a packed bed of spheres was studied by Wilson and Geankoplis by examining the dissolution of benzoic acid spheres in distilled water and a propylene glycol-water solution [84]. By varying the temperature as well as the fluid composition, a wide range of Schmidt numbers could be examined. Their results show that the Sherwood number depends on the Schmidt number, bed porosity, ε, and Reynolds number, Re, as shown in equation 2.36. The Reynolds number for a spherical bed is calculated with equation 2.37, where $\dot{V}$ is the volumetric flow of fluid through the bed, d is the diameter of spheres, and A_{CX} is the total cross sectional area (area of total flow if no spheres were present) [84]. Note that the definition of

Reynolds number in a packed bed can vary, so equation 2.37 adopts the notation of Wilson and Geankoplis and is denoted Re'. The correlation in equation 2.36 is valid for 55<Re'<1500 and 165<Sc<10690 [85].

Eq. 2.36 $$Sh = \frac{0.25}{\epsilon} Re'^{0.69} Sc^{1/3}$$

Eq. 2.37 $$Re' = \frac{\rho \dot{V} d}{\mu A_{CX}}$$

When a mass transfer correlation with proper bounds of applicability is not available, the Sherwood number can be calculated from a heat transfer correlation instead. Heat and mass transfer are well correlated for turbulent flows since both mechanisms are characterized by transport through turbulent eddy formation [83]. A common heat and mass transport relation is the Chilton-Colburn analogy, which is based upon empirical correlations and is applicable for turbulent flows with Reynolds numbers between $3 \cdot 10^4$ and 10^6 [85]. Terms in the analogy are referred to as "j-factors," where j_H is the j-factor for heat transfer and j_M is for mass. The j-factors are equivalent according to the analogy, as shown in equation 2.38. Thus if a heat transfer correlation for the Nusselt number (Nu) was available along with thermophysical property data to calculate the Prandtl number (Pr), then the Sherwood number could be calculated based on the Colburn analogy. An example of a widely used heat transfer relation is the Dittus-Boelter correlation, shown in equation 2.39, which is valid for turbulent flow in smooth tubes with 0.7<Pr<100 and Re>10,000 [86]. The Dittus-Boelter correlation can also be written with an exponent of 0.3 on the Prandtl number if the fluid is being cooled [86]. Prandtl numbers are calculated according to equation 2.40, where c_p is the specific heat of the fluid, μ is the fluid viscosity, and k is the fluid thermal conductivity.

Eq. 2.38 $$j_M = \frac{Sh}{ReSc^{1/3}} = j_H = \frac{Nu}{RePr^{1/3}}$$

Eq. 2.39 $$Nu = 0.023 Re^{0.8} Pr^{0.4}$$

Eq. 2.40 $$Pr = c_p \mu / k$$

As an alternative to heat transfer correlations, the j-factors can also be calculated from the friction factor for smooth tubes (f) as shown in equation 2.41. Mass transfer is associated with the friction factor as well since it is also dependent upon the degree of turbulence in the fluid. A simple

method for calculating the friction factor in adiabatic flows is with the McAdams relation in equation 2.42, which is valid for $10^4<Re<10^6$ [86]. Note that f is written in terms of the Fanning friction factor, instead of the Darcy friction factor which also appears in literature [86]. Combining equations 2.38 and 2.42, the Sherwood can be calculated based on the friction factor as shown in equation 2.43, which is very similar in structure to the Dittus-Boelter correlation.

Eq. 2.41 $$j_M = j_H = f/2$$

Eq. 2.42 $$f = 0.046Re^{-0.20}$$

Eq. 2.43 $$Sh = 0.023Re^{0.8}Sc^{1/3}$$

Because mass transfer in the salt has a central role in FHR tritium transport, the method for calculating the Sherwood number in each reactor region should be carefully considered. In an ideal scenario, actual experimental data from a Flibe test stand, or equivalently scaled experiment, would be compared to the available mass transfer coefficients in literature in order to gauge the most appropriate correlation. In the absence of validation data, the mass transfer coefficient should be selected based on whichever literature correlation has the most similar testing conditions as well as an appropriate range of applicability. However, using a correlation will always introduce some degree of modeling error. When using the Chilton-Colburn relation or another analogy, error is then being introduced by a correlation for friction factor or Nusselt number instead of a mass transfer correlation. Part of the error from a correlation is caused by the uncertainty in input parameters themselves. The values and uncertainties of compiled thermophysical parameters in Flibe are shown in Table 2.7 [87]. Whether a direct Sherwood number correlation or a friction factor correlation and the Chilton-Colburn analogy is used, Reynolds and Schmidt numbers are needed as inputs in all of the Sherwood number formulations discussed, and therefore uncertainty from Flibe density and viscosity is unavoidable.

Table 2.7. Thermophysical properties of Flibe and 95% confidence level uncertainties. From [87]. All temperatures are in Kelvin.

Property	Value	Uncertainty
Density ρ	2413-0.488T [kg/m^3]	2%
Viscosity μ	1.116e-4·exp(3755/T) [Pa-s]	20%
Heat Capacity c_p	2386 [J/kg-K]	3%
Thermal Conductivity k	1.1 [W/m-K]	10%

2.3.3. Evolution of Tritium from Flibe to Gas

The evolution of tritium from the salt into a cover gas is also a function of its transport in the liquid phase. In fact, it is typically assumed that mass transfer in the gas offers little or no resistance to the overall evolution process, and thus the transport in the salt phase is the rate-limiting step [48, 88, 89]. A simple schematic for the evolution process is shown in Figure 2.16 as an example for HT [88]. Tritium evolution is also possible for T_2 as well as TF [44, 47]. In Figure 2.16, tritium is assumed to be well mixed with a uniform concentration in the bulk fluid and the main concentration gradient is present is a thin, stagnant liquid film at the surface. The tritium concentration decreases across the film to the surface concentration value. At the surface, the tritium concentration in the salt can be related to the tritium gas partial pressure present according to the appropriate Henry's law constant for the given species [85]. The assumption of negligible gas phase mass transfer resistance also implies that the concentration profile is constant for tritium in the off-gas [89]. If the gas is continuously flowing and tritium is being removed, then the tritium concentration in the gas will approach zero [48].

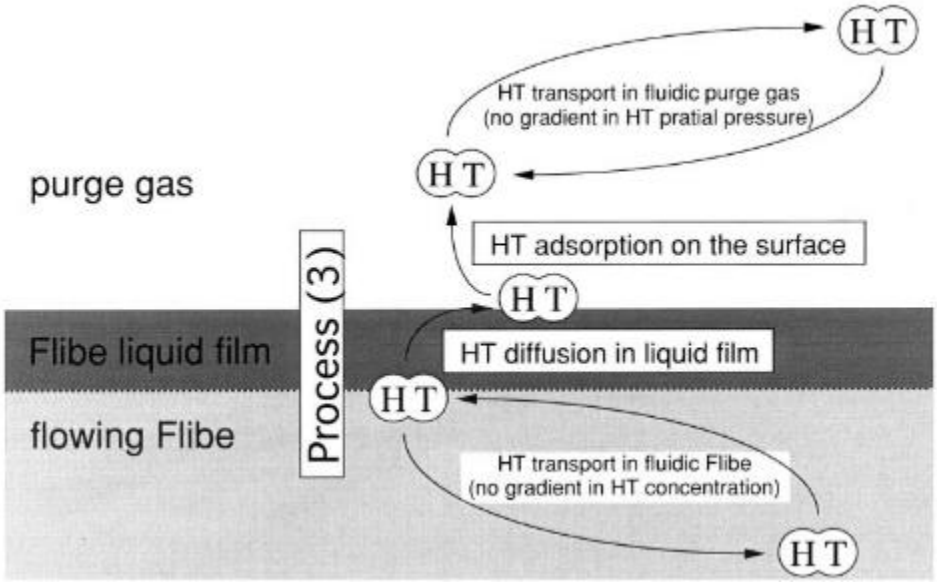

Figure 2.16. Conceptual description for the HT evolution process from Flibe to gas. From [88].

For the simple case of tritium evolution from a static salt, a mass transfer coefficient for evolution can be determined by monitoring the tritium release rate as a function of time. In the case of the Suzuki et al irradiations, tritium was produced through neutron irradiation of a static salt capsule and the production rate of tritium could be either calculated from a neutronic calculation or measured by the equilibrium release rate. The concentration of tritium was

calculated as the generation rate of tritium multiplied by the average residence time of tritium in the salt [48]. As shown in Figure 2.17, the residence time (τ) was determined based on the integral between the normalized total steady state release rate and the time-dependent release profile. The results shown are from an experiment with a He-10%H_2 sweep gas and therefore the tritium was assumed to exist as HT in the salt [48]. Using the measured evolution rate, interfacial area between the salt and gas (A), and the assumption of negligible gas phase concentration previously discussed, the mass transfer coefficient for HT evolution ($k_{E,HT}$) can be calculated according to equation 2.44. The same method was used to calculate a mass transfer coefficient to account for the permeating tritium in the experiment shown in Figure 2.17 [48].

Eq.2.44 $$HT\ Evolution\ \left[\frac{mol}{s}\right] = k_{E,HT}A\left(HT_{Salt} - HT_{gas}\right) \cong k_{E,HT}AHT_{Salt}$$

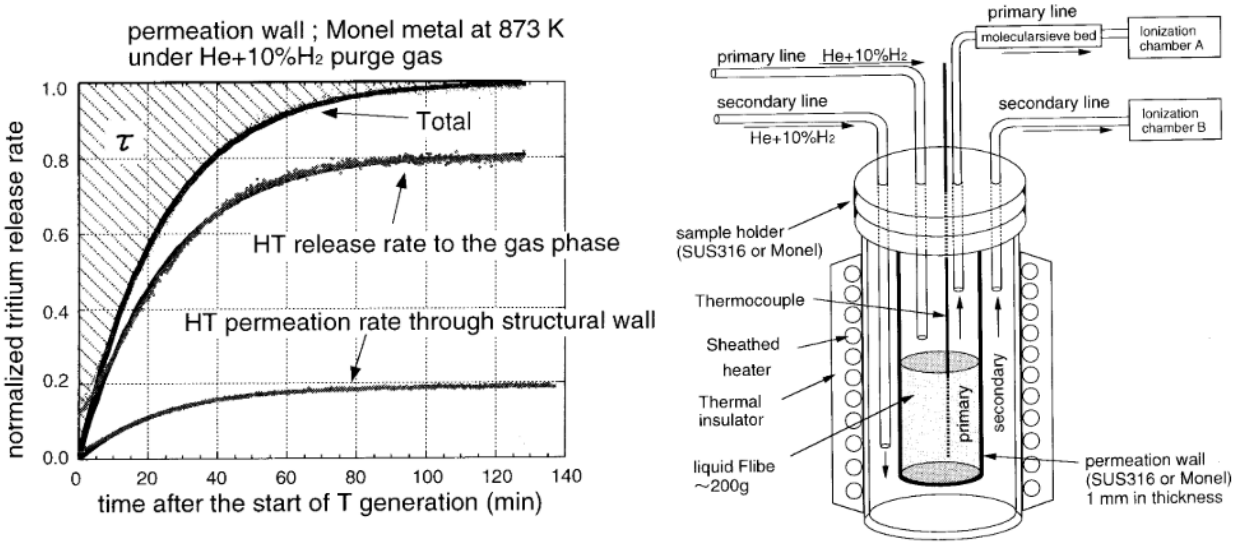

Figure 2.17. Measured evolution and permeation release of HT from Flibe at 873K under neutron irradiation with a He-10%H_2 sweep gas (left). The experimental design of the irradiation capsule is shown along with flow paths for sampling the cover gas and permeation zone (right) [48].

Evolution mass transfer coefficients for various salt temperatures are provided by Suzuki et al [88], but only for HT. This is likely because time-dependence of the TF release rate was difficult to observe with the experimental setup shown in Figure 2.17. A molecular sieve bed was placed in the primary off gas stream which removed TF from the gas while allowing HT/T_2 to continue to the tritium measurement systems. Another separation technique used by Oishi et al involved a set of two cold traps separated by a heated CuO bed [80]. In the first trap, condensable

species TF and HTO are removed from the gas stream. The HT/T_2 passes through the first trap, gets oxidized by the CuO bed, and then is condensed as HTO/T_2O in the second trap. Using a two-trap system allows for simultaneous measurement of TF and HT/T_2 in a gas stream, which Oishi et al leveraged to measure mass transfer coefficients for tritium evolving from static Flibe [80].

The measured evolution mass transfer coefficients from the static salt experiments are shown in Figure 2.18 along with proposed data fits for HT and TF. Data from the Suzuki et al measurements were used to create a data fit shown with the red line in Figure 2.18. Measurements were taken with several H_2 concentrations when salt temperature was 600ºC, which explains the spread in measurements at the inverse temperature of 1.145 (1000/K) [48]. However, only the point with a He-10%H_2 mixture was used for the data fit in order to stay consistent with the other temperature points. As shown in Table 2.8, the resulting data fit for the evolution mass transfer coefficient has an activation energy of 34 kJ/mol, which is similar to the activation energy of the tritium diffusion measurements previously discussed. An approximately similar activation energy for diffusion and evolution provides evidence for the theory that evolution of both TF and HT/T_2 is controlled by diffusion in a liquid film of Flibe [88]. Since there is considerable scatter in the TF evolution data and the temperature dependence is unclear, an evolution mass transfer coefficient for TF is proposed based on the HT data scaled to the ratio of diffusivities for TF and T_2. Considering all the options for diffusivities presented in Figure 2.14, the most consistent comparison between TF and T_2 is likely the results from atomistic simulation [81]. These diffusivities and the calculation of the evolution mass transfer coefficient fits are provided in Table 2.8. Since the Suzuki et al coefficient was measured for HT, an isotopic correction could be applied to represent the evolution of T_2, but is omitted for simplicity.

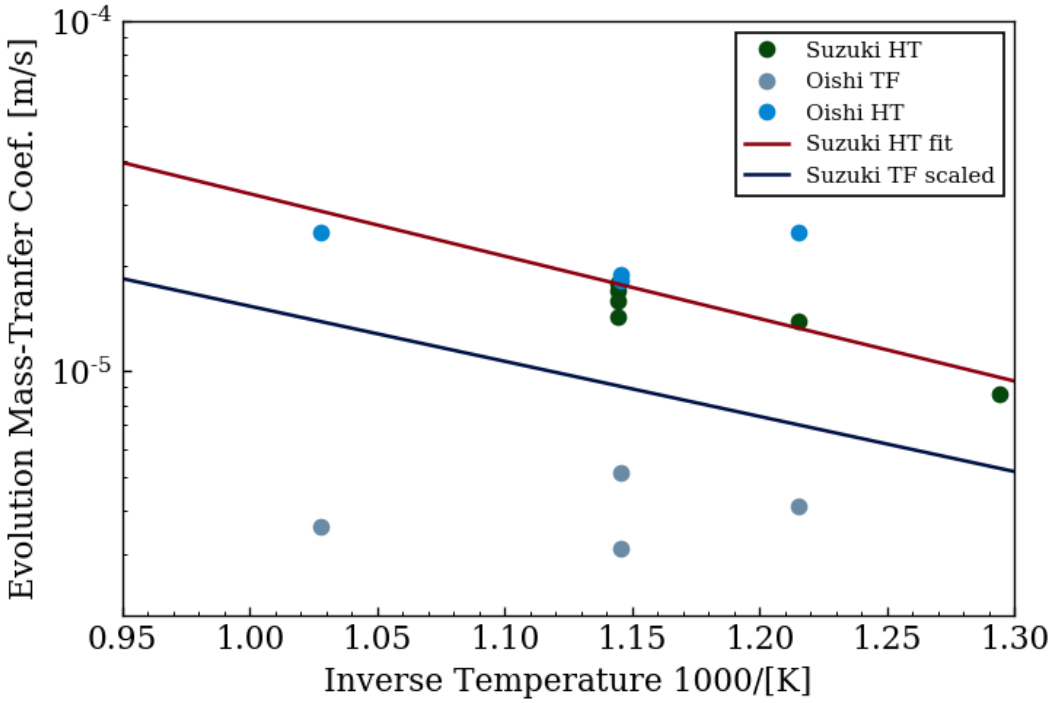

Figure 2.18. Evolution mass transfer coefficients for HT and TF [48, 80]. A fit of the Suzuki HT data is shown in red. The HT data fit was used to approximate a TF mass transfer coefficient by scaling the data to the ratio of TF to T2 diffusivity from atomistic simulations [81].

Table 2.8. Evolution mass transfer coefficients measured for HT along with diffusivities of TF and T_2 in Flibe calculated by atomistic simulation [48, 81]. A proposed evolution coefficient can be calculated for TF based on the ratio of TF:T_2 diffusivities.

Property	Value	Ref.
Atomistic D_{TF}	$2.758 \cdot 10^{-7} \exp(-40/RT)$ [m^2/s]	[81]
Atomistic D_{T2}	$9.349 \cdot 10^{-7} \exp(-36/RT)$ [m^2/s]	[81]
HT Evolution Coef. $k_{E,HT}$	$2.0 \cdot 10^{-3} \exp(-34/RT)$ [m/s]	[48]
TF Evolution Coef. $k_{E,TF}$	$(D_{TF}/D_{T2}) \cdot k_{E,HT}$ [m/s]	--

Another important consideration for evolution is the mass transport of salt occurring underneath the surface of the salt-gas interface. Even in the static salt irradiations, the small amount of convection occurring in the salt crucible likely had an influence on the evolution rate, as shown in the mechanism diagram in Figure 2.16. For example, tritium generated in the ~200g of Flibe in the Suzuki et al irradiation would have roughly a 2cm average diffusion length to reach the salt surface and evolve into gas. If the salt was perfectly stagnant, then the characteristic time of evolution could be estimated by the diffusion length squared divided by the diffusivity. Using the

Calderoni et al diffusivity of $2.86 \cdot 10^{-9}$ m^2/s at 600ºC results in a characteristic time of about 2300 minutes. However, as shown in Figure 2.17, the tritium release rate approached equilibrium after only 120 min. It was observed experimentally by Suzuki et al that bubbling of helium gas through Flibe further increased the evolution mass transfer coefficient by agitating the salt [88]. Furthermore, tritium evolution to the primary system off-gas of the MSRE was the largest release path from the reactor - accounting for over 44% of the total tritium generation [38]. In the MSRE, the off-gas system was tied to the pump which included a spray ring designed to strip xenon from the fuel salt [90]. Increased mass transfer in the pump bowl system can promote evolution both by increasing the evolution mass transfer coefficient as well as creating a larger surface area for gas-liquid contact compared to static salt. However, accurately modeling the mass transfer conditions at the salt-gas interfaces of a FHR require detailed design information of the primary pumping systems, which is not currently available.

2.4. Tritium Permeation in Metals

2.4.1. Permeation Mechanisms in a FHR

The ability of tritium to permeate through metals makes tritium management in FHRs a unique challenge compared to other radionuclides. As with tritium diffusivity, the tritium permeability in metals is an Arrhenius function which increases exponentially with temperature [76]. As a result, tritium will have a high degree of mobility in candidate structural materials at FHR operating temperatures [91].

Tritium and other hydrogen isotopes diffuse through metals in a monatomic state [48, 76]. Thus, the first step in the permeation process is the dissociation of T_2 into T atoms at the metal surface. The flux of T_2 atoms to the surface, $j_{d,T2}$, is related to the partial pressure of T_2 gas above the surface and a dissociation rate constant, k_d, as shown in equation 2.45. At the surface, dissociated tritium can also recombine into T_2 and reenter the gas phase. As shown in equation 2.46, the recombination flux is proportional to a rate constant, k_r, times the square of T concentration at the metal surface [92]. At equilibrium, the dissociation rate will equal the recombination rate and the partial pressure can be related to surface concentration through equation 2.47. The proportionality of dissolved hydrogen in metal to the square root of partial pressure is known as Sievert's law, and the constant K_S in equation 2.47 is the Sievert's law constant or the hydrogen solubility of the metal [76].

Eq. 2.45 $$j_{d,T_2} = k_d p_{T_2}$$

Eq. 2.46 $$j_{r,T_2} = k_r c_T^2$$

Eq. 2.47 $$c_T = K_S \sqrt{p_{T_2}}$$

In practice, the dissociation coefficient is difficult to measure and the Sievert's law constant is commonly used for analysis instead. A permeability is also defined for metals as the combined product of diffusivity and solubility. Although, here the diffusivity refers to monatomic T and the solubility has units of mol/m^3-Pa$^{1/2}$ to reflect the square root dependence with pressure [91]. A similar procedure as to the one described for salt permeation studies is used to measure the tritium transport properties in steel. In summary, the steady state flux of tritium through a metal sample is used to determine the permeability, the time-dependence of flux is used to analyze diffusivity, and the measured permeability divided by diffusivity results in the calculated solubility [91]. The flux of tritium through a 1-dimensional Cartesian geometry of thickness L is shown in equation 2.49.

Eq. 2.48 $$\Phi_{Metal} = D_T K_S$$

Eq. 2.49 $$j_{T_2,Steady} = \frac{\Phi_{Metal}}{L}\left(\sqrt{p_{T_{2,Up}}} - \sqrt{p_{T_{2,Down}}}\right)$$

As with the salt permeation experiments, the downstream partial pressure $p_{T2,Down}$ is usually neglected if the permeating tritium is continuously removed [76]. However, the downstream metal surface tritium concentration will not necessarily be zero unless the resistance of recombination is also negligible. From equation 2.46, it is shown that the recombination flux will decrease when the tritium concentration in the metal is low or if the recombination rate constant is reduced. In the case of negligible permeation resistance, a uniform tritium concentration in the sample, and a dominating recombination resistance, the flux of tritium can be calculated as shown in equation 2.50. Therefore, it is possible to gauge whether a permeation experiment is diffusion limited or surface-recombination limited based on the permeation flux dependence with T_2 partial pressure. In Figure 2.19, the permeation rate of deuterium through 304L stainless steel is shown as a function of temperature and D_2 pressure. As partial pressure of D_2 was reduced, the measured permeation rate deviated from a square root pressure dependence and approached a linear relationship [93].

Eq. 2.50 $$j_{T_2} = k_r K_S^2 p_{T_2}$$

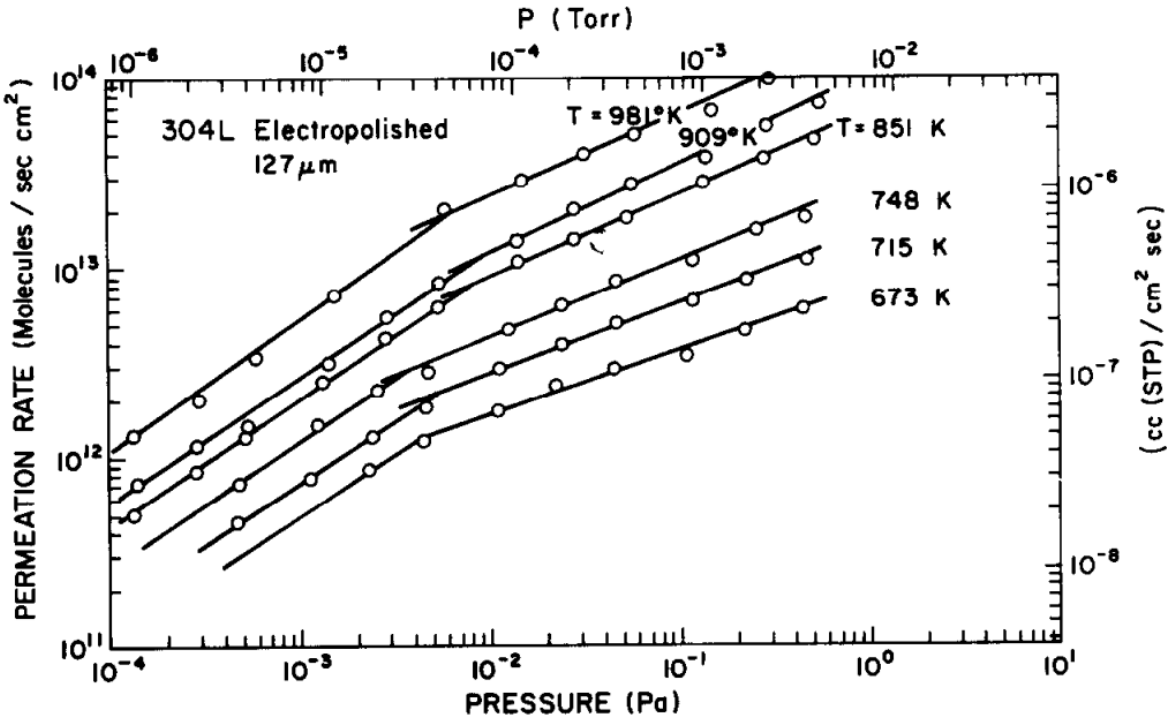

Figure 2.19. Deuterium permeation rate through 304L stainless steel as a function of temperature and D_2 pressure. Pressure dependence of permeation rate changed as the partial pressure was reduced [93].

Recombination resistance is also dependent on the rate constant, which captures properties of the underlying material as well surface conditions like oxidation and other impurities [94]. The recombination rate constant is a thermally activated parameter which can also be expressed by an Arrhenius equation. A variety of measured recombination coefficients are shown in Figure 2.20 for experiments with stainless steel. Figure 2.20 also shows coefficients calculated as a function of temperature in a theoretical model with upper and lower bounds based on a "sticking coefficient" of 0.5 and 5e-5 [95]. The theoretical model is fairly complex and contains several inputs [95]. Instead of the full theoretical form, the upper and lower bounds can be fit with simple equations as shown in Table 2.9 based on the data in Figure 2.20.

Table 2.9. Upper and low bound data fits for a theoretical recombination coefficient with various sticking coefficients [94, 95].

Recombination Condition	Sticking Coef.	Value
Upper Bound	0.5	$1.31\exp(-50.5/RT)$ [m^4/mol-s]
Lower Bound	5e-5	$1.19\cdot10^{-4}\exp(-49.8/RT)$ [m^4/mol-s]

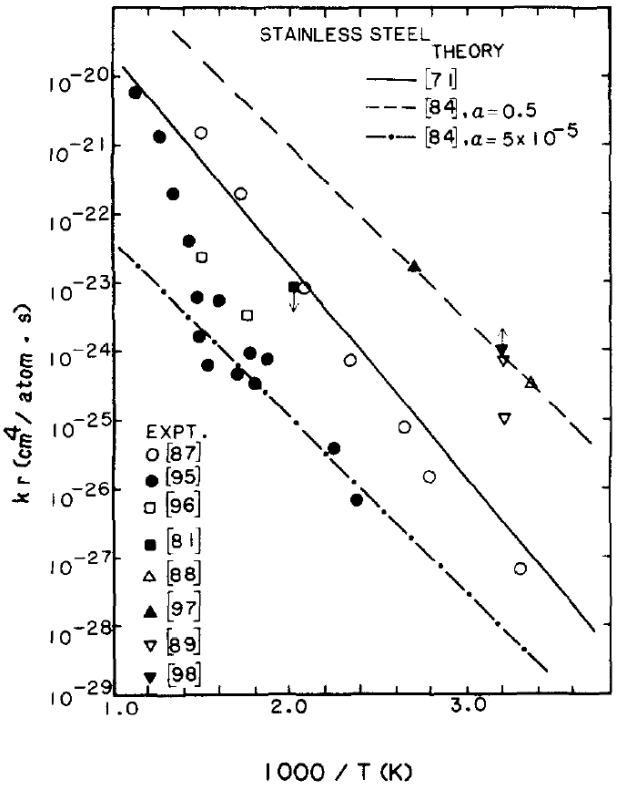

Figure 2.20. Measured recombination rate constants for hydrogen isotopes on stainless steels along with calculations from a theoretical model. References to experiments provided in [94].

In order to keep the effects of bulk permeation and surface reactions separate, permeability of materials should only be reported from experiments that verify diffusion-limited transport [76]. Therefore, diffusivity data can be compared with less obstruction from experimental procedures like surface preparation or testing environment. Another possible experimental difference is the isotopic effect in diffusivity from the selected hydrogen isotope. Experimental results examining the isotopic effect on permeability of austenitic stainless steel are shown in Figure 2.21. In some studies, the ratio of hydrogen to deuterium permeability was similar to the square root of two and constant with temperature as predicted by theoretical behavior [96]. Other results show a larger deviation between isotopes, which was more significant for 304SS than 316SS and larger at lower temperatures [97]. Diffusivity and solubility measurements from experiments that confirmed diffusion-limited permeation are shown in Figure 2.22 and Figure 2.23. All measurements are with hydrogen and 316 stainless steel and therefore the diffusivities are multiplied by $(1/3)^{1/2}$ to represent tritium. While a larger isotopic effect may exist, using the square root mass ratio provides a conservative estimate in order to prevent under prediction of tritium permeation.

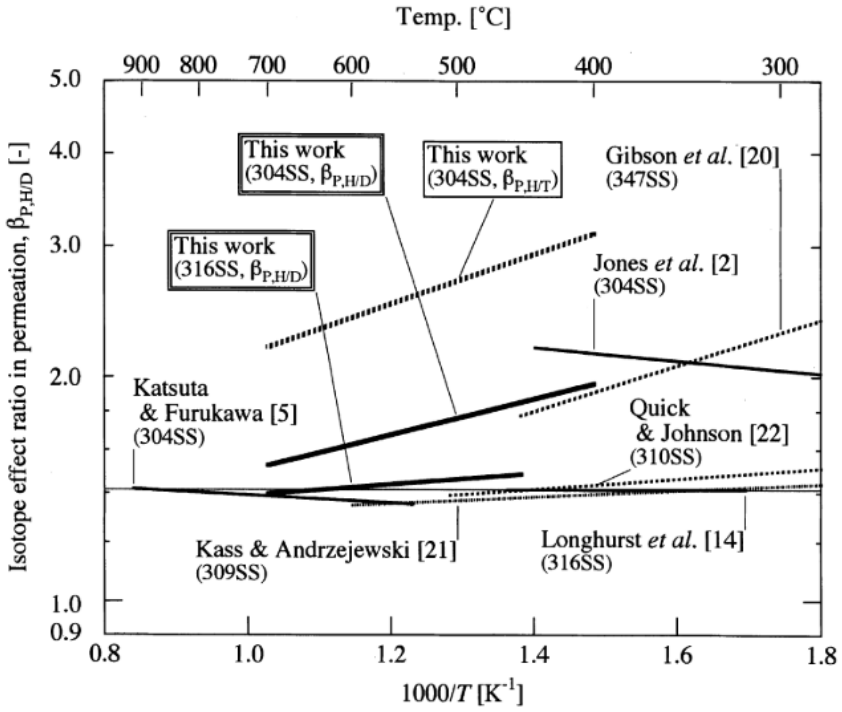

Figure 2.21. Ratio of hydrogen to deuterium permeabilities measured for various austenitic stainless steels. The isotopic effect for 316SS was similar to the square root of 2 and roughly constant with temperature, as predicted by Graham's law [97].

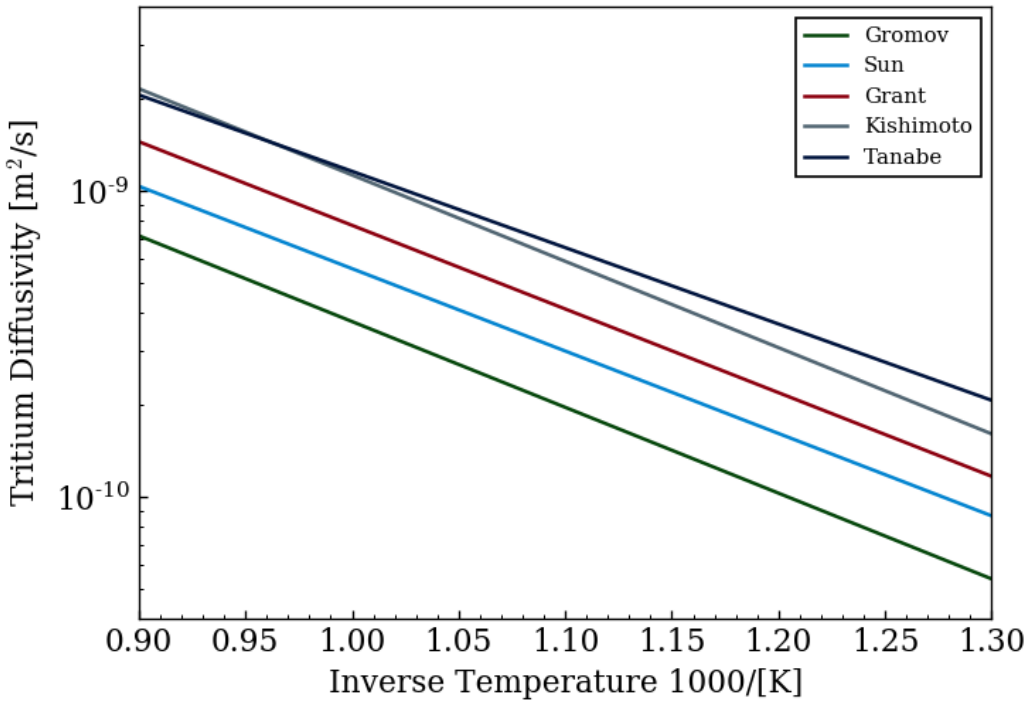

Figure 2.22. Diffusivity measurements of hydrogen in 316 stainless steel scaled to represent tritium diffusion. References provided in Table 2.10.

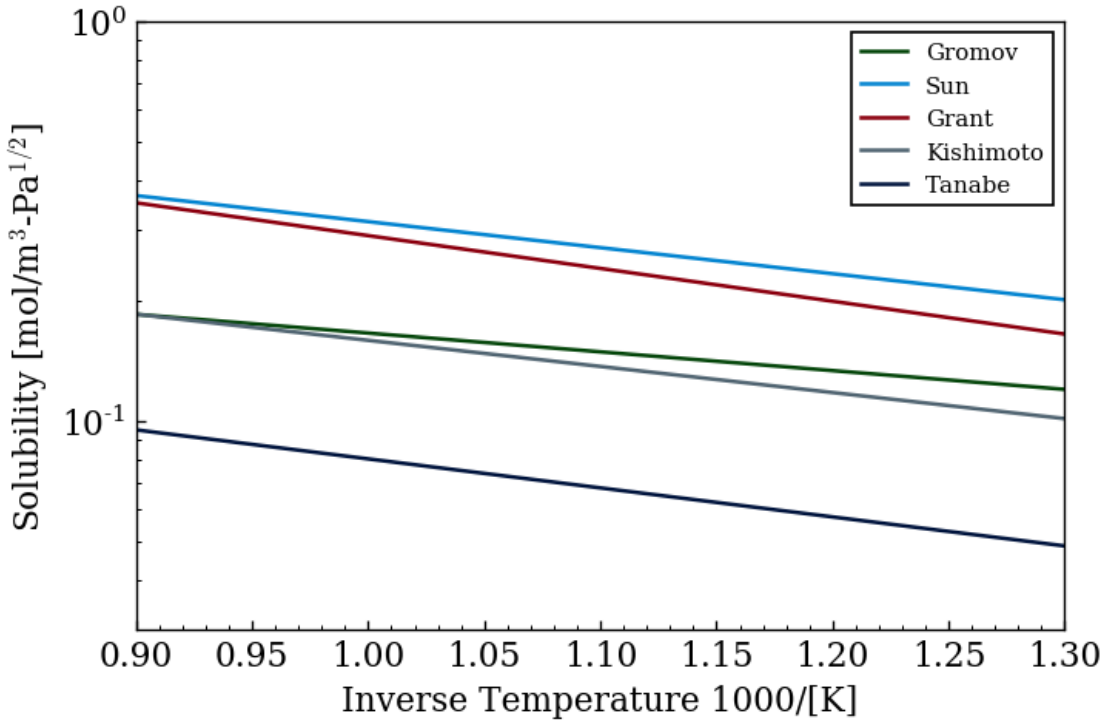

Figure 2.23. Sievert's law solubility coefficients for hydrogen in 316 stainless steel. References to experimental measurements provided in Table 2.11.

Table 2.10. Experimental measurements for hydrogen diffusivity in 316 stainless steel. Diffusivities in each experiment were measured over the temperature range provided. Since all measurements were conducted with hydrogen, the diffusivities are reduced by a factor of $(1/3)^{1/2}$ to represent tritium.

D_T Measurement	**Temp Range**	**Value [m^2/s]**	**D_T at 600°C [m^2/s]**	**Ref.**
Gromov et al	950-625K	$2.40 \cdot 10^{-7}$exp(-53.7/RT)	1.47E-10	[98]
Sun et al	473-703K	$2.77 \cdot 10^{-7}$exp(-51.6/RT)	2.26E-10	[99]
Grant et al	502-863K	$4.21 \cdot 10^{-7}$exp(-6300/T)	3.10E-10	[100]
Kishimoto et al	873-1173K	$7.51 \cdot 10^{-7}$exp(-54.0/RT)	4.42E-10	[101]
Tanabe et al	500-1200K	$3.65 \cdot 10^{-7}$exp(-47.8/RT)	5.04E-10	[91]

Table 2.11. Measurements of Sievert's law solubility of hydrogen in 316 stainless steel.

K_S Measurement	**Temp Range**	**Value [mol/m^{3}Pa$^{1/2}$]**	**K_S(600°C)[mol/m^{3}Pa$^{1/2}$]**	**Ref.**
Gromov et al	950-625K	0.488exp(-9.0/RT)	0.141	[98]
Sun et al	473-703K	1.41exp(-12.5/RT)	0.252	[99]
Grant et al	502-863K	1.92exp(-1890/T)	0.220	[100]
Kishimoto et al	873-1173K	0.714exp(-12.5/RT)	0.128	[101]
Tanabe et al	500-1200K	0.427exp(-13.9/RT)	0.0629	[91]

2.4.2. Permeation Barrier Coatings

Limiting permeation of tritium through the reactor system is a potential option to simplify tritium management in a FHR. Generally speaking, tritium partitioning and storage technologies are most effective when staged closest to the point of generation or release [102]. Therefore, allowing excessive tritium permeation into the ambient air of the reactor building or the working fluid of a power cycle may create a situation where the concentration is too dilute to allow for efficient capture. A permeation barrier coating is one potential option to reduce tritium release through structural metals into undesirable regions of the FHR power plant.

A simple model to analyze permeation barrier effectiveness is through the composite permeation model [103]. In this interpretation, tritium must fully permeate through a barrier layer as well as the underlying metal to transit through the material. As shown in equation 2.51, permeation flux will decrease with a larger barrier or metal thickness (L_B and L_M) or when the permeability of the barrier or metal (Φ_B and Φ_M) is reduced. Note that this form of the equation assumes a 1-D slab geometry, a driving partial pressure on the upstream side, and a negligible downstream tritium partial pressure. According to equation 2.51, the effective permeability of the metal is significantly reduced when L_B/Φ_B is much greater than L_M/Φ_M. In principle, this is not difficult to achieve since the hydrogen permeability of candidate coating materials is generally orders of magnitude lower than for stainless steel, as shown in Figure 2.24. A review of several more coating materials is also provided elsewhere [104]. However, it is important to note that the permeability measurements for barrier materials vary significantly in literature [76], and depend on material characteristics like microstructure or grain size [105]. Despite the differences in experimental measurements, several coating options exist that can create a significantly lower effective permeability when applied to stainless steel even for small coating thicknesses. For example, tungsten and erbia have permeabilities roughly three orders of magnitudes lower than 316SS as shown in Figure 2.24, and thus the permeation resistance of a steel subrate would be doubled according to equation 2.51 if a W or Er_2O_3 coating was applied with a thickness of 0.1% of the base 316SS metal.

Eq. 2.51
$$j_{T_2} = \frac{\sqrt{p_{T_2}}}{L_B/\Phi_B + L_M/\Phi_M}$$

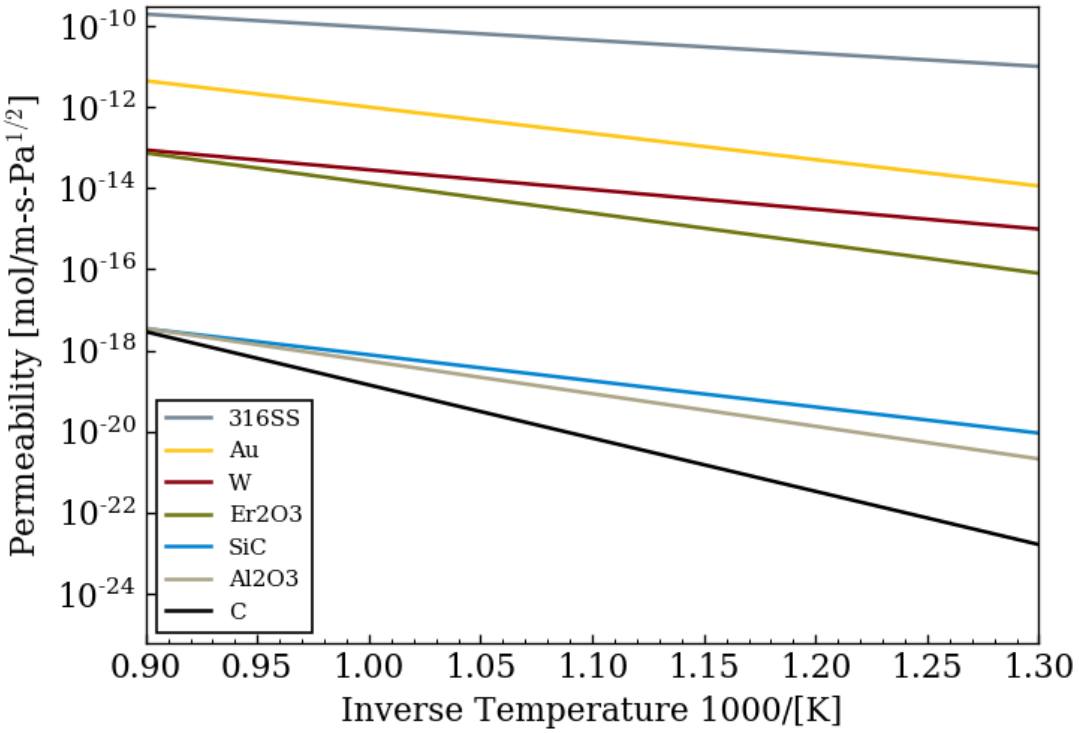

Figure 2.24. Hydrogen permeability of 316 stainless steel [91], along with candidate permeation barrier coating materials gold [106], tungsten [105], erbium oxide [107], silicon carbide [76], aluminum oxide [76], and fine-grain graphite [108].

The permeability of coating materials is often so low that transport through the coating itself can be effectively neglected, and only permeation through gaps and defects needs to be considered. This treatment is referred to as the areal-defect model [103], as shown in equation 2.52. The model is essentially permeation though the base metal, but scaled to the ratio of defect area (A_d) to total interface surface area (A_S). Additionally, the effective length (L_{eff}) is used instead of metal thickness to account for any additional distance tritium must travel through the metal to reach defect sites. The areal defect model can help explain why experimental measurements for hydrogen permeation often are much higher than expected permeability through the pure coating material. For example, permeation results for alumina coatings on stainless steel were several orders of magnitude higher on average than pure alumina for the measurements shown in Figure 2.25. In the areal-defect model, defects could refer to cracks in the coating material, grain boundaries, porosity, or any material imperfection that allows tritium to permeate faster than in the base coating material. An example of microcracks observed in an alumina permeation barrier coating on stainless steel is shown in Figure 2.26 [49].

Eq. 2.52

$$j_{T_2} = \frac{A_d}{A_S}\frac{\Phi_M}{L_{eff}}\sqrt{p_{T_2}}$$

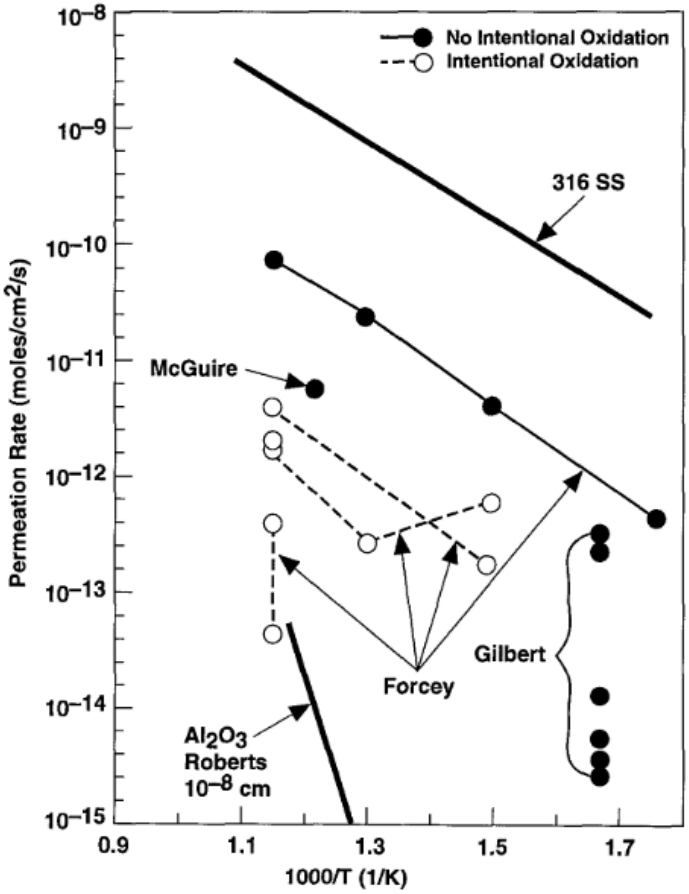

Figure 2.25. Comparison of hydrogen permeation flux measurements for 316SS and aluminized stainless steels at 101 kPa H_2 and various temperatures. From [103].

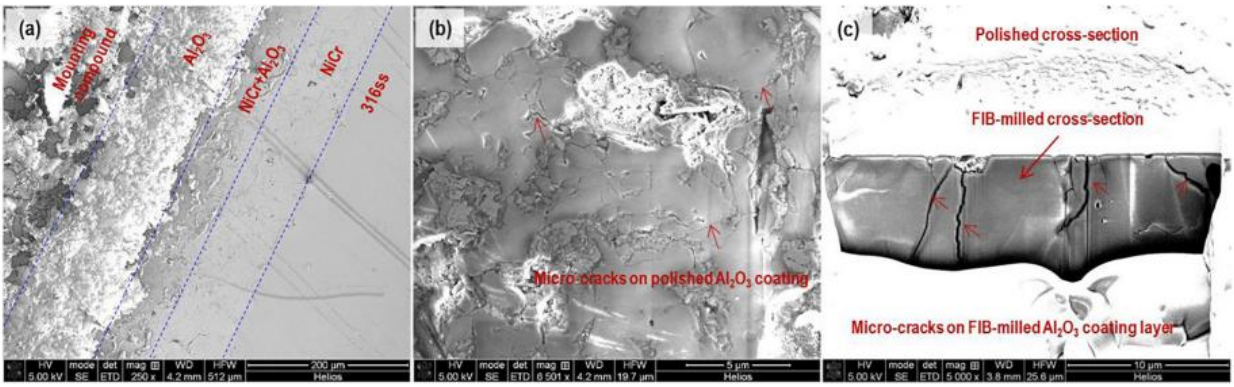

Figure 2.26. Cross-sectional SEM image of an alumina coating and transition coating layers on 316 SS (a) along with the top view of the polished alumina (b). Microcracks in the coating layer were observed with a FIB-milled cross-section (c). From [49].

Another factor supporting the areal-defect model is the observed temperature dependence of the permeation rate in coated samples. As shown in Figure 2.25, the slope of the permeation rate verses inverse temperature for two of the four measurements by Forcey et al roughly followed that of the 316 stainless steel substrate and was significantly lower than for pure alumina [109]. Similar behavior was observed with measurements of effective permeabilities of Al_2O_3/TiC coatings on steel, as shown in Figure 2.27 [110]. Since the slope of the permeation rate on an Arrhenius plot is proportional to the activation energy, similar slopes for coated and uncoated samples indicates that permeation through the substrate material is the rate limiting step for the permeation process [76]. If a significant fraction of permeation was occurring through the coating material, instead of just coating defects, then the activation energy for the coating would be reflected in the measured effective permeability of the sample. The similar slopes in permeability versus inverse temperature for the bare metal and coated samples in Figure 2.27 thus support the areal-defect model instead of the composite permeation treatment. A consequence of the areal-defect model is that the permeability of the chosen barrier material is less important than the ability to create low-defect coatings of the material with sufficient adhesion to the substrate. In other terms, an extremely low permeability material is not useful as a permeation barrier coating if tritium can bypass the coating through defects in the material.

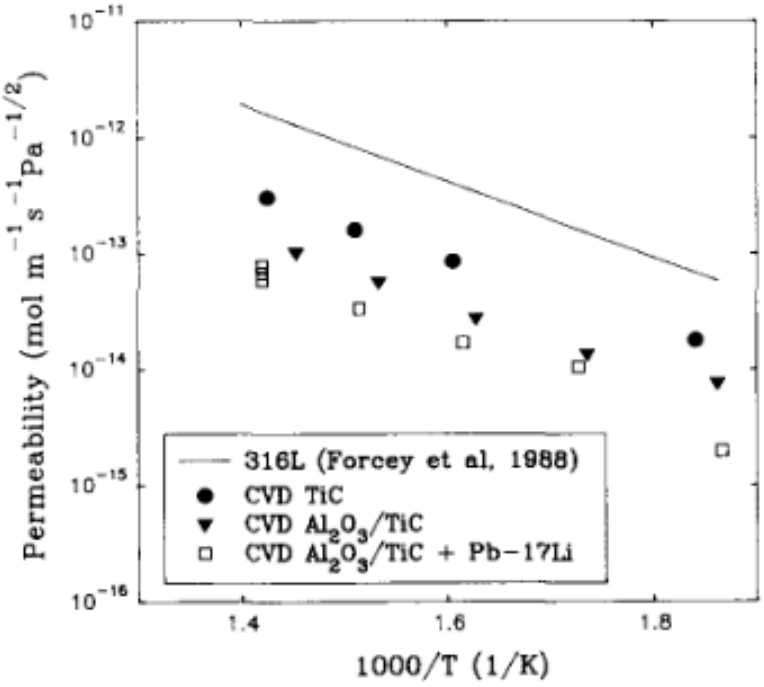

Figure 2.27. Effective deuterium permeability of Al_2O_3/TiC coated steel with and without the presence of liquid lead-lithium. Temperature dependence of permeation (i.e. slope of the permeability curves) through coated samples was similar to that of bare 316L. From [110].

While the areal-defect model may be a conceptually accurate calculation methodology, the actual interfacial defect area of a coating material is impractical to explicitly measure for engineering scale surfaces. Permeation performance from experimental results is often reported using a permeation reduction factor (PRF) instead. The PRF is the ratio of the permeability of the bare metal (Φ_M) to the effective permeability of the equivalent sample with the coating applied (Φ_{eff}), as shown in equation 2.53 [111]. The PRF can also be written in terms of the permeating tritium flux in the case of a thin barrier compared to the substrate material ($L_B << L_M$), as shown in equation 2.54. Since the PRF includes characteristics of the coatings as well as the substrate material, care should be taken when applying a PRF experimental measurement to model of a different base material or significantly dissimilar substrate thickness [111].

Eq. 2.53 $$PRF = \Phi_M / \Phi_{eff}$$

Eq. 2.54 $$j_{T_2,bare} = \frac{\sqrt{p_{T_2}}}{L_M/\Phi_M} \quad j_{T_2,coated} = \frac{\sqrt{p_{T_2}}}{(L_B + L_M)/\Phi_{eff}} \rightarrow PRF \cong \frac{j_{T_2,bare}}{j_{T_2,coated}}$$

An important consideration for applications of permeation barrier coatings is how the permeation resistance of the coating material will change over time. In laboratory tests with precise coating application methods, PRFs for Al_2O_3 from 1000 to above 10000 have been measured [103]. For Er_2O_3 on F82H steel, a PRF of roughly 5000 was measured [112]. However, the permeabilitiy significantly increased when the same sample was used at higher temperatures, as shown in Figure 2.28. The authors attribute the degradation in performance to cracks in the erbia layer caused by thermal stresses [112]. Radiation can also play a role in decreasing coating permeation resistance. In irradiation tests which simulated the blanket of a fusion reactor, PRFs of less than 150 were observed [103]. The difficulty of maintaining an ideal coating structure in a radiation field has led Causey et al to conclude that a PRF above 1000 "simply cannot be achieved in reactors" [76]. However, the issue of thermal, irradiation, or corrosion induced coating degradation can be alleviated by an environment that promotes growth and stability of the barrier. For example, a PRF between 10 and 20 has been measured just for the native chromium oxide layer on 316SS [113]. In a FHR, an oxide layer could reduce permeation into and out of an intermediate nitrate salt [114], or reduce permeation out of the primary system to the ambient air of the reactor building [38]. However, an oxide layer or oxide-based coating material would not be expected to maintain stability on the fluoride salt-facing surfaces of a FHR [51].

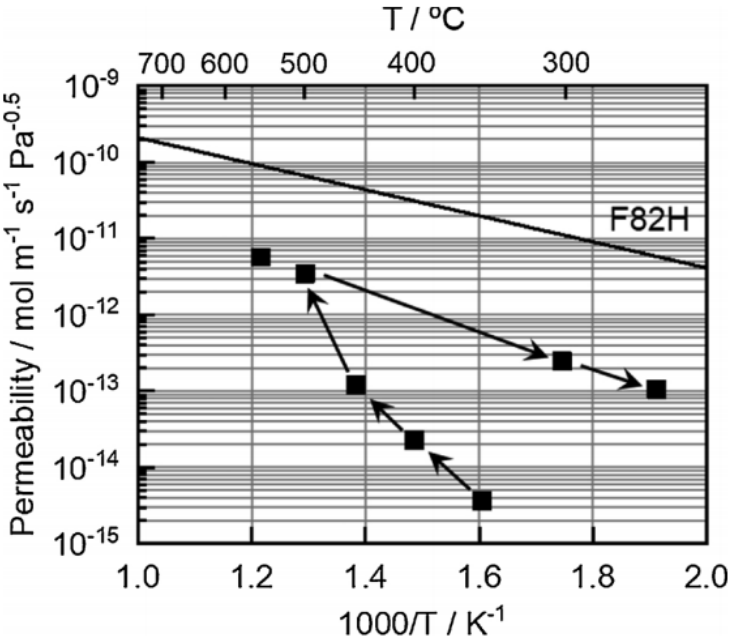

Figure 2.28. Deuterium permeability of Er_2O_3-coated F82H steel compared to an uncoated sample. The points and arrows indicate repeated measurements with the same sample, where the initial permeability increased significantly when experimental temperature increased [112].

2.5. Tritium Retention in Graphite

Interactions of tritium with graphite are an important aspect of FHR tritium transport because of the large inventory of graphite in the reactor. For example, the Mk-1 FHR design included a 5,940 kg central graphite reflector, 43,310 kg outer reflector, 204,000 3 cm diameter graphite moderator pebbles, and 440,000 3 cm diameter fuel pebbles in the core [5]. There are a variety of ways in which tritium could potentially interact with graphite such as physisorption and chemisorption [4], dissociative or molecular adsorption [115], or trapping at weak and strong defect sites [116]. The general term 'retention' is adopted here to refer to tritium movement from dissolution in the salt phase to capture by graphite without necessarily specifying the interaction mechanism within the material. However, the majority of previous literature on hydrogen interactions with graphite only involves gaseous H_2, D_2, or T_2, while very few studies investigate the role of molten salt in the retention process. Therefore, this section summarizes the total capacity for gaseous retention of hydrogen in graphite, the kinetics for gas retention, and then possible factors in which molten Flibe can influence each process.

2.5.1. Graphite Retention Capacity

The amount of hydrogen gas which can be retained by graphite depends strongly on microstructural properties of the material. In particular, the degree of graphitization is a fundamental characteristic which can influence retention behavior. Graphite is typically made from crushed coke particles of a desired size and coal-tar pitch. The mixture undergoes several forming and heat treatment steps, the hottest of which is referred to as the graphitization step [4]. Upon heating to temperatures between 1700°C and 3000°C, carbon materials begin to form continuous structures primarily through the alignment of smaller crystallites of graphite in the material [117]. As shown in Figure 2.29, a high degree of cross linking between crystallites prevents homogenous graphitization from occurring. However, a sufficiently high temperature during the graphitization step can eventually remove cross linking behavior [118]. The graphitization process for various temperatures is also illustrated in Figure 2.30.

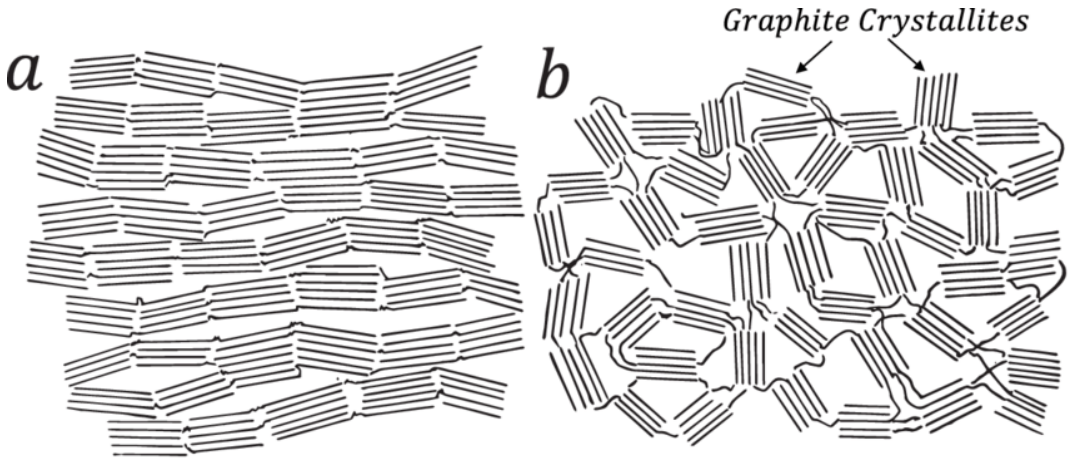

Figure 2.29. Two-dimensional schematic representation of graphitizing carbon (a) compared to the structure of non-graphitizing carbon (b). Adapted from [118].

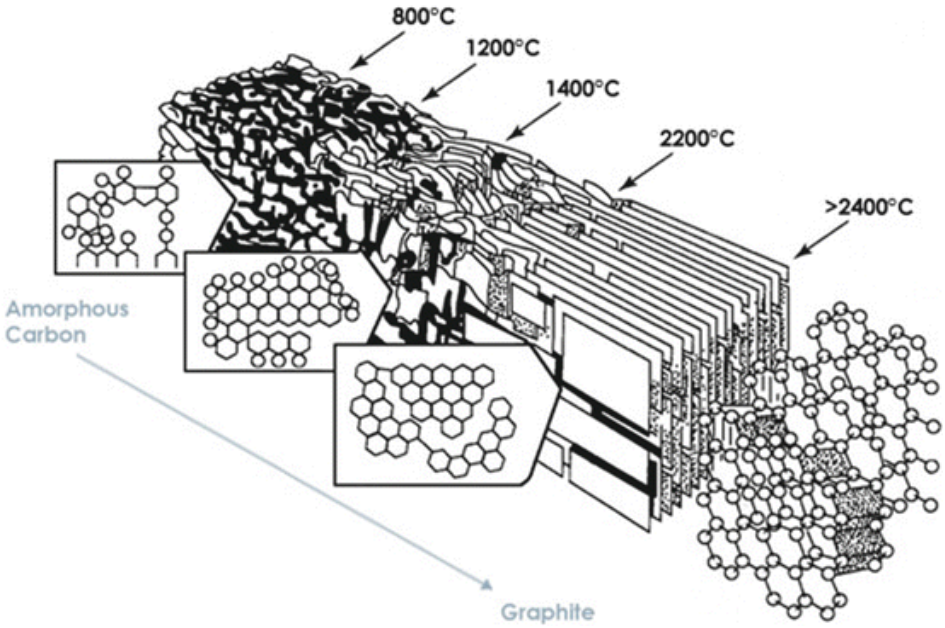

Figure 2.30. Changes to microstructure of carbon during graphitization at various temperatures [119]. Adapted from [120].

Degree of graphitization is important to consider because imperfections like dislocations, dangling carbon bonds, and porosity are the main drivers of hydrogen interactions – a fully crystallized and highly oriented graphite would experience very little hydrogen retention. This is evidenced by a review of hydrogen retention in various nuclear graphite grades by Atsumi et al shown in Figure 2.31 [121]. A relationship between lattice constant of the graphite and measured hydrogen retention was clearly observed. Lattice spacing measured by the d_{002} peak in X-ray diffraction can also be correlated to the degree of graphitization, G, according to equation 2.55

[122]. Therefore, the trend in Figure 2.31(a) shows that when the lattice constant approaches the theoretical constant for crystalline graphite, the retention of hydrogen in the graphite grade approaches zero [121].

Eq. 2.55 $$G = 1 - 3.41(d_{002} - 3.354)^{1/2}$$

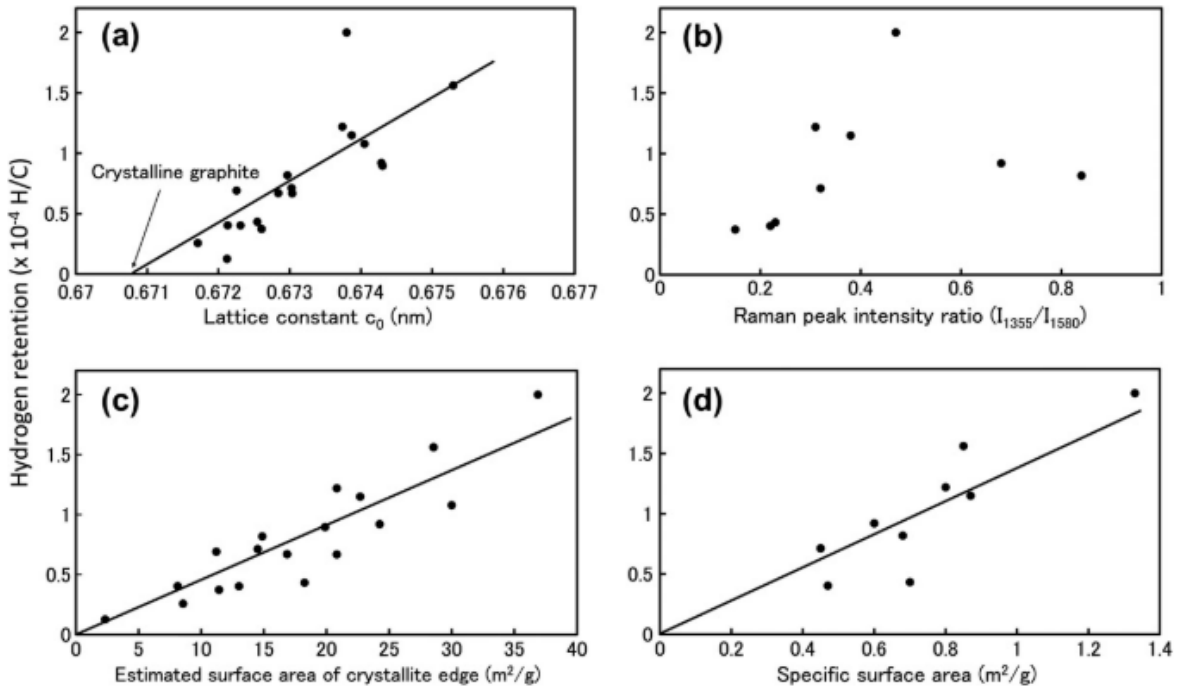

Figure 2.31. Hydrogen retention for various graphite grades verses measured material characteristics. Samples were changed with 10 kPa of hydrogen at 1273 K. From [121].

Another interesting trend is the observed increase in retention with specific surface area depicted in Figure 2.31(d). Nuclear graphites typically have densities between 1.7 g/cm^3 and 1.9 g/cm^3 [123], while the theoretical density of crystalline graphite is 2.26 g/cm^3. Therefore, roughly 20% of the internal volume is comprised of porosity which, in certain cases, is accessible to hydrogen gas. Specific surface area is a measure of the available surfaces inside of a material and is commonly measured based on the Brunauer, Emmett and Teller (BET) method [124]. For graphites with a higher specific surface area, more hydrogen retention was observed which indicates that the hydrogen interaction is a material surface effect [121]. However, not all surfaces within the graphite are equivalent in terms of capacity for hydrogen retention. As shown in Figure 2.31(c), a more robust correlation was found when Atsumi et al mapped the hydrogen retention onto the estimated crystallite edge area of each graphite grade [121]. This correlation supports the

theory that hydrogen can be retained in graphite by forming bonds with dangling carbon atoms at crystallite edge surfaces [123].

The total solubility of hydrogen in graphite follows the square root of hydrogen partial pressure that was previously discussed for Sievert's law. The square root dependence is consistent with a dissociative process where H_2 gas splits to form C-H bonds. Furthermore, the formation of the C-H bond is exothermic and solubility of hydrogen decreases with increasing temperature [125]. Hydrogen retention verses charging pressure are shown as a function of temperature with two nuclear graphite grades in Figure 2.32 – both grades roughly follow a square root relationship with total retention [125, 126]. Solubility values for other nuclear graphite grades of interest for the FHR are shown in Table 2.12.

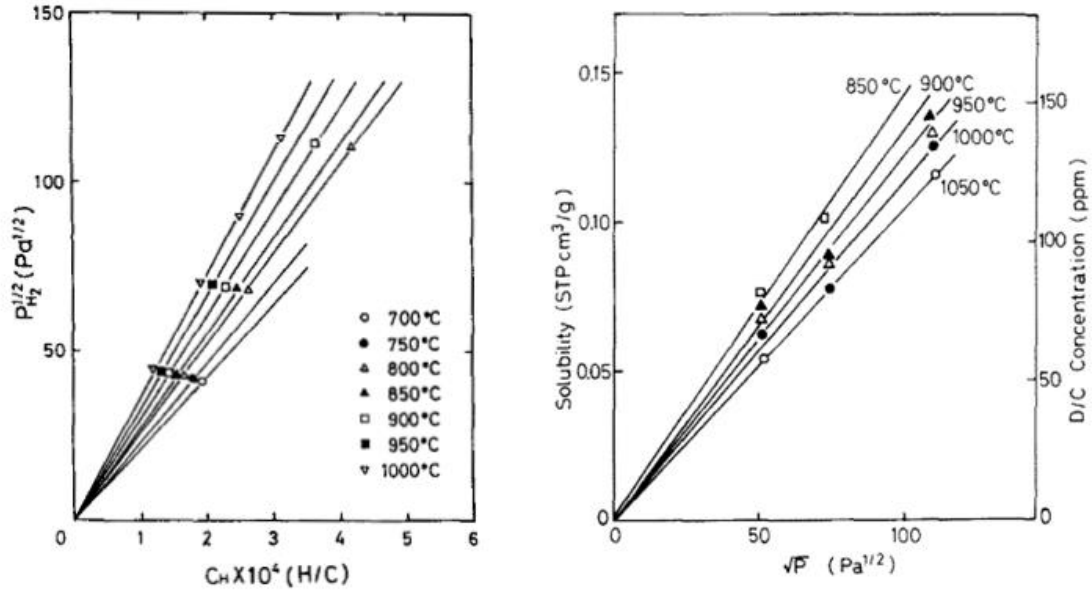

Figure 2.32. Hydrogen retention shown to follow the square root of charging pressure for ISO-88 graphite (left) and IG-110U (right) [125, 126]. Both graphites show a decrease in solubility for increasing temperatures. Note that the axes are flipped between graphs.

Table 2.12. Hydrogen Sievert's law constants for solubility in nuclear graphite grades. Graphite density, ρ, in units of g/cm^3 is used to convert solubilities into units of mol/m^3-$Pa^{1/2}$.

Graphite Grade	Density ρ	K_S [mol/m^3-$Pa^{1/2}$]	K_S at 600°C	Ref.
ISO-88	1.90 g/cm^3	(89.3ρ)·1.22e-4exp(19/RT)	2.84e-1	[126]
ISO-880U	1.90 g/cm^3	1e6(ρ/12.01) exp(-15.8+2640/T)	4.47e-1	[123, 125]
IG-110U	1.77 g/cm^3	1e6(ρ/12.01)exp(-14.5+2190/T)	9.13e-1	[123, 125]
POCO AXF-5Q	1.84 g/cm^3	1e6(ρ/12.01) exp(-15.6+2590/T)	4.99e-1	[125, 127]

The solubility measurements in Figure 2.32 are useful for understanding the total amount of hydrogen retained in graphite for a given temperature and partial pressure. However, the curves do not provide any information into the trapping mechanisms responsible for retention. One method to examine underlying retention characteristics is with Thermal Desorption Spectroscopy (TDS). In a TDS experiment, a graphite sample can be charged with hydrogen gas until the sample is fully saturated, then the sample is quenched and the desorption phase of the experiment begins. Typically, samples are desorbed with a linear temperature ramp which allows the desorption rate to be examined as a function of temperature. An example desorption experiment with ISO-880U graphite charged with D_2 gas at 1273K is shown in Figure 2.33 [115].

The desorption profile shows that deuterium release from graphite is not a simple function of temperature, but instead desorption occurs in distinct peak structures. Total release from each peak was estimated and correlated with the various D_2 charging pressures as shown on the right in Figure 2.33. Desorption from the lowest temperature peak increased linearly with charging pressures, which led the authors to conclude that molecular adsorption of D_2 in graphite pores was responsible for Peak 1 [115]. Peaks 2 and 3 follow roughly a square root relationship with charging pressure, although Peak 3 deviates significantly for low pressures. Because the position of peak 2 was altered by the charging pressure, Atsumi et al proposed that Peak 2 was desorption assisted by a recombination process – where a higher concentration of deuterium in the graphite led to more recombination and a lower peak release temperature [115]. The highest temperature peaks numbered 3 and 4 should correspond to trapping sites within the graphite. Peak 3 was assumed to be the dangling carbon bonds at crystallite edge sites that were previously discussed, which are also referred to as Trap 2 sites [115, 128]. An even higher energy trapping site (Trap 1) is proposed at interstitial clusters inside of the crystallites [128]. It was concluded that the highest temperature peak was responsible for the strongest energy trapping sites [115]. A schematic for hydrogen bonding at Trap 1 and Trap 2 sites is shown in Figure 2.34 [128].

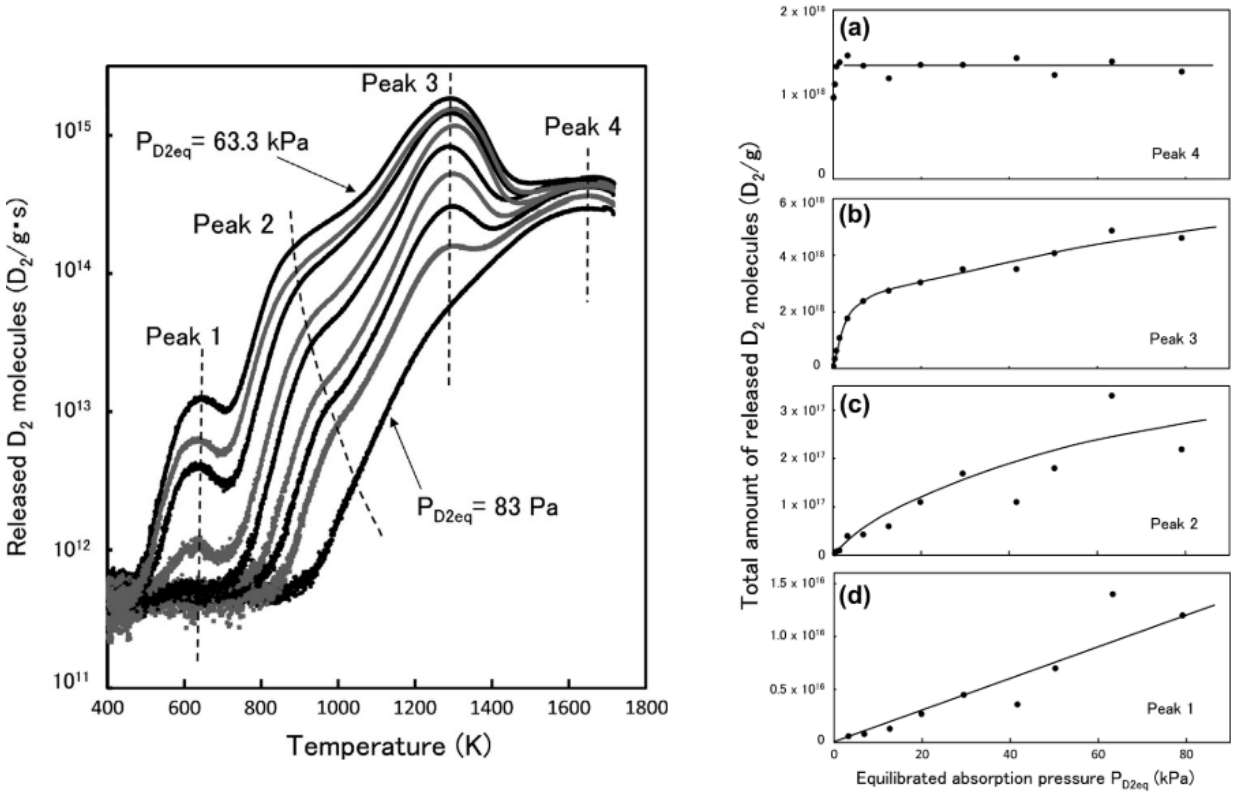

Figure 2.33. Thermal desorption profile for ISO-880U graphite charged with D_2 gas at 1273K and various pressures until saturation, then desorbed with a linear temperature ramp of 0.1K/s. Deuterium release rate is plotted as a function of desorption temperature (left) [129]. Total D_2 release from peaks identified in the desorption profile were correlated to the charging pressure (right) [115].

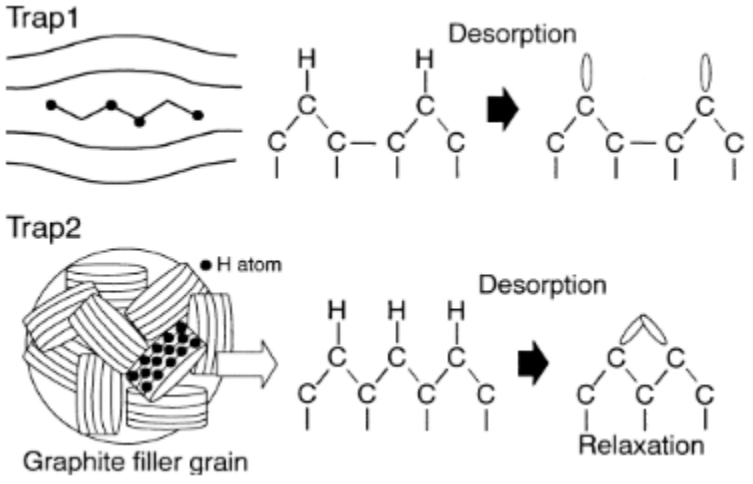

Figure 2.34. Illustration of H-C bonding at weak trapping sites at graphite crystallite edges and strong trapping sites at interstitial clusters. From [128].

The pressure dependence of strong energy trapping sites is displayed in the Peak 4 plot of Figure 2.33. While the retention in other peaks grows with additional charging pressure, the strong trapping remain roughly steady. Therefore, the strong trapping retention is likely limited by the total amount of Trap 1 sites available in graphite. The average Peak 4 retention line in Figure 2.33 corresponded to a retention of roughly $1.35 \cdot 10^{8}$ D_2 molecules per gram of graphite, which can be converted to a strong trap concentration of 8.5 mol/m^3. Saturation of high-energy trapping sites was also observed by Causey et al in POCO AXF-5Q graphite [127]. In their experiment, retention in a graphite sample did not increase at 1473K when charging pressure was raised from 0.66 Pa to 66 Pa [127]. The trap concentration based on the measured retention was $1.7 \cdot 10^{-5}$ traps/C atom or 2.6 mol/m^3. Lastly, strong trapping was observed for A3-3 matrix carbon by charging with H_2 gas at various pressures, desorbing the sample for 15 minutes at 700ºC, and repeating the absorption step, as shown in Figure 2.35 [130]. A detailed description of the experimental setup and procedure are available elsewhere [116]. An average of the strong trapping measurements after saturation at roughly 10 kPa of H_2 yields a trap concentration of 7.9 mol/m^3. Details of the three strong trapping measurements are summarized in Table 2.13.

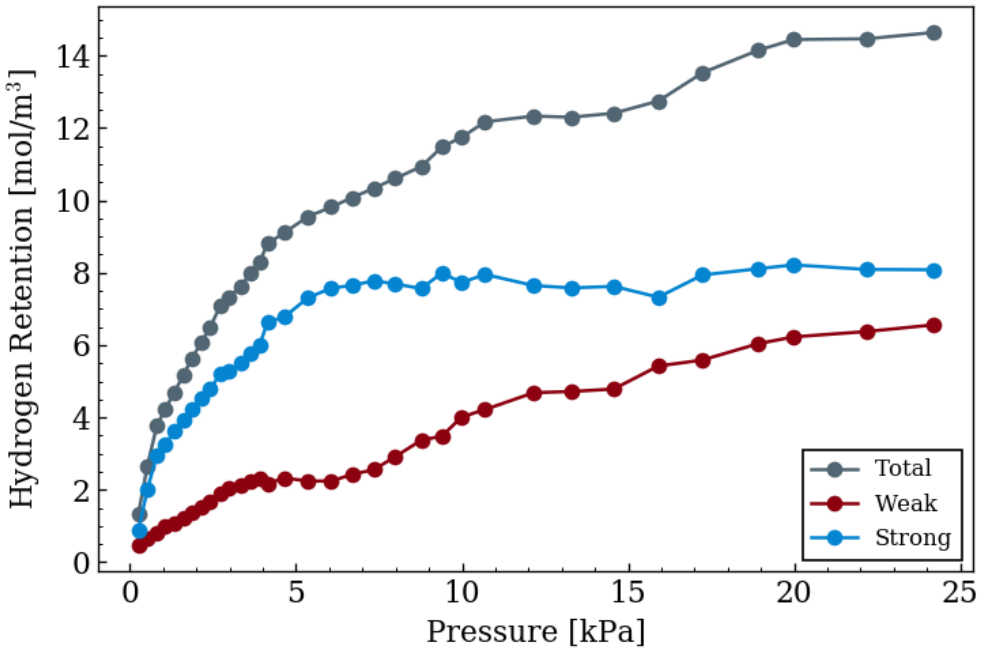

Figure 2.35. Measured total hydrogen retention as a function of pressure for A3-3 matrix carbon at 700ºC. After a 15 minute desorption at temperature under vacuum, the procedure was repeated to measure the weak retention. The difference between the total and weak isotherms is deemed the strongly trapped hydrogen. From [130].

Table 2.13. Summary of high-energy trap concentration measurements in nuclear graphite.

Graphite Grade	Measurement Technique	Trap concentration [mol/m^3]	Ref.
ISO-880U	TDS	8.5	[115]
POCO AXF-5Q	Absorption	2.6	[127]
A3-3	Absorption-Desorption	7.9	[130]

Another important factor for understanding hydrogen retention capacity in graphite for reactor applications is the interaction between neutron damage and trapping. In retention studies on irradiated graphites shown in Figure 2.36, hydrogen solubility increased dramatically for both strong and weak (Trap 1 and 2) sites. The additional retention from neutron damage saturated at a fairly low level of roughly 0.2 displacements per atom (dpa) [131]. For context, the central graphite reflector of the Mk-1 FHR was calculated to experience 2.21 dpa per year of reactor operation [5]. An increase in hydrogen trapping sites can be explained by changes in the graphite microstructure caused by neutron damage. For example, neutron irradiation increases the disorder in graphite and leads to a lower degree of graphitization, which is correlated with hydrogen retention as shown in Figure 2.37 [132].

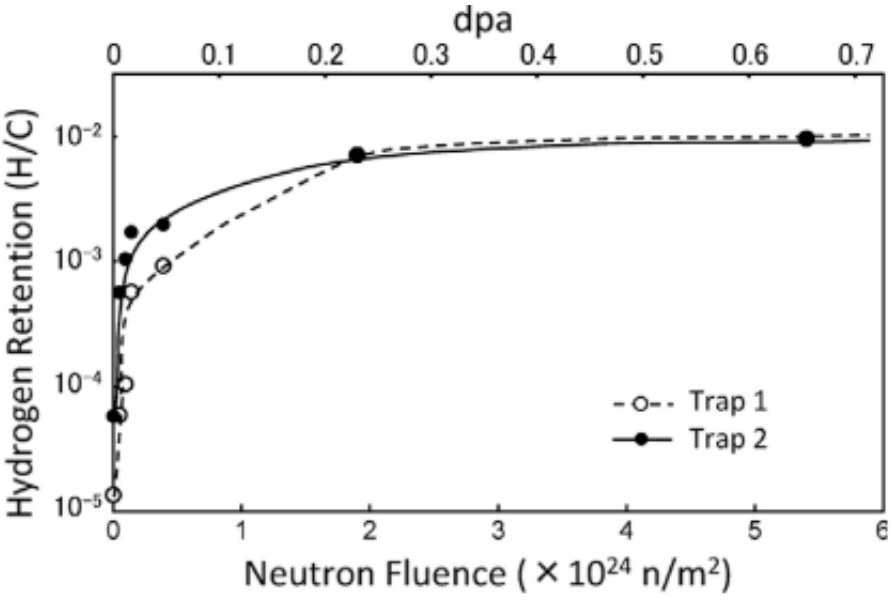

Figure 2.36. Hydrogen retention in IG-430U graphite for Trap 1 and 2 sites for various irradiation fluences. Samples were charged with hydrogen at 1273K and ~10 kPa. From [131].

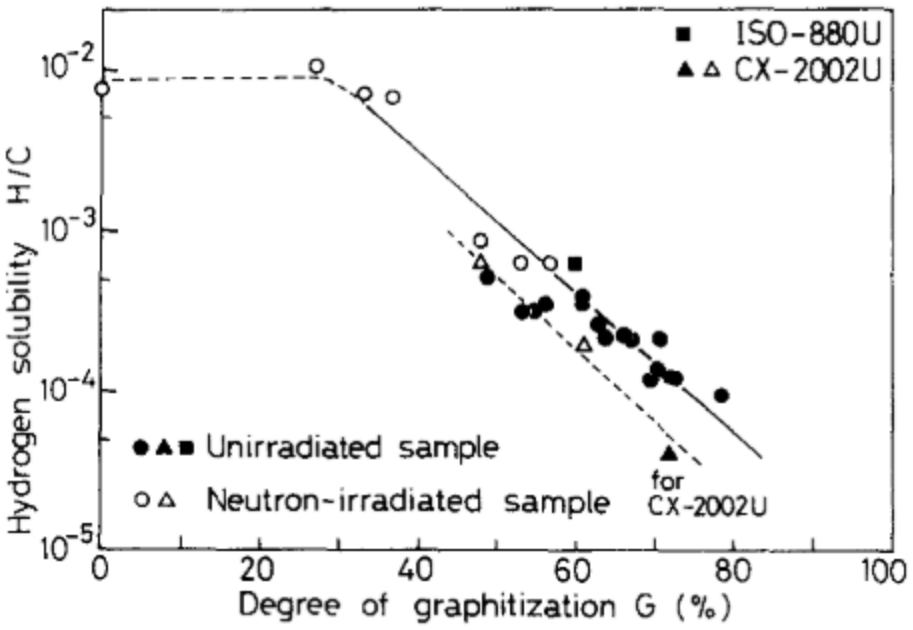

Figure 2.37. Hydrogen retention verses degree of graphitization measured by X-ray diffraction for irradiated and unirradiated samples. Graphites were charged at 1273K with 101 kPa of H_2 until saturation [132].

Hydrogen retention increases from irradiation also depend on the temperature of the radiation environment. Irradiations of various graphite grades presented in Figure 2.38 all led to significant increases in measured Trap 2 retention. However, each graphite grade saw less hydrogen retention in Trap 2 sites for irradiations at 541-582K verses a lower temperature of 416-456K [133]. The amount of decrease in hydrogen retention at the higher irradiation temperature varied significantly among the graphite grades studied. Trap 2 defect sites were observed to anneal out at lower temperatures than Trap 1 sites, but elevated hydrogen retention was observed for both trapping sites in irradiated samples even after annealing up to 1873K [133]. Total hydrogen retention in IG-110U and IG-430U graphite samples was also less for irradiations at 600ºC compared to irradiations at less than 200ºC [132]. Therefore, irradiation experiments at representative temperatures and neutron fluences are important for predicting the total tritium retention capacity for graphite components in a FHR.

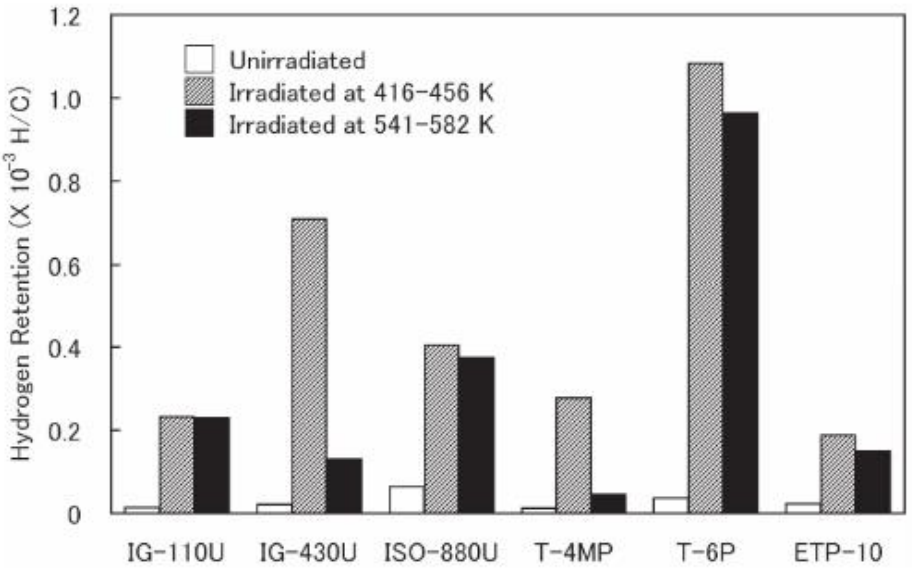

Figure 2.38. Hydrogen retention in weak trapping (Trap 2) sites for various graphite grades irradiated to a fluence of $3.9 \cdot 10^{23}$ n/m^2 and then charged at 1273K and 10 kPa H_2. From [133].

2.5.2. Tritium Transport in Graphite

The uptake of tritium into graphite components of a FHR is constrained by the total retention capacity as well as the kinetic limitations of transport inside graphite – both phenomena are important to understand in order to make accurate predictions of the tritium distribution in future FHR designs. Retention kinetics for hydrogen gas charging in graphite can be broadly observed from the TDS experiments plotted in Figure 2.39. Samples of ISO-880U graphite were all desorbed in linear temperature ramps of 0.1 K/s, but the D_2 gas charging times and temperature varied as shown in the plot [129]. The TDS experiment allows for the amount of tritium in each trapping site after the gas retention step to be examined. For the higher temperature retention experiment at 1273K, the desorption profile began to approach the profile of saturated graphite after roughly 20 minutes of charging. In contrast, the retention study at 973K showed a much slower retention rate since deuterium in each peak structure remained roughly an order of magnitude below saturation even after hours of charging [129]. Therefore, the retention process for each retention mechanism in graphite is facilitated by an increase in temperature. Total retention as a function of charging time in Peaks 4 and 5 from Figure 2.39 fit well with calculated results from a diffusion model, thus a diffusion-controlled process was proposed to describe how deuterium fills trapping sites inside graphite [129].

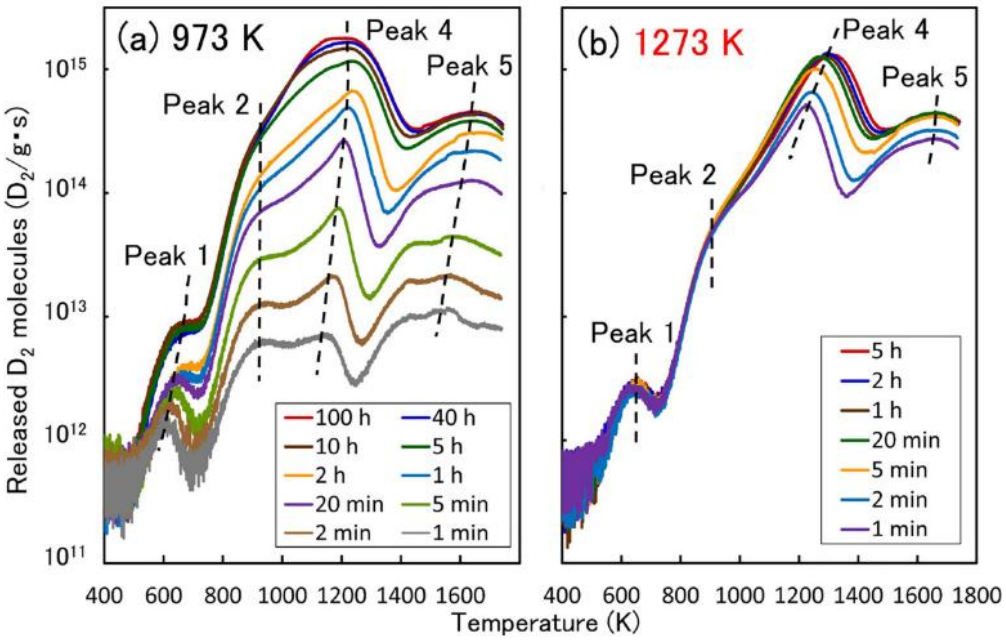

Figure 2.39. Thermal desorption of ISO-880U graphite samples heated at 0.1K/s after charging with 42 kPa of D_2 gas at 973K (left) and 1273K (right) for various charging times. From [129].

The characteristic diffusion length in the retention process was also proposed as the size of filler grains in the graphite, rather than the geometric dimensions of the graphite samples. In TDS measurements of graphites charged with 40 kPa of D_2 at 1273K, the maximum desorption rate occurred at a lower temperature for graphites with a lower grain size [123]. In Figure 2.40, the peak release temperature increases from ISO-880U, IG-110U, IG-430U, to ETP-10, which have grain sizes of 5, 14, 14, and 40 microns, respectively [123]. If the diffusivity of deuterium was similar inside the filler grains of each graphite grade, then the finer grains would reach full desorption earlier in the test procedure, which also explains the decrease in peak desorption temperature for the TDS experiments. Further evidence of grain-based diffusion is provided by isothermal desorption of tritiated graphite by Röhrig et al [134]. In their experiment, the ratio of measured reduced tritium diffusion coefficients (units of s^{-1}) between two HTGR graphite grades was similar to the ratio of squares of the grain radius in each graphite [134]. Lastly, Atsumi et al did not observe a shift in peak desorption temperature during a TDS experiment when the graphite sample size was reduced from 1.0 mm to 0.45 mm [126]. Therefore, they also suggested that desorption was limited by diffusion in the graphite grains and not in the bulk material [126].

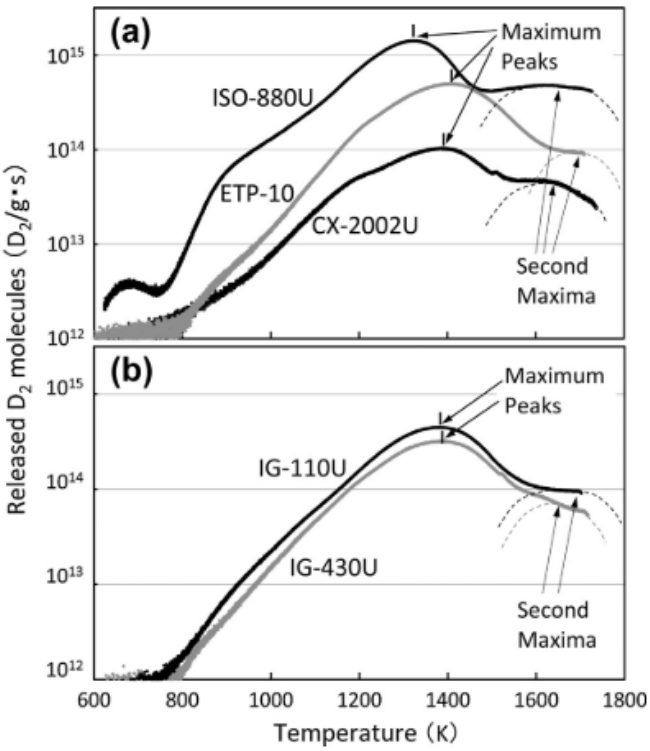

Figure 2.40. Thermal desorption spectra for various graphite grades and one carbon-fiber composite (CX-2002U). The temperature of maximum D_2 release was related to the grain size of each graphite. From [123].

While the diffusivity of tritium in graphite will increase with temperature, the solubility will ultimately dictate the amount of tritium retention in graphite when temperature becomes sufficiently high. For the isochronal absorption experiments by Causey et al shown in Figure 2.41, total retention increased in each 90 minute charging experiment up until roughly 1500K. The experiments after 1500K show a decrease in total retention with increasing temperature [108, 127]. At the lower temperatures, retention was kinetically limited by the diffusion of tritium into graphite and therefore the total retention after the 1.5 hour charge fell short of the equilibrium concentration. For the higher temperatures, the graphite was fully saturated but the total tritium solubility decreased because of additional detrapping at elevated temperatures. The retention results in Figure 2.41 also show good agreement with tritium transport model calculations of 10μm grains of POCO AXF-5Q graphite made with the DIFFUSE code [108]. Causey et al used the retention results and transport model to fit a value of tritium diffusivity in AXF-5Q graphite, which is shown along with other diffusivity measurements in Table 2.14. In each measurement the activation energy of diffusion is quite high, varying from roughly 250 to 300 kJ/mol. The high activation

energy led Atsumi et al to conclude that diffusion of hydrogen in graphite was actually a sequence of trapping and detrapping, rather than pure diffusion, which can be interpreted as an overall diffusion-like process [135].

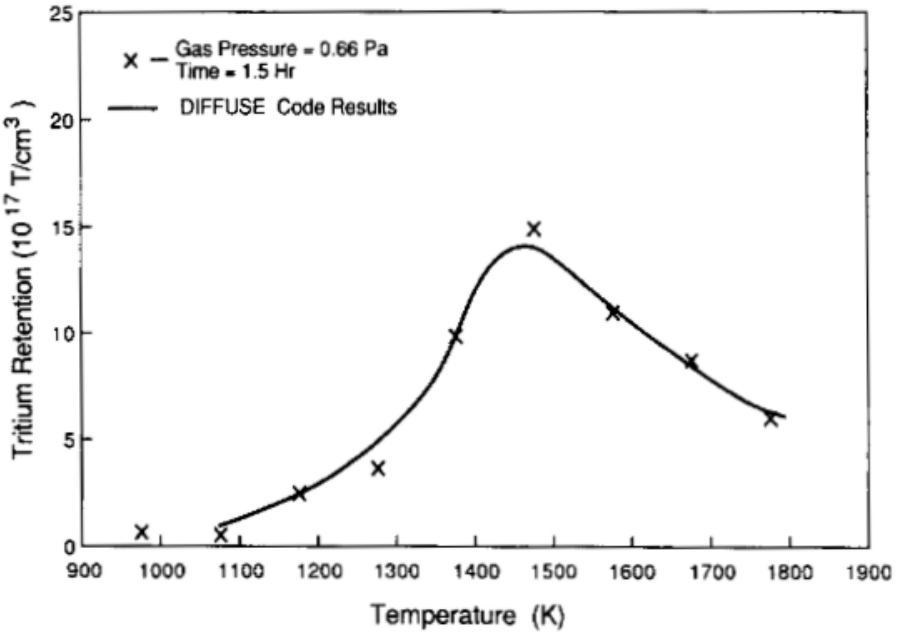

Figure 2.41. Tritium retention in POCO AXF-5Q graphite observed after 1.5 hours of gas charging at 0.66 Pa at the indicated temperatures. Measured retention results are compared to modeled results with the DIFFUSE code [108].

Table 2.14. Compiled results for tritium diffusivity in nuclear graphite, $D_{T,g}$. The ISO-880U diffusivity was not explicitly reported, but is estimated from a figure in reference [129].

Graphite Grade	**$D_{T,g}$ [m^2/s]**	**$D_{T,g}$ at 600ºC**	**Ref.**
ISO-88	$1.38 \cdot 10^{-4} \exp(-251/RT)$	$1.33 \cdot 10^{-19}$	[126]
ISO-880U	$8.11 \cdot 10^{-4} \exp(-305/RT)$	$4.61 \cdot 10^{-22}$	[129]
POCO AXF-5Q	$9.3 \cdot 10^{-5} \exp(-270/RT)$	$6.56 \cdot 10^{-21}$	[108]
ASI-500, AL2-500, HTGR Matrix	$4.0 \cdot 10^{-6} \exp(-268/RT)$	$3.71 \cdot 10^{-22}$	[134]

Other previous experimental measurements of hydrogen diffusivity in graphite vary significantly in both diffusivity magnitude and temperature dependence [136]. Only a subset of literature experiments with similar graphite grades and testing procedures are shown in Table 2.14. One example of a testing condition which can influence diffusivity data is the partial pressure of hydrogen present. Gas charging studies for three grades of graphite presented in Figure 2.42 show

that an increase in hydrogen pressure accelerated the absorption rate in all cases [136]. Additional hydrogen also had some effect on the absorption rate activation energy, but the results were not consistent among the graphite grades as shown by the slope of the lines at each pressure. The apparent diffusivity measurements in experiments with IG-110U graphite at 1273K are shown in Figure 2.43 in comparison to a proposed sigmoidal fit [136]. Additional research would be required to confirm the correct form of the change in diffusivity with pressure. However, a sigmoid fit with a mean shift is used here since the diffusivity increase appears to saturate at high hydrogen pressures and there should also be a non-zero diffusivity when hydrogen overpressure is zero. For example, the diffusivities measured in the thermal desorption experiments by Atsumi and Röhrig should be comparable to the zero overpressure condition since measurements occurred in evacuated furnaces and the only hydrogen present was the small amount desorbing from the sample [126, 134]. The data fit in Figure 2.43 can be used to estimate the change in diffusivity caused by hydrogen pressure. Using the ratio of the sigmoid fit to the diffusivity at zero pressure, a diffusivity amplification factor, A, can be calculated as shown in equation 2.56.

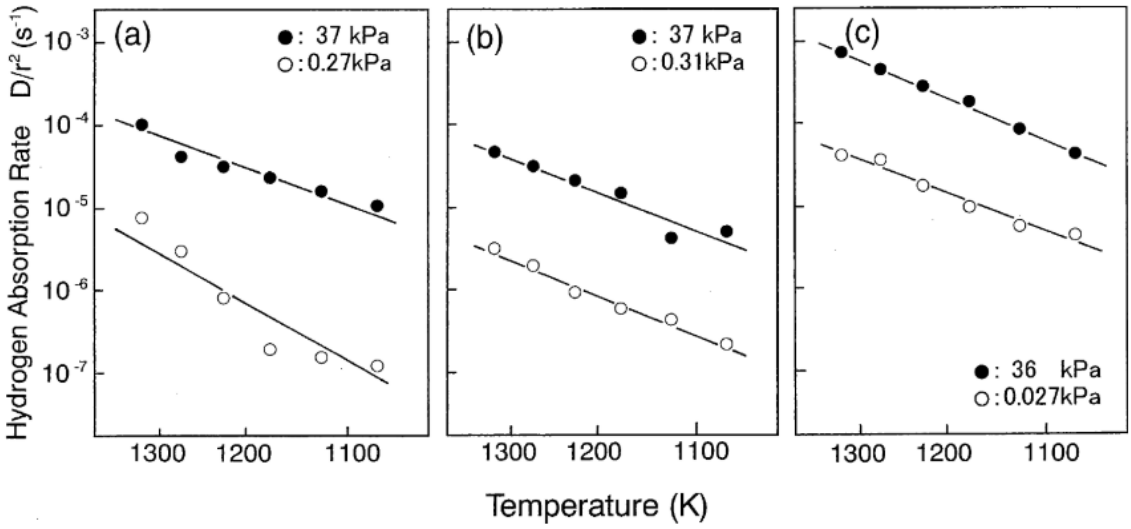

Figure 2.42. Hydrogen absorption rate for various temperatures and hydrogen pressures for IG-110U (a), IG-430U (b), and ISO-880U (c).

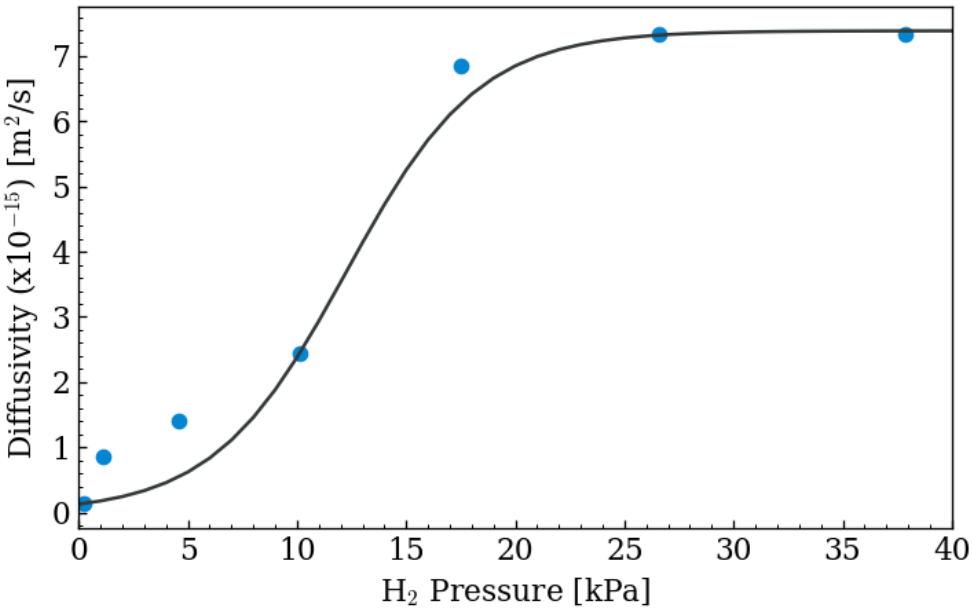

Figure 2.43. Observed hydrogen diffusivity in absorption experiments with IG-110U graphite at 1273K and various charging pressures. From [136]. The data is fit with a sigmoid function.

Eq. 2.56
$$A = \left(\frac{7.388 \cdot 10^{-15}}{0.1284 \cdot 10^{-15}}\right)\left(\frac{1}{1 + \exp(-0.329(P[kPa] - 12.3))}\right)$$

A significant decrease in the diffusion activation energy was observed for IG-110U tested in a hydrogen saturated condition of 37 kPa [136]. The measured energy of 125 kJ/mol is significantly less than the activation from other diffusivity measurements described in Table 2.14, and is also similar to the 121 kJ/mol activation energy of D_2 diffusion through pores of ISO-88 measured by Atsumi et al [126]. One possible explanation of the reduction in activation energy is that the high hydrogen pressures result in a larger fraction of occupied trapping sites in the graphite. Therefore, instead of trapping and detrapping at open sites, hydrogen tends to diffuse only though open pores in graphite once the number of vacant sites in sufficiently low. When the hydrogen pressure is below the saturation condition, both molecular diffusion through open pores and trapping in the graphite grains may occur. A complete illustration of the hydrogen retention process is shown in Figure 2.44 starting from uptake of H_2 into open pores, the trapping-detrapping diffusion process in grains, and finally trapping at high-energy sites in the crystallites [137].

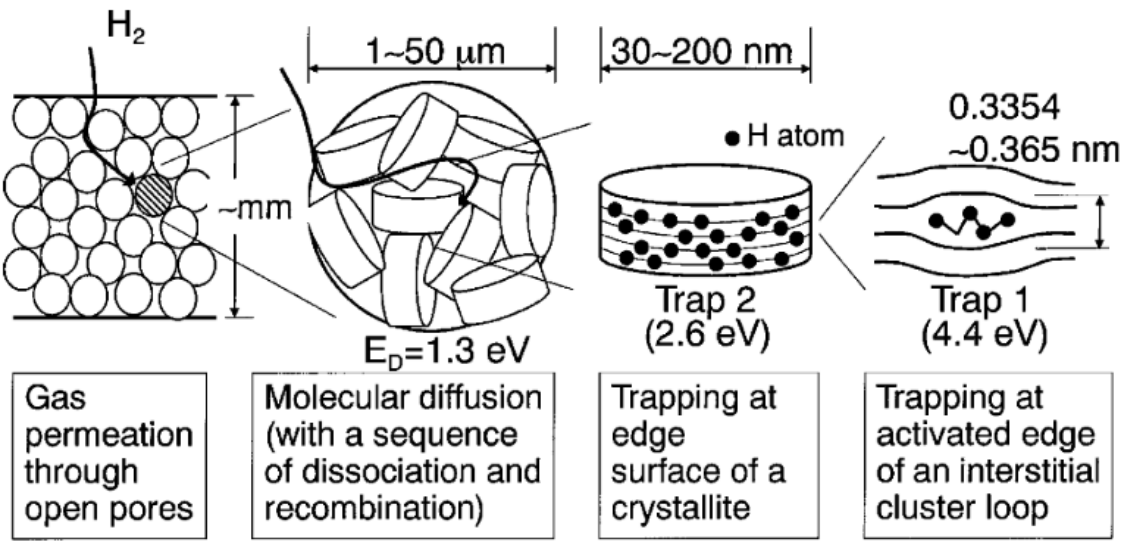

Figure 2.44. Illustration of hydrogen transport mechanisms in graphite open porosity, diffusion in filler grains, and trapping sites in crystallites. From [137].

Since diffusion in graphite grains is typically the rate limiting step for hydrogen retention, most retention models in previous studies do not factor in any considerations for molecular diffusion of hydrogen in graphite pores. For example, the DIFFUSE code results in Figure 2.41 were calculated for a single graphite filler grain modeled as a sphere [127]. Therefore, the model assumes that all grains inside the graphite were exposed to the same partial pressure of tritium during the 1.5 hour charging period. In high temperature or high partial pressure situations, the uniform concentration of hydrogen in graphite open pores is a reasonable assumption. However, tritium diffusion in graphite pores may be a significant factor in a FHR because temperatures and tritium partial pressures will be significantly lower than that of previous absorption studies. Graphite components in a FHR also have length scales much larger than the approximately millimeter thick samples used in most gas charging studies, which may result in significant tritium concentration gradients inside FHR graphite reflectors or fuel pebbles. Modeling tritium diffusion in graphite pores is one method to resolve these concentration gradients in the retention model. However, the available data for hydrogen diffusivity in graphite pores is very limited in literature.

As previously discussed, Atsumi et al calculated a pore diffusion coefficient for ISO-88 from TDS experiments [126]. Pore diffusion was distinguished from other mechanisms by considering that the desorption of Peak 1 corresponded to the release of D_2 retention in pores. Causey et al used a low temperature absorption study to estimate the tritium diffusivity in pores of POCO AXF-5Q graphite [108]. Therefore, the authors assumed that diffusion into grains was

negligible at low temperatures because of the high activation energy in the trapping and detrapping process. Thermal desorption experiments with helium as a proxy for hydrogen are another possible way to investigate gas diffusion in graphite pores. Helium has a similar molar mass to D_2 and can simulate the pore diffusion without any interference from interactions with trapping sites in graphite. Atsumi et al studied the thermal desorption of helium from various grades of nuclear graphite using a procedure similar to that of the hydrogen experiments [138]. While the diffusivity was not explicitly determined in the paper, a fit of the desorption profile can be used to calculate the helium diffusivity, as shown in Figure 2.45 for ISO-880U and IG-110U. The best available comparison between diffusivity measurements with hydrogen and helium are the ISO-88 and ISO-880U measurements, since ISO-880U is a higher purity grade with similar characteristics to ISO-88. As shown in the compiled pore diffusivity measurements in Table 2.15, the D_2 pore diffusivity in ISO-88 is roughly double the ISO-880U helium diffusivity at 600ºC. However, both measurements are significantly higher than the pore diffusivities of AXF-5Q and IG-110U graphite. A large spread in hydrogen grain diffusivity was also displayed in Table 2.14, which can reflect differences between graphite grades as well as overall uncertainty in the data. Therefore, a main limitation towards understanding tritium transport in graphite is a lack of precise measurements on the underlying transport phenomena.

Table 2.15. Measurements of tritium molecular diffusivity in graphite pores, $D_{T2,p}$. Values for ISO-880U and IG-110U graphite were fit from thermal desorption experiments with helium.

Graphite Grade	Measurement Technique	$D_{T2,p}$ [m^2/s]	$D_{T2,p}$ at 600ºC	Ref.
ISO-88	TDS	$1.47 \cdot 10^{-1} \exp(-121/RT)$	$8.50 \cdot 10^{-9}$	[126]
POCO AXF-5Q	Absorption	$1.2 \cdot 10^{-4} \exp(-86.8/RT)$	$7.70 \cdot 10^{-10}$	[108]
ISO-880U	TDS (Helium)	$2.05 \cdot 10^{-4} \exp(-77.5/RT)$	$4.74 \cdot 10^{-9}$	[138]
IG-110U	TDS (Helium)	$1.59 \cdot 10^{-5} \exp(-85.0/RT)$	$1.31 \cdot 10^{-10}$	[138]

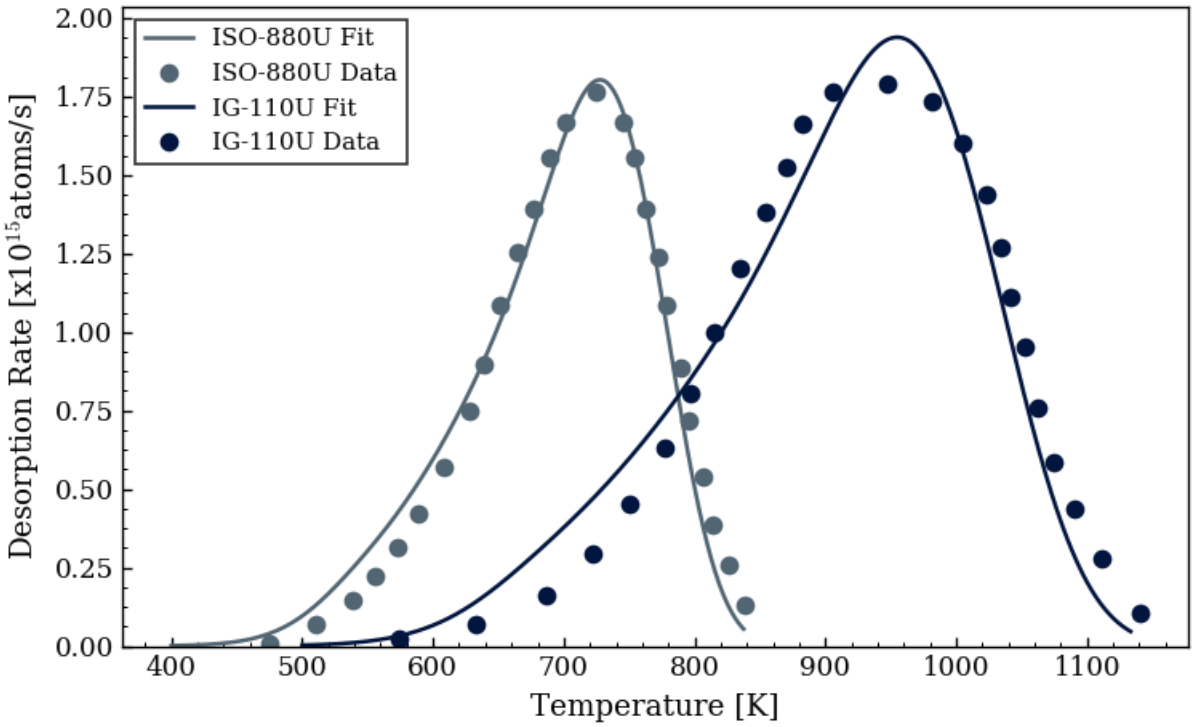

Figure 2.45. Thermal desorption of helium from ISO-880U and IG-110U graphite charged with 101 kPa of He for 1 hour and desorbed at 10ºC/min [138]. The desorption data was used with a diffusion model to fit a diffusivity for helium in graphite pores.

2.5.3. Influence of Molten Flibe on Tritium Retention

The previously described mechanisms for tritium transport and retention in graphite are only directly applicable to tritium dissolved as T_2 or HT gas in the Flibe coolant of a FHR, since the bulk of previous studies on hydrogen isotope retention in graphite were conducted with $H_2/D_2/T_2$ gas charging. This section describes a few examples of ways molten Flibe can influence the retention process from tritium generation, speciation, and physical properties of the salt itself. In situations where the influence of Flibe is non-negligible, the applicability of a HT/T_2 gas retention model should be evaluated and a more detailed transport model may be required for FHR results.

One potential discrepancy between tritium gas charging in graphite and tritium retention from Flibe comes from the tritium generation process itself. The tritium production reaction with lithium-6 is highly exothermic, and produces an ejected triton with an energy of 2.7 MeV following the neutron reaction [139]. If the ejected triton fully slows down in the salt, it could then be

expected to speciate into different chemical forms of the factors discussed in Section 2.2. However, there is also a possibility that the triton will be recoil implanted if it is born near graphite within the range of 2.7 MeV ions in Flibe. A range calculation for tritium ions in Flibe is shown below in Figure 2.46, which resulted in an average penetration depth of 47.1μm based on calculations with the SRIM code.

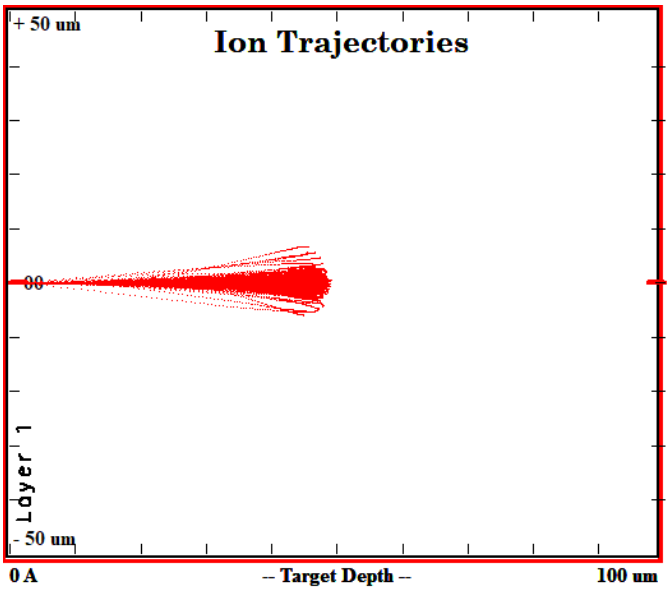

Figure 2.46. Range of 2.7 MeV tritium ions in 1.94 g/cm^3 Flibe calculated with SRIM.

Based on the SRIM range results, tritium retention can only occur through recoil implantation if it is born at a distance within roughly 50 μm of graphite. The MSRE can be used an example to assess the significance of recoil implantation to overall retention in graphite. An example MSRE fuel channel is shown on the left in Figure 2.47 below. The oval-shaped channel has an area of 287.5 mm^2 of which 3.63 mm^2, or 1.3%, is within a linear distance of 50 μm from the graphite wall. If the tritium generation is uniform in the salt throughout the fuel channel, then the 1.3% would represent the amount of tritium generated by lithium-6 which could be implanted. According to the isotopic generation numbers for the MSBR in Table 2.1, lithium-6 is expected to account for 50% of the total tritium generation. The other Flibe reactions, like with lithium-7, are endothermic and thus would have substantially lower triton recoil ranges. Therefore, 50% of the 1.3%, or 0.65% of total tritium retention can be explained by recoil retention in the MSRE. However, an estimated 15% of the total tritium generation throughout the MSRE operating lifetime was observed in the graphite moderator of the core [140].

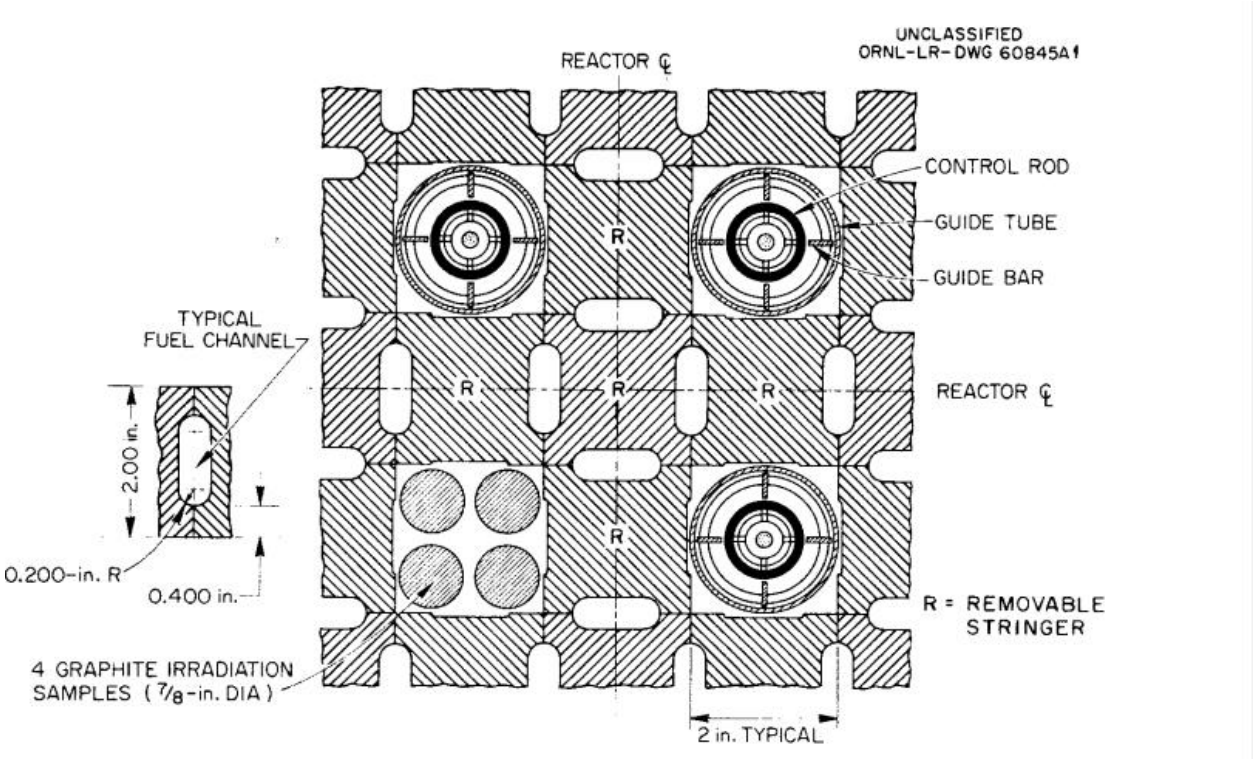

Figure 2.47. Control rod and moderator lattice in the MSRE with an example of a typical fuel channel. From [141].

The tritium concentration profile observed in the MSRE graphite also does not appear to be consistent with a recoil implantation process. Tritium content was analyzed in one of the removable graphite moderator stringers pictured in Figure 2.47 after the MSRE operating period was finished. The concentration profile was measured by successive cuts perpendicular to the graphite surface made with a 1.57 cm diameter rotating milling cutter [140]. Tritium concentration at the mean depth of each cut is plotted as a function of depth from the salt-graphite surface in Figure 2.48. The recoil range of tritons generated by lithium-6 was previously calculated to be 32μm for 1.89g/cm^3 pyrolytic graphite [142]. The tritium concentration in the MSRE graphite doesn't show any steep drop-off after the recoil range. Instead, it appears the tritium concentration decreases as continuous function of depth, which could be explained by a slow diffusion process into the MSRE graphite.

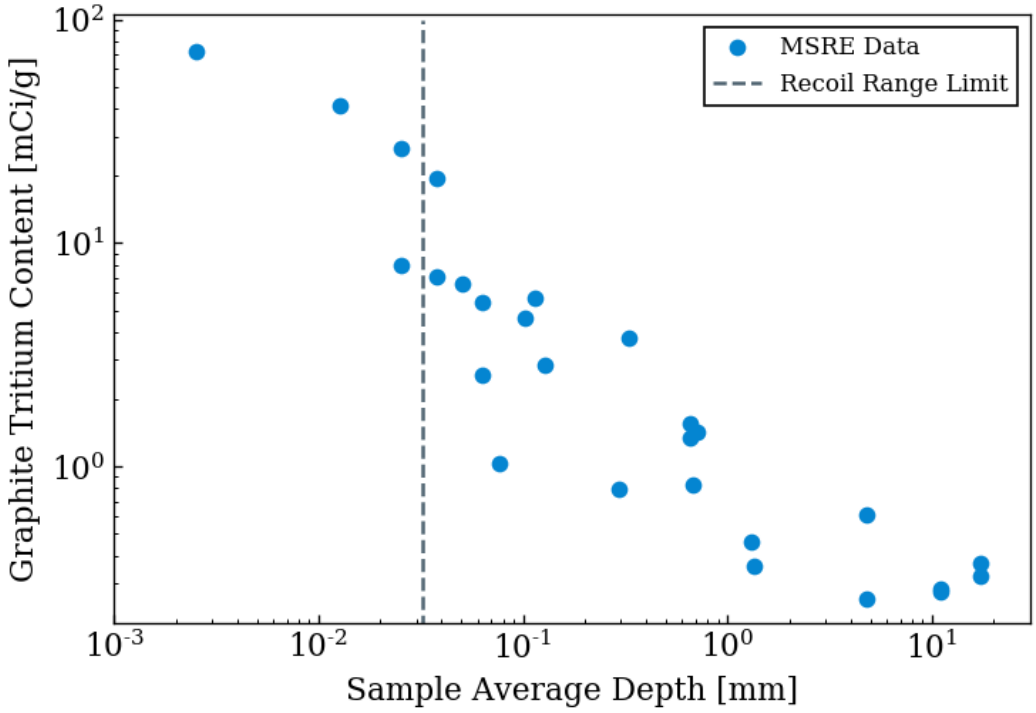

Figure 2.48. Tritium content in samples of the graphite moderator stringers after operation of the MSRE. The depth of measurements refers to the average of the starting depth and final depth in each sample taken from the graphite. From [140].

Another assumption in the previous section was that tritium diffuses as a gas inside the pores of the graphite, and therefore the graphite pores are not infiltrated by molten Flibe. Molten salt uptake into pores of the MSRE's moderator was inhibited by the physical properties of the CGB grade graphite. The graphite underwent multiple impregnation steps during fabrication to achieve an accessible porosity of only 4%, which was a precaution taken to reduce the penetration of fuel salt into the graphite pores [143]. Clean coolant salts without dissolved fuel result in less stringent graphite impregnation requirements for FHRs. However, molten Flibe infiltration is still a concern because it could damage graphite during melting and freezing cycles and could also affect the buoyancy of fuel and moderator pebbles in the salt. Flibe intrusion could potentially influence tritium retention in graphite by providing a mechanism for additional penetration of tritium into the graphite bulk. The main defense against Flibe intrusion is to use a graphite with a small enough pore size to prevent wetting of the graphite by salt. Four graphite grades were evaluated for Flibe intrusion by measuring the weight gain of samples before and after immersion in Flibe at 700ºC for 20 hours with results shown in Figure 2.49 [144]. An argon overpressure was

also adjusted for each experiment. At a certain critical pressure, the surface tension of the salt is overwhelmed and salt intrusion into the graphite begins to occur. The critical pressure increased with decreasing average pore sizes, which were 25μm, 4μm, 2μm, and 0.83μm for NBG-18, NG-CT-10, IG-110, and NG-CT-50, respectively [144]. As shown in Figure 2.49, Flibe infiltration is not expected to occur at atmospheric pressures for graphite with pore size at or smaller than the 2μm for IG-110.

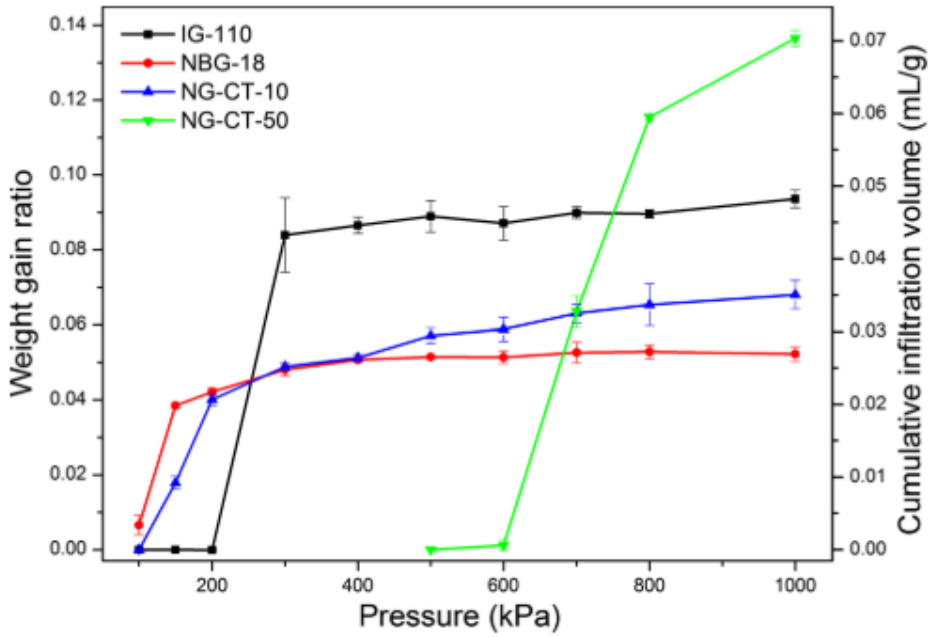

Figure 2.49. Weight change and cumulative infiltration of molten Flibe with various graphite grades tested at 700ºC for 20 hours. From [144].

An additional unknown in the Flibe-graphite system is the extent to which TF will interact with graphite. If TF can evolve to the off-gas above a salt, it will also likely diffuse as a gas into the open pores of graphite. Since retention in pores is a low portion of overall retention, the amount of total TF retention will depend on whether or not TF can engage with the same trapping sites as for T_2, or if there are additional trapping sites which can retain TF but not T_2. In tritium transport models made during the MSRE program, it was assumed that both TF and T_2 are retained equally by graphite [38]. However, in radiochemical analysis of the MSRE graphite after reactor operation, the graphite samples tested were dissolved in a boiling mixture of H_2SO_4 and HNO_3 and thus the chemical form of retained tritium could not be directly observed [140].

Better understanding of TF interactions with graphite is one motivation for additional experimental investigation into tritium retention in the Flibe-graphite environment. As shown in previous sections, even for T_2 there are also significant uncertainties caused by the spread in data reported on transport and trapping properties. Furthermore, most research on adsorption of hydrogen isotopes in graphite has been carried out at temperatures and charging pressure well above the relevant FHR range. Beyond retention in graphite, the integrated effects of tritium generation, speciation, and transport in molten Flibe create a range of uncertainties which make the tritium distribution in a FHR difficult to accurately predict. The tritium transport phenomena and current available data discussed in this section are important to understand in order to grasp the scope and limitations of models that can calculate tritium transport at the reactor-scale. In this study, observations from Flibe irradiation experiments at the MIT Reactor were analyzed in order to assess tritium transport behavior and identify knowledge gaps. Lessons learned from irradiation experiments were then used to propose a method for calculating tritium retention in system-level tritium transport models. Ultimately, the updated system-level model was used to explore tritium management strategies for a commercial-scale FHR.

3. Tritium Distribution in MITR Fluoride Salt Irradiations

The In-core fluoride-salt (FS) irradiations at the Massachusetts Institute of Technology Reactor (MITR) provide valuable insight into tritium transport mechanisms at prototypical FHR conditions. In particular, the tritium analysis of graphite samples from MITR experiments are the first retention measurements of graphite irradiated in Flibe since the MSRE program at ORNL. Measured partitioning between the irradiation off-gas and retention in graphite samples can also be used to determine the tritium distribution in each irradiation. To date, three in-core fluoride salt experiments have been completed at the MITR, which are denoted chronologically as FS-1, FS-2, and FS-3. The run dates for each experiment were September 13th to October 29th of 2013, July 8th to August 12th of 2014, and November 8th to December 18th of 2016 for FS-1, FS-2 and FS-3 respectively. One additional irradiation, FS-4, was also conducted in the MITR graphite reflector on April 26th and 27th of 2018. The unique features of the irradiation facility and test capsules are described in this section along with important observations on tritium transport and retention in graphite gained from each irradiation.

3.1. In-Core Experiment Design and Irradiation Facility

The three in-core Flibe experiments each contain similar features and design elements, but lessons learned from each test lead to design improvements for subsequent experiments. One common feature, for example, was the use of IG-110U graphite as the salt containing crucible material. The grade IG-110U refers to a high purity isotropic graphite manufactured by Toyo Tanso [17], and a large quantity of IG-110U procured prior to the FS-1 irradiation was used to manufacture crucibles and certain test samples for all three irradiations. Graphite crucibles prior to salt and test sample loading are shown in Figure 3.1. As shown in the figure, the number of axial graphite crucible sections increased from 1 to 3 from FS-1 to FS-3, respectively. Additional dimensions for the graphite crucibles in each experiment are provided in Appendix A. The graphite axial sections were contained inside of a Nickel 201 capsule with an Inconel 800H upper cap. Nickel was selected for chemical resistance against corrosion from salt vapor and unstable fluorides which can potentially be produced by radiolysis, although significant corrosion was not expected from normal experimental conditions. The Inconel 800H alloy was chosen to add strength for the threaded region which sealed the capsule body to the upper cap [40].

Figure 3.1. FS-1 graphite crucibles (left) and FS-2 graphite (center) along with nickel capsule used for east test. The FS-1 graphite holes are 1 cm in diameter and nickel capsules have similar diameters. Graphite crucibles for FS-3 are pictured on the right. From [17, 145].

Each in-core irradiation required Flibe with high levels of lithium-7 enrichment to prevent excessive tritium generation. There are currently no commercial suppliers for lithium-7 enriched to the levels required for FHR applications. For example, PWRs use enriched lithium-7 as an additive to the reactor coolant, but only at enrichments of 99.95% [30]. The salt for MITR Flibe irradiations was donated by ORNL and was sourced from the secondary coolant loop of the MSRE. The MSRE primary salt was enriched to 99.995% lithium-7, but the secondary Flibe coolant had a lithium-7 content between 99.990% and 99.991% as measured during the initial salt purification [57]. Prior to the MITR irradiations, the MSRE salt was regenerated to an acceptable chemical quality to alleviate potential degradation from decades of storage at ORNL [16]. The purification process resulted in Flibe with impurity levels of nickel, iron, and chromium that were below the targets set for the MSRE program [39]. Salt after the purification process is shown in Figure 3.2. Qualitative observations that demonstrate the salt quality and low impurity concentrations are the white color and large, translucent grains.

Figure 3.2. FS-1 Flibe (left) and FS-2 and FS-3 Flibe (right) after purification. From [60].

The Flibe salt, test samples, and graphite crucibles are sealed by the capsule and the process tubing in the primary gas boundary. Beyond the capsule region, the irradiation experiment assembly was contained in an additional secondary encapsulation, referred to as the 'thimble.' The thimble creates a gas-tight barrier with the MITR water and a separate gas region where tritium permeation from the capsule could be monitored. Titanium is used as the thimble material due to its relatively low neutron cross section and suitable decay time. The thimble occupies a fuel element slot in one of the central MITR core positions, as shown in Figure 3.3. Reactor water flow outside of the thimble provides heat removal for the titanium wall, which must be cooled sufficiently to prevent the onset of nucleate boiling with the primary water as specified by the MITR license requirements [146]. A cooled thimble wall is also useful for Flibe irradiation applications because it reduces tritium permeation through the titanium boundary and prevents tritium losses prior to the measurements.

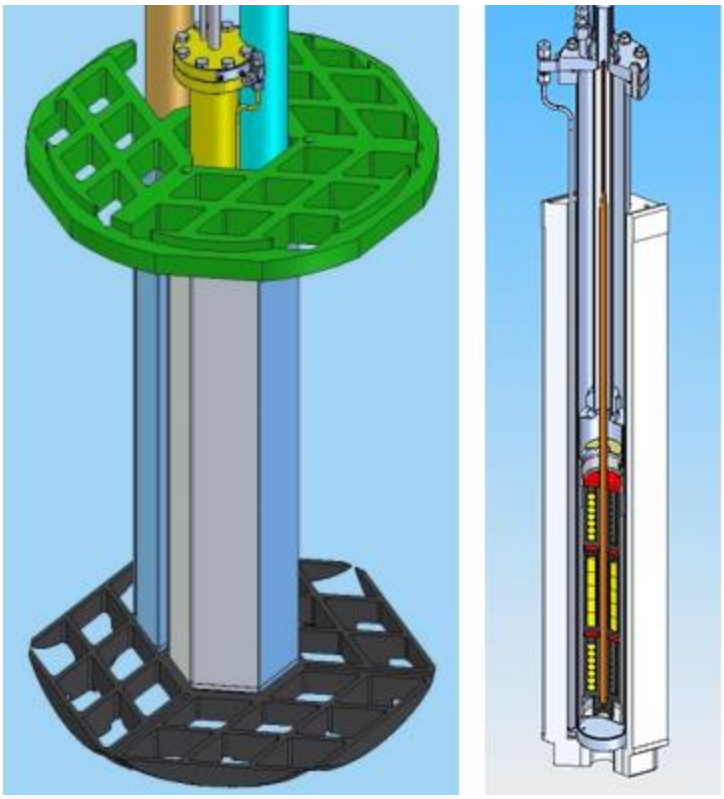

Figure 3.3. Arrangement for the FS-2 thimble (left) in the MITR core with other fuel elements removed and cross section of the FS-3 thimble and capsule internals, with samples pictured in yellow (right). From [40].

The primary source of heating for each Flibe experiment was nuclear heat from gamma and neutron energy deposition in the capsule materials. The heating rate can be calculated from a MCNP full core model of the MITR core which includes the fluoride salt experiment. For a MITR core power of 5.9 MW, the MCNP-calculated heating rates for the nickel, graphite, and Flibe in FS-3 were 2.5, 2.4, and 2.3 W/g respectively [40]. The desired irradiation temperature of 700ºC in the capsule is maintained by varying the ratio of helium to neon in the thimble sweep gas, where neon is added to decrease the gas thermal conductivity and raise temperatures. Using the MCNP-calculated heating rates, the capsule temperature profile was simulated using the ANSYS Fluent CFD code. Fluent models with 100% helium and 100% neon conditions produce the lower and upper limits for the experiment operating range, as shown in Figure 3.4, [40].

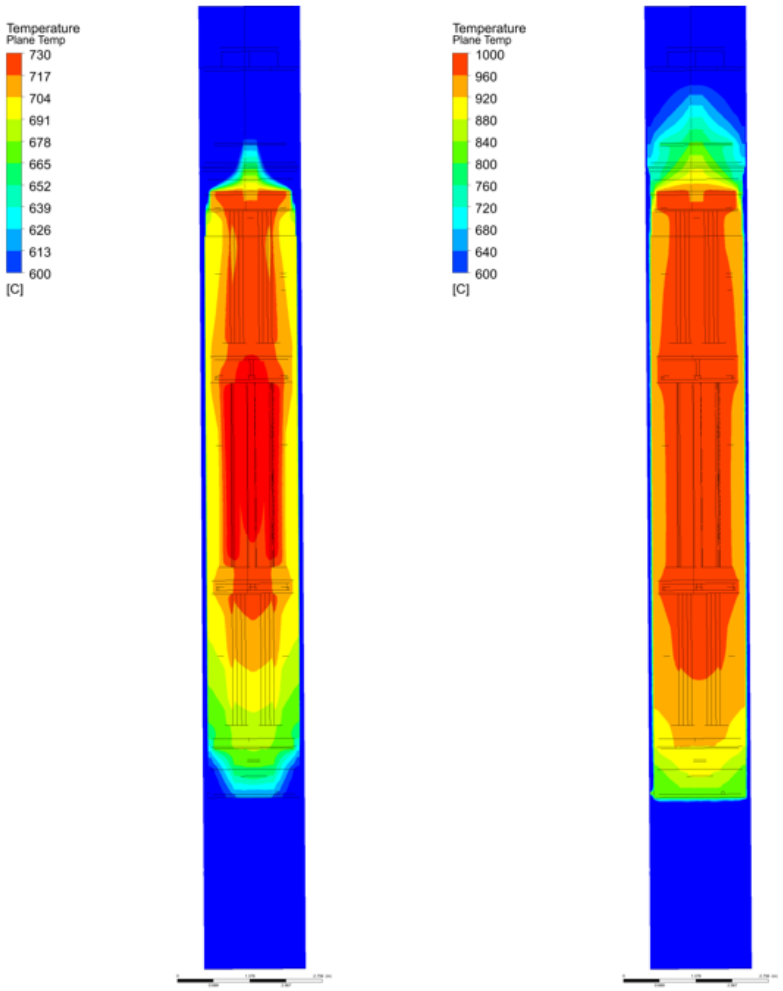

Figure 3.4. Thermal analysis for the FS-3 capsule with 100% helium thimble sweep gas (left) and 100% neon (right). Each model is shown with a separate temperature scale. From [40].

Capsule and thimble regions are continuously swept with an inert gas throughout the irradiation. The thimble contained a helium-neon mixture for temperature control, while the capsule gas is supplied with only helium. Total gas flow rates near 100 cc/min in each region were used, and gas flow inlets were placed towards the bottom of the capsule or thimble and swept upwards [17]. Each experiment was designed to allow for separate tritium sampling in each off-gas stream using a water bubbler trapping system supplied by TYNE Engineering [147]. A conceptual diagram of the water bubbler is shown in Figure 3.5. In the first three vials, water-soluble tritium forms are readily captured. Possible sources of water soluble tritium from the Flibe irradiations can be HTO, T_2O, or TF. The vials are placed in series in order to confirm that tritium is not carried out of the vial sets in significant quantities. There was usually an order of magnitude decrease in tritium concentration between vials, with less than 1% of the total tritium in each set

contained in the third vial. After the first three-vial set, the process gas stream is combined with a He-1%O_2 mixture in a furnace maintained at 450ºC. The palladium-coated alumina catalyst in the furnace oxidizes the insoluble forms of tritium, such as T_2 and HT, into soluble forms. Converted HT and T_2 are then captured in the second set of vials in the same manner as the initial set. The gas flowing out of the bubbler system passes through a backup water collector and a charcoal filter before exiting the reactor building ventilation system.

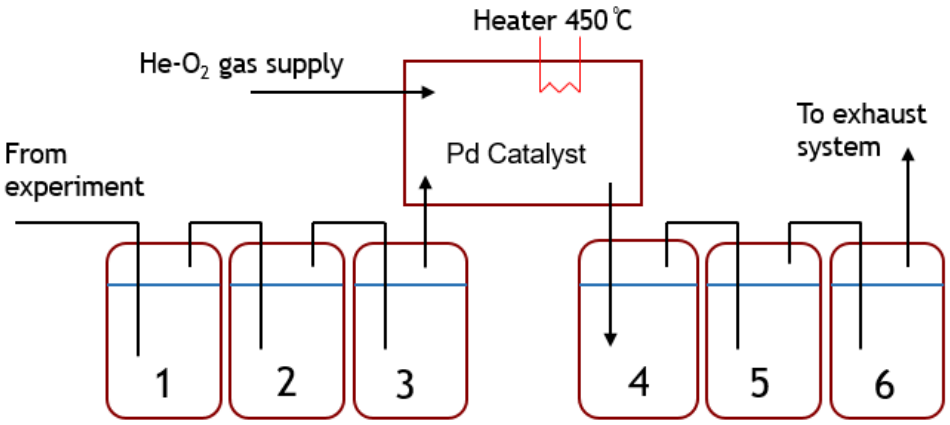

Figure 3.5. Conceptual diagram of the 6-vial water bubbler and catalyst furnace.

After collection in the water bubbler, the tritium concentration can be analyzed through liquid scintillation counting (LSC). A small sample of water from each vial is added to a scintillation mixture of PerkinElmer Opti-Fluor liquid which is then counted with a Packard TRI-CARB 2900TR Liquid Scintillation Analyzer [17]. The LSC specimens were prepared using 16 mL of scintillation fluid and a 0.1 mL sample of water from the vial taken with a micropipette. Volumes of each fluid were selected to create a condition where a beta particle decay would result in full energy deposition inside the fluid. Beta decay energies are determined by the detector, which are separated into energy bins to represent tritium, carbon-14, and phosphorus-32. Tritium has the lowest energy bin from zero to 18.6 keV, therefore the LSC can discriminate between tritium and high-energy beta emitters, although activity from other bins was typically very low compared to measured tritium. The total tritium content in each water bubbler vial is calculated based on the specific activity in the 0.1 mL sample. The tritium trapped in the vial sets divided by the time the vials were exposed to the off-gas stream results in a coarse calculation for the tritium release rate from the in-core experiment.

3.2. Tritium Release Measurements

There were several additional objectives of the MITR in-core Flibe irradiations beyond the tritium transport measurements discussed in this section. A wide range of candidate FHR materials were tested as well as Flibe salts at different chemical redox potentials to assess corrosion under irradiation [145]. In order to represent the neutron flux levels and temperatures expected in an FHR, these fluoride salt irradiations were carried out in the MITR core, where the spatial dimensions and allowable materials of each test are significantly constrained. Therefore, the tritium released from the experiment had to be trapped and measured by an external system on the reactor top. One challenge for the tritium release measurements in the MITR irradiations, and all other similar tritium experiments, is preventing losses and holdup of tritium during the transit through the gas piping from the in-core experiment to the tritium measurement systems. Experience gained from each in-core experiment provided insights into improved design features which enhanced the tritium sampling capability from one experiment to the next.

Quantifying the tritium production rate prior to the experiment is an essential step in understanding the tritium release observations. Before the irradiations took place, the amount of tritium generation was calculated with MCNP in units of mCi/MWd, where the megawatt-days refers to integrated power from the MITR core. Among the in-core irradiations FS-1, FS-2, and FS-3, the most significant factor in tritium production was the mass of Flibe loaded into the crucible, as shown in Table 3.1. However, the FS-4 production rate was orders of magnitude higher than the previous three experiments even though the salt mass was the lowest. This is because the FS-4 salt used natural-lithium Flibe at 7.59% Li-6 compared to the 0.01% Li-6 enriched salt used in the in-core irradiations [41]. Furthermore, the FS-4 tritium production rate is roughly two orders higher than the enriched salt irradiations despite the irradiation taking place in the MITR graphite reflector port where fast flux is negligible and thermal flux is roughly 1 order of magnitude lower than in-core [146]. Since the irradiation took place in a different facility and contained no graphite test samples, the FS-4 irradiation is not discussed in this section. Additional description of the FS-4 irradiation and tritium measurements are available elsewhere [49]. For the in-core irradiations, the calculated tritium generation values allow the observed release measurements from each experiment to be analyzed in terms of an overall tritium distribution.

Table 3.1. Flibe mass and tritium production from each MITR irradiation calculated by MCNP. The FS-4 experiment used natural-lithium Flibe while all others had lithium-7 enrichment.

Experiment	Flibe Inventory [g]	^{3}H Production Rate [mCi/MWd]
FS-1	121.2	2.63
FS-2	326.4	7.64
FS-3	101.5	2.71
FS-4	35.0	181

3.2.1. Tritium Release from Inert Off-Gas in FS-1 and FS-2

Several unexpected trends were observed in the tritium release measurements from FS-1. As shown in Figure 3.6, the initial capture rate measured in the capsule sweep gas was about 10% of the total estimated tritium generation rate. Release from the capsule decreased to less than 1% of the generation a few days into the experiment. A similar decreasing trend was also observed for tritium in the thimble sweep gas. Measured collection rates significantly lower than the calculated tritium generation rate suggest tritium interactions with the sweep-gas tubing prevented tritium from reaching the water bubbler system placed on the reactor top. Sweep gas flow and tritium sampling continued for several days after the 1000 hour irradiation when the reactor was shut down. In Figure 3.6, the collection rate appears to be unaffected by the reactor shutdown even though tritium production stopped after day 41 of the experiment. Therefore, the tritium measurements during FS-1 most likely reflected only the tritium coming to the water bubbler after a significant holdup time caused by interactions with the tubing. However, this explanation is not consistent with the higher collection efficiency observed during the beginning of the irradiation. It is possible that impurities such as oxygen or moisture in the gas tubing lines changed the surface conditions on the tubing interior which led to more interaction sites for tritium as the experiment progressed.

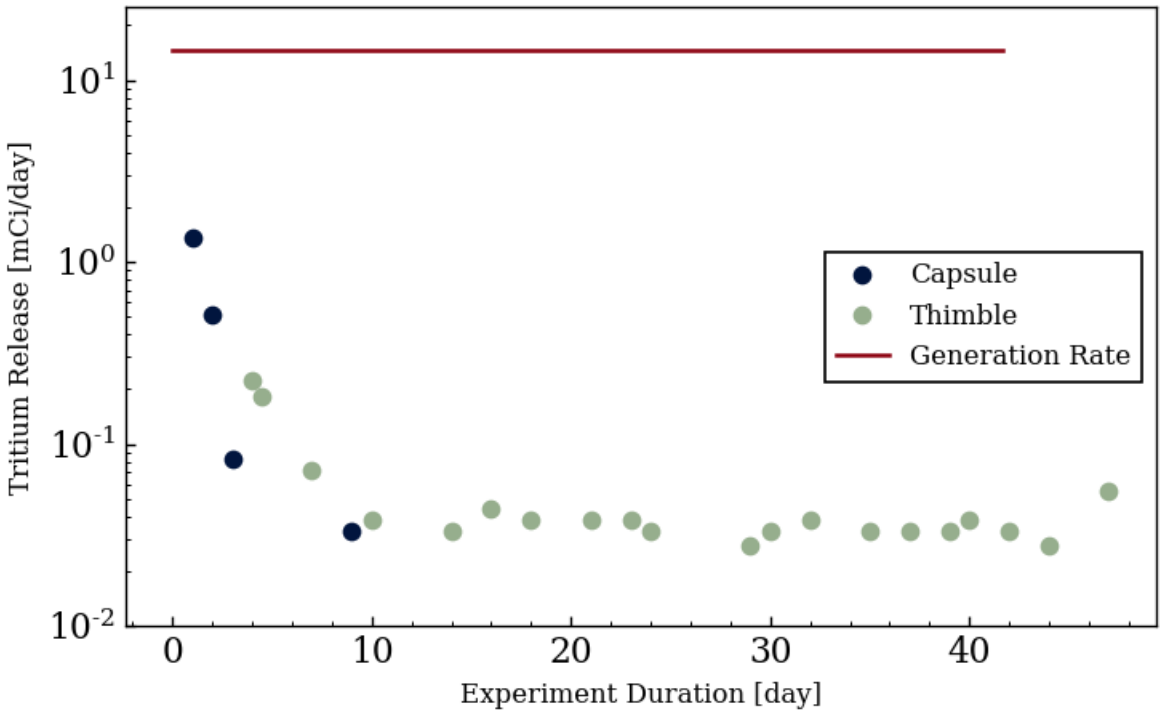

Figure 3.6. Tritium measurements in the FS-1 capsule and thimble regions as measured by the water bubbler system with periodic sampling and liquid scintillation counting. The observed release rate in each region was significantly lower than the calculated generation rate.

An additional issue observed in the FS-1 irradiation was a flow restriction which developed in the capsule off-gas line and interrupted tritium sampling near day ten of the experiment. The hypothesis for the flow blockage was condensation of volatile fluorides on the cold surfaces of the tubing above the heated zone [17]. Therefore, the FS-2 design used a modified the capsule line which was increased to a 1.27 cm (½-inch) diameter to reduce sensitivity to deposited vapors. A nickel flow-diverter plate was also added above the salt crucibles in order to force flow towards the cooler capsule upper plenum wall before exiting the exhaust line, thereby causing condensation onto the capsule walls instead of the tubing port. The release measurements in Figure 3.7 show that the added design improvements allowed for tritium sampling in both the capsule and thimble regions throughout the duration of the experiment. However, a collection rate of less than 1% was observed compared to the predicted generation rate, as seen in the FS-1 test. While the quantity of tritium release was lower than expected, the relative amounts measured between the capsule and thimble in FS-1 and FS-2 demonstrate that tritium was able to readily permeate through the nickel capsule at the irradiation temperature of 700ºC.

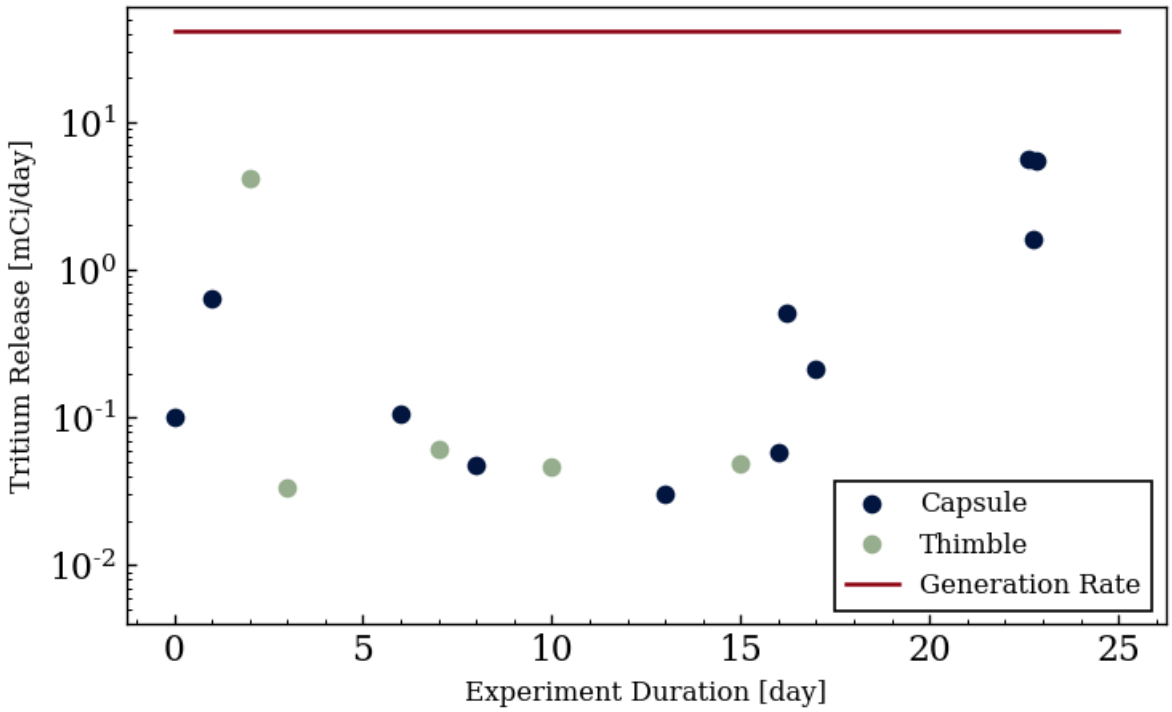

Figure 3.7. Tritium releases observed during the FS-2 irradiation plotted against the predicted generation rate.

Chemical form of captured tritium release during FS-1 and FS-2 was also monitored using the water bubbler system. The fraction of soluble tritium was calculated for each data point in Figure 3.6 and Figure 3.7, which is defined as the total activity in vials 1 to 3 prior to the catalyst furnace divided by the sum of activity in vials 1 to 6. Over half of the tritium measured at all points in both FS-1 and FS-2 was in a soluble form. The trend of solubility fraction shown in Figure 3.8 also shows some dependence of tritium chemical form on the experiment duration. At the beginning and end of each irradiation, the tritium release had a higher fraction of solubility than during the middle portions of the experiment. The trend with experiment duration also has some relation to the irradiation temperature, since samples were taken as the experiments were approaching their target temperatures as well as when the reactor was shut down and the salt capsules were cool [147]. One possible explanation is that gamma radiation from fission products in the MITR fuel could create free fluorine gas through radiolysis when the salt was frozen and the reactor was shut down prior to or after the irradiation period. It was observed during the MSRE program that irradiation of frozen Flibe liberates fluorine as a gas, but thermal recombination converts F_2 radiolysis products back to stable fluoride forms at temperatures above roughly 100ºC

[148]. Another explanation is the interaction of tritium with oxides on the tubing walls. In deuterium permeation studies with oxidized 316SS, the chemical form downstream of the sample shifted from D_2 to D_2O at temperatures below 500K [113]. However, it is difficult to make any conclusions about the overall chemical forms of tritium in each experiment since the low collection rate meant the majority of tritium was unaccounted for in FS-1 and FS-2 release measurements.

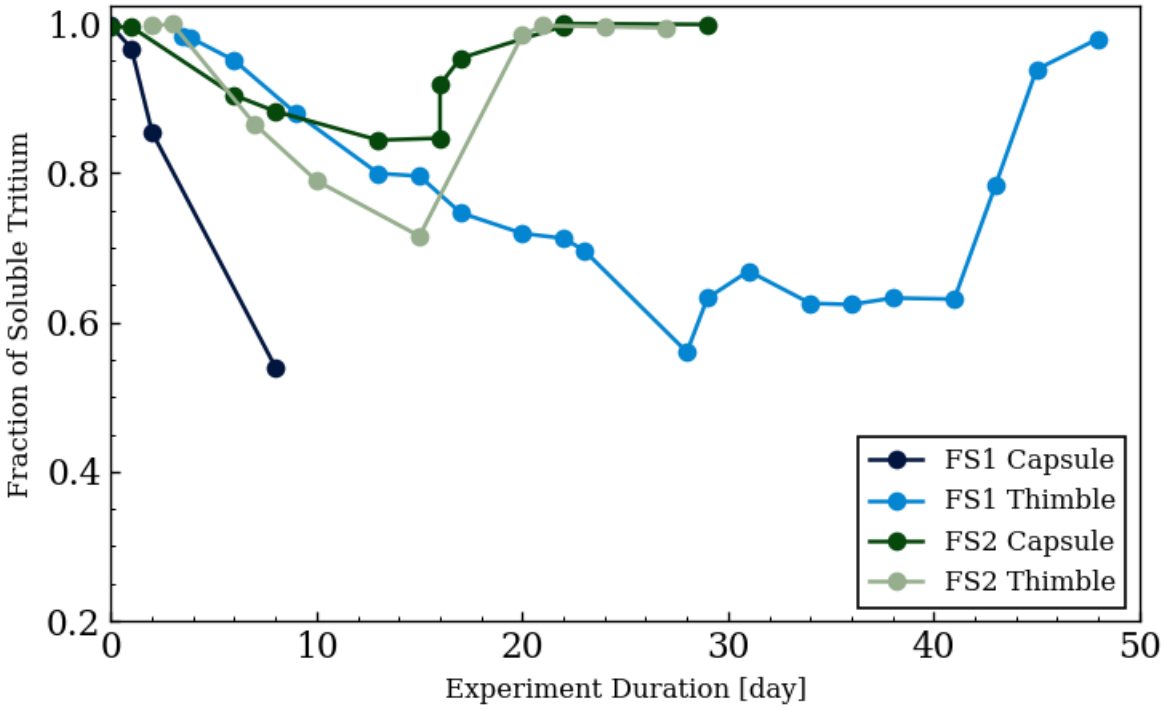

Figure 3.8. Ratio of tritium in vials 1-3 of the water bubbler verses tritium in all vials used to determine the fraction of tritium soluble in water during FS-1 and FS-2. Soluble forms would indicate either HTO/T_2O or TF while insoluble forms would be HT/T_2.

3.2.2. Tritium Release from Off-Gas with H_2 Addition in FS-3

A major change between FS-1/2 and FS-3 was the addition of hydrogen to the off-gas streams of the capsule and thimble to combat parasitic interactions of tritium with the gas tubing. The use of hydrogen in the first two experiments was avoided so that added hydrogen would not interfere in tritium interactions with sample materials in the capsule. For example, additional hydrogen could occupy trapping sites in graphite samples and crucibles of each experiment and prevent further retention by tritium. Because of the low tritium collection efficiency in FS-1 and FS-2, the decision was made to add a 50 cc/min He-3.5%H_2 (3.5% H_2 by volume) injection into

the 100 cc/min flow streams of the FS-3 capsule and thimble regions. Design precautions were made to limit the amount of hydrogen which could enter the capsule or thimble regions near the irradiation zone. The He-3.5%H_2 was added to the capsule flow gas stream in a separate flow tube which discharged into the central exhaust tube downstream of the capsule top. For the thimble, hydrogen was added in a junction near the thimble flange. Therefore, in both cases He-3.5%H_2 was injected into flow gas streams past the end of the encapsulated regions so that hydrogen could saturate interaction sites in the tubing in between the irradiation zones and the tritium bubbler system.

The hydrogen addition in FS-3 had a profound effect on the chemical form of tritium measured in the water bubbler system. As shown in Figure 3.9, the fraction of soluble tritium was below 1% for the majority of the irradiation in both the capsule and thimble regions. Like FS-1 and FS-2, there was also an increase in soluble tritium in samples at the beginning and end of the irradiation. A surprising result was the elevated soluble fraction in the thimble compared to the capsule – TF evolution would only occur in the capsule region and would register as soluble tritium. Therefore, the influence of TF in the capsule was likely less significant than HTO produced by interactions with oxide or moisture impurities in the process tubing. If the added hydrogen was able to back-diffuse into the capsule irradiation zone, then isotopic exchange in the salt phase could have produced HT in the same manner as in the Flibe irradiations conducted by Suzuki et al [44, 48]. Another possibility is that hydrogen was not present near the capsule, but isotopic exchange still converted HTO or TF into HT in the gas phase or on metal surfaces in the off-gas tubing.

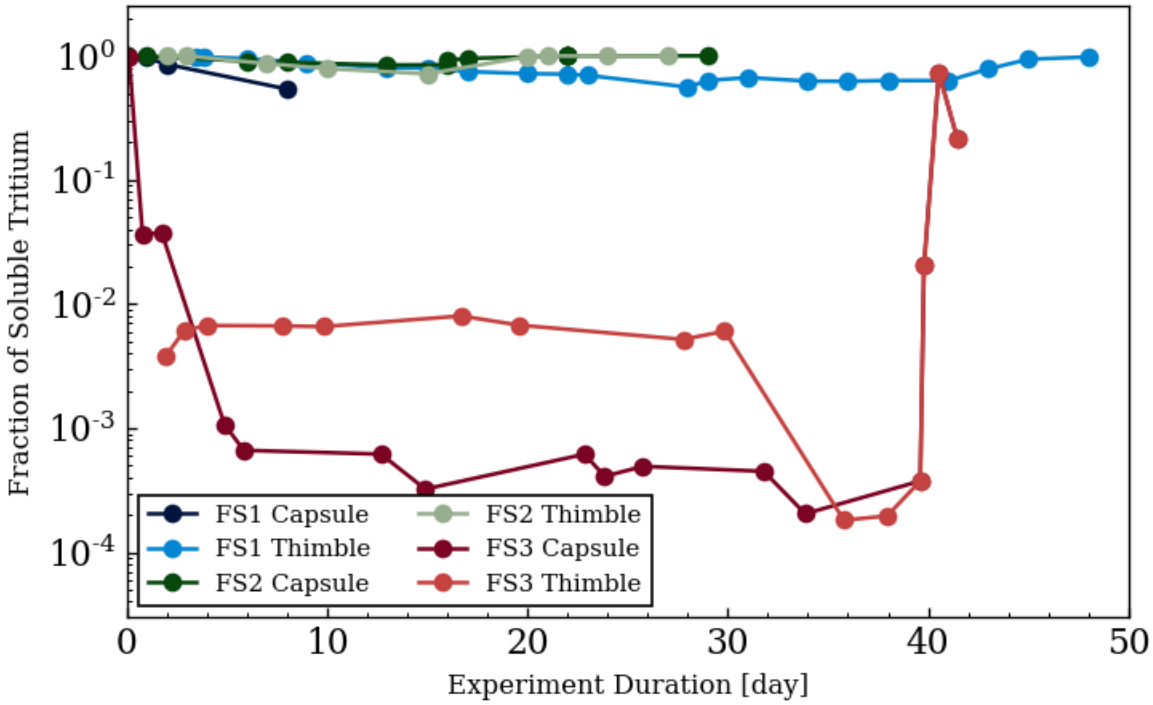

Figure 3.9. Fraction of soluble tritium in the three MITR in-core Flibe irradiations. Hydrogen addition into the FS-3 sweep gas resulted in predominantly insoluble tritium (T_2/HT) measured in the tritium water bubbler.

The addition of hydrogen into the sweep gas of the FS-3 experiment makes it difficult to determine what the original chemical form of tritium was upon release from the salt. However, the hydrogen addition significantly improved the tritium collection efficiency compared to FS-1 and FS-2. The measurements in Figure 3.10 show that the sum of tritium release in the capsule and thimble region was comparable to the total tritium generation rate. With the improved release measurements, more details are added to the FS-3 release plot in order to further describe tritium accountancy from the irradiation. For example, the tritium generation rate in Figure 3.10 accounts for changes in lithium-6 concentration during the experiment, which lead to an overall decrease in tritium generation rate of 3.3% after 40 days of MITR operation [41]. The MITR power was constant at 5.5MW during the 960-hour FS-3 irradiation except for a 3 hour downpower during the second day, which is neglected in this analysis.

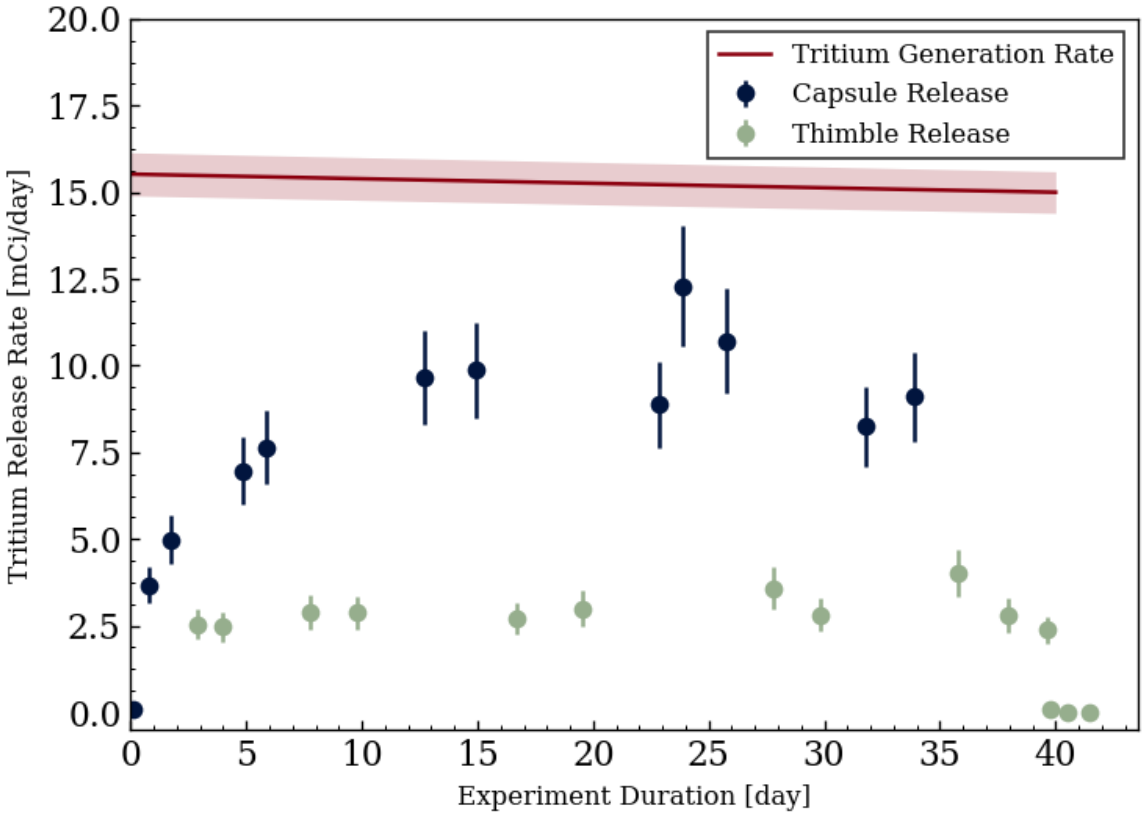

Figure 3.10. Tritium release from the capsule and thimble regions of the FS-3 experiment during the irradiation in comparison to the calculated total production. Uncertainty in tritium generation is represented in the shaded red region.

As shown in Figure 3.10, the sum of tritium releases in the capsule and thimble from the latter half of the experiment begins to approach the total generation rate. However, there is a notable low release rate from the capsule at the beginning of the experiment which increases towards equilibrium over roughly a 15 day period. The difference between the total releases and the generation rate can be used to estimate the amount of tritium retained inside the capsule materials. Since the bubbler could only sample one region at a time, a simple linear interpolation method was used to calculate the release rate in the unsampled region [18]. While other factors exist, the uncertainty in the tritium generation rate was calculated based on the uncertainty in lithium-6 concentration of the Flibe. During production of the MSRE secondary loop Flibe, 22 separate batches were made and the lithium isotopic assay was assessed in each batch. Of the batches listed, 13 had a lithium-6 wt% of 0.009 while 9 were measured at 0.010 [39]. Weighting each measurement by the kilograms in the batch and taking the standard deviation of the group

results in a relative standard deviation in the Li-6 value of 6%. Since Li-6 supplied 65% of total FS-3 tritium generation [41], the contribution of Li-6 composition uncertainty to the total tritium generation uncertainty is 4%. The integral of the tritium generation rate in Figure 3.10 along with the calculated uncertainty produces a calculated total tritium generation of 589±24 mCi during the FS-3 experiment.

For the capsule release rate uncertainty, the relative standard deviation is used from the 7 capsule data points starting with the point at day 12.7. Similarly for the thimble region, 6 thimble data points are used staring at day 16.7 until the point at day 38.0 (the point at day 39.6 includes some of the reactor shutdown period so it was not used in the thimble standard deviation). These relative standard deviations are 14% and 17% for the capsule and thimble, respectively. While the same measurement process is used for both regions, the difference in standard deviation between the thimble and capsule could be explained by different temperature and gas flow fluctuations in the regions along with unique tritium interactions with other materials present. Considering the overall release, there was then 350±49 mCi collected from the capsule and 110±19 from the thimble, which results in a total measured release with uncertainty propagated is 460±53 mCi. Therefore, the difference between tritium generation and the total release accounts for 22%±10% of the total tritium generation. Analysis of graphite samples after the irradiation was conducted to better understand whether or not retention in graphite could explain a significant fraction of the unreleased tritium.

3.3. Post-Irradiation Tritium Desorption of Graphite Samples

With tritium generation and releases quantified, understanding the amount of tritium retained in graphite components of each in-core irradiation was a vital step remaining towards understanding the tritium distribution of the experiment. Monitoring tritium contained in samples is a unique challenge because of the weak beta decay signal with a maximum energy 18.6 keV and no associated gamma emissions [149]. Therefore, accurately counting tritium in graphite typically requires an effective way of extracting the radioisotopes out of the sample. Several extraction methods are described in literature, such as dissolution of graphite in perchloric acid, dissolution in nitric and sulfiric acid, and combustion with oxygen [150, 151, 140]. A destructive technique like dissolution or combustion is useful for quantifying the total tritium content in a sample, but perturbs information on the storage mechanism and chemical form of tritium during the

measurement process. A less disruptive technique is oxidative thermal desorption, where samples are heated in the presence of oxygen to covert tritium to HTO and facilitate desorption [149]. Oxidative thermal desorption can provide information on desorption rate as a function of temperature, but will still convert tritium to HTO during desorption. Desorption of graphite samples against vacuum is another option used previously with studies on gas charging of hydrogen and deuterium [115, 126], but for tritium analysis this would require a complex vacuum system capable of handling tritium loads. Therefore, desorption of samples in inert gas was used in this work in order to best preserve the chemical form of trapped tritium and produce information for tritium desorption mechanisms.

3.3.1. Desorption of FS-2 Graphite Samples in a Steel Vessel Furnace

The design of a custom thermal desorption furnace for the MITR graphite samples was also informed by the lessons learned during tritium release measurements from FS-1 to FS-3. Several design features were added to prevent tritium interactions prior to the tritium measurement systems. Off-gas tubing as well heater internal surfaces create possible tritium interaction sites which can impede the measurement. Therefore, the furnace used an Ar-4%H_2 sweep gas mixture to saturate surface sites with hydrogen, as in the FS-3 test. For the furnace application, argon was suitable as the base gas instead of helium because the furnace was an out-of-core application. In addition to surface interactions, tritium permeation through the heater wall was a potential issue. A copper tube cooling water jacket was wrapped and brazed to the 304 stainless steel furnace vessel in order to cool the steel vessel and reduce the wall permeability. The water was circulated through a chiller throughout the experiment, with a typical cooling water outlet temperature below 30ºC. The water bubbler system used in FS-3 and described in Figure 3.5 was paired with the desorption experiment. Furnace internal components and the water cooling jacket are shown in Figure 3.11.

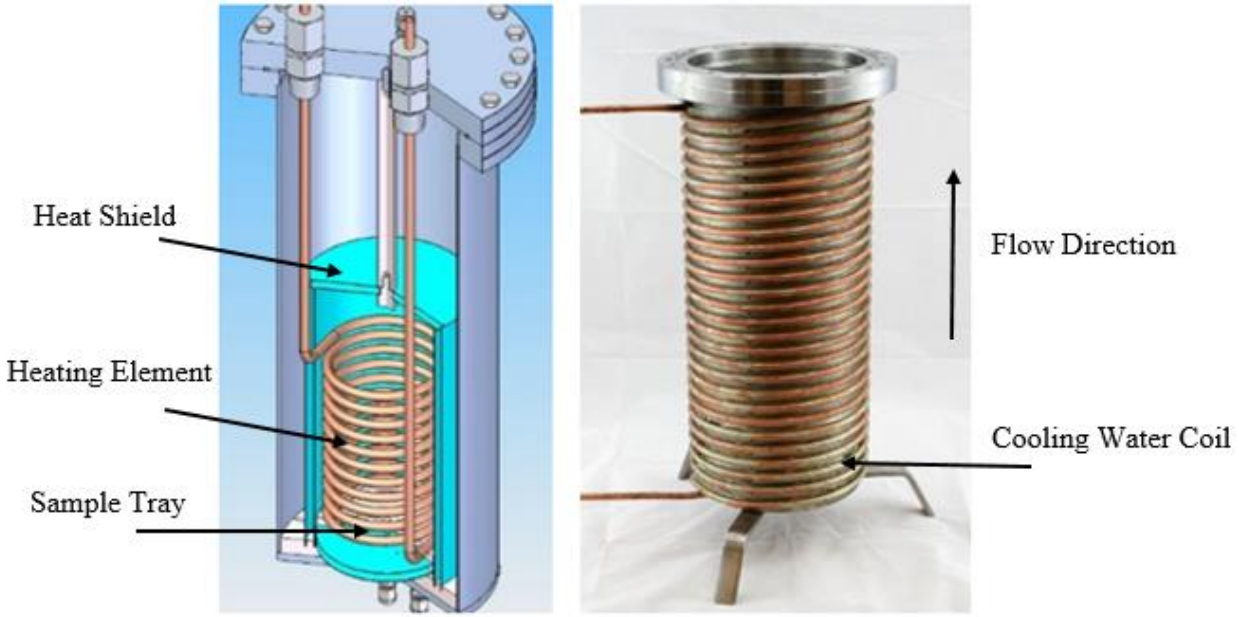

Figure 3.11. Steel vessel thermal desorption furnace cutaway drawing of internal features (left) and outer vessel showing the cooling coil (right). Water circulating through the exterior copper coil cools the body of the furnace to prevent tritium permeation losses. From [18].

High-temperatures required for the desorption furnace were enabled by a molybdenum disillicide heating coil provided by Micropyretics Heaters International. A large coil zone of 2.75" diameter and 5.5" height allowed flexible sample geometries to be tested. Around the heater, a cylindrical molybdenum heat shield radiatively insulated the coil. The heat shields are formed by cylindrical sheets in the lower assembly and circular plates that connect to the upper flange, as shown in light blue in Figure 3.11. Electrical isolation between the coil and furnace is provided by an alumina rod that connects the upper heat shields and insulating fittings that secure the coil to the upper flange. While the heating coil was capable of output temperatures up to 1850 ºC, the furnace in practice could only reach a maximum temperature of around 1000ºC, as measured by the thermocouples under the alumina sample. The heat shields only provided limited insulation and the active cooling of the furnace wall was a significant heat sink. A porous or ceramic insulation material in addition to the molybdenum sheets inside of the furnace vessel could raise achievable sample temperatures, but would create additional tritium interaction sites that might disturb the measurement process. The temperature limitations were a notable limitation of the initial steel furnace design.

Compared to the FS-3 release measurements, tritium analysis with the desorption furnace was greatly improved by the addition of a TYNE Engineering Model 7045 Tritium in Air Monitor.

The TYNE monitor produces a live readout of tritium activity in uCi/m^3 of the furnace off-gas during the experiment, which is important for extracting kinetic information of tritium desorption from samples. In contrast, the water bubbler system can only measure tritium release rates by pausing gas flow and sampling the vials periodically. The TYNE system was originally intended for reactor use during FS-3, but an equipment failure made it unavailable prior to the irradiation. The planned configuration in FS-3 was a two-pass flow through the ion chamber array. On the first pass, the gas is counted for beta decay in chamber M1 and ionization from gamma rays are compensated by chamber C1. The gas stream then flows through the water bubbler which captures both soluble and insoluble tritium. A second pass is then made through the ion chamber so that radioisotopes in the gas stream which pass through the bubbler, Ar-41 in particular, can be counted by M2/C2 and subtracted from the first-pass measurement to determine the tritium activity. Because tritium is the predominant radionuclide expected in the desorption furnace sweep gas, only a single pass is used and the second set of chambers is left open to the laboratory atmosphere for the furnace application. In addition to M1/C1 and M2/C2, a smaller fifth chamber in the center is used for a high range of tritium activities from 1000-999,999 uCi/m^3. The five-chamber system is shown below in Figure 3.12.

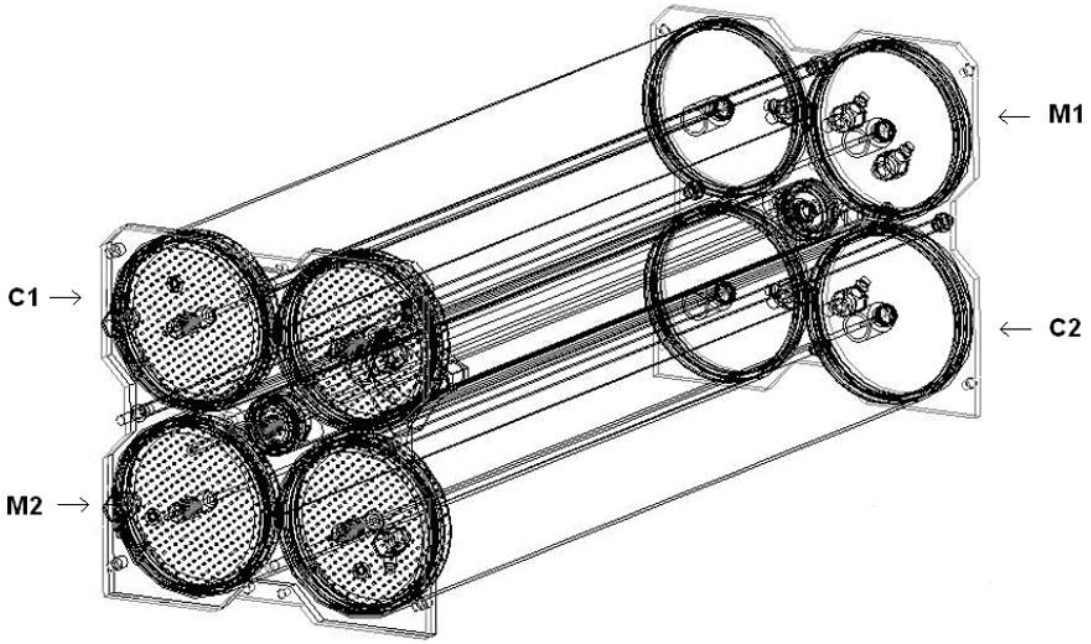

Figure 3.12. Configuration for the TYNE Tritium in Air Monitor ion chambers. M1 and C1 measure tritium and compensate for gammas, respectively. The second set of chambers are used to subtract out Ar-41, but are not needed in the desorption furnace application.

Since the ion chamber was originally calibrated for use with air, a correction must be applied for the particular sweep gas used in each experiment. The ion chamber detects the specific activity of tritium in a gas by measuring an ionization current. Converting the ionization current to a specific activity requires knowledge of the amount of energy required to produce an ion pair in the particular gas, which is referred to as a W factor with units of eV lost per ion pair produced. The W factor depends on the characteristics of the gas, type of radiation, and radiation energy, but is a relatively weak function of either variable [152]. Complied W factors for electron decays in various gases are shown in Table 3.2, which roughly correspond with the first ionization potential of the gas [153]. The ionization current, I_g, is inversely proportional to the W factor [154], and thus the ion chamber measurement of specific activity, C_g, can be converted to the appropriate condition using a ratio of W factors as in equation 3.1. There is limited guidance in literature regarding the treatment of specific gas mixtures, so a simple weighted average is used to produce a W factor of 26.8 for Ar-4%H_2. Therefore, measurements from the ion chamber are multiplied by 0.793 to represent the true specific activity in the argon hydrogen mixture.

Eq.3.1 $$C_g \propto I_g W_{Air} \cdot (W_{Ar/H_2}/W_{Air})$$

Table 3.2. Complied first ionization energies and W factor values for electrons in various gases. From [153].

Gas	First Ionization Potential [eV]	Electron W-Value [eV/ion pair]
Ar	15.7	26.4
He	24.5	41.3
H_2	15.6	36.5
N_2	15.5	34.8
Air	--	33.8
O_2	12.5	30.8
CH_4	14.5	27.3

The ion chamber only measures specific activity of a gas stream, and thus the flow rate must be measured in order to calculate the total tritium desorption rate from samples in the furnace. Total tritium release in a desorption profile can then be calculated based on the integral of the gas flow rate times the specific activity reading for the duration of the test as shown in equation 3.2. Flow of the Ar-4%H_2 sweep gas was held at a constant 312 cc/min by an Omega FMA5412A flow controller. For TDS experiments, a higher flow rate is desirable in order to minimize the delay between desorption and measurements during temperature changes. However, the flow rate in the

furnace needed to stay below roughly 500 cc/min, where excessive splashing in the bubbler vials starts to entrain water in the gas flow. Four timed measurements of flow into an evacuated graduated cylinder were used in order to calibrate the measurement for the particular gas mixture and the resulting times had a relative standard deviation of 4%. A He-1%O_2 gas mixture supplied to the catalyzer furnace was less rigorously controlled, and was adjusted to 25 cc/min according to the rising-bead visual flow meter on the bubbler front panel. Based on the bubbling rate in water vials of the He-1%O_2 flow compared to the calibrated flow stream, the He-1%O_2 was likely significantly higher than the 25 cc/min indicated on the rising-bead meter. The combined furnace, ion chamber system, and water bubbler setup is shown in Figure 3.13.

Figure 3.13. Thermal desorption facility used for FS-2 samples. Desorption occurs in the steel vessel furnace, gas flows into the ion chamber, and then tritium is trapped in the water bubbler.

Eq.3.2 $$^{3}H\ [mCi] = \left(\frac{1\ m^3}{1E6\ mL}\right)\left(\frac{1\ mCi}{1E3\ uCi}\right)\int_{t_0}^{t_f} Counts(t)\left[\frac{uCi}{m^3}\right] flow(t)\left[\frac{mL}{min}\right] dt$$

The desorption furnace underwent a series of tests with tritiated water and one FS-1 crucible section prior to tests with FS-2 research samples. A thorough description of the initial furnace trials and shakedown testing is described elsewhere [18]. In summary, the initial experiments helped to refine a desorption testing procedure and provided confidence in the ability of the furnace to efficiently collect tritium in the sweep gas. An example procedure for a 0.07595 gram sample of ARB graphite is shown below in Figure 3.14. A linear temperature ramp of 0.1 K/s was used for the sample, although the steel vessel furnace had some difficultly staying near the set point during heater pulses at temperatures below roughly 500°C. The furnace could achieve a maximum temperature between 960°C and 970°C, but the temperature ramp rate started to drop below the programmed slope after roughly 950°C. An additional temperature ramp down and hold at 800°C was used to allow for additional desorption and prevent rapid furnace cooling which could cause backflow of water into the tritium bubbler. As shown in Figure 3.14, a second temperature ramp of the sample at faster rate of 0.14 K/s led to a noticeable amount of desorption compared to the first cycle. Each sample underwent two ramp cycles as in the procedure shown in Figure 3.14 in order to assess the amount of tritium remaining in the sample which could be desorbed in the furnace temperature range. The ratio of first and second desorption amounts are shown in Table 3.3. Since the runs took place on different days over the course of two months, all values are corrected based on the day of measurement back to time time-center of the FS-2 experiment (July 26th, 2014) to normalize for tritium decay. For example, the IG2-6 measurement occurred on March 3rd, 2018 and therefore 18.3% of the tritium retained from the FS-2 experiment would have decayed by the time the sample was measured.

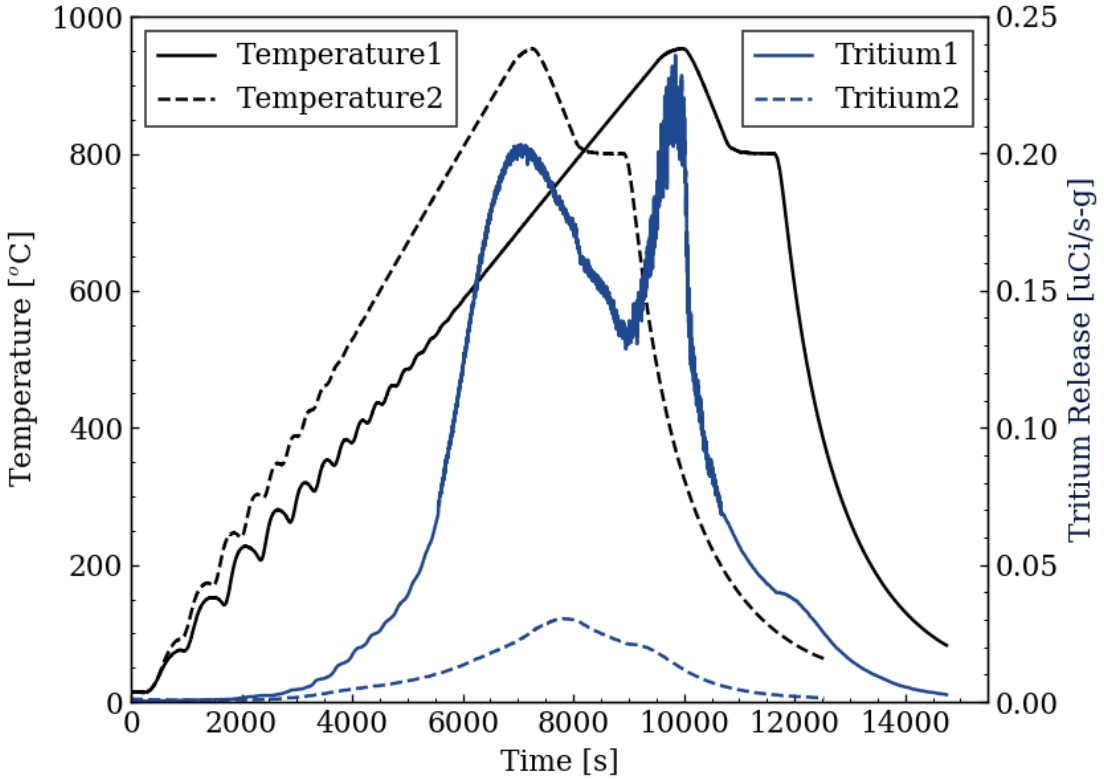

Figure 3.14. Desorption ramp procedure for FS-2 sample ARB-4 showing an initial temperature ramp of 0.1 K/s, a 20 minute ramp down to 800 C and a 10 minute hold. The profile is repeated for each sample with a 0.14 K/s ramp.

The first furnace trial of an irradiated sample used a fractured upper section of the FS-1 IG-110U crucible labeled GC1-1. Additional description and measurements from the GC1-1 test are available elsewhere [18]. As shown in Table 3.3, the GC1-1 sample had a tritium inventory roughly 5 times greater than the other samples which was unexpected since the position of the GC1-1 section in the FS-1 crucible was partially above the salt-fill level. The next sample tested, IG2-4, also saw an unexpectedly high 31% carryover of tritium from the first to second desorption cycle. Since the IG2-4 activity was lower than the GC1-1 sample, the high carryover can be explained by residual tritium from GC1-1 left in the furnace due to insufficient purging. For the tests after the IG2-4 sample, there was significantly less carryover with an average second:first desorption ratio of 11% for the remaining 7 samples. Assuming the same fractional decrease for a large number of repeated runs, the 11% suggests that the total tritium collected from each sample should be within 1-2% of the maximum releasable value [41].

Table 3.3. Total tritium release from samples with the steel vessel furnace after first and second desorption cycles. Runs are ordered chronologically based on testing date starting from GC1-1. Values are increased to account for decay between FS-2 and sample testing.

Sample	Initial Release [mCi]	Second Ramp [mCi]	Second/First
GC1-1	0.4459	0.0841	19%
IG2-4	0.1668	0.0524	31%
IG2-5	0.1021	0.0138	13%
IG2-6	0.0843	0.0099	12%
ARB-4	0.0727	0.0090	12%
IG2-8	0.1307	0.0125	10%
ARB-8	0.1734	0.0138	8%
ARB-9	0.0540	0.0068	13%
ARB-6	0.0696	0.0046	7%

The samples noted in Table 3.3 originated from larger disc samples immersed in Flibe during the FS-2 experiment. For desorption testing with the steel furnace, the IG-110U disc #2 and ARB disc #1 were used. The IG-110U sample discs were machined from the same supply of graphite used to produce the FS-2 and FS-3 crucibles. The ARB samples were provided by ORNL and are comprised of 64 wt% natural graphite, 16 wt% synthetic graphite, and 20 wt% resin blend. Details on the ARB fabrication process and material characterization are available in an ORNL report [155]. The IG-110U and ARB samples were contained in the sample crucible compartment during the FS-2 irradiation and thus would have experienced similar conditions of tritium uptake from the salt. A pre-irradiation photo of the FS-2 crucibles loaded with samples and Flibe salt is shown on the left in Figure 3.15. To allow for additional tests with each sample, the graphite discs were cut with a low speed saw in a fume hood capable of handling irradiated materials. After sectioning, the graphite pieces had a dose rate of roughly 0.1 mR/hr on contact [18]. An example subsection labeling diagram for the ARB graphite disc is shown on the right in Figure 3.15.

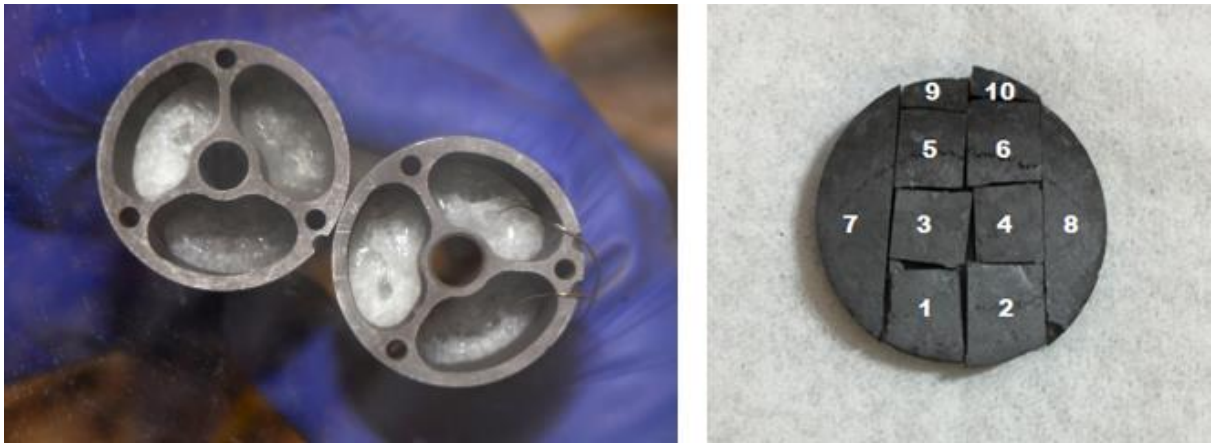

Figure 3.15. FS-2 graphite crucibles loaded with samples and filled with Flibe prior to irradiation (left). After the irradiation test, sample graphite samples were extracted from Flibe and cut into multiple subsections (right). Graphite crucibles were 39.7 mm in outer diameter and the graphite samples were 19mm in diameter and 2mm thick.

The first set of experiments after the GC1-1 initial test aimed to examine tritium trapping mechanisms through thermal desorption spectroscopy at various temperature ramp rates. In this method, the temperature at which the peak desorption rate occurs can be related to the activation energy [115]. The IG-110U internal subsections numbers 4, 5, and 6 were used for the ramp rate analysis since samples without the circumferential edge faces were expected to have more consistent tritium retention characteristics. Overall, the ramp rate study with the steel furnace was not successful in producing a measurement of desorption activation energy. As previously discussed, the IG2-4 data was contaminated by residual tritium from the GC1-1 test which could have influenced the desorption profile. Also, the IG2-6 test experienced a heater malfunction at 700°C and had to be cut short and repeated before a desorption peak could be observed. The desorption profiles from IG-110U sample internal sections 4, 5, and 6, along with edge section number 8 are shown together in Figure 3.16, where each tritium desorption rate in μCi/s is normalized to the mass of the graphite subsection. Only the portion of the desorption measurement is shown where the temperature followed the programmed linear ramp rate. Each plot spans from the experiment start at room temperature up until the ramp rate fell below 75% of the prescribed value near the maximum furnace temperature.

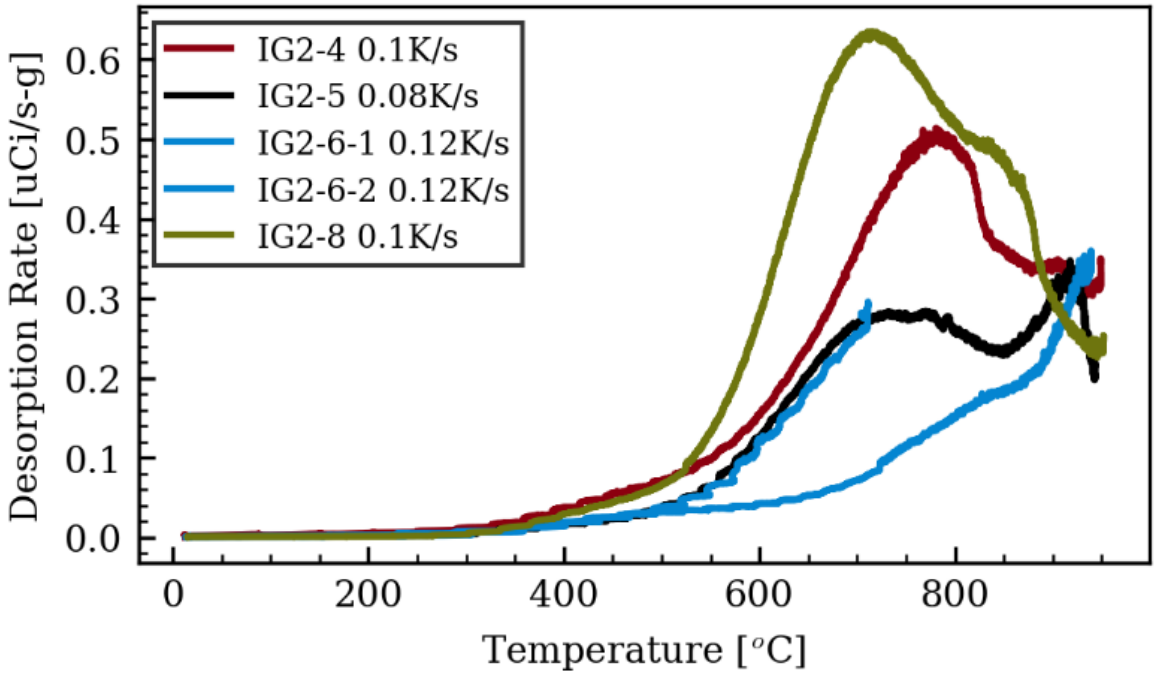

Figure 3.16. Desorption profile from IG-110U sample sections at various ramp rates. The IG2-6 test is broken up into two runs because of an unexpected heater malfunction in the first test.

While the previous thermal desorption experiments were not successful in identifying tritium retention mechanisms, they still could provide useful information on the total amount of tritium in each sample subsection. From the results in Figure 3.16, it also appeared that the amount of tritium retention per subsection mass was higher for the edge section number 8 than for the internal sections 4, 5, and 6. This was also clearly observed for subsections of the ARB graphite shown in Figure 3.17. The integral of the desorption profile as well as the height of the peak desorption rate at roughly 675°C both increased for edge samples ARB-8 and ARB-9 compared to the internal sample ARB-4. For each sample, the amount of Flibe-facing surface area per sample mass is also shown in the legend of Figure 3.17. Surface area was calculated with ImageJ using photos of each sample near a reference distance as in Figure 3.18. Uncertainty in the area calculation was assessed by observing the spread in areas from multiple photos of the same sample.

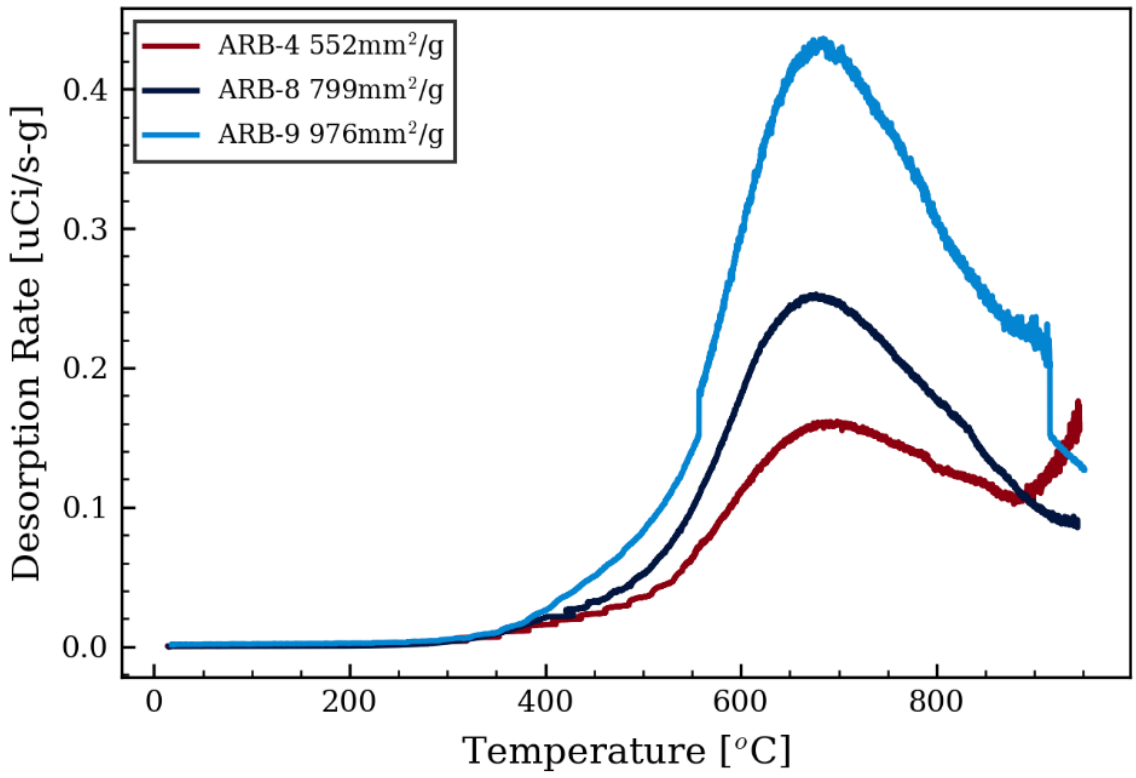

Figure 3.17. Tritium desorption profile from ARB internal subsection 4, and two edge subsections 8 and 9 with Flibe-facing surface area per sample mass indicated in the legend. All samples were desorbed at 0.1 K/s.

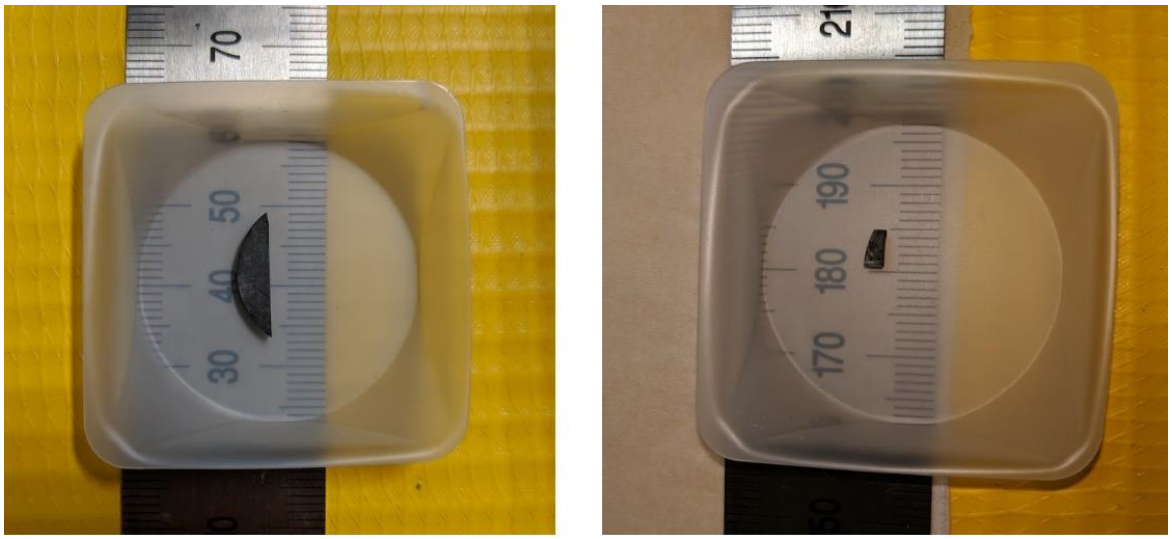

Figure 3.18. Photos of ARB-8 (left) and ARB-9 (right) used for the area calculation in ImageJ.

The Flibe-facing area, mass, and ion chamber-measured tritium content of each sample subsection is shown in Table 3.4 along with group averages for the IG-110U and ARB sections. Overall, the salt-facing area was a better predictor for tritium content than sample mass as gauged by the relative standard deviation of measurements for each graphite type. Therefore, based on the furnace desorption measurements it appeared that tritium desorption was more pronounced near the salt-graphite surface, rather than evenly distributed throughout the samples. The relative standard deviation of the area calculation was 3.2% on average, while the standard deviation of $\mu Ci/mm^2$ measurements was 10% for the IG-110U samples and 17% for the ARB samples. Thus the standard deviation of the entire measurement process cannot be explained by the area calculation alone and includes other factors such as ion chamber background counts, range switching effects, slight differences in temperature ramping procedure, and potential differences in tritium retention among the sample subsections.

Table 3.4. Ion chamber measurements for total tritium from samples along with measurements normalized by salt-facing surface area and by mass. Diving by area produced more consistent measurements within each sample group.

Sample	Mass [g]	Area [mm^2]	Total Tritium [mCi]	Tritium/Area [$\mu Ci/mm^2$]	Tritium/Mass [mCi/g]
IG2-5	0.07086	41.1±1.7	0.1158	2.82	1.634
IG2-6	0.06147	36.1±2.2	0.0942	2.61	1.532
IG2-8	0.06128	43.6±0.4	0.1433	3.29	2.338
			Average:	2.91	1.835
			$\sigma_{relative}$:	**10%**	**20%**
ARB-4	0.07595	41.9±0.3	0.0817	1.95	1.076
ARB-6	0.08722	48.2±1.1	0.0741	1.54	0.850
ARB-8	0.15265	122±2	0.1872	1.53	1.226
ARB-9	0.02721	26.6±1.8	0.0608	2.28	2.234
			Average:	1.83	1.347
			$\sigma_{relative}$:	**17%**	**39%**

The ion chamber was chosen as the preferred tritium analysis system since it produced a lower spread in measurements than observed with the water bubbler [18]. However, the water bubbler was still useful for assessing the chemical form of tritium present in the desorption gas stream. The fraction of water-soluble and insoluble tritium captured in the bubbler after each

sample desorption is shown in Figure 3.19. To prevent contamination between runs, a new set of glass vials and clean deionized water were used for each sample. Nonetheless, there appears to be a relationship between soluble tritium and the order of the runs as listed in chronological order of run date from left to right in Figure 3.19. The GC1-1 initial sample had the highest solubility fraction of 51%, which was thought to be caused by starting the temperature ramp too quickly before the furnace had changed over to an Ar-H_2 atmosphere. If there was remaining oxygen from ambient air in the furnace, tritium and hydrogen in the desorption gas could be converted to HTO and then be counted as soluble tritium. After the GC1-1 test, all other samples first underwent a purge of Ar-4%H_2 for at least 30 minutes prior to the desorption phase of the experiment. Therefore, one possible explanation for the decreasing soluble fraction is that HTO from the GC1-1 test was dispersed onto furnace internal surfaces or gas tubing which then was purged over time in the subsequent experiments. For the sample IG2-6 and the remaining sections, the fraction of insoluble tritium was over 80% of the total in each run.

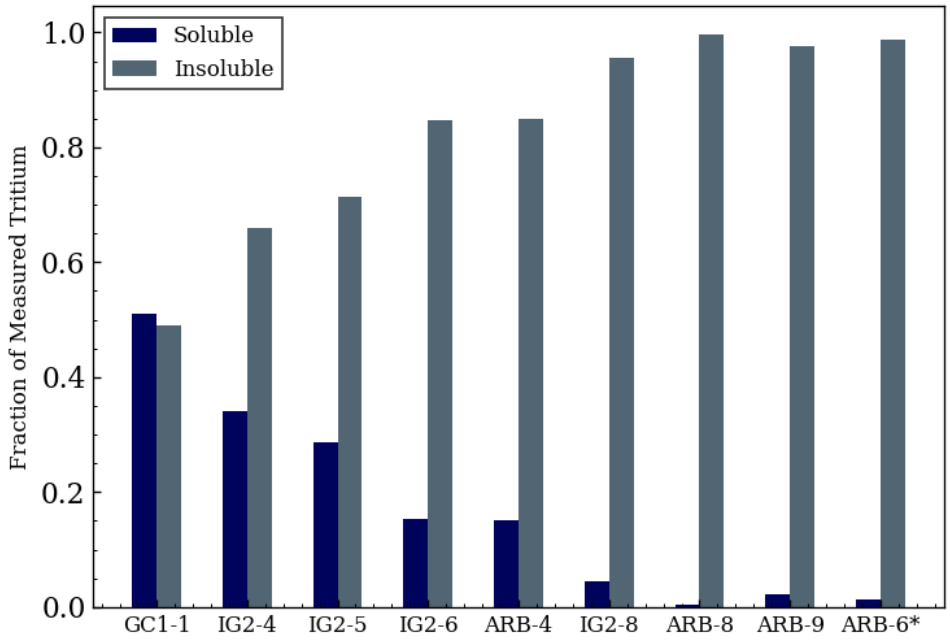

Figure 3.19. Fraction of soluble and insoluble tritium detected with the water bubbler system from experiments with IG-110U and ARB graphite in the steel furnace.

One issue in the solubility analysis is the potential influence of hydrogen in the Ar-4%H_2 sweep gas on the chemical form of tritium collected from each sample. Results of FS-3 and previous Flibe irradiations clearly show that excess hydrogen can shift tritium chemical form to

HT through isotopic exchange reactions [44, 18]. In the steel desorption furnace, the effect of hydrogen was examined by testing one sample, ARB-6, in a pure argon sweep gas. As shown in Figure 3.19, the resulting soluble fraction for ARB-6 was similar to other ARB sections tested in the Ar-4%H_2 gas. However, the sweep gas composition did have a noticeable effect on the tritium desorption profile measured as a function of temperature. Compared to the 4%H_2 gas, the test in pure Ar raised the peak desorption temperature of the ARB-6 sample roughly 150°C higher than for ARB-4, as displayed in Figure 3.20. The large discontinuity in the ARB-6 profile was caused by the ion chamber switching from low- to high-range measurement chambers. Range switching in the TYNE ion chamber occasionally had a seamless effect on the count rate, but in other cases, like the ARB-6 run, the change was very significant. The peak shift further into the desorption experiment could be caused by additional interactions and holdup of tritium in the furnace and transfer tubing without the saturation of surfaces by excess H_2. Another possibility is that H_2 in the sweep gas accelerated the diffusion of tritium out of the graphite sample and thus led to faster desorption of the sample and an earlier peak in the Ar-4%H_2 tests. Increased diffusion of D_2 in graphite was observed at partial pressures even below 4000 Pa in previous gas charging studies with IG-110U [136].

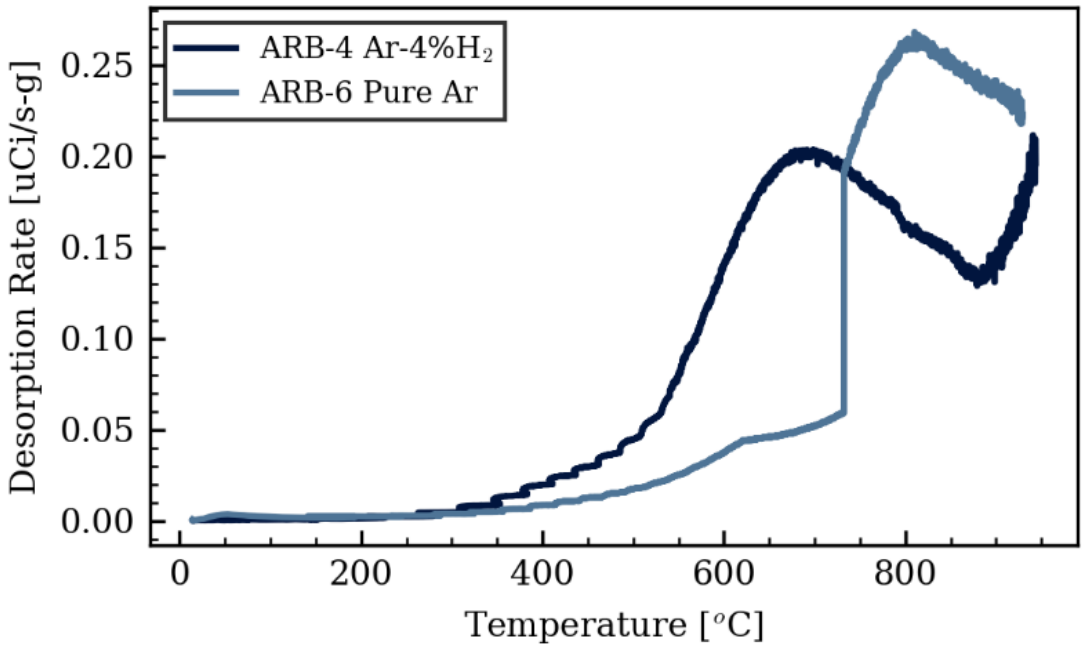

Figure 3.20. Influence of hydrogen in sweep gas composition between two ARB internal subsections desorbed at 0.1 K/s. The discontinuity in the ARB-6 measurement was caused by the ion chamber shift from low to high range.

One final observation from the steel furnace desorption tests was the presence of a high-temperature desorption peak observed in roughly half of the previously described runs. Deuterium gas charging studies on nuclear graphites have previously identified and discussed several desorption peaks which correspond to different trapping sites within graphite [115]. From the furnace tests alone, it is difficult to determine which trapping sites are responsible for the peak structures of the FS-2 sample desorptions. Furthermore, the high-temperature peak was mainly observed in samples tested towards the beginning of the set and was absent in the later runs. For example, in Figure 3.17 a peak beginning at 950°C was seen for ARB-4, but was not observed for the ARB-8 and ARB-9 samples tested afterwards. One explanation for the peak is again contamination in the furnace from the GC1-1 test run, which could have deposited HTO throughout the furnace internal surfaces. For the majority of the desorption experiment, the furnace body remains cool near the temperature of the water in the outer cooling jacket. Towards the maximum ramping temperatures, the furnace body also would also heat up to a temperature of roughly 100°C. Therefore, the upper temperatures of the experiment could also correspond to a condition where HTO impurities in the furnace also begin to evaporate and could appear in a high-temperature peak structure. To better investigate high-temperature tritium desorption in graphites from MITR Flibe irradiations, the next sets of experiments were conducted in a new furnace design with higher possible operating temperatures.

3.3.2. Desorption of FS-2 Samples in a Quartz Tube Furnace

The tritium desorption experiment was converted to a quartz tube furnace after successful demonstration of a similar facility in the FS-4 irradiation experiment [49]. Operating limits of the tube furnace permit a maximum heater temperature of 1100°C indefinitely or 1200°C for less than one hour. Desorption experiments were conducted with linear temperature ramp rates using a maximum temperature of 1150°C or less to provide margin against the designated limit. Heater temperatures were measured with a thermocouple installed near the furnace coils, while the sample temperature was measured with a sheathed thermocouple inside of the quartz tube. A heater temperature of 1150°C corresponded to a maximum temperature of 1000-1050°C near the sample. Therefore, the quartz tube furnace provided roughly 100°C of additional desorption temperatures above the range of the previous steel furnace. The quartz tube extends far enough out of the furnace zone where the ends are cool enough to be sealed by a steel flange that compresses a double set of silicone O-rings with maximum operating temperatures of 300°C. During testing, the flange

temperature reached a maximum of about 120°C at peak furnace temperatures. Quartz has a low permeability for tritium over the operating range of the furnace and therefore no effort was made to actively cool the tube. A portable tritium monitor was used to sample lab air during desorption experiments with both furnaces and a leak of tritium through the gas boundary was never detected. The quartz tube furnace desorption facility is described in Figure 3.21.

Figure 3.21. Quartz tube furnace with tritium measurement systems (left). Inside the furnace, an Inconel-sheathed thermocouple is positioned though one of the ceramic tube insulators while the samples rest on a high-temperature compatible sample tray in the quartz tube (right).

The first tritium desorption tests with the quartz tube furnace used the remaining subsections of the IG-110U disc tested with the steel vessel furnace in order to compare the collection efficiency of each facility. Since the tube furnace has a lower overall internal surface area than the steel furnace and thus potentially less interaction with tritium, an initial attempt was made to test a sample in a pure argon sweep gas without added hydrogen. Switching from Ar-4%H_2 to pure argon was also motivated by the reasonably high collection rate observed for the AR2-6 sample, which was less than the ARB sample average but higher than the AR2-8 sample in terms of measured μCi/mm^2 displayed in Table 3.4. However, the pure argon test with the IG2-9 sample in the quartz furnace resulted in a lower than expected amount of tritium desorption. The ramping procedure was repeated once with argon again, and then twice with Ar-4%H_2. A summary of runs with the sample is shown in Table 3.5, which shows that a significant fraction of tritium

was recovered upon switching the sweep gas in the third and fourth repeated runs. The same bubbler vials were used for the four runs and were samples after each test showed an increase in the total percentage of soluble tritium recovered at each stage. However, the source of soluble tritium was unclear since the furnace was also exposed to the lab atmosphere after each test and tritium could have interacted with moisture or oxygen in the ambient air.

Table 3.5. Summary of the first set of runs in the quartz tube furnace with repeated desorption measurements on a subsection of FS-2 IG-110U graphite. Each test used a ramp rate of 0.1 K/s up to sample temperature of 1050°C.

Sample	Sweep Gas	^{3}H Desorption [mCi]	Run/First Run	Total Soluble ^{3}H
IG2-9-1	Ar	0.0311	--	12%
IG2-9-2	Ar	0.0055	18%	19%
IG2-9-3	Ar-4%H_2	0.0084	27%	23%
IG2-9-4	Ar-4%H_2	0.0042	14%	24%

The low measurements for total desorbed tritium and high carryover on repeated runs with the IG2-9 sample prompted a switch back to the Ar-4%H_2 sweep gas. Another subsection of FS-2 IG-110U graphite was desorbed to better understand the tritium collection efficiency of the quartz tube furnace system. The desorption profile from the IG2-10 sample is shown in Figure 3.22, along with the first test of sample IG2-9 in the quartz tube furnace and a desorption profile of IG2-8 from the previous furnace. The desorption procedure was repeated for the IG2-10 sample, which resulted in 3% of the tritium measured in the second desorption compared to the first temperature cycle. The measured tritium per Flibe-facing surface area of the IG2-10 sample is compared to IG2-9 and the average of other samples tested in the previous furnace design in Table 3.6. Compared to the average of IG-110U samples from the steel furnace, the IG2-10 sample had a higher $\mu Ci/mm^2$ measurement and was above the standard deviation of the previous group. Therefore, the quartz tube furnace can either desorb the samples more thoroughly than the steel furnace or the system has a lower rate of parasitic losses prior to tritium measurement. However, further comparison was not possible due to a lack of remaining sample subsections from the FS-2 IG-110U #2 disc. Overall, the test of the IG2-10 sample provided confidence in the ability of the quartz tube furnace to conduct sample desorptions with a performance comparable or better than the steel furnace design.

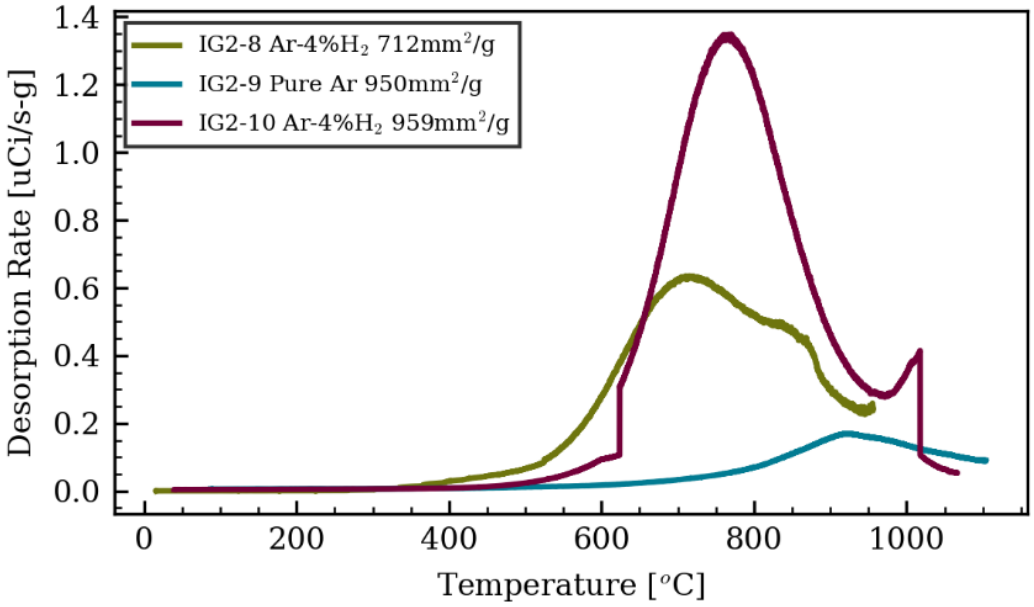

Figure 3.22. First desorption profiles of samples IG2-9 and IG2-10 in the quartz tube furnace compared to IG2-8 from the steel furnace design. All samples were desorbed in a linear temperature ramp of 0.1 K/s.

Table 3.6. Summary of comparison tests with the same sample of IG-110U graphite from FS-2. IG2-9 was tested with pure Ar sweep gas while IG2-10 and IG2-5, -6, and -8 used Ar-4%H_2.

Sample	Furnace	^{3}H per Area [μCi/mm^2]	Carryover	Total Soluble ^{3}H
IG2-9	Quartz	1.04	37%	24%
IG2-10	Quartz	3.31	3%	6%
IG2-5,6,8 Avg.	Steel	2.91±0.29	12%	16%

The sample subsection analysis was repeated to confirm the observation of surface-limited retention with higher possible desorption temperatures in the quartz tube furnace. For this study, the FS-2 IG-110U sample #1 was used and sectioned according to the diagram in Figure 3.23. The IG1-7 subsection in Figure 3.23 was fractured during the cutting process and therefore was not used. As shown in Figure 3.23, the IG1-2 section was further cut after its initial desorption run, but the remaining tritium in the subsections was too low to produce useful results and are not discussed. Overall larger subsections were used compared to the previous IG2 sample in order to promote the majority of the desorption profile into the high range of the ion chamber and avoid range switching near the desorption peak.

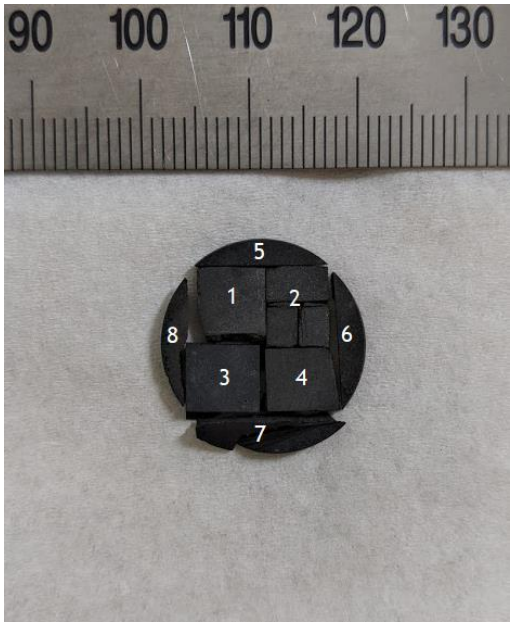

Figure 3.23. Sectioning diagram for the FS-2 IG-110U#1 sample. The IG1-2 sample was sectioned again into three pieces after its initial desorption. IG1-7 was unintentionally fractured during the sectioning process.

The IG-110U#1 sample subsections were tested in a similar ramping procedure to IG-110U#2. A maximum furnace set point of 1150ºC was used, which results in a temperature measurement from the thermocouple near the sample of 1050-1100ºC. After the maximum temperature, a 30 minute ramp down to 900ºC was used to prevent rapid cooling and backflow of the furnace. The samples were not cycled for a second run due to restrictions on laboratory time, but are preserved in storage if a second desorption is required at a later date. The low 3% carryover of the IG2-10 sample measurement provides some confidence that the total desorption in the quartz tube furnace is near the maximum releasable value after single run cycles. Desorption profiles for the three edge samples IG1-5, 6, and 8 are shown in comparison to one internal section, IG1-1, in Figure 3.24. The edge samples IG1-6 and IG1-8 show significantly larger tritium desorption peaks compared to IG1-1 when normalized to sample mass. However, the edge sample IG1-5 was noticeably below IG1-1. One possible explanation is that the IG-110U#1 sample disc was not fully submerged in the salt during the FS-2 experiment, and a portion of the sample which included the IG1-5 edge was not exposed to tritium directly from Flibe.

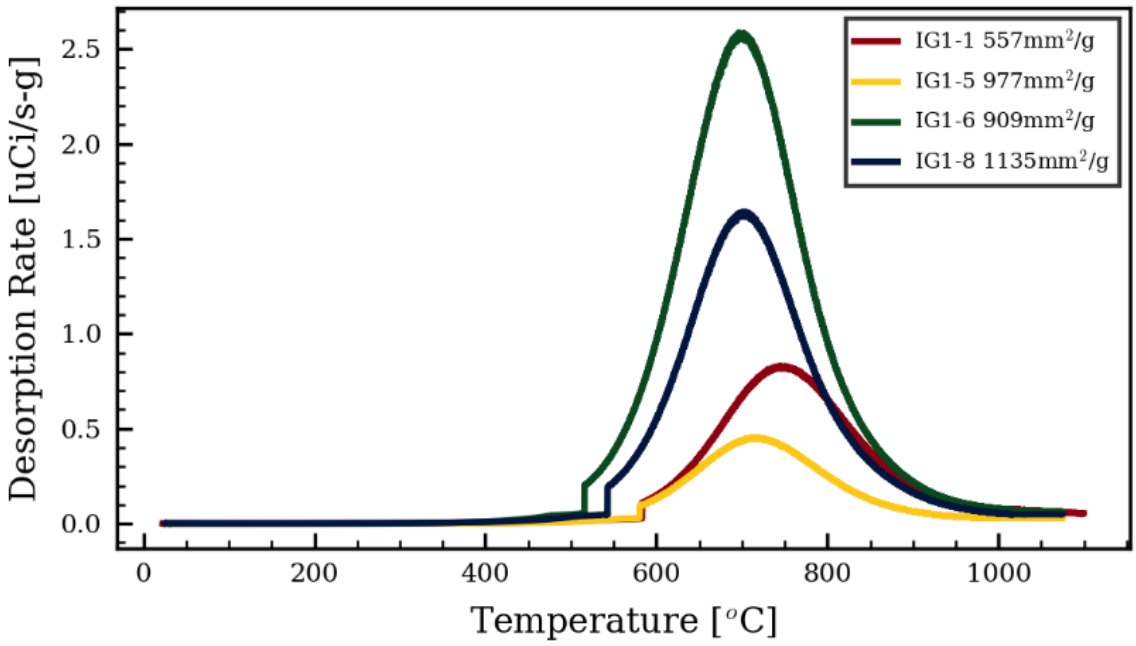

Figure 3.24. Desorption profile for edge samples IG1-5, 6, and 8 compared to internal sample IG1-1. All samples were desorbed in a linear ramp of 5ºC/min in Ar-4%H_2.

Despite the inconsistency between edge samples, the subsection desorption results reveal a similar conclusion to results from the previous furnace design – the standard deviation of tritium content normalized by sample Flibe-facing surface area is roughly half of that when measured tritium is normalized to sample mass. The standard deviation for tritium per area values is also shown to reduce significantly in Table 3.7 if the IG1-5 sample is removed as an outlier. Therefore, the IG-110U#1 sample disc from FS-2 also shows some indication that tritium retention in the graphite was not homogenously distributed, but more dependent on the surface area of the sample in contact with Flibe. It is also important to note that the IG1 μCi/mm^2 average was roughly 40% higher than the IG2 sample measured in the quartz furnace. The increased retention could be explained by differences in sample temperature or tritium concentration in salt caused by a slightly different position of samples in the FS-2 irradiation capsule. However, there should be minimal discrepancies caused by the sample material itself since both IG-110U sample discs were prepared from the same graphite block. As with the majority of desorption tests in the steel furnace, the dominant form of tritium captured by the water bubbler from IG1 sections was also in an insoluble form, either HT or T_2.

Table 3.7. Summary of tritium desorption measurements with the IG-110U#1 sample from FS-2.

Sample	Mass [g]	Area [mm^2]	Total Tritium [mCi]	Tritium/Area [$\mu Ci/mm^2$]	Tritium/Mass [mCi/g]	Soluble ^3H
IG1-1	0.14594	81.3±3.1	0.360	4.43	2.467	2.9%
IG1-2	0.14502	84.0±3.7	0.405	4.82	2.793	3.3%
IG1-3	0.15568	89.0±3.0	0.404	4.54	2.595	2.5%
IG1-4	0.13376	80.9±5.9	0.358	4.43	2.676	3.6%
IG1-5	0.07281	71.1±1.8	0.175	2.46	2.404	4.0%
IG1-6	0.07984	72.6±0.1	0.499	6.87	6.250	4.8%
IG1-8	0.05355	60.8±0.2	0.348	5.72	6.499	3.5%
			Average:	4.75	3.669	3.5%
			$\sigma_{relative}$:	**28%**	**50.5%**	
		$\sigma_{relative}$	without IG1-5:	**19%**	**49.9%**	

3.3.3. Measurement of Desorption Activation Energy

A thermal desorption spectroscopy measurement was conducted again with the FS-2 IG-110U samples after the previous unsuccessful attempt with the steel furnace. For this study, the activation energy of the tritium desorption process can be inferred from the desorption rate as a function of temperature during linear temperature profiles if multiple ramp rates are applied. The quartz tube furnace was better suited for the measurement because it offered more accurate temperature control during the linear ramp and a wider range of possible ramp rates due to less restrictive temperature limits. In order to best maintain consistent tritium retention characteristics among samples, only the internal subsections IG1-1, 2, 3, and 4 were used for the TDS study.

The applied temperature profiles and desorption rates as a function of time are shown in Figure 3.25 below. As previously discussed, the IG1 sample subsections were cut larger than for IG2 to keep the ion chamber in the high range for most of the experiment. For the IG1-1 sample, the Ar-4%H_2 flow rate was also reduced to 234 cc/min, which would further elevate the tritium sweep gas concentration for a given desorption rate. After the IG1-1 run, it was clear that tritium desorption rate was well above the chamber's low range, and therefore the flow rate was increased for the remaining samples to 546 cc/min to reduce the delay between desorption and tritium measurement. The change in flow rate had a detrimental effect on the trends in the desorption profiles. As seen in Figure 3.25 for IG1-2, 3, and 4, there was a noticeable relationship observed between peak desorption rate and temperature ramp rate, but the IG1-1 peak desorption rate was

roughly the same as IG1-2 despite the different ramp rate. The slower flow rate for IG1-1 could effectively smear out the desorption profile and produce a wider profile with a lower peak value. Additionally, the gas flow could influence the heat transfer inside the tube and change the temperature of the sample. Since the thermocouple is placed above the sample, but does not directly contact it, the true sample temperature could be noticeably different than the thermocouple reading for various flow rates. Because of these inconsistencies, the IG1-1 measurement was dropped from the analysis for activation energy measurement.

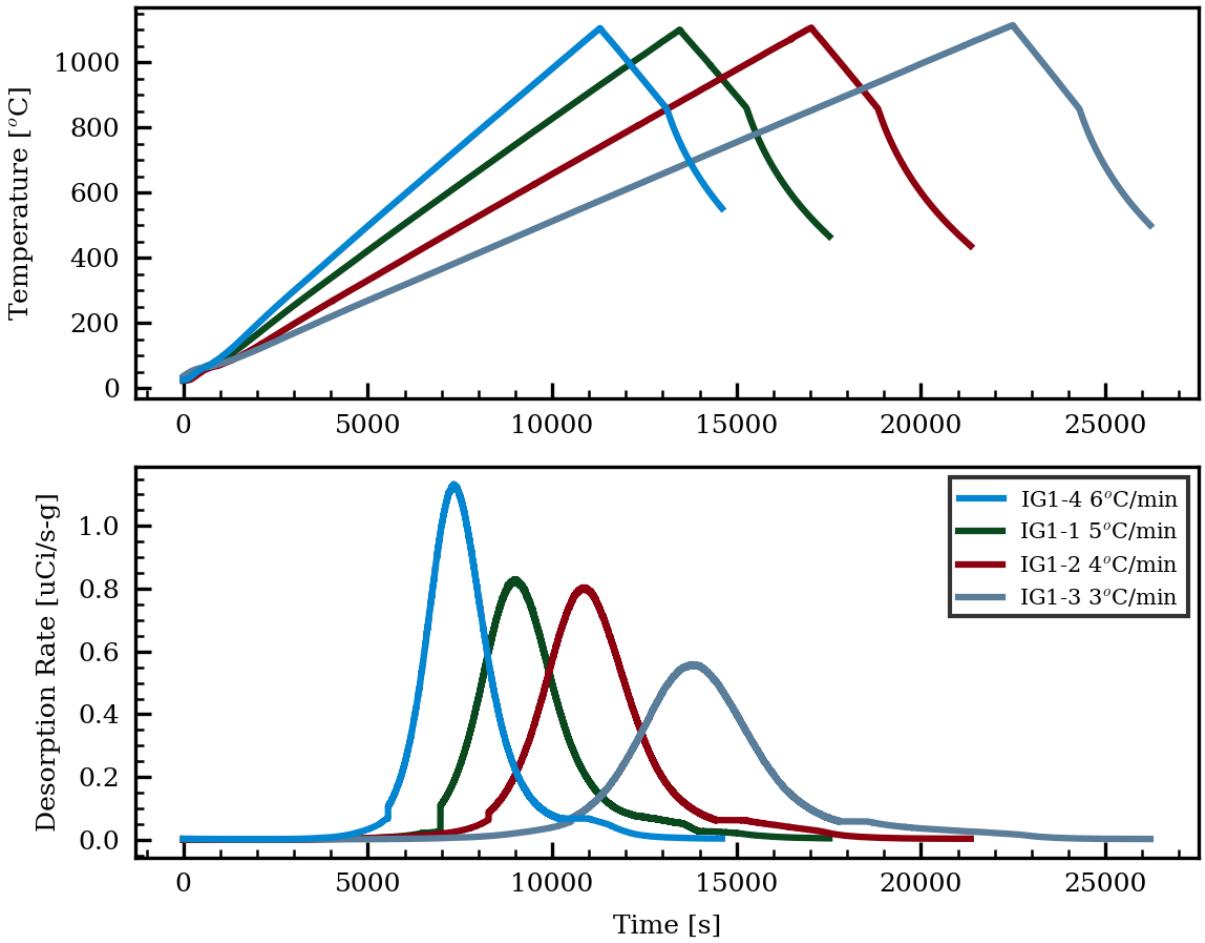

Figure 3.25. Temperature and tritium desorption profiles for FS-2 IG-110U#1 internal sample subsections desorbed at various ramp rates. All samples were tested with Ar-4%H_2 sweep gas.

For the IG1-2, 3, and 4 samples, the expected trend was observed for peak desorption rate as a function of temperature. As shown in Figure 3.26, the slowest ramp rate of 3ºC/min with IG1-3 resulted in a peak desorption rate at the lowest temperature of the set. A decreased ramp rate provides additional time for desorption prior to reaching a given temperature, and thus slower ramp

rates lead to more thorough desorption and shifts peak desorption rates to lower temperatures in the experiment. A similar trend was observed in TDS tests of ISO-880U graphite charged with D_2 gas [123]. The integral of the desorption verses time profiles were also used to calculate the total tritium in each sample subsection listed in Table 3.7.

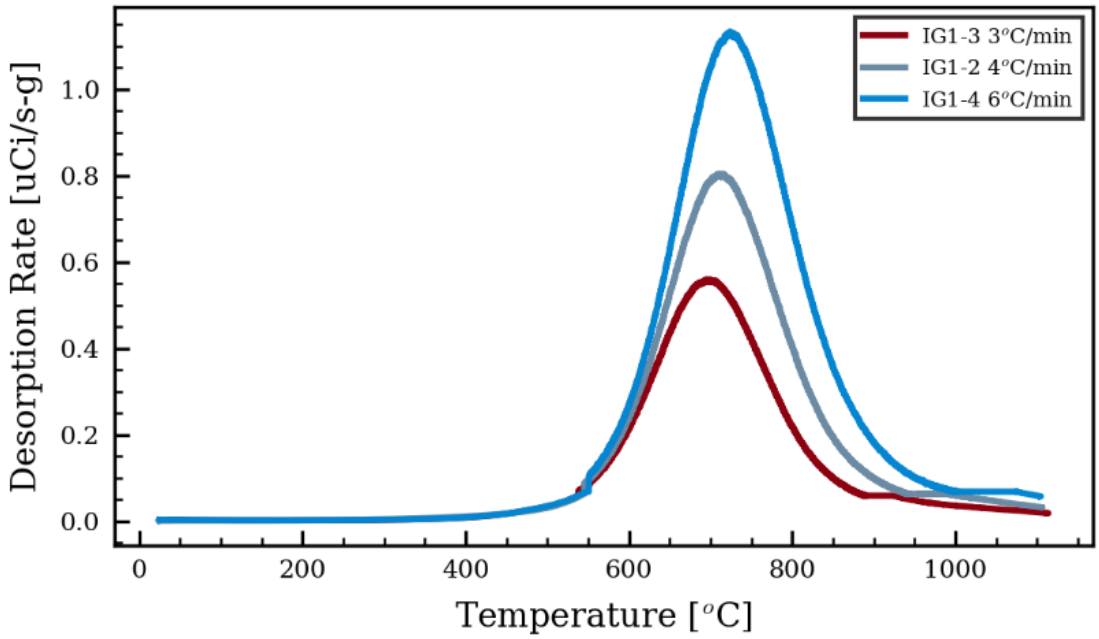

Figure 3.26. Desorption rate as a function of temperature for the FS-2 IG-110U#1 internal sample subsections tested with 546cc/min of Ar-4%H_2 and various ramp rates.

The temperature at which the peak desorption rate occurs can be used to determine the activation energy of the desorption process through the differential thermal analysis method developed by Kissinger [156]. The method was originally proposed for thermal decomposition of clays, but has seen wide use to study other phenomena [157]. A generic derivation can be applied for any thermally activated process that follows a first-order relationship with an Arrhenius rate constant as shown in equation 3.3. Here, x refers to the fraction of tritium desorbed from the sample, k is the desorption rate constant, A is a pre-exponential constant, E_a is the desorption activation energy, R is the universal gas constant, and T is the experimental temperature. Kissinger has demonstrated that the maximum reaction rate corresponds to the relationship shown in equation 3.4, where T_{max} is the temperature at the maximum dx/dt [156]. Rearranging the maximum condition allows activation energy to be calculated from the slope of $\ln(\beta/T^2_{max})$ verses $1/T_{max}$ as shown in equation 3.5, where β is the ramp rate of dT/dt.

Eq.3.3 $$\frac{dx}{dt} = k(1-x)\,;k = A \cdot exp(-E_a/RT)$$

Eq.3.4 $$A \cdot exp\left(-\frac{E_a}{RT_{max}}\right) = \frac{E_a}{RT_{max}^2}\frac{dT}{dt}$$

Eq.3.5 $$\frac{d\left(ln\left(\frac{\beta}{T_{max}^2}\right)\right)}{d\left(\frac{1}{T_{max}}\right)} = -\frac{E_a}{R}$$

As summarized in Section 2, the desorption of tritium from graphite occurs in a high activation energy process. Therefore, relatively small changes in the temperature position of the desorption peak can register as a large change in activation energy. One potential issue with the tube furnace in terms of thermal desorption spectroscopy measurements is the lag between desorption of tritium from the samples and measurement in the ion chamber. The largest potential region for time-lag is within the tube furnace itself, which has an internal volume of 1200cc compared to 93cc in the high range ion chamber and roughly 10cc of tubing volume. An attempt was made to correct for the flow delay using the relation shown in equation 3.6. The correction uses a simple assumption of a uniform concentration of tritium in the sweep gas, C_g, throughout the tube. Therefore, the molar balance of tritium in the tube increases with the true sample desorption rate, R(t), and decreases from the molar flow of tritium out of the tube, C_g times the volumetric flow rate $\dot{V}$. The original desorption profiles and flow adjustments are shown in Figure 3.27. As shown in the figure, the flow correction is largest for the fastest temperature ramp rate with IG1-4 since in that case the relative delay was the most significant.

Eq.3.6 $$\frac{dC_g}{dt} = \frac{R(t) - C_g\dot{V}}{V_{Tube}} \rightarrow R(t) = V_{Tube}\frac{dC_g}{dt} + C_g\dot{V}$$

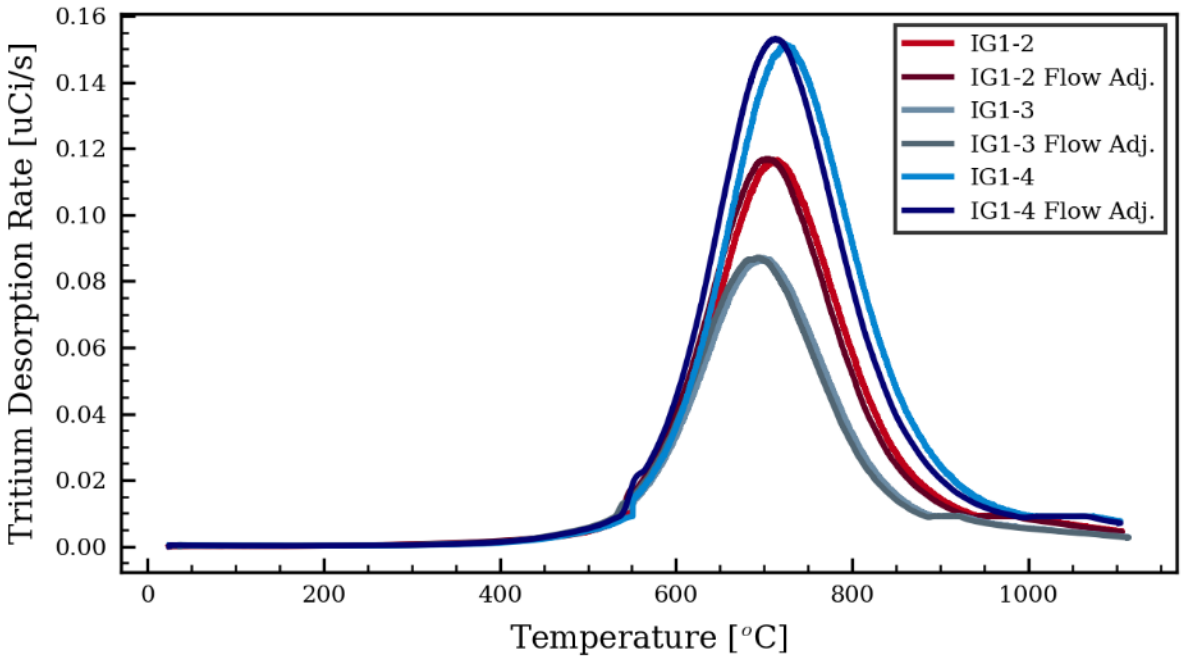

Figure 3.27. Original desorption profiles along with adjustments for delay from sweep gas flow according to equation 3.6.

Peak temperature and ramp rate data taken from Figure 3.27 are plotted for the activation energy calculation in Figure 3.28. The slope of the original and flow-adjusted lines led to calculated activation energies of 189 kJ/mol and 260 kJ/mol, respectively. Data from the IG1 desorption study is also summarized in Table 3.8. As determined by the R^2 values of the linear regression, the flow-adjusted values led to a slightly better fit. While the flow adjustment adds uncertainty to the calculation, the estimated uncertainty in the desorption furnace mass flow controllers is relatively low at 4% [18]. The flow-adjusted activation energy measurement of 260 kJ/mol is also more consistent with the activation energies for diffusion of tritium in graphite grains [126, 108]. Therefore, it is also possible that the observed tritium desorption profiles from the FS-2 samples are controlled by a diffusion process through the graphite. Thermal desorption experiments were also previously used to measure the activation energy of high-energy detrapping from ISO-880U graphite [123]. However, for the IG1 sample there was only one prominent peak observed. A higher-energy trapping peak might be inaccessible with the tube furnace temperature range. Another possibility is that the amount of tritium present in the high-energy trapping sites was too low to create a prominent signal.

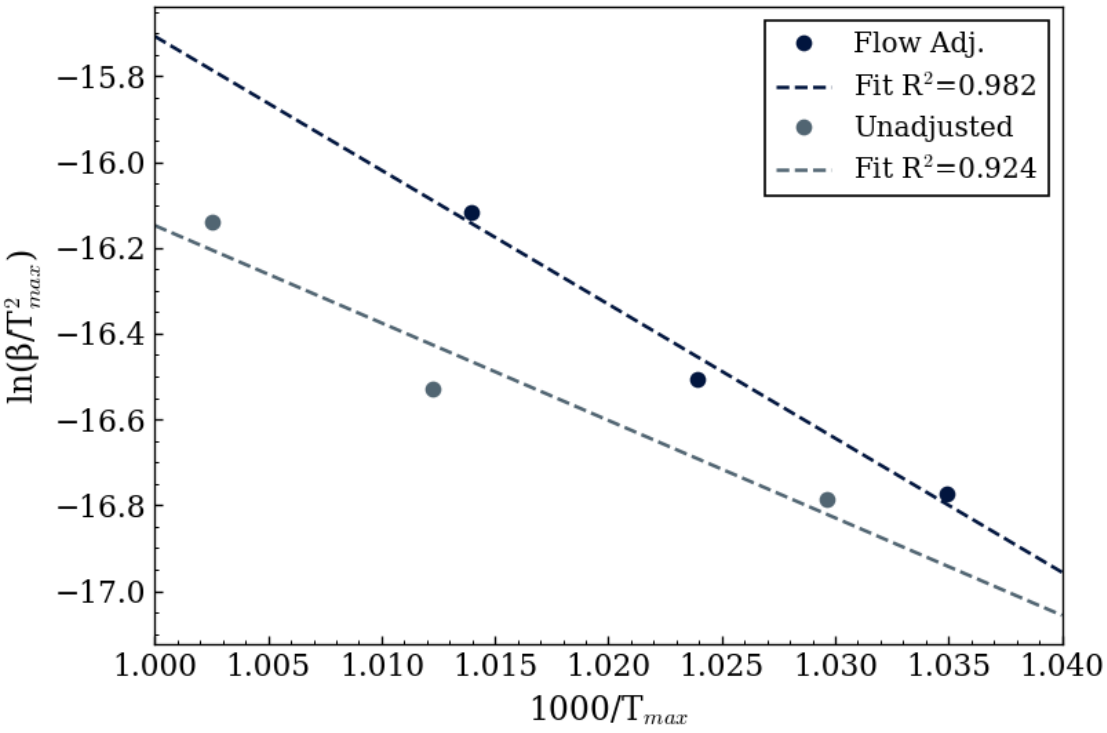

Figure 3.28. Kissinger plots of the original and flow-adjusted data used for calculating the desorption activation energy. Flow-corrected data produced a slightly better fit.

Table 3.8. Summary of results from the activation energy measurements with the FS-2 IG1 sample. The temperature ramp rate, β, was calculated from the sample thermocouple over the range of data from 600ºC-900ºC.

Sample	β [K/s]	T_{Max} [ºC]	Flow-Adj. T_{Max} [ºC]
IG1-2	0.06473	714.7	703.5
IG1-3	0.04844	698.1	693.1
IG1-4	0.09731	724.3	713.1
		E_a: 189 kJ/mol	**Ea: 260 kJ/mol**

3.3.4. Chemical Form of Tritium in the FS-1 Graphite Crucible

The 1000 hour FS-1 irradiation presented another opportunity to examine tritium retention in graphite. While there were no graphite samples in the FS-1 test matrix, the IG-110U crucible itself was examined using thermal desorption in the quartz tube furnace. In this study, roughly 4.5mm thick axial sections were cut with a low speed saw from the FS-1 crucible graphite, as shown in Figure 3.29. The graphite crucible sections used contained only silicon carbide samples and non-fueled surrogate Triso particles, and thus there were limited metallic impurities in the

crucible which would have elevated dose rates. A photo of the full FS-1 crucible prior to irradiation is shown in Figure 3.30. Molten Flibe and other samples were extracted from the graphite crucibles before sample sectioning for the tritium analysis took place. The top surface of the first section was 43mm above the bottom of the crucible and subsequent sections were cut moving towards the bottom face. Therefore, the designation LGC or "lower graphite crucible" was used to distinguish the samples from the broken upper piece, GC1-1, used for shakedown testing of the steel furnace.

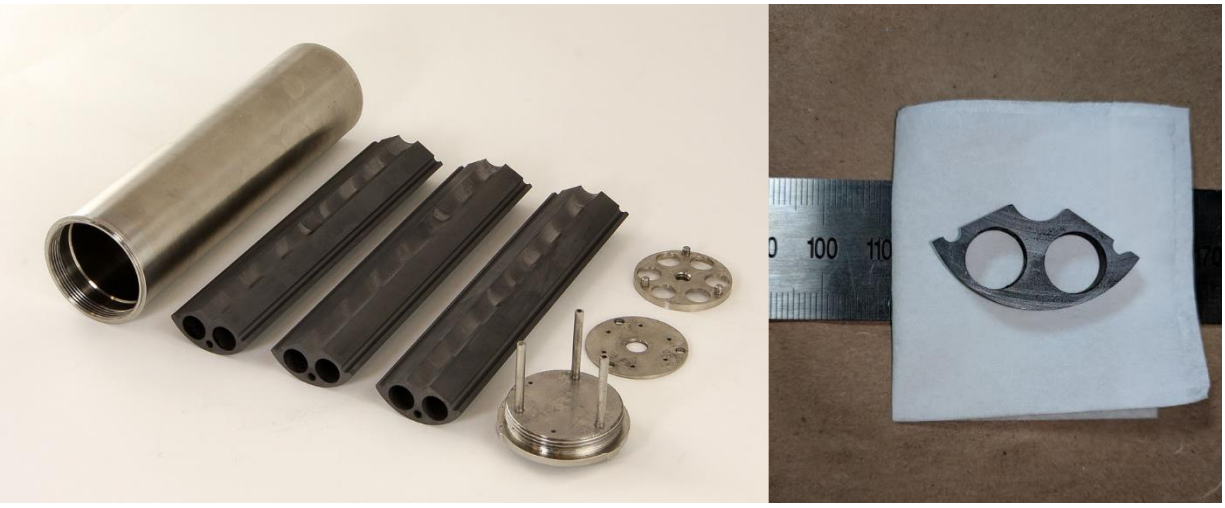

Figure 3.29. FS-1 experimental capsule and IG-110U graphite crucibles (left). One graphite crucible section was cut into several axial slices after the irradiation (right).

Figure 3.30. The FS-1 crucible loaded with samples and Flibe in a glovebox prior to irradiation. Samples for tritium analysis originated from the lower third section. From [17].

The FS-1 crucible sections offered a unique opportunity to examine loosely bonded tritium on the samples since they were not cleaned prior to sectioning. In contrast, the IG1, IG2, and ARB samples from FS-2 were soaked in deionized water overnight to dissolve any Flibe remaining on the graphite. Tritium dissolution was monitored during the sectioning of the FS-1 graphite samples in the roughly 200mL of water used as a lubricant for the saw blade. After each sample was cut, it was soaked in a beaker with 100mL of water for roughly two minutes in order to remove loose particles. One of the crucible sample sections (LGC-1) was soaked for an additional hour in a fresh 100 mL beaker to examine if additional leaching could occur. Periodic 0.1 mL samples were taken for LSC analysis during the hour, as shown in Figure 3.31. The LSC measurements were ten minute counts, which resulted in a relative uncertainty between 1% and 3% based on counting statistics. Some scatter in the plot can be explained by insufficient mixing in the beaker before LSC samples were taken. Water in the soaking beaker was only lightly stirred in order to prevent damage to the submerged graphite sample.

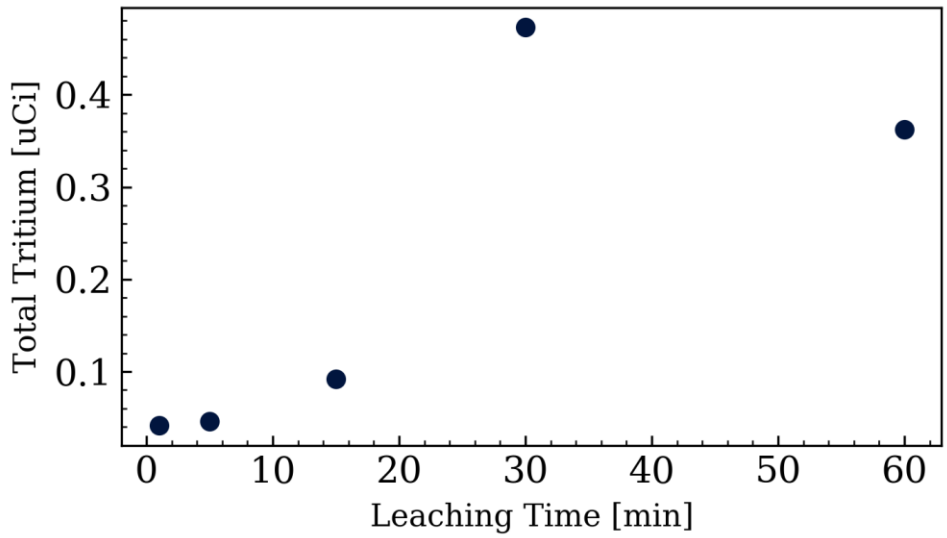

Figure 3.31. Tritium removed from the LGC-1 sample by 100 mL of deionized water as a function of soaking time based on 0.1mL samples taken at the given times.

Liquid scintillation counting of each water source showed 5.6 μCi of tritium in the cutting water tray and 1.2 μCi in the post-cutting soaking beaker. If tritium in the tray and beaker is divided evenly among the five samples prepared, and every sample is assumed to have 0.4 μCi of residual tritium that can be removed by extended soaking, as observed for LGC-1, then 1.8 μCi of easily removable, water soluble tritium was present on each graphite crucible section. Possible sources

are tritium contained in frozen salt residue on the graphite surface, TF retained in the graphite, or retained tritium which was converted to HTO during storage of the graphite. Tritium at high energy trapping sites in the graphite is not expected to easily dissolve into water during soaking.

The FS-1 graphite crucible sections were also desorbed in the quartz tube furnace following the water soaking analysis. Because of an observed lower tritium collection rate and high scatter observed in previous measurements with the water bubbler system compared to the ion chamber, the sweep gas was switched to Ar-0.5%H_2. The purpose of reducing the sweep gas hydrogen concentration from 4% to 0.5% was to increase the efficiency of the catalyst furnace in reacting HT/T_2 into HTO to promote tritium capture in water vials 4 through 6. Reducing excess H_2 was thought to decrease competition with HT/T_2 in the catalyzer and produce a higher conversion rate into HTO. A lower hydrogen concentration also potentially reduces the influence of the sweep gas on the chemical form of tritium, although in both 0.5% and 4% cases the concentration of H_2 is much greater than the tritium concentration in the sweep gas measured during desorption experiments. The 0.5%H_2 mixture was produced by adding a second mass flow controller and mixing a cylinder of argon with the previous Ar-4%H_2 cylinder into the tube furnace sweep gas supply inlet.

For the first three sections, a variable temperature ramp rate study was conducted to measure the activation energy of desorption. However, a thermocouple grounding issue occurred during the LGC-2 desorption which made mapping the desorption rate onto temperature difficult. The crucible sections were also much larger than the FS-2 samples previously tested and required special sample trays cut from machinable alumina. After the LGC-2 test, discoloration on the quartz tube was observed and the sample trays for the remaining experiments were switched to quartz cylinders cut from a 2.54 cm diameter tube. Switching from an opaque ceramic to the transparent quartz sample tray could have influenced the sample temperature in a way that was not measured by the thermocouple in the furnace. Therefore, an inconsistent trend was observed compared to the results from the IG1 sample. Temperature and desorption measurements from the LGC-1, 2, and 3 crucible sections are shown in Figure 3.32. The LGC-1 procedure was repeated a second time and a total desorption of 2% compared to the first run was observed. Since the LGC-1 test had the highest ramp rate and thus the least amount of desorption time, the 2% value could be considered as an upper limit to the remaining amount of tritium in the samples which could be desorbed by a second run in the quartz tube furnace.

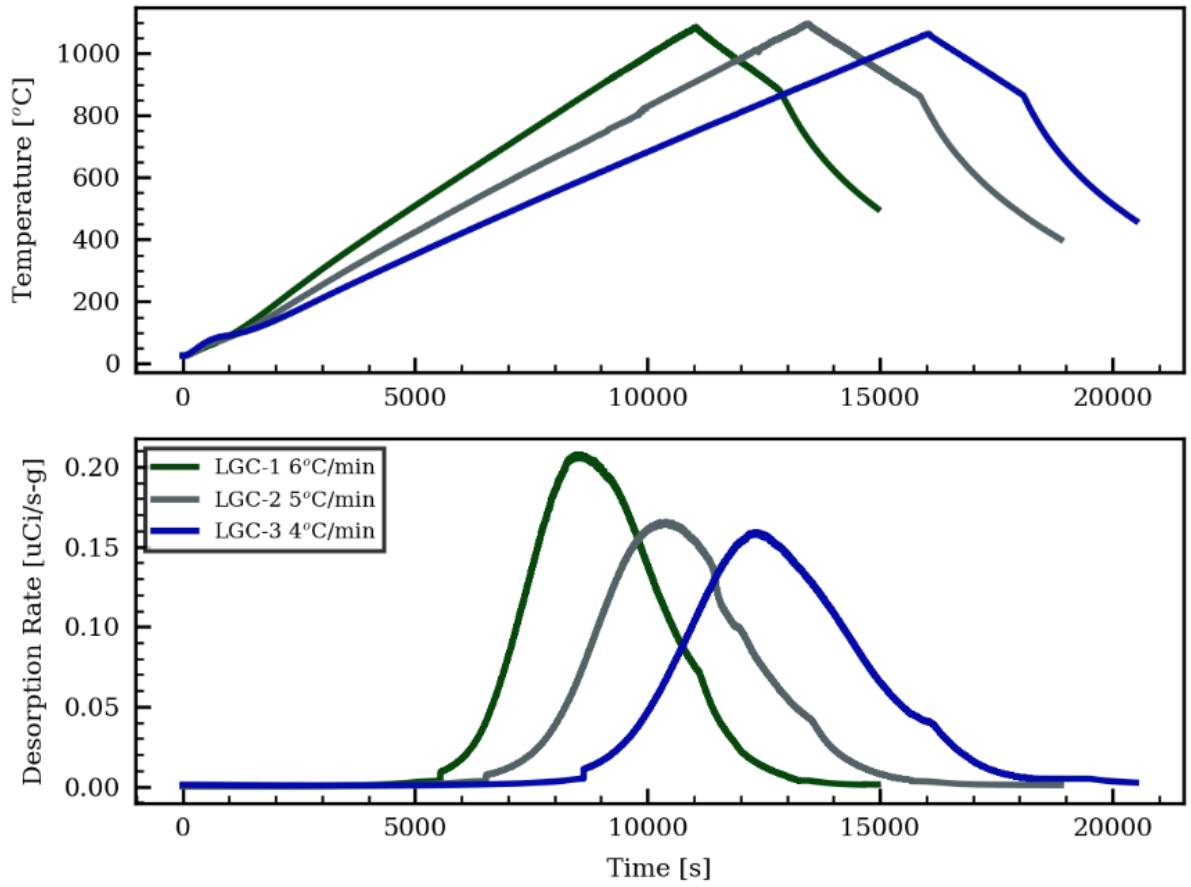

Figure 3.32. Temperature and tritium desorption profiles as a function of time for FS-1 graphite crucible sections LGC-1, 2, and 3. A 359cc/min sweep gas flow of Ar-0.5%H_2 was used.

Another important observation from the graphite crucible tests was that the peak desorption rate occurred at temperatures greater than 800ºC, compared to 675ºC-725ºC measured in the previous FS-2 IG-110U desorption experiments. The increase in peak desorption temperature was believed to be caused by the lower concentration of H_2 added to the furnace sweep gas. To test the theory, a sixth crucible section was cut and desorbed at a further reduced concentration of Ar-0.1%H_2, but with the same total gas flow rate. Desorption verses temperature for LGC-4 and 5 tested with Ar-0.5%H_2 are plotted with the Ar-0.1%H_2 LGC-6 test in Figure 3.33. The peak desorption rate occurred at 829ºC and 826ºC for LGC-4 and 5 respectively and 929ºC for LGC-6. Therefore, the decreased hydrogen concentration in the LGC-6 test sweep gas resulted in a peak temperature increase of roughly 100ºC. The shift in peak temperature could have been caused by an acceleration of tritium diffusion out of the graphite samples with elevated H_2 present [136].

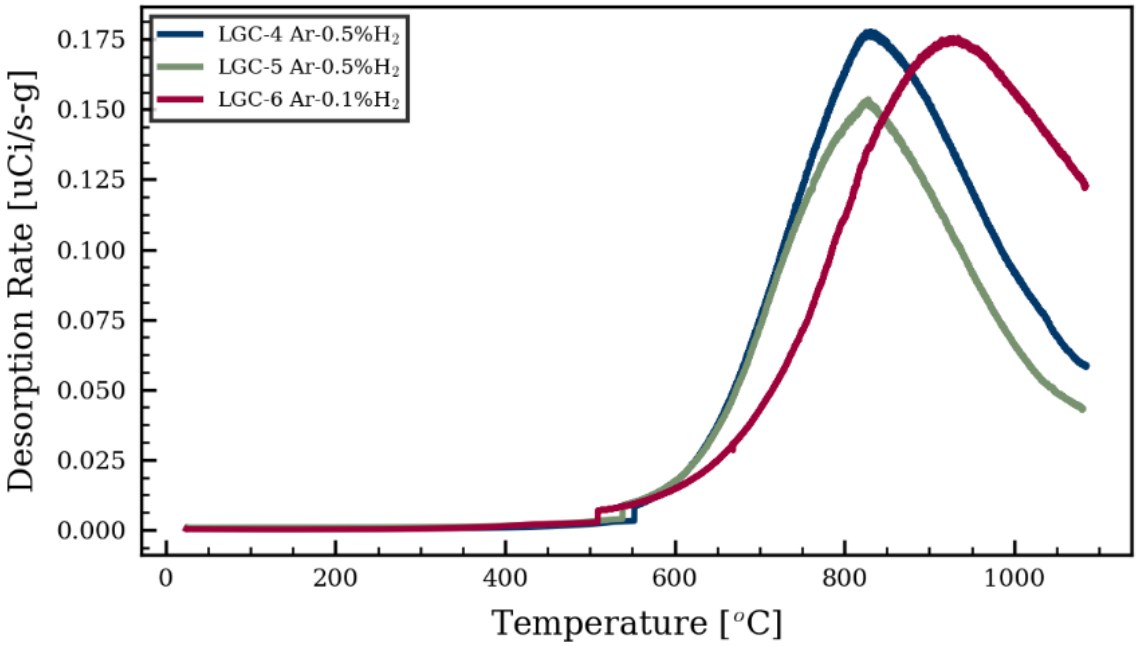

Figure 3.33. Desorption profile for the remaining FS-1 IG-110U graphite crucible sections at ramp rates of 5ºC/min. A peak shift in the LGC-6 desorption profile was caused by a lower H_2 concentration in the sweep gas.

Total measured tritium content in the FS-1 graphite crucible samples is shown in Table 3.9 below. Tritium content is again increased to account for decay and a W factor ratio of 0.783 is applied for the Ar-0.5%H_2 sweep gas. The values in Table 3.9 represent the tritium retention in the samples at the time-center of the FS-1 irradiation, or October 6th, 2013. Flibe-facing surface area was determined by taking several micrometer measurements of the sample thickness near the crucible holes. The thickness was then used to calculate the cylindrical area of the inner holes since the diameter was known from fabrication. As shown in the relative standard deviations in Table 3.9, the Flibe-facing surface area was a slightly more consistent normalization for tritium content than sample mass. However, since the samples were intended to be axial slices of the same vertical geometry there should ideally have been the same amount of Flibe-facing area per sample mass. Therefore, the μCi/mm^2 and mCi/g measurements are not useful for examining surface-limited or volumetrically-saturated retention. The tritium per area measurement is likely more consistent since it can partially account for deviations in the angle of cuts on the top and bottom faces of each sample. However, it is clear that the FS-1 crucible samples resulted in less tritium retention per sample mass than the previous FS-2 measurements. The LGC set contained roughly 5 times less tritium per mass than the FS-2 IG1 sample, which roughly corresponds to the specific areas of the

samples (181 mm^2/g for FS-1 LGC and 690 mm^2/g for FS-2 IG1, on average). Therefore, it is also likely that the FS-1 graphite samples experienced tritium retention concentrated near the Flibe-graphite interface, rather than homogenous retention in the crucible.

Table 3.9. Tritium measurement summary from the FS-1 IG-110U crucible sections.

Sample	Mass [g]	Area [mm^2]	Total Tritium [mCi]	Tritium/Area [$\mu Ci/mm^2$]	Tritium/Mass [mCi/g]	Soluble ^3H
LGC-1	1.55791	302±11	1.206	3.99	0.7741	1.3%
LGC-2	1.69241	296±11	1.196	4.04	0.7067	1.4%
LGC-3	1.20344	220±12	0.921	4.19	0.7653	2.5%
LGC-4	1.86737	325±12	1.438	4.44	0.7701	2.0%
LGC-5	1.54778	269±10	0.998	3.71	0.6448	4.1%
LGC-6	2.19866	407±27	1.929	4.74	0.8774	13.7%
			Average:	4.18	0.7564	4.2%
			$\sigma_{relative}$:	8.6%	10.3%	

Tritium solubility results in Table 3.9 also show a similar trend to the FS-2 IG1 sample, where the majority of tritium was measured in an insoluble form as HT or T_2. One clear outlier, however, was the LGC-6 sample tested with the Ar-0.1%H_2 sweep gas. The LGC-6 sample also saw drastically less tritium per sample mass than the other five samples as measured by the water bubbler. An average of 0.242 mCi/g was measured for the LGC-1 through LGC-5 samples compared to 0.091 mCi/g for LGC-6. A malfunction with catalyst furnace could have occurred where soluble tritium was collected at the same rate but a greater fraction of insoluble tritium was able to pass through the water bubbler. Removing the LGC-6 sample, the remaining five crucible sections saw an average soluble tritium percentage of 2.3%. The average soluble percentage from the FS-2 IG1 sample was higher at 3.5% even though the samples were tested with Ar-4%H_2 instead of Ar-0.5%H_2. Therefore, it does not appear that the percentage of soluble tritium measured with the tube furnace is a strong function of the concentration of H_2 added to the sweep gas. For the first five FS-1 crucible samples, 2.3% of the 1.083 mCi average measured corresponds to 25μCi, which is totals to 26.8μCi or 2.5% of tritium retained per sample in a soluble form when the amount from the water leaching measurement is included. The low soluble fraction measured on the FS-1 crucible sections and other samples provides justification for focusing on insoluble forms of HT or T_2 when examining tritium retention mechanisms in graphite in the molten Flibe environment.

3.3.5. Observations from the Desorption of FS-3 Graphite Samples

Tritium desorption measurements of FS-3 graphite samples are important for understanding the distribution and partitioning of tritium in the Flibe experiments. As discussed previously, the FS-3 test was the only MITR Flibe in-core irradiation where a significant fraction of tritium release in the off-gas was observed. Therefore, desorption testing of the FS-3 samples helps to frame the total tritium retention in graphite in terms of the calculated generation and observed release. However, as the largest test of the three irradiations, 95 total graphite samples were present in FS-3 along with the three IG-110U crucibles. The desorption tests of five graphite samples from FS-3 presented in this section can provide preliminary values to help quantify the overall tritium retention, as well as identify important factors in graphite retention mechanisms through analysis of the desorption profiles. Samples used in this study were 8 mm diameter, 2 mm thick discs – the same geometry used for 70 of the 95 FS-3 samples. The remaining 25 samples were larger 8 mm diameter, 16 mm height cylinders reserved for mechanical testing [40]. Seven IG-110 disc samples from the #4 compartment of the upper crucible are shown in Figure 3.34.

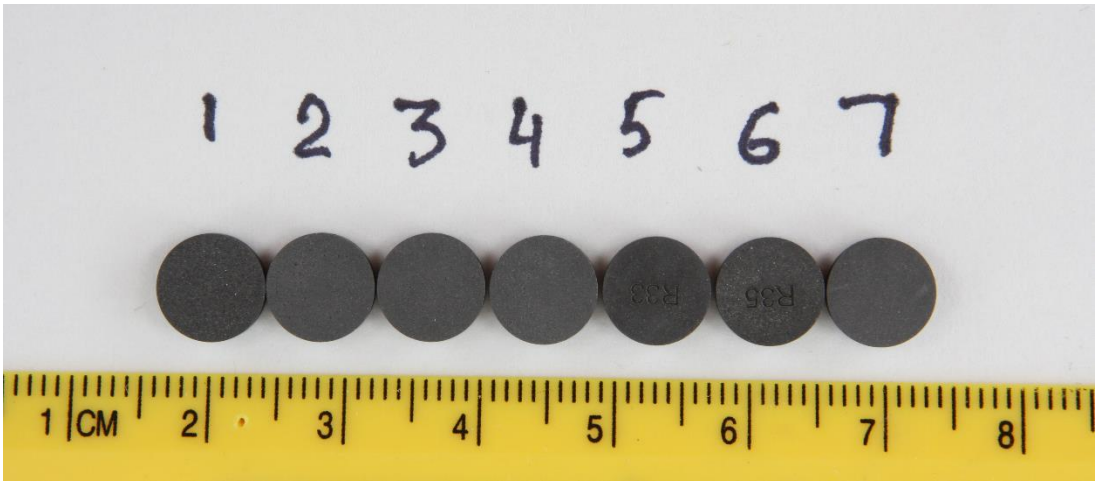

Figure 3.34. IG-110 graphite disc samples from the upper crucible compartment #4 (U4) shown prior to irradiation. The first sample is the deepest submerged in the salt.

The graphite disc samples were inserted in groups of seven into the crucible compartments, where the samples in each compartment were all of the same graphite grade. Compartments were machined with additional slots which maintained the discs in a vertical position with flat faces of the disc perpendicular to the crucible upper face. The crucible design and dimensions are shown in Figure 3.35 – an identical design was used for the upper and lower crucibles. Samples are

inserted according to the number of the set, with the #1 sample being the first and thus the deepest in the crucible compartment. A metal plate in contact with each crucible upper face was in contact with the #7 samples and thus a contact chain from sample to sample kept the graphite discs submerged in the salt. Temperature was measured with a thermocouple in a smaller hole drilled near the edge of each crucible (feature B in Figure 3.35). The thermocouple measured the temperature at the middle of the salt compartment depth and thus was most representative for the #3 and #4 samples in the seven sample sets. Graphite crucibles assembled onto the FS-3 test assembly are shown in Figure 3.36.

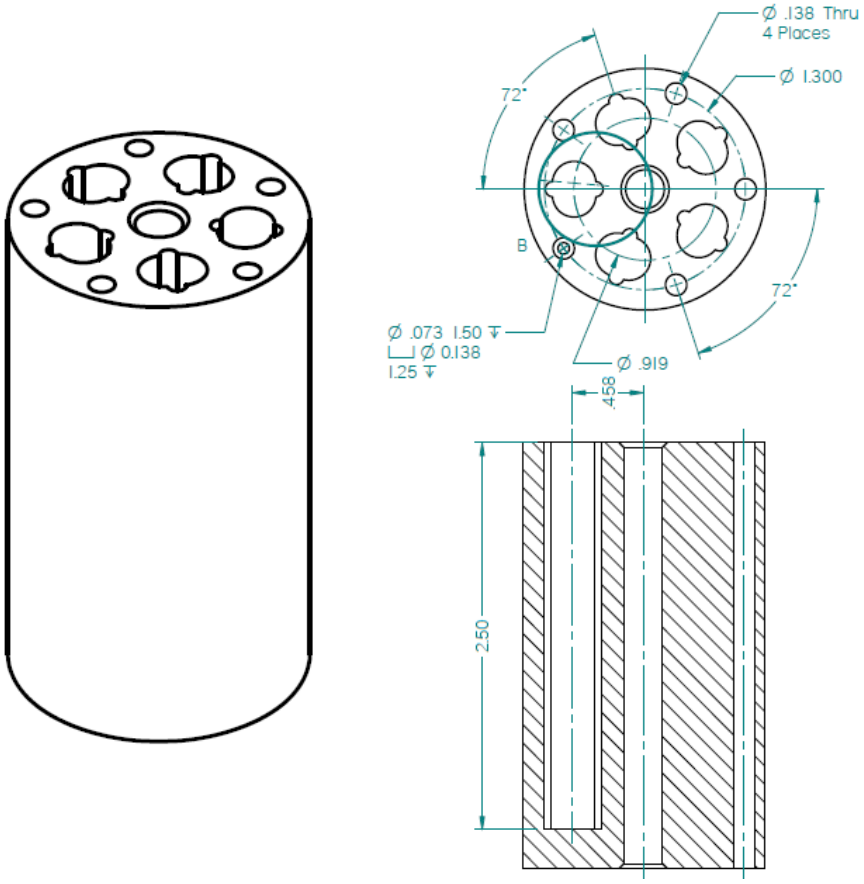

Figure 3.35. Lower and upper crucible design for FS-3. Disc samples are vertically oriented by the slots machined into the five salt compartments. All dimensions are in inches.

Figure 3.36. Graphite crucibles and nickel capsule cover in an assembly test prior to Flibe filling and the FS-3 irradiation.

The first desorption tests with the FS-3 samples used IG-110U discs from the lower crucible #3 compartment (L3) and aimed to confirm previous results on effects of H_2 in the desorption sweep gas. As shown in the tritium desorption profiles of Figure 3.37, there was a noticeable shift in the peak desorption rate to higher temperatures as the H_2 concentration was decreased between samples from 4%, to 1%, and then 0.25%. The initial desorption peak occurred at a temperature of 865ºC, 901ºC, and 953ºC for L31, L32, and L33, respectively. Observing the peak shift at the relatively high concentrations of 4% and 1% H_2 helps to rule out interactions of tritium in the quartz tube as the cause of the desorption peak shift. Therefore, the desorption tests with the FS-3 L3 samples provides evidence supporting that hydrogen in the sweep gas accelerates diffusion of tritium in the graphite samples and leads to an earlier desorption peak at higher H_2 concentrations.

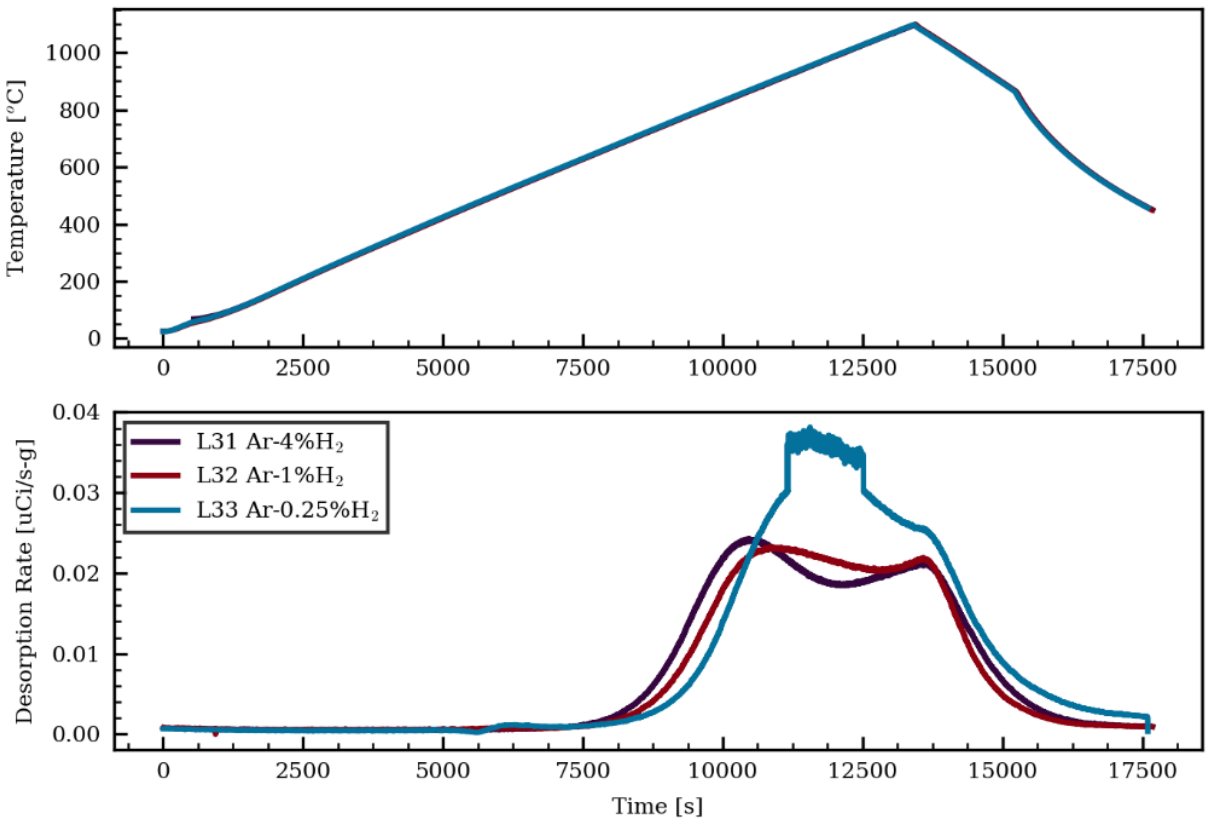

Figure 3.37. Applied temperature profile and desorption rate as a function of time for IG-110U sample discs from the lower crucible of FS-3. Samples were desorbed at 5ºC/min with various sweep gas compositions. An ion chamber range switch obstructed the L33 measurement.

There were several key differences between the FS-3 sample desorptions and the previous results shown from FS-1 and FS-2. The most obvious is the presence of a second peak near the maximum temperature of the tube furnace. In this case the peak is not fully resolved and the desorption rate starts decreasing because the furnace temperature reaches its maximum set point. A higher temperature peak was observed in some of the early steel furnace measurements, but could have been explained by tritium contamination from previous testing. No high-temperature peak was seen in the quartz tube furnace tests with the IG-110U crucible sections from FS-1 and the IG1 sample from FS-2. Since these samples all originated from the same IG-110U graphite source, there should be minimal differences in material properties that could influence tritium retention.

Other significant features of the FS-3 L3 sample desorptions were the elevated position of the initial desorption peak and the much lower overall tritium retention. The L31 peak desorption temperature of 865ºC with Ar-4%H_2 was even higher than the 827.5ºC average of the LGC-4 and

LGC-5 samples despite their use of Ar-0.5%H_2 sweep gas. Peak desorption rates for L31, L32, and L33 were also roughly an order of magnitude lower than the LGC samples in terms of μCi/s per sample mass. All of the differences between the L3 desorption profiles and the FS-1 and FS-2 samples can potentially be explained by the addition of He-3.5%H_2 into the FS-3 sweep gas.

While He-3.5%H_2 injection occurred downstream of the irradiation zone, even a small amount of hydrogen back-diffusion into the capsule or permeation from the thimble to capsule could create a situation where hydrogen present near the graphite greatly outnumbered tritium. For example, the equilibrium tritium release rate in the capsule was estimated to be 9.83 mCi/day during FS-3 [18], which corresponds to $1.57 \cdot 10^{-6}$ mol T/m^3 in the 150 cc/min capsule sweep gas. In comparison, the concentration of H in He-3.5%H_2 is roughly six orders of magnitude higher at to 2.844 mol/m^3. Considering just the salt instead of the gas, if the 589 mCi of tritium generated during the FS-3 irradiation never left the 101.5g of Flibe in the capsule, the concentration of T in the salt would be 0.388 mol/m^3, and thus still lower than the hydrogen concentration in He-3.5%H_2.

When the hydrogen concentration exceeds the tritium concentration, both hydrogen and tritium will be retained in graphite, but the amount of overall tritium retention in the multi-isotope case will be less than if there were only tritium present. This can be explained by the square root relationship with hydrogen solubility in graphite – as total hydrogen partial pressure increases, a lower relative amount of H and T will be retained from the gas phase. If the solubility followed a linear relationship with partial pressure, then equal fractions of hydrogen and tritium would be retained in the graphite at any given partial pressure. The multi-isotope effects between H and T solubility in graphite helps explain why the FS-3 samples had significantly higher peak desorption temperatures than FS-1 and FS-2. It is likely that the total retention of H and T in the FS-3 graphite was much greater than T alone in FS-1/2, and FS-3 samples could even have approached volumetric saturation. If tritium in the FS-3 graphite was evenly dispersed throughout the volume instead of concentrated near the surface, then the total diffusion length for desorption would increase for the FS-3 samples which would also be reflected in an increase in the peak desorption temperature.

Another significant observation from the FS-3 tritium analysis was the difference in desorption profiles between samples irradiated in the lower and upper crucibles. In addition to the three L3 samples, two IG-110 discs from the upper crucible #4 compartment (U4) were desorbed in the quartz furnace. The U43 sample desorption profile shown in Figure 3.38 displays a

substantial increase in the high-temperature peak compared to L31. A repeated desorption of the U43 sample shows that the first peak at roughly 850ºC was thoroughly desorbed, but significant fraction of tritium remained in the high-temperature peak. The most significant difference between the lower and upper crucibles was the irradiation temperature during FS-3. Since FS-3 had the largest test capsule among the MITR Flibe irradiations, there was also a notable temperature gradient from the bottom to top of the irradiation zone. Thermocouples positioned near the axial center of each crucible read an average of 600.3ºC, 698.6ºC, and 719.4ºC for the lower, center, and upper crucibles, respectively. The increase of over 100ºC in irradiation temperature for the upper crucibles may have assisted in tritium diffusion towards, and bonding with, high-energy trapping sites. These result show some consistency with retention studies by Causey et al, where trapping at high energy sites became significant at temperatures above 1000K [127]. Since the 960 hour FS-3 irradiation was much longer than the 1.5 hour experiments by Causey et al, the transition to high energy trapping sites could occur at a lower temperature.

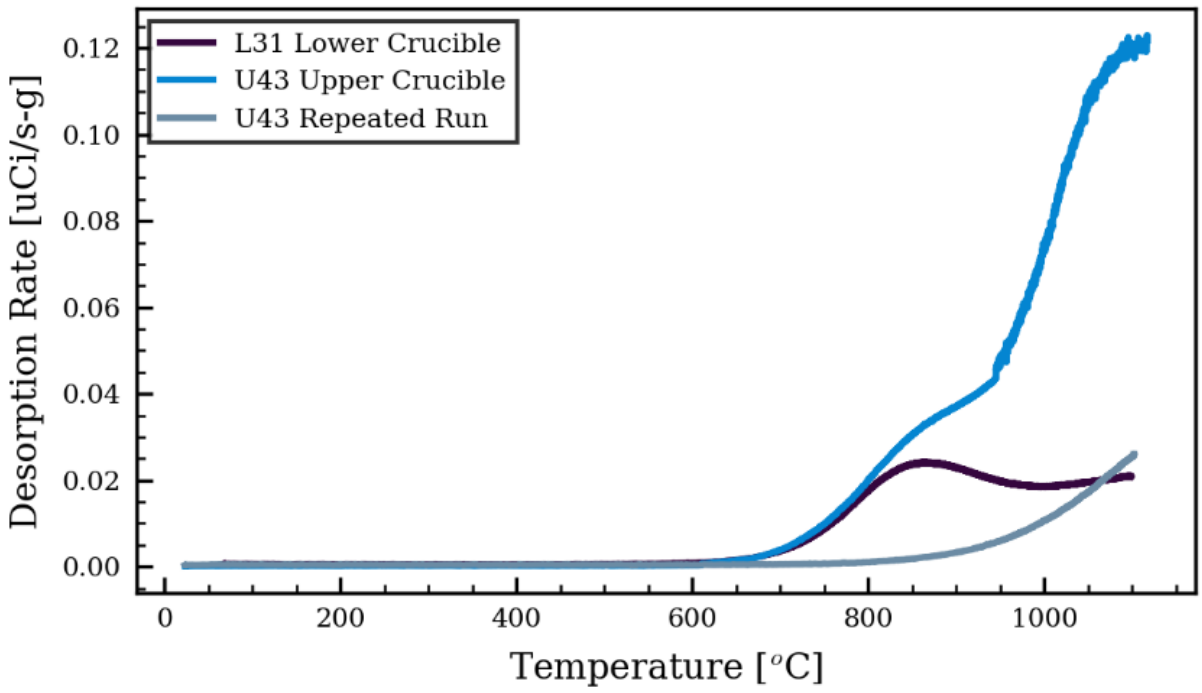

Figure 3.38. Comparison of samples irradiated in the upper and lower crucibles of FS-3. Both samples were tested at 5ºC/min with Ar-4%H_2.

Observing surface-limited retention or volumetric saturation was also important for understanding whether or not additional hydrogen had influenced the FS-3 graphite tritium retention characteristics. Therefore, the subsection analysis was repeated for the #4 IG-110 sample disc in the upper crucible #4 slot (U44). The FS-3 sample discs were significantly smaller than previously used for FS-2, and thus the number of subsections had to be reduced to 4 total. As shown in Figure 3.39, the U44 sample was cut off-center in order to create samples that varied in mass as well as Flibe-facing area. Complied desorption profiles in Figure 3.40 show similar results to that of the U43 sample, where the first desorption peak at roughly 850ºC was significantly smaller than a high-temperature peak near the furnace maximum range. Another important observation was the similarity of mass-normalized desorption rates between samples, despite the variation of specific surface areas from 818 mm^2/g to 983 mm^2/g.

Figure 3.39. Subsection labeling diagram for the FS-3 IG-110 sample U44 from the upper crucible.

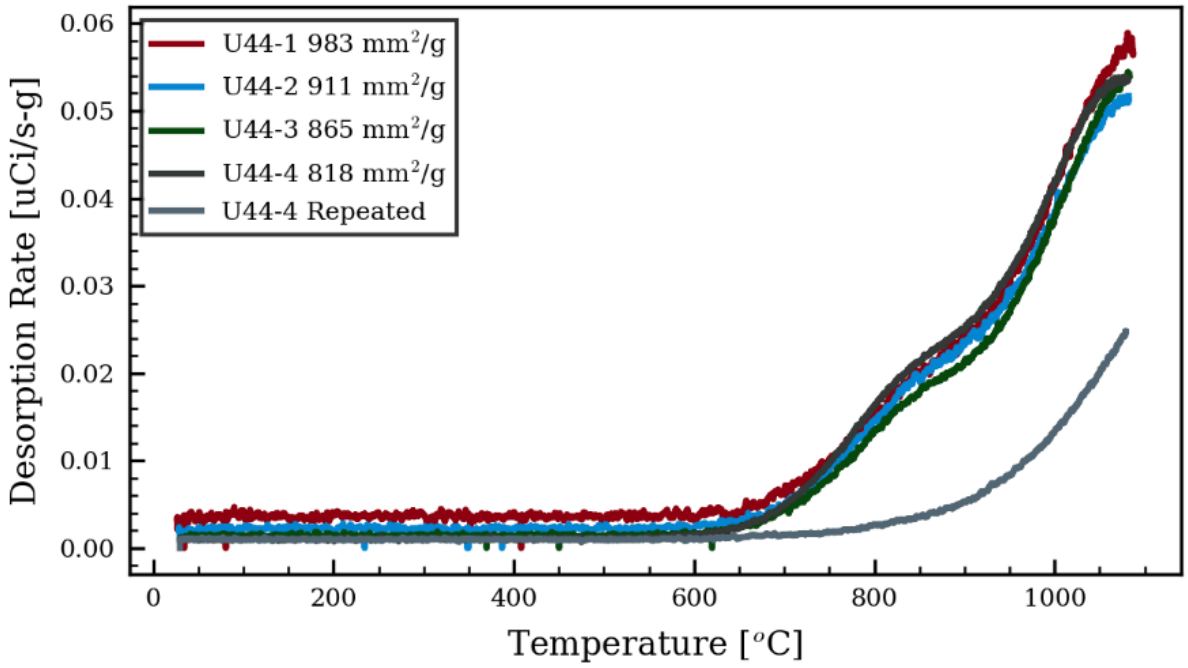

Figure 3.40. Desorption verses temperature for the FS-3 IG-110 sample U44 subsections tested with ramp rates of 5ºC/min and Ar-4%H_2 sweep gas.

Total tritium content from the subsection desorption tests are shown in Table 3.10. Tritium measurements are again adjusted to the time-center of the FS-3 irradiation (November 28th, 2016) to account for the decrease in activity from decay. Sample Flibe-facing area still provided a slightly more consistent normalization than sample mass as seen in other subsection desorption testing. However, the relative difference in group standard deviations between μCi/mm^2 and mCi/g measurements was less than that measured for FS-2 samples – tritium per mass had twice the relative standard deviation for the IG1 sample, 2.3 times for the ARB sample, and was a factor of 2.6 higher than tritium per area for IG2, compared to a factor 1.7 for U44. As shown in Figure 3.41, a zero-intercept linear fit between tritium content and sample mass had a slightly higher R^2 value than for tritium content verses area, in part because a wider range existed between sample mass than for sample area. The subsection analysis cannot conclusively show that the U44 sample had a homogenous distribution of tritium, but there was clear evidence that U44 was closer to volumetric saturation than the FS-2 samples.

Table 3.10. Tritium desorption results from the subsections of FS-3 upper crucible sample U44.

Sample	Mass [g]	Area [mm^2]	First Desorption [mCi]	Tritium/Area [μCi/mm^2]	Tritium/Mass [mCi/g]	Soluble ^{3}H
U44-1	0.02086	20.5±0.5	0.00640	0.312	0.3068	17%
U44-2	0.03266	29.8±1.0	0.00845	0.284	0.2587	0.9%
U44-3	0.05111	44.2±0.9	0.01277	0.289	0.2499	3.3%
U44-4	0.07235	59.2±0.2	0.01891	0.319	0.2614	0.7%
			Average:	0.301	0.2692	
			$\sigma_{relative}$:	**5.7%**	**9.5%**	

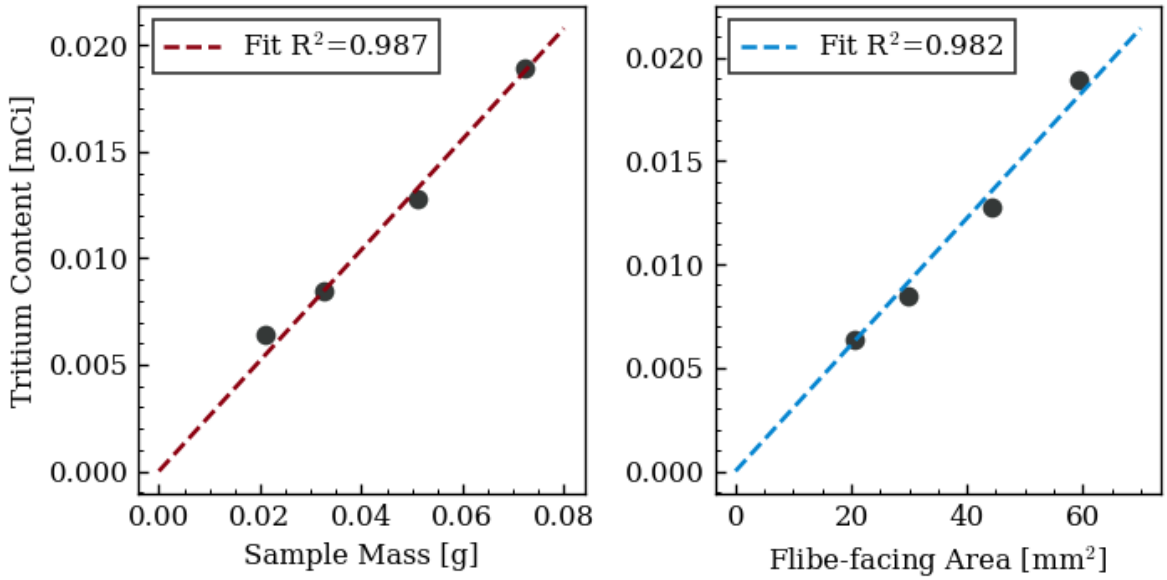

Figure 3.41. Tritium content versus sample mass and area for the subsections of FS-3 IG-110 sample U44. Sample mass led to a slightly better fit than sample area in terms of a zero-intercept linear relationship.

Results from the FS-3 sample desorption measurements are summarized together in Table 3.11. Because of the significant differences in tritium content between lower crucible and upper crucible samples, a separate average was used for each group. The significant amount of tritium in the high-temperature peak also resulted in a large amount of additional desorption in the repeated runs, where 19.1% of the initial release was observed for the U43 sample second run and 38.1% occurred for U44-1. A lower fraction in the second run was seen for the U43 sample because the maximum furnace set point was raised from the typical value to observe more of the high-

temperature peak. The resulting maximum temperature was 37ºC higher for the U43 sample compared to U44-1 and thus a more complete desorption occurred. Because of the high additional desorption, another column is added to Table 3.11 to account for the remaining tritium in the samples which could be desorbed by the quartz tube furnace. An infinite amount of additional runs at with 19.1% carryover would lead to a total amount of tritium in the sample being 23.6% greater than the initial measurement – for the U44 carryover of 38.1% the total amount would be 61.5% greater than the initial run. Unfortunately a second desorption of an L3 sample was not conducted, but the lesser of the two increase factors was applied in Table 3.11 because of the relatively lower amount of desorption from the high-temperature peak. The desorption results show that on average the U4 samples had three times more tritium content than the L3 samples. As previously stated, the higher irradiation temperature of 719.4ºC in the upper crucible during FS-3 compared to 600.3ºC in the lower crucible is believed to be the cause of both the increased high-energy trapping as well as the elevated total tritium in the U4 samples.

Table 3.11. Tritium content in the L3 IG-110U and U4 IG-110 samples from the FS-3 irradiation

Sample	Mass [g]	Area [mm^2]	First Run [mCi]	Predicted Total [mCi]	Tritium/Area [$\mu Ci/mm^2$]	Tritium/Mass [mCi/g]
L31	0.18285	152	0.0216	0.0267	0.176	0.1459
L32	0.18068	152	0.0198	0.0245	0.161	0.1353
L33	0.18459	152	0.0260	0.0321	0.211	0.1741
				Average:	0.183	0.1518
				$\sigma_{relative}$:	14%	13%
U43	0.17906	151	0.0702	0.0868	0.574	0.4849
U44	--	--	0.0465	0.0752	0.486	0.4350
				Average:	0.530	0.4599
				$\sigma_{relative}$:	12%	7.7%

3.4. Tritium Distribution in FS Irradiations and Summary of Observations

3.4.1. Estimation of Overall Tritium Retention in Graphite

Examining the distribution of tritium between release from the salt and retention in graphite is important for understanding overall tritium transport behavior as well as consistency between measurements from the FS-1, FS-2, and FS-3 irradiations. Since only a small subset of graphite samples were tested from each experiment, total retention calculations rely on a method for extrapolating the tritium desorption results to predict retention on other graphite components. One beneficial factor is IG-110U graphite samples were tested from each experiment and were also sourced from the same supply of graphite as the salt-containing crucibles in each test. Therefore, the tritium retention measurements are representative of a large fraction of the graphite material present in each test capsule. However, as demonstrated by the FS-3 desorption results, temperature gradients as well as differences in tritium concentration throughout the salt are potential reasons why retention levels in graphite could vary throughout the capsule. The analysis in this section therefore provides only a preliminary accounting of the tritium distribution from each in-core irradiation.

For FS-1, the total graphite retention can be estimated by taking the tritium content per Flibe-facing area measured from the six crucible sections multiplied by the total surface area of graphite in contact with the salt. The FS-1 measurements themselves did not measure whether tritium was homogenously distributed in graphite or concentrated near the surface. However, tritium content per area is used here since the results were more consistent with the FS-2 IG-110U#1 sample, where 4.18 $\mu Ci/mm^2$ and 4.75 $\mu Ci/mm^2$ were measured between FS-1 LGC and FS-2 IG1 samples, respectively. The tritium per mass measurements were significantly farther apart since 0.7563 mCi/g was measured for FS-1 but 3.669 mCi/g was observed for FS-2. The FS-1 crucible had six compartments 10.3 mm in diameter and 143 mm in depth, which results in a total internal surface area of 28,263 mm^2 [158]. Area multiplied by $4.18 \cdot 10^{-3}$ mCi/mm^2 corresponds to 118 mCi of total tritium retention in the graphite crucible, and a retention of 19.6% considering the 602.5 mCi of total generation from FS-1 [158]. Using the same 4% uncertainty in generation rate discussed for FS-3 along with the 8.6% uncertainty in LGC $\mu Ci/mm^2$ measurements, the uncertainty in retention is 9.5% of 19.6% or 1.9% overall. Therefore, based on the area extrapolation method the retention of tritium in the IG-110U crucible graphite accounted for 19.6±1.9% of the tritium generated during FS-1.

After the FS-1 experiment, a small piece of Flibe was measured to have a tritium content of only 1.5 nCi/mg, although it was expected that this measurement should be a lower bound [147]. This concentration would result in a total of 0.18 mCi in all of the FS-1 salt, which is much lower than the 118 mCi of tritium estimated in the crucible graphite. Tritium retention could have also existed in the Hastelloy N, 316SS, SiC/SiC, and Triso particle samples tested in FS-1, but these samples were not examined. The total surface area of samples was 6763 mm^2 or about 17% of the area of the crucible. Metallic samples also have a lower expected solubilty for tritium than graphite - the solubility of tritium in graphite is roughly five times higher than 316 stainless steel at 700ºC [91, 126]. Therefore, the estimation of tritium retention in the graphite crucible should account for the majority of tritium retention in the FS-1 capsule materials.

An integrated MITR power of 74.2 MWd occurred during the FS-2 irradiation which resulted in 566.9 mCi of total tritium generation [145]. In contrast to the FS-1 desorptions, the subsection analysis of the FS-2 IG-110U#1, IG-110U#2, and ARB#1 samples did demonstrate that tritium per Flibe-facing area was a more consistent measurement than tritium per sample mass. Therefore, the same previous procedure is used to estimate the total retention in the FS-2 graphite. The two crucibles had a total Flibe-facing area of 45,882 mm^2 along with 1380 mm^2 of IG-110U samples and 1377 mm^2 of ARB.

Samples from FS-2 were desorbed in both the steel furnace and quartz tube designs, but the quartz tube furnace should be considered the more representative measurement because of improved features like higher maximum temperature and better temperature control. An average of $4.75 \cdot 10^{-3}$ mCi/mm^2 was measured for the IG1 subsections along with $3.31 \cdot 10^{-3}$ mCi/mm^2 from the IG2-10 subsection. While the difference between samples is significant, it is important to consider both for the full extrapolation because the spread in samples could be representative of the true changes in tritium retention throughout the FS-2 capsule graphite. Therefore, an average of 4.03 mCi/mm^2 can be used to calculate a retention of 191 mCi of tritium in the IG-110U crucibles and disc samples. The ARB graphite was not tested in the tube furnace, but the retention can be estimated by taking the ratio of ARB to IG-110U measurements in the steel furnace times the IG1 value which results in $2.53 \cdot 10^{-3}$ mCi/mm^2. Therefore, the total estimated retention in FS-2 graphite is 194 mCi and the retention accounts for 34% of the total tritium generation. Assuming that the uncertainty in retention is equal to the 28% measured for the IG1 subsection set and generation uncertainty is again 4%, the retention fraction with uncertainty would be 34±10%.

In contrast to FS-1 and FS-2, desorption from the FS-3 graphite samples showed that tritium content had a relatively stronger trend with sample mass. Therefore, total retention can be estimated based on mass of graphite instead of Flibe-facing area. The discrepancy between retention in samples from lower and upper crucibles requires a separate accounting in each zone. A total graphite mass of 464.71 g was present in the FS-3 capsule [40], which consisted of 145.45 g each in the lower and upper zones and 173.80 g in the center crucible. The L3 sample retention of 0.1518 mCi/g then results in 22.08 mCi along with 66.89 mCi from the 0.4599 mCi/g in U4. Tritium retention in the center crucible was not measured, but a value of 0.4061 mCi/g can be estimated from a linear interpolation based on the 698.6ºC irradiation temperature of the center crucible compared to 600.3ºC and 719.4ºC for L3 and U4, respectively. The total retention predicted in the center crucible is then 70.58 mCi and the overall retention of 159.55 mCi is 27.1% of the total generation. The uncertainty in retention is the quadratic sum of the 2.92 mCi, 6.79 mCi, and 5.14 mCi uncertainties of retention in the lower, center, and upper crucibles, respectively, or 9.00 mCi. Combined with a 4% uncertainty in generation, the overall retention in FS-3 is 27.1±1.9%. Repeating the same analysis with Flibe-facing area instead of mass yields a total retention of 4±1%. Therefore, the extrapolation based on mass appears to be more appropriate considering the results from the FS-1 and FS-2 irradiations. Tritium retention results from the three irradiations are summarized in Table 3.12.

Table 3.12. Compiled results for the percentage of total tritium generation in each experiment estimated to be retained in graphite.

In-Core Irradiation	Irradiation Time [hr]	Retention in Graphite	Method of Calculation
FS-1	1000	19.6±1.9%	Retention extrapolation based on Flibe-facing area
FS-2	300	34±10%	Retention extrapolation based on Flibe-facing area
FS-3	960	27.1±1.9%	Retention extrapolation based on graphite mass
FS-3	960	4±1%	Retention extrapolation based on Flibe-facing area
FS-3	960	22±10%	Difference between release and total generation

The estimations for tritium retention in graphite shown in Table 3.12 reveal important features of tritium measurements from the FS-1, FS-2, and FS-3 in-core irradiations. Finding that the estimated retention in the FS-3 graphite based on the mass-based extrapollation represents the difference between generation and release within the margin of error provides some confidence in the values of tritium retention measured in thermal desorption experiments. The release measurements from FS-3 also show that tritium evolution to the capsule gas was lowest at the beginning of the irradiation, then release increased over a roughly 15-day period before stabilizing. If the increase in release rate was caused by a decreasing rate of retention in graphite, then the elevated retention in the FS-2 experiment could also be explained by the fact that FS-2 had the lowest in-core irradiation time. The differences in retention between the experiments motivates the need for understanding how tritium retention rates in graphite changes over time in the molten Flibe environment.

While the estimated graphite retention percentages of total generation in Table 3.12 allow for simple comparisons between experiments, it is worth reiterating that these values provide only a partial accounting of tritium from each irradiation. Only a small subset of material from each experiment was used to extrapolate the total tritium conent in graphite, as previously discussed. The FS-1 and FS-2 experiments also contained metallic samples immersed in the salt, which were not analyzed for tritium inventory - the full sample matrix from each irradiation experiment is provided in Appendix A. Tritium releases from the irradiation capsule were only measured in significant quantities during the FS-3 experiment due to the addition of H_2 into the capsule and thimble sweep gas. From all experiments, residual tritium on the gas tubing surfaces or within the capsule and tubing metal itself is also another potential final tritium location which was not measured. A summary of all tritium measurements relevant to tritium accounting from each experiment is provided in Table 3.13. For reference, graphite samples were soaked in water prior to all tritium desorption measurements, but the water was only analyzed for tritium content with the FS-1 LGC samples. The water soaking showed 0.0018 mCi of easily removable water-soluble tritium per sample, which is extrapolated in Table 3.13 to represent the full crucible mass. Flibe after FS-1 was also analyzed for tritium content by dissolution in water, which measured 1.5 nCi/mg of Flibe and thus a total extrapolated salt inventory of 0.18 mCi.

Table 3.13. Summary of tritium generation calculations and tritium analysis measurements from each MITR irradiation. All values in mCi.

In-Core Irradiation	Tritium Generation	Tritium Release	Graphite Water Soaking	Graphite Thermal Desorpion	Salt Dissolution in Water
FS-1	603±24	--	[1]0.17	[2]118±10	[1]0.18
FS-2	567±23	--	--	[2]194±54	--
FS-3	589±24	460±53	--	[1]160±9	--

[1]Extrapolated to experiment total based on mass
[2]Extrapolated to experiment total based on Flibe-facing surface area

3.4.2. Observations from Thermal Desorption of Graphite Samples

One central motivation of using thermal desorption for tritium analysis instead of other techniques like combustion or dissolution in acid was to observe the release of tritium from the graphite samples as a function of temperature. The temperature-dependent desorption rate can then be used to examine the tritium retention mechanisms in graphite which occurred as a result of the MITR in-core Flibe irradiations. Since the measurements in this section are the only thermal desorption studies available on tritium retention from molten Flibe irradiations, the next most suitable comparisons are gas charging and thermal desorption of deuterium in nuclear graphites, of which several studies have been conducted [115, 127]. Deuterium desorption as a function of temperature is shown for several graphite grades in Figure 3.42 [159]. Desorption profiles show an initial peak between 600K and 700K which was proposed to be caused by molecular retention of D_2 in graphite pores [115]. The pore retention peak was only noticeable for some grades, and was also shown to follow a linear relationship with charging pressure [115]. The pore desorption peak was not observed in tritium desorption profiles in this work, which can be explained by the low tritium partial pressure expected in Flibe during the MITR irradiations. A maximum D_2 desorption rate occurred between 1300K and 1400K, which was 1346K and 1384K for ISO-880U and IG-110U, respectively according to Figure 3.42 [159]. Differences between peak position among the graphite grains were explained by grain sizes, where ISO-110U had the lowest grain size at 5 μm, was the fastest to desorb thoroughly, and thus had the earliest peak desorption temperature [123]. Another peak can be seen from the results, which is the most clear for ISO-880U at 1664 K. The high temperature peak was explained by the presence of high-energy trapping sites within graphite crystallites [115].

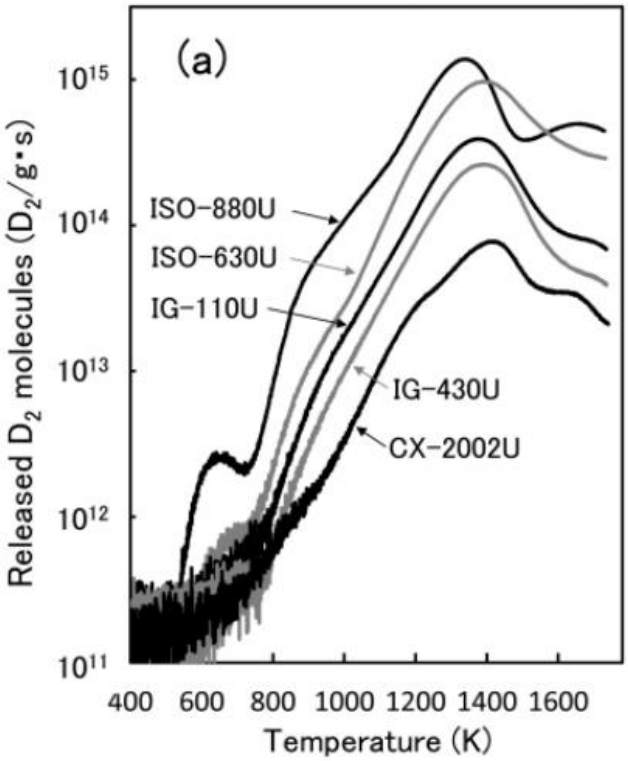

Figure 3.42. Thermal desorption spectra of deuterium in several nuclear graphite grades charged with 42 kPa D_2 for 8-30 hours at 1000ºC and desorbed at 6ºC/min. From [159].

The mechanism for the 1300K-1400K D_2 desorption peak was proposed as deuterium from crystallite edge trapping sites released in a diffusion-controlled process through the graphite filler grains [115]. It is possible that the initial desorption peak from the FS-1, FS-2, and FS-3 sample desorptions also shares this mechanism. One supporting data point was that the desorption activation energy for the peak in FS-2 IG1 samples was calculated to be 260 kJ/mol, which is similar to the 251 kJ/mol and 270 kJ/mol grain diffusion activation energies for ISO-88 and POCO AXF-5Q graphites, respectively [126, 108]. Therefore, it is reasonable to assume that tritium desorption from the initial IG1 peak was also controlled by a diffusion process through graphite grains. However, the temperature location of the peak was significantly different between the tritium desorption measurements in this work and the D_2 gas charging results in literature. For example, the peak desorption rate for the IG1-1 subsection occurred at 1020K while the IG-110U graphite had a maximum desorption at 1384K [159], even though both desorption experiments used ramp rates of 6ºC/min. One explanation is that the FS-2 samples were not fully saturated, which was observed in the subsection analysis of the ARB, IG1, and IG2 samples. An insufficient saturation would result in a higher concentration profile near the outer surface, a lower average

diffusion length required for desorption, and thus an earlier peak temperature in a desorption profile. Similar results were observed in the D_2 gas charging studies, where a peak shift to lower temperatures occurred for samples charged below the point of saturation, as seen in Figure 3.43 [123].

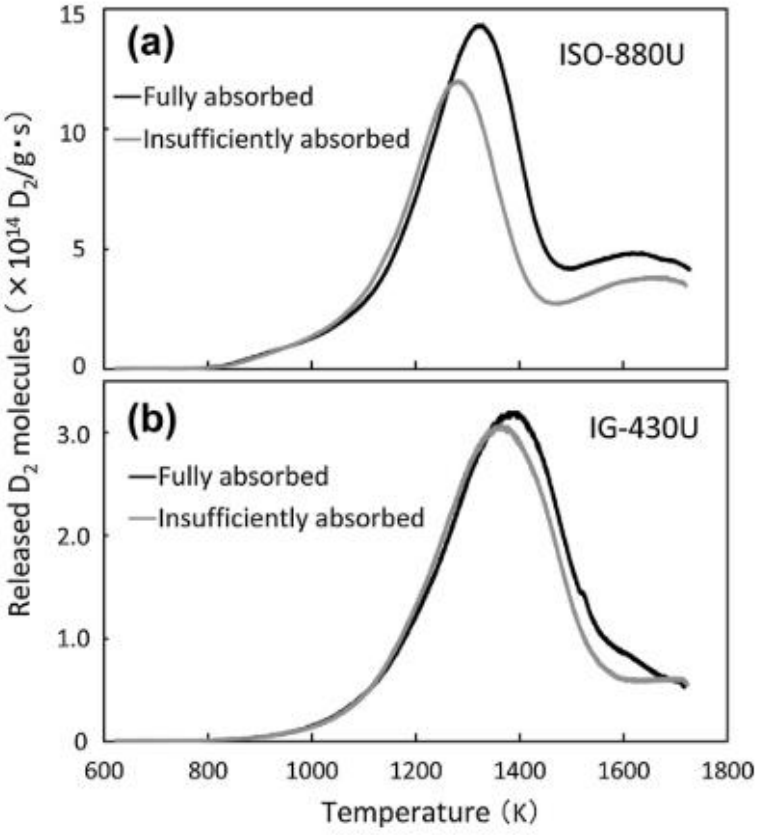

Figure 3.43. Thermal desorption of graphites at saturated conditions compared to profiles at lower charging times. The ISO-880U saturation time was 30,000s compared to 1000s for insufficient charging. For IG-430U, the times were 30,000s and 6000s. From [123].

Another factor contributing to the lower peak desorption temperature was the presence of hydrogen in sweep gas of the furnace desorption experiments. The deuterium thermal desorption studies were all conducted against vacuum, and thus the excess hydrogen concentration can be treated as zero. As previously discussed, excess hydrogen can accelerate diffusion in graphite [136], which also leads to a lower peak temperature if release is controlled by a diffusion process. A comparison of graphite sample groups tested with the same ramp rates but different hydrogen concentrations are shown in Figure 3.44, where in all cases a lower hydrogen concentration led to a higher temperature location of the initial desorption peak. The relationship is best observed from the L3 sample set, since three different hydrogen concentrations were used. A simple exponential

fit of the data assuming the 4%H_2 peak location as the asymptotic value is shown in equation 3.7. From the equation, the desorption peak with zero excess hydrogen would have occurred at 1054ºC, or 1327K. Subsection analysis of the FS-3 U44 sample showed that the graphite was closer to volumetric saturation then the FS-2 samples, which explains why the FS-3 L3 samples had a higher desorption peak temperature than the FS-2 ARB sample and the FS-1 IG-110U crucible sections. However, the predicted L3 peak temperature of 1327K is still lower than the 1384K observed for IG-110U in the D_2 gas charging studies. The remaining 57K difference could be explained by close, but still insufficient saturation in the L3 samples or the 5ºC/min ramp rate used for the L3 group compared to 6ºC/min used in the D_2 studies. Accounting for isotopic differences would move the results farther apart, since deuterium diffuses faster than tritium and the D_2 desorption results would shift to slightly higher temperatures when adjusted to T_2. Nonetheless, the FS-3 desorption results show at least some consistency with D_2 gas desorption studies and do not prohibit using the diffusion-controlled release of tritium from trapping sites in the graphite grains as an explanation of the desorption mechanism in MITR measurements.

Eq.3.7 $$T_{Peak} = 189°C \cdot \exp(-1.19 \cdot \%H_2) + 865°C$$

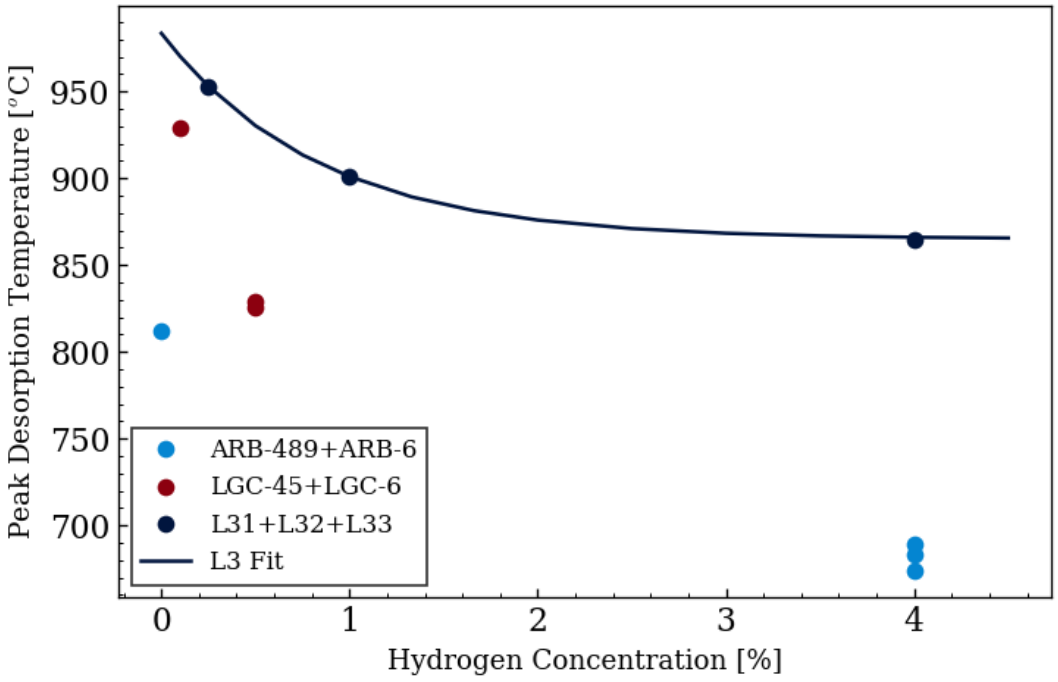

Figure 3.44. Complied results for temperature of initial tritium desorption peaks verses hydrogen concentration used in the steel or quartz furnace sweep gas.

The role of high-energy trapping sites in tritium retention from the FS-1, FS-2, and FS-3 experiments is also important to discuss. A high-temperature peak was clearly observed in the FS-3 sample, but was only occasionally observed in the FS-2 graphite and was not present in the FS-1 crucible sections. As previously discussed, the cause of the high-temperature peak in the FS-2 samples could have been a result of other tritium contamination present in the furnace from previous runs. Therefore, one explanation for the significant high-energy trapping in the FS-3 samples was the possibility of additional hydrogen present from the He-3.5%H_2 addition to the irradiation sweep gas. In hydrogen gas charging studies shown in Figure 3.45, retention in ISO-880U graphite was observed to occur in two stages. In the first stage, the hydrogen retention measured from decrease in pressure corresponded well to the theoretical curve of a diffusion process in the graphite grains [133]. The next stage involved a slower retention rate which lasted for a longer duration of the experiment. Retention in two stages was explained by differences in trapping mechanisms, where retention in weak trapping sites occurred first before retention in strong sites was significant [133]. In terms of the FS-3 experiment, the tritium plus excess hydrogen could have caused sufficient retention in weak trapping sites where the transition to strong trapping began to occur. For FS-1 and FS-2, no additional hydrogen existed and tritium retention was likely not sufficient to fill weak trapping sites. Furthermore, the difference between the high-temperature peak magnitude in the L3 and U4 sample tests shows that an increase in temperature from 600.3ºC to 719.4 ºC had a significant role in accelerating the trapping rate of tritium into the high-energy trapping sites.

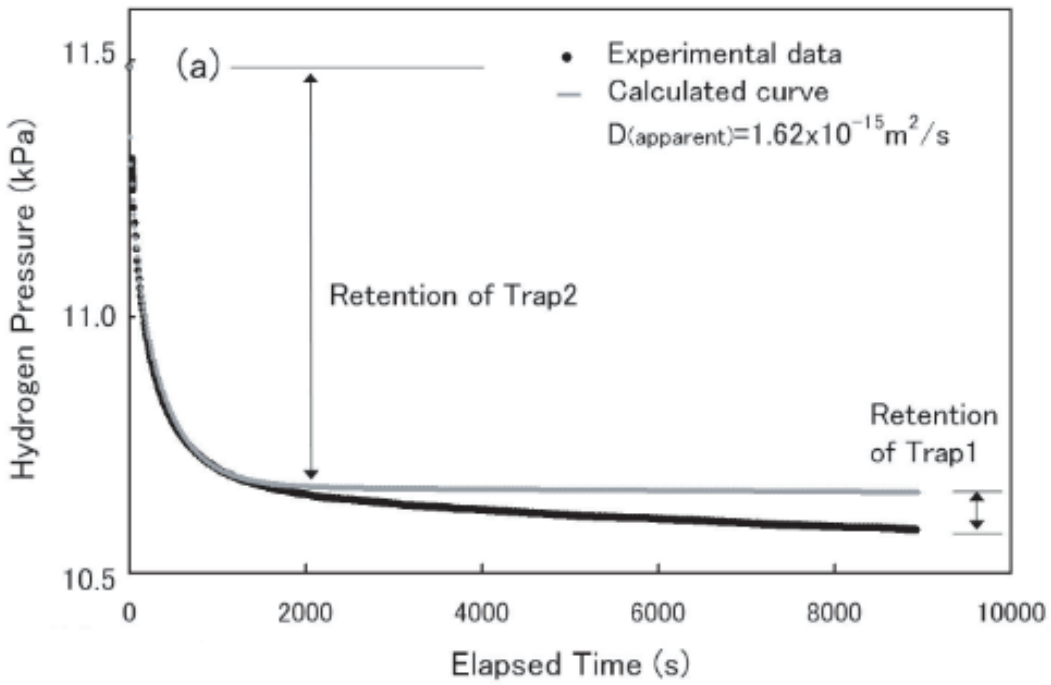

Figure 3.45. Hydrogen pressured measured during charging of an ISO-880U sample at 1273K where a decrease in pressure corresponds to increased retention in the sample. Hydrogen retention first occurs in weak trapping sites (Trap 2) followed by movement in strong trapping sites (Trap 1). From [133].

Lastly, the chemical form of measured tritium provides some information into the tritium retention process in the Flibe-graphite system. In desorption tests from each experiment, the majority of tritium was measured in an insoluble form, of which the HT and T_2 are possible. The average soluble tritium percentage from samples in each irradiation is shown in Table 3.14. There was no clear trend for measured fraction of solubility with sweep gas H_2 concentration, and therefore isotopic exchange reactions are not believed to be a significant source of the insoluble tritium from the samples. Soluble tritium was also examining by soaking a graphite crucible section from FS-1 in water for one hour, along with measuring tritium content in water used during the sample sectioning process. An average tritium content of 1.083 mCi was measured for the thermal desorption of samples compared to 0.0018 mCi per sample observed from water leaching. Therefore, the amount of weakly bonded soluble tritium that can be removed by water is also small part of the total tritium retention.

Table 3.14. Summary of average soluble tritium measured by the water bubbler system in the samples during desorption of samples from each in-core irradiation.

In-Core Irradiation	Sample Sets	Soluble ^{3}H
FS-1	LGC	4.2%
FS-2	ARB, IG1, IG2	11.2%
FS-3	L3, U3, U4	7.2%

In summary, observations of thermal desorption from graphite samples tested during MITR Fluoride salt irradiations have several similarities to studies on the retention of gaseous hydrogen in graphite. The activation energy of desorption from FS-2 IG-110U graphite was measured to be similar to that of hydrogen diffusion in similar graphite grades. Tritium desorption profiles were influenced by the concentration of H_2 used in each experiment, and the change in desorption as function of temperature was consistent with the proposed acceleration of diffusion at increased H_2 partial pressures. Desorption also occurred in distinct peak structures which are indicative of the weak and strong trapping sites typically occupied when graphite is charged with hydrogen gas. Finally, the majority of tritium measured in each desorption experiment was in a chemical form similar to H_2. Therefore, the thermal desorption measurements from the MITR in-core Flibe irradiations support the use of previously proposed mechanisms for hydrogen gas retention in graphite to explain the uptake and trapping of tritium in the Flibe-graphite environment.

4. Modeling Tritium Transport in Graphite under FHR Conditions

The degree to which tritium is retained in the FHR core graphite is important to understand in order to predict the tritium distribution in the reactor, tritium source term, and optimal strategies to mitigate environmental release. Based on experience from the MSRE as well as observations from the MITR Flibe irradiations, tritium uptake into graphite is expected to comprise a significant fraction of the overall tritium distribution. In the MSRE, it was estimated that 15% of the total tritium generated during the reactor's operation was retained in the graphite moderator stringers in the core [57]. The tritium retention in a pebble bed FHR could potentially be higher for several reasons. Tritium uptake into the MSRE's moderator could have been inhibited by the physical properties of the low-porosity CGB grade graphite [143]. Furthermore, in a pebble bed FHR the fuel and moderator elements can be circulated through the core and desorbed for tritium before reinsertion, which can accelerate tritium retention by continuously freeing up tritium trapping sites from graphite in the core. Therefore, a method for calculating the retention rate of tritium in graphite as a function of time is necessary to understand how tritium concentrations will evolve in FHR graphite components.

4.1. Bulk-Diffusion Retention Model

As discussed in Section 2, the retention of gaseous hydrogen in nuclear graphite has been extensively studied in literature. The tritium desorption results in Section 3 also suggest that similar transport mechanisms from gas charging of graphite can be used to describe tritium retention in graphite if T_2 or HT is present in Flibe. Therefore, the methods for modeling tritium retention in this section rely heavily on the mechanisms previously discussed in literature. However, one major challenge is that previous hydrogen gas charging studies typically have taken place at significantly higher temperatures and partial pressures compared to the expected conditions in a FHR. A typical method to model retention in these studies is to approximate the graphite grains as spheres and solve for the diffusion of tritium into the grains assuming a uniform partial pressure of hydrogen in the graphite pores, as depicted in Figure 4.1. If the H_2 pressures varies within pores as a function of depth in the material, then a concentration gradient could exist in the graphite bulk. Understanding the concentration gradient is important because the amount of tritium at the graphite surface will affect the boundary condition for salt-graphite interfaces in a FHR.

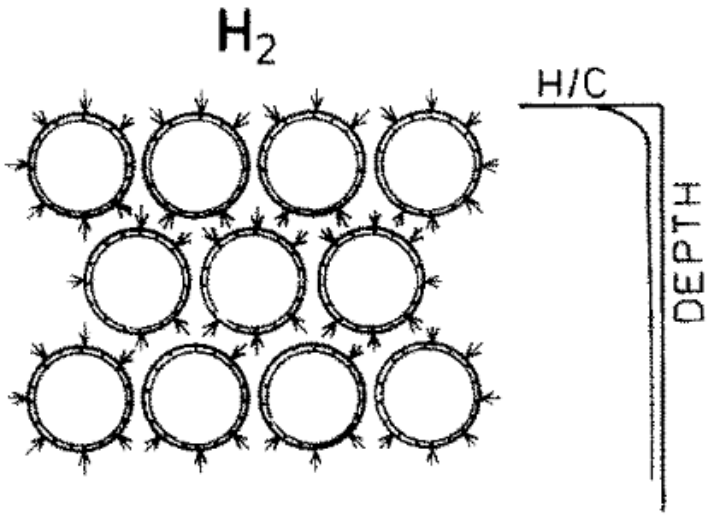

Figure 4.1. Model for retention of hydrogen in graphite grains approximated as spheres. A concentration gradient in the material can exist if the partial pressure of H_2 varies in the graphite pores. From [160].

Results of tritium retention from irradiated Flibe demonstrate that the concentration gradient within the graphite bulk is important to resolve. In the MSRE moderator graphite, the tritium activity decreased roughly two orders of magnitude from surface samples to sections taken at a depth of 1.52 mm [57]. An additional sample of POCO graphite was exposed to the MSRE salt for the final 1786 hours of operation and a surface activity of 0.02 Ci/g was observed compared to less than $4.5 \cdot 10^{-5}$ Ci/g in the graphite interior [140]. Subsection analysis of graphite samples from the MITR FS-1 and FS-2 irradiations also show that tritium retention was more predominant near the surface than in the graphite bulk. Therefore, modeling tritium retention using a uniform tritium partial pressure in pores of graphite components in a FHR would likely not lead to an accurate prediction of the tritium concentration within the graphite bulk, especially for materials with large physical dimensions like the graphite reflector.

A simple method to represent the spatial dependence of tritium concentration in graphite is to combine the diffusion of tritium in pores and grains into a single bulk-diffusion process. In this method, there is no accounting for the heterogeneous features of the microstructure and the graphite is treated as a homogenous material. As shown in Figure 4.1, a smooth distribution in the overall retention profile can exist even if individual grains in graphite have different retention characteristics [161]. Since the length of diffusion in this method is the geometric dimensions of the graphite, rather than the scale of grain length proposed in literature, the bulk-diffusion method requires a new input for tritium diffusivity which has not been previously measured.

The kinetics of tritium diffusion in graphite can be examined through the desorption profiles of nuclear graphite grades measured by Atsumi et al [123, 159]. In Figure 4.2, thermal desorption spectra are shown for graphite samples initially saturated with deuterium then desorbed in linear temperature ramps of 0.1 K/s [159]. The desorption profile of POCO AXF-5Q1 is of interest because POCO AXF-5Q was also tested by Causey et al in an absorption experiment at a low tritium partial pressure [127]. The difference between AXF-5Q and AXF-5Q1 is the purity, where the 5Q1 designation has a total impurity content of 5 ppm or less [162]. For grain size, density, and microstructure, there is minimal difference between the two grades. In the desorption profile, the AXF-5Q1 desorption peak at roughly 1350K is proposed to be the result of a diffusion-like trapping and detrapping process between crystallite edge sites in the graphite filler grains [159]. A similar peak from desorptions of ISO-880U was fit well with a diffusion-controlled process [129]. Therefore, an attempt was made to reconstruct the diffusivity by modeling the desorption profile over the sample geometry instead of within the graphite grains.

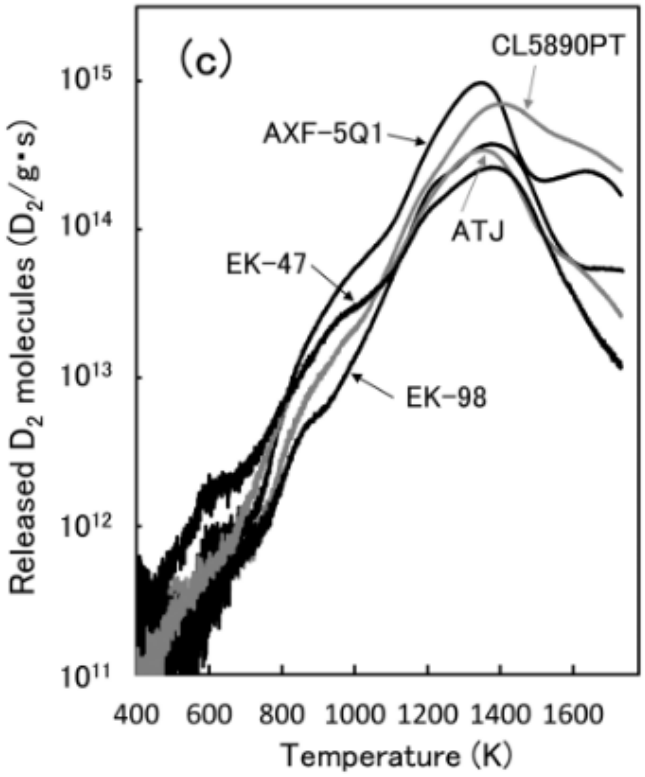

Figure 4.2. Thermal desorption profiles of various graphite grades charged with 42 kPa of D_2 gas at 1273 K for 8-30 hours and desorbed at 0.1 K/s. From [159].

Solving for bulk-diffusion requires a solution over a representative sample geometry. The graphites tested in Figure 4.2 were cut from thin sheets and had dimensions of 33×5×1 mm [159]. Therefore, for isotropic diffusion and equal conditions on all surfaces, the concentration gradient during the desorption experiments would be most significant in the dimension of the 1 mm thickness. The concentration profile would also be symmetric through the midplane in the 1 mm direction, therefore a two-dimensional geometry of 5 mm in length and 0.5 mm in thickness could be used to represent the concentration profile in the sample. A further reduction to a one-dimensional geometry can be justified by the length of the two-dimensional cross section being a factor of 10 larger than the thickness. Thus, a simplified method for calculating concentrations as a function of time can be carried out with Fick's second law in one Cartesian dimension shown in equation 4.1. Although deuterium was used to charge the graphite samples in the Atsumi et al measurement, the notation for diffusing tritium, T_d, is adopted here to be consistent with other equations in this section.

Since the graphite samples in the desorption experiment started at a saturated condition [159], an initial condition of a uniform concentration, C, is used for the simulation. The desorption took place under vacuum where the D_2 concentration can be treated as zero. In the absence of surface resistance to desorption, the concentration profile at the edge of the geometry ($x = x_L$) would also be near zero. These initial and boundary conditions for the desorption simulation are also summarized in equation 4.1. Temperature of the material can then be increased according to the 0.1 K/s rate used in the experiment and the diffusion-controlled desorption rate, R(t), can be calculated by monitoring the flux across the boundary at x_L, as in equation 4.2. To fit the desorption profile from the experiment, the bulk diffusivity, $D_{T,Bulk}$, can be varied by changing the diffusion activation energy, E_a, as well as the pre-exponential constant, D_o, described in equation 4.3. Calculated desorption profiles with a varying pre-exponential constant are shown in Figure 4.3. The desorption simulation used a forward time centered space scheme with 100 evenly spaced points and a constant time step of 0.05 seconds.

Eq. 4.1 $$\frac{\partial T_d}{\partial t} = D_{T,Bulk}\frac{\partial^2 T_d}{\partial x^2} \; : T_d(x, t = t_0) = C : T_d(x = x_L, t) = 0$$

Eq. 4.2 $$R(t) = \; -D_{T,Bulk}\frac{\partial T_d}{\partial x}\Big|_{x=x_L}$$

Eq. 4.3 $$D_{T,Bulk} = \; D_o \exp(-E_a/RT)$$

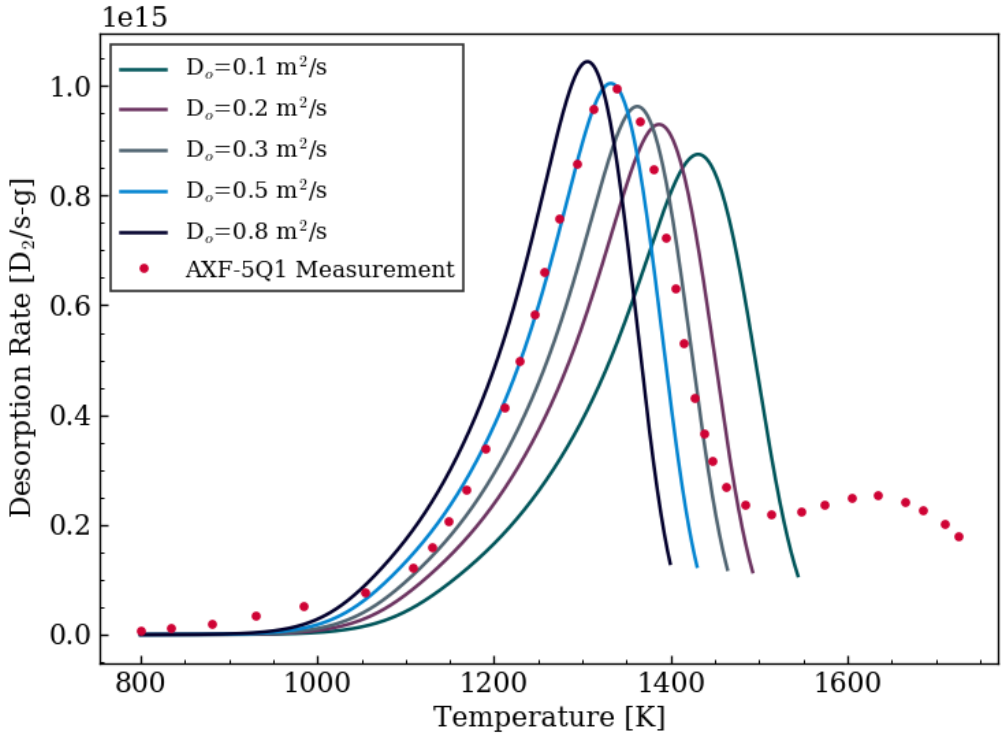

Figure 4.3. Desorption simulation for POCO AXF-5Q1 graphite using a bulk deuterium diffusivity with an activation energy of 235 kJ/mol and various pre-exponential factors. Results are compared to experimental measurements from [159].

The modeled results in Figure 4.3 only attempt to reconstruct the peak caused by the diffusion-controlled release of deuterium. Therefore, the desorption rate continues to decrease after the maximum desorption rate and another peak from detrapping at high-energy trapping sites was not represented. The initial concentration of the desorption simulation was set so that the integral of the profile would be similar to the experimental measurement without the high-temperature peak included. In this analysis, the integral of the diffusion-controlled peak was estimated to comprise measured desorption rates up until 1425K. Error was calculated in each simulation based on the sum of absolute values of the difference in desorption rates between the model and sampled points of the Atsumi et al experiment. Total errors for several combinations of D_o and E_a are shown in Figure 4.4.

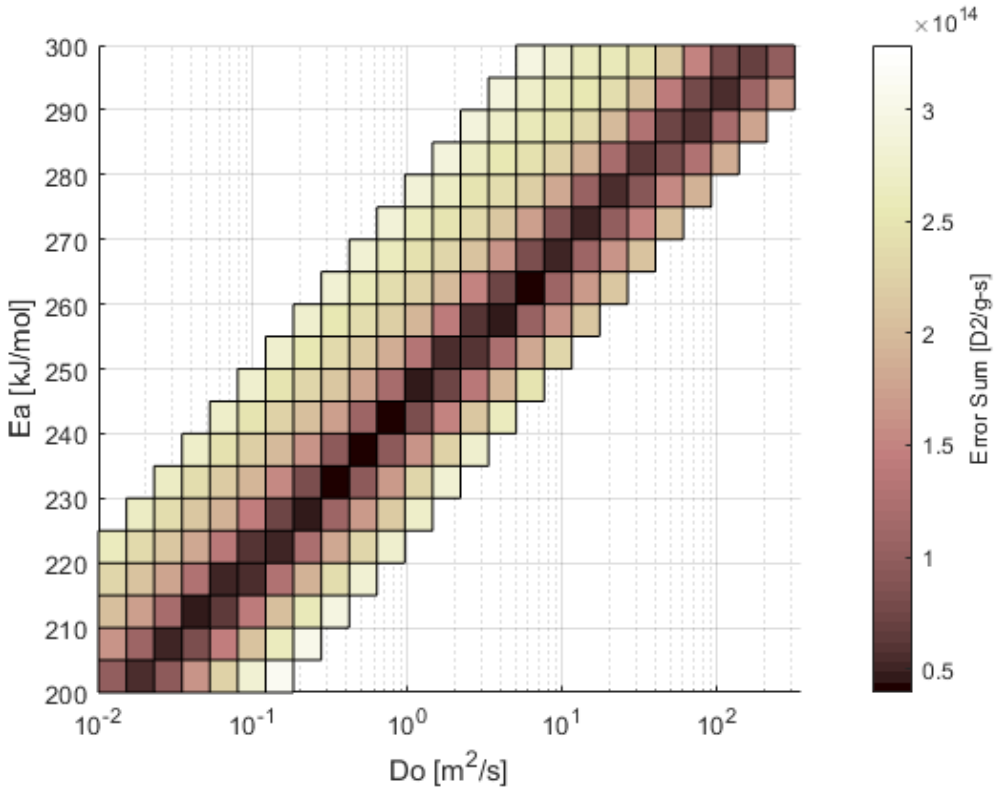

Figure 4.4. Sum of errors between modeled desorption profiles and the experimental measurement for POCO AXF-5Q1 graphite using a bulk diffusivity model with various activation energies and pre-exponential factors.

The compiled results in Figure 4.4 show that the bulk-diffusivity model can represent the experimental desorption profile reasonably well for certain combinations of D_o and E_a. The bounds in activation energy for the analysis were chosen to represent the range of grain-diffusion activation energies measured in literature, assuming that a bulk-diffusivity of deuterium in graphite would also follow a similar temperature dependence. Pre-exponential factor bounds were then chosen so that the fitting error for each activation energy had a local minimum somewhere between the lowest and highest values of D_o in each set. In general, the activation energy determines the rate at which desorption changes with temperature, and therefore has some control over the width of the diffusion-controlled desorption peak. Data from Figure 4.4, shows that the lowest error occurred with activation energies in the range of 230 kJ/mol to 260 kJ/mol. For activation energies outside of the 230-260 kJ/mol range, the peak width at the most suitable D_o was either too wide or narrow which increased the calculated error. The minimum error in the data set occurred with an activation energy of 235 kJ/mol and pre-exponential factor of 0.417, which is plotted along with the diffusion peak data from Atsumi et al in Figure 4.5.

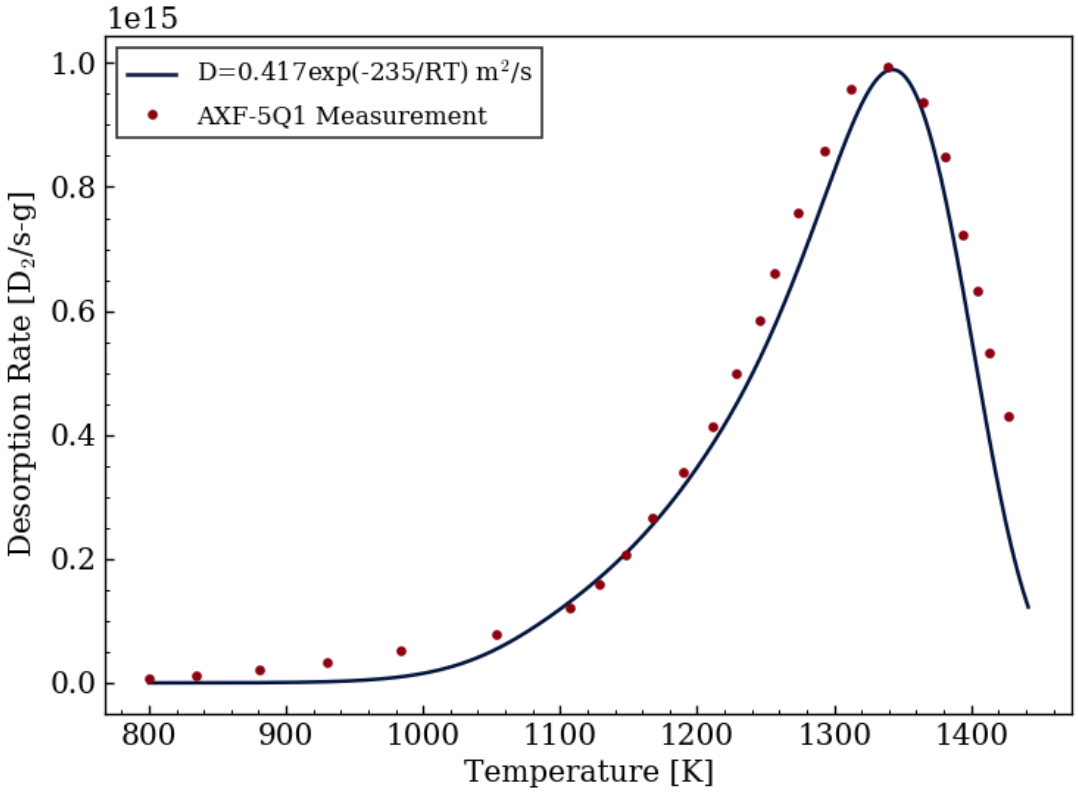

Figure 4.5. Best fit POCO AXF-5Q1 deuterium bulk-diffusivity from the D_o and E_a search results compared to experimental measurements from [159].

In comparison to experimental results, the best fit for POCO AXF-5Q1 graphite diffusivity is significantly larger than measured diffusion coefficients based on graphite grains, but also less than the diffusivity measured for graphite pores. The bulk-diffusivity is roughly four orders of magnitude higher than the diffusion coefficient in grains, which can be explained by the square of ratio of length-scales – the samples in the desorption study were 1 mm thick [159], while the grain size of POCO AXF-5Q graphite is 10 μm [127]. Experimental measurements for grain and pore diffusivities scaled to represent tritium are plotted along with the best fit for bulk-diffusivity in Figure 4.6.

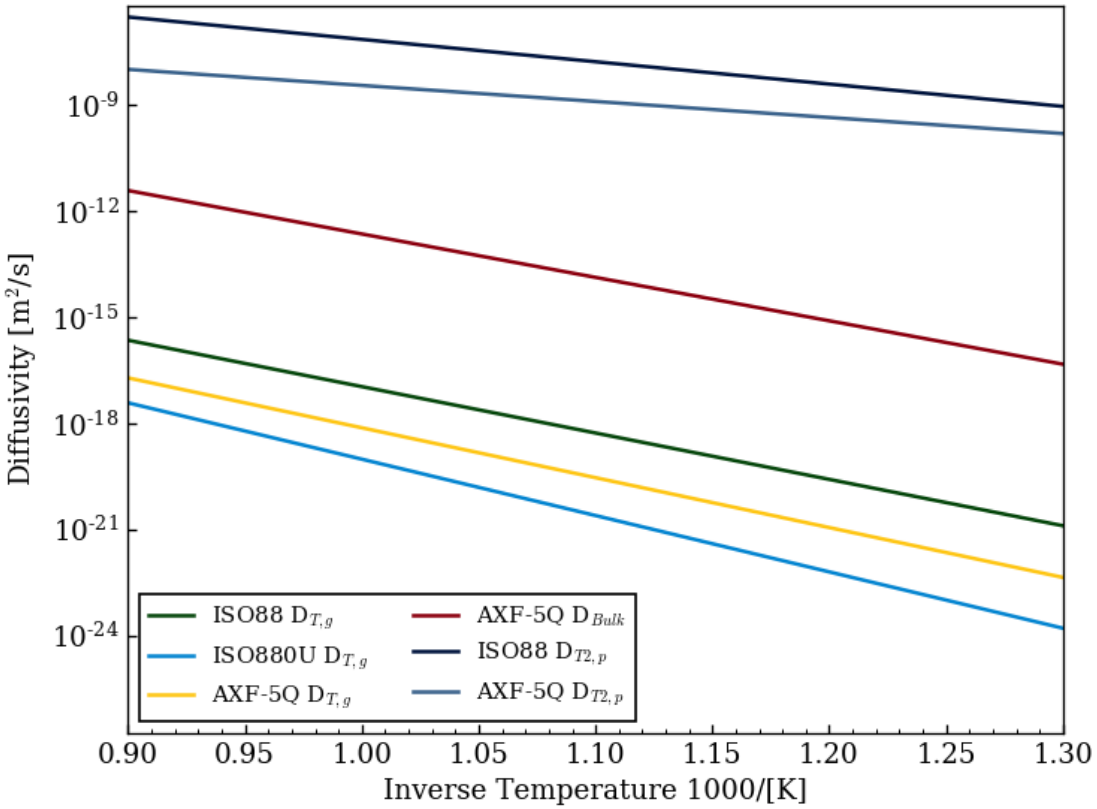

Figure 4.6. Comparison of measured tritium diffusivities in graphite grains ($D_{T,g}$) [126, 108, 129], plotted along with measurements for diffusivity in graphite pores ($D_{T2,p}$) [126, 108]. The best-fit for a bulk-diffusion coefficient in POCO AXF-5Q is in between values of pore and grain diffusivities.

The bulk-diffusivity fit from the desorption profile can be paired with a representation for high-energy trapping in order to better represent the overall tritium transport and retention process in graphite. A modified version of the equations presented by Atsumi and Morita et al are proposed to calculate tritium transport inside FHR graphite components with the bulk-diffusion model [136, 163]. As shown in equations 4.4 and 4.5, two categories of tritium are tracked: tritium diffusing through the graphite bulk, T_d, and tritium contained in high-energy trapping sites, T_t. Both diffusing and trapped tritium can vary in space and time, but only the diffusing tritium has a diffusion transport term. In contrast, trapped tritium is stationary but can increase in time as diffusing tritium transitions into high-energy traps. Tritium is conserved in the trapping process such that the increase of tritium in trapping sites at a specific location would be balanced by a decrease of diffusing tritium. Trapped tritium increases and decreases based on trapping and detrapping rate constants, or Σ_t and Σ_d, respectively, shown in equation 4.5.

Eq. 4.4
$$\frac{\partial T_d(x,t)}{\partial t} = D_{T,Bulk}\,\frac{\partial^2 T_d(x,t)}{\partial x^2} - \frac{\partial T_t(x,t)}{\partial t}$$

Eq. 4.5
$$\frac{\partial T_t(x,t)}{\partial t} = \Sigma_t\, T_d(x,t) - \Sigma_d T_t(x,t)$$

The trapping and detrapping rate constants are based on the form used for trapping calculations in the TMAP code [92]. However, since the TMAP expressions were developed for the scale of the material lattice, a modification is again required for the bulk representation of tritium transport in pores and grains in graphite. A modified version of the trapping rate constant is shown in equation 4.6. The trapping rate constant is an Arrhenius function with temperature which also depends on the concentration of empty trapping sites, or the total concentration of sites minus the current trapped tritium concentration (C_t° - T_t). For POCO AXF-5Q graphite, the concentration of high-energy trapping sites was measured at 2.6 mol/m^3 [127]. Another simplification was to assume that the trapping rate constant in the bulk model would follow the same temperature dependence as the TMAP formulation, which uses a trapping activation energy, E_t, equal to the diffusion activation energy or 270 kJ/mol as measured for AXF-5Q graphite [108]. The detrapping rate constant in equation 4.7 is a simple Arrhenius function with no species concentration dependence. A pre-exponential factor, ν_o, is representative of the detrapping attempt frequency and several sources suggest a value of 10^{13} s^{-1} [92, 164, 165]. Therefore, the remaining factors are the trapping rate constant pre-exponential factor, Σ_{to}, and the detrapping activation energy, E_d.

Eq. 4.6
$$\Sigma_t = \Sigma_{to}\exp\left(\frac{-E_t}{RT}\right)\cdot\left(C_t^o - T_t(x,t)\right)$$

Eq. 4.7
$$\Sigma_d = \nu_o\exp(-E_d/RT)$$

Values of remaining trapping and detrapping parameters were assessed using the tritium retention measurements in POCO AXF-5Q graphite by Causey et al [127]. In the experiment, the tritium gas was charged into samples for 1.5 hours and at various temperatures. The four data points from 1200ºC to 1500ºC represent a condition where the sample is saturated, but total retention begins to decrease with increasing temperature because of additional detrapping [127]. Therefore, the saturated conditions can be used to fit trapping and detrapping parameters in order to represent the decrease in total retention at very high temperatures. Reaching a saturated

condition means that the time derivatives of T_d and T_t in equations 4.4 and 4.5 would be zero at some point in the experiment. There would also then be no spatial dependence in either the diffusing or trapped tritium concentrations. In this case, the diffusing tritium would be equal to the value predicted by Sievert's law and the trapped tritium concentration as a function of temperature could be solved for using equation 4.8. Here the Sievert's law solubility of ISO-88 is used to stay consistent with other data fitting performed by Causey et al [126, 108]. The total equilibrium tritium retention, or sum of T_d and T_t, is shown in Figure 4.7 for a Σ_{to} of $1 \cdot 10^9$ s^{-1} and various detrapping activation energies.

Eq. 4.8
$$T_d = K_{S,g}\sqrt{P_{T_2}} \; : \; T_t = \frac{\Sigma_{to} \exp\left(\frac{-E_t}{RT}\right) T_d C_t^o}{\Sigma_d + \Sigma_{to} \exp\left(\frac{-E_t}{RT}\right) T_d} \quad as \; t \to \infty$$

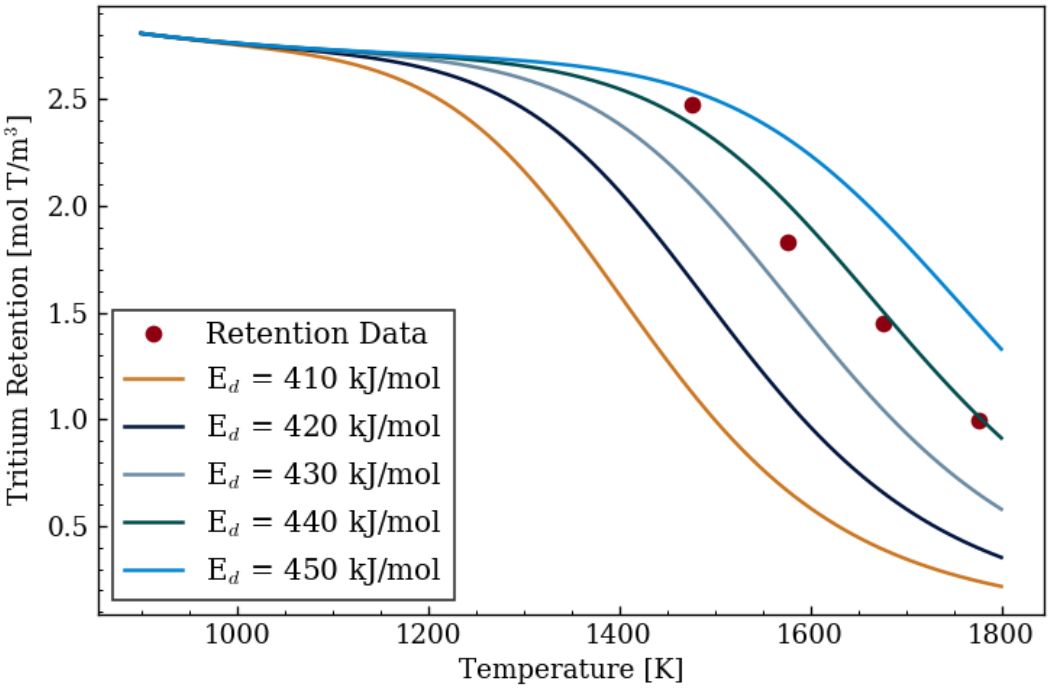

Figure 4.7 Model for equilibrium tritium retention at 0.66 Pa charging pressure in POCO AXF-5Q graphite as a function of temperature. Results are compared to experimental measurements where saturation is expected [108].

The best fit for Σ_{to} and E_d according to the 1200ºC through 1500ºC points of the Causey et al retention study occurred with a with a trapping pre-exponential factor of $1.13 \cdot 10^9$ s^{-1} and detrapping activation energy of 437 kJ/mol. Using these parameters, the full bulk-diffusion and trapping model can be examined over the remaining temperature range of the experiment. For the

data points below 1200ºC, an equilibrium condition in the AXF-5Q graphite would not be expected. Therefore, a model which can solve the time and spatial dependence of equations 4.4 and 4.5 is required to calculate tritium retention prior to saturation. Diffusing and trapped tritium concentrations can be solved in a combined matrix equation based on a forward time centered space finite difference scheme as shown in equation 4.9. As with the desorption simulation, a one-dimensional geometry with a symmetry condition across the center is used to represent the graphite sample dimensions. In the retention measurements, graphite samples were 10 mm by 15 mm sheets that varied from 0.36 mm to 0.42 mm in thickness [127]. Half of the average sample thickness is 0.195 mm, which is over 50 times smaller than the next largest sample dimension, which justifies modeling tritium transport in the sample in only the dimension of sample thickness. An explicit symmetric boundary condition is used for T_d^1 and T_t^1, where the superscript of 1 refers to the point on the symmetric boundary on the sample midplane. At the sample surface, the diffusing tritium concentration is set with a constant-value boundary condition with a value of $K_{S,g}(0.66\ Pa)^{1/2}$ determined by the experimental charging condition. Trapped tritium at the surface still increases and decreases in the same manner as the internal points, but changes in T_d^N are decoupled from T_t^N since the diffusing tritium concentration remains fixed by the boundary condition. The remaining internal terms in the coefficient matrix are the finite difference representation of the differential equations in equations 4.4 and 4.5.

Eq.4.9

$$\begin{bmatrix} T_d^1 \\ T_d^2 \\ \dots \\ T_d^{N-1} \\ T_d^N \\ T_t^1 \\ T_t^2 \\ \dots \\ T_t^{N-1} \\ T_t^N \end{bmatrix}^{t+\Delta t} = \begin{bmatrix} 0 & 1/\Delta t & & & & & & & & \\ \frac{D}{\Delta x^2} & -\frac{2D}{\Delta x^2}-\Sigma_t & \frac{D}{\Delta x^2} & & & & \Sigma_d & & & \\ & \frac{D}{\Delta x^2} & -\frac{2D}{\Delta x^2}-\Sigma_t & \frac{D}{\Delta x^2} & & & & \Sigma_d & & \\ & & \frac{D}{\Delta x^2} & -\frac{2D}{\Delta x^2}-\Sigma_t & \frac{D}{\Delta x^2} & & & & \Sigma_d & \\ & & & & 1/\Delta t & & & & & \\ & & & & & 0 & 1/\Delta t & & & \\ & \Sigma_t & & & & & -\Sigma_d & & & \\ & & \Sigma_t & & & & & -\Sigma_d & & \\ & & & \Sigma_t & & & & & -\Sigma_d & \\ & & & & & \Sigma_t & & & & -\Sigma_d \end{bmatrix} \begin{bmatrix} T_d^1 \\ T_d^2 \\ \dots \\ T_d^{N-1} \\ T_d^N \\ T_t^1 \\ T_t^2 \\ \dots \\ T_t^{N-1} \\ T_t^N \end{bmatrix}^t \Delta t + \begin{bmatrix} T_d^1 \\ T_d^2 \\ \dots \\ T_d^{N-1} \\ T_d^N \\ T_t^1 \\ T_t^2 \\ \dots \\ T_t^{N-1} \\ T_t^N \end{bmatrix}^t$$

The finite difference model was examined using a sphere geometry test case with a constant flux input boundary condition and zero initial concentrations. If trapping is neglected, an analytical solution for the diffusing tritium as function of time and radial position is available [166]. As shown in equation 4.10, the analytical concentration profile depends on the flux boundary condition, J_o, the sphere radius, R, and diffusivity, D. The values α_n are the positive roots of $\alpha_n R\cot(\alpha_n R)=1$, where the first six roots are used for the comparison with values of 0, 4.4934, 7.7253, 10.9041, 14.0662, and 17.2208 [166]. To simplify the test case, a J_o of 1 mol/m^2-s is used along with a D of 1 m^2/s and R of 1m. The results of the finite difference model are shown to approach the analytical solution in Figure 4.8 when additional mesh points are modeled inside the sphere.

Eq. 4.10
$$T_d(r,t) = \frac{J_o R}{D}\left(\frac{3Dt}{R^2} + \frac{r^2}{2R^2} - \frac{3}{10} - \frac{2R}{r}\sum_{n=1}^{\infty}\frac{\sin(\alpha_n r)}{\alpha_n^2 R^2 \sin(\alpha_n R)}\exp(-D\alpha_n^2 t)\right)$$

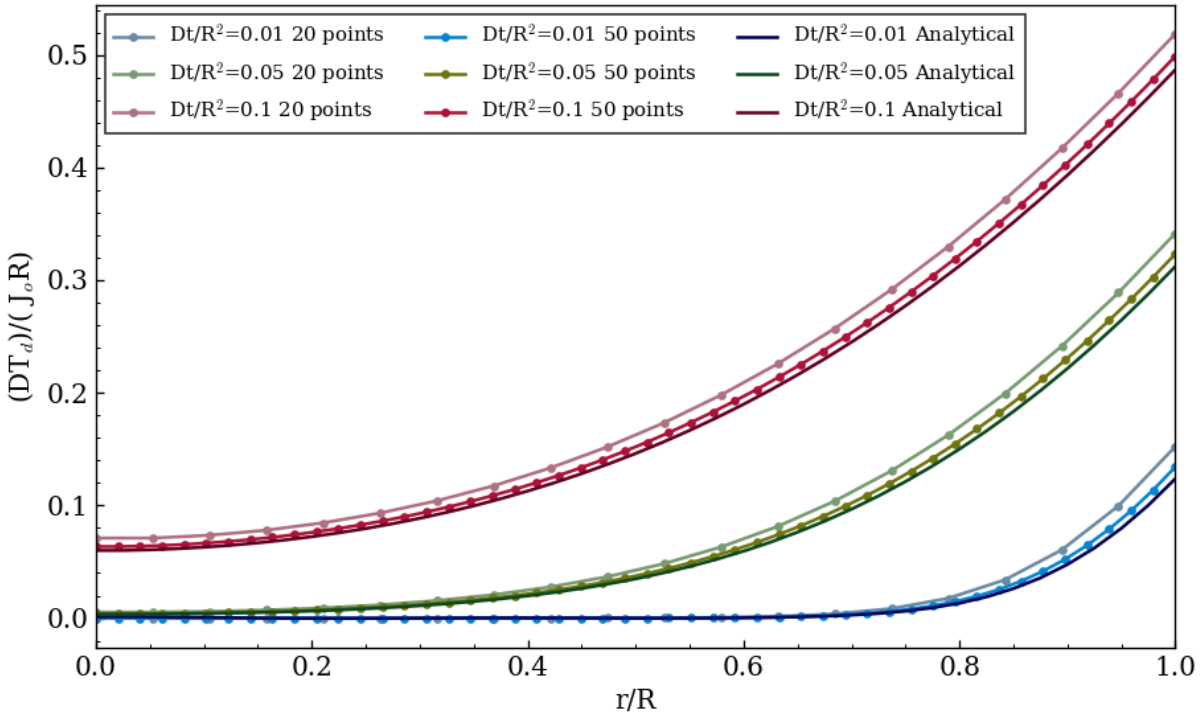

Figure 4.8. Comparison of Matlab finite difference diffusion model to analytical solutions of a sphere with constant flux into the outer surface at three different times. Analytical solutions obtained from [166].

Obtaining an analytical solution for the case of diffusion and trapping is significantly more complicated than for diffusion alone. A solution can be derived through the Method of Manufactures Solutions, but only in the effective diffusivity regime where the influence of trapping is minimal [167]. Therefore, the finite difference model with diffusion and trapping was verified against a separate implementation in the commercial multiphysics code STAR-CCM+. Diffusion was simulated using the Passive Scalar utility in a 3 dimensional parallelepiped geometry. Four sides of the geometry were set to zero-flux boundaries so that diffusion occurred only one dimension, as pictured in Figure 4.9. A comparison of STAR-CCM+ results to the Matlab finite difference model is shown in Figure 4.10 for a simulated flux of $1 \cdot 10^{-6}$ mol/m^2-s up to a time of 10 seconds. Differences between models could be caused by different spatial discretizations or the solution method. The STAR-CCM+ results used a second-order implicit time solver while the Matlab model uses a first-order explicit integration.

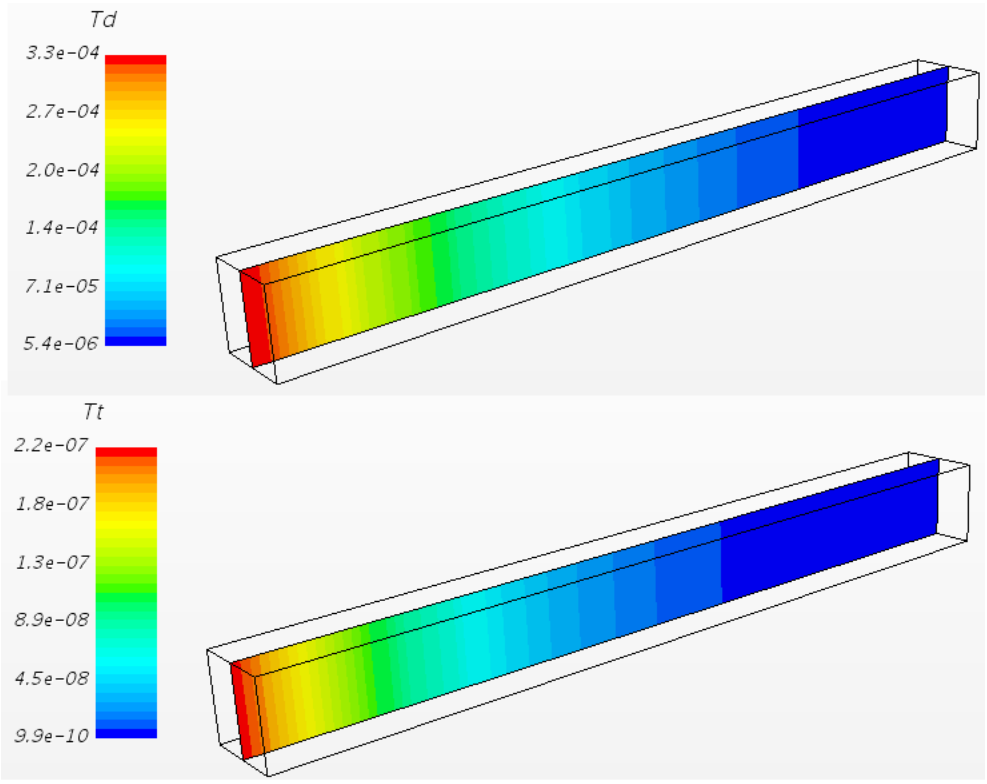

Figure 4.9. Simulation of diffusion and trapping in STAR-CCM+ using a constant flux boundary condition on the left-most face and a symmetric boundary on all other faces.

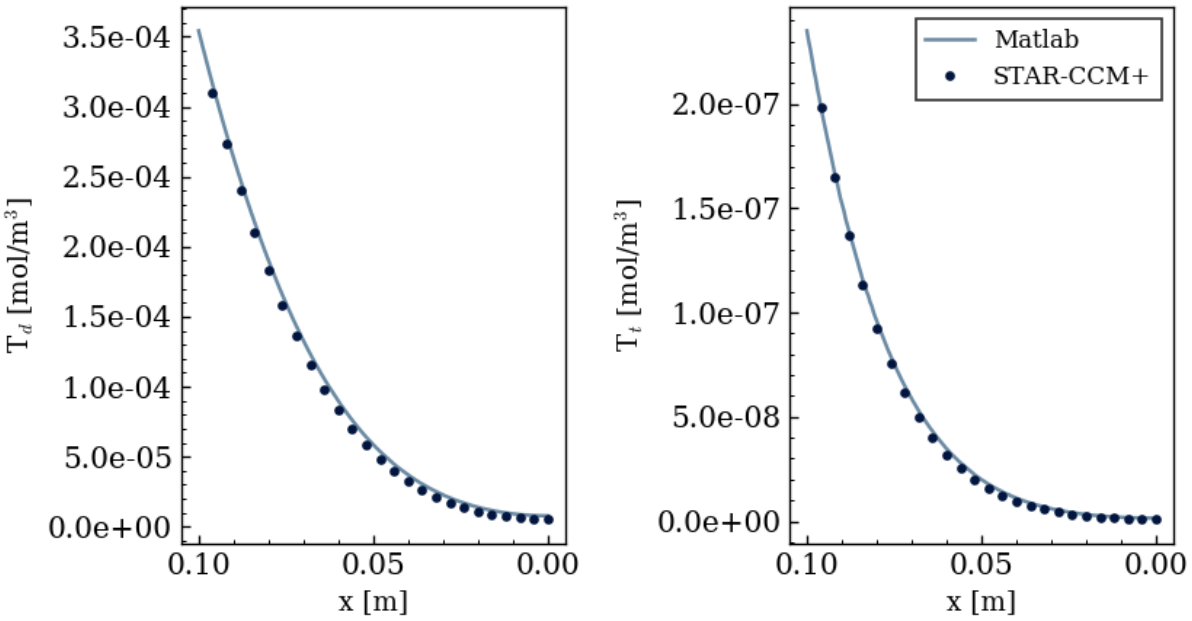

Figure 4.10. Comparison of Matlab finite difference and STAR-CCM+ models of tritium diffusion and trapping.

Beyond the test cases, the finite difference diffusion and trapping model was also used to reproduce results from experimental measurements. In the case of retention studies by Causey et al, individual simulations were conducted for 1.5 hours of retention starting from 900 K and repeated every 25 K until the total retention was near the equilibrium value. There were 100 internal mesh points in the simulation and the time step for the 900 K simulation was 1 second. The time step was decreased as temperature increased according to the ratio of diffusivities at 900 K to the current temperature in order to limit temporal discretization error from run to run. Results from the model are compared to experimental measurements in Figure 4.11, where the modeled results are shown to reach equilibrium retention at temperatures roughly 200 K lower than the experimental data. The simulation used the tritium bulk-diffusivity calculated from the desorption profile of a 1 mm thick graphite sample. Since the graphite thickness in the Figure 4.11 model was only 0.39 mm, the bulk-diffusivity calculated with a longer diffusion length overestimates the rate at which the tritium concentration profile evolves in the sample.

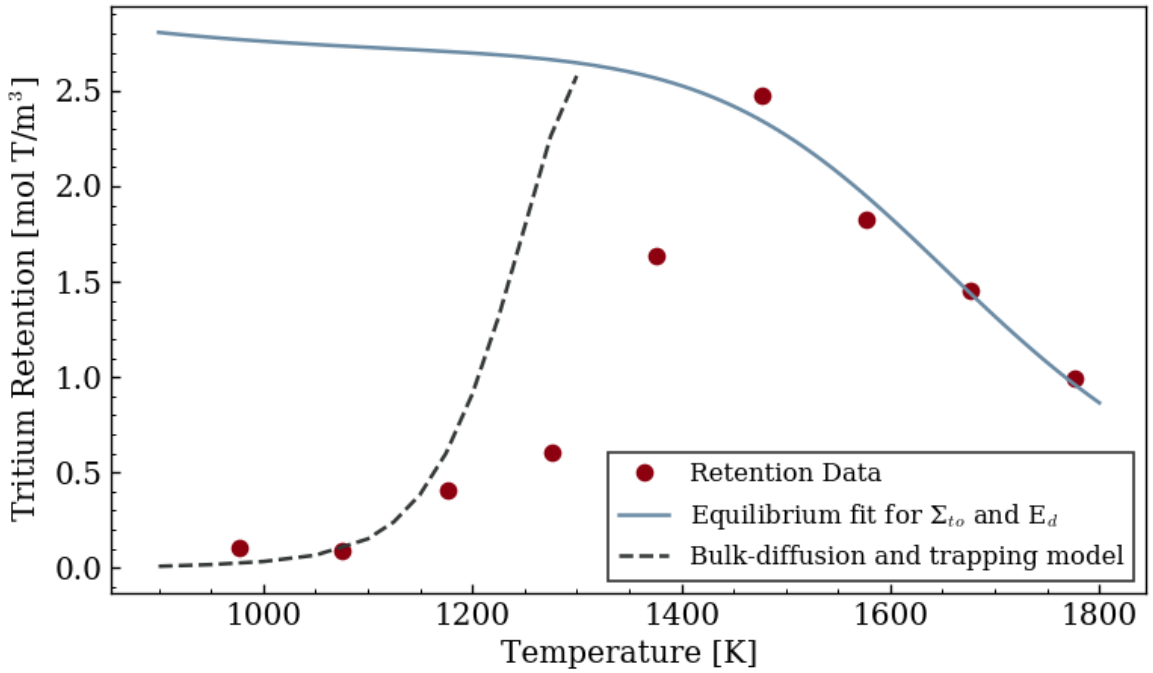

Figure 4.11. Bulk diffusion and tritium retention model simulations of 1.5 hour tritium charging in POCO AXF-5Q graphite with 0.66 Pa T_2. The modeled results reach saturation at equilibrium at earlier temperatures than the experimental data [108].

The inconsistency in retention results between samples with different dimensions is a significant disadvantage of the bulk-diffusivity model. For example, when the diffusivity is tuned to match the results of a certain diffusion length, it may misrepresent the results at a different length-scale. Therefore, the bulk-diffusivity model may create a significant error if fitted values from the millimeter scale gaseous retention and desorption experiments are applied to the FHR, where graphite dimensions of interest are at least an order of magnitude larger. One compensating factor could be that retention in the FHR may only be significant within a few millimeters of the graphite surface, as observed in the MSRE [57]. However, either a retention experiment with a larger length scale or a direct measurement of the tritium concentration profile at representative FHR conditions would be required in order to better support the results from the bulk-diffusion retention model.

4.2. Pore and Grain Diffusion Model

Tritium retention calculations can better represent proposed retention mechanisms if diffusion of molecular tritium in pores and diffusion of tritium within filler grains are both separately modeled, instead of combining the two steps into a single bulk-diffusion process. Previous research has identified that the length scale of hydrogen diffusion is the size of grains within nuclear graphite [134, 123]. At elevated temperatures and high hydrogen partial pressures, total retention results agree well with diffusion models that only consider transport within graphite grains [126, 129]. However, an assumption in these models is that all graphite grains within the bulk material are exposed to the same partial pressure of hydrogen in graphite pores.

Because of the significant tritium concentration gradients observed in graphite from retention with molten Flibe [140], applying a uniform T_2 pressure throughout all pores in graphite would likely over predict the penetration of tritium into the bulk material for the low tritium concentrations and 550ºC-700ºC temperature range expected in FHR designs. Modeling a tritium diffusion process through the pores paired with uptake and diffusion into graphite grains is one method to represent the varying concentrations of tritium across graphite bulk dimensions. An illustration of the combined hydrogen transport process in graphite is shown in Figure 4.12. Uptake of H_2 into graphite first occurs through the open pores, labeled as Path 1 in the figure. Trapping and detrapping at crystallite edge sites in a diffusion-controlled process then occurs within the graphite filler grains (Path 2). Another process labeled Path 3 is proposed for the diffusion of hydrogen through basal planes of the crystallite to the high-energy trapping sites [121]. The spatial dependence of the high-energy trapping within crystallites can be neglected since the crystallite size is typically 30-200 nm [128], compared to 5-40 μm for grain size [123].

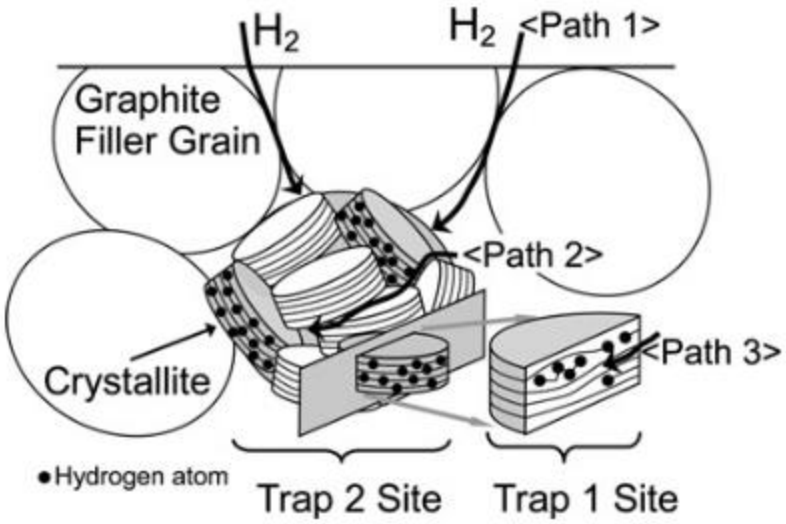

Figure 4.12. Schematic for different mechanisms of hydrogen transport in graphite. From [121].

One disadvantage of modeling tritium transport in both pores and grains is the addition of another dimension into the numerical representation of graphite. At minimum, one representative grain needs to be modeled at each position where the tritium concentration in pores is tracked. A T_2 concentration gradient within pores of the graphite bulk can then be linked to the evolving concentration profiles of tritium within filler grains at various depths from the graphite surface. Equations for the three tracked tritium species in graphite are shown below. In equation 4.11, the diffusing tritium is modeled in a similar manner to the bulk-diffusivity model. However, here the diffusivity of tritium in the filler grain, $D_{T,g}$, is used and the equation is written in a radial geometry to represent grains approximated as spheres [126]. Similarly in equation 4.12, the trapped tritium is tracked in a spherical geometry with the radial position within the grain denoted as r_g. In the case of the thin graphite sheets from the Atsumi et al desorption measurements or the Causey et al absorption study [126, 127], the bulk material can be represented by a one-dimensional Cartesian geometry. The diffusing tritium in pores, $T_{2,p}$, is modeled over the sample dimensions instead of inside the pores, where the position x_p in equation 4.13 refers to position in the graphite bulk. Modeling pore diffusion also requires a separate diffusivity for tritium transport in graphite porosity, $T_{2,p}$. A one-dimensional illustration of the pore and grain representation is shown in Figure 4.13 for a one-dimension slab geometry with a symmetric center condition. An additional point outside the domain (x_{p+1}) is used to apply a flux boundary condition.

Eq. 4.11
$$\frac{\partial T_d(r_g,t)}{\partial t} = D_{T,g}\,\nabla^2 T_d(r_g,t) - \frac{\partial T_t(r_g,t)}{\partial t}$$

Eq. 4.12
$$\frac{\partial T_t(r_g,t)}{\partial t} = \Sigma_t\, T_d(r_g,t) - \Sigma_d T_t(r_g,t)$$

Eq. 4.13
$$\frac{\partial T_{2,p}(x_p,t)}{\partial t} = D_{T_2,p}\,\frac{\partial^2 T_{2,p}(x_p,t)}{\partial x^2} + \mathrm{s}(x_p,t)$$

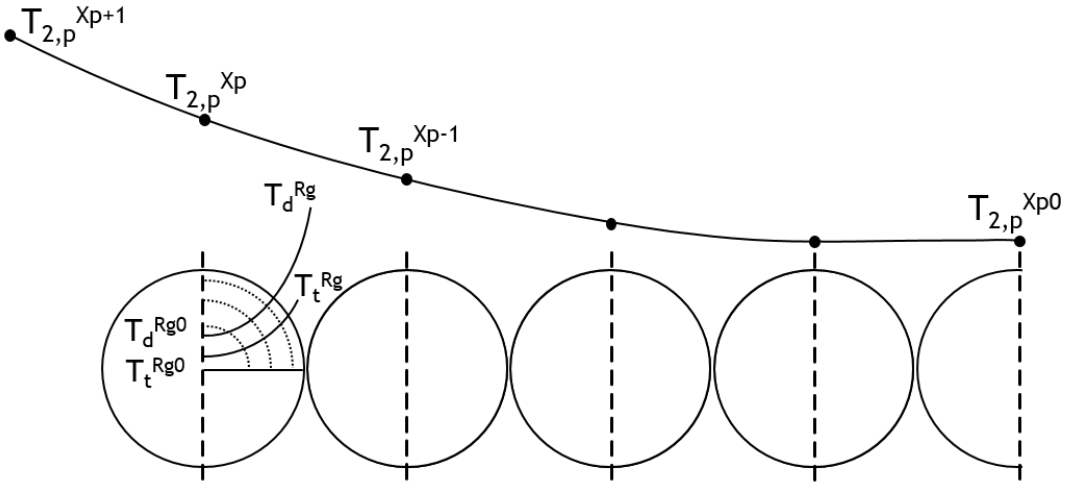

Figure 4.13. Conceptual tritium concentration profiles of a 1-D discretization for tritium diffusion in pores and grains of a one-dimensional graphite slab. The T_2 concentration in pores is tracked from the slab center, Xp0, to the surface. At each pore node, a representative spherical filler grain of radius R_g is modeled with concentration profiles for diffusing and trapped tritium.

Tritium diffusing in pores is converted to grain-diffusing and trapped tritium through a source term, s, shown in equation 4.13. The amount of tritium transfer at each pore node obeys the tritium balance in equation 4.14. On the left side, the change in T_2 concentration in pores after one time step is multiplied by the geometric volume of the node, V_N, and the porosity of the graphite in order to determine the change in mols of tritium. The graphite porosity, φ, is calculated based on the density of the graphite grade and the theoretical density of crystalline graphite at 2.266 g/cm^3 [168]. A factor of 2 is also applied since tritium in pores diffuses as T_2 but diffusing and trapped tritium in grains is tracked as T. To calculate the change in tritium within grains at the node, the integral of the diffusing and trapped tritium is taken over the volume of the grain. Since only one representative grain is modeled per node, the integral is multiplied by the number of grains in the node found by the ratio of node volume to grain volume, V_N/V_{Grain}. The number of grains is also scaled down by a factor of 1-φ to account for partial node volume of void space in

pores. A negative sign on the right side of equation 4.14 is used because the change in mols of tritium in the pores is matched by an opposite change in the grains. By rearranging and simplifying the equation, the tritium balance is converted to represent a T_2 source term in equation 4.15.

Eq. 4.14
$$2\phi V_N\left(T_{2,p}^{t} - T_{2,p}^{t-\Delta t}\right) = -\frac{(1-\phi)V_N}{V_{Grain}}\left(\int (T_d + T_t)^{t}\, dV_G - \int (T_d + T_t)^{t-\Delta t}\, dV_G\right)$$

Eq. 4.15
$$s\left(r_p, t\right) = -\frac{1-\phi}{2\phi V_{Grain}}\left(\int (T_d + T_t)^{t}\, dV_G - \int (T_d + T_t)^{t-\Delta t}\, dV_G\right)$$

In addition to the conservation equation, tritium in pores and grains should also obey a Sievert's law relationship. As in equation 4.16, the concentration of diffusing tritium at each grain surface, T_d^{Rg}, should be equal to the Sievert's law constant in graphite, $K_{s,g}$, times the square root of T_2 partial pressure at the pore node. The partial pressure is equal to the concentration of T_2 at the pore node, $T_{2,p}$, times the universal gas constant and temperature, R and T, if T_2 in pores is treated as an ideal gas. Equation 4.16 creates a boundary condition for the grain surface, which then dictates the amount of additional diffusion into the grain at each time step and thus the amount of T_2 added or removed from the pores with the source term. Since the grains occupy only a portion of the volume, while void space in pores occupies the remainder, the Sievert's law constant is increased by a factor of $(1-\varphi)^{-1}$ to provide the same total values of tritium concentration at the bulk scale. A similar conversion is also applied to the concentration of high-energy trapping sites in the crystallite.

Eq. 4.16
$$T_d^{Rg} = \frac{K_{S,g}}{1-\phi}\sqrt{T_{2,p}RT}$$

The square root of T_2 partial pressure in equation 4.16 prevents the direct, simultaneous solution of both pore and grain concentrations using a set of matrix equations. Therefore, an indirect solution is used based on an iterative method. At each time step, a diffusion-only step for T_2 in pores is conducted with the source term set to zero. Then at each pore node the T_2 concentration is varied, the surface concentration of T_d in the grain is updated according to equation 4.16, and a diffusion and trapping step in the grain is completed. Iteration of the $T_{2,p}$ value continues until the change of tritium in pores matches the source term calculated from the updated T_d and T_t concentration profiles. The iteration is based on a bisecting search between upper and lower limits, $T_{2,High}$ and $T_{2,Low}$, described in equation 4.17. During an absorption process, the upper

limit of T_2 concentration at a pore node is determined from the initial pore diffusion step where the source term is set to zero. A value of zero can be used for the lower limit, $T_{2,Low}$, which doesn't increase convergence time significantly as long as the converged value is closer to zero than to the upper limit. At each iteration, the difference between the current value of T_2 in the pore node and the upper limit, diffusion-only value ($T_{2,p}^{i}$ - $T_{2,p}^{s=0}$) is compared to the source term calculated from integrating the tritium in the grains in order to calculate the iteration error. If the error is greater than zero, the value of $T_{2,p}$ needs to be reduced and the upper limit is set to the value at the current iteration. The T_2 value at the current pore node for the next iteration is then calculated from the average of updated upper and lower limits. A convergence example from the surface node in a 4 cm diameter graphite sphere absorption test case is shown in Figure 4.14. Values in the figure originate from the early on in the simulation, where the retention capacity in the grains is high and the concentration of T_2 in pores needs to be significantly reduced to match the increase in grain retention during the time step.

$$Err = \left(T_{2,p}^{i} - T_{2,p}^{s=0}\right) - s$$

Eq. 4.17

$$Err > 0 : T_{2,High} = T_{2,p}^{i} \; ; Err < 0 : T_{2,Low} = T_{2,p}^{i}$$

$$T_{2,p}^{i+1} = \left(T_{2,High} + T_{2,Low}\right)/2$$

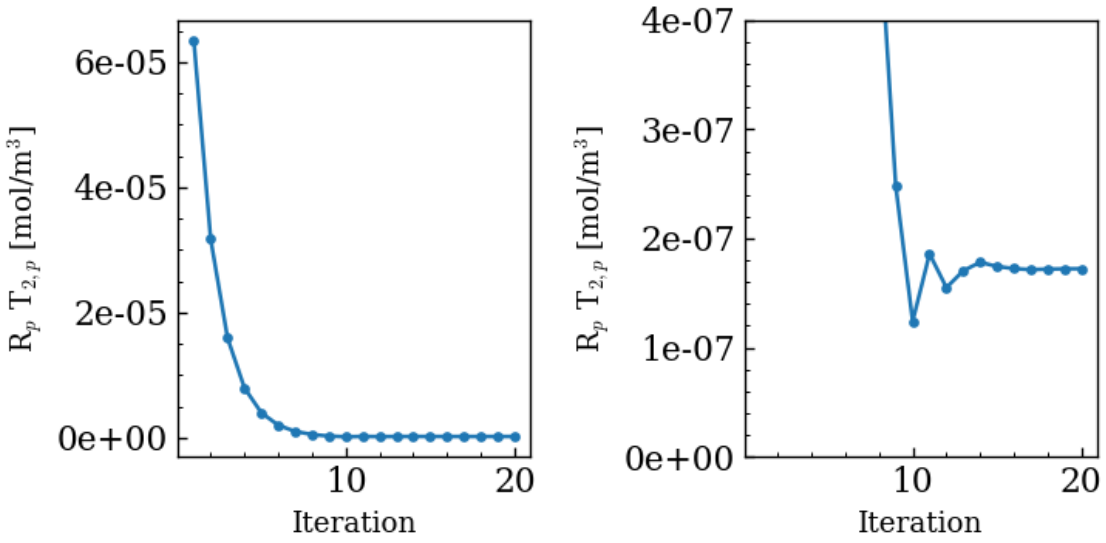

Figure 4.14. Pore T_2 concentration iterations for the surface node ($r=R_p$) in a test simulation of flux into a 4 cm graphite sphere. A time step of 1500 seconds is used and iterations are shown for the third time step. Calculated T_2 values decrease by a factor of two for the first ten iterations (left) then calculations reach the convergence value by 20 total steps (right).

Since the iteration method solves for pore diffusion and grain transport separately, additional steps need to be taken to account for the fact that both processes happen simultaneously in physical systems. For example, repeating the same convergence procedure for all pore nodes based on the initial $T_{2,p}$ concentrations from the diffusion-only step would lead to increasing over-predictions of tritium retention in grains further into the graphite bulk. To better conserve total tritium in each step, the concentration profile in the diffusion-only step should be reduced to account for tritium transfer into the grains at the previous nodes. This can be done by starting the iteration procedure at the pore node closet to the surface in the case of a tritium absorption simulation. Converging the value of $T_{2,p}$ also results in a calculated value for the source term, s, at the pore node. The pore diffusion step can then be repeated according to equation 4.13 with a partially-filled source term vector – the source values are included for nodes that have previously been calculated, but are left as zeros for the remaining positions. Repeating the diffusion step allows the partial source term to remove previously retained tritium in order to better calculate the value of $T_{2,p}^{s=0}$ for the next pore node.

Concentration of T_2 in pores as a function of radial position and iteration using this method are shown in Figure 4.15. The values were taken from the previous simulation also described in Figure 4.14. Compared to the initial diffusion-only step, the T_2 concentration in pores needs to be decreased significantly to converge with the amount of retention in grains. As seen in Figure 4.15, more iterations are needed to further reduce the $T_{2,p}$ values to convergence as depth into the graphite sphere increases. The results shown use fully converged values for illustrative purposes, although in the test case the T_2 concentration is reduced to nearly zero roughly 1 mm into the graphite sphere. To accelerate the pore and grain calculation in a larger simulation, the total number of iterations can be capped or the simulation at the given time step can be stopped once the $T_{2,p}$ concentration falls below a set lower limit.

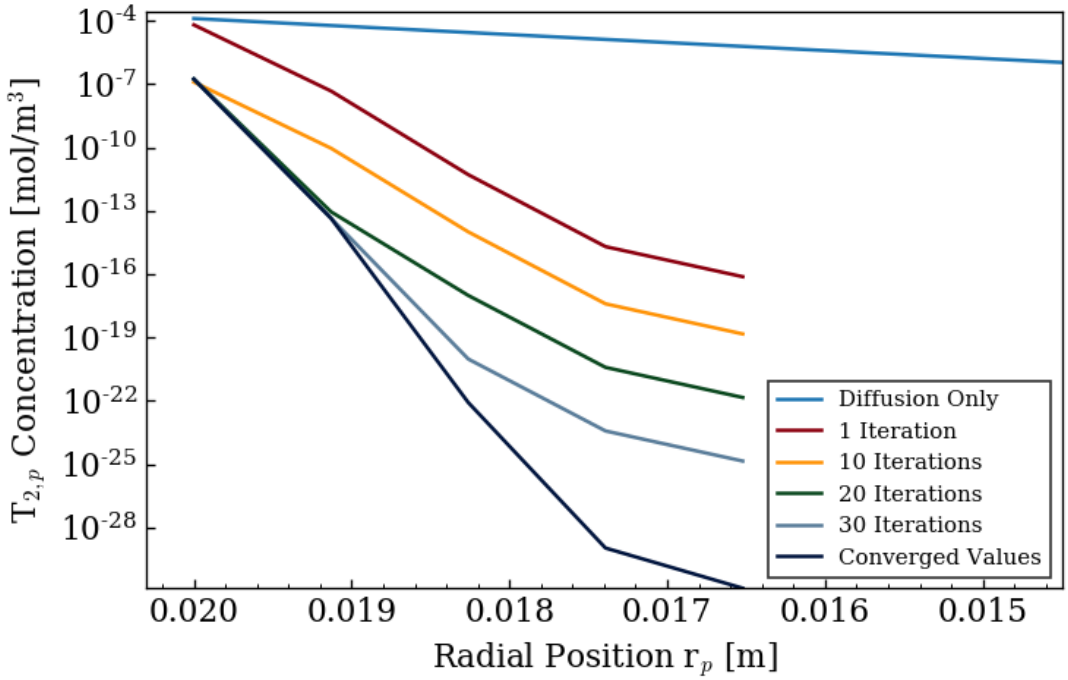

Figure 4.15. Test simulation of $2.5 \cdot 10^{-10}$ mol T_2/m^2-s flux into a 4 cm graphite sphere. Results are shown at t=4500s for Δt=1500s. An initial diffusion-only step is used to transport tritium into graphite pores. The values for T_2 at pore nodes are then reduced and converged with tritium retention in grains.

While it requires an additional spatial dimension, third species of tracked tritium, and an iterative solution method, one important advantage of the pore and grain diffusion model is that each input parameter has previously been measured in literature and solutions do not require a fitted diffusivity. The structure of the trapping and detrapping rate constants can also be used in the forms previously demonstrated for the TMAP code [92]. As shown in equation 4.18, the trapping rate constant follows the temperature dependence of the tritium grain diffusivity and depends on the lattice parameter, λ, and number density, N, of the material. In this case the number density of carbon in a graphite crystal is used along with both the a and c lattice parameters of graphite. The detrapping rate constant structure is the same for both the bulk-diffusivity and pore and grain diffusion model. However, adjusting the trapping rate constant requires the value of the detrapping activation energy to be adjusted in order to maintain consistency with experimental results.

Eq. 4.18
$$\Sigma_t = \frac{D_{T,g}}{\lambda^2 N}\left(C_t^o - T_t(x,t)\right)$$

The Causey et al 1.5 hour absorption measurements can be used again to examine the behavior of the pore and grain tritium retention model. Setting the time and spatial derivatives of equations 4.11, 4.12, and 4.13 to zero, the four highest-temperature measurements from the data set can be used to test the equilibrium trapping behavior. The best fit of experimental data from the equilibrium curve should have reproduced the values determined in the original study [127]. However, the authors did not state the exact values used in their model, so there are slight differences in the concentration of high-energy trapping sites and the detrapping energy from the values reported in the paper and the parameters used in this work. The trapping rate inputs fit from the high-temperature data points and other model parameters inputs are compiled in Table 4.1.

Table 4.1. Summary of input parameters used for the simulation of tritium retention in POCO AXF-5Q graphite with the pore and grain transport model. Unreferenced parameters were fit from the 1200ºC through 1500ºC points of the Causey et al measurements [127].

Parameter	Value	Ref.
$D_{T,g}$	$9.3 \cdot 10^{-5}$exp(-270.2 kJ/mol /RT) [m^2/s]	[108]
$D_{T2,p}$	$1.2 \cdot 10^{-4}$exp(-86.8 kJ/mol /RT) [m^2/s]	[108]
$K_{S,g}$	$1.22 \cdot 10^{-4}$(P [Pa])exp(19 kJ/mol /RT) [STP cc/g]	[126]
C_t^0	2.76 [mol/m^3]	
E_d	418.6 kJ/mol	
λ	(a) $2.464 \cdot 10^{-10}$ [m], (c) $6.711 \cdot 10^{-10}$ [m]	[169]
N	188160 [mol C/m^3]	[169]
ν_0	$1 \cdot 10^{13}$ [s^{-1}]	[164]

In the retention studies by Causey et al, the total tritium contained in a sample of POCO AXF-5Q graphite was measured after exposure to 0.66 Pa of a D/T gas mixture for 1.5 hours [127]. As shown in Figure 4.16, the retention is kinetically limited in the range of 700ºC-1200ºC and the measured tritium falls short of the solubility limit. At higher temperatures, the graphite is saturated but the retention decreases because of elevated rates of detrapping. This data set was used to calculate a fitted diffusivity for POCO AXF-5Q using a transport model of a spherical grain in the DIFFUSE code [108]. The reported diffusivity along with the parameters shown in Table 4.1 can be used to recreate the DIFFUSE results by modeling a representative 5μm radius grain with a constant surface tritium concentration set by the graphite solubility ($T_d^{Rg} = K_{S,g}(0.66\ Pa)^{1/2}$) and a

zero initial internal concentration. When the diffusion of T_2 in graphite pores is added to the model, the pore-grain and grain only results are similar over the 900-1100K range and then begin to deviate. Concentration profiles during the pore and grain model simulation are shown in Figure 4.17. Since the T_2 porous diffusivity in AXF-5Q was measured at 573-773K [108], it is possible that the reported diffusivity under predicts the pore diffusion at elevated temperatures. Another possibility is that the true diffusivity in the AXF-5Q grains is higher than the reported value, since the original diffusivity came from a data fit with a grain-only transport model which neglected any resistance to tritium retention caused by diffusion through the pores.

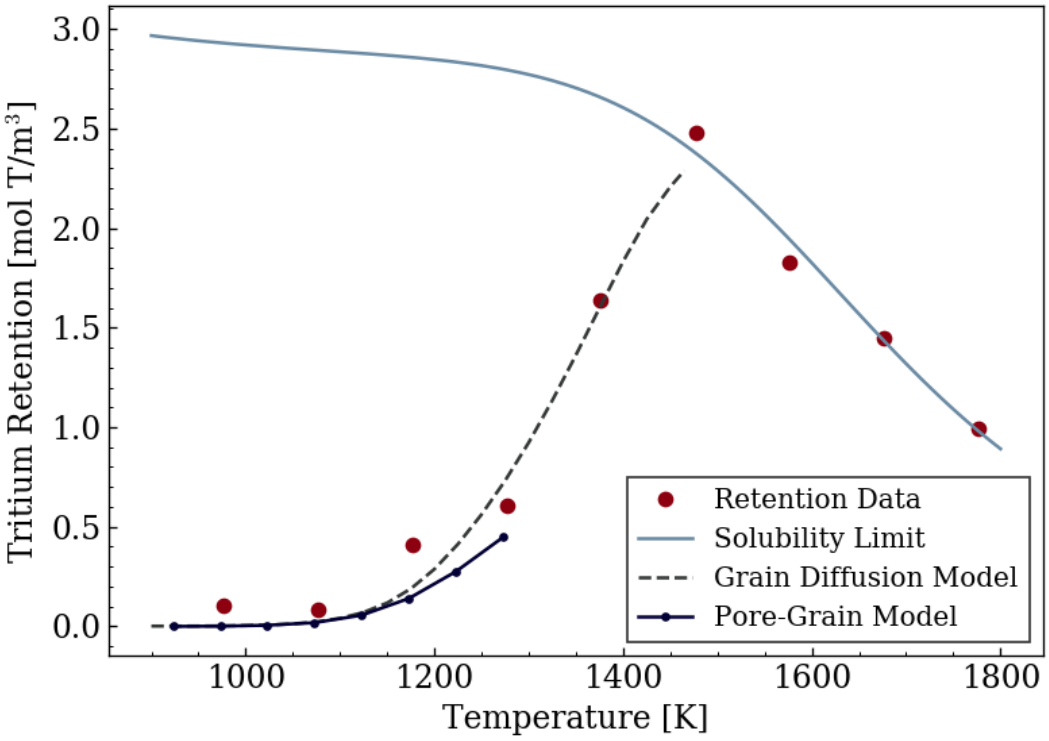

Figure 4.16. Tritium retention in a sample of POCO-AXF-5Q graphite after exposure to 0.66 Pa of tritium gas for 1.5 hours [127], plotting alongside results from the pore and grain transport model, a simplified model of the grains only, and the predicted total solubility limit.

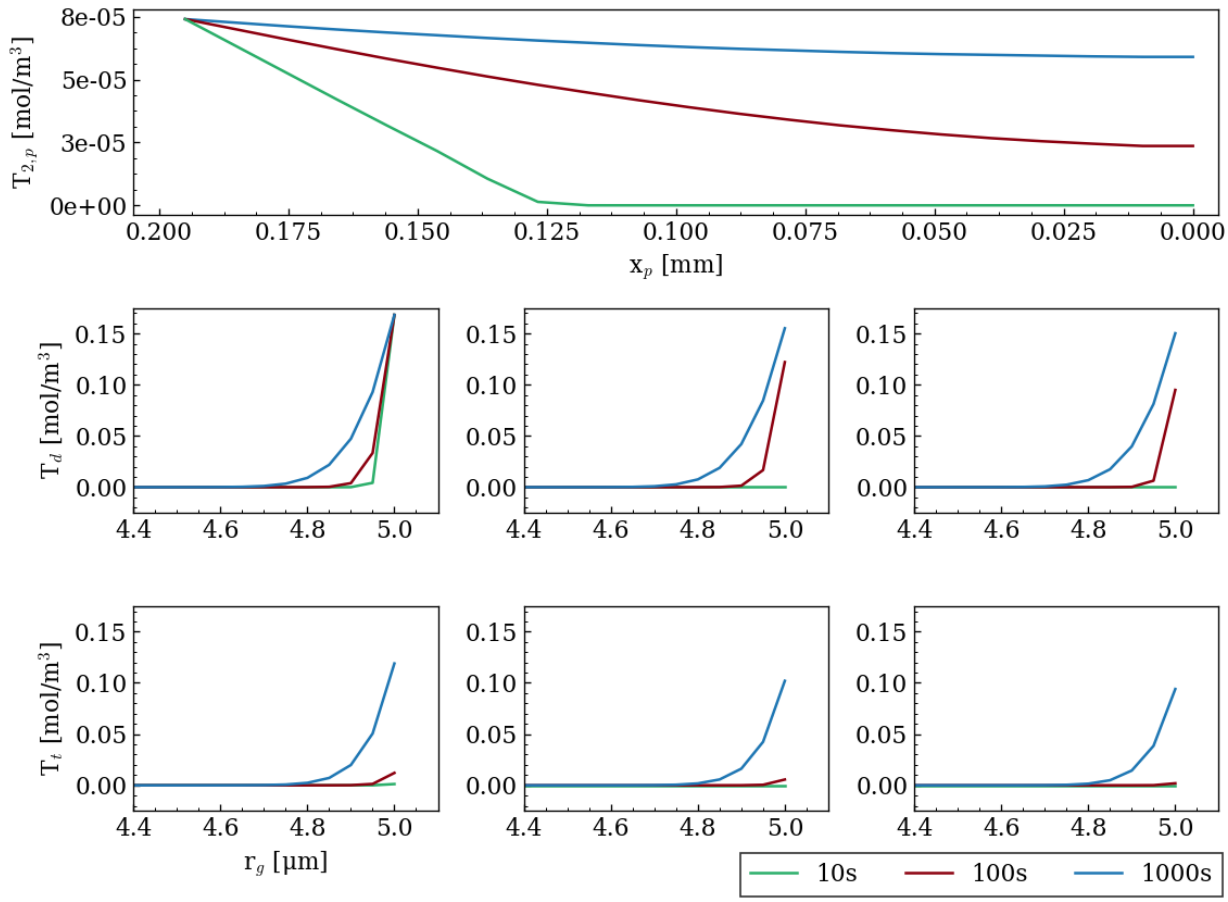

Figure 4.17. Tritium concentration profiles in simulated absorption in AXF-5Q graphite at 800ºC. Concentration of T_2 in pores is shown from the surface, x_p=0.195mm, to the sample center, x_p=0mm, in the upper row. In the center and lower rows, the concentration of diffusing and trapped tritium is plotter for the outer 0.6µm of the 10µm diameter graphite grains. The left column of T_d and T_t plots concentrations at the surface-representative grain, the center column shows a grain at a depth of 0.1 mm from the surface, and the right column shows the innermost grain modeled at the sample center.

Another relevant experiment to examine with the pore and grain diffusion model is the retention study with ISO-88 graphite performed by Atsumi et al [126]. In their experiment, 10 mm by 10 mm sheets of graphite with a thickness of 1 mm were charged with 60 kPa of D_2 gas for 5 hours at various temperatures. As shown in Figure 4.18, the retention as a function of temperature shows a similar trend to the Causey et al measurements – at lower temperatures the retention is kinetically limited and falls short of the solubility limit, while at higher temperatures the total retention is driven down by a decrease in solubility of D_2 in graphite [126]. Because of the high charging pressure, trapping and detrapping at high-energy sites is not likely a significant factor in

the total retention. For example, the equilibrium concentration of deuterium in ISO-88 graphite is 51.4 mol/m^3 at 700ºC and 60 kPa, while the total number of strong trapping sites was previously calculated to be 2.76 mol/m^3. The Sievert's law constant was originally reported as $1.9 \cdot 10^{-4}$exp(19 [kJ/mol] /RT) in units of STPcm^3/g [126]. However, this value significantly over predicts the retention values measured at 700ºC, 800ºC, 900ºC in the 5 hours of gas charging. Maintaining the adsorption enthalpy of 19 kJ/mol, the best fit for the 700-900ºC points occurred with a solubility of $1.22 \cdot 10^{-4}$exp(19 [kJ/mol] /RT), which was used for the modeled results in Figure 4.18 along with other calculations in this study where the solubility of ISO-88 is needed. One notable feature of the measurements is that a peak in retention was measured at 700ºC, compared to 1200ºC in the Causey et al study [127]. This could be a result of the longer charging time, faster diffusivity of ISO-88 compared to POCO AXF-5Q, or the higher charging pressure. As shown in Figure 4.18, the results from the pore and grain transport simulation only approach the measured results when the diffusivity is adjusted to account for acceleration from high D_2 partial pressures. For 60 kPa, the diffusivity is increased by a factor of 57.5 based on the results in Figure 2.43 and the corresponding data fit in equation 2.56. With the acceleration factor applied, the model still under predicts retention at 500ºC and 600ºC. This may be because the diffusion acceleration was fit from data with IG-110U, not ISO-88, and the acceleration factor was assumed to be constant with temperature. Nonetheless, the model is able to capture the general retention trends as a function of temperature.

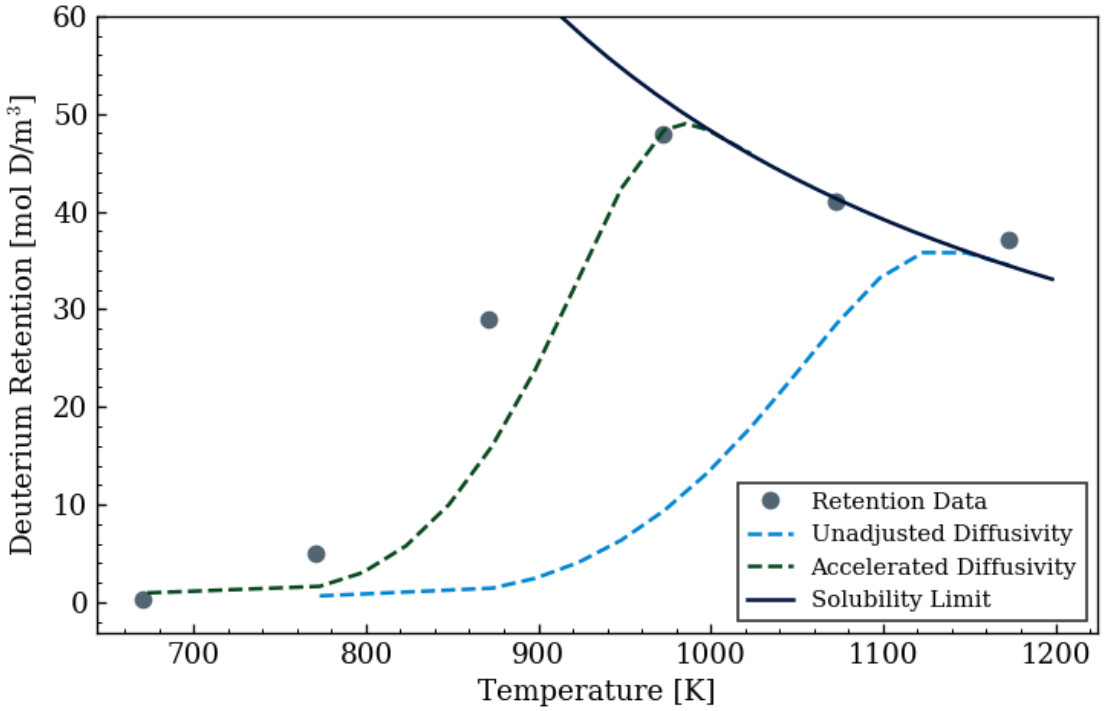

Figure 4.18. Measurements of deuterium retention in ISO-88 graphite after charging with 60 kPa of D_2 for 5 hours at various temperatures. Modeled results are shown with and without a factor of 57.5 applied to the diffusivity to account for faster diffusion at high charging pressures.

While the previous comparisons have focused on modeling tritium absorption, simulating high-temperature desorption of tritium from graphite is also of interest to tritium transport models of a FHR. For example, a graphite pebble recirculation system could be designed to include a desorption step prior to reinsertion back into the core. Desorbing graphite pebbles on each pass through the core is a potential method to remove trapped tritium and promote the uptake and removal of tritium in the reactor through retention on graphite. Because of the deviation observed at high temperatures in Figure 4.16, desorption calculations for the pebble recirculation application are carried out with the grain-only diffusion model. Desorption results from a grain-only diffusion and detrapping model can be compared to experimental measurements by Atsumi et al [159].

Thermal desorption profiles for POCO AXF-5Q1 graphite are compared to a diffusion model of a 5μm radius grain in Figure 4.19. Initial concentrations for the simulation are set according to the gas charging conditions, which were 42 kPa of D_2 and 1273K [159]. The desorption rate is then tracked by setting the diffusing tritium surface concentration to zero and increasing the temperature at a linear rate of 0.1 K/s from 700K up to 1800K. The central

desorption peak has a higher desorption rate and a narrower width than the experimental data. If a grain size distribution is used instead of the uniform grain size, then the desorption profile would be broader with respect to temperature [123]. Similarly, the high temperature desorption peak can better fit the data when a dispersion of trapping energies are used [129]. For simplicity, a uniform size grain model with a single trapping energy is used for desorption calculations in this work. While there is significant error in the desorption rate, the results from Figure 4.19 demonstrate that the diffusion and detrapping model is able to recreate the separation between desorption peaks as a function of desorption temperature. Therefore, the desorption model can help inform what temperatures are required to remove trapped tritium from graphite in a theoretical pebble recirculation system.

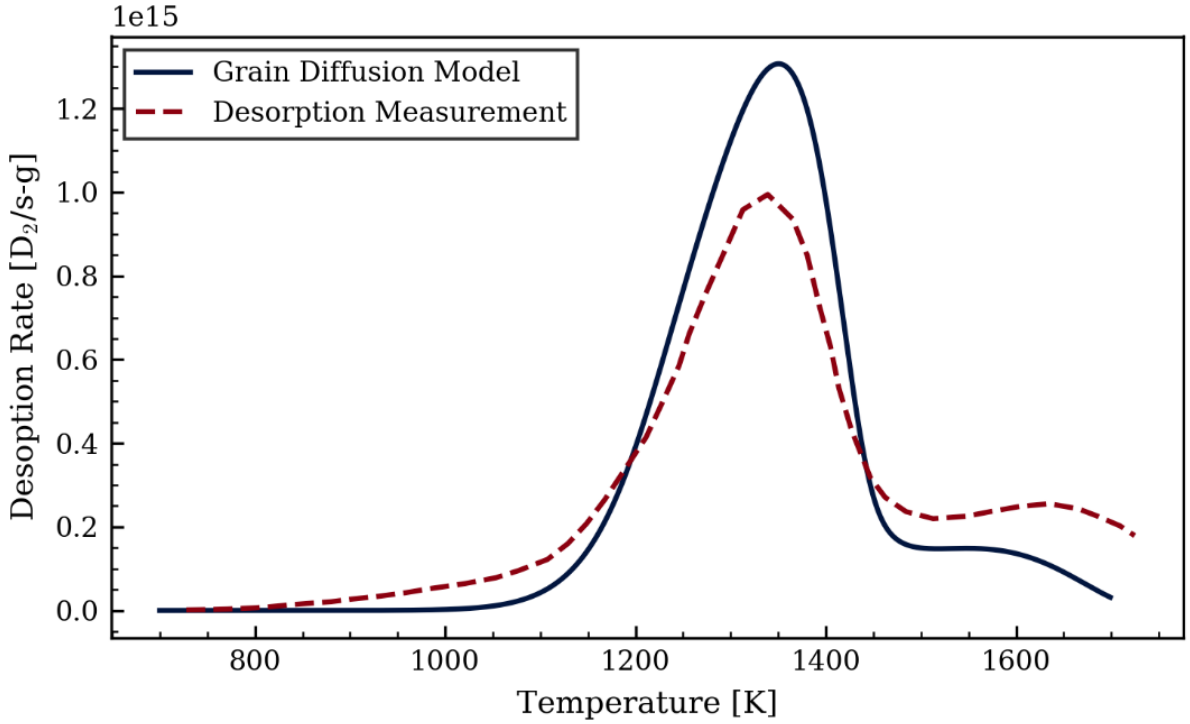

Figure 4.19. Modeled desorption of POCO AXF-5Q1 graphite charged with D_2 gas at 1273K and 42kPa then desorbed in a linear temperature ramp of 0.1K/s. Model results are compared to experimental desorption measurements [159].

In summary, the pore and grain diffusion model results are consistent with experimental data from low pressure and moderate temperature retention studies in POCO AXF-5Q graphite [127]. However, the calculated retention begins to deviate below the experimental results at temperatures above roughly 900ºC. The model results were in better agreement with high pressure

charging studies with ISO-88 graphite [126], but only when a factor was applied to the diffusivity to account for faster diffusion at the elevated charging pressure. In desorption calculations with a grain-only transport model, desorption occurred in peak structures with temperature positions similar to experimental data, but with noticeable differences in desorption rates. While differences in modeled and experimental results exist, one advantage of the pore and grain diffusion method is that diffusivities from literature can be used directly, and thus there is no reliance on a fitted bulk-diffusivity. As a result, the pore and grain model will maintain consistent results for retention in graphite as the physical dimensions of the graphite geometry are changed. For example, the ISO-88 graphite was over twice the thickness of the POCO AXF-5Q samples in the previously modeled experimental results. It may be possible to accurately represent the tritium retention process in graphite using a bulk-diffusion coefficient. However, there is currently limited data available to validate the assumptions of the bulk-diffusivity model such as experimental conditions with low tritium partial pressures, large physical dimensions, and FHR representative temperatures. Therefore, the pore and grain diffusion method is used for baseline calculations in this work for the system-level model of tritium transport in a FHR.

5. System-Level Tritium Transport Model Development

The ability to predict the transport and release of tritium among different regions in a FHR is an essential prerequisite in determining the optimal set of tritium management strategies for the design. Efforts to model the tritium distribution in molten salt reactors at the system-level scale began during the MSRE program [170]. Because of its low power level as a test reactor, tritium generated from the MSRE itself was not a significant radiological hazard and releases were compliant with proper health standards [171]. However, it was understood that the unmitigated releases of tritium in a commercial-scale MSR plant would potentially violate environmental release limits, as 63% of generated tritium was expected to permeate through the primary and secondary heat exchangers into the steam system [38]. If the steam system water was discharged at the rates of similar sized steam cycle plants, then the tritium concentration in released water was estimated to be 80 times the allowable limit for water effluents [38].

Early models for tritium transport in the MSRE focused on the steady-state concentration of tritium in each reactor system, which were separated into zero-dimensional regions to solve for the gains and losses of tritium in each zone [170]. More recently, system-level models for other reactor designs have been developed, such as the TRIDENT model for pebble bed FHRs [43], TAPAS for prismatic FHRs [172], and TMSR-TTAC for liquid-fueled molten salt reactors [173]. In this work, system-level tritium transport is modeled based on the TRIDENT code framework. The significant modifications to the model and key results are summarized in this section.

5.1. System Description and Summary of Features

The TRIDENT (TRITium Diffusion EvolutioN and Transport) model was first developed at MIT in 2015 as part of a PhD thesis by Stempien [3]. Model results were designed to represent the Mk-1 FHR design concept, which uses a single salt loop paired with an open-air Brayton power cycle [8]. Since the initial development of TRIDENT, there has been growing interest in FHRs coupled with a nitrate salt intermediate loop, primarily through design efforts of Kairos Power [20]. A conceptual diagram of relevant components in the Kairos Power Fluoride Salt-Cooled High-Temperature Reactor (KP-FHR) core is shown in Figure 5.1. The new features of the KP-FHR prompted additional investigation into tritium transport modeling for the design. Furthermore, as the KP-FHR design has progressed past the technological maturity level of the Mk-1 FHR concept, additional regions can be added into TRIDENT to more accurately describe the tritium distribution

in the reactor. Tritium distribution results presented in this section are therefore modeled for a pebble bed FHR with a nitrate salt intermediate loop, power level of 320 MWth, and an inlet/outlet temperature of 550ºC/650ºC. The model inputs are intended to be representative of a generic reactor similar to the KP-FHR, but specific design parameters from the reactor are not used in order to provide a general analysis for the reactor type.

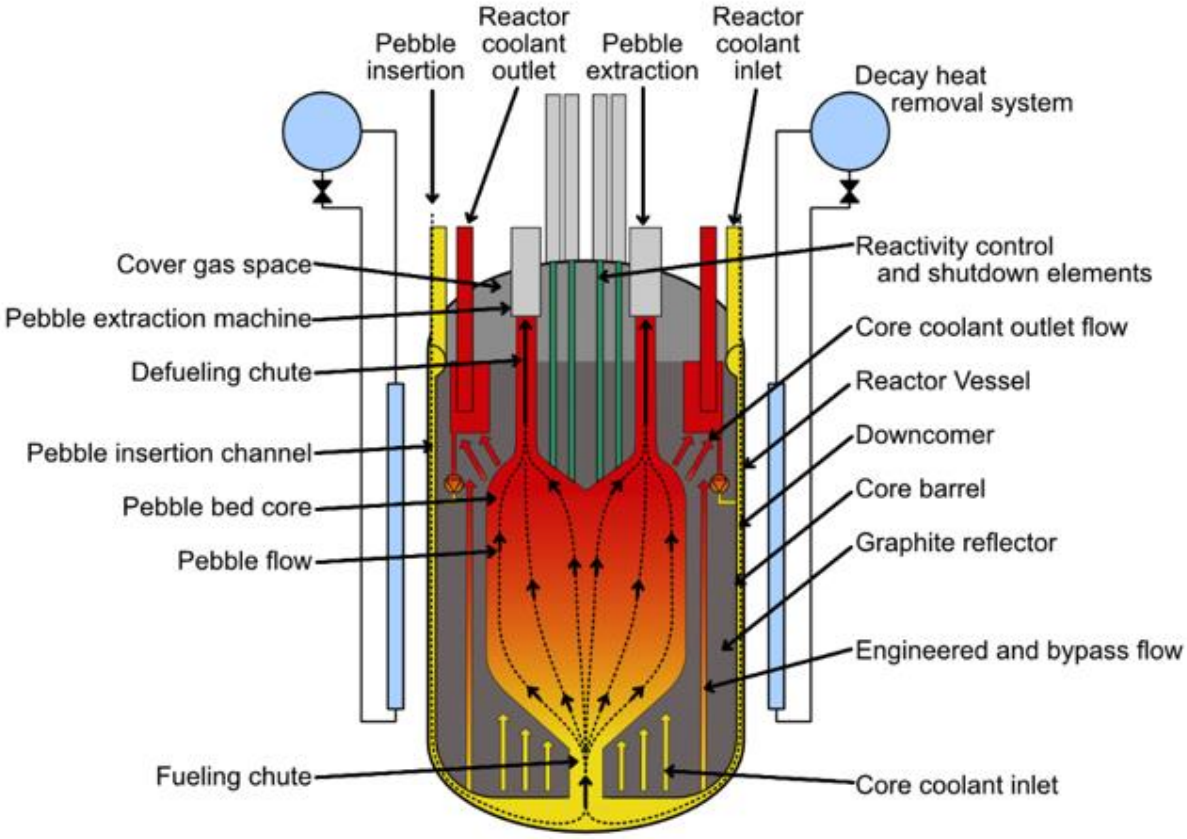

Figure 5.1. Illustration of features and components for the KP-FHR core [174].

A thorough description of the original TRIDENT methodology for calculating tritium generation, transport to surfaces, and permeation through metals is available elsewhere [3]. In this work, the previously described methods in Section 4 are implemented to calculate the tritium retention in the fuel and graphite moderator pebbles in the core. Additionally, new regions were added into the model to calculate tritium permeation through the primary loop hot leg and cold leg, which are modeled before and after the heat exchanger. After the cold leg, the salt enters the downcomer region where tritium permeation through the reactor vessel and tritium retention on the graphite reflector outer surface occur simultaneously before the salt returns to the core inlet. In

the core, the pebble recirculation calculation was updated to account for continuous recirculation, pebble removal and replacement, and different pebble desorption scenarios. At the core exit, a node was also added to simulate tritium evolution into the off-gas of the reactor vessel. Because of the several new regions, the TRIDENT code was moved from Matlab to Matlab Simulink, which allows for simplified swapping and interconnections between individual subroutines for each modeled region. The FHR tritium release paths calculated by the model are summarized in Table 5.1, and the reactor representation in the updated model is illustrated in Figure 5.2. The system discretization is set so that the first calculated node is located at the core inlet and there are 11 total nodes in each region and 10 evenly spaced subdivisions. At each node the concentration of TF and T_2 is tracked in units of mol/m^3, then the gains and losses of tritium are calculated in the subdivisions between the concentration nodes. At the outlet of each region, the molar flow of TF and T_2 in mol/s is calculated and passed to the inlet of the following region.

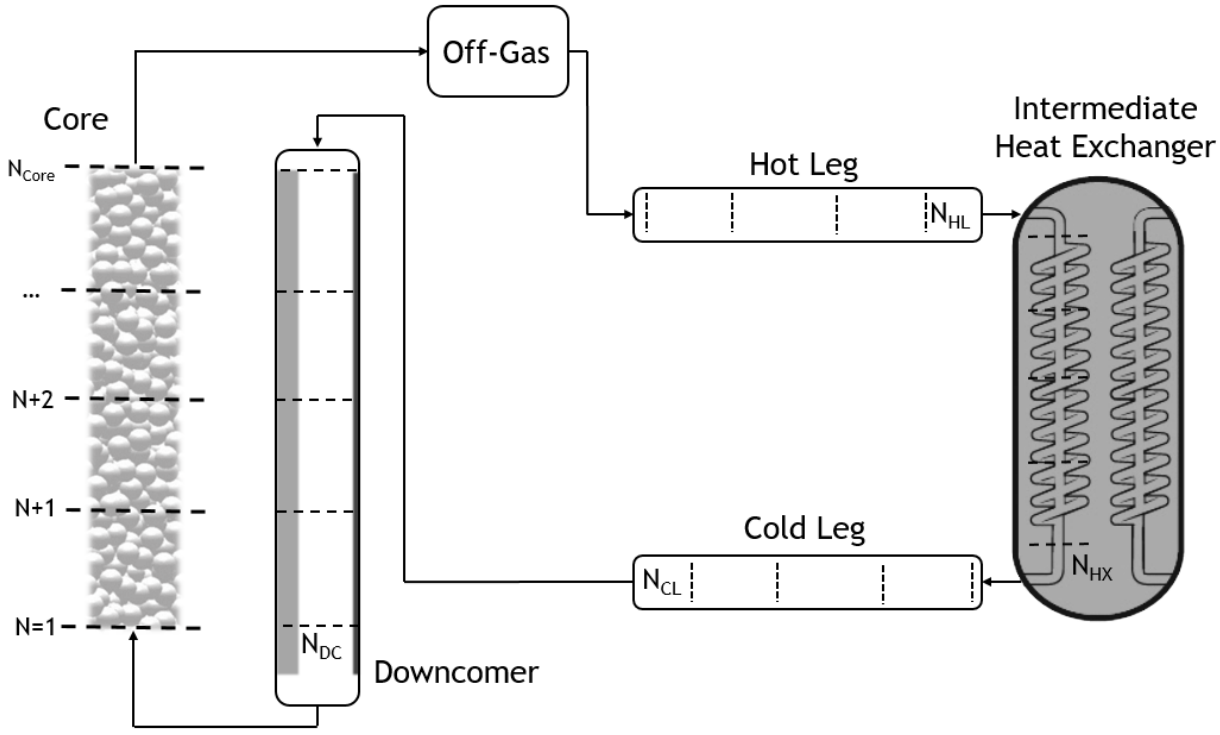

Figure 5.2. System-level model flow path and discretization diagram. The first simulation node is positioned at the core inlet. There are 11 concentration nodes per region and thus 10 subdivisions between nodes. Heat Exchanger diagram from [175].

Table 5.1. Reactor regions and tritium release pathways for the FHR primary system.

Region	Tritium Release Pathway
Core	Retention in fuel element and graphite moderator pebbles Evolution to off-gas above core
Downcomer	Retention in graphite reflector Permeation through reactor pressure vessel to reactor building
Hot leg	Permeation to reactor building
Primary HX	Permeation to secondary coolant
Cold leg	Permeation to reactor building

TRIDENT solves a transient simulation in order to calculate tritium transport and releases in each FHR region. However, time-dependence is only built into equations relevant to the tritium distribution. Details such as the coolant flow rate and temperature profiles are set during the initialization of the simulation and remain steady throughout the simulation. In the simplified baseline case, a constant axial power profile in the core is assumed along with linear temperature changes in the core and heat exchanger. Additionally, the hot leg, cold leg, and downcomer regions are assumed to be isothermal. While a more accurate temperature profile could be built into the model, the piecewise linear profile has the benefit of making model results easier to interpret in terms of the underlying tritium transport phenomena. The simplified temperature profile distribution among simulation nodes is shown in Figure 5.3 for the case of a 550ºC core inlet and 650ºC core outlet temperature. Temperature dependent thermophysical and transport properties are tabulated at each node in the loop according to the prescribed temperature distribution only once at the beginning of the simulation so the property calculations are not unnecessarily repeated.

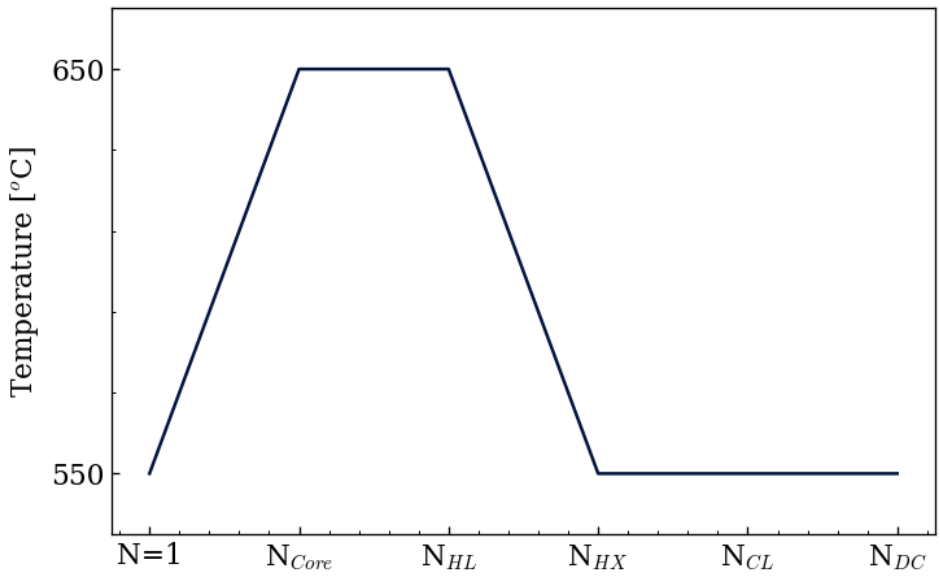

Figure 5.3. Temperature profile in TRIDENT regions among different nodes. The first node is set to the core inlet. A simplified profile is used with linear temperature changes in the core and heat exchanger and constant temperatures in other regions.

Another simplification in the KP-FHR TRIDENT representation is to focus the model only on tritium transport in the primary loop. Tritium which permeates through the heat exchanger to the intermediate nitrate salt as T_2 is expected to rapidly oxidize into T_2O [176], either through conversion of nitrates into nitrites, as shown for sodium nitrate in equation 5.1, or through reaction with oxygen in the intermediate loop cover gas, as in equation 5.2. Both reaction pathways have a significant thermodynamic driving force [114]. Assuming that all tritium is converted into T_2O or HTO, and further reactions of T_2O/HTO into T_2 or HT are prevented by the oxide layers in the intermediate loop, then back-permeation into the Flibe salt becomes negligible and the tritium transport in the intermediate loop is decoupled from the primary loop solution. For $NaNO_3$ and KNO_3, the T_2O can be removed from the intermediate salts by gas stripping or dehumidifying the intermediate loop off-gas [114]. However, the gas stripping is less effective in the case of $LiNO_3$ because of the stability of LiOT dissolved in the salt [177]. The current KP-FHR intermediate loop concept features a mixture of $NaNO_3$ and KNO_3 in the intermediate loop [20], thus capture of T_2O in the intermediate off-gas systems should be feasible.

Eq.5.1 $$NaNO_3 + T_2 \rightarrow NaNO_2 + T_2O$$

Eq.5.2 $$T_2 + 1/2\ O_2 \rightarrow T_2O$$

The system configuration for the KP-FHR is shown in Figure 5.4, where the primary loop systems are pictured in red. Two circuits for the primary loop are shown in the figure, but assuming there are identical conditions in each, only one circuit is modeled in the code with a factor of 2 applied to the area of the hot leg and cold leg. The HX areas listed in Table 5.2 are the total areas for the two intermediate heat exchangers. Other input parameters are shown in Table 5.2 for the generic FHR design used in the system-level tritium transport model.

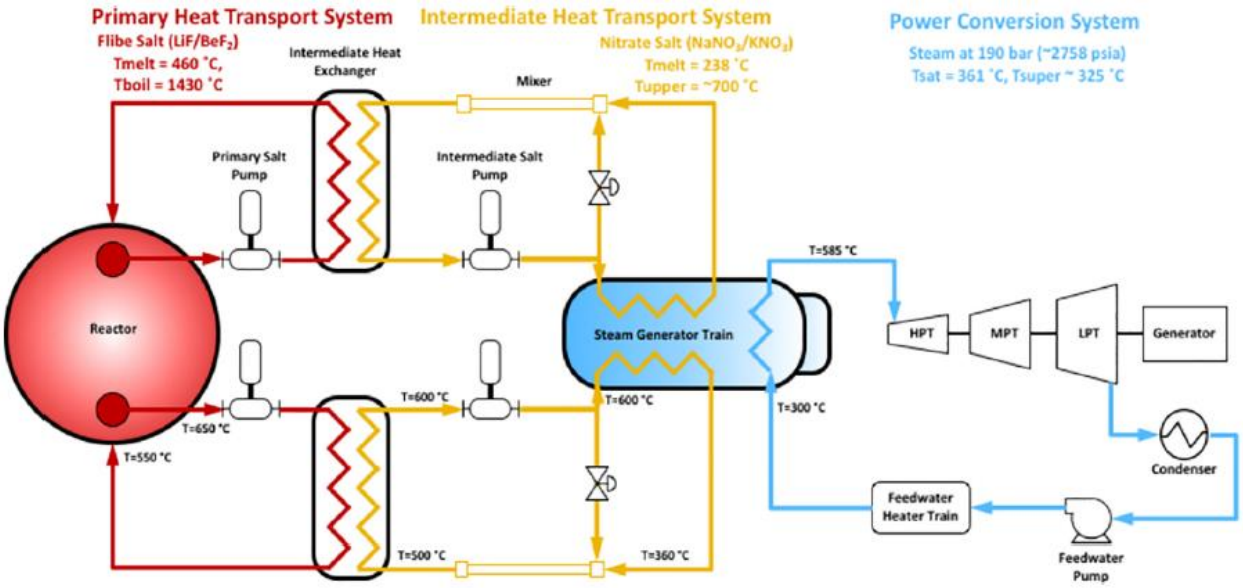

Figure 5.4. System illustration and flow paths for the KP-FHR paired with a steam power cycle. From [20].

Table 5.2. Generic FHR design parameters used as inputs for the tritium transport simulations. Cold leg dimension are set to be identical to the hot leg.

Parameter	***Value***
HX tube thickness [m]	1.25e-3
HX tube ID [m]	1.25e-2
HX inner area [m^2]	5750
HX tube length [m]	10
Hot leg tube thickness [m]	1e-2
Hot leg tube length [m]	15
Hot leg tube ID [m]	0.375
Vessel ID [m]	3.75
Vessel thickness [m]	0.05
Graphite Reflector OD [m]	3.66
Downcomer height [m]	6.5
Graphite pebble diameter [m]	0.04
Number of pebbles	335000
Core cross sectional area [m^2]	5.2
Core free-surface evolution area [m^2]	5.75
Core salt volume [m^3]	7.5
Total primary loop salt volume [m^3]	50
Salt Li-7 enrichment [mol%]	99.995

To differentiate between model results in this study and the previous TRIDENT methodology [3], the designation TRIDENT Mod1 is applied to represent the new reactor configuration and additional features. A summary of features in each code is provided in Table 5.3. The additional permeation zones added to TRIDENT Mod1 – the hot leg, cold leg, and reactor vessel – use a similar methodology to TRIDENT, although a recombination step was added to each exterior-surface node. A node between the core and hot leg was also added to represent evolution to the reactor cover gas based on an evolution mass transfer coefficient. The most significant change to the underlying methodology was the implementation of the graphite retention models described in Section 4. Simulating the kinetics of graphite transport also allows for desorption conditions in a pebble recirculation system to be simulated in TRIDENT Mod1. Not all features from TRIDENT were moved to TRIDENT Mod1, such as the corrosion model and corrosion product transport simulation. Since the focus of this study is tritium management strategy development, the corrosion models were not currently required. Furthermore, by using the fixed-

potential equilibrium redox assumption to calculate chemical forms of tritium, the tritium speciation process is decoupled from salt redox potential changes under various corrosion product concentrations.

Table 5.3. Summary of features in the original TRIDENT model [3], along with alterations and new features made in TRIDENT Mod1.

	TRIDENT	**TRIDENT Mod1**
Computer Program	MATLAB	MATLAB Simulink
Reactor Configuration	Pebble bed FHR with open-air Brayton cycle or fluoride salt intermediate loop	Pebble bed FHR with nitrate salt intermediate loop decoupled from the simulation
Reactor Regions	Core, Heat Exchanger, Extraction Systems	Core, Off-gas, Hot leg, Heat Exchanger, Cold leg, Downcomer, Extraction Systems
Graphite Calculation	Solubility limited	Diffusion and trapping model
Redox Dependence	Equilibrium or corrosion-controlled	Equilibrium or sub-loop controlled
Pebble Recirculation	Full removal	Full removal or time- and temperature-dependent desorption calculation
Permeation Barrier Coatings	Exterior surfaces	Exterior surfaces and Flibe-facing surfaces
Tritium Evolution	None	Evolution to Core cover gas
Recombination Resistance	None	Recombination built into permeation calculation
Corrosion Reactions	Simulated corrosion in metals	None
Corrosion Product Transport	Flibe mass transfer corrosion product transport	None

5.2. Overview of Calculation Methodology and Implementation

The important phenomena relevant for tritium transport in FHRs have been previously discussed in Section 2. Here, each process is described in terms of the specific implementation into the current TRIDENT Mod1 code. There are several similarities in each implementation strategy to the original TRIDENT methodology, which is discussed in detail elsewhere [3]. The overlapping features are also discussed in this section to provide a complete description of the current TRIDENT Mod1 calculation process and to aid in the interpretation of presented results.

5.2.1. Options for Tritium Generation and Speciation

The tritium generation equation is an essential input which creates a source term for tritium in the simulation. As shown in Section 2, tritium generation from neutron reactions in Flibe are the focus of the simulation since other sources of tritium generation such as ternary fission and impurities in graphite are only expected to account for 2% of total tritium generation. Within Flibe, lithium-6 and lithium-7 are the major sources of direct tritium production. The next most significant reaction occurs from fluorine-19, which was calculated to produce 0.38% of the tritium compared to the sum of lithium-6 and lithium-7 for the MSBR [38], and 0.025% compared to lithium-6 and lithium-7 in the FS-3 irradiation [41]. Therefore, TRIDENT and TRIDENT Mod1 use a tritium generation calculation based on tritium producing reactions of lithium-6 and lithium-7 only [43]. However, it is also important to account for changes in lithium-6 concentrations in the salt if when conducting beginning-of-life to equilibrium simulations. A differential equation governing the lithium-6 concentration in the primary loop salt is shown in equation 5.3, which increases based on production from Be-9(n,α)He-6 reactions and decreases from neutron absorption from lithium-6 [43]. Integrating equation 5.3 to find the lithium-6 concentration as a function of time results in the time dependent tritium generation rate, g(t), shown in equation 5.4 [178]. An explanation of terms in equations 5.3 and 5.4 is provided in Table 5.4.

Eq.5.3
$$\frac{dN_{Li6}}{dt} = \phi N_{Be9}\sigma_{Be9}^{n,\alpha}V_C/V_L - \phi N_{Li6}\sigma_{Li6}^{n,abs}V_C/V_L$$

Eq.5.4
$$g(t) = \phi\sigma_{Li7}^{n,n'}N_{Li7} + \phi\sigma_{Li6}^{n,t}\left(N_{Li6}^{o}\exp\left(-\frac{V_C}{V_L}\phi\sigma_{Li6}^{n,abs}t\right) + \frac{\phi\sigma_{Be9}^{n,\alpha}N_{Be9}}{\phi\sigma_{Li6}^{n,abs}}\left(1-\exp\left(-\frac{V_C}{V_L}\phi\sigma_{Li6}^{n,abs}t\right)\right)\right)$$

Table 5.4. Description of input parameters in the tritium production equation.

Parameter	Explanation [Units]
ϕ	Neutron flux [n/cm^2-s]
$\sigma_{Li7}^{n,n'}$	Lithium-7 tritium production microscopic cross section [barn]
N_{Li7}	Lithium-7 atomic number density [atoms/cm^3]
$\sigma_{Li6}^{n,t}$	Lithium-6 tritium production microscopic cross section [barn]
N_{Li6}^{o}	Lithium-6 initial (time=0) number density [atoms/cm^3]
V_C	Volume of Flibe in the core [m^3]
V_L	Total volume of Flibe in the primary loop [m^3]
$\sigma_{Li6}^{n,abs}$	Lithium-6 total neutron absorption microscopic cross section [barn]
$\sigma_{Be9}^{n,\alpha}$	Beryllium-9 n,α reaction microscopic cross section [barn]

The values in the tritium production equation are based on neutronic analysis originally carried out for the Mk-1 FHR [178]. Therefore, the generation is scaled by the ratio of reactor thermal powers (320 MW/236 MW) to account for additional tritium generated in the FHR design used for this analysis. However, the one-group cross sections shown in equation 5.4 also depend on the neutron energy spectrum seen by the salt. Therefore, a tritium generation neutronic analysis specific to a FHR design should be completed once more detailed results are required. In the case of the scaled Mk-1 FHR generation values and reactor design parameters in Table 5.2, a 320 MWth FHR would produce 3390 Curies of tritium per day at the reactor beginning-of-life and 981 Curies per day at equilibrium. Tritium production rates as a function of time are plotted in Figure 5.5 for several lithium-7 enrichments. The time scale of over ten years to reach an equilibrium tritium generation rate in the case of 99.995% lithium-7 is significantly longer than the times required to reach an equilibrium tritium distribution in the simulation. For example, with a constant tritium generation rate the slowest tritium release to equilibrate is typically the permeation rate through the vessel which takes roughly one year. Therefore, a constant production term equal to the equilibrium tritium generation rate is used to accelerate scoping studies presented in this work.

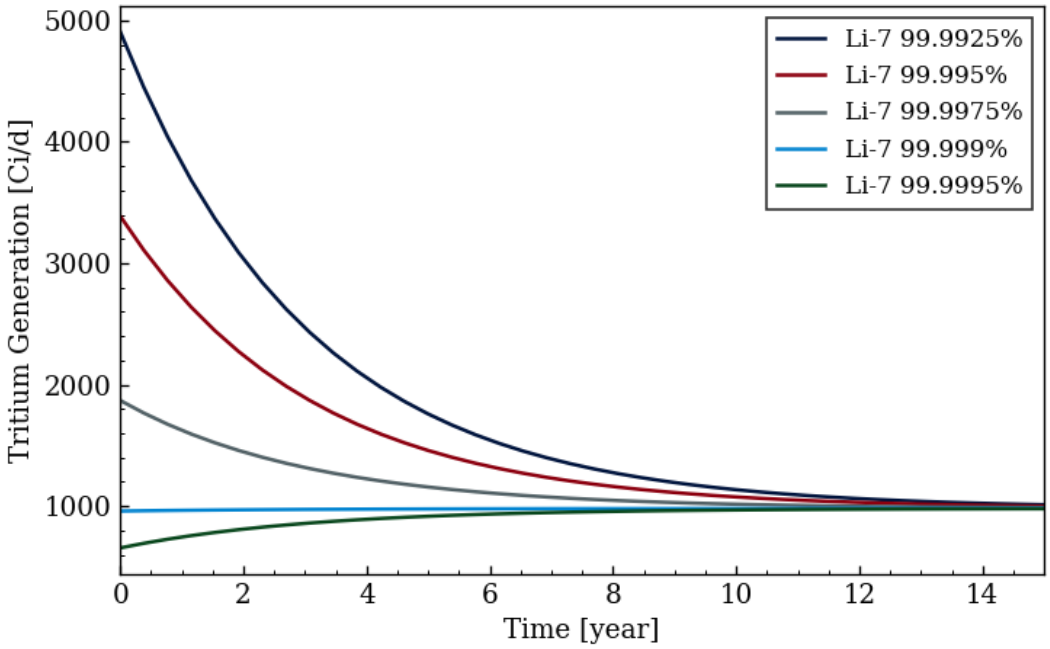

Figure 5.5. Tritium generation as a function of time and lithium-7 enrichment based on calculations with equation 5.4.

The total tritium generation rate must then be split among the nodes of the core for the TRIDENT Mod1 simulation. A linear temperature profile in the core for the simplified baseline case implies a constant axial power distribution, and thus a uniform flux in the salt at each core node. Since the salt density changes with temperature, the total tritium generation in each node, G_N, is calculated based on a weighted average of densities in each core node as shown in equation 5.5. Simply dividing the total generation by the number of nodes would not cause a significant change from the calculation in equation 5.5 because Flibe density only varies 2.4% from 550ºC to 650ºC [179]. However, using an axial vector for tritium generation allows for more complicated flux distributions to be implemented if additional detail in the model is required later on.

Eq. 5.5
$$G_N = \frac{g(t)\rho_N V_C}{\sum_{N=1}^{N_{Core}} \rho}$$

After the generation calculations, tritium is partitioned into TF and T_2 based on the desired options for speciation. If a simulation of only T_2 is desired, then the speciation into TF can be set to zero. Tritium could also be generated fully as TF in the core, and then a chemical speciation calculation can performed elsewhere in the reactor loop. The option most commonly used in the presented results is to generate TF and T_2 according to the Flibe redox potential, which is a set

input in the simulation. By rearranging the definition of fluorine potential ($\Delta\bar{G}_{F2}$) presented in Section 2.2.1 for equation 2.12, the ratio of TF partial pressure to square root of T_2 partial pressure can be determined according to equation 5.6. The partial pressure ratio, abbreviated as P_R, is shown in Table 5.5 for examples of salt chemistry conditions discussed in Section 2 as calculated at 600ºC where the standard free energy of formation of HF gas (ΔG^o_{TF}) is -277.9 kJ/mol [180]. Since the definition of fluorine potential uses pressures in units of atmospheres, while Pascals are used in TRIDENT Mod1, the pressure ratios are converted as shown in Table 5.5 using a factor of $101325^{1/2}$ to produce units of $Pa^{1/2}$ from $atm^{1/2}$.

Eq. 5.6
$$\frac{p_{TF}}{\sqrt{p_{T_2}}} = \exp\left(\frac{\Delta\bar{G}_{F_2} - 2\Delta G^0_{TF}}{2RT}\right)$$

Table 5.5. Ratio of partial pressure of TF to square root of T_2 partial pressure for various chemical conditions and fluorine potentials.

Redox Condition	**$\Delta\bar{G}_{F2}$**	**P_R [$atm^{1/2}$]**	**P_R [$Pa^{1/2}$]**
Purification with 1:10 H_2/HF	-590.0 kJ/mol	$9.485\cdot10^{-2}$	$3.019\cdot10^{1}$
Experimental Redox Measurements	-676.8 kJ/mol	$2.403\cdot10^{-4}$	$7.649\cdot10^{-2}$
MSRE Target Chemistry 1:100 UF_3/UF_4	-700.5 kJ/mol	$4.698\cdot10^{-5}$	$1.495\cdot10^{-2}$
Beryllium Fully-Reduced Redox Potential	-902.5 kJ/mol	$4.265\cdot10^{-11}$	$1.357\cdot10^{-8}$

The pressure ratio for a given redox potential is used to determine the amount of tritium in each chemical form. First, the total tritium molar flow in the node or region, $M_{\Sigma T}$, is calculated based on the incoming molar flow of T_2 and TF which are represented by $M_{T2,in}$ and $M_{TF,in}$, respectively, with units of mol-T/s in equation 5.7. Tritium added to the node by generation is calculated using the specific tritium generation per node from equation 5.5. By substituting concentration times volumetric flow rate to replace molar flows, and then using the definition of Henry's law in place of concentrations, the tritium balance can be written in terms of T_2 and TF partial pressures as in equation 5.8. Dividing each term by $p_{T2}^{1/2}$ allows for the pressure ratio calculated from the redox condition, P_R, to be substituted in as a coefficient in the quadratic equation for $p_{T2}^{1/2}$ shown in 5.9. Solving the equation for p_{T2} and converting the pressure back into a concentration with Henry's law produces equation 5.10, which calculates the total molar flow of T_2 in the node or region. The additional T_2 produced in a node from tritium generation in units of mol-T_2/s, $G_{T2,N}$, as calculated by equation 5.11 is also useful for other TRIDENT Mod1 functions.

Eq. 5.7 $$M_{\Sigma T} = 2M_{T_2,in} + M_{TF,in} + G_N$$

Eq. 5.8 $$M_{\Sigma T} = 2\dot{V}K_{H,T2}p_{T_2} + \dot{V}K_{H,TF}p_{TF}$$

Eq. 5.9 $$2\dot{V}K_{H,T2}p_{T_2} + \dot{V}K_{H,TF}P_R\sqrt{p_{T_2}} - M_{\Sigma T} = 0$$

Eq. 5.10 $$M_{T_2} = \dot{V}\left(\frac{1}{4}\sqrt{\frac{P_R^2K_{H,TF}^2}{K_{H,T_2}} + \frac{8M_{\Sigma T}}{\dot{V}}} - \frac{P_RK_{H,TF}}{\sqrt{K_{H,T_2}}}\right)^2 : M_{TF} = M_{\Sigma T} - 2M_{T_2}$$

Eq. 5.11 $$G_{T_2,N} = M_{T_2} - M_{T_2,in}$$

Outside of the core, the balance between TF and T_2 shifts because of differential release rates between the two species. For example, in the heat exchanger the T_2 concentration in the salt decreases because of permeation, but the TF concentration remains the same because no TF release paths in the heat exchanger are modeled. Therefore, the TF and T_2 concentrations are adjusted at the outlet of each TRIDENT Mod1 region in order to maintain a balance according to the set redox potential. The tritium molar flows leaving one region can be rebalanced using equation 5.10 prior to entering the next region. However, the G_N term is set to zero since no tritium generation occurs outside of the reactor core. In the cases where tritium generation is set to TF only, the rebalancing based on redox potential in between reactor regions is the only source of T_2 in the simulation.

5.2.2. Tritium Transport to Core Graphite Pebbles

While tritium is added to the core through the generation term, tritium is also removed from Flibe in the core through uptake and retention on graphite pebbles. A notable simplification in the core model is that no distinction is made between fuel pebbles and graphite moderator pebbles, which will be simultaneously present in a FHR core [5]. The temperature profile within pebbles is also assumed to be isothermal and equal to the salt temperature at the particular axial core node. Adding transport parameters specific to graphite grades selected for a FHR as well as detailed pebble temperature profiles are areas in which the tritium retention calculation in graphite could be improved as FHR designs progress in maturity or design details become available in open literature.

The tritium retention calculation first requires a mass transfer coefficient to represent tritium transit from the salt bulk to the graphite pebble surface. The Wilson and Geankoplis correlation for mass transfer in a packed bed of spheres in used to calculate the Sherwood number

as discussed in Section 2.3.2 for equation 2.36 [85]. A mass transfer coefficient for the core is then calculated based on equation 5.12, where the characteristic length is the pebble diameter, d_{pebble}, or 4 cm. As previously discussed, only the uptake of T_2 in the core pebbles is modeled in the graphite retention methodology, so equation 5.12 uses the diffusivity of T_2 in Flibe as opposed to TF. The mass transfer coefficient is converted into a flux of T_2 through multiplying by a concentration gradient, which depends on the bulk concentration of T_2 throughout the node ($T_{2,Bulk}$) and the concentration in the salt phase at the pebble surface ($T_{2,Surf}$) as shown in equation 5.13.

Eq. 5.12 $$k_{T_2,Core} = ShD_{T_2}/d_{pebble}$$

Eq. 5.13 $$j_{T_2} = k_{T_2,Core}\left(T_{2,Bulk} - T_{2,Surf}\right)$$

The salt phase concentration of T_2 at the pebble surface depends on the tritium retention characteristics on the graphite side of the interface. Therefore, tritium retention in the graphite pebble sets a boundary condition which changes the concentration gradient in the salt and ultimately determines the extent to which tritium is transferred into graphite. The basis for the boundary condition calculation is that the salt and graphite will both be exposed to the same partial pressure of T_2 at the interface of the two materials [181]. If the bulk-diffusion model for graphite is used, then the tritium concentration at the salt surface can be related to the diffusing tritium concentration at the graphite pebble surface (T_d^{Rp}) by combining Henry's law for the salt and Sievert's law for graphite as shown in equation 5.14. The retention process with flux of T_2 from the salt, concentration of T_2 and T_d and the interface, and concentration profile of T_d within the pebble is illustrated conceptually in Figure 5.6.

Eq. 5.14 $$p_{T_2} = T_{2,Surf}/K_{H,T_2} = \left(T_d^{Rp}/K_{S,g}\right)^2$$

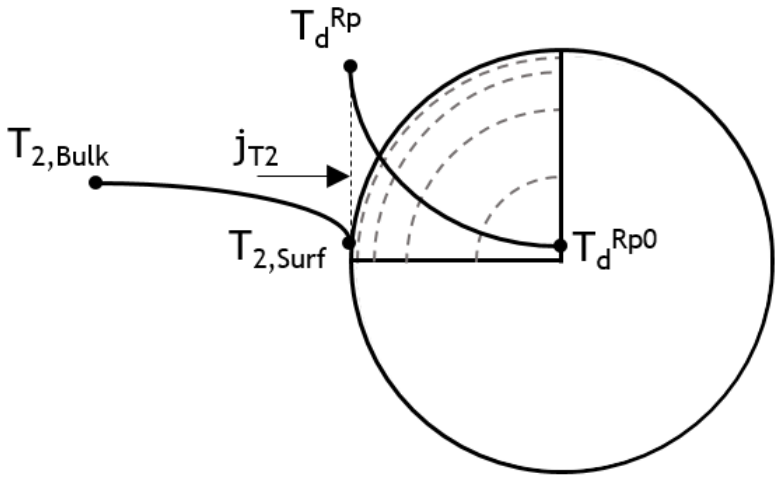

Figure 5.6. Illustration of T_2 mass transfer from Flibe salt to graphite pebbles in the bulk-diffusion model for tritium retention in graphite.

A retention calculation is performed at each axial subdivision in the core, where one representative pebble is modeled per division. All graphite pebbles are modeled with identical material and tritium transport properties, in this case as POCO AXF-5Q graphite since the grade offers the most complete set of experimental data for the graphite transport and trapping equations. In a FHR, the fuel pebbles will likely be made with a graphite matrix material, such as the A3-3 grade used in HTGRs [182]. There could also be unfueled graphite pebbles used for additional neutron moderation in the core. The grade of the moderator pebbles could be selected based on the desired tritium management strategy – grades with high hydrogen solubility and trap concentrations could be selected if tritium retention in graphite is a desirable feature, or low solubility if retention is to be minimized. Tritium retention parameters for other graphite grades and the ability to model retention in multiple grades simultaneously would be required for the use of TRIDENT Mod1 in a detailed, design-specific FHR model.

The purpose of modeling tritium generation and retention over an axial discretization in the core, rather than as a single lumped system, is to allow for properties to vary in each position as well as to account for tritium gains and losses between nodes. If the flux of T_2 to pebbles is known, then the concentration of T_2 entering the next node (T_2^{N+1}) can be solved for according to equation 5.15. Only one pebble is modeled per node, so the total area of pebble (A_{node}) is calculated based on the area each pebble times the total number of pebbles in each core axial subdivision. Two different volumetric flow rates for the previous node and following node ($\dot{V}^N$ and $\dot{V}^{N+1}$) are used since the volumetric flow rate can change as temperature of Flibe in the core increases. The

discretization notation for T_2 concentrations along with tritium sources and losses for the core divisions are shown in Figure 5.7. In the baseline cases, there were 11 concentration nodes modeled for the core and thus 10 axial subdivisions. The bulk concentration values, graphite surface concentrations, and graphite pebble concentration profiles are modeled at the subdivisions and are considered to represent the midpoint between the concentration nodes.

Eq. 5.15 $$T_2^{N+1} = \left(T_2^N \dot{V}^N + G_{T_2,N} - j_{T_2} A_{node}\right)/\dot{V}^{N+1}$$

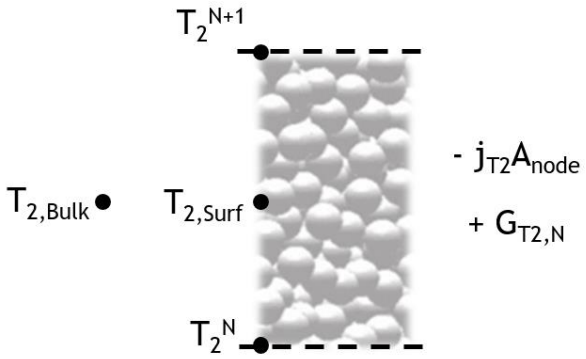

Figure 5.7. Notation for tritium gains and losses between concentration nodes in the TRIDENT Mod1 core discretization.

As shown in equation 5.13, the bulk T_2 concentration across the node is needed in order to calculate the flux of T_2 into the graphite pebbles. Typically, tritium concentration will increase throughout the core because of the generation term, and therefore using the T_2 concentration at the previous node (T_2^N) as the bulk concentration would under predict the T_2 flux. For small changes in concentrations between nodes, as is typical of equilibrium conditions in TRIDENT Mod1 simulations, the bulk concentration is equal to the average of T_2 concentrations at the preceding and following concentration nodes. For significant concentration changes, the bulk concentration can be derived from the differential equation shown in equation 5.16, where the derivative of T_2 concentration with respect to normalized axial position, z, depends on the linear tritium generation rate, G', and the flux of tritium to pebbles. The term $k_{T2}A_{node}/\dot{V}$ is substituted with the character λ for simplicity. Integrating with the boundary condition that T_2 concentration initially is equal to the previous node concentration ($T_2(z=0) = T_2^N$), the T_2 concentration between concentration nodes can be determined with equation 5.17. The bulk concentration across the node is shown in equation 5.18, which is produced by solving for the average of $T_2(z)$ from the beginning to the end of the node, z=0 to z=1.

Eq. 5.16 $$\frac{dT_2(z)}{dz} = \left(G'(z)/\dot{V} - \lambda\left(T_2(z) - T_{2,Surf}\right)\right) : \lambda = k_{T_2} A_{node}/\dot{V}$$

Eq. 5.17 $$T_2(z) = T_2^N exp(-\lambda z) + \left(\frac{G_{T_2,N}}{\dot{V}\lambda} + T_{2,Surf}\right)\left(1 - exp(-\lambda z)\right)$$

Eq. 5.18 $$T_{2,Bulk} = \left(\frac{G_{T_2,\mathrm{N}}}{\dot{V}\lambda^2} - \frac{\left(T_2^N - T_{2,Surf}\right)}{\lambda}\right)\exp(-\lambda) + \frac{1}{\lambda}\left(T_2^N - T_{2,Surf} + \frac{G_{T_2,N}}{\dot{V}}\right) - \frac{G_{T_2,N}}{\dot{V}\lambda^2} + T_{2,Surf}$$

The purpose of equation 5.18 is to calculate an average T_2 concentration in the salt between the concentration nodes in order to produce a more representative value for the flux of T_2. However, equation 5.18 also depends on the concentration of T_2 at the graphite surface, which in turn depends on the additional tritium retention during the calculation step caused by the flux of T_2 to pebbles. Even if an average of T_2^N and T_2^{N+1} is used to calculate the T_2 bulk concentration in place of equation 5.18, the calculation of T_2^{N+1} requires the flux of T_2 to be known. Therefore, a system of equations must be solved simultaneously, which is carried out in TRIDENT Mod1 using the fsolve function in Matlab [3]. The function uses a non-linear solver to minimize the error in the solution of the set of three equations shown in equation 5.19 by iterating on the three variables shown in bold: j_{T2}, $T_{2,Surf}$, and $T_{2,Bulk}$. Concentration of diffusing tritium at the outer surface of the pebble is not known initially, but can be calculated using the current iteration value of j_{T2} using the graphite retention methodology described in Section 4. Similarly, the T_2^{N+1} is calculated at every iteration using equation 5.15. Once the three variables are determined, TRIDENT Mod1 then begins the same calculation for the next axial position, and T_2^{N+1} becomes T_2^N.

Eq. 5.19 $$\begin{bmatrix} \boldsymbol{j_{T_2}} = k_{T_2,Core}\left(\boldsymbol{T_{2,Bulk}} - \boldsymbol{T_{2,Surf}}\right) \\ \boldsymbol{T_{2,Surf}}/K_{H,T_2} = \left(T_d^{Rp}/K_{S,g}\right)^2 \\ \boldsymbol{T_{2,Bulk}} = (T_2^N + T_2^{N+1})/2 \end{bmatrix}$$

There are a few important differences in the previous equations if the pore and grain diffusion model is used to solve for tritium retention in graphite instead of the bulk diffusivity model. Because the methodology assumes that tritium retention in graphite first occurs by diffusion into graphite pores, the full area of the pebbles in not considered when calculating the total loss of tritium by the retention flux. Instead, the total surface area of pebbles in the node is scaled down by the porosity, φ, to calculate tritium flux only into the porous regions of the graphite. The resulting tritium balance for the pore and grain retention model for core concentration nodes

is then shown by equation 5.20. Since T_2 flux into graphite is only assumed to take place in pores, the boundary condition at the salt-graphite interface is then set by the concentration of tritium in pores at the pebble surface, $T_{2,p}^{Rp}$, instead of the diffusing tritium concentration. Therefore, the boundary condition becomes a combination between Henry's law for the salt and the ideal gas law for T_2 in the pores, as shown in equation 5.21. In both the pore and grain model and the bulk-diffusivity representation, the transport of tritium within graphite is important to solve because the concentration profiles create a surface boundary condition which determines how much tritium will be retained by graphite in the core.

Eq. 5.20
$$T_2^{N+1} = \left(T_2^N \dot{V}^N + G_{T_2,N} - j_{T_2} \phi A_{node}\right) / \dot{V}^{N+1}$$

Eq. 5.21
$$p_{T_2} = \frac{T_{2,Surf}}{K_{H,T_2}} = T_{2,p}^{Rp} \cdot RT$$

5.2.3. Graphite Pebble Recirculation and Desorption

Once tritium is retained in the graphite, it can be removed from the FHR through the pebble recirculation system either through desorption of existing pebbles or replacement with new pebbles. Since fuel pebbles are buoyant in Flibe, the fuel is introduced to the bottom of the FHR and extracted out of the top of the core [6]. Individual pebbles are not tracked in TRIDENT Mod1, and therefore an approximate method is required for representing the recirculation process within the single representative pebble modeled at each axial core subdivision.

A pebble recirculation process is approximated at each time step by moving and averaging a portion of the tritium concentration profiles from each axial subdivision into the above neighboring position. An example of the recirculation calculation for the diffusing tritium at axial position N (T_d^N) is shown in equations 5.22 and 5.23 below, where N_{Core}-1 is the number of axial subdivisions in the core, Δt is the simulation time step, and τ_{RT} is the residence time of pebbles in the core. A similar calculation is repeated for the trapped tritium in grains as well as T_2 in pores at each node. Since the number of pebbles in each axial division is $N_{Pebble}/(N_{Core}-1)$, and the number of pebbles leaving a node in each time step is $N_{Pebble}\Delta t/\tau_{RT}$, the fraction of pebbles leaving the node is $(N_{Core}-1)\Delta t/\tau_{RT}$. Therefore, the $(N_{Core}-1)\Delta t/\tau_{RT}$ term is used to calculate the fraction of circulating tritium in each time step. At the top of the core ($N=N_{Core}-1$ for the pebble positions), tritium is removed by recirculation to the bottom of the core and a portion of the pebbles are also moved to spent fuel storage. Therefore, the top node concentration profiles are decremented with an

additional time constant based on the pebble total lifetime, τ_{LT}, as shown in equation 5.24 for diffusing tritium in graphite grains. In the simulations presented in this work, a pebble residence time of 50 days is used along with a total lifetime of 500 days. The pebble lifetime was chosen to be similar to the Mk-1 FHR pebble full power lifetime of 1.4 years [6].

Eq. 5.22 $$T_d{}^N = T_d{}^N - (\mathrm{N_{Core}} - 1)(\Delta t/\tau_{RT})T_d{}^N$$

Eq. 5.23 $$T_d{}^{N+1} = T_d{}^{N+1} + (\mathrm{N_{Core}} - 1)(\Delta t/\tau_{RT})T_d{}^N$$

Eq. 5.24 $$T_d{}^{N_{\mathrm{Core}}-1} = T_d{}^{N_{\mathrm{Core}}-1}\left(1 - (\mathrm{N_{Core}} - 1)\frac{\Delta t}{\tau_{RT}}\right)\left(1 - (\mathrm{N_{Core}} - 1)\frac{\Delta t}{\tau_{LT}}\right)$$

The amount of tritium returning back to the core in the recirculation system depends on the fraction of tritium removed by desorption. Although a FHR design may or may not include a dedicated pebble desorption facility in the pebble recirculation system, the desorption process can be explored with the graphite retention model. At certain points in the TRIDENT Mod1 simulation, a desorption of a single pebble is modeled based on the concentration profiles in the top core position as the initial condition. The desorption is simulated with the grain-only transport model, in the same manner as the simulation of the Atsumi et al comparison shown in Section 4. A desorption factor is calculated separately for the diffusing and trapped tritium of each modeled grain inside of the pebble, as defined in equation 5.25 for diffusing tritium. Desorption options are either full desorption (DF=1), no desorption (DF=0), or a desorption calculation based on a specified temperature and duration. The returning diffusing tritium for the lowest axial core node (N=1) is shown in equation 5.26. The difference between the tritium leaving the top node and the tritium returning to the core is the total removed in the pebble recirculation system. Note that tritium decay is currently not simulated in the model for tritium retained in graphite, which would have a small impact on the full desorption calculations, but would be notable for the zero desorption treatment with pebble removal the 500 day cycle. For example, a pebble with a given tritium inventory would experience 0.768% tritium decay over 50 days and 7.42% over 500 days. The decay of tritium into helium would have the effect of freeing tritium trapping sites and allowing additional retention to occur.

Eq. 5.25 $$DF_d = \left(\int T_{d,Initial}dV_G - \int T_{d,Final}dV_G\right) / \int T_{d,Initial}dV_G$$

Eq. 5.26 $$T_d{}^1 = T_d{}^1 + T_d{}^{N_{\mathrm{Core}}-1}\left(1 - (\mathrm{N_{Core}} - 1)\frac{\Delta t}{\tau_{LT}}\right)\cdot(1 - DF_d)(\mathrm{N_{Core}} - 1)\frac{\Delta t}{\tau_{RT}}$$

5.2.4. Tritium Evolution to Reactor Cover Gas

After the core simulation, evolution is calculated at a single node in between the core and hot leg regions in TRIDENT Mod1. The purpose of the node is to simulate the process of tritium transfer from the salt phase to the gas plenum above the core inside of the reactor vessel. Other evolution processes could also exist in FHR designs beyond the reactor vessel region. For instance, if a gas space is present in the primary salt pumping system, and a sweep gas is purged through the pump gas volume, then tritium evolution to the pump system sweep gas would occur. Evolution into the pump bowl off-gas was the largest single source of tritium release measured in the MSRE [38], potentially because the pump was designed with a special spray ring to aid with stripping of fission product gases [90]. Because detailed designs of pump components for FHRs are not yet openly available, tritium evolution from the primary pumping system is not modeled.

Based on experimental observations [44], both TF and T_2 are expected to evolve from the salt to gas. The evolution rate of T_2 in mol/s is calculated based on equation 5.27, where the concentration of T_2 at the core outlet is calculated based on the molar flow of T_2 at the final core node, N_{Core}, divided by the volumetric flow rate of Flibe at the outlet. Tritium concentration in the off-gas is neglected, based on the assumption at the primary system off-gas will be continuously purged through a tritium capture system. A salt-gas interfacial area of 5.75 m^2 is used in the calculation, which is slightly more than half of the total cross-sectional area based on the vessel inner diameter. An area less than the total vessel area is used to account for other components in the core which may extend above the salt fill level and reduce the surface area for evolution. For TF evolution in equation 5.28, the same evolution mass transfer coefficient as T_2 is used, but a scaling factor based on diffusivity ratio of TF and T_2 is applied since the limiting step in evolution is thought to be diffusion through Flibe [47]. The TF and T_2 diffusivities in Flibe for the scaling factor are taken from atomistic simulations [81], as TF and T_2 diffusivities from separate experiments can vary significantly.

Eq.5.27 $$T_2\ Evolution\ = k_{E,T_2} A\left(M_{T_2,N_{Core}}/\dot{V}_{N_{Core}}\right)$$

Eq.5.28 $$TF\ Evolution\ = \frac{D_{TF}}{D_{T_2}} k_{E,T_2} A\left(M_{TF,N_{Core}}/\dot{V}_{N_{Core}}\right)$$

The evolution mass transfer coefficient is based on the experimental measurements from static Flibe irradiations conducted by Suzuki et al [48]. Applying the mass transfer coefficient to evolution in a FHR relies on the assumption that there will be similar mass transport characteristics

between the static irradiation experiment and the FHR salt-gas interface. The applicability of the static-salt mass transfer coefficient depends on the reactor core and vessel design parameters, which makes the true evolution coefficient in the FHR difficult to predict without a detailed design. Because the salt flow from the core outlet to the hot leg could potentially influence the mass transfer occurring at the salt free surface, the evolution rates predicted based on the static-salt mass transfer coefficient should be considered a lower estimate.

5.2.5. Tritium Permeation in the Hot Leg, Heat Exchanger, and Cold Leg

In the TRIDENT Mod1 FHR layout, the salt flows through the hot leg, heat exchanger, and cold leg after passing through the off-gas plenum and core coolant outlet. Outside of the core there is no tritium generation, but tritium loss still occurs by permeation of T_2 through the primary system. As with tritium retention in graphite, the permeation rate through structural metals depends on the rate of T_2 mass transfer in the salt which is calculated from the Sherwood number in the region. The hot leg, heat exchanger, and cold leg use a similar calculation methodology since the only tritium release path in each region is tritium permeation. However, the mass transfer in each region varies significantly because of the different cross sections of pipe flow. The Reynolds and Schmidt numbers for each region, which are used as inputs to calculate the Sherwood number, are shown below in Table 5.6. Inlet and outlet values for the heat exchanger are shown in order to display the range which occurs in the region due to the change in temperature. In contrast, the dimensionless numbers for mass transfer are constant in the hot leg and cold leg since they are assumed to be isothermal zones.

Table 5.6. Reynolds and Sherwood numbers used for permeation calculations in the hot leg, heat exchanger, and cold leg.

Region	Re	Sc
Hot Leg	$3.36 \cdot 10^5$	$8.83 \cdot 10^2$
Heat Exchanger (Inlet)	$1.38 \cdot 10^3$	$8.83 \cdot 10^2$
Heat Exchanger (Outlet)	$8.87 \cdot 10^2$	$2.75 \cdot 10^3$
Cold Leg	$2.05 \cdot 10^5$	$2.75 \cdot 10^3$

For the hot leg and cold leg, two experimental Sherwood number correlations for turbulent flow in pipes are shown in equations 5.29 and 5.30 [85, 183]. Based on the values in Table 5.6, both correlations have a range of applicability which includes the variation of Schmidt numbers in Flibe between 550ºC and 650ºC. Conversely, the Reynolds numbers in the hot leg and cold leg

each exceed the upper applicability bounds in equations 5.29 and 5.30. The Chilton-Colburn analogy could be used to produce a Sherwood number valid over a larger Reynolds number range. However, the analogy is noted to produce results about 20% lower than experimental measurements over the Reynolds number range of $3 \cdot 10^4$ to 10^6 [85]. Since permeation is generally considered undesirable, the experimental correlations are used to provide a conservative prediction for release from the reactor. Among the two options presented, equation 5.29 has a Reynolds number range closer to the hot leg and cold leg values and is therefore used in baseline simulations.

Eq. 5.29 $$Sh = 0.0096 Re^{0.913} Sc^{0.346} \qquad 10^4 < Re < 10^5 \ : \ 430 < Sc < 100{,}000$$

Eq. 5.30 $$Sh = 0.023 Re^{0.83} Sc^{1/3} \qquad 2{,}100 < Re < 35{,}000 \ : \ 0.6 < Sc < 3{,}000$$

In the heat exchanger, the Schmidt numbers are in between the values of the hot leg and cold leg, but the Reynolds numbers are significantly lower since there is a total cross-sectional flow area of 17.97 m^2 in the heat exchanger tubes compared to only 0.22 m^2 in the hot or cold leg piping. For internal flows with Reynolds number less than 2100, a Sherwood number with a constant value of 4.36 can be used [85, 184]. Using equation 5.30, the Sherwood number at 600ºC in the heat exchanger would be 8.95, although the Reynolds number falls below the lower limit of applicability for the correlation. An alternate correlation for mass transfer at low Reynolds numbers is shown in equation 5.31 [85], which varies based on Reynolds and Schmidt numbers and also depends on the ratio of tube diameter to tube length (d/L). The heat exchanger Sherwood number at 600ºC calculated with equation 5.31 is 18.1. The highest of the three is again used in TRIDENT Mod1 for conservative predictions of tritium permeation. Additionally, if elliptical twisted tube heat exchangers are used in a FHR [20], then the mass transfer may be more significant than for standard straight tube banks, and using a higher Sherwood number could be more representative of the true mass transfer rates.

Eq. 5.31 $$Sh = 4.36 + \frac{0.023(d/L)ReSc}{1 + 0.0012(d/L)ReSc} \qquad Re < 2{,}100$$

Once the Sherwood number is calculated, a mass transfer coefficient can be produced for the region to represent the movement of T_2 from the bulk of the salt to the inner surfaces of the metal walls. An example mass transfer coefficient calculation for the heat exchanger is shown in equation 5.32, where the characteristic length is the heat exchanger tube inner diameter, d_{tube}. The

mass transfer coefficient is converted into a flux in a similar manner to other regions, as shown in equation 5.33. As with graphite in the core, the boundary condition for metallic regions is created by assuming the Flibe and metal are exposed to the same partial pressure of T_2 at the interface [181], and then relating concentration in each phase with the Henry's law coefficient in the salt and the Sievert's law solubility for 316 stainless steel as in equation 5.34. The bulk concentration of T_2 across the node can be solved using the previous formulation in equation 5.18, but with tritium generation set to zero as shown in equation 5.35. While the surface boundary condition for graphite is solved with a non-linear solver, there is less of a need to iterate on the boundary condition for metallic components since changes in T_2 flux from the salt result in only small changes in the surface concentrations calculated by equation 5.34. Thus, the set of equations below is solved explicitly using the T_2 salt surface concentration from the previous time step. The surface boundary condition for typical structural metals is less influential than for graphite because the tritium diffusivity in metals is much higher. For example, the diffusivity of tritium in 316 stainless steel at 600ºC is $5.04 \cdot 10^{-10}$ m^2/s [91], while the bulk-diffusivity in POCO AXF-5Q1 graphite was $3.65 \cdot 10^{-15}$ m^2/s as determined in Section 4. Therefore, diffusion away from the surface is typically rapid enough that the inner metal surface concentration does not lead to a high T_2 concentration at the salt surface. When the salt T_2 surface concentration is low, the overall permeation resistance of the metal is negligible and the main limitation for permeation is only mass transfer in the salt phase.

Eq. 5.32 $$k_{T_2,HX} = ShD_{T_2}/d_{tube}$$

Eq. 5.33 $$j_{T_2} = k_{T_2,HX}\left(T_{2,Bulk} - T_{2,Surf}\right)$$

Eq. 5.34 $$p_{T_2} = T_{2,Surf}/K_{H,T_2} = \left(T^i_{HX}/K_{S,316}\right)^2$$

Eq. 5.35 $$T_{2,Bulk} = \frac{1}{\lambda}\left(T_2^N - T_{2,Surf}\right)(1 - \exp(-\lambda)) - T_{2,Surf}$$

The faster diffusion of tritium in metals compared to graphite also requires a different approach for the numerical solution in TRIDENT Mod1. A second order centered time centered space scheme is used as shown in equation 5.36. The scheme is also known as the Crank-Nicolson method, and is inherently stable for all time step values [185]. In contrast, the maximum time step before which the forward time centered space (FTCS) scheme would become unstable is determined by $\Delta x^2/2D$ [185], or 62 seconds for 6 evenly spaced mesh points in the heat exchanger.

In the simulations in this study, time steps near 1000 seconds were typically used. While the Crank-Nicolson scheme remains stable at time steps above the FTCS limit, using a significantly larger step decreases the accuracy in modeling the transient behavior of the solution. However, the time dependence of tritium diffusion in the heat exchanger is not important to resolve in TRIDENT Mod1 since the heat exchanger offers very little permeation resistance to the overall permeation process, and is therefore mainly decoupled from the rest of the simulation. In the other permeation zones, the stability conditions is less restrictive – the $\Delta x^2/2D$ condition results in a time step of 1085 seconds for 9 points in the hot leg and 18,900 seconds for 15 points in the reactor vessel.

Eq. 5.36

$$\begin{bmatrix} T_{HX}^{i} \\ T_{HX}^{i+1} \\ \cdots \\ T_{HX}^{o-1} \\ T_{HX}^{o} \end{bmatrix}^{t+\Delta t} = \begin{bmatrix} 1 & & & \\ -\frac{D\Delta t}{2\Delta x^2}\left(1+\frac{D\Delta t}{\Delta x^2}\right) & \cdots & -\frac{D\Delta t}{2\Delta x^2} & \\ & \cdots & \cdots & \cdots \\ & & -\frac{D\Delta t}{2\Delta x^2}\left(1+\frac{D\Delta t}{\Delta x^2}\right) & -\frac{D\Delta t}{2\Delta x^2} \\ & & & 1 \end{bmatrix}^{-1} \begin{bmatrix} 1 & & & \\ \frac{D\Delta t}{2\Delta x^2}\left(1-\frac{D\Delta t}{\Delta x^2}\right) & \cdots & \frac{D\Delta t}{2\Delta x^2} & \\ & \cdots & \cdots & \cdots \\ & & \frac{D\Delta t}{2\Delta x^2}\left(1-\frac{D\Delta t}{\Delta x^2}\right) & \frac{D\Delta t}{2\Delta x^2} \\ & & & 1 \end{bmatrix} \begin{bmatrix} T_{HX}^{i} \\ T_{HX}^{i+1} \\ \cdots \\ T_{HX}^{o-1} \\ T_{HX}^{o} \end{bmatrix}^{t}$$

Before the diffusion step, the flux-in boundary condition is applied by increasing the inner surface concentration as shown in equation 5.37. The heat exchanger is used as an example region and T_{HX}^{i-1} is tritium concentration in the metal at the point nearest to the point at the salt-metal interface, T_{HX}^{i}. In the case of zero recombination resistance and negligible downstream T_2 concentration, the tritium concentration at the outer metal surface, T_{HX}^{o}, would be equal to zero. To simulate recombination resistance, the outer surface concentration is increased and is set so that the diffusion flux in the metal towards the outer interface matches the recombination flux, as shown in equation 5.38. Solving the equation for the recombination-adjusted surface concentration, T_r, results in equation 5.39. In this case, the solution for T_r is approximate since it relies on the value of T_{HX}^{i-1} calculated by a diffusion step where the previous value of T_r was used. Once the concentration T_2 flux is calculated and the concentration profile in the metal is updated, the T_2 concentration at the next node can be calculated by equation 5.40. The overall permeation process using the previously described calculation steps is summarized in Figure 5.8.

Eq. 5.37

$$T_{HX}^{i} = T_{HX}^{i-1} + \frac{2j_{T2}\Delta x}{D_{T,316}}$$

Eq. 5.38
$$j_r = \frac{D_{T,316}}{\Delta x}\left(T_{HX}^{o-1} - T_r\right) = 2k_r T_r^2$$

Eq. 5.39
$$T_r = \frac{1}{4k_r}\left(-\frac{D_{T,316}}{\Delta x} + \sqrt{\left(\frac{D_{T,316}}{\Delta x}\right)^2 + \frac{D_{T,316}}{\Delta x} 8k_r T_{HX}^{i-1}}\right)$$

Eq. 5.40
$$T_2^{N+1} = \left(T_2^N \dot{V}^N - j_{T_2} A_{node}\right)/\dot{V}^{N+1}$$

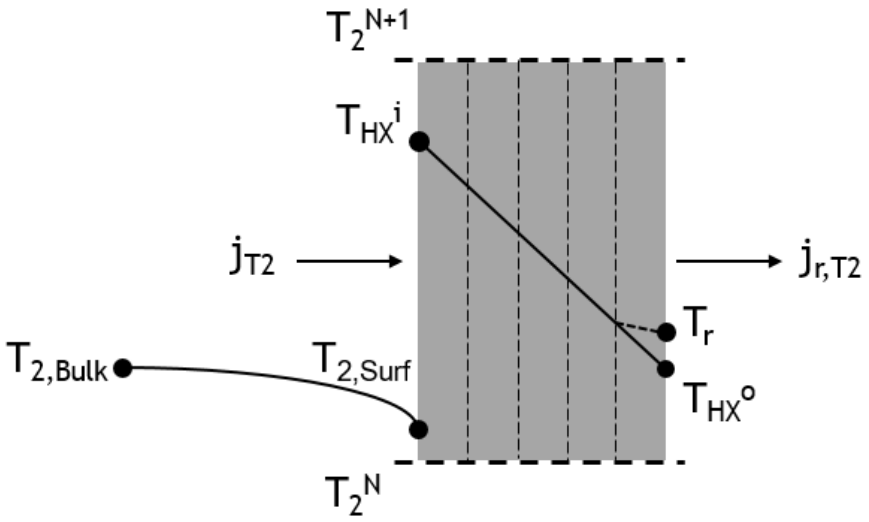

Figure 5.8. Conceptual illustration of the tritium permeation calculation for one node in the heat exchanger. Salt flow is shown moving upwards from node N to N+1.

Permeation barrier coatings in TRIDENT Mod1 can be simulated on inner, Flibe-facing surfaces or on outer surfaces. Coatings can also be applied globally or only onto specified regions. In all cases, the coated condition is implemented with the permeation reduction factor based on tritium fluxes. The PRF is a specified input and does not explicitly consider any characteristics of the coating material itself. Therefore, in a simulation with coatings applied, the PRF should be chosen based on experimental evidence of what material performance is achievable in the specified environment. In the simulation, a permeation step is first conducted in the same manner previously described for the uncoated metals. Then, the flux is reduced using the PRF to represent the coated sample. For coatings on the Flibe-facing surfaces, the coating-adjusted flux, $j_{T2,C}$, is calculated just by dividing the previously determined value of j_{T2} by the inner coating reduction factor, PRF_{in}, shown in equation 2.54. The outer coating reduction factor is implemented after the recombination calculation, thus the PRF_{out} value is applied to the previously calculated recombination flux of T_2,

$j_{r,T2}$. In order to reduce the flux at the outer boundary, the outer surface concentration (T_{HX}^{o} for the heat exchanger) is recalculated according to equation 5.42. As shown in the equation, for very large values of PRF_{out} the outer surface concentration matches the concentration at the neighboring node, T_{HX}^{o-1}, and the gradient across the boundary approaches zero. The inner and outer coating implementation is summarized conceptually in Figure 5.9.

Eq. 5.41
$$j_{T_2,C} = \frac{j_{T_2}}{PRF_{in}}$$

Eq. 5.42
$$T_{HX}^{o} = T_{HX}^{o-1} - \frac{2j_{r,T2}\Delta x}{PRF_{out}D_{T,316}}$$

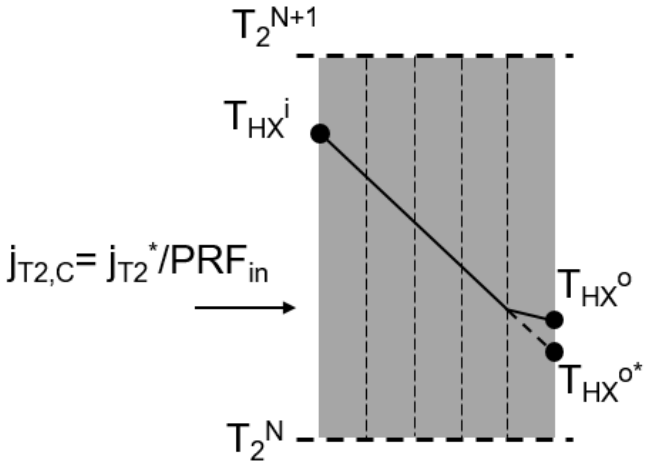

Figure 5.9. Adjustments to the permeation calculation to simulate coatings. Inner surface flux is divided by the specified PRF_{in} value. The outer surface concentration is increased to reduce the outward flux by a factor of PRF_{out}. T_{HX}^{o}* and j_{T2}* refer to values calculated for the uncoated condition.

5.2.5. Retention and Permeation in the Downcomer Region

The last region in the reactor flow path before the salt returns to the core inlet is the reactor downcomer. In the downcomer, the salt is in contact with graphite from the reflector as well as the structural metal of the reactor pressure vessel. Therefore, the downcomer will undergo tritium retention in a similar mechanism to that of the core pebbles as well as permeation through the reactor vessel. In the one-dimensional TRIDENT Mod1 representation, the downcomer is modeled as an annular flow region with the reflector as the inner diameter and the vessel as the outer layer. Because the downcomer region has a flow with a Reynolds number of 20,700 and Schmidt number of 2,750, the Sherwood number correlations in equation 5.29 and 5.30 both have a valid range of

applicability. However, the correlation from equation 5.29 is used to provide consistency with the hot leg and cold leg regions. The characteristic length for the Reynolds number is the downcomer annulus hydraulic diameter, as calculated by equation 5.43, where d_{RPV} is the inner diameter of the reactor pressure vessel and d_{DC} is the outer diameter of the core graphite reflector. The mass transfer coefficient for the downcomer also uses the hydraulic diameter. Both the reflector and vessel are modeled with the same mass transfer coefficient, which is shown in equation 5.44.

Eq. 5.43 $$d_H = d_{RPV} - d_{DC}$$

Eq. 5.44 $$k_{DC,T_2} = ShD_{T2}/d_H$$

Tritium retention in the reflector graphite is modeled with the same transport and trapping equations as the pebbles in the reactor core. However, characteristics of the downcomer region are generally unfavorable for tritium retention. First, the temperature is considered to be the temperature of the heat exchanger outlet and thus the lowest in the loop, which slows both the diffusion into graphite and the transition of diffusing tritium to high energy trapping sites. Also, the flow of salt will typically be more turbulent than in the core and the reflector will see a higher flux of tritium for a given tritium concentration. Both of these factors lead to a high tritium concentration at the graphite surface of the reflector which then limits tritium uptake according to the salt-graphite boundary condition. Therefore, TRIDENT Mod1 does not currently mesh the entire reflector graphite in order to reduce the matrix size for the diffusion equation solution, but only focuses on the surface region instead. Neglecting the deep regions in the reflector is justifiable since interior mesh points typically have a negligible tritium concentration in TRIDENT Mod1 simulations of multiple reactor years.

To model retention in the reflector graphite, the nonlinear solver is again used as with the core pebbles. However, additional equations must be merged into the solution matrix since the tritium concentration available for retention also depends on the amount of permeation occurring through the vessel. The solution matrix in the downcomer consists of five total equations, as shown in equation 5.45, with the five unknown variables in bold. Both the downcomer reflector and the reactor vessel have an equation that relates the flux of T_2 towards each surface to the mass transfer coefficient times the concentration gradient (rows 1 and 3). Similarly, there are two equations that relate the tritium concentrations at each interface based on solubility relations in each material (rows 2 and 4). Lastly, the average tritium concentration across the node is solved for based on the

average of the previous and next node tritium concentrations (row 5). The T_2 concentration at the next node, T_2^{N+1}, is determined based on the current iteration values for the flux of T_2 to the reflector and vessel as in equation 5.46, where the areas of the reflector and reactor vessel per node (A_{Refl} and A_{RPV}) are used to calculate total tritium losses. An illustration of the calculation process for one node in the downcomer is pictured in Figure 5.10.

Eq. 5.45

$$\begin{bmatrix} \boldsymbol{j_{DC,T_2}} = k_{DC,T_2}\left(\boldsymbol{T_{2,Bulk}} - \boldsymbol{T_{2,DC,Surf}}\right) \\ \boldsymbol{T_{2,DC,Surf}}/K_{H,T_2} = \left(T_d^{Rp}/K_{S,g}\right)^2 \\ \boldsymbol{j_{RPV,T_2}} = k_{DC,T_2}\left(\boldsymbol{T_{2,Bulk}} - \boldsymbol{T_{2,RPV,Surf}}\right) \\ \boldsymbol{T_{2,RPV,Surf}}/K_{H,T_2} = \left(T_{RPV}^{i}/K_{S,316}\right)^2 \\ \boldsymbol{T_{2,Bulk}} = (T_2^N + T_2^{N+1})/2 \end{bmatrix}$$

Eq. 5.46

$$T_2^{N+1} = \left(T_2^N \dot{V}^N - j_{DC,T_2}A_{Refl} - j_{T_2}A_{RPV}\right)/\dot{V}^{N+1}$$

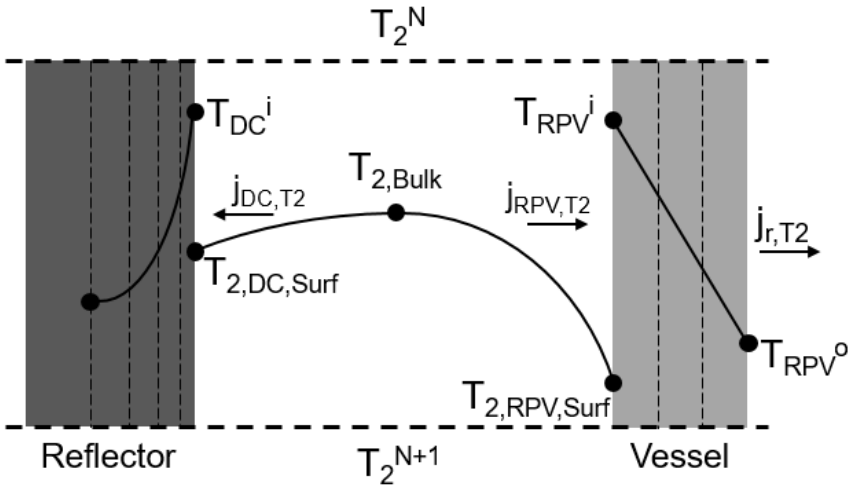

Figure 5.10. Notation for tritium flows in one node of the downcomer region. Salt flow is shown moving downwards from node N to N+1.

5.3. Tritium Distribution Results under Baseline Conditions

The system requirements and optimal strategies for tritium management in a FHR first depend on the baseline distribution of tritium in the reactor. Several simulations are presented in this section to describe the tritium release paths when no tritium management strategies are imposed. Key features of the results are examined in order to explain the calculated distribution in terms of the fundamental tritium transport behavior.

5.3.1. Summary of Input Parameters and Conditions

While some parameters have been previously stated, the full set of inputs into the TRIDENT Mod1 code are presented in this section to provide a complete overview of the calculation process. The reactor operating parameters shown in Table 5.7 have a notable influence on several other inputs in the model. For example, tritium diffusivities, tritium solubilities, and salt thermophysical properties all have a temperature dependence, and the range each parameter in the simulation depends on the core inlet and outlet temperature. The mass flow rate of salt is also calculated from the core temperature change, $T_{out} - T_{in}$, reactor thermal power, $\dot{Q}$, and Flibe specific heat capacity, c_p, as shown in equation 5.47 [3]. The redox potential is also shown in Table 5.7, which is selected to represent Flibe which has been fully reduced by beryllium metal [54]. Therefore, the baseline tritium distribution mainly focuses on the tritium distribution of T_2 in the reactor, since very little TF is present at an equilibrium condition of -902.5 kJ/mol.

Table 5.7. Reactor operation parameters used for the TRIDENT Mod1 baseline simulations.

Parameter	Value
Core inlet temperature [K]	823.15
Core outlet temperature [K]	923.15
Reactor power [MWth]	320
Pebble residence time in-core [day]	50
Pebble lifetime [day]	500
Redox Potential [kJ/mol]	-902.5

Eq. 5.47
$$\dot{Q} = \dot{m} c_p (T_{out} - T_{in})$$

The tritium production parameters shown in Table 5.8 were originally calculated for the Mk-1 FHR design [178]. To represent a 320 MWth FHR, the neutron flux is scaled by the ratio of thermal powers, where the Mk-1 FHR was designed for 236 MWth [8]. The parameters in Table 5.8 can be used to determine the tritium production as a function of time caused by changes in the salt lithium-6 concentration, but the equilibrium generation rate is used in the baseline analysis for simplicity.

Table 5.8. Tritium production parameters. From [178].

Parameter	Value
1-group Flux [n/cm^2-s]	(320/236)*3.41e14
Lithium-7 tritium production x-section [m^2]	1e-27
Lithium-6 tritium production x-section [m^2]	148.026e-24
Lithium-6 total absorption x-section [m^2]	148.032e-24
Beryllium-9 n,α x-section [m^2]	3.63e-27

Thermophysical properties of Flibe along with tritium transport properties are compiled in Table 5.9. The thermophysical properties were selected based on the recommendations in literature reviews [179]. For the tritium transport properties, a smaller set of data is available from previous studies and the selection of each property depends on which experimental data source should be considered the most reliable. For example, the T_2 diffusivity in Flibe was taken from the Calderoni et al experiment [75], since their measured diffusivity is nearest to the diffusivity calculated from recent atomistic simulations [81]. The T_2/H_2 solubility measurements in Flibe generally fall into two groups, some relatively low measurements and other measurements which are several orders of magnitude higher. A solubility measurement from Malinauskas et al is used since it was a direct measurement of H_2 solubility in Flibe [82], whereas other measurements were observed indirectly from permeation experiments [75, 78].

Table 5.9. Temperature dependent properties. All temperatures, T, are in Kelvin and the universal gas constant, R, is in units of kJ/mol-K.

Parameter	Symbol	Value	Ref.
Flibe density [kg/m^3]	ρ	2415.6-0.49072T	[179]
Flibe viscosity [Pa-s]	μ	1.116e-4exp(3755/T)	[179]
Flibe heat capacity [J/kg-K]	c_p	2386	[179]
T_2 diffusivity in Flibe [m^2/s]	D_{T2}	9.3e-7exp(-42/RT)	[74]
TF diffusivity in Flibe [m^2/s]	D_{TF}	6.4854e-26(T)^5.7227	[80]
Henry's law coefficient for T_2 in Flibe [mol/m^3-Pa]	$K_{H,T2}$	2.714e-8exp(4.235e-3(T-273.15))	[3, 82]
Henry's law coefficient for TF in Flibe [mol/m^3-Pa]	$K_{H,TF}$	1.707e-3 exp(-4.26e-3(T-273.15))	[3, 72]
T diffusivity in 316SS [m^2/s]	$D_{T,316}$	sqrt(1/3)6.32e-7exp(-47.8/RT)	[91]
Sievert's law coefficient for T in 316SS [mol/m^3-Pa$^{1/2}$]	$K_{S,316}$	0.427exp(-13.9/RT)	[91]
[1]Hydrogen recombination rate constant for 316SS (lower bound) [m^4/mol-s]	k_r	1.19e-4exp(-49.8/RT)	[186]
[1]Hydrogen recombination rate constant for 316SS (upper bound) [m^4/mol-s]	k_r	1.31exp(-50.5/RT)	[186]
[1]T_2 evolution mass transfer coefficient [m/s]	$k_{E,T2}$	$2.0\cdot10^{-3}$exp(-34/RT)	[187]
[2]TF evolution mass transfer coefficient [m/s]	$k_{E,TF}$	$k_{E,T2}$(0.295exp(-4/RT))	[81]

[1]Estimated from figures, not explicitly reported in references
[2]Arrhenius term is the ratio of TF to T_2 diffusivity in atomistic simulations

Once the mass flow rate and thermophysical properties are calculated, the mass transport parameters can be determined through Sherwood number correlations. As shown in Table 5.10, the highest Sherwood numbers occur in the hot leg and cold leg, while the lowest value is present in the heat exchanger. The core has a significantly higher Sherwood number than the heat exchanger despite having a salt flow with similar Reynolds and Schmidt numbers. Ultimately the T_2 mass transfer coefficient is used as an input for determining tritium flux to surfaces, which is calculated by multiplying the Sherwood numbers in Table 5.10 by the diffusivity of T_2 and dividing by the characteristic length in each region.

Table 5.10. Reynolds numbers and Schmidt numbers in each region used to compute the Sherwood number correlations [85]. Sherwood numbers are then used to calculate the mass transfer coefficient for T_2.

Region	Re	Sc	Sh Correlation	Sh Value	k_{T2} [m/s]
Core Average	$1.25 \cdot 10^3$	$1.81 \cdot 10^3$	$(0.25/0.4)Re^{0.69}Sc^{1/3}$	$1.04 \cdot 10^3$	$7.43 \cdot 10^{-5}$
Hot Leg	$3.36 \cdot 10^5$	$8.83 \cdot 10^2$	$0.0096Re^{0.913}Sc^{0.346}$	$1.11 \cdot 10^4$	$1.16 \cdot 10^{-4}$
Heat Exchanger Average	$1.13 \cdot 10^3$	$1.81 \cdot 10^3$	$4.36+0.023(d/L)ReSc /(1+0.0012(d/L)ReSc)$	$1.81 \cdot 10^1$	$3.66 \cdot 10^{-6}$
Cold Leg	$2.05 \cdot 10^5$	$2.75 \cdot 10^3$	$0.0096Re^{0.913}Sc^{0.346}$	$1.05 \cdot 10^4$	$5.63 \cdot 10^{-5}$
Downcomer	$2.07 \cdot 10^4$	$2.75 \cdot 10^3$	$0.0096Re^{0.913}Sc^{0.346}$	$1.30 \cdot 10^3$	$2.90 \cdot 10^{-5}$

Lastly, there is another set of input parameters which are used for calculations of tritium retention in graphite, both in the core graphite pebbles and the reflector in the graphite. The pore and grain diffusion model is used as the standard methodology for the TRIDENT Mod1 baseline results. Input parameters in this case are identical to those presented for the comparison case study for POCO AXF-5Q graphite, as shown in Table 4.1. When the bulk diffusion model is used instead for retention calculations, the graphite-related transport parameters are shown in Table 5.11. The unreferenced parameters in Table 5.11 originate from the data fitting of experimental studies with POCO AXF-5Q graphite presented in Section 4.

Table 5.11. Tritium transport parameters for TRIDENT Mod1 calculations using the bulk-diffusion model to simulate tritium retention in graphite.

Parameter	Symbol	Value	Ref.
Bulk-diffusivity of tritium in graphite	$D_{T,Bulk}$	$0.417\exp(-235/RT)$ [m^2/s]	
Tritium solubility in graphite	$K_{S,g}$	$1.22 \cdot 10^{-4}$(P [Pa])exp(19/RT) [STP cc/g]	[126]
Concentration of high-energy trapping sites	C_t^0	2.6 [mol/m^3]	[127]
Trapping rate constant pre-exponential factor	Σ_{to}	$1.13 \cdot 10^9$ [s^{-1}]	
Trapping rate constant activation energy	E_t	270 kJ/mol	[108]
Detrapping attempt frequency	ν_0	$1 \cdot 10^{13}$ [s^{-1}]	[164]
Detrapping activation energy	E_d	437 [kJ/mol]	

5.3.2. Tritium Distribution with Baseline Conditions

The tritium distribution and release paths can be simulated with TRIDENT Mod1 using the previously described FHR reactor dimensions, operating conditions, and input parameters. Examining the tritium distribution first with all retention in graphite set to zero is useful for understanding the calculation process and results from the reactor loop outside of the core. When graphite is treated as a perfect tritium barrier, tritium will only be removed from the salt in the model by permeation through structural metals or evolution to the reactor off-gas. As shown in Figure 5.11, permeation through the heat exchanger is the largest source of tritium release, mainly because of the significantly higher surface area compared to other regions. The time dependence in permeation rates depends on the temperature of the region as well as the thickness of the metal. Since the vessel has the largest thickness at 5cm, compared to 1cm of the hot and cold leg piping and 1.25mm for the heat exchanger tubes, vessel permeation is the slowest to equilibrate. The downcomer is also modeled as an isothermal region at the minimum temperature in the loop, so the diffusivity of tritium in the 316 stainless steel of the vessel is lower than the average diffusivity in the heat exchanger tubes or the hot leg pipe. As the tritium concentration in the vessel builds up, the concentration at the salt side of the interface also increases according to the defined boundary condition. Therefore, the flux of tritium to the vessel surface gradually decreases over time, as shown on the right in Figure 5.11.

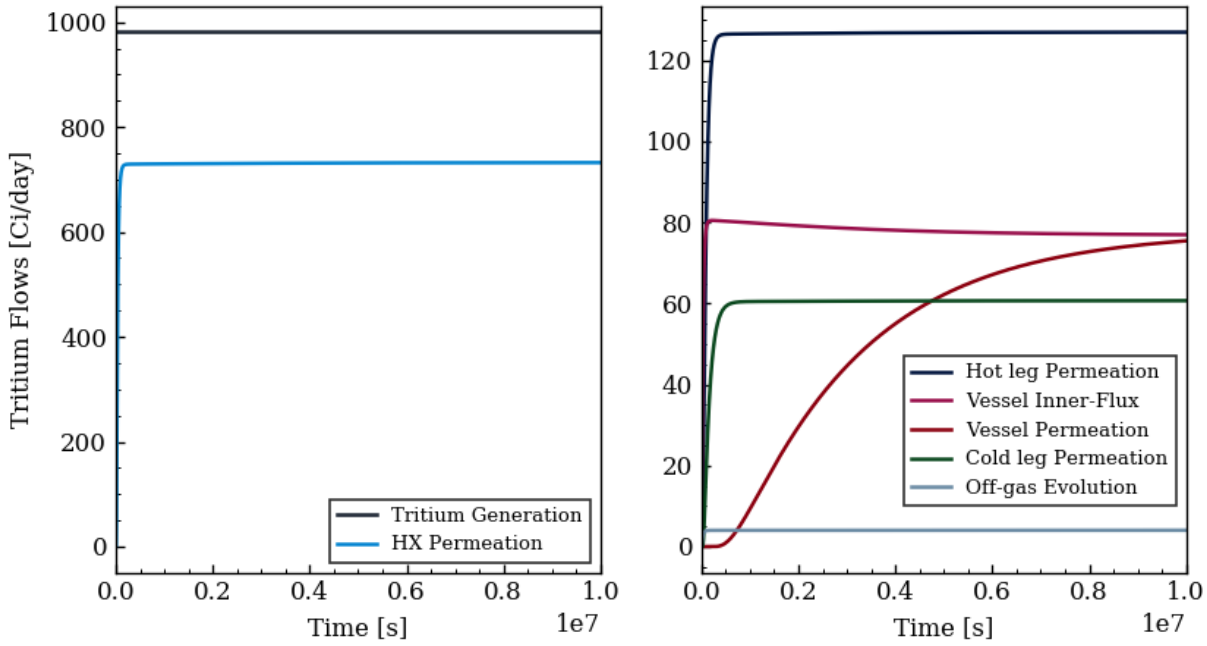

Figure 5.11. Tritium permeation and evolution rates through various regions of the modeled FHR with tritium retention in graphite set to zero. Permeation through the heat exchanger is the main release path for tritium.

The time required to reach an equilibrium tritium concentration in the salt is generally faster than the equilibration in permeation releases. An equilibrium tritium concentration in the salt occurs once the tritium generation rate matches the rate of tritium removal from the salt. For both tritium evolution and tritium permeation, the flux of tritium out of the salt depends on the tritium concentration. Therefore, the removal rate of tritium starts out low and grows over time as the tritium concentration in Flibe increases. Furthermore, the steady-state tritium concentration is not determined by the solubility of tritium in the salt, unless the solubility has a strong influence on the rate at which tritium transports out of the salt phase. In Figure 5.12, the concentrations of T_2 and TF over time are plotted from the beginning of the zero-retention simulation. As previously discussed, a fully-reduced redox potential of -902.5 kJ/mol was used in the baseline simulations, which explains why the TF concentration in Figure 5.12 is several orders of magnitude lower than that of T_2.

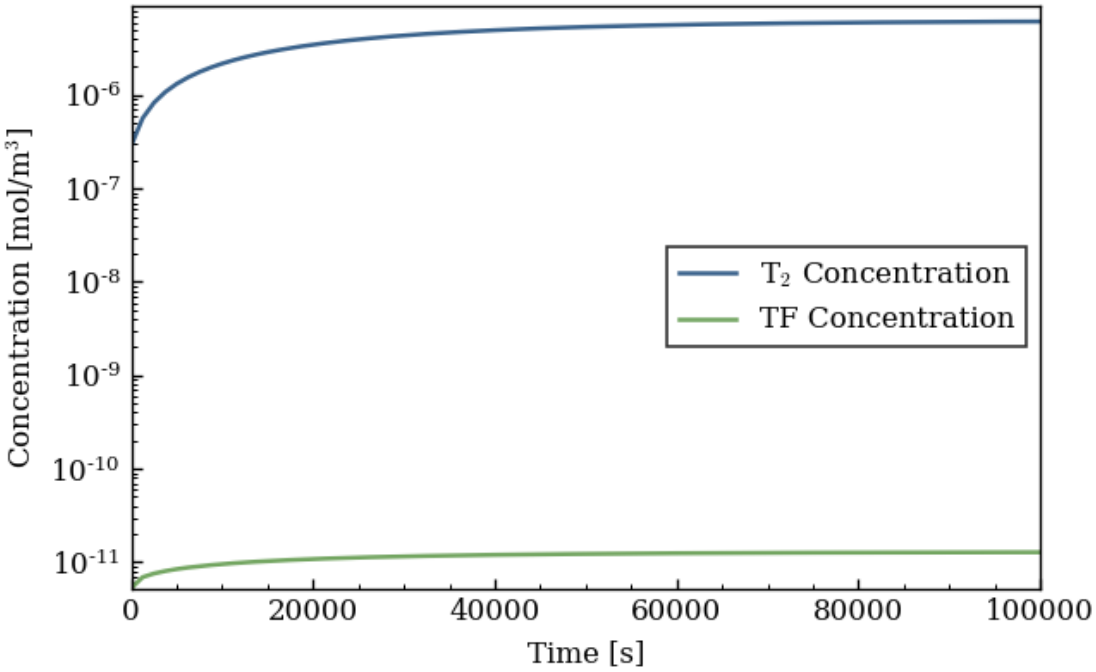

Figure 5.12. Concentration of T_2 and TF in Flibe from simulations with tritium retention in graphite neglected. At the fully beryllium-reduced redox potential, the concentration of TF is orders of magnitude below T_2.

The contribution of each tritium release path to the calculated total in Figure 5.11 is shown in the rightmost column of Table 5.12. One way to assess results from TRIDENT Mod1 is by comparing calculated release fractions to the product of the Flibe T_2 mass transfer coefficient and the total inner-surface area of each region. Assuming a constant tritium concentration in the salt and resistance to release caused only by mass transfer in the salt, the product of the mass transfer coefficient and area ($k_{T2}A$) compared to the sum of $k_{T2}A$ values would provide a general prediction for the contribution to total release from each reactor zone. As shown in Table 5.12, the release predictions based on the $k_{T2}A$ percentage of the reactor total in each region correlate well with the results from the TRIDENT Mod1 simulation in Figure 5.11. There are some differences between the predictions and TRIDENT Mod1 results in Table 5.12 which can be explained by small effects from permeation resistance. For example, the hot leg, cold leg, and vessel have a small, but higher permeation resistance than the heat exchanger, and thus their release values from TRIDENT Mod1 are below the $k_{T2}A$ predictions.

Table 5.12. Mass transfer coefficients for T_2 (k_{T2}) and Flibe-facing surface area of each reactor region with the core pebbles and graphite reflector neglected. The fraction of $k_{T2}A$ in each region corresponds with the percentage of total tritium release calculated by TRIDENT Mod1.

Region	k_{T2} [m/s]	Area [m^2]	$k_{T2}A$ Fraction	TRIDENT Result
Hot Leg	$1.16 \cdot 10^{-4}$	35.3	13.9%	12.3%
Heat Exchanger	$3.66 \cdot 10^{-6}$	5750	71.4%	74.0%
Cold Leg	$5.63 \cdot 10^{-5}$	35.3	6.7%	5.8%
Reactor Vessel	$2.90 \cdot 10^{-5}$	76.6	7.5%	7.4%
Off-gas	$2.38 \cdot 10^{-5}$	5.75	0.5%	0.4%

The product of the mass transfer coefficient times the surface area represents the total potential for tritium permeation at a given tritium concentration in the salt. When permeation resistance in the metal is significant, the concentration gradient in the salt decreases and the flux of T_2 to the metal surface is reduced. The consistency between model results and $k_{T2}A$ predictions in Table 5.12 suggests that resistance to the overall permeation process created by tritium diffusion through 316 stainless steel in a FHR is small compared to the mass transfer resistance in the salt itself. In an analytical analysis of a nickel permeation window system, it was also determined that permeation was mainly limited by mass transport of tritium in Flibe, rather than diffusion through the nickel tubes [188].

Permeation resistance from the metal can be quantified by comparing the T_2 concentration in Flibe at the metal interface to the T_2 concentration in the bulk salt. The metal surface concentrations in each region are plotted along with the bulk salt T_2 concentration in Figure 5.13. An average over each region results in a T_2 interface concentration of 3.68e-8, 6.30e-12, 3.88e-8, and 3.12e-7 mol-T_2/m^3 for the hot leg, heat exchanger, cold leg, and reactor vessel, respectively. The permeation resistance caused by the metal can be observed by dividing the average surface concentration by the bulk salt concentration, which was 6.30e-6 mol-T_2/m^3 in Figure 5.12. In this manner, the metal creates 4.95% resistance to permeation in the reactor vessel, 0.62% in the cold leg, 0.58% in the hot leg, and 1e-4% in the heat exchanger. Therefore, in all permeation zones in TRIDENT Mod1, the resistance to permeation caused by diffusion in the metal is not a major limitation in the overall permeation process for the baseline reactor conditions.

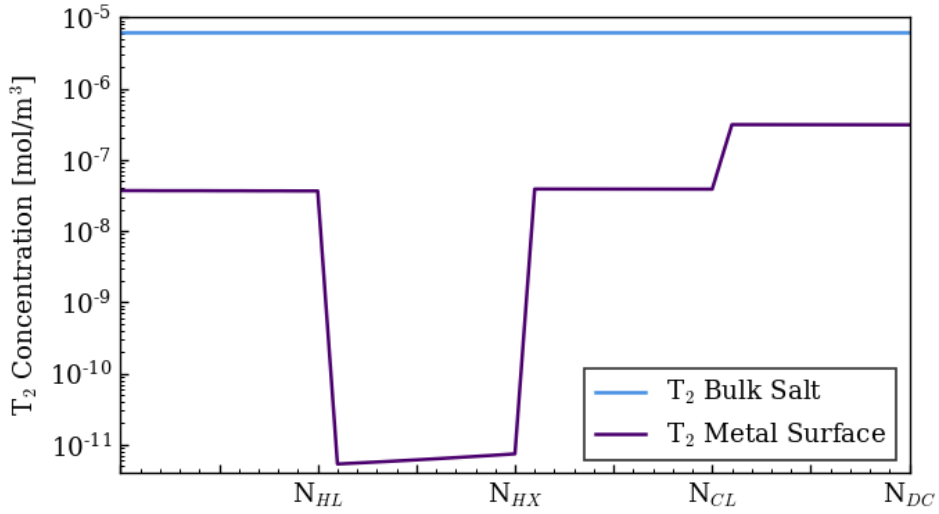

Figure 5.13. Comparison of T_2 bulk salt concentration compared to the T_2 salt-metal interface concentration in the hot leg, heat exchanger, cold leg, and reactor vessel.

When graphite in the FHR is treated as a perfect sink for tritium, instead of a perfect barrier, retention in graphite becomes the dominant mechanism of tritium removal from the salt. The mass transfer coefficient and surface area analysis is repeated in Table 5.13, but with the pebbles in the core and the graphite reflector included. While the heat exchanger has a larger surface area than the graphite in the core, the elevated mass transfer in the pebble bed results in the core having the largest total product of mass transfer coefficient times area, as shown in Table 5.13. The significant potential for tritium retention in graphite motivates the need for modeling tritium transport within graphite regions of the FHR. If tritium diffusion and trapping in graphite is a limiting factor in the overall retention process, then the total uptake in graphite would be significantly over predicted by a model which considers only limitations of mass transfer in flowing Flibe.

Table 5.13. Mass transfer coefficients and surface areas in various FHR regions. The $k_{T2}A$ in each region shows potential for tritium release when mass transfer in Flibe is rate-limiting.

Region	**k_{T2} [m/s]**	**Area [m^2]**	**$k_{T2}A$ [m^3/s]**	**$k_{T2}A$ Fraction**
Core Pebbles	$7.43 \cdot 10^{-5}$	1684	$1.25 \cdot 10^{-1}$	79.8%
Hot Leg	$1.16 \cdot 10^{-4}$	35.3	$4.09 \cdot 10^{-3}$	2.6%
Heat Exchanger	$3.66 \cdot 10^{-6}$	5750	$2.10 \cdot 10^{-2}$	13.4%
Cold Leg	$5.63 \cdot 10^{-5}$	35.3	$1.99 \cdot 10^{-3}$	1.3%
Reactor Vessel	$2.90 \cdot 10^{-5}$	76.6	$2.22 \cdot 10^{-3}$	1.4%
Graphite Reflector	$2.90 \cdot 10^{-5}$	74.7	$2.17 \cdot 10^{-3}$	1.4%
Off-gas	$2.38 \cdot 10^{-5}$	5.75	$1.37 \cdot 10^{-4}$	0.1%

When graphite interactions are added into the TRIDENT Mod1 simulation, tritium permeation through the heat exchanger decreases because a sizeable share of tritium becomes retained by pebbles in the core. Simulation results are plotted in Figure 5.14 for the heat exchanger permeation rate, graphite uptake rate, and removal rate through the pebble recirculation system assuming full desorption of pebbles with a 50 day core residence time along with addition removal of pebbles on a 500 day cycle. The transport of tritium inside the core and reflector graphite is modeled with the pore and grain diffusion method discussed in Section 4. Retention in the core pebbles also decreases the permeation rates through the hot leg, reactor vessel, and cold leg, which are plotted along with the reflector retention and off-gas evolution in Figure 5.15.

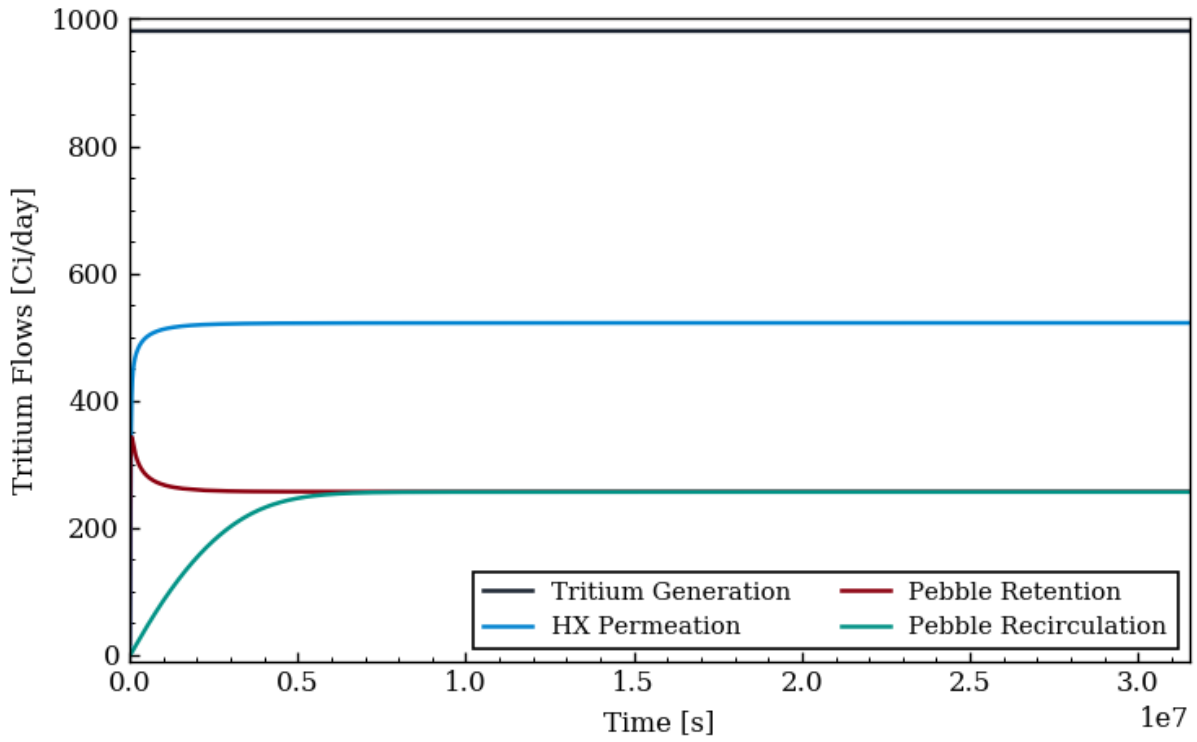

Figure 5.14. Tritium release through the heat exchanger and pebble recirculation system for a one year simulation calculated with the pore and grain diffusion methodology for graphite.

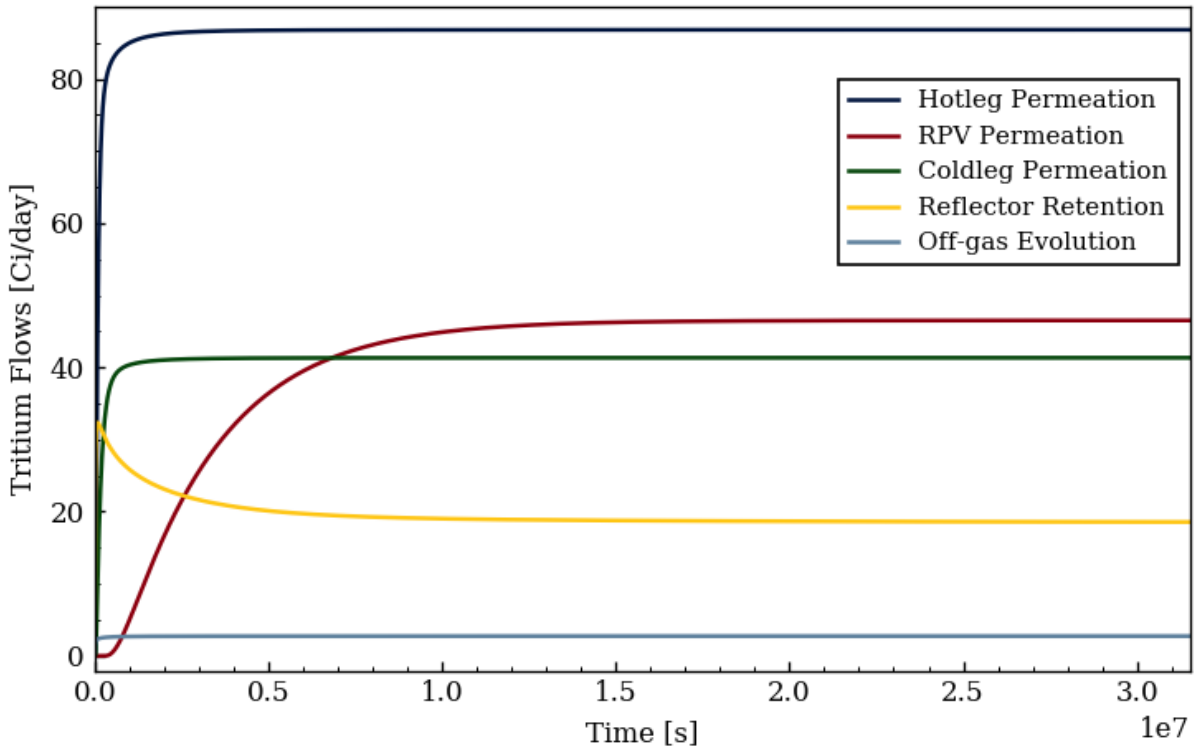

Figure 5.15. Baseline tritium distribution for remaining FHR regions with a lesser contribution to overall release.

As shown in Figure 5.14, tritium retention in the graphite pebbles begins at above 300 Curies per day at the start of the simulation then decreases to its equilibrium value, which is equal to the removal rate through the pebble recirculation system. The decrease in retention rate can be explained by the accumulation of tritium near the surface of the graphite, followed by a decrease in the flux to graphite pebbles as the T_2 surface boundary condition increases. The tritium retention rate also decreases over time in the graphite reflector as shown in Figure 5.15, although at a slower pace than the core pebbles. Since the reflector is not desorbed or replaced like the pebbles, the retention rate will eventually approach zero in longer simulations. The rate of tritium retention in core graphite pebbles shown in Figure 5.14 is clearly less than the 79.8% predicted by the $k_{T2}A$ values in Table 5.13. As a result, there must be a source of additional resistance in the retention process besides the mass transport from the bulk salt to the pebble surface. Comparing the T_2 bulk salt concentrations to the T_2 surface concentrations in each region can again be used to monitor the resistance to tritium uptake caused by the boundary condition in each material. As shown in Figure 5.16, the T_2 surface concentrations for graphite pebbles in the core and the downcomer

reflector are both noticeably higher than surface concentration of the metal regions. Dividing the average bulk T_2 concentration by the surface concentration results in 47% and 57% for the core and downcomer, respectively. Therefore, the flux of tritium into graphite in the FHR is significantly inhibited by the surface boundary condition, which increases during the simulation because of the buildup of tritium near the salt-facing surfaces in graphite materials.

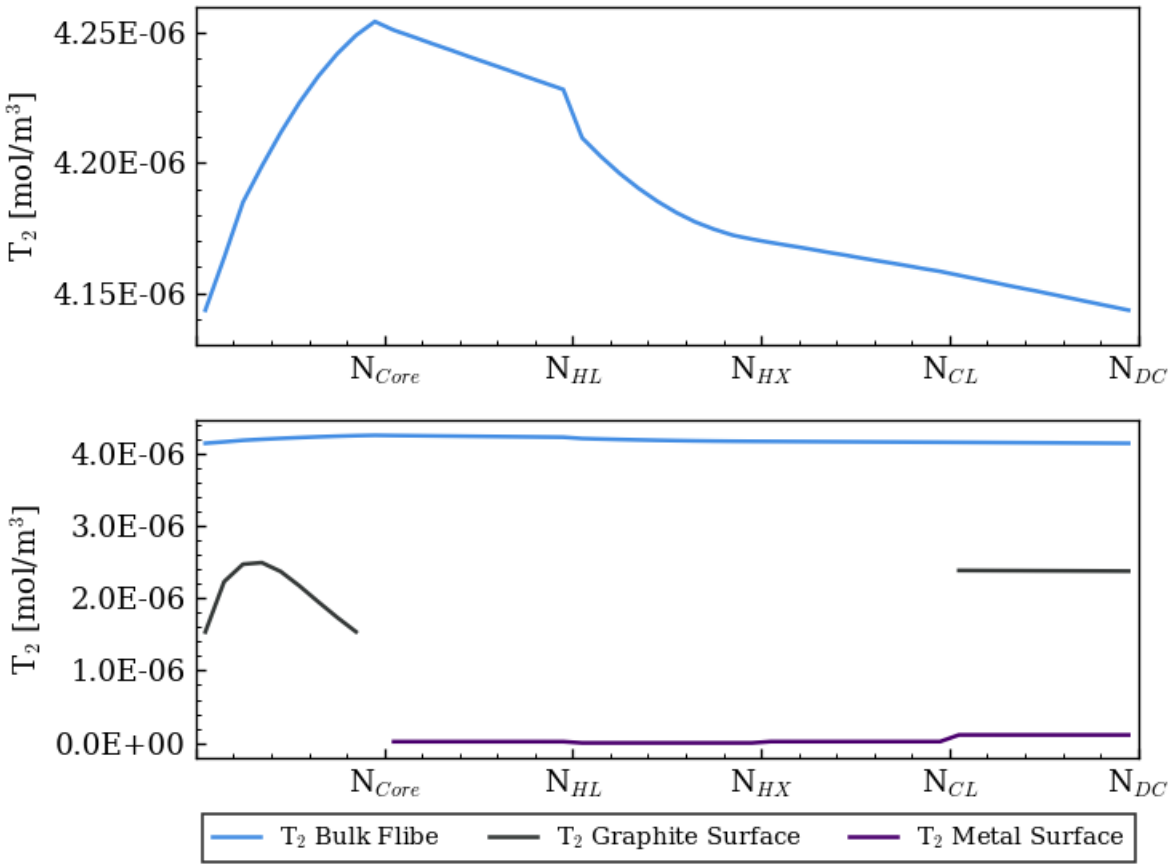

Figure 5.16. Flibe bulk T_2 concentration throughout the FHR primary loop (top). The salt T_2 surface concentrations are significantly higher for graphite materials in the core and downcomer compared to the structural metals (bottom).

Another notable observation from the Figure 5.16 concentrations is the change in graphite T_2 surface concentration throughout the nodes in the core. The T_2 pebble surface concentration starts out low at the first axial position in the core, reaches a maximum at the fourth node, and then begins decreasing from the fourth node up until the top of the core. Pebbles are modeled at evenly spaced axial positions in the core, and since a linear core temperature distribution is applied, the axial node number is directly proportional to the simulated temperature of each pebble.

Low surface concentrations near the core inlet are caused by several reasons. First, when salt temperatures are reduced, the corresponding T_2 surface boundary condition decreases as shown in equation 5.21 because the solubility of T_2 in Flibe increases [82]. Another reason for the initially low T_2 surface concentration is because the mass transfer coefficient in Flibe nearly doubles across the core because of increasing diffusivity with temperature – k_{T2} vaired from $5.10 \cdot 10^{-5}$ m/s at the core inlet to $9.19 \cdot 10^{-5}$ m/s at the outlet. Therefore, less tritium transfer occurs into the pebbles at the lower axial positions in the core. Calculated concentration profiles of T_2 diffusing in the pores of the graphite pebbles ($T_{2,p}$) are shown in Figure 5.17, where the $T_{2,p}$ pebble surface concentrations increase from the lowest core position (N=1) up until the third node. The third and fourth nodes have a similar $T_{2,p}$ surface value. However, because of temperature effects, the resulting T_2 salt surface concentration calculated with equation 5.21 is the highest for the fourth node.

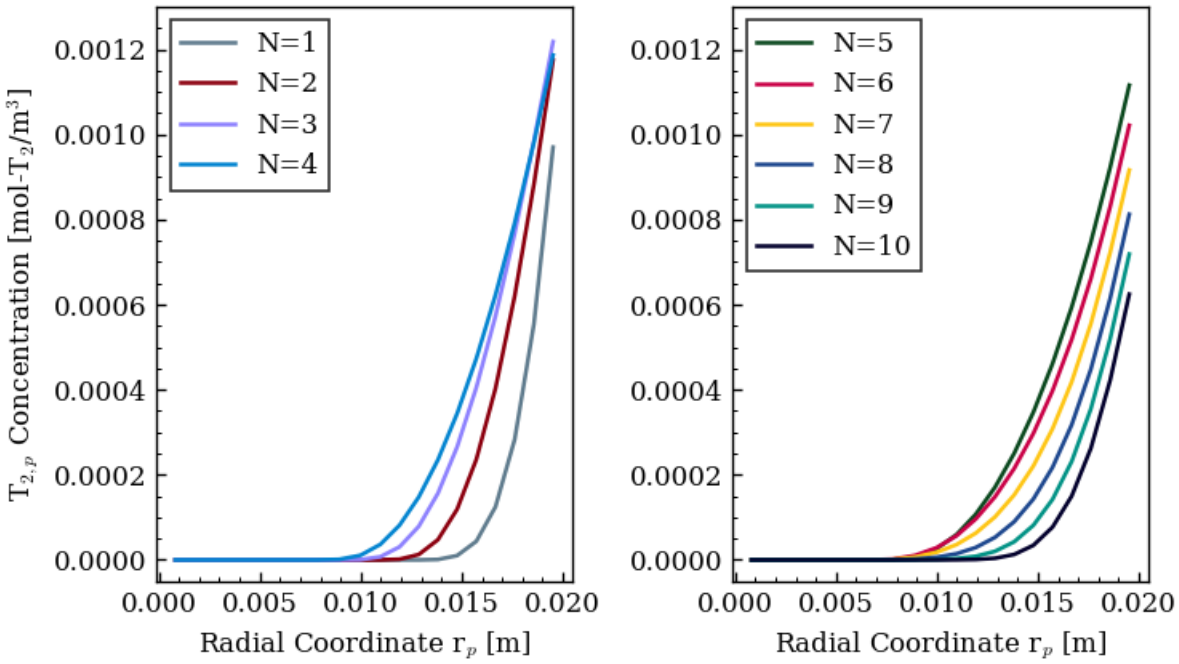

Figure 5.17. Pore tritium concentrations ($T_{2,p}$) as a function of radial position for the ten graphite pebbles modeled at axial subsections in the core. The $T_{2,p}$ concentration at the pebble surface is the largest at the third node, then concentrations decrease for the higher axial positions.

Concentration profiles for the tritium diffusing in graphite grains (T_d) also follow a similar trend among the axial positions in the core. As temperature increases, the tritium diffusivity in the graphite grains increases substantially, which allows for deeper penetration into the graphite bulk at higher axial nodes as shown in Figure 5.18. However, elevated temperature also increases the amount of diffusing tritium which transitions into high-energy trapping sites since the grain diffusivity and trapping rate constant are modeled with the same activation energy. The total amount of tritium in high-energy trapping sites increases at each axial position, as shown in Figure 5.19. For the upper nodes in the core, the trapped tritium concentration is roughly twice as large as the concentration of tritium diffusing in the grains. Therefore, the conversion of tritium into high-energy trapping sites has a significant role in decreasing the diffusing tritium concentration in grains and pores at higher temperature positions in the core, which ultimately explains the decreasing T_2 salt-graphite surface concentration after the mid-core nodes in Figure 5.16.

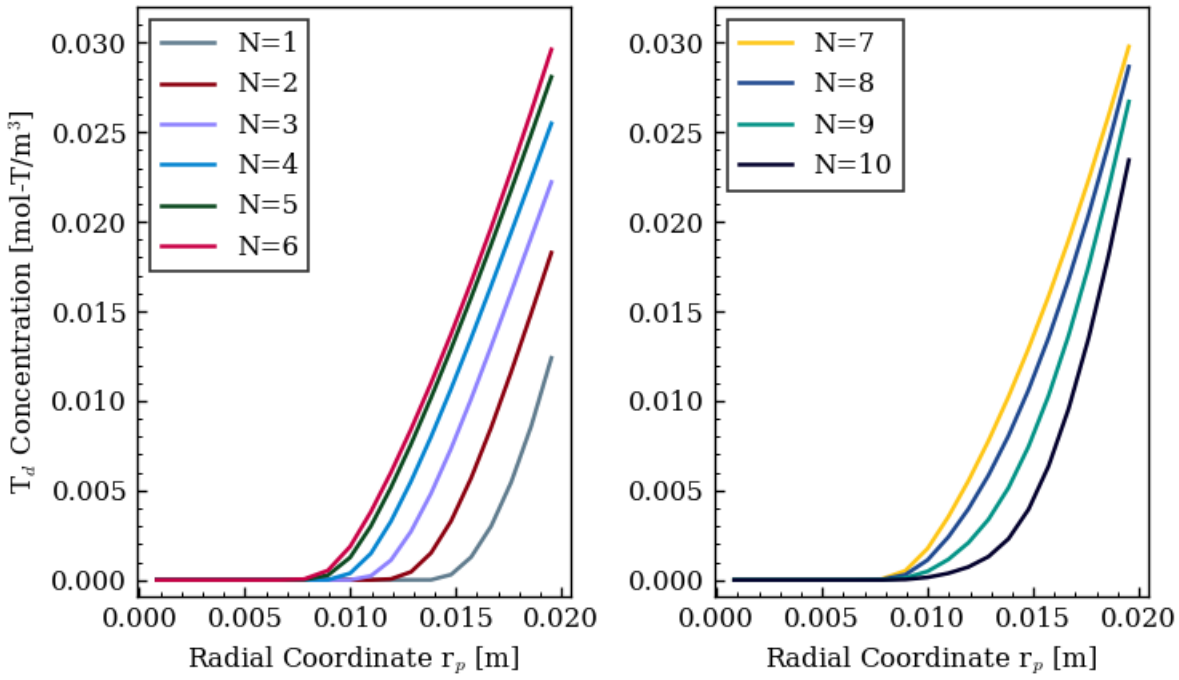

Figure 5.18. Diffusing tritium (T_d) concentration as a function of radial position for the ten graphite pebbles modeled at axial subsections in the core. The diffusing tritium has the highest overall concentration profile at the sixth node (left), then concentrations decrease for the higher axial positions (right).

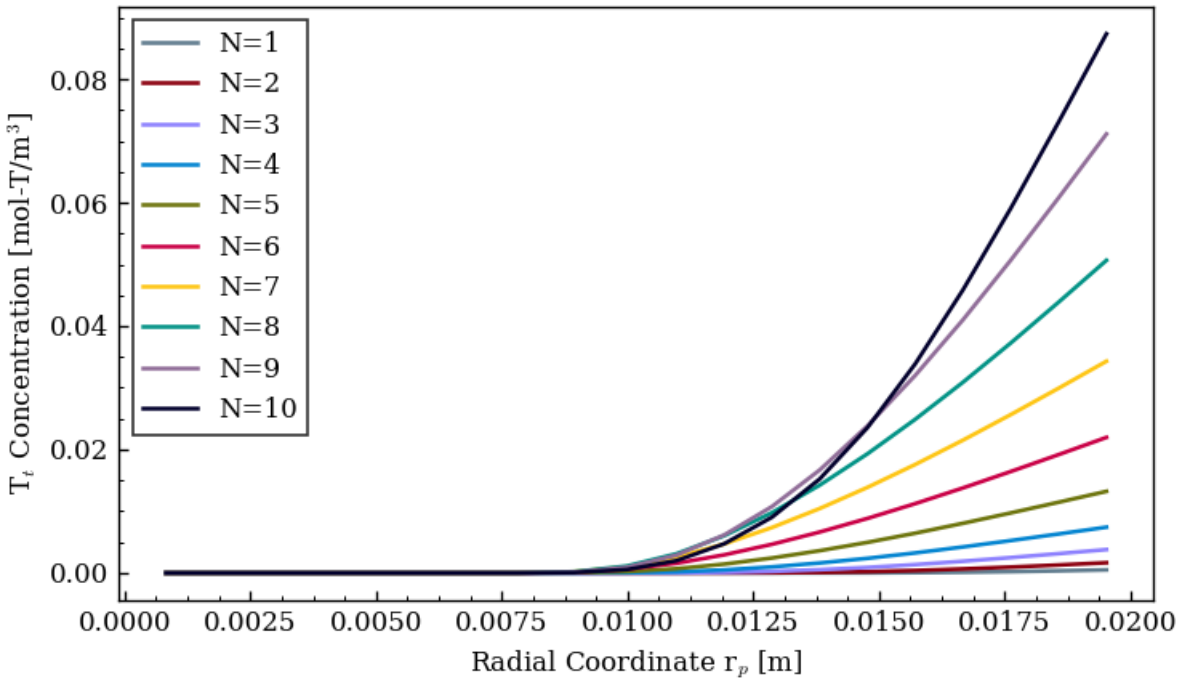

Figure 5.19. Tritium in high-energy trapping sites (T_t) as a function of radial position in the pebbles and axial position in the core. The higher-temperature of the upper core nodes facilitates the transition of tritium into trapping sites.

As shown in Figure 5.19, a significant change in the rate of high-energy trapping is predicted from the graphite pebbles surrounded by 550ºC salt at the core inlet to the 650ºC pebbles at the core outlet. In this manner, the calculated results with the pore and grain transport methodology are similar to the tritium desorption results from the FS-3 graphite samples. As discussed in Section 3, the tritium desorption rate in the high temperature peak was over five times higher for IG-110U samples irradiated in the upper crucible at 719.4ºC compared to the lower crucible samples at 600.3ºC. Therefore, FHR operating temperatures appear to be near a critical temperature range where tritium trapping in high-energy sites can become a significant fraction of total tritium retention. The total tritium retention in the graphite pebbles is also somewhat consistent with the MITR sample tritium desorption measurements. Since substantial tritium concentration gradients in the FHR pebbles are shown in Figure 5.17 through Figure 5.19, the tritium inventory in the pebbles is better described by an activity per surface area value, rather than activity per pebble mass. Using the equilibrium retention rate of 256.3 Ci/day in Figure 5.14, the pebble tritium inventory is 7.61 Ci/m^2. Factors used in the calcluation are 1684 m^2 from total pebbles circulating with a core residence time of 50 days, or a circulation rate of 33.68 m^2/day.

Therefore, the TRIDENT Mod1 pebble retention predictions are somewhat near the 4.18 Ci/m^2 average for the FS-1 crucible samples and the 4.75 Ci/m^2 average from the FS-2 IG1 sample. Although there are several important differences in tritium transport conditions between the FHR environment and the MITR in-core Flibe irradiations, the observation that TRIDENT Mod1 predictions are not severely higher or lower than the experimental values gives some confidence that the tritium retention calculations are realistic values.

Another method to assess the tritium distribution predictions is by comparing the previous results with the pore and grain tritium transport methodology to calculations with the bulk-diffusion treatment for graphite. In both cases, all graphite is considered to be POCO AXF-5Q grade, but the bulk-diffusion model uses the fitted parameters in Table 5.11 instead of the diffusivity measurements in literature – all other inputs and assumptions were maintained. As shown in Figure 5.20, a similar trend in pebble retention in the core is observed for the bulk diffusion model, where the retention rate starts out higher initially, but decreases over time to the equilibrium removal rate. The bulk-diffusion model predicts an equilibrium retention rate of 194 Ci/day from the core pebbles, which is lower than the pore and grain method result of 256 Ci/day. Heat exchanger permeation, pebble retention, and tritium removal through pebble recirculation are plotted from the bulk-diffusion simulation in Figure 5.20.

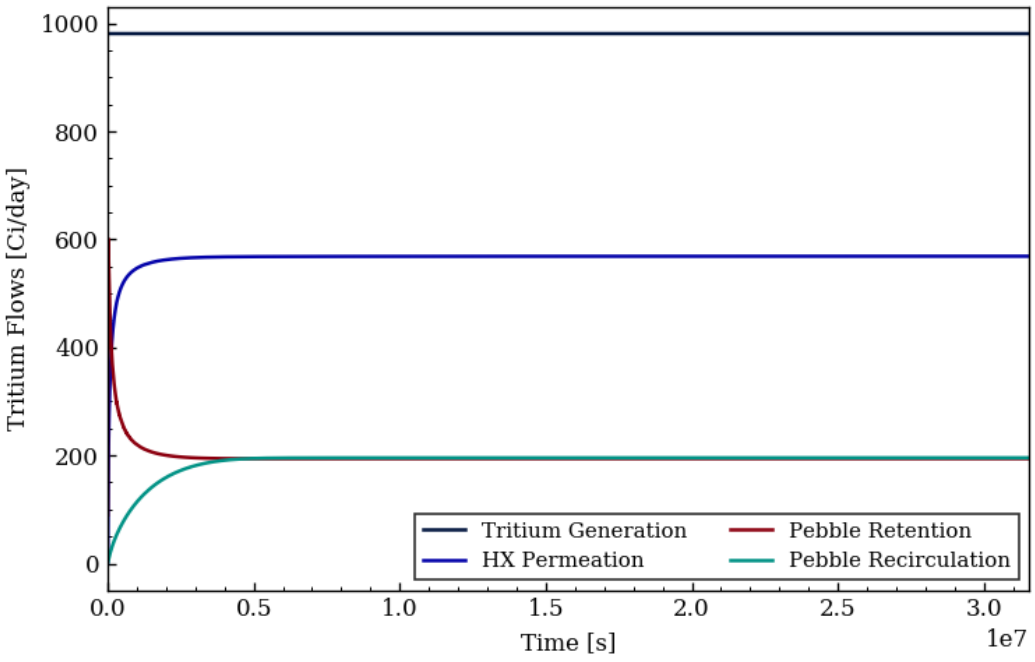

Figure 5.20. Heat exchanger permeation and pebble retention calculated using the bulk-diffusion methodology for calculating tritium retention in graphite.

One other significant difference between the bulk-diffusion and pore and grain transport model is the calculated rate of tritium retention in the downcomer graphite. As shown in Figure 5.21, the retention rate in the downcomer drops fairly quickly, and has an uptake rate of 0.743 Ci/day after one year compared to 18.6 Ci/day shown previously in Figure 5.15. Therefore, the bulk-diffusion method is more restrictive in terms of tritium retention than the pore and grain diffusion method for the lower temperatures in the downcomer region. With the bulk-diffusion method, slow diffusion of tritium in graphite leads to a high surface concentration, which in turn will raise the T_2 concentration in the salt at the interface and inhibit further retention. In contrast, slow diffusion into graphite grains at lower temperatures allows T_2 to diffuse further into the graphite bulk. Ultimately, the surface boundary condition also increases with the pore and grain methodology as the outer surfaces of graphite grains saturate with tritium and uptake of T_2 from pores increases. However, it is clear that the pore and grain methodology allows for a larger surface area of graphite to engage in the uptake of tritium compared to the bulk-diffusion method, where only the geometric surface area of the reflector is considered. The additional degree of freedom between tritium diffusion into pores and tritium uptake into grains allows for elevated retention in the reflector over time with the pore and grain diffusion calculation.

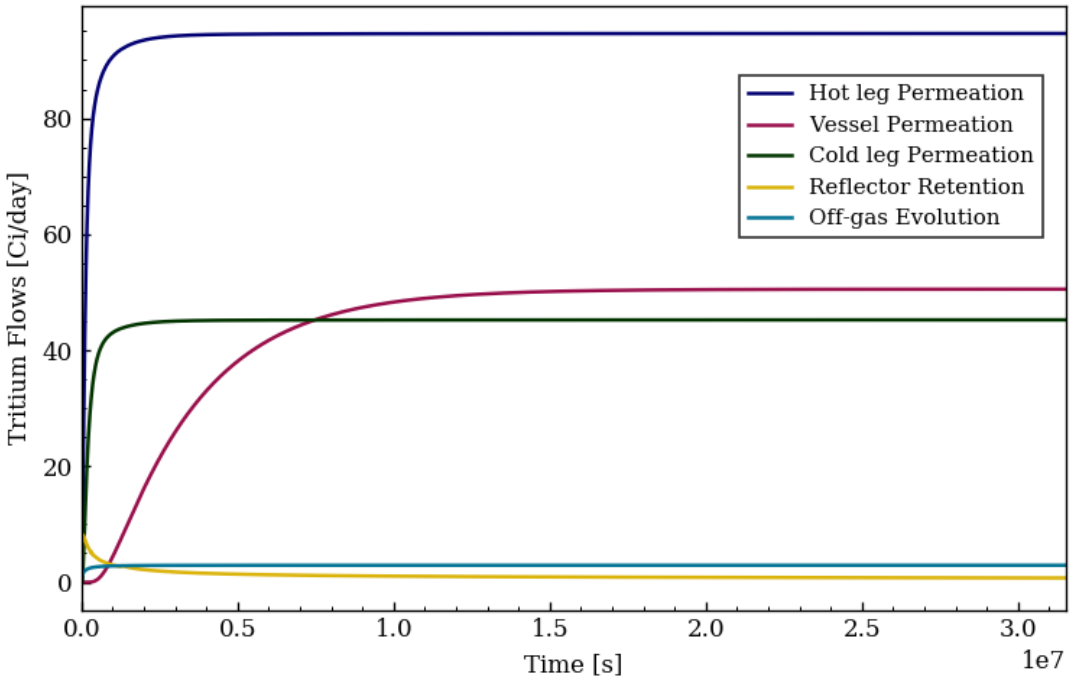

Figure 5.21. Tritium transport to other FHR regions calculated using the bulk-diffusion treatment for the core pebbles and graphite reflector.

The calculated tritium distribution after one year simulations is compared in Table 5.14 for the pore and grain transport and bulk-diffusion methods. Differences in core pebble and graphite reflector retention also cause a small shift in the other release FHR paths between the two methods. In both cases, the tritium retention rate on the outer surface of the graphite reflector in the downcomer region accounted for less than 2% of the total distribution after one year. Because of the low outer-reflector contribution, tritium retention on the inner surfaces of the graphite reflector facing the core pebbles is currently not modeled. Modeling the reflector also more than doubles the TRIDENT Mod1 simulation run time, since the downcomer region requires a five equation fsolve matrix compared to the three equation matrix in the core. As shown in Figure 5.1, the graphite reflector may also feature salt cooling channels which could allow for additional tritium uptake from the salt to occur. Similarly, a detailed FHR design will have several design features which deviate from the simplified, one-dimensional representation of the reactor currently used in TRIDENT Mod1. However, the release pathways described in Table 5.14 should account for the majority of Flibe-facing surfaces areas in the reactor and thus provide a general understanding for the tritium release expected in each region.

Table 5.14. Comparison of the contribution to total tritium release in each region with the two proposed methods for calculating tritium retention in graphite. The percentages are taken with respect to the sum of tritium flows after a one year simulation.

Release Pathway	Pore and Grain	Bulk-Diffusion
Heat Exchanger	53.6%	59.4%
Core Pebbles	26.3%	20.3%
Hot Leg	8.9%	9.9%
Reactor Vessel	4.8%	5.3%
Cold Leg	4.2%	4.7%
Graphite Reflector	1.9%	0.1%
Off-Gas	0.3%	0.3%

The tritium distribution results in Table 5.14 also demonstrate that when either retention methodology is used, the percentage of tritium uptake into graphite is significantly less than the amount expected based on mass transfer in Flibe alone. For example, based on the T_2 mass transfer coefficient in Flibe and the salt-facing surface area, tritium retention in graphite pebbles would account for 79.8% of total tritium release, as shown in Table 5.13, if a similar concentration gradient was present among all FHR surfaces and graphite had an unlimited retention capacity.

Considering the 15% tritium retention observed in the MSRE graphite [57], along with the 19.6%, 34%, and 27.1% calculated for FS-1, FS-2, and FS-3, respectively, treating graphite as a perfect absorber of tritium would over predict the observed values since the share of graphite area was likely a larger percentage of total surfaces than the percentage of tritium retention in each case. The TRIDENT Mod1 results demonstrate the importance of modeling tritium transport within graphite in order to produce a salt-graphite interface boundary condition. The calculated boundary condition governs the rate at which tritium uptake into graphite can occur, which in turn has a strong influence on the overall tritium distribution in the reactor.

5.4. Assessment of Model Inputs and Assumptions

The FHR tritium distribution calculated with TRIDENT Mod1 will vary depending upon the input parameters used in the model. Additionally, the true operating conditions in a FHR may be significantly different from the baseline considerations used in the previous calculations. The impact of parameter changes and deviations from baseline conditions can be explored using a series of TRIDENT Mod1 simulations in order to develop an understanding of possible scenarios in which the FHR tritium distribution will be altered. Because of the low contribution calculated in the baseline distribution, tritium retention in the graphite reflector is neglected for all of the results in this section in order to accelerate the runtime of the scoping studies.

5.4.1. Sensitivity of Tritium Transport and Thermophysical Properties

Calculations in TRIDENT Mod1 rely on input values measured in previous experimental studies. A review of experiments and data relevant to tritium transport has been previously carried out in Section 2. The tables and plots of experimental data in Section 2 can give a qualitative sense of the typical spread in the measurements for each parameter. Here, the quantitative impact of each parameter is evaluated by varying individual inputs in TRIDENT Mod1 and monitoring the relative change in tritium distribution compared to the baseline calculations. Tritium release paths are combined into three categories based on a theoretical plant layout, and then release into each zone is used as a figure of merit for a sensitivity analysis. Since an increase in tritium release through a certain pathway will be offset by decreases in other regions, it is important to examine the full tritium distribution when assessing the influence of individual parameters.

For the hot leg, cold leg, and reactor vessel, tritium permeation through the structural metals will be directly released into surrounding areas in the power plant, which is referred to in

this analysis generically as the reactor building. Further subdivisions in the reactor building could exist in future FHR designs which would isolate each zone, but the three regions are combined here to simplify the distribution analysis. Near the reactor core, tritium is released from the salt directly through evolution to the reactor vessel gas plenum, or indirectly through retention on graphite and desorption in a pebble recirculation system. Evolution and pebble recirculation are combined into a primary system release category since both systems would likely use inert cover gas, and the physical locations in the plant could allow for both tritium release streams to be processed with the same primary off-gas collection system. Lastly, permeation through the heat exchanger will require design considerations for tritium control in the intermediate loop, which is treated as a separate zone. Tritium release paths into the primary system, reactor building, and intermediate loop collection zones are summarized in Figure 5.22.

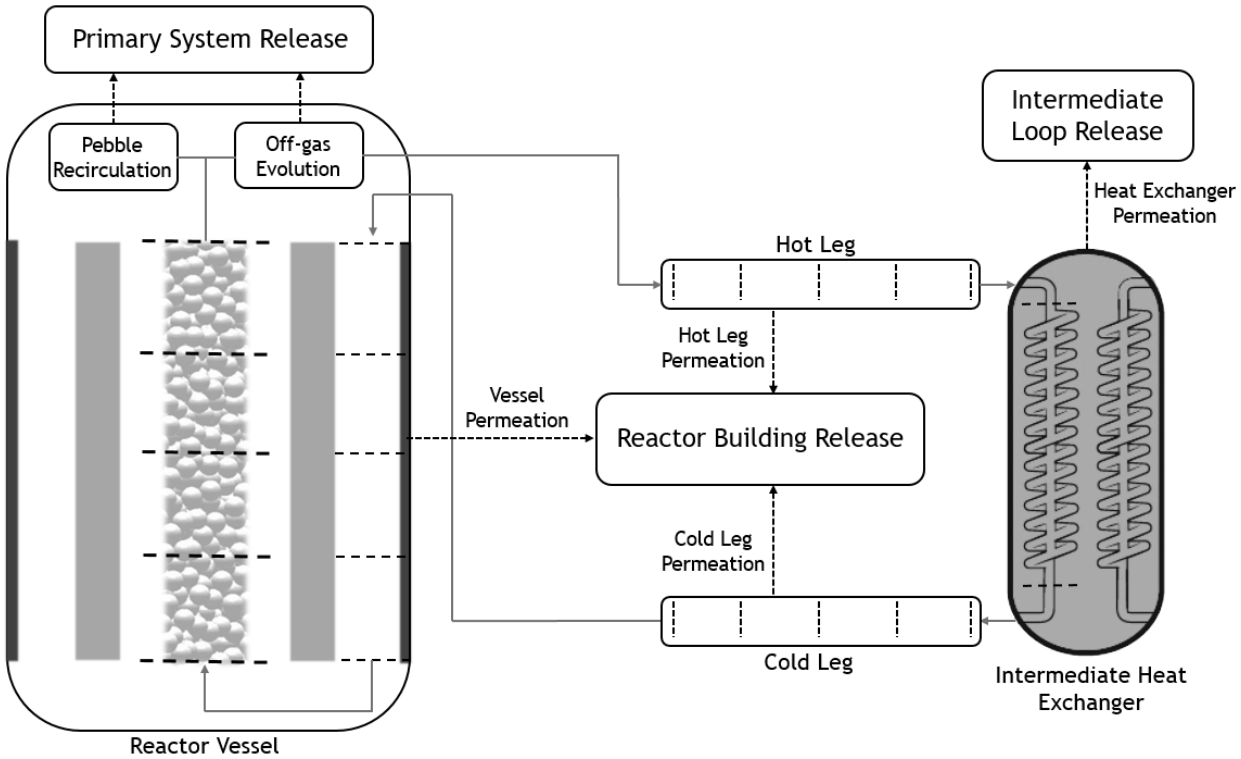

Figure 5.22. Illustration of tritium release path categorization for primary system releases, permeation releases into the reactor building, and release into the intermediate loop.

The experimental measurements discussed in Section 2 for various TRIDENT Mod1 input parameters are compiled in Table 5.15. For each parameter, the standard deviation of the set of experimental measurements was taken to represent the parameter uncertainty. Note that Table 5.15 does not include every model input, but only the thermophysical and transport related properties

which have three or more experimental measurements available in literature. Since a small set of values are available for certain parameters, the standard deviations provide only a rough understanding of the uncertainty in each parameter. The baseline value for each parameter was selected by assessing which experiment was the highest quality or most representative of the FHR conditions, rather than using an average of the experimental measurements. Values from single, appropriate studies were used instead of group averages because of the generally high relative standard deviations shown in Table 5.15

Table 5.15. Average values of input parameters and standard deviations calculated from the experimental measurements of each value summarized in Section 2.

Parameter	Symbol	Average Value	Standard Deviation	σ_{rel}
Flibe density[1]	ρ	1.99e3 [kg/m^3]	39.7	2%
Flibe specific heat[1]	c_p	2.39e3 [J/kg-K]	71.6	3%
Flibe viscosity[1]	μ	8.55e-3 [Pa-s]	1.71e-3	20%
Tritium diffusivity in 316SS	$D_{T,316}$	3.26e-10 [m^2/s]	1.48e-10	45%
Sievert's law constant in 316SS	$K_{S,316}$	1.61e-1 [mol/m^3-Pa$^{1/2}$]	7.56e-2	47%
Sievert's law constant in graphite	$K_{S,g}$	5.36e-1 [mol/m^3-Pa$^{1/2}$]	2.68e-1	50%
Strong trap site concentration	C_t^0	6.33 [mol/m^3]	3.25	51%
T_2 diffusivity in Flibe	$D_{T2,Flibe}$	1.95e-9 [m^2/s]	1.62e-9	83%
Henry's law constant in Flibe	$K_{H,T2}$	2.60e-4 [mol/m^3-Pa]	2.68e-4	103%
Diffusivity of T_2 in graphite pores	$D_{T2,p}$	3.54e-9 [m^2/s]	3.89e-9	110%
Tritium diffusivity in graphite grains	$D_{T,g}$	3.51e-20 [m^2/s]	6.53e-20	186%

[1]Thermophysical property uncertainties assume constant temperature and steady-state operation

The relative standard deviations from Table 5.15 were used to represent the uncertainties of the baseline parameter values selected in Table 5.9. Once the standard deviations are determined, the sensitivity of the tritium distribution to the parameter uncertainty, S, can be evaluated using equation 5.48. In the equation, the figure of merit (FOM) - either release through to primary system,

reactor building, or intermediate loop – is monitored for a simulations with a single parameter adjusted above and then below the baseline value by one standard deviation. Nearly all of the parameters in Table 5.15 vary with temperature, so the standard deviation is taken from the experimental values tabulated at 600ºC, then added or subtracted to the baseline value. In several cases the 600ºC standard deviation is greater than the parameter value, so only the positive perturbation can be applied and equation 5.49 is used to calculate the sensitivity. The sensitivity values ranked in order of magnitude for each zone are shown in Table 5.16.

Eq. 5.48
$$S = \frac{(FOM_{\sigma+} - FOM_{\sigma-})}{2 \cdot FOM_o}$$

Eq. 5.49
$$S = \frac{(FOM_{\sigma+} - FOM_o)}{FOM_o}$$

Table 5.16. Sensitivity values of various inputs for tritium release into the primary system, reactor building, and intermediate loop tritium collection zones calculated from equation 5.48 or equation 5.49.

Primary Systems		**Reactor Building**		**Intermediate Loop**	
Parameter	Sensitivity	Parameter	Sensitivity	Parameter	Sensitivity
$K_{H,T2}$	-21.7%	μ	-7.62%	$K_{H,T2}$	8.3%
$K_{S,g}$	15.9%	$K_{H,T2}$	6.37%	$D_{T2,Flibe}$	6.2%
$D_{T,g}$	15.2%	$K_{S,g}$	-5.68%	$K_{S,g}$	-5.8%
$D_{T2,Flibe}$	-12.4%	$D_{T,g}$	-5.40%	$D_{T,g}$	-5.5%
$D_{T2,p}$	6.98%	$D_{T2,Flibe}$	3.26%	μ	3.1%
C_t^0	1.49%	$D_{T2,p}$	-2.48%	$D_{T2,p}$	-2.5%
μ	-1.13%	$D_{T,316}$	2.39%	C_t^0	-0.57%
$D_{T,316}$	-0.47%	c_p	-1.35%	c_p	0.56%
ρ	0.20%	C_t^0	-0.53%	$D_{T,316}$	-0.54%
c_p	0.08%	$K_{S,316}$	0.32%	ρ	0.16%
$K_{S,316}$	-0.06%	ρ	-0.10%	$K_{S,316}$	-0.08%
Sum[1]	76%	Sum[1]	36%	Sum[1]	33%

[1]Based on absolute values

The sensitivity values in Table 5.16 are a function of both the importance of each parameter in the model as well as the relative uncertainty. As a result, the parameters which create a larger change in the tritium distribution are also generally parameters with the greater relative uncertainties, as shown in the lower rows of Table 5.15. One counterexample of a parameter with a mid-range sensitivity and an outsized impact is the Sievert's law solubility for tritium in graphite

($K_{S,g}$), which ranks in the top two sensitivities for all regions in Table 5.16. Although the $K_{S,g}$ values are only used for calculations in the core, an increase in tritium retention under elevated graphite solubility values results in less tritium available for permeation into the reactor building and intermediate loop. A similar trend is also observed for the diffusivity of tritium in graphite pores and grains, $D_{T,g}$ and $D_{T2,p}$, respectively. The sum of sensitivity values in each column provides a relative gauge of the tritium distribution uncertainty. Since the graphite retention calculation uses several parameters with high uncertainties like the tritium diffusivities, the primary system release has the largest sum of sensitivities. Therefore, the fraction of tritium which is retained by the core graphite can be considered as the most uncertain aspect of the FHR tritium distribution.

One example of a parameter with a mixed effect is the Henry's law coefficient for T_2 solubility in Flibe. A higher value for the coefficient results in a preference for T_2 to remain in the salt phase, rather than permeate into metals or diffuse into graphite. The phase preference for T_2 is determined through the interface boundary conditions, where a higher $K_{H,T2}$ value creates a greater T_2 concentration in the salt at the surface and a lower overall concentration gradient for mass transfer in the bulk salt. Surface T_2 concentrations for the graphite pebbles and structural metals in the FHR are plotted in Figure 5.23 with and without the standard deviation added to the Henry's law coefficient. Adding the standard deviation results in an elevated T_2 graphite surface concentration as well as higher surface concentrations for the hot leg, cold leg, and reactor vessel, which decreases the resistance to retention in graphite as well as permeation in the reactor building zones. Even with a Henry's law coefficient increased by one standard deviation, the permeation resistance of the heat exchanger tubes remains negligible, and release to the intermediate loop is further increased compared to the reactor hot leg, cold leg, and reactor vessel.

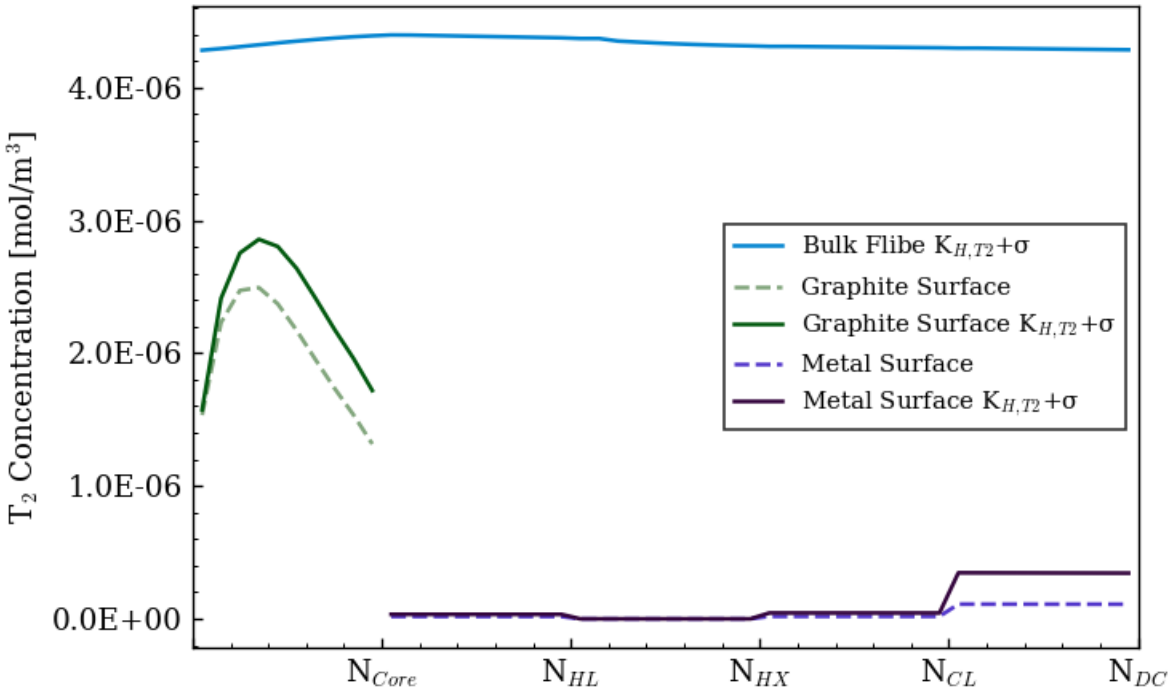

Figure 5.23. Surface concentrations of T_2 for the core pebbles, hot leg, heat exchanger, cold leg, and reactor vessel before and after the Henry's law coefficient is raised from the baseline value by one standard deviation.

The low permeation resistance in the heat exchanger is also evidenced by the negative sensitivity values from 316 stainless steel solubility and diffusivity perturbations shown in Table 5.16. Increasing either parameter will reduce the overall permeation resistance in the metal regions. However, since there is almost zero permeation resistance initially in the heat exchanger, the permeation rate into the intermediate loop decreases when the solubility or diffusivity of tritium in 316SS is raised since more permeation into the reactor building occurs. Release into the reactor building increases slightly with higher $D_{T,316}$ and $K_{S,316}$ values since there is non-negligible permeation resistance in the hot leg, cold leg, and reactor vessel at baseline conditions.

Another method to calculate sensitivity is to vary parameters by the same relative magnitude, instead of by the calculated standard deviations. In this manner, the impact of each parameter in the model can be evaluated separately from the experimental uncertainty. The calculation procedure is shown in equation 5.50, where each parameter is increased by 10% above and below the value at 600ºC. A factor of 0.2 is applied to the denominator to normalize for the 20% spread in the numerator value. Sensitivity results using this method are shown for the three permeation zones in Table 5.17.

Eq. 5.50
$$S = \frac{(FOM_{10\%+} - FOM_{10\%-})}{0.2 \cdot FOM_o}$$

Table 5.17. Sensitivity values of various TRIDENT Mod1 inputs for tritium calculated from equation 5.50 by varying each parameter ±10%.

Primary Systems		**Reactor Building**		**Intermediate Loop**	
Parameter	Sensitivity	Parameter	Sensitivity	Parameter	Sensitivity
$K_{S,g}$	27.5%	c_p	-45.2%	c_p	18.6%
$K_{H,T2}$	-25.4%	μ	-37.4%	μ	15.3%
$D_{T2,Flibe}$	-22.5%	ρ	-11.3%	$D_{T2,Flibe}$	11.4%
$D_{T,g}$	13.2%	$K_{S,g}$	-9.8%	$K_{S,g}$	-9.9%
$D_{T2,p}$	10.7%	$K_{H,T2}$	7.9%	$K_{H,T2}$	9.6%
Σ_T	6.2%	$D_{T2,Flibe}$	6.2%	$D_{T,g}$	-4.8%
μ	-5.7%	$D_{T,g}$	-4.7%	$D_{T2,p}$	-3.9%
ρ	4.0%	$D_{T2,p}$	-3.4%	Σ_T	-2.2%
c_p	2.7%	$D_{T,316}$	2.8%	ρ	1.9%
C_t^0	2.6%	$K_{S,316}$	2.4%	C_t^0	-1.4%
$D_{T,316}$	-0.5%	Σ_T	-2.2%	$D_{T,316}$	-0.7%
$K_{S,316}$	-0.4%	C_t^0	-0.1%	$K_{S,316}$	-0.6%
Σ_D	-0.0%	Σ_D	0.0%	Σ_D	0.0%

The sensitivity results in Table 5.17 show a ranking of parameters that is significantly different from the previous values in Table 5.16. For example, the Flibe thermophysical properties of density, heat capacity, and viscosity had low sensitivity ratings in Table 5.16 because of their relatively low experimental measurement uncertainty. In contrast, when all inputs are varied evenly, the thermophysical parameters have large impacts because they change the mass transport properties in Flibe. The influence of thermophysical property perturbations on Sherwood numbers is shown in Figure 5.24, where each axis is has the same relative scaling in order to display the spread caused by the ±10% parameter adjustments. The largest change in Sherwood numbers occurs for the hot leg, cold leg, and reactor vessel since the correlation used depends on $Re^{0.913}$ and $Sc^{0.346}$ compared to $Re^{0.69}$ and $Sc^{1/3}$ for the core. An increase in either of the three thermophysical properties leads to a lower Sherwood number in the hot/cold leg and reactor vessel, which is reflected by the negative sensitivity values for reactor building release in Table 5.17. Among the permeation regions, the heat exchanger is least affected by changes to thermophysical parameters. In the Sherwood number correlation used, there is also no dependence and salt viscosity in the heat exchanger since the Reynolds and Schmidt numbers are raised to the same

power. Therefore, as the density and heat capacity increases also lead to lower Sherwood numbers in the heat exchanger, but the overall change is smaller than the other permeation zones and thus permeation to the intermediate loop increases because reactor building release is reduced significantly.

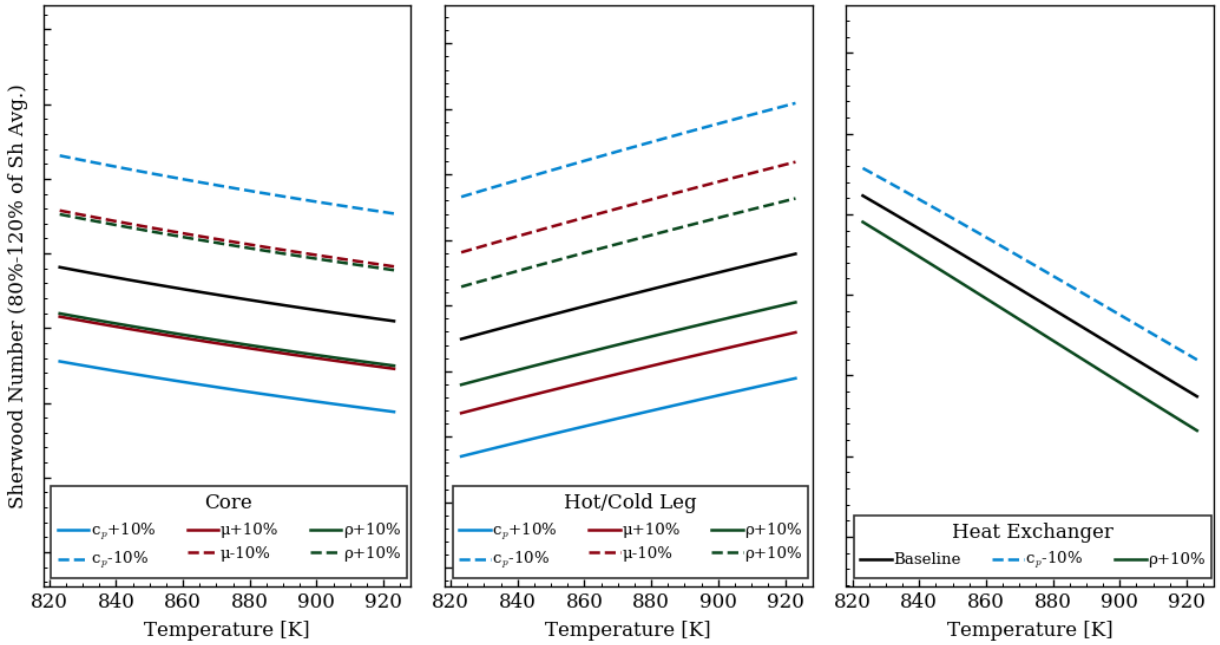

Figure 5.24. Sherwood numbers in the core, hot or cold leg pipe, and heat exchanger tubes as a function of temperature when Flibe heat capacity, density, and viscosity are varied by ±10%. Each y axis has lower and upper limits of 80% and 120% of the average baseline Sherwood number value in each zone.

Results in Table 5.17 also reveal important features of the tritium retention model for the core pebbles. The most significant parameter was the solubility of tritium in graphite, which has a strong influence on determining the amount of tritium which can enter the graphite grains at each time step. Similarly, the diffusivity of tritium into grains and diffusivity of T_2 in pores determine the uptake rate of tritium in graphite, and ultimately change the boundary condition at the pebble surface which governs the concentration gradient in the core salt. In terms of tritium trapping at high-energy sites, the trapping rate constant has a notable influence on overall retention since the conversion of diffusing tritium into strong trapping sites can allow for additional uptake into the graphite grains. In contrast, the detrapping rate constant had the lowest overall impact since the 550ºC-650ºC operating range of the simulated FHR was well below the temperatures required for significant desorption from high-energy sites. Strong trapping site desorption was not observed

until above 1000ºC for the FS-3 samples desorbed in Ar-4%H_2 and above 1300ºC for graphite samples charged with deuterium gas and desorbed in a vacuum [159]. Therefore, to best improve tritium retention predictions under steady-state conditions at normal operating temperatures, future experimental work should focus on improving measurements for the Sievert's law constant for solubility as well as diffusivities of tritium in graphite. Beyond graphite parameters, the diffusivity and solubility of T_2 in Flibe also create a significant uncertainty in all aspects of the FHR tritium distribution, as shown in Table 5.17.

5.4.2. Impact of Assumptions on the Chemical Form of Tritium

The previous baseline tritium distribution and sensitivity calculations were all conducted assuming a Flibe redox potential fully reduced by beryllium metal. While a strongly reducing salt may be desirable for corrosion control, the achievable redox potential in a FHR will depend on design characteristics and operation parameters of FHR chemical control systems. As discussed in Section 2, the addition of beryllium metal into Flibe does not guarantee that the salt will become fully reduced. The true redox potential in Flibe may depend more on the kinetic limitations of chemical interactions with redox agents, as well as the presence of other impurities in the salt.

The tritium distribution under various salt chemical conditions can be observed by varying the input redox potential. By enforcing the set redox potential throughout the reactor loop, the balance between tritium chemical forms can then be calculated with equation 5.10. Equilibration of TF and T_2 concentrations in TRIDENT Mod1 for three Flibe fluorine potentials are shown in Figure 5.25. The baseline condition of fully beryllium-reduced salt at a potential of -902.5 kJ/mol is shown for reference. Two additional cases at more oxidizing conditions are plotted as well. In the first, the MSRE target chemistry of 100:1 UF_4:UF_3 is used, which corresponds to a fluorine potential of -700.5 kJ/mol in un-fueled Flibe salt. Lastly, the average measured redox potential of the three experiments plotted in Figure 2.6 is used, which produced an average of -676.8 kJ/mol. As shown in Figure 5.25, the more oxidizing redox potentials lead to significant increases in the TF concentration in the salt as well as the overall equilibration time.

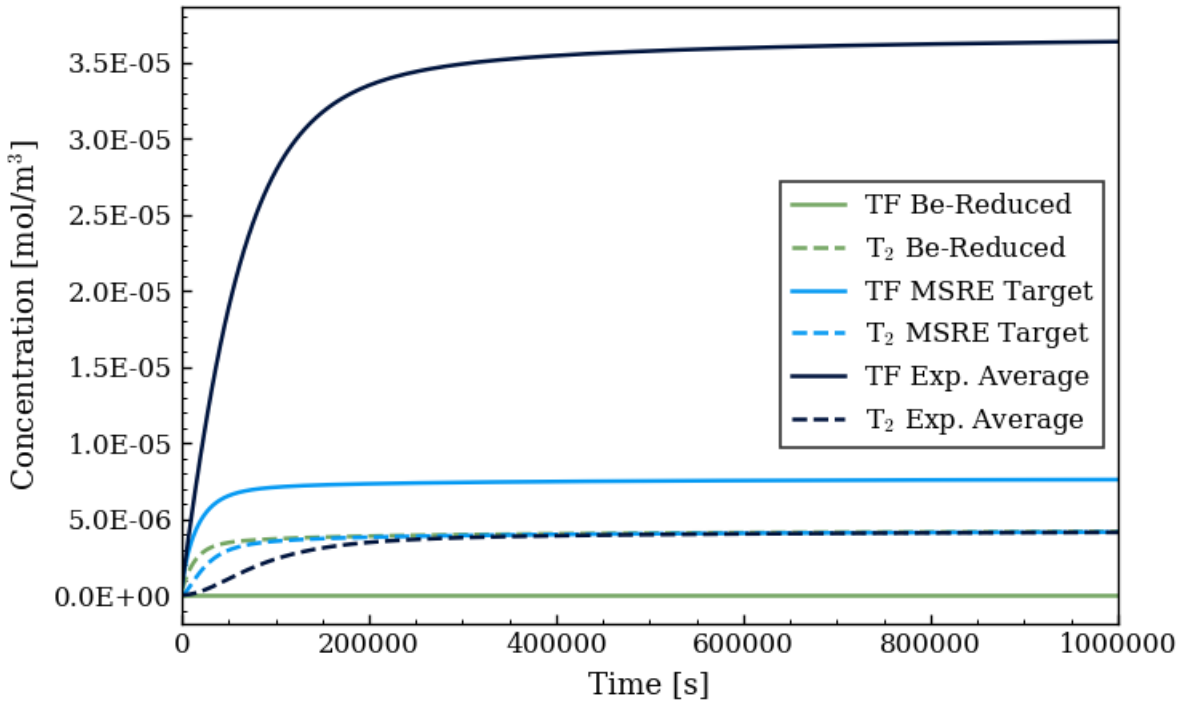

Figure 5.25. TF and T_2 concentrations in Flibe obtained from TRIDENT Mod1 simulations at three redox potentials: -902.5 kJ/mol, -700.5 kJ/mol, and -676.8 kJ/mol.

The results in Figure 5.25 show that the redox potential has a strong influence on the total tritium concentration in the salt, which is mainly driven by increasing TF concentrations at oxidizing conditions. For example, at a redox potential of -676.8 kJ/mol, the TF concentration in Flibe is almost ten times that of T_2. However, within the range of redox potentials discussed, the greater TF concentration does not lead to a significant change in the overall tritium distribution. As previously discussed, the permeation of TF through metals and retention of TF on graphite is currently neglected in TRIDENT Mod1 due to a lack of experimental evidence on the occurrence of each phenomenon. Therefore, the only modeled release path for TF in the FHR is evolution into the reactor vessel plenum. Evolution is thus limited to a 5.75 m^2 salt-gas interface above the core. Furthermore, the evolution mass transfer coefficient is lower for TF than that of T_2 since TF is expected to have a slower diffusivity in the salt [81]. The evolution rate for the three redox cases is plotted on the left in Figure 5.26, where the evolution rate rises from 2.73 Ci/day at the beryllium-reduced potential to 4.77 Ci/day at -676.8 kJ/mol. An increased evolution rate leads to small decreases in the other release paths, such as permeation through the heat exchanger. The distribution of releases and other relevant parameters for each case is shown in Table 5.18.

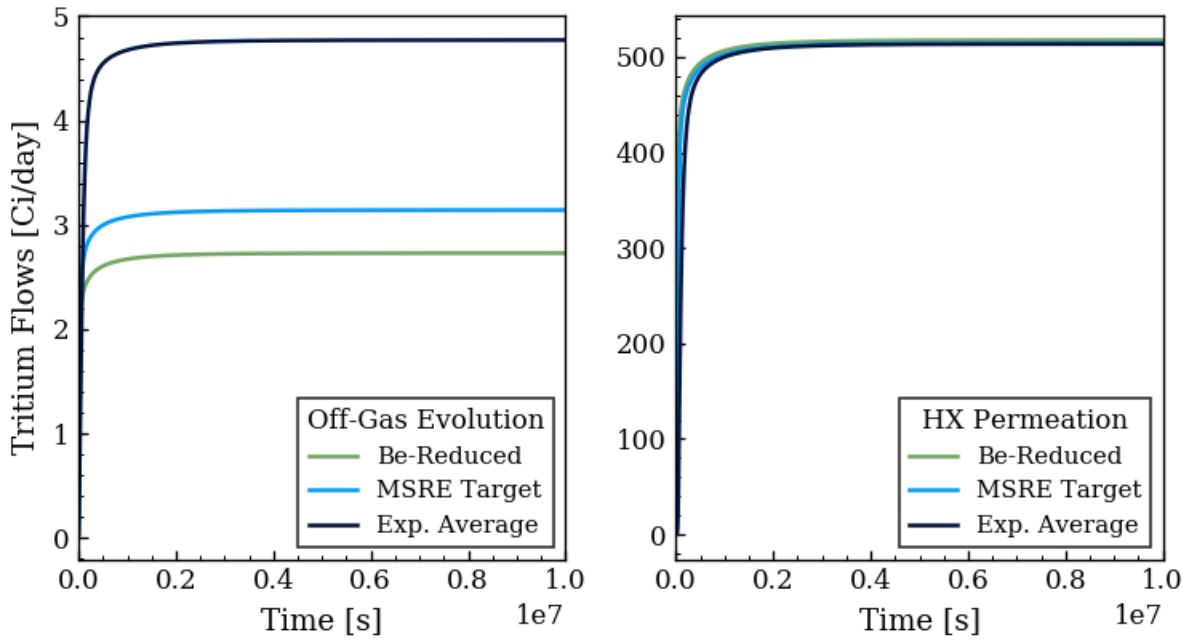

Figure 5.26. Tritium evolution to off-gas and permeation through the heat exchanger for the three previous redox cases.

Table 5.18. Tritium concentrations and release distributions for three redox potential conditions.

Value	Be-Reduced	MSRE Target	Exp. Average
Fluorine Potential	-902.5 kJ/mol	-700.5 kJ/mol	-676.8 kJ/mol
T_2 [mol/m^3]	$4.26 \cdot 10^{-6}$	$4.22 \cdot 10^{-6}$	$4.19 \cdot 10^{-6}$
TF [mol/m^3]	$1.15 \cdot 10^{-11}$	$5.78 \cdot 10^{-5}$	$1.15 \cdot 10^{-4}$
Heat Exchanger	54.0%	53.7%	53.6%
Core Pebbles	26.8%	27.2%	27.2%
Hot Leg	9.0%	8.9%	8.9%
Reactor Vessel	5.6%	5.6%	5.6%
Cold Leg	4.3%	4.3%	4.2%
Off-Gas	0.28%	0.33%	0.50%

Because the fluorine potential is defined based on partial pressures of each species [54], the ratio of TF to T_2 concentration at chemical equilibrium also depends on the Henry's law coefficients for TF and T_2 in Flibe. As previously shown, the Henry's law coefficient for T_2 solubility in Flibe has the highest relative uncertainty among parameters which have been measured in several studies. Only one study was available for the TF Henry's law coefficient in

Flibe [72], and thus the uncertainty in $K_{H,TF}$ is unknown. Figure 5.27 provides an example of how TF to T_2 ratios will change based on the redox potential of the salt and the value used for the Henry's law coefficient. The Henry's law coefficient is shown increasing on the x-axis based on the ratio of the input value to the measured value by Malinauskas et al [82]. If the Henry's law coefficient for T_2 increases, then relatively less TF will be present in the salt for a given redox potential.

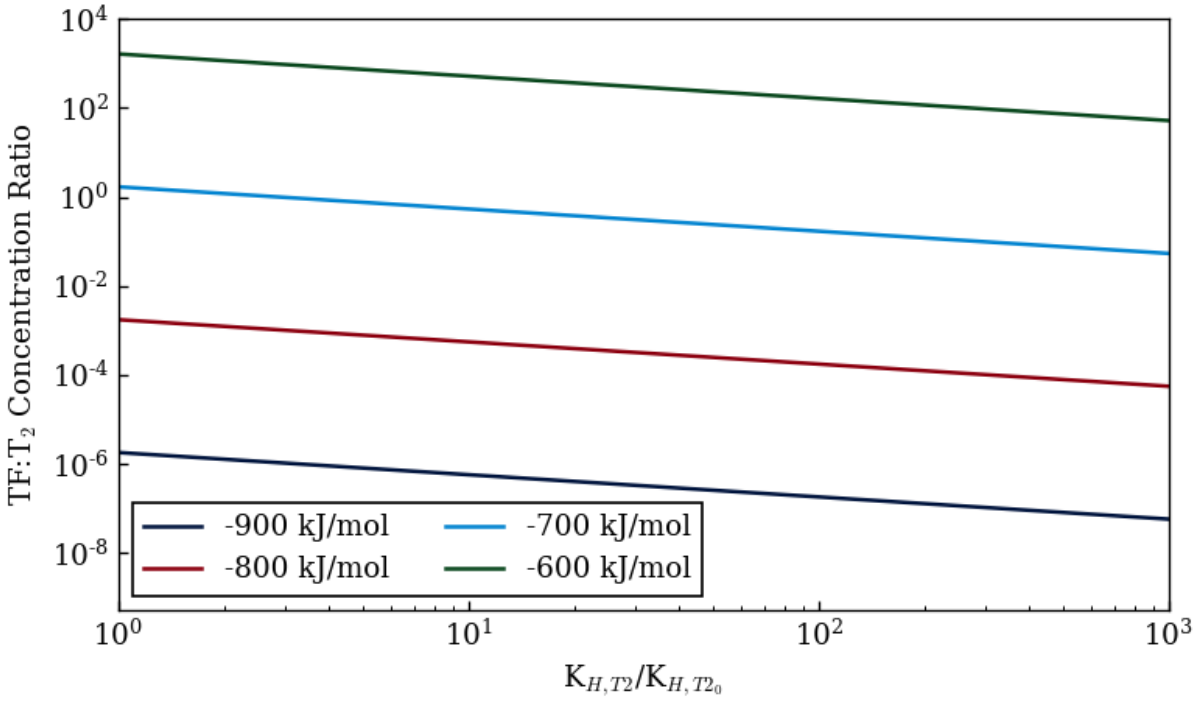

Figure 5.27. TF to T_2 concentration ratios for a T_2 concentration of 4.3e-6 mol/m^3 as the Henry's law coefficient for T_2 in Flibe is increased from the values reported by Malinauskas et al [82].

The previous results demonstrate how the tritium distribution predictions in TRIDENT Mod1 will vary if the Flibe redox potential increases above the beryllium-reduced lower limit. In each case, tritium in Flibe was generated at the TF:T_2 ratio dictated by the salt potential and the concentrations were rebalanced at every time step to adjust for T_2 and TF releases. The physical interpretation for this assumption is that tritium speciation occurs quickly and uniformly throughout the salt, and a chemical equilibrium occurs for all tritium in the primary loop. If tritium is instead generated as TF, and a chemical reaction is required for conversion to T_2, then kinetic limitations in the tritium speciation process could also lead to elevated concentrations of TF in the salt. Because of a lack of information on tritium reaction kinetics in a FHR environment,

TRIDENT Mod1 relies on the equilibrium chemical assumption instead of directly modeling the speciation process. Therefore, the TRIDENT Mod1 code does not currently predict whether or not the TF:T_2 ratio will deviate significantly from equilibrium.

One method to conceptually build in kinetic limitations to tritium speciation is to add a chemical control sub-loop to the TRIDENT Mod1 reactor model. A chemical control system in a FHR could provide capabilities for salt filtering, oxide removal, and corrosion control in addition to preventing tritium fluoride buildup [5]. As shown in Figure 5.28, the chemical control loop takes a percentage of the flow from the hot leg, adjusts the TF:T_2 ratio, then returns the salt to the cold leg. In this case, all tritium is generated initially as TF and the only source of T_2 is the sub-loop through the rebalancing process in equation 5.10. The sub-loop calculation would be representative of a FHR where TF:T_2 ratios deviate from equilibrium in the primary loop, but fully equilibrate inside of a chemical control system with special design features to create a sufficiently reducing and reactive environment. Tritium concentrations are shown for the sub-loop simulations in Figure 5.29 with a beryllium-reduced redox potential applied for sub-loop flows of 5%, 1%, 0.5%, and 0.1%. The T_2 concentration remains fairly steady at the various flow conditions, but the TF concentration is shown to build up significantly as the chemical control flow is decreased.

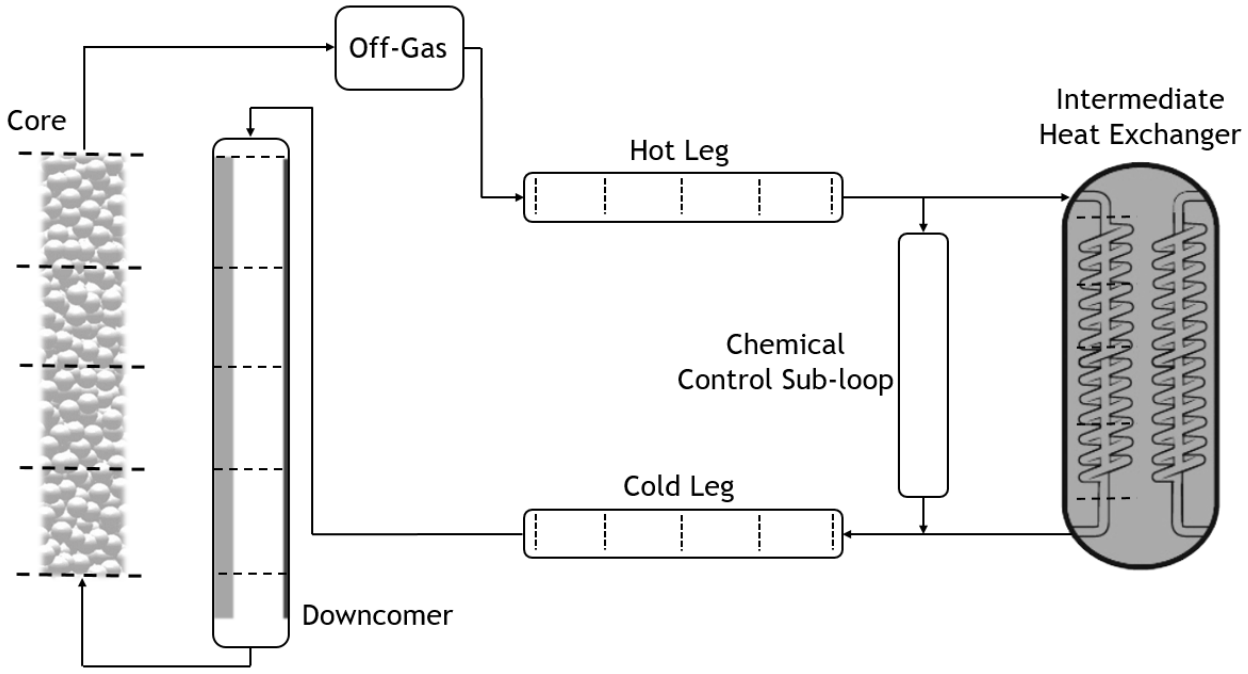

Figure 5.28. TRIDENT Mod1 reactor model layout for calculations where redox rebalancing only occurs for a fraction of the primary flow in a chemical control sub-loop.

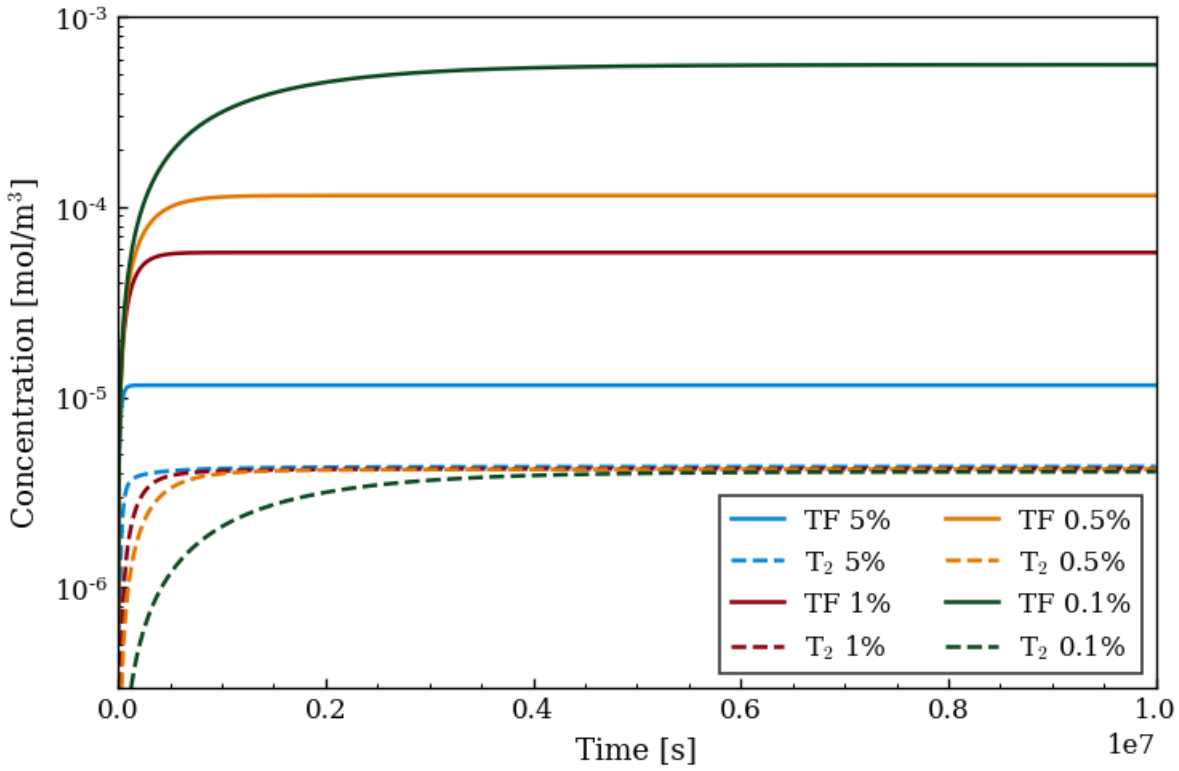

Figure 5.29. TF and T_2 concentrations in the chemical control calculations where tritium is generated as TF and only converted to the beryllium-reduced redox potential in the sub-loop.

The increase in TF concentration from lower sub-loop flows has a similar effect on the tritium distribution as higher redox potentials – higher TF values lead to more evolution to the reactor off-gas and less release through other pathways. Off-gas evolution is plotted along with retention in the core pebbles for various sub-loop flows in Figure 5.30. As shown in Table 5.19, decreasing the sub-loop flow from 5% to 0.1% of the total primary flow lead to an increase in evolution from 0.4% to 3.5% of total tritium release. Therefore, for both the sub-loop analysis and oxidizing redox potentials, the large increase in TF concentration did not lead to a significant shift in the overall tritium distribution. The low sensitivity of tritium distributions to TF concentrations is a result of evolution being the only modeled pathway for TF release. For more favorable evolution conditions, such as a larger salt-gas interfacial area or enhanced mass transfer near the free surface, the increase in TF concentration could have a larger influence on calculated releases and the overall tritium distribution.

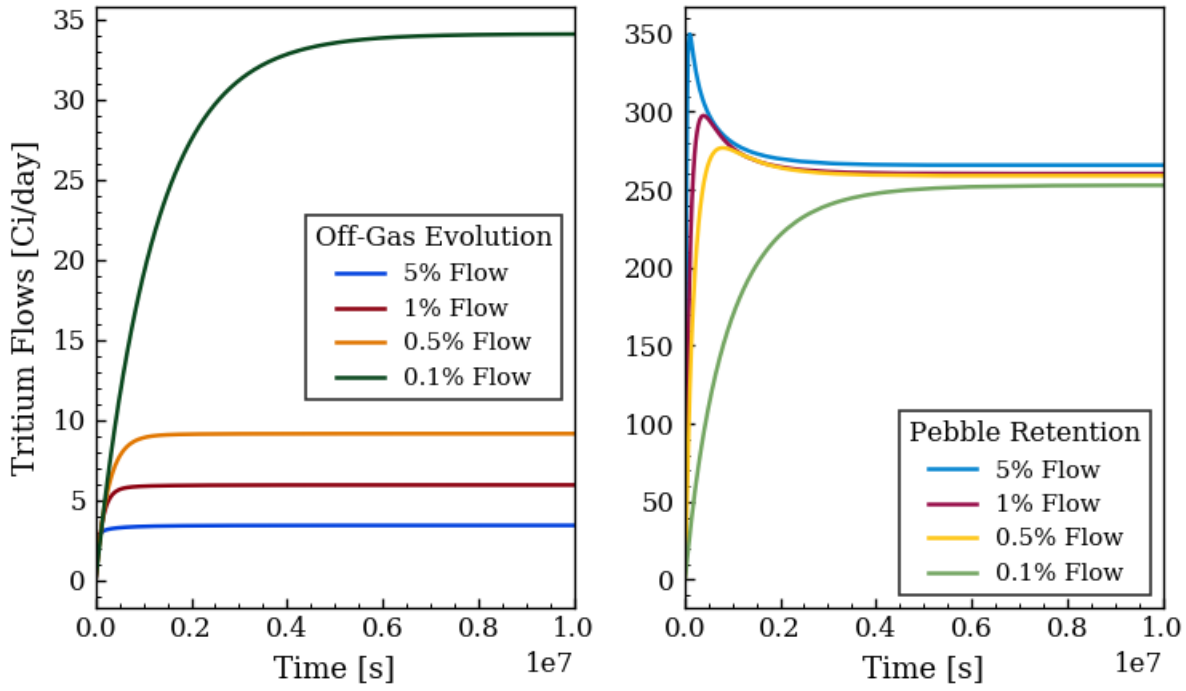

Figure 5.30. Tritium evolution to off-gas and retention in the core pebbles as a function of percent flow through the chemical control sub-loop.

Table 5.19. Tritium concentrations and release fractions for various flow percentages through a chemical control sub-loop.

Value	5% Flow	1% Flow	0.5% Flow	0.1% Flow
T_2 [mol/m^3]	$4.33 \cdot 10^{-6}$	$4.22 \cdot 10^{-6}$	$4.19 \cdot 10^{-6}$	$4.07 \cdot 10^{-6}$
TF [mol/m^3]	$1.16 \cdot 10^{-5}$	$5.78 \cdot 10^{-5}$	$1.15 \cdot 10^{-4}$	$5.61 \cdot 10^{-4}$
Heat Exchanger	52.1%	52.9%	52.8%	51.4%
Core Pebbles	27.7%	27.1%	27.0%	26.3%
Hot Leg	9.1%	8.9%	8.8%	8.6%
Reactor Vessel	6.1%	6.0%	5.9%	5.8%
Cold Leg	4.7%	4.5%	4.5%	4.4%
Off-Gas	0.4%	0.6%	1.0%	3.5%

5.4.3. Influence of Pebble Desorption Conditions

An underlying assumption in the previous simulation results is the treatment for the desorption of pebbles in the recirculation system. In the baseline results, sensitivity studies, and redox control simulations, complete pebble tritium desorption was considered to occur for each pass in the recirculation process. Numerically, the full desorption condition was applied by using a desorption factor of one in equation 5.26 for both the diffusing and trapped tritium. Another option in TRIDENT Mod1 is to simulate the tritium desorption in pebbles during the simulation in order to calculate and periodically update desorption factors for the recirculation system. In this case, the desorption factors would be less than one, with lower desorption temperatures and times resulting in desorption factors closer to zero.

Currently in TRIDENT Mod1, the desorption process is modeled for a fixed temperature and total duration, which remain constant throughout the simulation. The desorption calculation uses the pebble tritium concentration profiles from the top core axial node as the initial starting condition. Next, a pebble desorption subroutine runs a transient desorption simulation for the specified duration. Tritium diffusion and detrapping is calculated using the grain-only transport method, as done for the simulation of the Atsumi et al desorption profile in Section 4. In Figure 5.31, example concentration profiles of trapped tritium (T_t) are provided before and after desorption at 900ºC for 100 hours, 1000ºC for 10 hours, and 1000ºC for 100 hours. The trapped tritium concentration for 900ºC and 10 hours was nearly equal to the initial profile and thus was omitted from the plot. In all four cases, the weakly-bonded diffusing tritium (T_d) was successfully desorbed to nearly zero (DF_d=1). Comparing the differences between trapped tritium for the 900ºC-100hr and 1000ºC-100hr cases verses the 1000ºC-10hr and 1000ºC-100hr cases, raising the desorption temperature is generally more effective in increasing the desorption fraction compared to increasing the desorption duration.

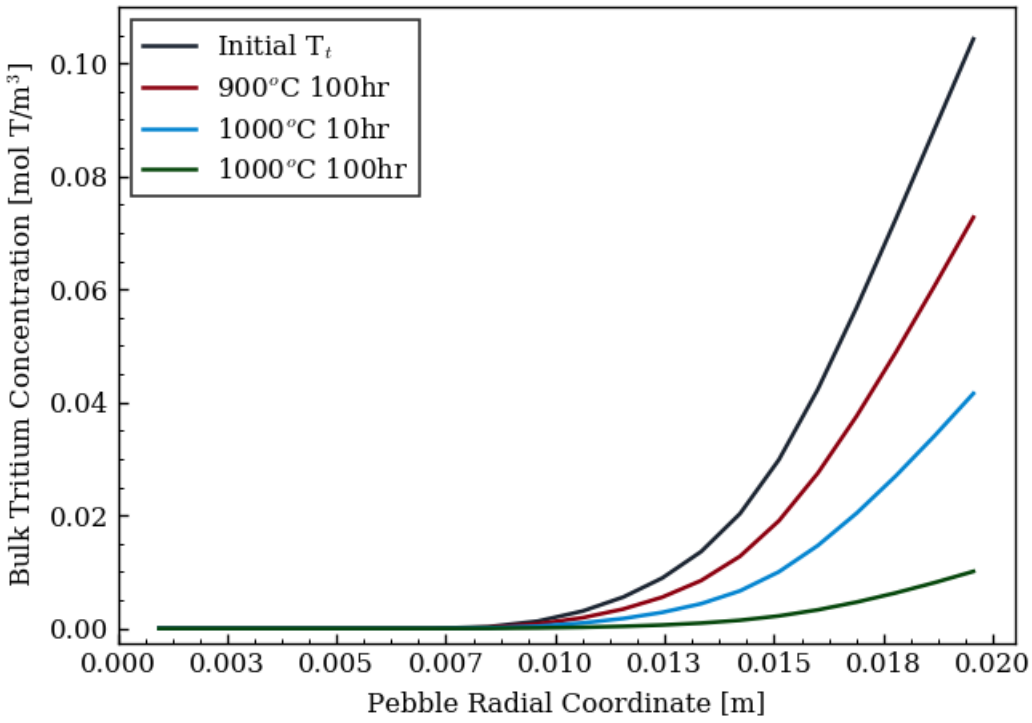

Figure 5.31. Trapped tritium (T_t) concentration profiles before and after desorption simulations. The concentration profiles are shown for a fixed temperature and desorption time in three cases: 900ºC for 100 hours, 1000ºC for 10 hours, 1000ºC and for 100 hours.

Simulating a pebble desorption for 10 to 100 hours adds significant computational time to the TRIDENT Mod1 simulation. Additionally, solving the diffusion equations at temperatures of 900ºC and above requires time steps of less than one second in the desorption subroutine. Therefore, the desorption calculation is only completed once for every 100 time steps in the TRIDENT Mod1 loop simulation, or every 125,000 seconds for a baseline simulation step of 1250s. Updating the desorption calculation only periodically is justifiable since the desorption factors change gradually throughout the simulation and the equilibration in pebble retention rate occurs over much larger timescales than the 125,000 seconds between desorption factor updates.

The influence of desorption conditions on the FHR tritium distribution is shown in Figure 5.32. Aside from the desorption parameters, all other conditions were consistent with the previous baseline tritium distribution simulations. As shown in Figure 5.32, the weaker desorption conditions led to less tritium removal through pebble recirculation, which was mainly offset by increased permeation through the heat exchanger. The other permeation regions also increased slightly as desorption decreased. There was only a 20% relative decrease of tritium retention in

graphite pebbles for the fully-desorbed case compared to zero desorption. However, the zero desorption case took much longer to reach equilibrium since the time dependence was based only on the 500 day pebble lifetime instead of the 50 day core residence time. Equilibrium release fractions for the desorption cases plotted in Figure 5.32 are shown in Table 5.20.

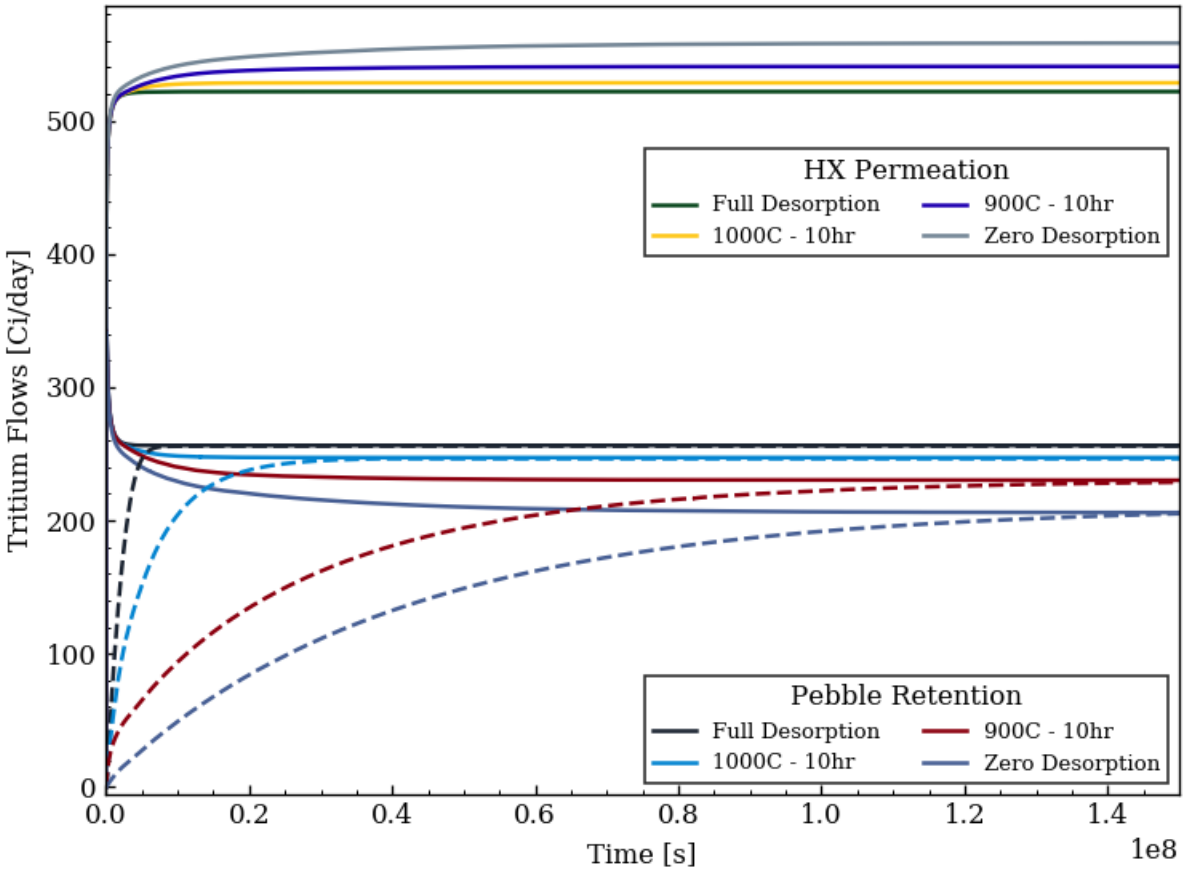

Figure 5.32. Permeation through the heat exchanger, tritium retention in core graphite pebbles (solid lines) and tritium removal in the pebble recirculation system (dashed lines) for four different desorption conditions. Pebbles were simulated with a 50 day core residence time and a 500 day total lifetime.

Table 5.20. Tritium distribution summary for the case of 1000ºC and 900ºC desorption in the pebble recirculation system for 10 hours in comparison to the baseline case (full desorption) and the case where pebbles are not desorbed but are removed after a 500 day residence time.

Release Pathway	Full Desorption	1000ºC-10hr	900ºC-10hr	Zero Desorption
Heat Exchanger	53.6%	54.3%	55.5%	57.3%
Core Pebbles	26.3%	25.4%	23.6%	21.2%
Hot Leg	8.9%	9.0%	9.2%	9.5%
Reactor Vessel	4.8%	4.8%	4.9%	5.1%
Cold Leg	4.2%	4.3%	4.4%	4.5%
Graphite Reflector	1.9%	1.9%	2.0%	2.0%
Off-Gas	0.3%	0.3%	0.3%	0.3%

As shown in Table 5.20, tritium retention rates in the core pebbles remained fairly steady despite significantly different desorption conditions. The effect can be partially explained by changes in the bulk salt and graphite surface T_2 concentrations, as shown in Figure 5.33. For the weaker desorption conditions, the tritium inventory in the pebbles increases and the T_2 concentration at the graphite surface is also raised. The higher T_2 surface concentration lowers the overall retention rate in the pebbles. However, since retention in the core pebbles is a significant fraction of the overall tritium distribution, a lower retention rate increases the T_2 concentration in the bulk salt which in turn allows for more retention to occur. Therefore, the changing T_2 concentration in Flibe creates a mitigating factor which partially compensates for the decrease in retention rate during low- or zero-desorption scenarios.

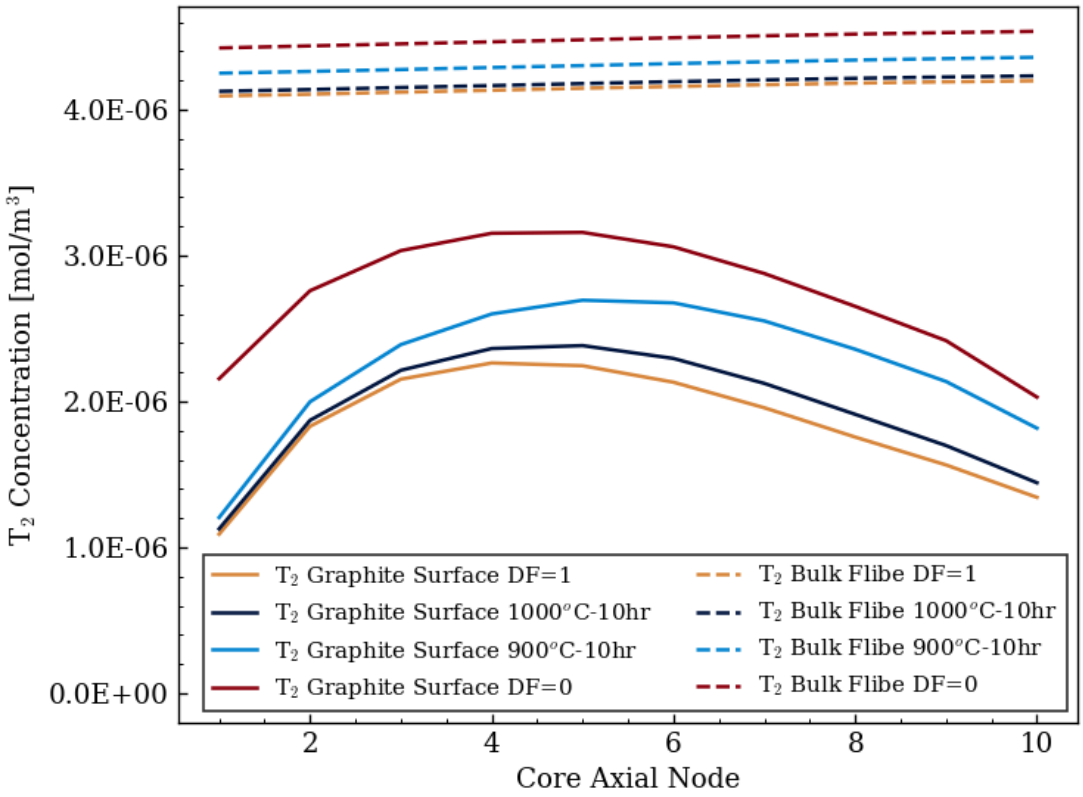

Figure 5.33. Concentration of T_2 at the graphite pebble surfaces and in the bulk salt for the various pebble desorption cases.

Another factor which allows for additional retention at various desorption conditions is the recirculation of pebbles – in all cases, pebble recirculation in the core was simulated with the same 50 day residence time. As shown in Figure 5.34, the flux of T_2 remains highest at the upper nodes of the core despite the changing graphite surface concentrations for each desorption scenario. For a pebble recirculation system which fully desorbs tritium, each pebble then only passes through the high T_2 flux region of the core once before being desorbed. In contrast, recirculating the pebbles without full desorption allows for several passes through the high flux zones, although at a relatively lower T_2 flux because of the increasing graphite surface concentration. Therefore, the recirculation of pebbles also contributes to the moderation of retention rates during low-desorption cases. Based on the desorption simulations in TRIDENT Mod1, designing a thorough desorption apparatus in the pebble recirculation system of a FHR will reduce the tritium inventory in the core pebbles, but the desorption conditions are not expected to have a significant influence on the overall tritium distribution in the reactor.

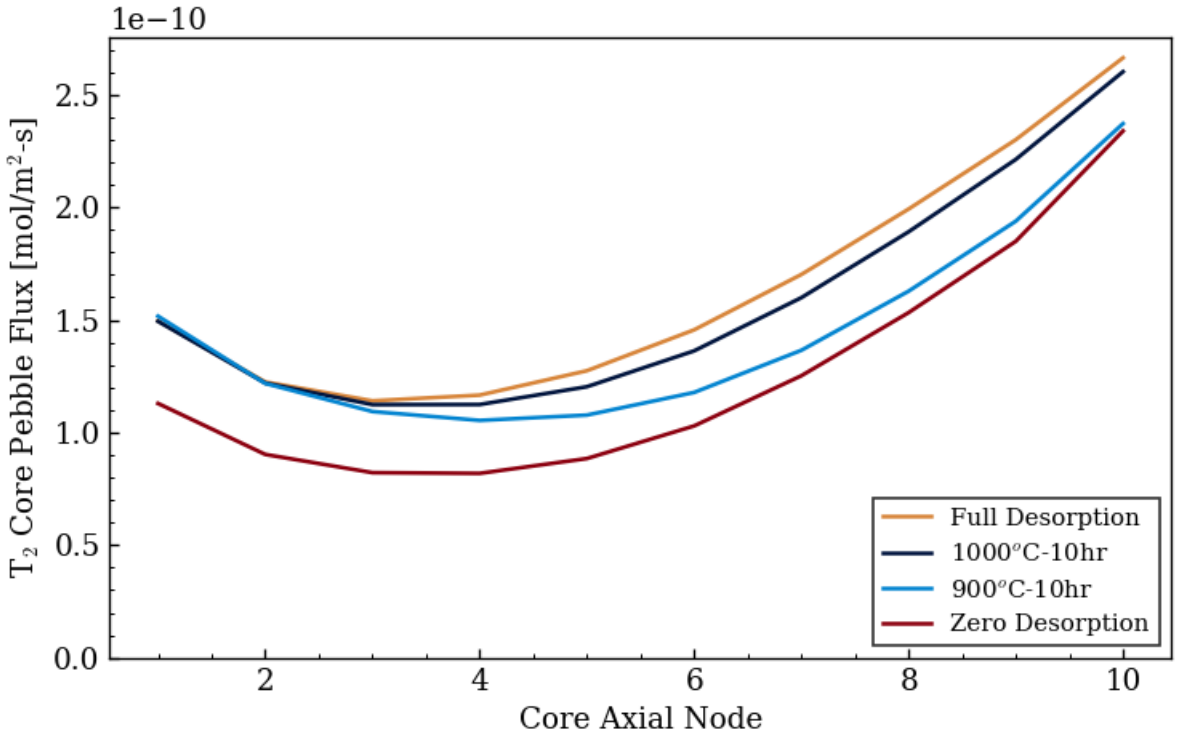

Figure 5.34. Flux of T_2 to core pebbles verses axial node in the core for each desorption case.

6. Overview of Tritium Management Strategies for the FHR

The previous results in Section 5 discuss the expected tritium release paths under baseline FHR conditions in a generic reactor design. Additionally, the change in tritium distribution among reactor regions is shown as input parameters are varied and the model assumptions are adjusted. In this section, the FHR design parameters are modified to represent various tritium control strategies and the resulting tritium releases are simulated with the TRIDENT Mod1 code. Ultimately, a FHR tritium management strategy will involve several systems and components which are not currently modeled. For example, tritium capture systems will be required to collect releases from a given reactor region and subsequent steps following capture may be required in order to convert collected tritium into a stable form for long term storage. Therefore, the full tritium management plan for a FHR cannot be determined from TRIDENT Mod1 alone until tritium collection and storage technologies are selected and incorporated into the reactor design. However, the FHR tritium distribution calculated with TRIDENT Mod1 when various tritium control systems are applied can provide useful information in understanding the potential impact of each design implementation. Furthermore, the release rates predicted by the model are helpful in determining the size and efficiency required by tritium collection systems in various regions of the plant. In this section, predicted FHR tritium releases are compared to representative values from other designs such as pressurized water reactors which discharge 800 Ci/GWe-yr and heavy water reactors which release 25,000 Ci/GWe-yr on average [29].

6.1. Technology Options for Tritium Capture and Storage

Features of the FHR design can be modified in order to promote tritium transport into favorable release streams and prevent releases in undesirable regions. Whether or not a certain type of tritium release is desirable depends, in part, on the technologies selected for tritium capture and storage. For example, the potential for tritium sequestration in a certain material will depend on the chemical form of tritium. As previously discussed, tritium which permeates into the nitrate salt intermediate loop is expected to oxidize into HTO/T_2O, permeation through metals is expected to predominantly produce HT/T_2, and HT/T_2 and TF can be present in the off-gas of the primary system. Therefore, different tritium capture strategies will be required for each region and the effectiveness of each system may vary. Methods to capture each form of tritium are summarized briefly in this section along with advantages and limitations of each technology.

Considering the tradeoffs of tritiated water storage can provide a useful frame of reference when discussing other storage options. Tritium is difficult to store in highly concentrated liquid concentrations because the addition of HTO in water can create a corrosive environment through radiolytic production of H_2O_2 [189]. Specific activities greater than 1PBq/m^3, or 27 Ci/L, were measured to shift an iron-water environment from a passivated state into the active corrosion region [189]. It is also difficult to rely on tritium decay to reduce corrosivity over time since the amount of H_2O_2 radicals produced per H-3 disintegration increases with decreasing specific activity [189]. Therefore, in order to store tritiated water in low-alloy steel vessels, the 981 Ci/day produced at equilibrium in a FHR would need to be diluted into 36.3 liters of water per day which amounts to a tritiated water production of 13.3 m^3 per year. Using storage vessels with greater corrosion resistance would increase the allowable activity and reduce the required volumes. However, any tritiated water storage system would also need to strictly limit leaks of liquid water as well as release of evaporating HTO vapor. For these reasons, among other considerations, the tritium which builds up in the heavy water coolant and moderator of CANDU reactors is typically extracted through a process such as combined electrolysis and catalytic exchange [190, 191].

Collecting HTO on an adsorbent material, instead of storage as a liquid, can alleviate potential concerns from tritiated water liquid leaks or evaporated moisture releases. For molecular sieve materials such as SiO_4-AlO_4 zeolites, water is captured through strong interactions and the adsorption capacity for water can reach 19.6%, as measured by the ratio of captured water mass to mass of sieve material [192]. Radiolysis of tritiated water will also occur from HTO stored on molecular sieve, but corrosion is less of a concern since the zeolites are chemically inert [192]. However, the radiolysis of tritiated water will liberate H_2 from the molecular sieve [192], and thus production of HT is also likely possible. Therefore, a system to recombine HT back into HTO should be included in a storage vessel if molecular sieve is intended to be used as a long term tritium sequestration material. If a HT recombination system is feasible, then HTO can be stored on molecular sieves in concentrations up to the potential water loading limits of the adsorbent. Recombiner systems could also be used during the tritium capture process to convert HT/T_2 into HTO/T_2O to allow for adsorption onto molecular sieve. However, since HTO is 10,000 times more biologically hazardous than HT [25], a recombiner system should only be employed in certain conditions where HT/T_2 capture is exceedingly difficult, the HT/T_2 concentrations are high and cannot be released, and conversion to HTO significantly improves capture efficiency.

In practice, the specific of activity of tritium on an adsorbent will depend on the concentration of other moisture impurities present, since both H_2O and HTO will be collected together on the sieve. Thus, the molecular sieves would be the most effective in the off-gas system of the intermediate loop, where tritium is expected to oxidize into HTO/T_2O and dry cover gas will likely be used to limit corrosion from the nitrate salt [193]. Molecular sieve detritiation systems have previously shown capacity to maintain gases as dew points of -60ºC [194], which corresponds to 6.59 ppm H_2O by mass [195]. For an intermediate loop cover gas flow of 100 liters/min pre-dried to the -60ºC dew point, a total mass of 1.16 g of H_2O and 0.676 g of HTO would be produced per day assuming a tritium source equal to the full 981 Ci/day equilibrium generation. The tritiated water could then be captured using 8.98 g of molecular sieve per day or 0.0136 L/day of sieve volume at an adsorbent density of 0.66 g/cc [196]. While the 0.0136 L/day is a significant improvement over the volume required for liquid water storage, the molecular sieve volume could be further reduced by decreasing the gas flow rate or the lowering moisture impurity levels.

Another tritium capture method with a high capacity for specific activity is storage as a metal hydride on a getter bed. For example, titanium metal is used as the primary storage technology for tritium which is extracted from the heavy water coolant and moderator of CANDU reactors [197]. The titanium getter beds used at the Wolsong CANDU plant tritium removal facility are designed to contain 18.5 PBq (500,000 Ci) of tritium on 1 kg of titanium sponge inside of a 6.5 L vessel [34]. Therefore, 981 Ci/day from a FHR would require 0.0128 L/day of storage using similar vessels at the same utilization rates. It is also possible that titanium metal could be used to capture TF by first converting the tritium through equation 6.1, which is written with a variable valence state for TiF_2, TiF_3, or TiF_4 [198]. However, the reaction of titanium would reduce the storage capacity of the getter bed since titanium fluoride is more stable than titanium hydride [199]. Similarly, the oxidation of titanium from ambient air would also prevent a hydride getter bed from effectively capturing tritium. Therefore, a titanium getter bed would best be used in the inert gas environments of a FHR, such as in the primary system off-gas or the cover gas of a pebble desorption facility.

Eq. 6.1
$$xTF + Ti \rightarrow TiF_x + \frac{x}{2}T_2$$

When considering molecular sieve or metal hydrides as a tritium storage form, the reactor building will likely be the most difficult region to capture tritium from in a FHR. Analyzing reactor building tritium control would require additional details of a FHR plant design, and evaluating the overall dose consequence of releases will depend on the chemical forms of tritium, the dilution rate in the ventilation systems, and potential mitigations through a large release stack. Considering tritium capture only, general concepts can be taken from other design sources for preliminary estimations. A schematic of the proposed Mk-1 FHR reactor building design is shown below in Figure 6.1. It may be possible to isolate regions in the building for dedicated tritium removal, so taking 10% of the full volume of the cylindrical shield building shown in Figure 6.1 results in 2,239 m^3. Air circulation rates in the Mk-1 FHR reactor building were not explicitly set in the design, but the ventilation rate of a commercial reactor could be used as a substitute since both systems should have similar safety functions. The ventilation rate of the GE BWR Mark II secondary containment, for example, is designed to limit the inleakage of ambient air to 50% of secondary containment volume per day [200]. Applying a 1,120 m^3 per day air inflow with an optimistically low dew point of 0ºC (3640 ppm H_2O by mass) produces roughly 5 kg of water per day which requires 38.4 L/day of molecular sieve. Filling the reactor building with inert gas would enable the use of titanium getter beds, but would also prohibit personnel from performing online maintenance in inerted regions of the building. With a 1ppm O_2 impurity concentration and the same inleakage flow rate, the amount of oxygen entering the building would still outnumber the mols of tritium produced at 0.0474 mol O_2/day and 0.0338 mol-T/day. Therefore, the capacity of titanium getter beds would likely be below their expected performance under an inert gas environment in the reactor building.

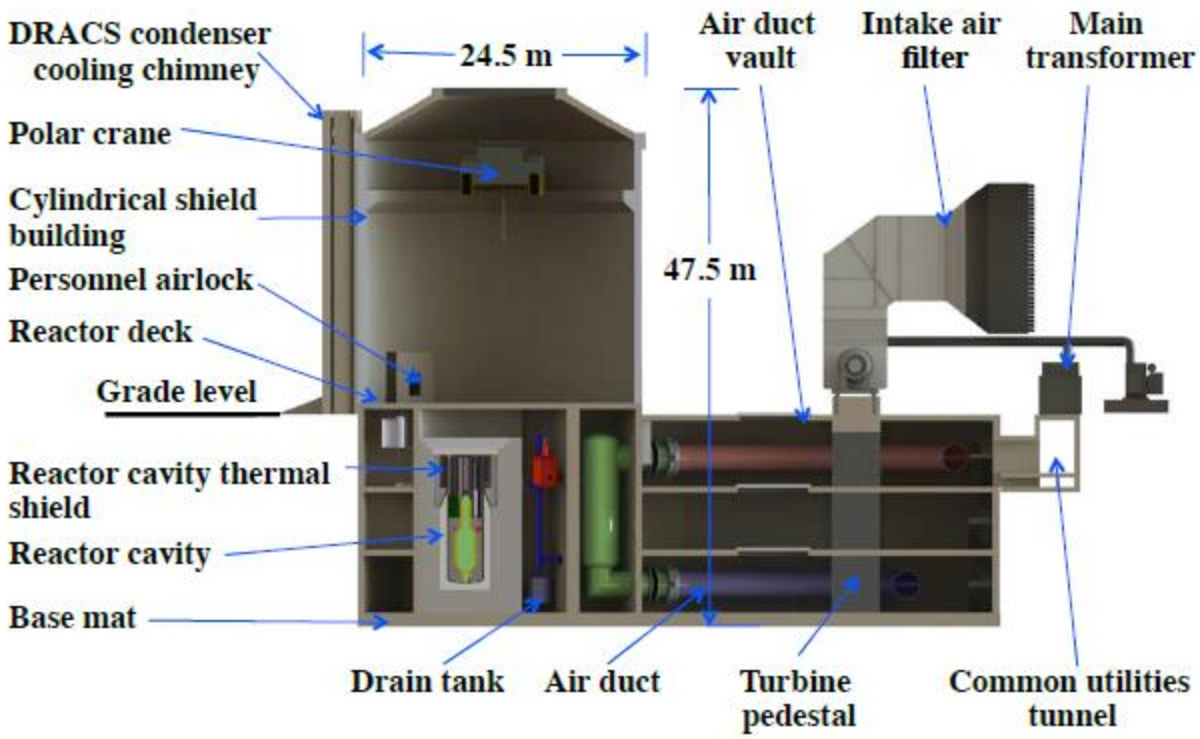

Figure 6.1. Mk-1 FHR reactor building diagram. From [5].

In summary, potential tritium capture technologies exist for the FHR which have been previously demonstrated in other systems. The storage of tritium on titanium getter beds has been extensively used in CANDU reactors [34, 201], and molecular sieve beds have been used on the exhaust detritation system of the JET tokamak as well as other laboratory applications [194, 202]. Molecular sieve driers could be used to capture HTO/T_2O from the nitrate salt intermediate loop off-gas while titanium beds could be used to capture T_2 from the primary loop. Both technologies have the potential to create stable long-term waste forms with attractive storage volume utilization. Among various regions of the FHR plant, the reactor building will likely present the most challenging conditions for tritium capture because of the large volume and higher potential concentrations of moisture and oxygen, which compete against tritium for storage on metal hydrides and molecular sieve adsorbents. Therefore, tritium distribution calculations with TRIDENT Mod1 were performed with the intent to identify strategies to limit the permeation of tritium through the reactor vessel, hot leg, and cold leg. Limiting permeation through these zones into the reactor building will likely provide the greatest benefit towards lowering the cost and complexity for a tritium management strategy which focuses on capturing tritium prior to environmental release.

6.2. Influence of Permeation Barrier Coatings

Permeation barrier coatings can assist in creating a favorable tritium distribution in a FHR by reducing permeation through unwanted zones and promoting release in other regions. One significant limitation of a tritium management strategy which purely relies on permeation barriers is that coating performance may degrade over time in the reactor environment. As previously discussed in Section 2.4.2, even small changes in the integrity of barrier layers can degrade the overall permeation resistance [203]. As a result, a permeation reduction factor practical upper limit of 1000 was suggested for any coating used in an irradiation environment [76]. The significance of radiation damage, corrosion, and other degradation mechanisms may vary for coating applications in different regions of a FHR. Furthermore, coating environments will be significantly different depending on whether they are applied on inner, Flibe-facing surfaces or on the exterior of the primary system structural metals. Verifying the long-term performance of permeation barriers in a FHR environment will require further experimental testing in prototypical conditions. In this section, the coating materials themselves are not explicitly modeled in TRIDENT Mod1. Instead, a fixed PRF is set for a given set of regions and the resulting tritium distribution is calculated. Therefore, the TRIDENT Mod1 results can demonstrate what impacts on the overall tritium distribution are possible for varying levels of coating performance, and thus can assist in providing coating performance requirements for future FHR designs.

6.2.1. Coatings Applied to Flibe-Facing Surfaces

One initial reference case is to consider a Flibe-facing internal coating on all metallic surfaces of the FHR: hot leg, heat exchanger, cold leg, and reactor vessel. A fully-coated scenario could be pursued in the case that permeation into the reactor building as well as the intermediate loop is intended to be minimized, and thus tritium collection in the primary system would be the main management strategy. Considering the previously discussed permeation reduction factor practical limit of 1000 for reactor applications, as well as the unknown influence of molten Flibe on long-term coating stability, a limit of 500 was used for the PRFs applied in TRIDENT Mod1. The model input values for PRFs were also selected based on discussions with FHR designers to confirm the feasibility of the modeled PRF range compared to preliminary experimental results [174]. As shown in Section 5, the permeation reduction factor for inner-surface coatings directly reduces the flux of T_2 to metallic surfaces. However, the resulting release rate is not simply the

baseline value divided by the PRF since the bulk T_2 concentration in Flibe also increases as release rates are reduced. As shown in Figure 6.2, the retention rate of tritium in the graphite pebbles increases significantly because of the increased bulk concentration. Graphite pebbles were still well below the capacity limits in high-energy trapping sites since a full desorption was assumed with a pebble core residence time of 50 days. Applying zero-desorption instead, the decrease in pebble retention rate compared to the full-desorption case in Figure 6.2 would result in a more significant drop in retention rates compared to the baseline cases in Section 5.4.3. Therefore, designing for thorough desorption conditions in the pebble recirculation system and applying coatings to the inner-surfaces of structural metals in a FHR is one method to reduce permeation through the heat exchanger and promote the retention in pebbles into the dominant tritium transport pathway.

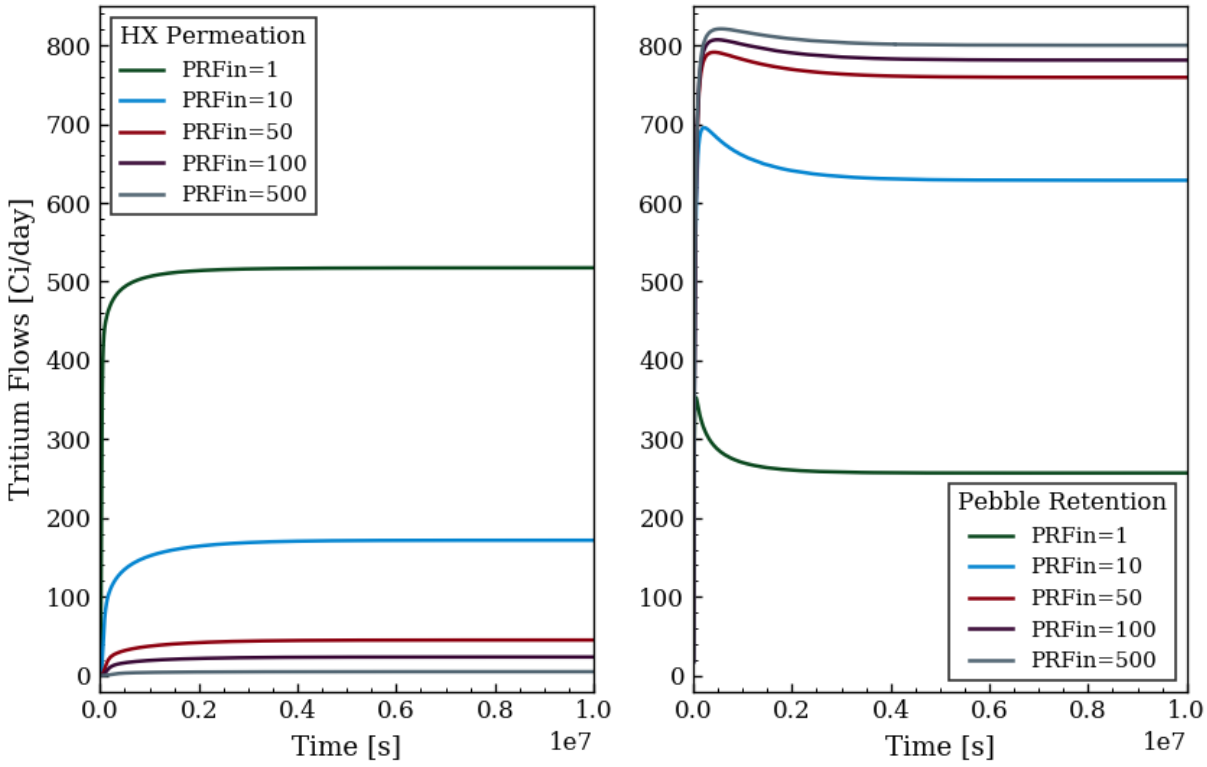

Figure 6.2. Tritium permeation through the heat exchanger and retention on core pebbles when coatings of a specified PRF are applied to all Flibe-facing metallic surfaces in a FHR.

As with the heat exchanger, the permeation rates through the hot leg, cold leg, and reactor vessel are similarly reduced as inner-coating permeation resistance increases. The buildup of tritium concentration in Flibe also increases the evolution rate to the primary off-gas system, but still the tritium evolution does not become a major release path in the overall distribution. Tritium evolution could be further increased by a higher redox potential, but TF was negligible in all cases since the fully-reduced redox potential was imposed for each simulation. Release rates from the remaining FHR regions in the fully-coated scenario are plotted in Figure 6.3. The increase in T_2 concentration and decrease in permeation rates for the higher PRF cases is summarized in Table 6.1.

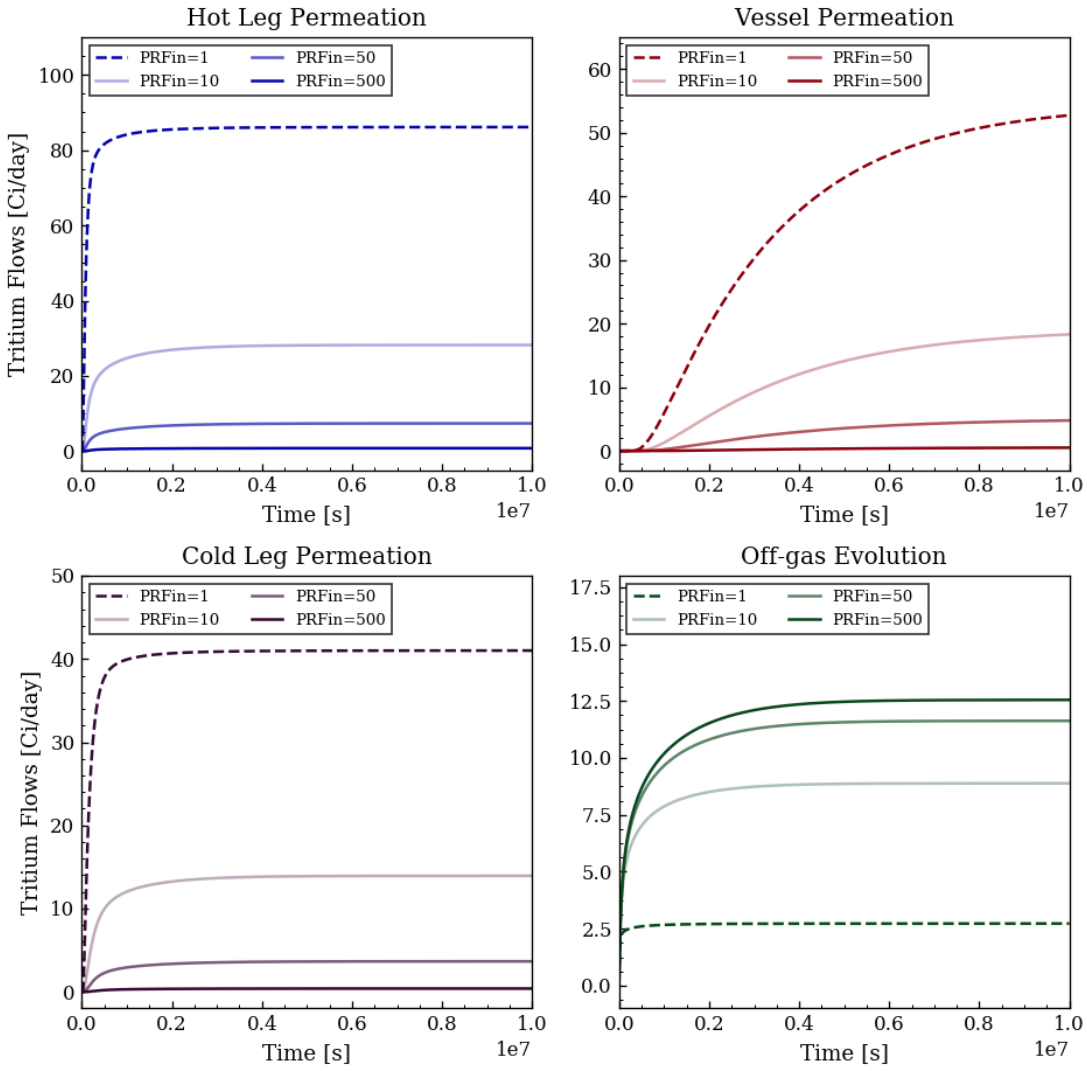

Figure 6.3. Remaining tritium release pathways for the Flibe-facing coatings on applied to all FHR metallic regions.

Table 6.1. Bulk Flibe T_2 concentration and tritium releases for Flibe-facing coatings applied to all FHR regions.

Value	Baseline	PRF_{in}=10	PRF_{in}=50	PRF_{in}=100	PRF_{in}=500
T_2 [mol/m^3]	$4.26 \cdot 10^{-6}$	$1.38 \cdot 10^{-5}$	$1.82 \cdot 10^{-5}$	$1.89 \cdot 10^{-5}$	$1.96 \cdot 10^{-5}$
Heat Exchanger	54.0%	19.5%	5.41%	2.84%	0.593%
Core Pebbles	26.8%	72.5%	91.3%	94.7%	97.7%
Hot Leg	8.99%	3.21%	0.888%	0.466%	0.0973%
Reactor Vessel	5.62%	2.16%	0.600%	0.315%	0.0658%
Cold Leg	4.28%	1.59%	0.440%	0.231%	0.0483%
Off-gas	0.285%	1.01%	1.40%	1.47%	1.53%

As shown in Table 6.1, the sum of tritium permeation from all regions amounts to 0.804% of the tritium distribution under a PRF_{in}=500 scenario. For an equilibrium generation rate of 981 Ci/day, the 0.804% permeation still results in a release of 2880 Ci/yr into the reactor building and intermediate loop. In comparison, a typical pressurized water reactor (PWR) will discharge 800 Ci/GWe-yr while a heavy water reactor (HWR) will release 25,000 Ci/GWe-yr. Scaling the release values to the electricity output of a 140 MWe FHR results in 112 Ci/yr and 3500 Ci/yr to match PWR and HWR discharge levels, respectively. Therefore, unmitigated releases to the reactor building and intermediate loop in a FHR with a 500 PRF coating on all metal surfaces would produce less environmental discharge than a HWR, but significantly more release than a PWR. If the PRF_{in} value was 100, then the FHR releases to the reactor building and intermediate loop would amount to 13,800 Ci/yr and would thus be above both HWR and PWR values. In summary, a fully-coated FHR would require permeation barriers with a PRF_{in} of near 500 throughout the reactor life in order to maintain releases below HWR levels if tritium capture was only designed for the primary system. For lower permeation resistance from inner-surface coatings, tritium control systems would likely also be required in the reactor building and intermediate loop.

In all inner-coating cases shown in Table 6.1, the heat exchanger remains as the greatest release path for tritium in the metallic permeation zones. The TRIDENT Mod1 results demonstrate the difficulty in achieving a tritium distribution through inner-surface coatings where permeation to the heat exchanger can be freely released without additional mitigation. Therefore, a more strategic arrangement of barriers would be to apply coatings to the hot leg, cold leg, and reactor vessel inner-surfaces while leaving the heat exchanger uncoated and adding a tritium capture system to the intermediate loop. Compared to the fully-coated cases, the partial coating scenario

has the added benefit of maintaining a similar T_2 concentration in the salt in all cases, since the main release path remains as permeation into the heat exchanger and retention on core pebbles, as shown in Figure 6.4. As a result, the coatings have a greater effect in reducing permeation into the reactor building for a given PRF_{in} value since reducing hot leg, cold leg, and reactor vessel permeation has only a mild effect on the buildup of T_2 concentration in the primary loop. The sources of permeation into the reactor building in the partially-coated cases are shown in Figure 6.5, while the full distribution and bulk T_2 concentration from each simulation is summarized in Table 6.2.

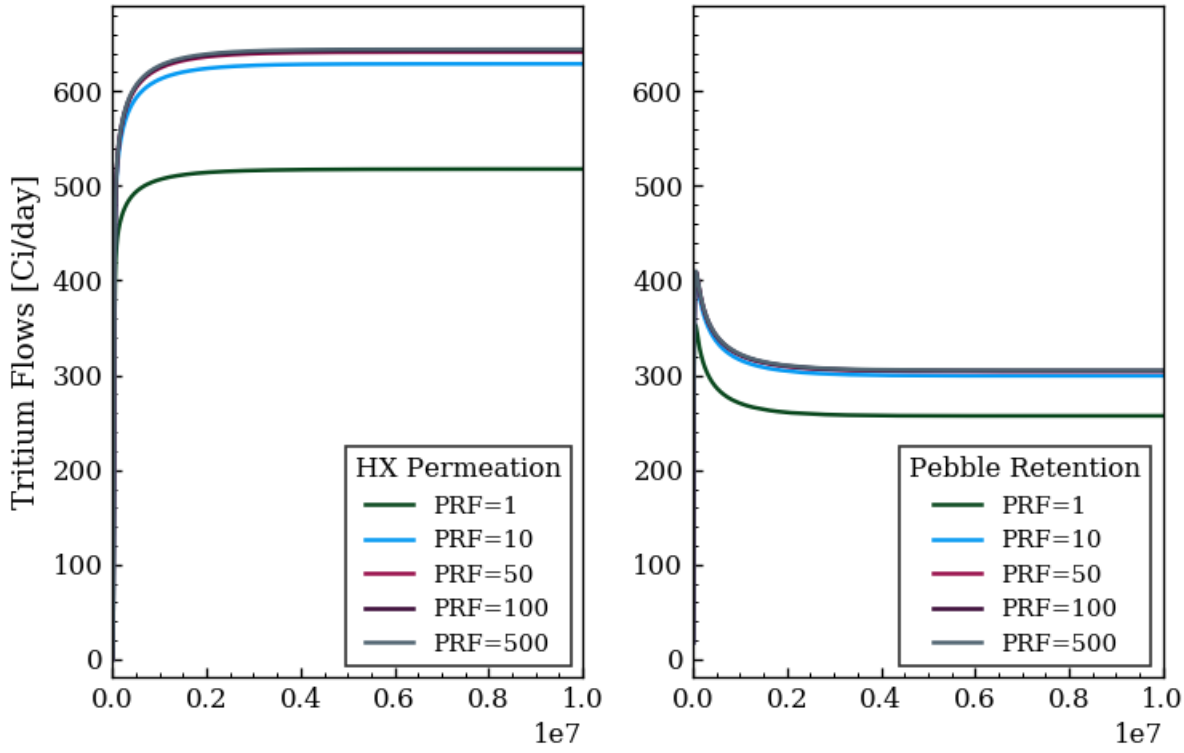

Figure 6.4. Heat exchanger permeation and retention on core pebbles in when coatings of various PRFs are applied to the Flibe-facing surfaces of the hot leg, cold leg, and reactor vessel.

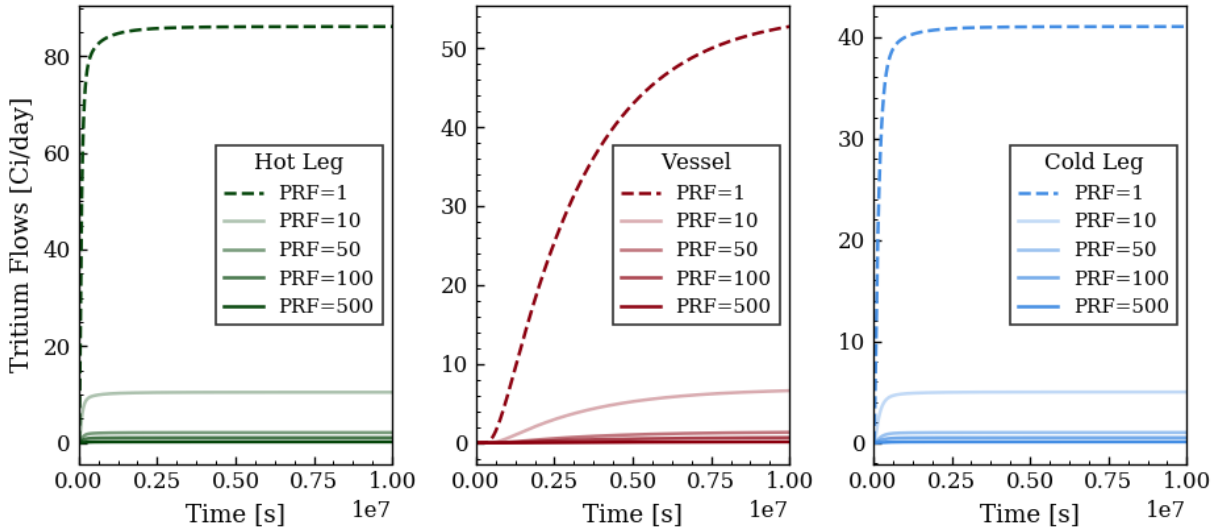

Figure 6.5. Permeation rates through the regions where Flibe-facing coatings are applied in the partially-coated FHR scenario.

Table 6.2. Bulk Flibe T_2 concentration and tritium releases when the Flibe-facing coatings of various permeation resistance are applied to the hot leg, cold leg, and reactor vessel only.

Value	Baseline	PRF_{in}=10	PRF_{in}=50	PRF_{in}=100	PRF_{in}=500
T_2 [mol/m^3]	$4.26 \cdot 10^{-6}$	$5.15 \cdot 10^{-6}$	$5.25 \cdot 10^{-6}$	$5.26 \cdot 10^{-6}$	$5.27 \cdot 10^{-6}$
Heat Exchanger	54.0%	65.9%	67.3%	67.4%	67.6%
Core Pebbles	26.8%	31.4%	31.9%	32.0%	32.0%
Hot Leg	8.99%	1.10%	0.224%	0.112%	0.0225%
Reactor Vessel	5.62%	0.716%	0.146%	0.073%	0.0147%
Cold Leg	4.28%	0.525%	0.107%	0.054%	0.0108%
Off-gas	0.285%	0.346%	0.353%	0.353%	0.354%

If tritium capture is feasible in both the intermediate loop and primary systems, then there are clear benefits in coating only the hot leg, cold leg, and reactor vessel. First, the partially-coated scenario requires permeation barriers on only 2.5% of the surface area as the fully-coated condition, since the sum of inner surface areas for the hot leg, cold leg, and vessel amounts to 123.8 m^2 compared to 5750 m^2 from the heat exchanger. The overall permeation reduction into the reactor building is also greater for the partially-coated case. As shown in Table 6.2, at a PRF_{in} of 50, the reactor building permeation accounts for 0.447% of the total tritium distribution. For an equilibrium generation rate of 981 Ci/day, the PRF_{in}=50 case results in a reactor building release of 1710 Ci/yr, which is lower than the average 3500 Ci/yr HWR tritium discharge rate scaled to

FHR power output [29]. The same is not true for the fully-coated case, where reactor building permeation would be 6900 Ci/yr using the values in Table 6.1. When the PRF_{in} is raised to 500 for the hot leg, cold leg, and vessel, the reactor building release is 172 Ci/yr, which approaches the PWR release goal of 112 Ci/yr. Therefore, the partial coating scenario is an efficient way to utilize inner-surface coatings to reduce permeation into the reactor building. However, whether or not tritium control in the reactor building is required will depend on the achievable coating performance, the efficiency of tritium capture systems in various FHR regions, and the true release targets set by future FHR designs.

6.2.2. Coatings on Exterior Reactor Surfaces

When considering coatings on the inner- and outer-surfaces of FHR structural metals, there are numerous advantages to the use of exterior coatings. Most notably, the exterior coatings are not in contact with Flibe salt and therefore only require corrosion resistance against ambient air at elevated temperatures in the case of the reactor building surfaces, or molten nitrate salt for secondary-side heat exchanger coatings. Using coatings in these environments allows for a wider range of possible coating materials when the condition for stability against molten Flibe is removed. Furthermore, coatings on the exterior surfaces of a FHR will be easier to inspect during operation and could potentially be reapplied during the reactor lifetime if a degradation in performance is observed.

One significant drawback to exterior coatings is that, as previously discussed, the permeation process in a FHR will be mainly limited by mass transport in Flibe, rather than by diffusion of tritium in the metal. Therefore, outer-surface coatings can only provide permeation resistance if the tritium concentration in the metal increases significantly and the boundary condition at the salt-metal interface begins to limit the concentration gradient in the salt. In contrast, coatings on Flibe-facing surfaces can provide permeation resistance by preventing tritium from initially entering the metal regions. As shown in Section 5, various degrees of permeation resistance are created by the 316 stainless steel in the FHR depending on tritium concentrations in each metal region. Tritium in the metal increases with higher fluxes of T_2 from the salt, and longer transit times during diffusion from thicker metal components or lower temperatures. As a PRF is applied to the metal outer surface, the concentration of diffusing tritium in the metal increases roughly linearly with the strength of the coating. However, for PRF_{out} values of up to 500, the rise

in concentration of tritium in the heat exchanger metal does not significantly decrease in the influx of T_2 from Flibe. The heat exchanger permeation and pebble retention rates for various PRF_{out} values applied to all primary loop exterior surfaces are shown in Figure 6.6. Results from Figure 6.6 confirm the observations from the Mk-1 reactor simulations in the original TRIDENT model, where outer-surface coatings delayed the permeation rate, but were not able to significantly decrease the equilibrium permeation through the heat exchanger [3]. In fact, the heat exchanger permeation rate actually increases with stronger outer-surface coatings since a higher PRF_{out} has some influence on decreasing permeation rates though the other reactor zones.

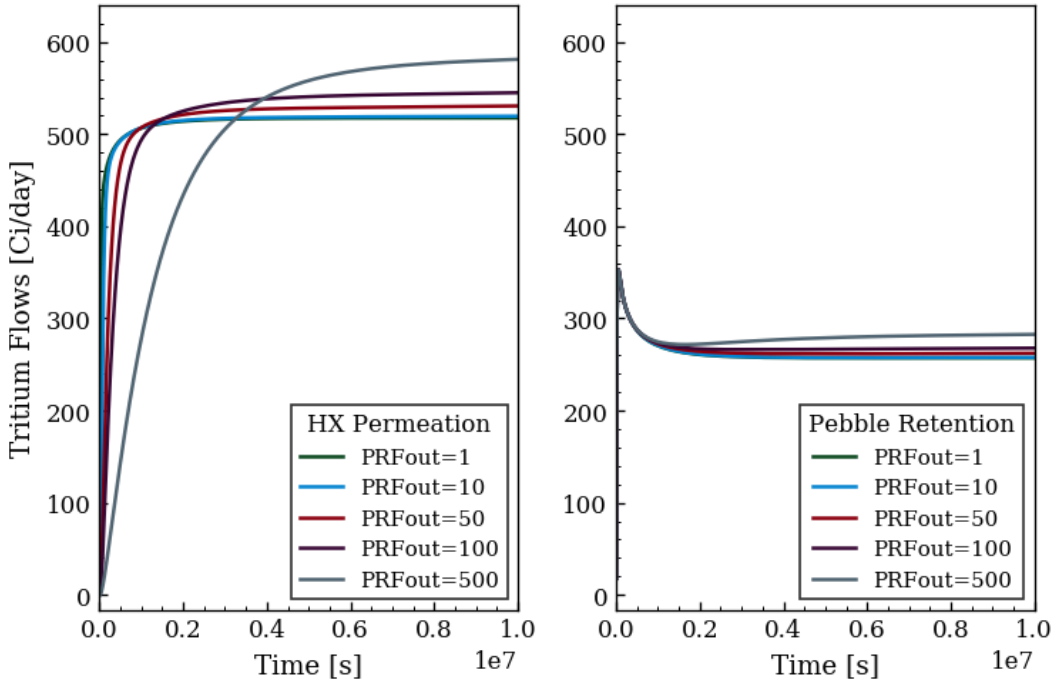

Figure 6.6. Permeation through the heat exchanger and retention on core pebbles as coatings of various PRFs are applied to all exterior metal surfaces of the primary system.

The varying effect of exterior coatings on the permeation rates can be further explained by examining the concentration profiles within the 316 stainless steel of FHR regions. Concentration profiles for the heat exchanger outlet and the cold leg are plotted in Figure 6.7 to provide an example of two metal regions both modeled at 550ºC. For the baseline case of with a PRF_{out} of 1, the concentration at the exterior surface is slightly greater than zero because of the modeled recombination resistance. The slope in the concentration profile is proportional to the tritium flux, which is significantly higher in the cold leg than the heat exchanger because the mass transfer coefficients in Flibe are $5.63 \cdot 10^{-5}$ m/s and $3.66 \cdot 10^{-6}$ m/s for each region, respectively. A higher

PRF_{out} value has the effect of raising the entire concentration profile in the metal. However, at a PRF_{out} of 500, the concentration of tritium in the heat exchanger at the salt interface (depth of zero) is only slightly above the baseline cold leg surface concentration. As previously stated, the cold leg creates less than 1% of overall permeation resistance from diffusion in the metal at the baseline, uncoated conditions. Therefore, permeation resistance in the heat exchanger does slightly increase at high PRF_{out} values, but the greater increase in permeation resistance in the hot leg, cold leg, and reactor vessel results in an overall higher rate of heat exchanger permeation when outer surface coatings are applied to all metal exteriors.

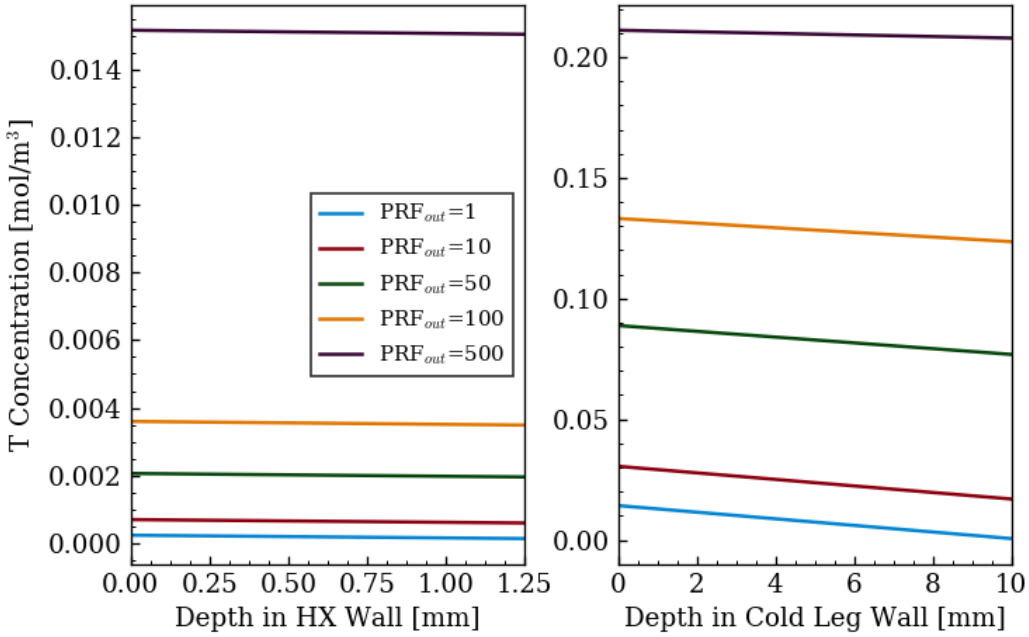

Figure 6.7. Tritium concentration profile inside the 316SS out the heat exchanger outlet (left), and average concentration profile in the cold leg (right) for various outer coating PRFs.

The buildup of diffusing tritium concentration in the cold leg metal shown in Figure 6.7 does lead to a noticeable increase in overall permeation resistance, which leads to a decrease in the equilibrium permeation rate through the region. Similarly, a decrease in permeation rate for the hot leg and vessel also occurred for greater outer barrier reduction factors, as shown in Figure 6.8. Among the regions shown in Figure 6.8, the relative decrease in permeation rate for each PRF was largest for the reactor vessel. As the thickest metal region at the lowest temperature in the loop, the reactor vessel was shown to have the highest permeation resistance of the structural metal zones under baseline FHR conditions. Therefore, the exterior coating surfaces best amplify the

permeation resistance of the vessel compared to other metallic regions. For example, the ratio of permeation fractions for the PRF_{out} of 500 case to the baseline case was 0.244 for the hot leg, 0.238 for the cold leg, and 0.157 for the vessel, as shown by the distribution results in Table 6.3. While higher tritium concentration in metals leads to additional permeation resistance, elevated tritium concentrations produced by exterior-surface coatings could potentially lead to embrittlement issuses from tritium decay into helium-3, which is discussed in Appendix B.

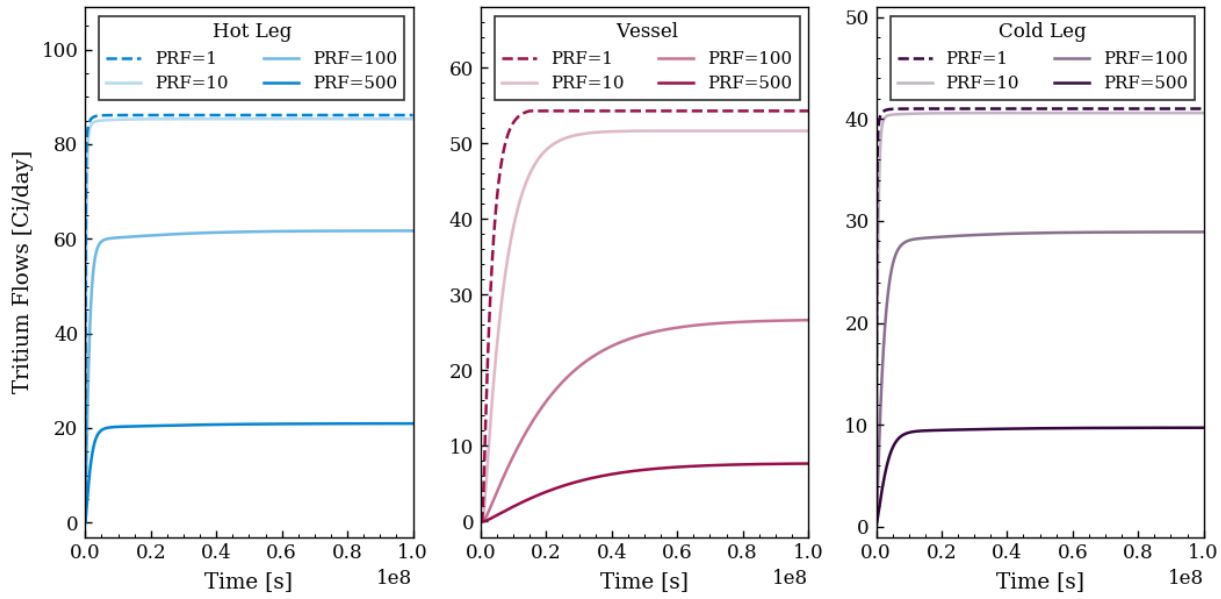

Figure 6.8. Permeation rates in the hot leg, vessel, and cold leg when outer-surface coatings of various permeation reduction factors are applied to all regions.

Table 6.3. Tritium distribution and bulk Flibe T_2 concentrations for tritium permeation barrier coatings applied to all exterior surfaces in TRIDENT Mod1.

Value	**Baseline**	**PRF_{out}=10**	**PRF_{out}=50**	**PRF_{out}=100**	**PRF_{out}=500**
T_2 [mol/m^3]	$4.26 \cdot 10^{-6}$	$4.29 \cdot 10^{-6}$	$4.44 \cdot 10^{-6}$	$4.62 \cdot 10^{-6}$	$5.07 \cdot 10^{-6}$
Heat Exchanger	54.0%	54.3%	56.4%	58.8%	64.6%
Core Pebbles	26.8%	26.9%	27.8%	28.7%	31.0%
Hot Leg	8.99%	8.90%	7.94%	6.45%	2.19%
Reactor Vessel	5.62%	5.32%	3.89%	2.76%	0.88%
Cold Leg	4.28%	4.24%	3.75%	3.02%	1.02%
Off-gas	0.285%	0.286%	0.297%	0.309%	0.340%

The distribution results in Table 6.3 show that exterior permeation barrier coatings are not effective in reducing tritium release through the heat exchanger. Repeating the runs with coatings removed from the heat exchanger but maintained in other regions resulted in nearly the same tritium distributions – heat exchanger permeation was 0.1% higher in terms of overall release for the PRF_{out}=500 case when coatings were simulated only on the hot leg, cold leg, and reactor vessel. In the fully-coated cases, permeation rates were reduced for the hot leg, cold leg, and reactor vessel, but the decrease in permeation was relatively less than for the Flibe-facing coatings at a given permeation reduction factor. Reactor building releases in the fully-coated case amount to 14,600 Ci/yr for a PRF_{out} of 500 based on the distribution values in Table 6.3. Therefore, unless outer coatings can maintain permeation reduction factors of over 500, it is unlikely that an exterior-surface coating can be used as the sole defense against unmitigated releases of tritium into the reactor building. If a reactor building tritium control system is then needed, and the cost and complexity of the system requirements scales with of the total amount of tritium collection required, then outer-surface coatings would be beneficial in lowering the release of tritium into the reactor building and reducing the design limits required for corresponding tritium capture technologies.

In summary, coatings on the outer surfaces of FHR structural metals are only likely to provide a supporting role in the overall tritium management strategy. Compared to Flibe-facing barriers, outer surface coatings have a weaker influence because the permeation process in FHRs is mainly limited by mass transfer in Flibe, rather than diffusion through metals. Coatings on outer-facing surfaces can only suppress permeation if an increase in tritium concentration in the metal leads to a significantly higher T_2 boundary value at the salt-metal interface. In the heat exchanger, for example, the T_2 boundary condition is very low in the uncoated scenario, and remains negligible up to permeation reduction factors of 500 on outer surface coatings. Therefore, practical exterior surface coatings can only be used to reduce permeation from the hot leg, cold leg, and reactor vessel. However, the expected permeation rates with PRFs of 500 will still be sufficiently high as to require tritium control systems in the reactor building if exterior coatings are used as the sole mitigation strategy. Tritium capture systems could be avoided with PRFs above 500, but a more effective exterior coating will also potentially lead to a degradation of mechanical properties through a higher helium-3 concentration caused by tritium decay. At a PRF_{out} value of 500, outer surface coatings applied to the hot leg, cold leg, and reactor vessel could reduce the permeation

rate into the reactor building to 21.7% of the rate calculated for the uncoated case, based on values in Table 6.3. A useful application for outer-surface coatings could exist if a tritium capture system is designed into the FHR reactor building, and the tritium capture and storage characteristics of the system have a significant dependence on the release rate of tritium into the building.

6.3. Tritium Extraction System Concepts and Performance

Permeation barrier coatings are a type of tritium management intervention which does not significantly change the design of the FHR reactor and supporting systems. The efficacy of a tritium management strategy based on coatings relies on the permeation resistance and long-term stability of the barrier materials, but does not require any major new systems to be added to the plant. In contrast, another approach is to incorporate a large-scale tritium extraction system into the primary coolant loop. The purpose of a tritium extraction system is to create a favorable collection stream for tritium release, contain a significant fraction of the overall tritium distribution, and minimize tritium releases in other regions of the plant where tritium capture is more difficult. Since the tritium extraction system must compete for releases against the tritium transport paths native to the rest of the FHR design, the requirements for size and surface areas of any extraction system will typically be similar to that of other main components in the reactor, such as the intermediate heat exchanger. However, one advantage for extraction systems over coatings is that the design of tritium extraction systems can proceed without the development and demonstration of novel materials. For example, a tritium permeator could be fabricated with 316 stainless steel as with the other FHR structural materials and a graphite retention bed could utilize the same nuclear graphite material as the reactor core. There is currently no consensus for the preferred tritium extraction technology in FHRs since no system has yet been demonstrated in a representative large-scale test [204].

A comparative analysis of a tritium permeator, graphite retention bed, and gas stripping system was performed by Stempien using the TRIDENT model applied to the Mk-1 FHR design [3]. In this section, the analysis is repeated with an emphasis on optimization and sizing of example extraction systems. Furthermore, the graphite retention system was modeled using the updated graphite retention methodology based on pore and grain diffusion described in Section 4. The gas stripping system was modeled previously using an assumed equilibrium condition in several separation stages [3]. An equilibrium analysis can provide an estimate of the tritium extraction

efficiency of the gas stripping system, but calculating the size and pressure drop of a gas stripping column requires values for the tritium mass transfer coefficients in the gas and liquid films of a prototypical system [85], which have not been previously measured. Therefore, an analysis of the tritium permeator and retention bed is only included in this work. As with the original TRIDENT model, the tritium extraction systems are represented after the core outlet. In this manner, tritium can be removed from the salt first before flowing into the hot leg, heat exchanger, and remaining regions of the primary loop. Additionally, the higher temperatures near the core outlet should benefit each extraction process, since the mass transfer coefficient for tritium transport to metal surfaces increases with higher T_2 diffusivities in Flibe and the retention flux to graphite was previously shown to be greatest for the higher-temperature regions of the core. An illustration of the TRIDENT Mod1 reactor layout with a tritium extraction system is shown in Figure 6.9.

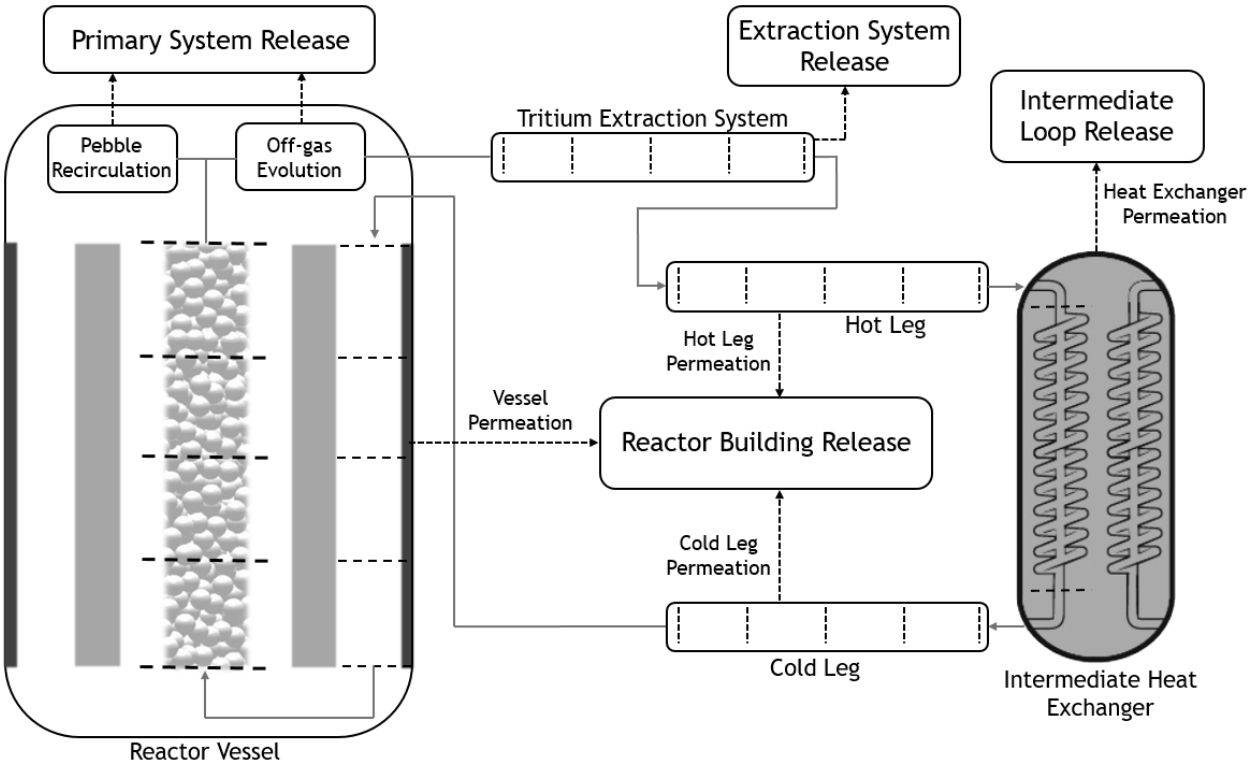

Figure 6.9. TRIDENT Mod1 calculation overview of regions and releases with the addition of a tritium extraction system following the core outlet.

6.3.1. Tritium Permeator Design Optimization

Extraction systems based on tritium permeation through metal membranes have been previously studied for potential use in breeding blankets of fusion reactor concepts [205, 206]. For use in a FHR, a tritium permeator system can be modeled using the same methodology employed for the intermediate heat exchanger. A conceptual schematic for a single permeator tube is shown in Figure 6.10 [205], while a design using several tubes and a single tritium collection volume is also possible. The concept in Figure 6.10 uses a vacuum on the downstream collection zone to effectively neglect any back-permeation of tritium and maximize the concentration gradient from the tritiated fluid to the boundary. Tritium concentration can also be treated as zero in the collection area if an inert sweep gas is used and continuously circulated through a tritium capture system. Since tritium permeation through metals at FHR temperatures would produce a predominatly T_2 chemical form in the collection zone [113], titanium or other metal hydride-forming getter beds would be a suitable tritium capture option to pair with the permeator extraction system. An important performance metric of the permeator system is the removal efficiency, η, which is defined as the decrease in tritium concentration from the fluid inlet to outlet divided by the inlet concentration, as shown in equation 6.2.

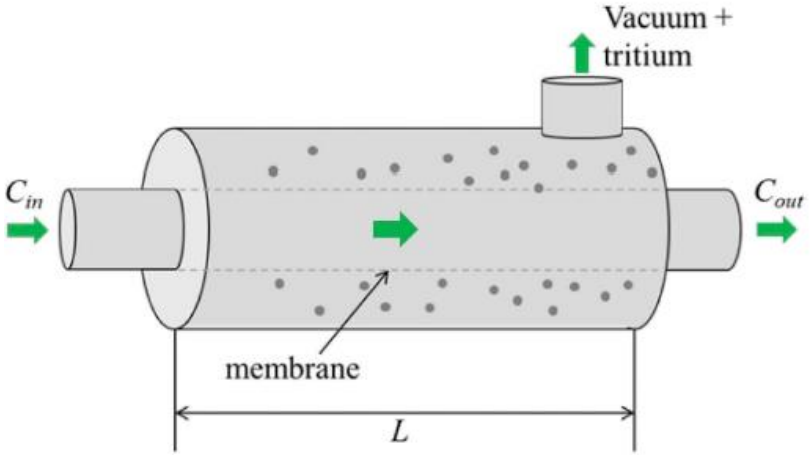

Figure 6.10. Permeator system illustration shown for extraction of tritium from a fluid in the center concentric tube.

Eq. 6.2 $$\eta = (C_{in} - C_{out})/C_{in}$$

Before implementation into the system-level model, an analysis of various permeator designs was conducted assuming an inlet T_2 concentration of $4.3 \cdot 10^{-6}$ mol/m^3 in 650ºC Flibe to simulate the core outlet conditions of the previous FHR baseline simulations. The test case is simulated with the constant inlet concentration, and then efficiency is calculated once the concentration of tritium in the permeator 316SS tubes reaches equilibrium. Initially, the effect of tube diameter on removal efficiency was examined using a 1000-tube permeator with a 1m length and 1mm tube thickness. The removal rate increases as tube diameter is decreased because the mass flow rate is held constant and the smaller diameters lead to a higher Flibe velocity, thereby accelerating mass transfer in the salt. A higher flux of T_2 from increased mass transfer also increases the steel tritium concentration and thus the permeation resistance created by the metal.

An optimal removal efficiency occurs at a certain tube inner diameter once the benefits of additional mass transfer in Flibe are counterbalanced by increases in permeation resistance. As shown in Figure 6.11, the optimal removal efficiency occurs at larger tube diameters and overall lower efficiencies for more restrictive conditions at the tube outer surface. The higher and lower bounds on the tritium recombination coefficient (referred to as High k_r and Low k_r) discussed in Figure 2.20 of Section 2.4.1 were applied along with a PRF_{out} of 10 to simulate a characteristic permeation reduction caused by an oxide layer on the stainless steel [113]. Figure 6.11 also shows the pressure drop across the permeator tube bundle as calculated by equation 6.3, where L is the tube length, d is the inner diameter, ρ is the density of Flibe, and v is the bulk velocity of Flibe in each tube [86]. The friction factor, f, is calculated with the McAdams correlation for Reynolds numbers above 10^4 and the Blasius relation for Reynolds numbers between $4 \cdot 10^3$ and 10^4 [86]. Permeator systems with Reynolds numbers significantly below $4 \cdot 10^3$ have a low degree of tritium mass transfer in Flibe and are typically out of the range of interest for design optimization.

Eq. 6.3
$$\Delta P = f \frac{L}{d} \frac{\rho v^2}{2}$$

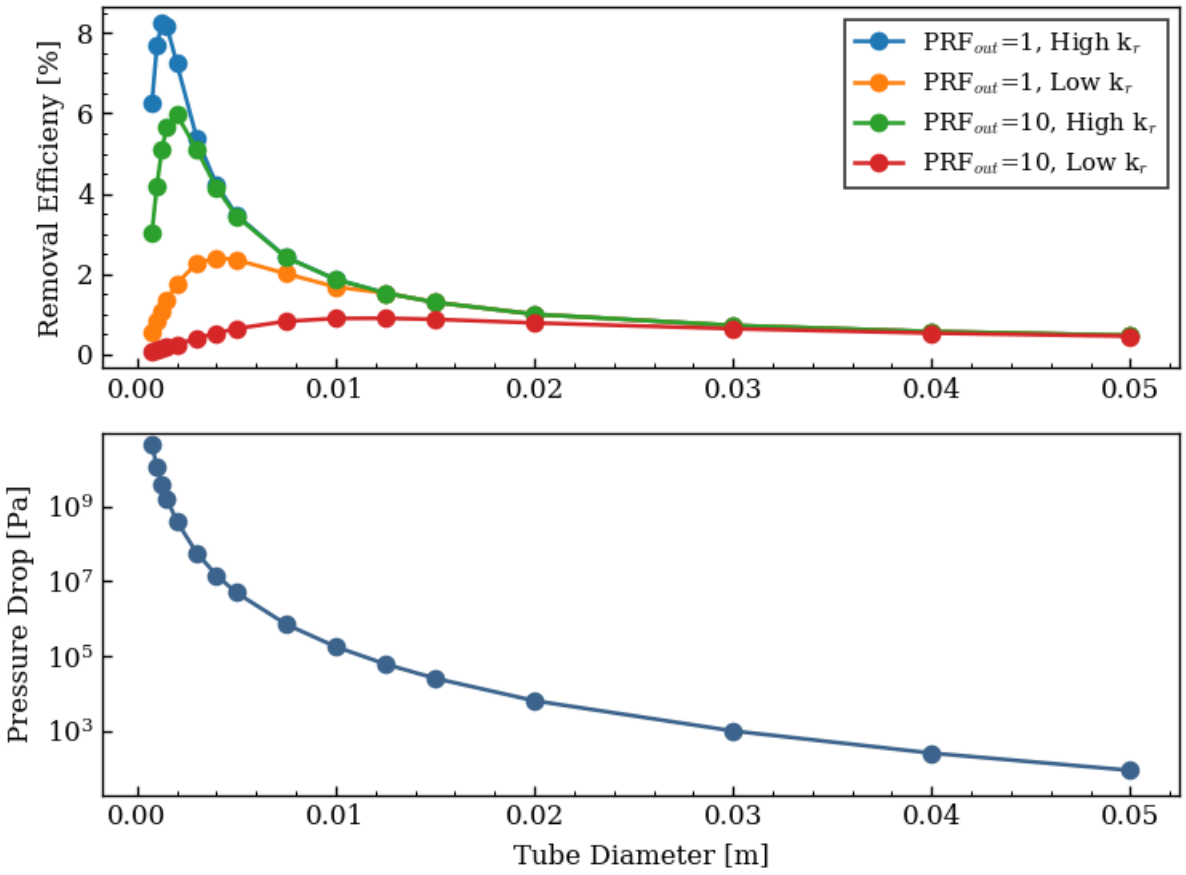

Figure 6.11. Removal efficiency for a permeator system with 1000 tubes of 1m length, 1mm in thickness, and various inner diameters. Upper and lower bounds for a 316SS recombination constant were used along with PRF_{outs} of 1 and 10 to simulate a bare tube exterior and a chromium oxide layer. The tube diameter at the maximum removal efficiency depends on the outer surface conditions and pressure drop across the system increases with decreasing diameter.

Since the pressure drop in Flibe over the permeator system increases significantly with smaller tube diameters, as shown in Figure 6.11, the maximum removal efficiency for a system constrained to a certain pressure drop will not necessarily utilize the tube diameter where mass transfer and permeation resistances are optimized. To further constrain the analysis, a pressure drop limit of 2 atmospheres can be imposed, which was selected based on the ΔP of the primary heat exchanger in the Mk-1 FHR design [5]. The pressure drop of the permeator scales linearly with tube length, as shown in equation 6.3, and thus the calculated pressure decrease for a given tube diameter in the 1m length calculations can be used to determine the tube length at a ΔP of 2 atm. As shown in Figure 6.12, a relationship exists between the total volume of Flibe inside the permeator and the tritium removal efficiency once the total pressure drop in each case is fixed. The

removal efficiency increases when the tube diameter is raised, the pressure drop decreases, and the overall length is extended to reach ΔP = 2 atm. Since the total volume of Flibe in the FHR primary loop was 50 m^3 with the baseline dimensions in Table 5.2, achieving a high-efficiency permeator system requires a significant addition of Flibe inventory to the reactor.

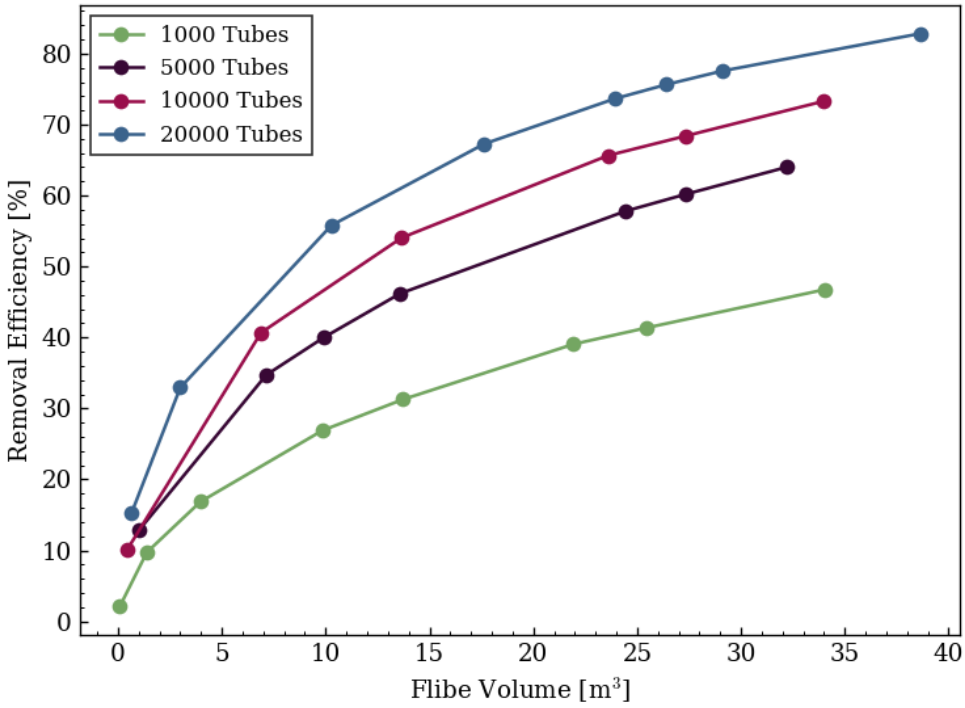

Figure 6.12. Calculated removal efficiencies for permeator systems with various numbers of tubes and increasing tube diameters. The tube length is set to create a pressure drop of 2 atm for all results and the total volume of Flibe in each case is used as the x coordinate. All simulations use the ideal exterior surface conditions of PRF_{out}=1 and a high recombination coefficient.

Taking the number of tubes, length of tubing at ΔP = 2 atm, and tube thickness of 1mm can produce the amount of steel used in each permeator system case from Figure 6.12. A clear relationship is present between the volume of steel in the permeator and the tritium removal efficiency, as shown in Figure 6.13. The relationship can be explained by the removal rate being proportional to the total inner-surface area, and the geometry of the tubes is roughly that of a thin cylindrical shell where volume is directly proportional to inner area. Slight deviations in efficiency from the trend exist because of varying degrees of permeation resistance in the metal as well as concentration differences across the length of the tubing in each case. Since there are diminishing returns in overall efficiency as the steel volume increases, the amount of steel should also be considered in selecting the size of a permeator system to implement in a FHR.

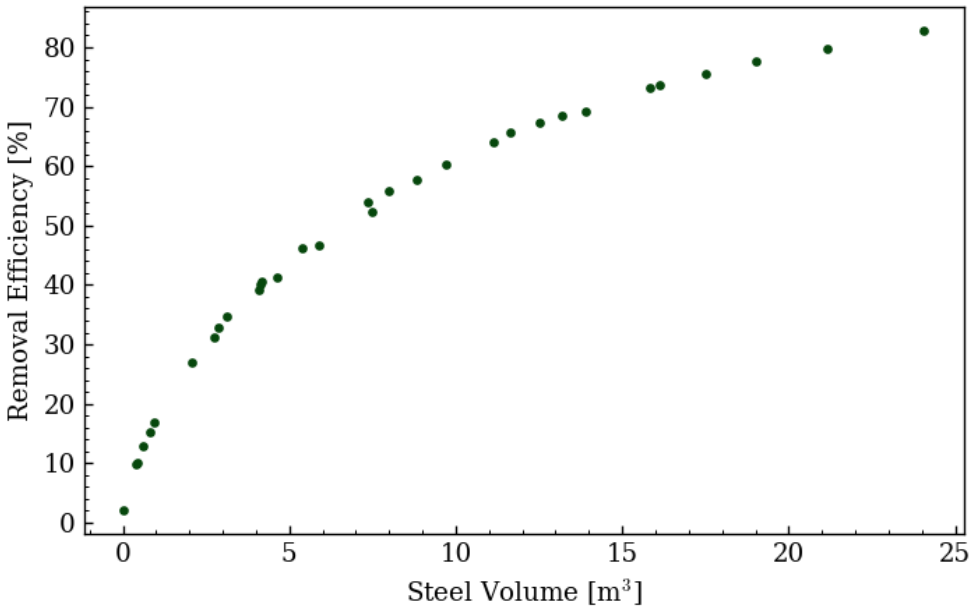

Figure 6.13. Tritium removal efficiency verses the total volume of steel in the permeator cases shown in Figure 6.12.

Another trend present in Figure 6.12 is the increase in removal efficiency with a greater number of tubes. The higher tube number cases divide the flow and reduce the pressure drop while allowing for smaller diameter tubes with higher removal efficiencies. Therefore, for a given salt volume and pressure drop, the higher tube number systems will have a lower tube diameter and a decreased length. Shortening the length of the system also has the benefit of better utilizing each incremental length of the tube. In long systems, the tube surfaces near the permeator outlet will remove relatively less tritium from the fluid since the concentration of T_2 continuously decreases across the permeator length. However, as shown in Figure 6.14, there are diminishing returns in removal efficiency for increasing the number of tubes once the system pressure drop and total Flibe volume are fixed. To further constrain the permeator dimensions, Figure 6.14 shows the optimized efficiencies at a total Flibe volume equal to half that of the original FHR inventory, or 25 m^3. The cases were repeated for the pessimistic assumptions of exterior surface conditions of a PRF_{out} at 10 to represent oxidation and a lower estimate for the 316 stainless steel hydrogen recombination coefficient. At each tube length, the change in surface conditions represented roughly a 6% decrease in overall removal efficiency. Dimensions for each permeator case plotted are shown in Table 6.4.

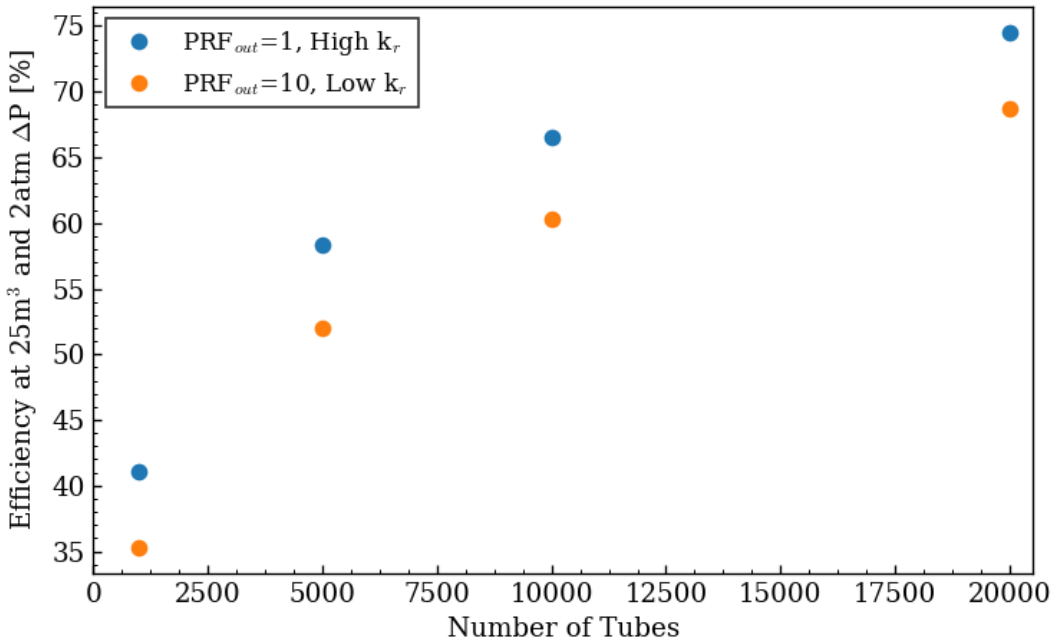

Figure 6.14. Permeator efficiency for bounding surface conditions when inner tube diameters are set to create a Flibe volume of 25 m^3 and pressure drop of 2 atm.

Table 6.4. Permeator dimensions and removal efficiencies for the cases plotted in Figure 6.14.

Number of Tubes	Tube Inner Diameter [cm]	Permeator Length [m]	Steel Volume [m^3]	η PRF_{out}=1 High k_r	η PRF_{out}=10 Low k_r
1000	2.293	60.49	4.55	41.04%	35.30%
5000	1.204	43.91	8.99	58.28%	52.00%
10000	0.907	38.61	12.22	66.49%	60.28%
20000	0.684	33.97	16.74	74.53%	68.67%

Using the dimensions in Table 6.4, a model region can be implemented into TRIDENT Mod1 to calculate the influence of the permeator extraction system on the FHR tritium distribution. The permeator release, heat exchanger permeation, and core pebble retention rate are shown in Figure 6.15 using the dimensions of the 20,000 tube permeator. As shown in the figure, the permeator extraction rate becomes the dominant path for tritium release while diminishing the releases through other regions. The remaining FHR release paths from the same simulation are plotted together in Figure 6.16.

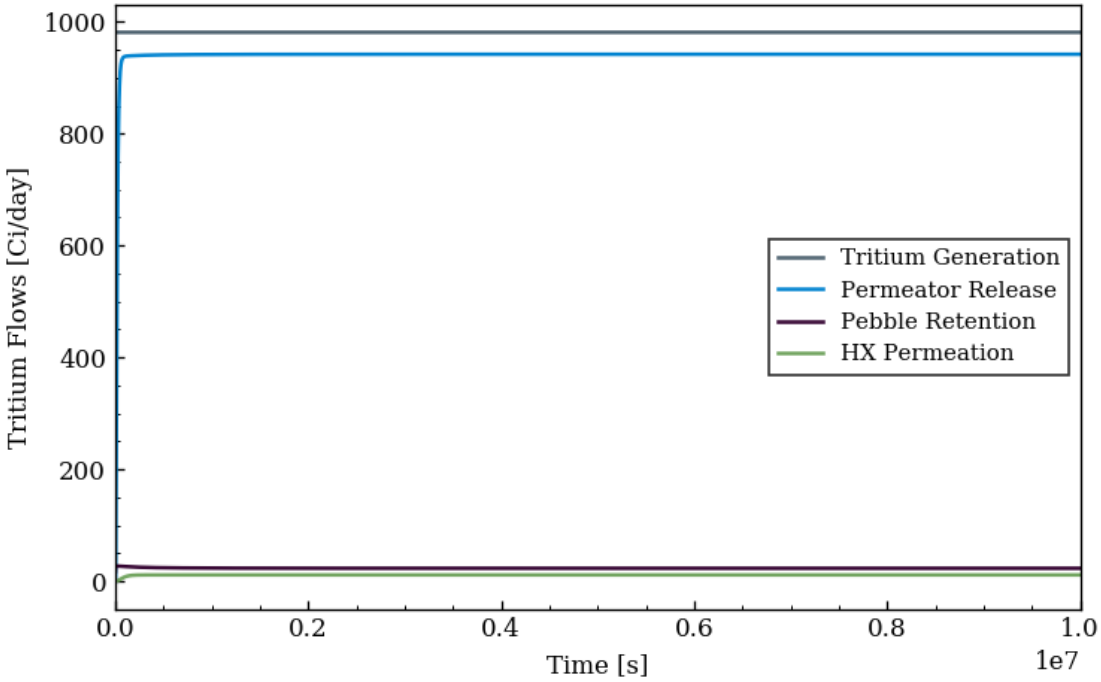

Figure 6.15. Tritium generation and release rate through a 20,000 tube permeator plotted along with the retention rate in core pebbles and heat exchanger permeation rate.

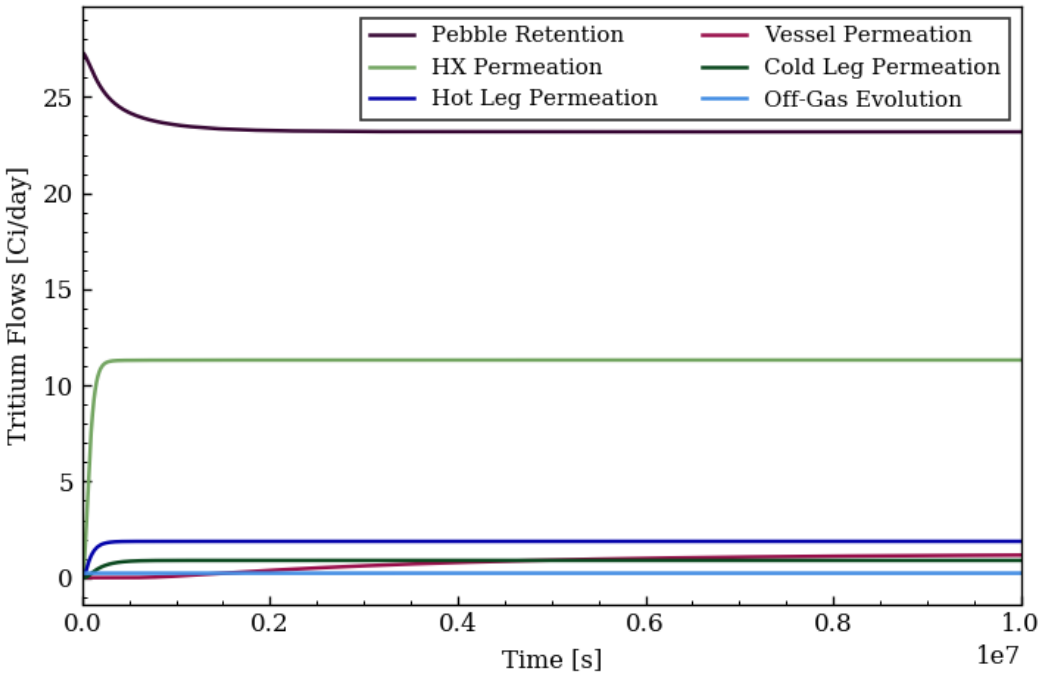

Figure 6.16. Tritium releases through all baseline FHR regions when the 20,000 tube permeator is used between the core and hot leg.

Permeator systems with 10000 tubes, 5000 tubes, and 1000 tubes were also simulated in TRIDENT Mod1 according to the system dimensions in Table 6.4. As the number of tubes decreases, the removal efficiency of the system is reduced, but the release through the permeator remains as the dominant tritium transport path in the FHR as shown in Figure 6.17. The tritium distribution in the FHR for each permeator design is summarized in Table 6.5. Compared to the test cases at a constant inlet concentration of $4.3 \cdot 10^{-6}$ mol-T_2/m^3, the efficiency of each permeator system slightly increased in the system-level implementation in TRIDENT Mod1. When the extraction systems are added, the T_2 concentration in the salt is significantly reduced, as shown in Table 6.5. Lower concentrations create more favorable boundary conditions at the salt-metal interface, since the partial pressure of T_2 in the salt is linear with concentration, whereas the concentration of T_2 in metals for a given partial pressure follows the square root of partial pressure [3]. Therefore, lower T_2 concentrations can slightly decrease some of the permeation resistance produced by tritium diffusion through the permeator tube walls. The difference between test case efficiencies and values from the TRIDENT Mod1 simulations decreases as T_2 in the salt increases.

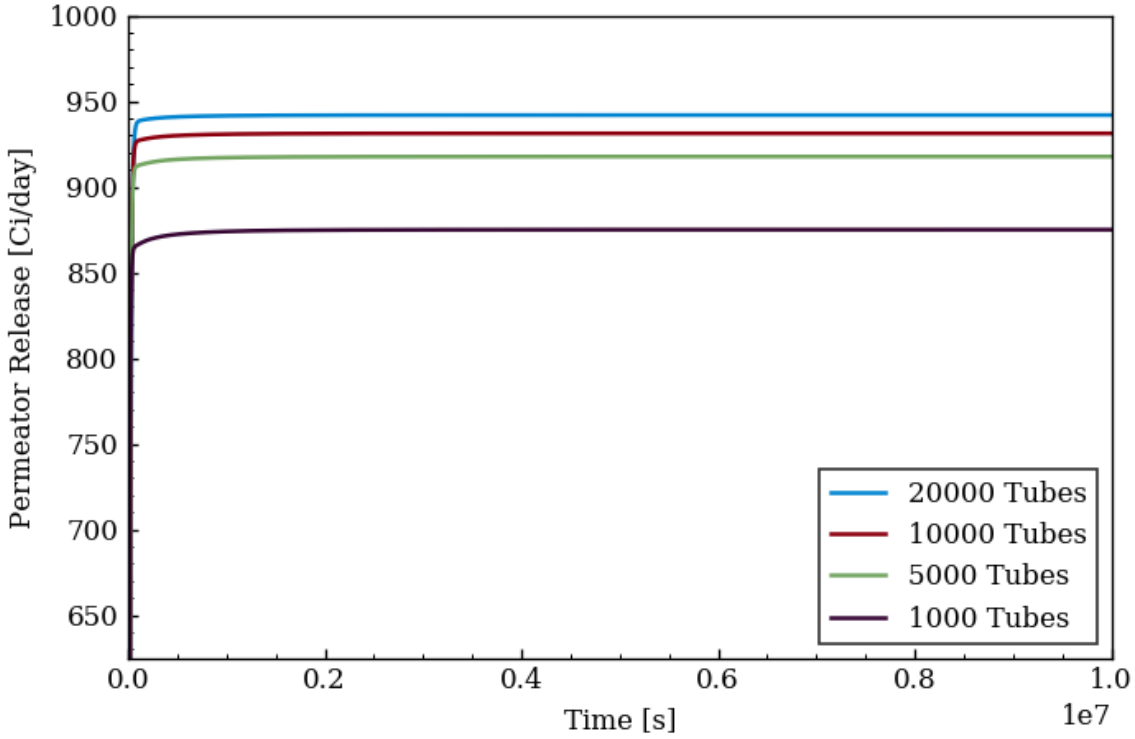

Figure 6.17. Tritium removal through a permeator simulated in TRIDENT Mod1 using the system dimensions in Table 6.4.

Table 6.5. Comparison of permeator efficiency calculated in the TRIDENT Mod1 simulations compared to the constant inlet concentration test case. The tritium distribution from each simulation is shown along with the T_2 concentration at the core outlet.

Value	Baseline	20k Tube	10k Tube	5k Tube	1k Tube
Test Case η	--	74.53%	66.49%	58.28%	41.04%
TRIDENT η	--	74.91%	66.88%	58.65%	41.36%
T_2 [mol/m^3]	$4.26 \cdot 10^{-6}$	$3.72 \cdot 10^{-7}$	$4.11 \cdot 10^{-7}$	$4.62 \cdot 10^{-7}$	$6.25 \cdot 10^{-7}$
Permeator	--	96.0%	95.0%	93.6%	89.4%
Heat Exchanger	54.0%	1.2%	1.7%	2.4%	4.5%
Core Pebbles	26.8%	2.4%	2.7%	3.1%	4.4%
Hot Leg	8.99%	0.19%	0.28%	0.40%	0.76%
Reactor Vessel	5.62%	0.12%	0.18%	0.26%	0.49%
Cold Leg	4.28%	0.09%	0.13%	0.19%	0.36%
Off-gas	0.29%	<0.01%	0.01%	0.05%	0.09%

The percent of overall tritium removal by the permeator is much greater than the single pass extraction efficiencies in Table 6.4. If all other FHR regions were treated as one removal system, then the FHR single pass efficiency could be estimated from the ratio of the salt volume exchange rate to the residence time of tritium. For 50 m^3 of salt in the FHR flowing at 0.729 m^3/s in the primary loop, the characteristic flow time through the loop would be 74.1 s. The residence time for tritium can be estimated from the inventory in the salt divided by the total production rate [48]. For the baseline result of $4.3 \cdot 10^{-6}$ mol/m^3 of T_2 and negligible TF, there is a steady-state inventory of 12.5 Ci in the salt and the residence time is 1101s based on a tritium production of 981 Ci/day. Therefore, the combined single-pass removal efficiency of all FHR regions is roughly 6.7%, and the 20,000 tube permeator is over 12 times more effective. For a FHR with a uniform tritium concentration throughout the primary loop, the ratio of tritium extraction through the permeator (R_{EX}) can be estimated by equation 6.4, where η_{EX} is the removal efficiency of the extraction system and η_{FHR} is the 6.7% removal rate in the FHR estimated by the characteristic times for flow around the loop and residence time of tritium. If the extraction system removes tritium first before all other FHR regions, then equation 6.5 can be used to account for the lesser tritium concentration occurring after the initial extraction. In the FHR model, tritium extraction occurs before the hot leg, heat exchanger, cold leg, and vessel, but there is still unavoidable tritium retention on the core pebbles which occurs once prior to the permeator system. Therefore, the TRIDENT Mod1 results for removal fraction verses permeator efficiency fall between the estimates of equations 6.4 and 6.5, as shown in Figure 6.18.

Eq. 6.4
$$R_{EX} = \frac{\eta_{EX}}{\eta_{EX} + \eta_{FHR}}$$

Eq. 6.5
$$R_{EX} = \frac{\eta_{EX}}{\eta_{EX} + \eta_{FHR}(1 - \eta_{EX})}$$

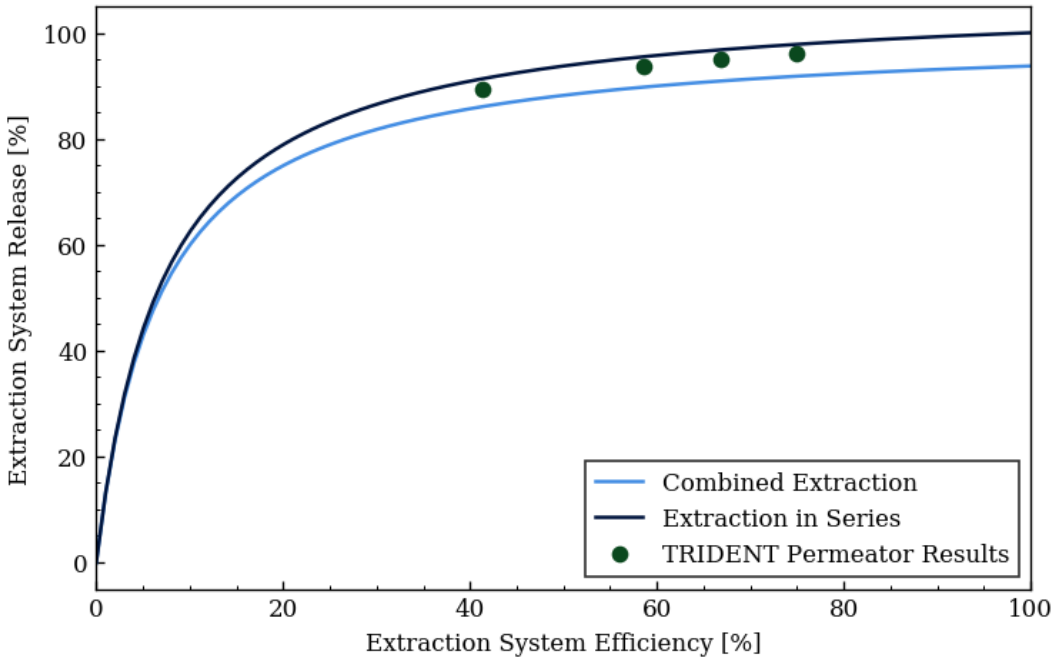

Figure 6.18. Permeator release fraction verses efficiency from TRIDENT Mod1 results in Table 6.5 compared to the estimates based on a constant-concentration combined extraction process (equations 6.4) and an extraction in series with the permeator leading (equation 6.5).

Results from TRIDENT Mod1 as well as estimations in Figure 6.18 demonstrate that a permeator design with reasonable constraints can constitute the majority of tritium releases in a FHR and become the most significant release path from the reactor. However, the results also show the difficulty in utilizing an extraction system as the sole tritium release mitigation strategy. For example, the sum of hot leg, cold leg, and reactor vessel permeation from the 20,000 tube permeator simulation in Table 6.5 amounts to a release of 1432 Ci per year into the reactor building, which is below the average HWR tritium discharge rate of 3500 Ci/yr but increases to 5729 Ci/yr if the intermediate loop tritium FHR releases are also unmitigated. Therefore, either a larger permeator than the 20,000 tube design or a dedicated tritium control system for the intermediate loop would be required to maintain overall FHR releases below HWR levels. To match the PWR discharge rate of 112 Ci/yr using only the permeator extraction system, the sum of all other FHR release would have to be 0.3068 Ci/day, or 0.03127% of the total distribution. Using equation 6.5 as an upper estimate, the efficiency of the permeator in this scenario would have to be at least 99.5% in order to freely release tritium from all other regions of the FHR. As previously demonstrated, there are diminishing returns on permeator extraction efficiencies as system dimensions are

increased. Therefore, depending on FHR design goals for tritium release, it is not likely that a tritium permeator system can be practically used as the single tritium control system in the plant. A more efficient implementation would be to use a permeator or other tritium extraction system in tandem with additional tritium mitigation and control technologies in the FHR.

6.3.2. Tritium Extraction with a Graphite Retention Bed

Another possible tritium extraction technology involves separating tritium from liquid Flibe through retention onto a graphite pebble bed. Advantages of a graphite bed over a permeator system are the enhanced mass transfer in a bed of spheres compared to straight tubes as well as a potentially higher surface area per system volume, depending on the diameter of pebbles in the bed and the volume requirements for the tritium collection area between tubes in the permeator system. However, the buildup of tritium inventory in the graphite will decrease the flux of tritium to the spheres over time in a similar process to that of the core pebbles in previous TRIDENT Mod1 simulations. Therefore, a graphite retention bed can be paired with an absorber sphere circulation and desorption system in order to maintain a useful extraction rate of tritium from the salt. One likely orientation for a conceptual system would be to rely on the same pebble recirculation technology used for the core, where the movement of pebbles is driven by the buoyancy of graphite spheres in molten Flibe and fresh pebbles are injected into the bottom of the retention bed, as shown in Figure 6.19. A counter-current of Flibe and graphite spheres can also lead to a more efficient axial utilization the bed – since tritium concentration continuously decreases in the direction of salt flow, graphite pebbles with the lowest tritium inventory and highest retention potential can assist in increasing tritium retention rates in the lower sections of the bed when injected near the salt outlet.

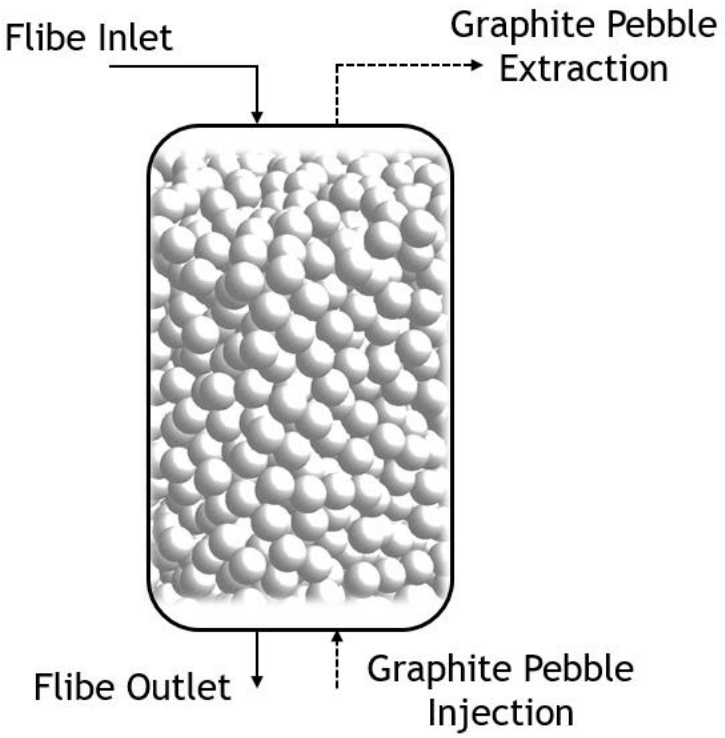

Figure 6.19. Illustration of salt and pebble movement in a counter-flow graphite retention bed system with Flibe flowing from the top to bottom of the absorber column. Sphere diagram from [207].

The graphite retention bed can be simulated using the same subroutine implemented for the reactor core in the TRIDENT Mod1 system-level model. As with the permeator system, the graphite bed was modeled as an isothermal region at 650ºC since the intended position is directly following the core outlet. The graphite retention bed was examined using the same test case conditions as the permeator system: an inlet T_2 concentration of $4.3 \cdot 10^{-6}$ mol-T_2/m^3, negligible TF, and a Flibe mass flow rate equal to 100% of the FHR primary loop flow. A sphere packing fraction of 0.6 was used to be consistent with the FHR core [3], which is in the range of most likely packing fractions of a randomly oriented bed [208]. The total pressure drop over the graphite bed was also constrained to 2 atm, which was calculated using the Foumeny correlation shown in equation 6.6 [209]. In addition to the Flibe density, viscosity, and superficial velocity, the correlation also includes the effect of bed porosity, ε, and the ratio of bed diameter to pebble diameter, D_B/d_p.

Eq. 6.6
$$\frac{\Delta P}{L} = \frac{130\mu v}{d_p^2}\left(\frac{(1-\epsilon)^2}{\epsilon^3}\right) + \frac{\rho v^2}{d_p}\left(\frac{1-\epsilon}{\epsilon^3}\right)\left(\frac{D_B/d_p}{0.335 D_B/d_p + 2.28}\right)$$

In the test case simulation, the removal efficiency of the bed decreases over time as the tritium inventory in absorber spheres increases. The equilibrium efficiency in each retention bed geometry depends on the recirculation rate of pebbles, as shown in Figure 6.20. Desorption of pebbles on each recirculation was assumed to be 100% efficient, and thus graphite pebbles with an internal tritium concentration of zero were returned to the lower node of the retention bed. Recirculation parameters for the absorber spheres were selected based on factors applied to the volumetric flow rate of fuel pebbles in the core, which is 0.225 m^3 of graphite per day for 4 cm pebbles at the baseline core residence time value of 50 days. Results in Figure 6.20 therefore refer to recirculation rates 1, 5, 10, 20, and 30 times that of core pebble handling system. During the simulation, the equilibrium values were calculated once the removal efficiency had a relative decrease of less than 0.01% over a 10,000s length of time.

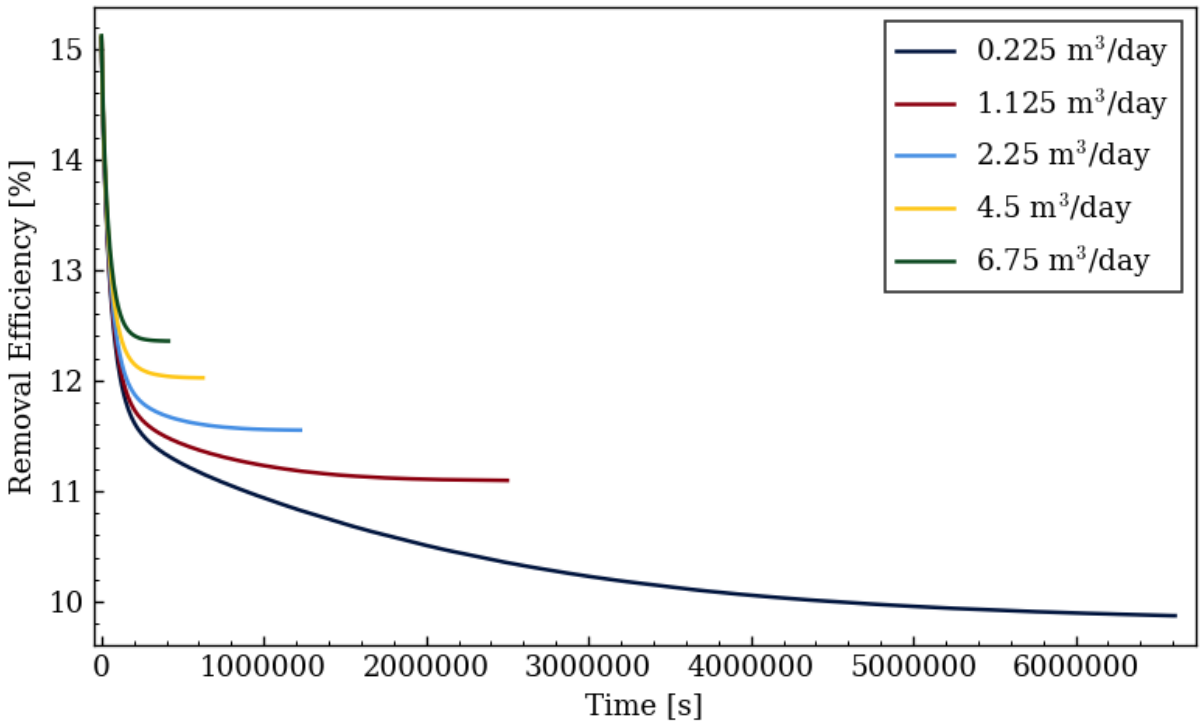

Figure 6.20. Example retention bed test case output of removal efficiency over time for various absorber sphere volumetric recirculation rates. An absorber sphere diameter of 2.5 cm was used along with a cylindrical bed diameter of 2.5 m and overall length of 8.099 m to create a pressure drop of 2 atm.

Additional graphite retention bed cases were investigated in order to determine the effects of design parameters on system performance. Figure 6.21 shows the tritium removal efficiency for various absorber sphere diameters and recirculation rates for a 2.5m and 3m diameter bed. In each case, the length of the system was set based on the bed and sphere diameters to create a pressure drop of 2 atm as calculated by equation 6.6. Smaller diameter spheres lead to a higher pressure drop per system length, but create a higher surface area per volume for retention to occur. As shown by the 2.5m diameter bed cases, there is a higher potential efficiency for smaller sphere systems, but only at higher pebble recirculation rates. Spheres with lower diameters are more sensitive to the recirculation rate since they will approach their retention capacity faster than larger diameter pebbles. Increasing the diameter of the graphite bed has a similar effect to increasing the number of tubes in the permeator study – the salt velocity decreases when the retention bed diameter is raised, which decreases the pressure drop per until length and allows for larger volume systems with higher removal efficiencies. As shown for the 3m bed cases in Figure 6.21, retention beds with a larger volume require even higher recirculation rates to benefit from smaller pebble diameters.

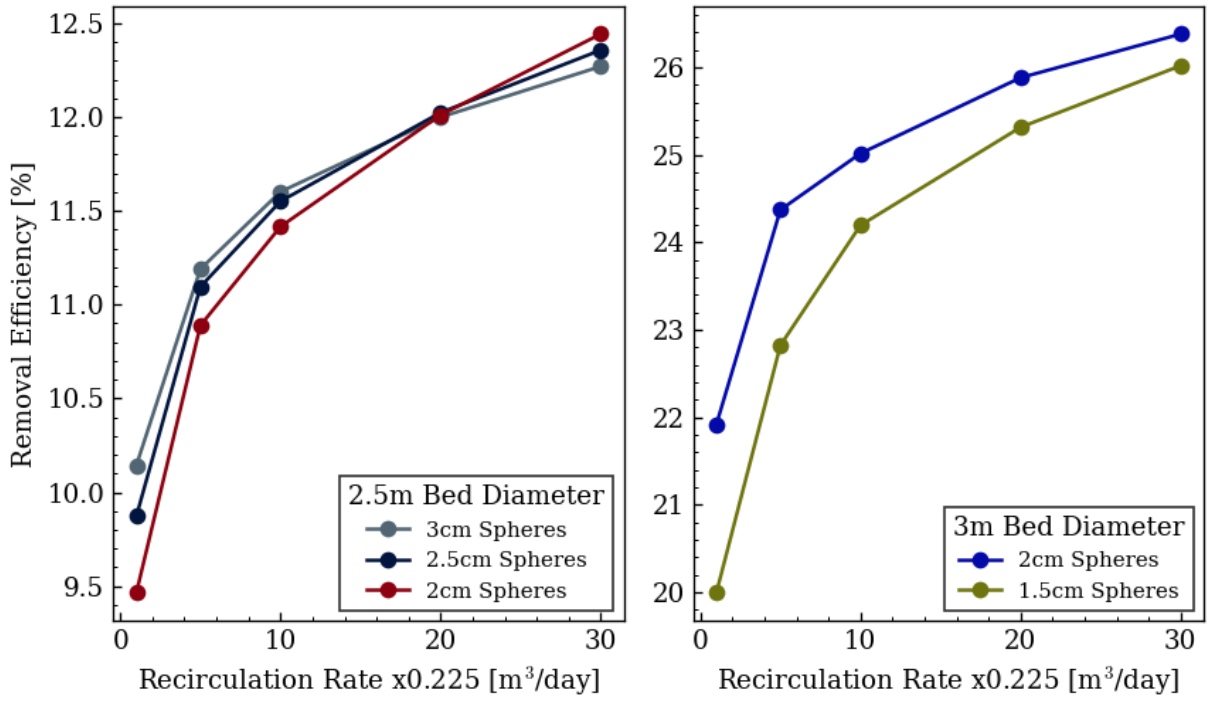

Figure 6.21. Retention bed removal efficiency for a 2.5m and 3m bed diameter, various pebble diameters, increasing recirculation rates, and various lengths set to produce an overall pressure drop of 2 atm in each case.

The total Flibe volume from each of the cases in Figure 6.21 varies since the system length was adjusted to match a pressure drop of 2 atm. As seen in the permeator results, the potential removal efficiency of the retention bed increases with additional Flibe volume. However, the removal efficiencies throughout all Flibe volumes in the retention bed simulations are lower than the results from the 1000 tube permeator test case, as shown in Figure 6.22. The graphite bed results at each recirculation rate are shown in the figure, as well as open circles which represent the graphite bed efficiency at an infinite volumetric flow of absorber spheres. An infinite recirculation rate was calculated by maintaining a zero T_2 boundary condition at the salt-graphite interface of all spheres. The same treatment could be applied to represent an infinite solubility of tritium within the spheres. In both cases, the only limitation on tritium retention in the bed is mass transfer to the pebble surfaces in Flibe.

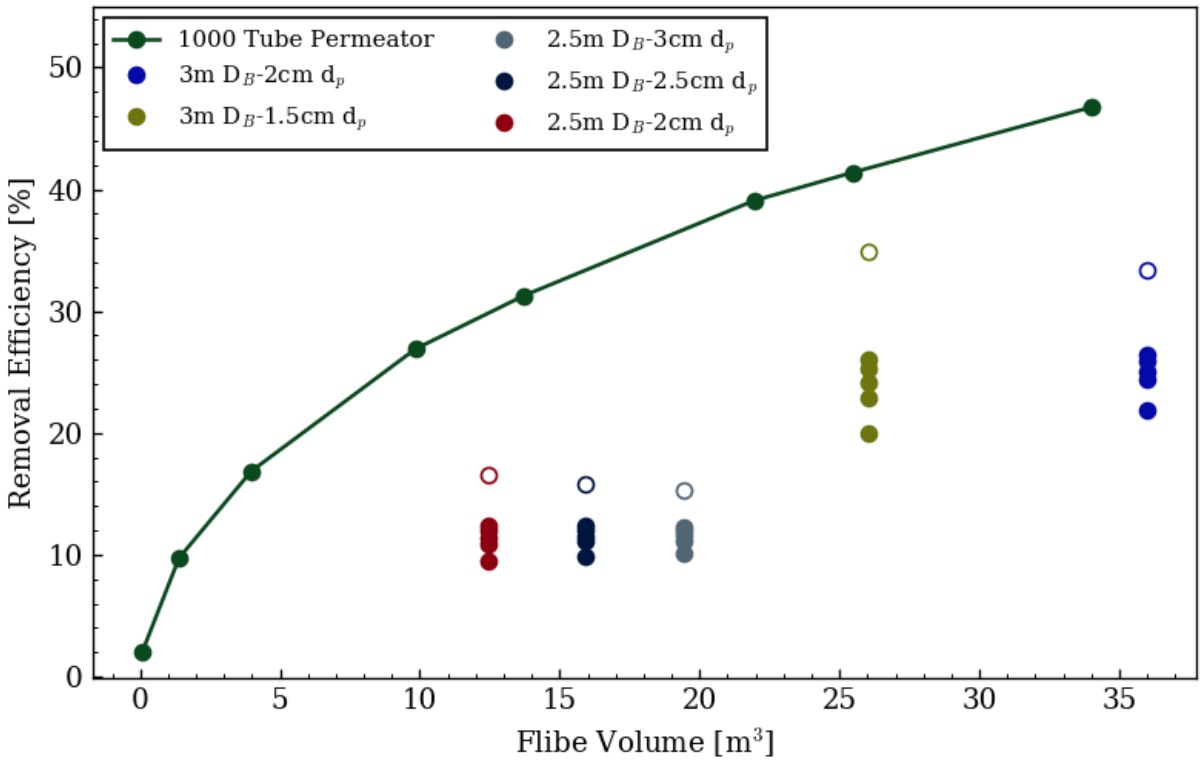

Figure 6.22. Comparison of retention bed tritium removal efficiencies from Figure 6.21 to the 1000-tube permeator results. The open circles in the retention bed cases represent infinite recirculation rates.

For the infinite recirculation results with the retention bed, the extraction efficiencies remain lower than the permeator cases despite a greater geometric surface area of pebbles than Flibe-facing area of tubes per system volume in some designs. The lower efficiency occurs because the model simulates an influx of T_2 only into the pores of graphite first, where the open pore area is calculated by the geometric surface area time the graphite porosity, φ. Mass transfer potential in Flibe can be examined for each system through the product of the overall Flibe-facing area times the T_2 mass transfer coefficient. As shown in Table 6.6, the $k_{T2}A$ values for the retention bed designs simulated are all greater than the values of the 1000-tube and 5000-tube permeators, while the 3m diameter retention beds have $k_{T2}A$ numbers above all permeator cases. However, when the area is scaled down by a factor of φ, or 0.1858 for AXF-5Q graphite [127], the retention bed falls below the permeator $k_{T2}A$ values in each design. Table 6.6 also shows removal efficiency calculations if the retention bed was a perfect absorber of tritium, where the full surface area of the graphite was applied when calculating the flux of T_2 to pebble surfaces. In these cases, the retention bed maximum performance was higher than most permeator results.

Table 6.6. Comparison of relevant dimensions and results for the retention bed and permeator test cases. The permeator specific volume was calculated assuming a 50% occupancy of tubes inside a tube bundle and 50% void space.

Graphite Bed:	**2.5m D_B, 3cm d_p**	**2.5m D_B, 2.5cm d_p**	**2.5m D_B, 2cm d_p**	**3m D_B, 2cm d_p**	**3m D_B, 1.5cm d_p**
Bed Length [m]	9.911	8.099	6.331	12.722	9.217
Flibe Volume [m^3]	19.46	15.90	12.43	35.97	26.06
Specific Area [m^2/m^3]	120	144	180	180	240
$k_{T2}A$ [m^3/s]	0.611	0.634	0.664	1.494	1.578
$\varphi k_{T2}A$ [m^3/s]	0.114	0.118	0.123	0.278	0.293
Infinite Recirculation η	15.31%	15.84%	16.52%	33.39%	34.89%
Perfect Absorber η	59.11%	60.46%	62.16%	88.77%	90.06%
Permeator:	**1k Tube**	**5k Tube**	**10k Tube**	**20k Tube**	
Tube Length [m]	60.49	43.91	38.61	33.97	
Flibe Volume [m^3]	25	25	25	25	
Specific Area [m^2/m^3]	74	122	148	175	
$k_{T2}A$ [m^3/s]	0.365	0.603	0.755	0.945	
Test Case η	41.04%	58.28%	66.49%	74.53%	

Model assumptions based on whether or not the full graphite pebble surface can retain an influx of tritium, or trapping sites can only be accessed first by diffusion through pores, will influence the resulting retention bed efficiency under high pebble recirculation rates. However, at pebble volumetric flow rates thirty times that of the FHR core and below, the removal efficiency of the graphite bed is significantly lower than the infinite recirculation values because the main limitation in the retention process is the tritium diffusion and trapping rate in graphite and not mass transfer in Flibe. Similarly, the performance of the retention bed is more dependent on the rate of tritium transport into graphite, rather than the total capacity for tritium retention in the spheres. For example, results from the 2.5m retention bed case with 2.5cm spheres made of stainless steel instead of graphite are shown below in Figure 6.23. The solubility of tritium in graphite is roughly five times higher than 316 stainless steel at FHR temperatures [91, 126], but the faster diffusion of tritium into steel results in a greater total inventory of tritium in the pebbles since a larger fraction of the sphere volume is engaged in the retention process. Time dependence of removal efficiency in the steel retention bed differs from the graphite system because the T_2 surface boundary condition does not begin to increase significantly until tritium diffuses towards the center and saturates the metal sphere. Note that this analysis is not intended to support development of a steel sphere tritium retention bed concept, but only to illustrate the importance of considering both tritium capacity and retention kinetics for any retention bed design.

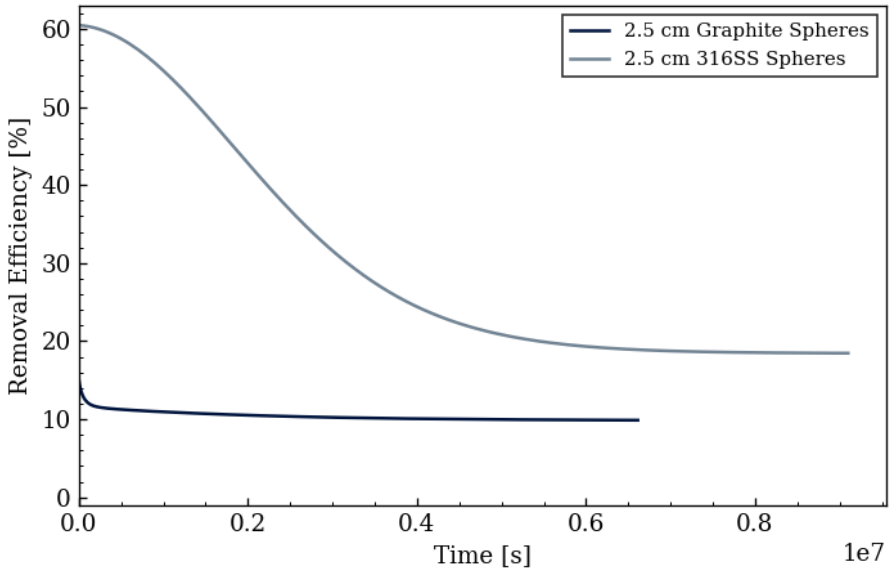

Figure 6.23. Removal efficiencies in a 2.5m diameter bed 8.099m in length using 2.5cm POCO AXF-5Q graphite or 316 stainless steel spheres in the constant T_2 inlet condition test case.

In summary, the removal efficiency of a graphite retention bed as predicted by the pore and grain tritium transport model is lower than that of permeator systems at similar Flibe volumes and pressure drops. Because of the low solubility of T_2 in Flibe, along with the relatively high diffusivity and solubility of tritium in steel, the permeation process in FHRs is predominantly limited by mass transfer in Flibe rather than diffusion in the metal. All tritium extraction systems are limited by the rate at which tritium can transfer through Flibe to the extraction surfaces, and thus using an extraction technique based on permeation through metals is one method which creates very little additional resistance to the overall tritium exchange process. In contrast, the diffusion of tritium into graphite bulk appears to be slow enough as to limit the total useful retention volume in a graphite bed extraction system. The tritium diffusion and trapping limitations in the graphite retention process can also explain the significant tritium concentration gradient observed in the MSRE graphite moderator as well as the difference between mCi/g and $\mu Ci/mm^2$ values measured in desorptions of the FS-2 irradiation samples [140, 41]. Regardless of the removal efficiency of the graphite retention bed, the same conclusions from the TRIDENT Mod1 permeator analysis apply – the majority of tritium generated by a FHR can be removed by a 10-20% efficient extraction system (using the analysis in Figure 6.18), but an extraction system efficiency of greater than 99% is likely required to allow unmitigated tritium releases in all other regions of the reactor.

6.3.3. Summary of TRIDENT results and Tritium Management Options

The implementation of a tritium extraction system or permeation barrier coating into the design of a FHR will require significant levels of investment and effort in order to fully demonstrate the efficacy of each approach. To justify the necessity of any tritium management related design intervention, FHR designers should first have a thorough understanding of the tritium control and capture systems required to maintain acceptable release rates with a generic FHR plant layout. For this purpose, the results from TRIDENT Mod1 or a similar system-level tritium transport code can provide useful predictions for understanding the baseline tritium distribution expected in FHR designs.

As previously discussed, potential candidate materials for long term tritium storage are hydride getter beds for HT/T_2 and molecular sieve adsorbents for HTO/T_2O. For both storage materials, the capture mechanisms are based on chemical interactions, and thus tritium and other hydrogen isotopes will be captured at roughly equivalent rates. Therefore, the efficiency of each tritium capture method depends on the amount of hydrogen-containing molecules or otherwise undesirable species present in each collection flow path. As the largest volume region and likely the most difficult to fully isolate from impurities, the reactor building can be considered the most difficult region in which to deploy a tritium capture system. Tritium collection efficiency could be improved in these areas by constructing gas-tight enclosures surrounding the sources of tritium release into the reactor building, which in the current TRIDENT Mod1 code are permeation through the hot leg, cold leg, and reactor vessel. Isolating a smaller volume in the reactor building dedicated to tritium capture could allow for effective HTO/T_2O collection in very dry air or HT/T_2 capture in an inert cover gas. The cost and complexity of any proposed tritium control system or design change should then be weighed against the reactor building modifications required to achieve a given tritium release design goal in a baseline FHR design.

If reactor building design modifications and subsequent tritium control systems are found to be not practical, the release rate through the hot leg, cold leg, and reactor vessel can be reduced through permeation barrier coatings. Coatings applied to the outside of metal surfaces reduce releases by amplifying the permeation resistance in the metal. However, the permeation resistance created by diffusion through steel is small at normal FHR conditions. At the highest outer-coating performance case studied, the permeation rate through the hot leg, cold leg, and reactor vessel was reduced from 67,600 Ci/yr in the baseline simulation to 14,600 Ci/yr with a PRF_{out} value of 500.

Considering that a HWR releases only 3,500 Ci/yr for an equivalent electrical output [29], the outer coating release reduction appears to be insufficient to leave tritium releases uncontrolled in the reactor building and prevent the implementation of building tritium control systems.

Permeation barrier coatings on Flibe-facing surfaces of structural materials are more effective in reducing permeation rates because the coatings directly reduce the flux of T_2 into the material. Disadvantages of inner-facing coatings also exist, such as potential corrosion concerns from molten Flibe and the added difficulty in inspecting or replacing coatings during service life. When coatings are applied to all inner-surfaces of the FHR, permeation rates are significantly reduced, but the concentration of T_2 in the salt also increases which adds to the concentration gradient and initial flux of T_2 from Flibe. The permeation rate to the reactor building when all inner-surfaces are coated with a PRF_{in} of 500 amounts to 757 Ci/yr. A more efficient use of coatings, both in terms or required surface areas and release reductions per PRF_{in} applied, is to allow permeation through the heat exchanger and utilize coatings only on the hot leg, cold leg, and reactor vessel. In this case, the buildup of T_2 concentration in the salt is prevented because the heat exchanger remains as the dominant tritium release path, and permeation into the intermediate loop is preferred over the reactor building since suitable tritium capture systems exist for the nitrate salt cover gas. For coatings with PRF_{in} values of 500 applied to the hot leg, cold leg, and reactor vessel only, the reactor building release rate decreases to 172 Ci/yr.

A tritium extraction system implemented into the FHR primary loop can lower releases in all regions by decreasing the equilibrium concentration of tritium in Flibe. The removal efficiency of an extraction system depends on the dimensions of each design. For example, the volume of Flibe in the extraction system generally increased the removal efficiency for both the permeator and graphite retention beds examined in this Section. Considering the time constants of Flibe flow and tritium residence time in the FHR, the sum of releases in the primary loop amount to a removal efficiency of 6.7% per salt pass through the primary loop. Therefore, an extraction system will begin to absorb the majority of tritium releases once the system single-pass removal efficiency surpasses that of the overall FHR, which is readily achievable with each of the permeator and retention bed designs studied in this section. However, to achieve a tritium release rate equal to PWR levels of 112 Ci/yr for an equivalent FHR electrical output, an extraction system would have to be at least 99.5% efficient to allow unmitigated releases from all other regions in a FHR. Furthermore, the removal efficiency of an extraction system will increase diminishingly as the

scale of the system is raised, as exhibited by the steel volumes and number of tubes verses performance of permeator systems analyzed previously. Therefore, it is increasingly difficult to achieve an extraction system efficiency of 99.5% without attempting to first restrict the baseline release rates of the other FHR regions.

The TRIDENT Mod1 results reveal the difficulty in relying on only a single design change to achieve a release rate below that of current PWRs – either Flibe-facing coatings with PRF_{in} values greater than 500 must be demonstrated for a strategy solely based on coatings, or an extraction system with a removal efficiency of greater than 99.5% would be required if the extraction system outlet was the only region where tritium capture took place. Since tritium permeation through the heat exchanger and tritium retention on the core pebbles are the two main release pathways in a baseline FHR, the requirements for additional tritium control systems are significantly relaxed if design considerations are implemented to recover tritium from the intermediate loop and the core graphite pebbles. Retention on the core pebbles is maximized when pebbles are fully desorbed on each pass through the core, but the retention rate remains significant if recirculation without desorption occurs and pebbles are simply replaced on a 500 day residence time. Therefore, permeation through the heat exchanger and retention on graphite pebbles can both be leveraged as a partial tritium control solution regardless of whether a desorption facility is integrated into the pebble desorption system.

Because suitable candidate tritium collection options exist to recover tritium from the core pebbles and the intermediate loop cover gas, in addition to the fact that these transport pathways are the most difficult to minimize in any tritium control strategy, the FHR design should incorporate focused efforts to reduce and control tritium releases into the reactor building. To this end, a combination of technologies will likely be more effective than a single solution. For example, the majority of tritium extraction in a FHR can be achieved with a small system capable of 10-20% extraction efficiency. Pairing a minor tritium extraction system with various levels of Flibe-facing coatings results in significantly lower coating PRF_{in} requirements for a given release rate, as shown in Figure 6.24. Adding permeation barriers to Flibe-facing surfaces also appears to greatly reduce the overall release rate, even at much lower extraction efficiencies than the permeator results plotted vertically at $PRF_{in}=0$ in Figure 6.24.

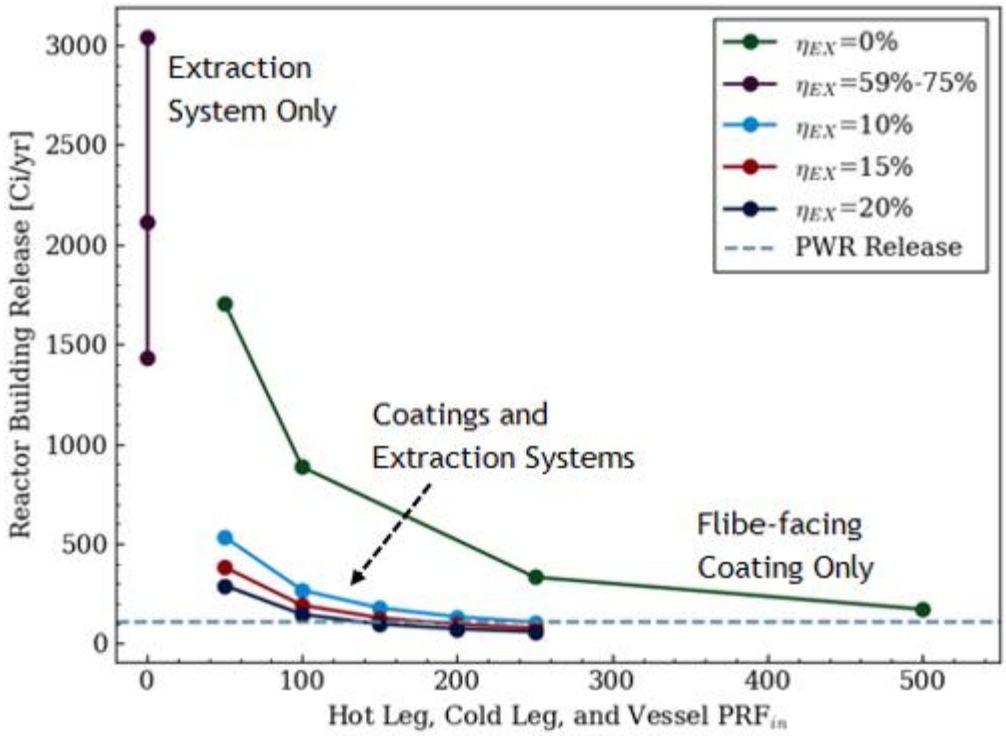

Figure 6.24. Annual release into the reactor building simulated by TRIDENT Mod1 for the 5k, 10k, and 20k tube permeator cases (η_{EX}=58.65%, 66.88%, and 74.91%) along with cases without extraction systems but permeation barriers applied to the hot leg, cold leg, and reactor vessel. Additional cases with permeation barriers and extraction systems of efficiencies between 10% and 20% outperform results from coating- or extraction-only simulations.

The combination of Flibe-facing coatings and minor extraction systems can lead to release rates into the reactor building which are lower than that of average PWR tritium discharge values according to simulations with TRIDENT Mod1. As shown in Figure 6.25, release values are below the PWR average for extraction system efficiencies of 10%, 15%, and 20% when coatings with PRF_{in} values of 250, 200, and 150, respectively, are applied to the hot leg, cold leg, and reactor building. In this strategy, determining the required margin from the tritium release design goal will ultimately depend on the capture efficiency of tritium control systems employed for the primary releases and intermediate loop. If effective tritium capture systems can be implemented for the remaining release paths, then a combination of a modest tritium extraction system and Flibe-facing permeation barrier coatings on the hot leg, cold leg, and reactor vessel is an efficient strategy to minimize overall tritium release from a FHR plant.

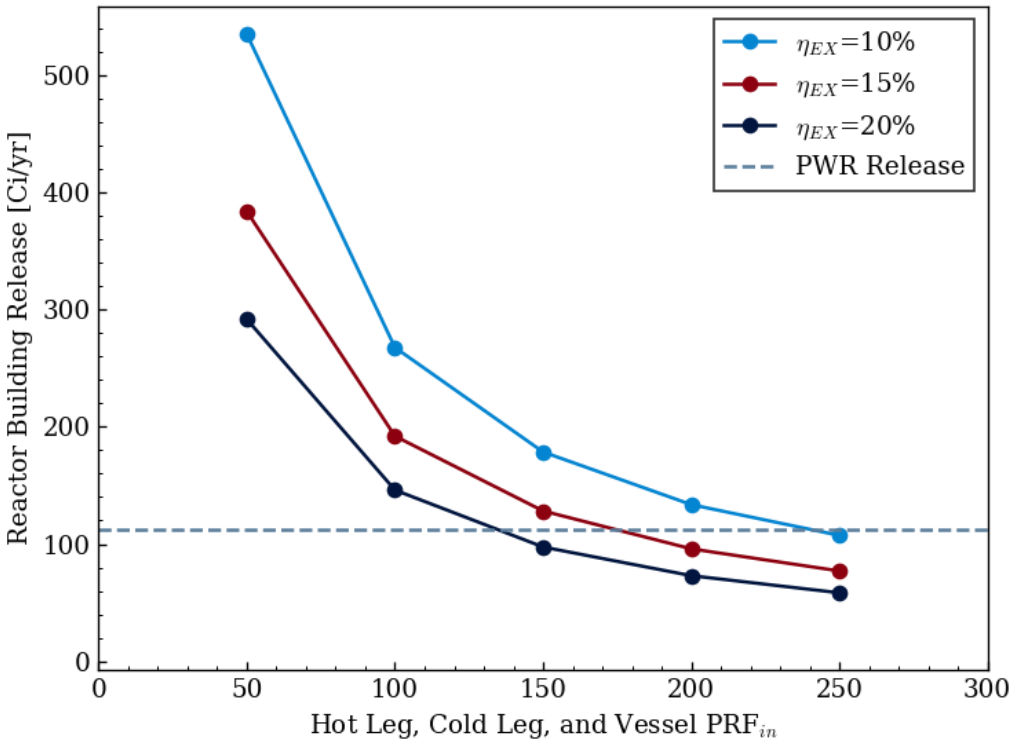

Figure 6.25. Annual reactor building release for various combinations of Flibe-facing coating permeation resistance and extraction system efficiencies compared to average PWR discharge rates [29].

7. Conclusions and Future Research Needs

While several design features of the Fluoride-Salt-Cooled High-Temperature Reactor have been successfully demonstrated in previous reactor designs, the eventual realization of the FHR depends on the ability to address key technical challenges. One such challenge is the need to mitigate the environmental release of tritium generated by neutron irradiation of the Flibe coolant salt. Implementing design and engineering controls to limit tritium release from the plant first requires an understanding of how and where tritium release will occur from the primary system, whether by permeation through metals, evolution to the reactor cover gas, or retention on graphite in the core. The TRIDENT system-level tritium transport code originally developed by Stempien [3], and expanded upon in this study, was utilized to determine the rates of tritium release by various modes and in multiple regions of a FHR design. The model was then be used to explore design changes which promote tritium release to favorable collection streams and reduce release into undesirable zones, thus outlining the basis for an overall tritium management strategy.

In any FHR design, the majority of surface areas in contact with Flibe salt will likely consist of structural metals from components such as the heat exchanger, reactor vessel, and primary piping. The permeation process at typical FHR conditions is mainly limited by mass transfer in Flibe, rather than diffusion through metals, which was proved analytically for Flibe and nickel systems and was shown numerically for Flibe and 316 stainless steel in TRIDENT Mod1 [188]. Therefore, the permeation rates through various regions in a FHR can be predicted based solely on the mass transport characteristics of Flibe flow in each zone. However, if the only limitation towards retention in graphite was tritium transport to graphite surfaces, then the core pebbles would absorb the majority of generated tritium, or 79.8% of the total tritium for the FHR design modeled in this study.

Modeling the transport of tritium within graphite materials is a solution to represent other phenomena which may add resistance to the overall tritium retention process. The inclusion of graphite transport and trapping kinetics into the TRIDENT Mod1 code can therefore produce more representative values for the expected rates of tritium retention in the graphite pebbles and reflector regions in a FHR. In this study, tritium analysis of graphite samples from in-core irradiations at the MIT Reactor were used to understand contributing factors which influence tritium retention mechanisms in the Flibe and graphite environment. Experimental measurements were then used to construct and justify a method for simulating the transport of tritium inside graphite materials

at FHR conditions. The graphite retention methodology was then implemented into the TRIDENT system-level model to examine the baseline distribution of tritium in a FHR and explore potential tritium management solutions. Conclusions from each individual step in this research process are summarized below.

7.1. Conclusions from Experimental Measurements

The main conclusions from the experimental measurements presented in Section 3 can be summarized as follows:

- **Retention in graphite accounted for a significant fraction of the total tritium generation in the FS-1, FS-2, and FS-3 in-core irradiations.** The total retention in graphite from each irradiation was estimated through tritium desorption experiments which measured the total tritium content in several samples. An average of each sample set was extrapolated to represent the total graphite inventory of the particular experiment, either by using the tritium content per Flibe-facing surface area measured for FS-1 and FS-2 samples or the tritium activity per sample mass in FS-3. The estimated percent of total tritium generation retained by graphite was then 19.6±1.9% for FS-1, 34±10% for FS-2, and 27.1±1.9% for FS-3. Considering that the difference between calculated tritium generation and measured releases from the FS-3 experiment was 22±10% of the total production, tritium retention in graphite is the main reason for total release being less than the overall generation. While there are several differences between the MITR Flibe experiments and the tritium transport conditions of a FHR, the significant fraction of tritium retained by graphite samples in the FS-1, FS-2, and FS-3 irradiations demonstrates the need to consider tritium retention in graphite in full-scale FHR models.

- **Tritium content in FS-2 graphite samples was concentrated near the salt-facing surfaces, and not evenly distributed through the graphite volume.** Three graphite disc samples from the FS-2 experiment were split into subsections with various amounts of Flibe-facing exterior surface areas per sample mass. Sample subsections originating from the same disc should have similar tritium retention characteristics, and the tritium inventories measured in each individual subsection test were compared by normalizing the tritium activity to the subsection area and subsection mass. For all three disc sample sets, the normalization by sample area provided

more consistent values than normalization by sample mass, as judged by the relative standard deviation of each group. Relative standard deviations by mass and area were 20% and 10% for the IG2 sample, 39% and 17% for the ARB sample, and 50% and 28% for the IG1 sample, with the lower value in each case being the tritium activity per surface area deviation. A subsection analysis could not be completed for the FS-1 crucible samples, but the similarities between tritium per area measurements compared to tritium per sample mass between FS-2 and FS-1 samples also suggests that retention in the FS-1 crucible was better explained by surface-concentrated retention rather than volumetric saturation. For example, the activity per surface area average was 4.75 $\mu Ci/mm^2$ for the IG1 sample and 4.18 $\mu Ci/mm^2$ for the FS-1 crucible sections, compared to 3.669 mCi/g for IG1 and 0.7563 mCi/g for the FS-1 crucible. The MITR tritium desorption measurements, as well as post-operation analysis of MSRE moderator graphite [140], reveals that the regions closest to the salt-graphite interface are preferentially engaged in tritium retention. Therefore, a method to calculate the tritium transport into bulk graphite is required in order predict the tritium inventory in FHR core materials, rather than relying only on the volumetric capacity of graphite to calculate the total retention.

- **Tritium desorption measurements of nuclear graphites irradiated in Flibe demonstrate several similarities to mechanisms observed in retention of gaseous hydrogen.** A central assertion made from the experimental measurements in this study is that there are several parallel observations between desorption testing of MITR Flibe irradiation samples and previous studies on the retention of gaseous hydrogen isotopes in graphite. Therefore the mechanisms proposed for the H_2 gas retention process can also be used to describe tritium transport in the Flibe-graphite system. The observed similarities are summarized below.

- **Tritium desorption from MITR Flibe irradiation samples occurred in distinct peak structures which are indicative of trapping sites in graphite.** All thermal desorption experiments of samples from the FS-1, FS-2, and FS-3 irradiations displayed a central peak tritium desorption rate at temperatures in the range of 650ºC to 900ºC. Another distinct desorption peak at temperatures above 1000ºC was clearly observed for the FS-3 samples, but not consistently shown in FS-1 and FS-2 samples. A tritium desorption profile with two main

peaks is consistent with previous observations of nuclear graphites charged with deuterium gas [115]. Peaks in the desorption profile observed in previous gaseous retention studies were proposed to be a result of active sites in graphite with distinct trapping energies [123]. Peak desorption rates occurred at lower temperatures in the MITR sample desorptions than for the D_2 retention studies in literature, which can be explained by the graphite samples being below the point of saturation [123]. For example, the FS-3 graphites were the closest of the MITR samples to being saturated as judged by the subsection analysis of the U44 IG-110U sample, and thus the FS-3 samples had relatively higher peak desorption temperatures than observed for FS-1 and FS-2 graphites of the same grade.

- **Tritium desorption as a function of temperature was influenced by the presence of additional H_2 in the furnace sweep gas.** A shift to lower peak desorption temperatures was observed as hydrogen concentration increased during the analysis of FS-1 crucible sections, the ARB samples from FS-2, and the lower crucible IG-110U samples from FS-3. In each case, increasing the H_2 concentration in the furnace sweep gas led to peak desorption temperatures earlier in the experiment and at lower overall temperatures. Studies on the absorption of hydrogen gas have shown that the effective diffusivity of H_2 in graphite increases as the partial pressure of H_2 is raised [136]. Therefore, adding hydrogen to the sweep gas of the desorption furnace would lead to a peak desorption rate at lower temperatures if the desorption release was controlled by a diffusion process through the graphite sample. The effect of hydrogen in the furnace sweep gas can also explain a portion of the difference between the lower peak desorption temperatures from MITR graphite samples and gas retention studies in literature, where desorption occurred in a vacuum and no additional H_2 was present [123, 159].

- **The measured activation energy for tritium desorption in MITR graphite samples was consistent with previously proposed mechanisms.** When graphite samples are charged with hydrogen gas and desorbed at high temperatures, the rate limiting step in the desorption process is described as the diffusion-controlled transport of tritium through graphite filler grains [115, 123, 159]. Several experiments have measured the diffusivity of hydrogen in graphite grains, and the four studies described in Section 2 present diffusivities with an average activation energy of 273.5 kJ/mol [126, 129, 127, 134]. The activation energy corresponding to the central

desorption peak from the MITR IG1 sample subsections was measured by observing the shift in peak desorption temperature as the temperature ramp rate was varied. An activation energy of 260 kJ/mol was calculated for the IG1 sample set, which is consistent with a tritium desorption process being rate-limited by diffusion through graphite grains since the range of grain diffusivity activation energies varied from 251 to 305 kJ/mol in the previous studies. A tritium desorption process controlled by diffusion also helps to explain why the desorption rates of MITR samples as a function of temperature were influenced by sweep gas hydrogen concentration.

- **The chemical forms of tritium retained on FS-1, FS-2, and FS-3 graphite samples were mainly HT/T_2.** The chemical form of tritium desorbed from the MITR samples could be examined by detecting whether or not the species were soluble in the first three vials of the water bubbler collection system. The resulting average soluble tritium fraction of each sample group was 4.2% for FS-1, 11.2% for FS-2, and 7.2% for FS-3 samples. Therefore, the majority of tritium desorption in all cases occurred from a water-insoluble form, of which HT/T_2 are the most likely. The chemical form of tritium measured from MITR samples then also supports the use of transport mechanisms proposed for gaseous hydrogen to describe the retention process in graphite of tritium originating from molten Flibe under neutron irradiation.

7.2. Conclusions from Graphite Tritium Transport Model Development

The central takeaways from the development of the graphite transport and trapping model are summarized below.

- **A bulk-diffusivity model can be used to represent tritium transport in graphite, but only when diffusion length scales are controlled.** Treating graphite as a homogenous medium with a single diffusivity was used to replicate the thermal desorption of deuterium in 1mm thick POCO AXF-5Q1 samples from previous studies [159]. Using the experimental desorption profile, a bulk-diffusivity was fit from the data by varying the diffusion activation energy and pre-exponential factor. The resulting bulk diffusivity from the data fit had values in between that of previous measurements for the diffusivity of hydrogen in graphite pores and the diffusivity inside graphite grains. Therefore, a bulk-diffusivity can be used to represent the diffusion in graphite pores and grains with a single process. However, since the grain size stays

constant in graphite while bulk dimensions can vary, the bulk-diffusivity fit from a single experiment cannot be generally applied to other graphite systems with different diffusion length scales. For example, when the bulk-diffusivity from the 1mm desorption experiment was used to model the retention of a 0.39mm thick sample from a separate study, the retention rate for a given time and temperature was over predicted by the model since then sample length scale was significantly reduced. To apply the bulk-diffusivity model to retention calculations in a FHR, an experimental data source would be required with temperatures, hydrogen partial pressures, and physical dimensions similar to that expected in the reactor.

- **Modeling tritium transport in graphite pores along with tritium diffusion and trapping in graphite grains can provide a more general approach towards simulating tritium retention in graphite.** Models which simulate tritium diffusion and trapping in graphite grains have demonstrated an ability to reproduce results from gaseous retention experiments [127, 108]. However, one assumption made in previous models is that grains inside graphite are exposed to the same partial pressure of tritium throughout the graphite bulk. Considering that a significant tritium concentration gradient may be present in graphite at FHR conditions, a retention model for a FHR requires some representation for the change in tritium partial pressures which may occur over the physical dimensions of graphite materials in the core. Modeling the diffusion of molecular tritium through graphite pores in connection with the uptake, diffusion, and trapping of tritium in grains is one method in which a tritium retention can be solved for as a function of depth into graphite. A pore and grain transport solution is a more general approach than the bulk-diffusivity method since each input into the model has been previously measured in literature and no additional data fitting is required. However, as significant uncertainty in some parameters exists, calculations from the pore and grain diffusion method would benefit from additional experimental investigation into tritium transport properties in graphite grades of interest.

- **Both tritium retention calculation methods demonstrate that tritium transport in graphite limits the overall retention rate in a FHR.** Using the baseline FHR description outlined in Section 5, tritium retention on the core graphite pebbles accounted for 26.3% of the total tritium distribution with the pore and grain transport methodology and 20.3% with the

bulk-diffusion treatment. Both values are significantly below the 79.8% retention estimate which would have occurred if tritium retention in graphite was only limited by mass transfer in Flibe. As a result, tritium transport into graphite adds a considerable resistance to the overall retention process at expected FHR conditions according to the transport models proposed in this study.

7.3. Conclusions from Proposed Tritium Management Strategies

The updated tritium retention methodology for graphite was implemented into the TRIDENT Mod1 system-level tritium transport model to calculate the baseline FHR tritium distribution and explore tritium management strategies. While the strategies implemented were not an exhaustive list of potential options, the resulting changes to the tritium distribution can provide general guidance towards the effect from similar tritium management solutions.

- **Permeation through the hot leg, cold leg, and reactor vessel comprises a significant fraction of the baseline tritium distribution.** In addition to implementing the graphite retention methodology, the updates to TRIDENT from this work included development of additional regions in the FHR to better describe the complete tritium distribution in the reactor. One surprising result was that tritium permeation through the hot leg, cold leg, and reactor vessel produced 17.9% of total tritium releases, despite accounting for only 1.9% of the total surface areas in contact with Flibe in the primary loop. The elevated permeation in these regions occurs because of the significant turbulence and enhanced mass transfer characteristics. For an equilibrium tritium generation rate of 981 Ci per day, the baseline releases from the hot leg, cold leg, and reactor vessel amount to 64093 Ci per year. Considering that permeation from these regions will lead to release into the reactor building where tritium capture may be the most difficult, it is important factor these releases into the overall tritium management strategy for the FHR.

- **Permeation barrier coatings applied to exterior surfaces only marginally reduce permeation into the reactor building, and are not practical for limiting permeation into the intermediate loop.** In the TRIDENT Mod1 code, permeation barrier coatings applied to the exterior surfaces of structural metals have the effect of increasing the concentration of diffusing tritium. Increased tritium concentration in the metal can in turn amplify the

permeation resistance through increasing the boundary T_2 value at the salt-metal interface. However, since the heat exchanger has negligible permeation resistance under baseline conditions, exterior coatings with permeation reduction factors up to 500 were not effective in reducing the permeation rate into the intermediate loop. In contrast, there is a small, but notable permeation resistance created by tritium diffusion through the hot leg, cold leg, and vessel at baseline FHR conditions. For exterior coatings with PRF_{out} values of 500 applied to these regions, the sum of permeation releases is estimated to decrease from the baseline value of 64093 Ci/yr to 14,600 Ci/yr.

- **Flibe-facing coatings can reduce permeation rates, and can be most efficiently leveraged in strategies which also employ tritium capture in the intermediate loop.** For coatings applied to the inner surfaces in the primary loop, the flux of T_2 into the metal is directly reduced according to the specified PRF_{in} value. Applying coatings to all Flibe-facing surfaces decreases permeation rates, but also increases the T_2 concentration in the salt as tritium release paths are diminished. The sum of permeation rates from the hot leg, cold leg, and reactor vessel was 757 Ci/yr when all inner-surfaces were simulated with a PRF_{in} of 500. By leaving the heat exchanger uncoated instead, and thus assuming that tritium capture systems can be effectively employed in the intermediate loop, the significant increase in T_2 concentration can be prevented and permeation through the heat exchanger remains as the dominant release path. For a PRF_{in} of 500 applied only to the hot leg, cold leg, and vessel, the permeation rate into the reactor building was calculated to be 172 Ci/yr. In this case, the amount of Flibe-facing coating surface area required is only 2.5% of the fully-coated case.

- **A tritium extraction system in the primary loop can remove substantial tritium releases, but other FHR transport pathways remain significant even at high removal efficiencies.** The calculated tritium residence time in the FHR primary systems along with the Flibe flow transit time reveals that 6.7% of the salt tritium inventory is removed upon each pass through the primary loop. Therefore, a tritium extraction system will start to absorb the majority of tritium releases from the reactor once a single-pass removal efficiency of 6.7% is exceeded. A removal efficiency of greater than 10% was readily achieved for the permeator and graphite retention bed designs considered in Section 6. For example, a permeator system constrained to

a 25 m^3 internal Flibe volume and 2 atm overall pressure drop had a calculated removal efficiency of 41.04% for a 1000 tube design and 74.53% for a 20,000 tube design. However, the sum of all other FHR release paths still amounted to 5729 Ci/yr when the 20,000 tube permeator design was implemented in TRIDENT Mod1. A simple formula discussed in Section 6 suggests that the required removal efficiency of an extraction system would have to be greater than 99.5% in order to achieve releases from all other FHR regions equal to the average PWR discharge rate of 112 Ci/yr [29]. In both the permeator and graphite bed designs studied, there were diminishing returns on extraction performance as the dimensions of each system increased. Therefore, achieving a PWR-equivalent release rate would require an impractically large extraction device in the primary loop if the extraction system was the only region where tritium was captured from the FHR.

- **Combining a low efficiency tritium extraction system with moderate strength Flibe-facing coatings leads to tritium releases from the hot leg, cold leg, and reactor vessel which are lower than a reference PWR annual tritium release rates.** As the dominant tritium release path in the baseline FHR simulations, permeation through the heat exchanger is the most difficult to minimize in any tritium management strategy. If a nitrate salt is used as an intermediate coolant, tritium which permeates through the heat exchanger is expected to undergo oxidation and thus be restrained from further permeation [176, 114]. A tritium management strategy which implemented controls to sequester tritium from the intermediate loop would thus not necessarily require limitations on the permeation rate through the heat exchanger. Focusing then on releases to the reactor building, Flibe-facing permeation barriers can be applied to the hot leg, cold leg, and reactor vessel while the heat exchanger is left uncoated. Adding a low efficiency tritium extraction system to the primary loop can significantly reduce the coating requirements for permeation resistance while maintaining low release rates into the reactor building. For example, TRIDENT Mod1 simulations demonstrate that reactor building releases below the PWR annual discharge rate can be achieved for PRF_{in} values and extraction system efficiencies of 250 and 10%, 200 and 15% or 150 and 20%, respectively. As previously shown, a coating with a PRF_{in} above 500 would be required to achieve the same results without the added extraction system.

7.4. Data Needs and Opportunities for Future Improvement

The TRIDENT Mod1 code relies on numerous experimentally measured parameters in order to perform system-level tritium transport calculations. Additional experiments to measure certain parameters would improve the confidence in the predicted tritium distribution. The sensitivity study discussed in Section 5 can provide information as to which experiments would be the most valuable in future studies, as summarized below.

- **The Henry's law coefficient for T_2 solubility in Flibe ($K_{H,T2}$):** The $K_{H,T2}$ values had a notable sensitivity to tritium release in all FHR regions. Measurements of $K_{H,T2}$ fall into two groupings in literature studies – either relatively low values from direct measurements of solubility, or relatively high values measured during permeation experiments. Future measurements could help to rule out one group of measurements over the other, and thus significantly reduce the relative uncertainty in the parameter. For example, the relative standard deviations of the low and high groupings are 55% and 41%, compared to a combined relative standard deviation of 103%. Therefore, the uncertainty could be reduced by half through an experiment which identifies which grouping is more appropriate.

- **Solubility of tritium in graphite ($K_{S,g}$):** Sensitivity values for $K_{S,g}$ were among the top three highest in all reactor regions, despite the moderate relative uncertainty. The solubility of tritium in graphite influences the total tritium capacity and also partially governs the transition of from pores to grains in graphite. High sensitivity values from $K_{S,g}$ also highlight the need to understand how the solubility of tritium in graphite will change under neutron irradiation at FHR conditions.

- **Diffusivity of tritium in graphite grains ($D_{T,g}$):** The $D_{T,g}$ input value had the highest relative uncertainty in literature measurements, and also the third largest impact on the tritium release to primary systems. One cause of the high uncertainty is that previous measurements on several grades of graphite as well as significantly different testing conditions were used to calculate the relative uncertainty. Once the graphite grades of interest are selected for the FHR, directed testing on these materials at suitable FHR conditions could lead to significant improvements on the spread in observed data.

- **Diffusivity of tritium in graphite pores ($D_{T2,p}$):** Varying the diffusivity of tritium in graphite pores has a similar effect to that of graphite grains, although at a slightly lower sensitivity. Only two measurements on the diffusivity of hydrogen in nuclear graphite pores were found in literature [126, 108], and the data set was supplemented with estimations on the diffusivity of helium calculated from thermal desorption profiles [138]. In addition to more measurements, there is also a need for data to be taken over a larger range of FHR-representative temperatures.

- **Diffusivity of T_2 in Flibe ($D_{T2,Flibe}$):** The diffusivity of tritium in Flibe has a fairly high uncertainty in previous experimental measurements, and has a notable impact on tritium transport to all regions in a FHR. Further resolving the T_2 diffusivity in Flibe is also important when determining the removal efficiency of any candidate tritium extraction system for the FHR. Additionally, the $D_{T2,Flibe}$ value had the second largest sensitivity in terms of tritium release to the intermediate loop. Therefore, tritium management strategies which rely on tritium capture in the nitrate salt will require higher certainty in diffusivity values in order to accurately predict the amount of tritium control required in the intermediate loop.

- **Trapping rate constant (Σ_T):** No experimental studies which explicitly measure a trapping rate constant were found in the literature review and TRIDENT Mod1 relies on the Σ_T structure proposed by the TMAP code [92]. When all parameters were varied by 10%, the trapping rate constant had the sixth highest sensitivity on the amount of tritium retention in the core. Further studying the temperature dependence of the trapping rate constant will be important in determining the fraction of tritium which is converted to high-energy trapping sites in graphite. As shown for the baseline TRIDENT Mod1 results, the amount of high-energy trapping significantly varied between the graphite pebbles near the 550ºC core inlet and pebbles near the 650ºC core outlet. Furthermore, the FS-3 desorption experiments show that there was a large difference between strong trapping behavior in the lower crucible samples which had an irradiation temperature of 600ºC and the upper crucible samples at 720ºC. Therefore, the range of FHR operating temperatures appears to be near transition temperatures where high-energy trapping in graphite becomes significant.

Beyond the input parameter sensitivity study, other possibilities were explored to examine how the tritium distribution in a FHR would change if the baseline assumptions varied. For example, the assumptions on the chemical form of tritium in Flibe were varied by using more oxidizing redox potentials in the salt, as well as modeling a delay in redox equilibration with a chemical control sub-loop. In both scenarios, the TF concentration in the salt significantly increased, as was well above the T_2 concentration in some cases. However, substantial increases in the TF concentration in Flibe did not lead to a large deviation from the baseline tritium distribution because evolution to the reactor cover gas was the only modeled path for tritium release. If FHR-representative systems are indeed found to exhibit high levels of TF relative to T_2, then the underlying assumptions on TF release paths should be revisited.

One reason why TRIDENT Mod1 results were not sensitive to large changes in tritium chemical forms is that evolution to the reactor cover gas had the lowest contribution to overall release in the baseline results. The evolution rate calculation relies on an experimentally measured mass transfer coefficient, where in the current model a value from a static Flibe irradiation is used [48]. It should be noted that the evolution mass transfer coefficient is comparable to other values in TRIDENT Mod1 – it is higher than the mass transfer coefficient in the heat exchanger and 82% of the value for the mass transfer coefficient in the vessel downcomer. However, evolution rates could be still higher in actual FHR designs if there is a significant rate of additional mass transfer occurring near the top of the vessel. For example, integral pumps in the vessel head could enhance the evolution mass transfer coefficient and potentially increase the potential salt-gas interfacial area if the salt surface is continuously disturbed. For these reasons, the current evolution rates predicted by TRIDENT Mod1 could be considered as lower bound estimates.

For tritium management strategies, the TRIDENT Mod1 results provide a preliminary understanding or design considerations for different tritium management solutions. With the extraction system analysis, the results demonstrate the size and scale of equipment needed to achieve various amounts of tritium release. For coatings, the tritium distribution results show what permeation reduction factors would be required from candidate coating materials. The TRIDENT Mod1 tritium management results were evaluated based on release out of the primary systems in gross terms of Curies of tritium per day. However, the true targets to minimize are the radiation hazards of tritium release and the potential for environmental contamination, which depend not only on the total amount of tritium release but also on the tritium effluent concentrations and

chemical forms. Future work should be carried out to connect the modeled results for tritium distribution in the primary FHR systems shown in this study to the release and potential tritium capture in the FHR plant, and then eventually to solve for tritium dose and radiation hazards in a site-scale mechanistic release model.

The tritium management discussion in Section 6 also did not examine any economic factors of the proposed solutions since little concrete information is available for certain aspects of each strategy. Overall costs of each approach will also significantly depend on the implementation of each solution into the FHR design, which requires a further detailed analysis. Since compliance with tritium release regulations will be required for licensing and operation of the reactor, a challenge for FHR designers exists in selecting and demonstrating a tritium management strategy for the plant that does not create a significant cost burden which diminishes the prospects for future FHR commercialization.

8. References

[1] C. Forsberg, L.W. Hu, P. Peterson and K. Sridharan, "Fluoride-Salt-Cooled High-Temperature Reactor (FHR) for Power and Process Heat," Massachusetts Institute of Technology, 2014.

[2] Williams, D. F.; Toth, L. M.; Clarno, K. T., "Assessment of Candidate Molten Salt coolants for the Advanced High-Temperature Reactor (AHTR)," ORNL/TM-2006/12, 2006.

[3] J. Stempien, "Tritium Transport, Corrosion, and Fuel Performance Modeling in the Fluoride-Salt-Cooled High-Temperature Reactor," Massachusetts Institute of Technology, PhD Thesis, 2015.

[4] S. T. T. Lam, "Managing Tritium Inventory and Release with Carbon Materials in a Fluoride Salt-Cooled High-Temperature Reactor," Massachusetts Institute of Technology, SM Thesis, 2017.

[5] C. Andreades et. al., "Technical Description of the “Mark 1” Pebble-Bed Fluoride-Salt-Cooled High-Temperature Reactor (PB-FHR) Power Plant," Department of Nuclear Engineering, University of California, Berkeley, 2014.

[6] C. Andreades, A. T. Cisneros, J. K. Choi, A. Y. K. Chong, M. Fratoni, S. Hong, L. R. Huddar, K. D. Huff, J. Kendrick, D. L. Krumwiede, M. R. Laufer, M. Munk, R. O. Scarlat and N. Zweibau, "Design Summary of the Mark-I Pebble-Bed Fluoride Salt-Cooled, High-Temperature Reactor Commercial Power Plant," *Nuclear Technology,* vol. 195, pp. 223-238, 2016.

[7] Jacopo Buongiorno, Michael Corradini, John Parsons, David Petti et al, "The Future of Nuclear Energy in a Carbon-Constratined World," MIT Energy Initiative, 2018.

[8] C. Forsberg and P. F. Peterson, "Basis for Fluoride Salt-Cooled High-Temperature Reactors with Nuclear Air-Brayton Combined Cycles and Firebrick Resistance-Heated Energy Storage," *Nuclear Technology,* vol. 196, pp. 13-33, 2016.

[9] N. Baghdasaryan and T. Kozlowski, "Review of Progress in Coated Fuel Particle Performance Analysis," *Nuclear Science and Engineering,* vol. 194, pp. 169-180, 2020.

[10] C. Forsberg, D. Wang, E. Shwageraus, B. Mays, G. Parks, C. Coyle and M. Liu, "Fluoride-Salt-Cooled High-Temperature Reactor (FHR) Using British Advanced Gas-Cooled Reactor (AGR) Refueling Technology and Decay Heat Removal Systems that Prevent Salt Freezing," *Nuclear Technology,* vol. 205, pp. 1127-1142, 2019.

[11] D. L. Krumwiede, R. O. Scarlat, J. K. Choi, T. M. Phan and P. F. Peterson, "Three-Dimensional Modeling of the Pebble-Bed Fluoride-Salt-Cooled, High-Temperature Reactor (PB-FHR)," *Transactions of the American Nuclear Society,* 2013.

[12] International Atomic Energy Agency, "High Temperature Gas Cooled Reactor Fuels and Materials," IAEA-TECDOC-1645, Vienna, 2010.

[13] H. G. MacPherson, "The Molten Salt Reactor Adventure," *Nuclear Science and Engineering,* vol. 90, pp. 374-380, 1985.

[14] C. W. Forsberg, P. F. Peterson, K. Sridharan, L. W. Hu, M. Fratoni and A. K. Prinja, "Integrated FHR Technology Development: Tritium Management, Materials Testing, Salt Chemistry Control, Thermal Hydraulics, Associated Benchmarking and Commercial Basis," MIT-ANP-TR-180, 2018.

[15] G. Zheng, B. Kelleher, G. Cao, M. Anderson, T. Allen and K. Sridharan, "Corrosion of 316 Stainless Steel in High Temperature molten Li2BeF4 (FLiBe) Salt," *Journal of Nuclear Materials,* vol. 461, pp. 143-150, 2015.

[16] B. Kelleher, K. Dolan, P. Brooks, M. Anderson, K. Sridharan;, "Batch-Scale Hydrofluorination of 7Li2BeF4 to Support Molten Salt Reactor Development," *Journal of Nuclear Engineering and Radiation Science,* 2015.

[17] D. M. Carpenter, M. Ames, G. Kohse, Y. Ostrovsky and L.-w. Hu, "Fluoride Salt High-Temperature Reactor Materials Irradiation Test at the MIT Research Reactor," in *Proceeding of ICAPP 2014*, Charlotte, NC, 2014.

[18] K. Dolan, "Tritium Thermal Desorption Testing of Nuclear Graphites Irradiated at Fluoride-Salt-Cooled High-Temperature Reactor Conditions," Massachusetts Institute of Technology, SM Thesis, 2018.

[19] D. Zhang, L. Liu, M. Liu, R. Xu, C. Gong, J. Zhang, C. Wang, S. Qiu and G. Su, "Review of conceptual design and fundamental research of molten salt reactors in China," *International Journal of Energy Research,* vol. 42, pp. 1834-1848, 2018.

[20] E. Blandford, K. Brumback, L. Fick, C. Gerardi, B. Haugh, E. Hillstrom, K. Johnson, P. F. Peterson, F. Rubio, F. S. Sarikurt, S. Sen, H. Zhao and N. Zweibaum, "Kairos power thermal hydraulics research and development," *Nuclear Engineering and Design,* vol. 364, 2020.

[21] E. M. Baum, M. C. Ernesti, H. D. Knox, T. R. Miller and A. M. Watson, "Nuclides and Isotopes: Chart of the Nucliedes," Knolls Atomic Power Laboratory, Seventeenth Edition - 2009.

[22] M. F. Fitzsimons, M. C. Lohan, A. D. Tappin and G. E. Millward, "4.04 - The Role of Suspended Particles in Estuarine and Coastal Biogeochemistry," *Reference Module in Earth Systems and Environmental Sciences,* vol. 4, pp. 71-114, 2011.

[23] M. T. Mustonen and J. Suhonen, "Beyond low beta-decay Q values," in *American Institute of Physics Conference Proceedings 13014, 401*, 2010.

[24] Canadian Nuclear Safety Commission, "Implementation of Recommendations from the Tritium Studies Synthesis Report," 2019.

[25] K. Eckerman, J. Harrison, H.-G. Menzel and C. H. Clement, "Compendium of Dose Coefficients based on ICRP Publication 60," International Commission on Radiological Protection, ICRP Publication 119. Ann. ICRP 41(Suppl.), 2012.

[26] D. Grabaskas, T. Fei and J. Jerden, "Technical Letter Report on the Assessment of Tritium Detection and Control in Molten Salt Reactors: Final Report," Argonne National Laboratory, ANL/NSE-20-15, 2020.

[27] United States Nuclear Regulatory Commission, "Advanced Reactor Stakeholder Public Meeting," August 20, 2020.

[28] E. L. Albenesius, "Tritium as a product of fission," *Physical Review Letters,* vol. 3, 1959.

[29] International Atomic Energy Agency, "Management of waste containing tritium and carbon-14," Vienna, 2004.

[30] World Nuclear Association, "Information Library - Current and Future Generation - Lithium," October 2017. [Online]. Available: https://www.world-nuclear.org/information-library/current-and-future-generation/lithium.aspx.

[31] M. J. Colomb, "Supplemental Special Report for Tritium Discovered Onsite Vermont Yankee Nuclear Power Station," Entergy, BVY 10-039, 2010.

[32] T. Dadabbo, "Vermont Yankee Nuclear Power Plant Tritium Incident," 19 April 2017. [Online]. Available: http://large.stanford.edu/courses/2017/ph241/dadabbo2/.

[33] Canadian Nuclear Safety Commission, "Tritium Releases and Dose Consequences in Canada in 2006," INFO-0793, 2009.

[34] S.-H. Son, S.-K. Lee and K.-S. Kim, "Tritium production, recovery, and application in Korea," *Applied Radiation and Isotopes,* vol. 67, pp. 1336-1340, 2009.

[35] B. W. Gainey, "A Review of Tritium Behavior in HTGR Systems," General Atomics, GA-A13461, 1976.

[36] National Nuclear Data Center, "ENDF/B-VII.1 Evaluated Neutron Library," Brookhaven National Laboratory, 2011.

[37] M. Rubel, "Fusion Neutrons: Tritium Breeding and Impact on Wall Materials and Components of Diagnostic Systems," *Journal of Fusion Energy,* vol. 38, pp. 315-329, 2019.

[38] R. B. Briggs, "Tritium in Molten-Salt Reactors," *Reactor Technology,* vol. 14, no. 4, 1971-1972.

[39] J. H. Shaffer, "Preparation and Handling of Salt Mixtures for the Molten Salt Reactor Experiment," ORNL-4616, Oak Ridge National Laboratory, 1971.

[40] MIT-Nuclear Reactor Laboratory, "Irradiation of Materials in Molten Fluoride Salt in a Dedicated In-Core Facility (FS-3)," 2016.

[41] K. Dolan, G. Zheng, K. Sun, D. Carpenter and L.W. Hu, "Tritium Generation, Release, and Retention from In-core Fluoride Salt Irradiations," *(Submitted).*

[42] J. Cao, L. Zhang, F. Xie, B. Xia and S. T. T. Lam, "Source Term Study on Tritium in HTR-PM: Theoretical Calculations and Experimental Design," *Science and Technology of Nuclear Installations,* vol. 2017, 2017.

[43] J. D. Stempien, R. G. Ballinger and C. W. Forsberg, "An integrated model of tritium transport and corrosion in Fluoride Salt-Cooled High-Temperature Reactors (FHRs) - Part I: Theory and benchmarking," *Nuclear Engineering and Design,* vol. 310, pp. 258-272, 2016.

[44] A. Suzuki, T. Terai and S. Tanaka, "Change of tritium species in Li2BeF4 molten salt breeder under neutron irradiation at elevated temperature.," *Journal of Nuclear Materials,* Vols. 258-263, pp. 519-524, 1998.

[45] M. Shimada and R. J. Pawelko, "Tritium permeability measurement in hydrogen-tritium system," *Fusion Engineering and Design,* vol. 129, pp. 134-139, 2018.

[46] A. L. Mathews and C. F. Baes, "Oxide Chemistry and Thermodynamics of Molten LiF-BeF2 Solutions," *Inorganic Chemistry,* vol. 7, no. 2, pp. 373-382, 1968.

[47] A. Suzuki, T. Terai and S. Tanaka, "Mechanism on Change of Tritium Species in Li2BeF4 Molten Salt Breeder Under Neutron Irradiation at Elevated Temperature," *Fusion Technology,* vol. 34, pp. 526-530, 1998.

[48] A. Suzuki, T. Terai and S. Tanaka, "Tritium release behavior from Li2BeF4 molten salt by permeation through structural materials," *Fusion Engineering and Design,* Vols. 51-52, pp. 863-868, 2000.

[49] G. Zheng, D. Carpenter, K. Dolan and L.W. Hu, "Experimental investigation of alumina coating as tritium permeation barrier for molten salt nuclear reactors," *Nuclear Engineering and Design,* vol. 353, 2019.

[50] H. Moriyama, S. Maeda, T. Ohmura, K. Moritani and J. Oishi, "Chemical Behaviors of Tritium Formed in a LiF-BeF2 Mixture," *Journal of Nuclear Materials,* vol. 148, pp. 211-216, 1987.

[51] T. R. Allen, K. Sridharan, L. Tan, W. E. Windes, J. I. Cole and D. C. Crawford, "Materials Challenges for Generation IV Nuclear Energy Systems," *Nuclear Technology,* vol. 162, pp. 342-357, 2008.

[52] G. D. D. Cul, D. F. Williams, L. M. Toth and J. Caja, "Redox Potential of Novel Electrochemical Buffers Useful for Corrosion Prevention in Molten Fluorides," *Proc. 13th Internation Symposium on Molten Salts, 201st Meeting of the Electrochemical Society.*

[53] C. F. Baes, "The Chemistry and Thermodynamics of Molten Salt Reactor Fuels," *Nuclear Metallurgy,* vol. 15, 1969.

[54] D. Olander, "Redox Condition in Molten Fluoride Salts Definition and Control," *Journal of Nuclear Materials,* no. 300, pp. 270-272, 2002.

[55] L. M. Toth and L. K. Felker, "Fluorine Generation by Gamma Radiolysis of a Fluoride Salt Mixture," *Radiation Effects and Defects in Solids,* vol. 112, pp. 201-210, 1990.

[56] B. Kelleher, K. Dolan, M. Anderson and K. Sridharan, "Observed Redox Potential Range of Li2BeF4 Using a Dynamic Reference Electrode," *Nuclear Technology,* vol. 195, pp. 239-252, 2016.

[57] R. E. Thoma, "Chemical Aspects of MSRE Operations," Oak Ridge National Laboratory, Oak Ridge, TN, 1971.

[58] L. Olson, "Materials Corrosion in Molten LiF-NaF-KF Eutectic Salt," PhD Thesis, University of Wisconsin - Madison, 2009.

[59] D. L. Manning, G. Mamantov, "Recent Electroanalytical Studies in Molten Fluorides," *Characterization of Soluted in Nonaqueous Solvents,* pp. 289-309, 1978.

[60] B. Kelleher, *Purification and Chemical Control of Molten Li2BeF4 for a Fluoride Salt Cooled Reactor,* University of Wisconsin - Madison, 2015.

[61] Valery K. Afonichkin, Andrey L. Bovet, Victor V. Ignatiev, Alexander V. Panov, Vladimir G. Subbotin, Alexander I. Surenkov, Andrey D. Toropov, Aleksey L. Zherebtsov, "Dynamic Reference Electrode for Investigation of Fluoride Melts Containing Beryllium Difluoride," *Journal of Fluorine Chemistry,* vol. 130, pp. 83-88, 2009.

[62] J. R. Keiser, J. H. DeVan and D. L. Manning, "The Corrosion Resistance of Type 316 Stainless Steel To Li2BeF4," Oak Ridge National Laboratory, 1977.

[63] T. Terai, A. Suzuki and S. Tanaka, "In-Situ Tritium Release Experiment from Molten Li2BeF4 Salt under Neutron Irradiation at Elevated Temperatures (INTREXFLIBE)," *Fusion Technology,* vol. 30, pp. 911-915, 1996.

[64] T. Terai, A. Suzuki and S. Tanaka, "Tritium Release from Li2BeF4 Molten Salt Breeder Under Neutron Irradiation at Elevated Temperature," *Fusion Technology,* vol. 39, pp. 768-772, 2001.

[65] M. Hara, Y. Hatano, M. F. Simpson, G. R. Smolik, J. P. Sharp, Y. Oya, K. Okuno, M. Nishikawa, T. Terai, S. Tanaka, R. A. Anderl, D. A. Petti and D.-K. Sze, "Interactions between molten Flibe and metallic Be," *Fusion Engineering and Design,* vol. 81, pp. 561-566, 2006.

[66] S. Fukada, M. F. Simpson, R. A. Anderl, J. P. Sharpe, K. Katayama, G. R. Smolik, Y. Oya, T. Terai, K. Okuno, M. Hara, D. A. Petti, S. Tanaka, D.-K. Sze and A. Sagara, "Reaction rate of beryllium with fluorine ion for Flibe redox control," *Journal of Nuclear Materials,* Vols. 367-370, pp. 1190-1196, 2007.

[67] S. Delpech, C. Cabet, C. Slim and G. S. Picard, "Molten fluorides for nuclear applications," *Materials Today,* vol. 13, no. 12, 2010.

[68] C. S. Marchi, B. P. Somerday, R. S. Larson and S. F. Rice, "Solubility of hydrogen and its isotopes in metals from mixed gases," *Journal of Nuclear Materials,* vol. 372, no. 2-3, pp. 421-425, 2008.

[69] W. M. Jones, "Thermodynamic function for tritium and tritium hydride. The dissociation of tritium and tritium hydride.," *The Journal of Chemical Physics,* vol. 16, no. 11, 1948.

[70] E. Herms, J. M. Olive and M. Puiggali, "Hydrogen embrittlement of 316L type stainless steel," *Materials Science and Engineering,* vol. A272, pp. 279-283, 1999.

[71] A. P. Malinauskas, D. M. Richardson, J. E. Savolainen and J. H. Shaffer, "Apparatus for the Determination of the Solubility of Hydrogen in Molten Salts," *Industrial & Engineering Chemistry Fundamentals,* vol. 11, no. 4, pp. 584-586, 1972.

[72] P. E. Field and J. H. Shaffer, "The solubilities of hydrogen fluoride and deuterium fluoride in molten fluorides," *The Journal of Physical Chemistry,* vol. 71, pp. 3218-3222, 1967.

[73] W. Henry, "Experiments on the quantity of gases absorbed by water, at different temperatures, and under different pressures," *Philosophical Transactions of the Royal Society of London,* 1802.

[74] S. Fukada and A. Morisaki, "Hydrogen permeability through a mixed molten salt of LiF, NaF and KF (Flinak) as a heat-transfer fluid," *Journal of Nuclear Materials,* vol. 358, pp. 235-242, 2006.

[75] P. Calderoni, P. Sharpe, M. Hara and Y. Oya, "Measurement of tritium permeation in flibe (2LiF-BeF2)," *Fusion Engineering and Design,* vol. 83, pp. 1331-1334, 2008.

[76] R. Causey, R. Karnesky and C. S. Marchi, "Tritium Barriers and Tritium Diffusion in Fusion Reactors," in *Comprehensive Nuclear Materials,* Oxford, Elsevier, 2012, pp. 511-549.

[77] Y. Zeng, W. Liu, W. Liu, Y. Qian, N. Qian, X. Wu, Y. Huang, S. Wu and G. Wang, "Behavior characteristivs of hydrogen and its isotope in molten salt of LiF-NaF-KF (FLiNaK)," *Nuclear Engineering and Technology,* vol. 51, pp. 490-494, 2019.

[78] A. Nakamura, S. Fukada and R. Nishiumi, "Hydrogen isotopes permeation in a fluoride molten salt for nuclear fusion blanket," *Journal of Plasma Science and Fusion Research,* vol. 11, 2015.

[79] R. Andrel, S. Fukada, G. Smolik, R. Pawelko, S. Schuetz, J. Sharpe, B. Merrill, D. Petti and N. Nishimura, "Deuterium/tritium behavior in Flibe and Flibe-facing materials," *Journal of Nuclear Materials,* Vols. 329-333, pp. 1327-1331, 2004.

[80] J. Oishi, H. Moriyama, S. Maeda and Y. Asaoka, "Tritium Recovery from Molten LiF-BeF2 Salt," *Fusion Engineering and Design,* vol. 8, pp. 317-321, 1989.

[81] S. Lam, "Accelerated atomistic prediction of structure, dynamics and material properties in molten salt," Massachusetts Institute of Technology, PhD Thesis, 2020.

[82] A. P. Malinauskas and D. M. Richardson, "The Solubilities of Hydrogen, Deuterium, and Helium in Molten Li2BeF4," *Industrial & Engineering Chemistry Fundamentals,* vol. 13, pp. 242-245, 1974.

[83] R. S. Brodkey and H. C. Hershey, Transport Phenomena: A Unified Approach, Columbus, Ohio: Brodkey Publishing, 1988.

[84] E. J. Wilson and C. J. Geankoplis, "Liquid mass transfer at very low reynolds numbers in packed beds," *I&EC Fundamentals,* vol. 5, no. 1, 1966.

[85] R. H. Perry and D. W. Green, Perry's Chemical Engineers' Handbook, New York: McGraw-Hill, 2008.

[86] N. E. Todreas and M. S. Kazimi, Nuclear Systems, Boca Raton: Taylor & Francis Group, 2011.

[87] R. R. Romatoski and L. W. Hu, "Fluoride-Salt-Cooled High-Temperature Test Reactor Thermal-Hydraulic Licensing and Uncertainty Propogation Analysis," *Nuclear Technology,* vol. 205, pp. 1495-1512, 2019.

[88] A. Suzuki, T. Terai and S. Tanaka, "In-situ HT release behavior from molten Li2BeF4 salt," *Fusion Engineering and Design,* Vols. 39-40, pp. 781-785, 1998.

[89] F. N. Peebles, "Removal of Xenon-135 from circulating fuel salt of the MSBR by mass transfer to helium bubbles," ORNL-TM-2245, Oak Ridge National Laboratory, 1968.

[90] P. G. Smith, "Development of Fuel- and Coolant-Salt Centrifugal Pumps for the Molten-Salt Reactor Experiment," ORNL-TM-2987, Oak Ridge National Laboratory, 1970.

[91] T. Tanabe, Y. Yamanishi, K. Sawada and S. Imoto, "Hydrogen Transport in Stainless Steels," *Journal of Nuclear Materials,* Vols. 122-123, pp. 1568-1572, 1984.

[92] G. R. Longhurst, "TMAP7 User Manual," INEEL/EXT-04-02352, Idaho National Engineering and Environmental Laboratory, 2008.

[93] H. K. Perkins and T. Noda, "Deuterium transport through 304 and 304L stainless steel at low driving pressures and 15 KeV deuteron bombardment," *Journal of Nuclear Materials,* vol. 71, pp. 349-364, 1978.

[94] K. Wilson, "Hydrogen Recycling Properties of Stainless Steels," *Journal of Nuclear Materials,* vol. 103&104, pp. 453-464, 1981.

[95] M. Baskes, "A calculation of the surface recombination rate constant for hydrogen isotopes on metals," *Journal of Nuclear Materials,* vol. 92, pp. 318-324, 1980.

[96] N. .. Quick and H. H. Johnson, "Permeation and Diffusion of Hydrogen and Deuterium in 310 Stainless Steel, 427K to 779K," *Metallurgical Transactions A,* vol. 10A, 1979.

[97] T. Shiraishi, M. Nishikawa, T. Yamaguchi and K. Kenmotsu, "Permeation of multi-component hydrogen isotopes through austenitic stainless steels," *Journal of Nuclear Materials,* vol. 273, pp. 60-65, 1999.

[98] A. I. Gromov and Y. K. Kovneristyi, "Permeability, diffusion, and solubility of hydrogen in Cr-Ni and Cr-Mn austenitic stainless steels," *Metal Science and Heat Treatment,* vol. 22, pp. 321-324, 1980.

[99] X. K. Sun, J. Xu and Y. Y. Li, "Hydrogen permeation behaviour in austenitic stainless steels," *Materials Science and Engineering,* vol. 114, pp. 179-187, 1989.

[100] D. M. Grant, D. L. Cummings and D. A. Blackburn, "Hydrogen in 316 steel - Diffusion, permeation and surface reaction," *Journal of Nuclear Materials,* vol. 152, pp. 139-145, 1988.

[101] N. Kishimoto, T. Tanabe and T. S. e. al, "Hydrogen diffusion and solution at high temperatures in 316L stainless steel and nickel-base heat-resistant alloys," *Journal of Nuclear Materials,* vol. 127, pp. 1-9, 1985.

[102] Canadian Nuclear Safety Commission, "Evaluation of Facilities Handling Tritium," INFO-0796, 2010.

[103] G. W. Hollenberg, E. P. Simonen, G. Kalinin and A. Terlain, "Tritium/hydrogen barrier development," *Fusion Engineering and Design,* vol. 28, pp. 190-208, 1995.

[104] K. Katayama, J. Izumino, H. Matsuura and S. Fukada, "Evaluation of hydrogen permeation rate through zirconium pipe," *Nuclear Materials and Energy,* vol. 16, pp. 12-18, 2018.

[105] M. Shimada and R. J. Pawelko, "Tritium permeability in polycrystalline tungsten," *Fusion Engineering and Design,* vol. 146, pp. 1988-1992, 2019.

[106] G. R. Gaskey and R. G. Derrick, "Trapping of deuterium during permeation through gold," *Scripta Metallurgica,* vol. 10, pp. 377-380, 1976.

[107] T. Chikada, A. Suzuki, C. Adelhelm, T. Terai and T. Muroga, "Surface behaviour in deuterium permeation through erbium oxide coatings," *Nuclear Fusion,* vol. 51, 2011.

[108] R. A. Causey, "The Interaction of Tritium with Graphite and its Impact on Tokamak Operations," *Journal of Nuclear Materials,* Vols. 162-164, pp. 151-161, 1989.

[109] K. S. Forcey, D. K. Ross and C. H. Wu, "The formation of hydrogen permeation barriers on steels by aluminizing," *Journal of Nuclear Materials,* vol. 182, 1991.

[110] K. S. Forcey and A. Perujo, "Tritium permeation barriers in contact with liquid lithium-lead eutectic (Pb-17Li)," *Journal of Nuclear Materials,* vol. 218, pp. 224-230, 1995.

[111] C. Linsmeier, M. Rieth, J. Aktaa, T. Chikada, A. Hoffmann, J. Hoffmann and A. H. e. al, "Development of advanced high heat flux and plasma-facing materials," *Nuclear Fusion,* vol. 57, 2017.

[112] H. Fujita, T. Chikada, J. Engels, J. Mochizuki, S. Horikoshi, M. Matsunaga, T. Tanaka and T. Terai, "The relationship between structural changes of ceramic coatings and gamma-ray irradiation effect on deuterium permeation," *Fusion Engineering and Design,* vol. 146, pp. 2255-2258, 2019.

[113] Y. Oya, M. Kobayashi, O. J, M. Suzuki, A. Hamada, K. Matsuoka, Y. Hatano, M. Matsuyama, T. Hayashi, T. Yamanishi and K. Okuno, "Effect of surface oxide layer on deuterium permeation behaviors through a type 316 stainless steel," *Fusion Engineering and Design,* vol. 87, pp. 580-583, 2012.

[114] E. G. Bohlmann, "Heat Transfer Salt for High Temperature Steam Generation," Oak Ridge National Laboratory, ORNL-TM-3777, 1972.

[115] H. Atsumi, Y. Takemura, T. Konishi, T. Tanabe and T. Shikama, "Thermal Desorption of Hydrogen from Carbon and Graphite at Elevated Temperatures," *Journal of Nuclear Materials,* vol. 483, pp. S963-S966, 2013.

[116] S. Lam, K. Dolan, W. Liu, R. Ballinger and C. Forsberg, "Weak and strong hydrogen interactions on porous carbon materials in high-temperature systems," *Journal of Nuclear Materials,* vol. 519, pp. 173-181, 2019.

[117] R. E. Franklin, "Homogeneous and Heterogeneous Graphitization of Carbon," *Nature,* no. 4501, p. 239, 1965.

[118] R. E. Franklin, "Crystallite growth in graphitizing and non-graphitizing carbons," *Proceedings of the Royal Society A,* 1951.

[119] A. Celzard and V. Fierro, "Carbon, a unique model material for condensed matter physics and engineering science," in *Fandamental and Applied Nano-Electronics,* Springer, Dordrecht, 2016.

[120] H. Marsh and J. Griffiths, "Model of the carbonisation/graphitisation process," in *International Symposium on Carbon, New Processes and Applications,* 1982.

[121] H. Atsumi, T. Tanabe and T. Shikama, "Hydrogen behavior in carbon and graphite before and after neutron irradiation - Trapping, diffusion and the simulation of bulk retention," *Journal of Nuclear Materials,* vol. 417, pp. 633-636, 2011.

[122] R. E. Franklin, "The Structure of Graphitic Carbons," *Acta Crystallographica,* vol. 4, p. 253, 1951.

[123] H. Atsumi, Y. Takemura, T. Miyabe, T. Konishi, T. Tanabe and T. Shikama, "Desorption of hydrogen trapped in carbon and graphite," *Journal of Nuclear Materials,* vol. 442, pp. S746-S750, 2013.

[124] International Organization for Standardization, "Determination of the specific surface area of solids by gas adsorption -- BET method," 2010.

[125] Y. Shirasu, S. Yamanaka and M. Miyake, "Thermodynamic analysis of hydrogen solubility in graphite," *Journal of Nuclear Materials,* vol. 200, pp. 218-222, 1993.

[126] H. Atsumi, S. Tokura and M. Miyake, "Absorption and Desorption of Deuterium on Graphite at Elevated Temperatures," *Journal of Nuclear Materials,* Vols. 155-157, pp. 241-245, 1988.

[127] R. A. Causey, M. I. Baskes and K. L. Wilson, "The retention of deuterium and tritium in POCO AXF-5Q graphite," *Journal of Vacuum Science & Technology A: Vacuum, Surfaces, and Films,* vol. 4, no. 3, pp. 1189-1192, 1986.

[128] H. Atsumi and K. Tauchi, "Hydrogen absorption and transport in graphite materials," *Journal of Alloys and Compounds,* Vols. 356-357, pp. 705-709, 2003.

[129] H. Atsumi and Y. Kondo, "Retention and release of hydrogen isotopes in carbon materials priorly charged in gas phase," *Fusion Engineering and Design,* vol. 131, pp. 49-53, 2018.

[130] S. Lam, "Unpublished Work," *Massachusetts Institute of Technology,* 2018.

[131] H. Atsumi, T. Tanabe and T. Shikama, "Bulk hydrogen retention in neutron-irradiated graphite at elevated temperatures," *Journal of Nuclear Materials,* Vols. 390-391, pp. 581-584, 2009.

[132] H. Atsumi, M. Iseki and T. Shikama, "Trapping and Detrapping of Hydrogen in Carbon-Based Materials Exposed to Hydrogen Gas," *Journal of Nuclear Materials,* vol. 212, pp. 1478-1482, 1994.

[133] H. Atsumi, N. Shibata, T. Tanabe and T. Shikama, "Hydrogen absorption into neutron-irradiated graphite and estimation of the trapping effect," *Physica Scripta,* vol. T128, pp. 72-75, 2007.

[134] H. Rohrig, P. Fischer and R. Hecker, "Tritium Balance in High-Temperature Gas-Cooled Reactors," *Journal of the American Ceramic Society,* vol. 59, no. 7-8, pp. 316-320, 1976.

[135] H. Atsumi, "Mechanism of Hydrogen Trapping and Transport in Carbon Materials," *Physica Scripta,* vol. T103, pp. 77-80, 2003.

[136] H. Atsumi, "Hydrogen bulk retention in graphite and kinetics of diffusion," *Journal of Nuclear Material,* Vols. 307-311, pp. 1466-1470, 2002.

[137] H. Atsumi, "Hydrogen retention in graphite and carbon materials under a fusion reactor environment," *Journal of Nuclear Materials,* Vols. 313-316, pp. 543-547, 2003.

[138] H. Atsumi, T. Yamauchi and M. Miyake, "Dissolution and diffusion of helium in graphite," *Journal of Nuclear Materials,* Vols. 179-181, pp. 227-230, 1991.

[139] K. Uchida, M. Akabori, K. Noda, T. Tanifuji and S. Nasu, "Recoil range of 2.7 MeV tritons produced by the Li-6(n,alpha)H-3 reaction in Li2O single crystals," *Journal of Nuclear Materials,* vol. 89, pp. 92-98, 1980.

[140] E. L. Compere, S. S. Kirlis, E. G. Bohlmann, F. F. Blankenship and W. R. Grimes, "Fission Product Behavior in the Molten Salt Reactor Experiment," Oak Ridge National Laboratory, ORNL-4865, 1975.

[141] P. N. Haubenreich, J. R. Engel, B. E. Prince and H. C. Claiborne, "MSRE Design and Operations Report," ORNL TM-730, Oak Ridge National Laboratory , 1964.

[142] R. A. Causey, T. S. Elleman and K. Verghese, "Hydrogen Diffusion and Solubility in Pyrolytic Carbon," *Carbon,* vol. 17, pp. 323-328, 1979.

[143] H. E. M. Jr. and J. R. W. Jr., "Materials Development for Molten-Salt Breeder Reactors," Oak Ridge National Laboratory, ORNL-TM-1854, 1967.

[144] H. Tang, W. Qi, Z. He, H. Xia, Q. Huang, C. Zhang, X. Wang, J. Song, P. Huai and X. Zhou, "Infiltration of graphite by molten 2LiF-BeF2 salt," *J. Mater. Sci.,* vol. 52, pp. 11346-11359, 2017.

[145] D. Carpenter, M. Ames, G. Kohse, Y. Ostrovsky and L.-w. Hu, "Findings of the second round of fluoride salt high temperature reactor materials irradiation tests at the MIT research reactor," in *Proceedings of ICAPP 2015,* Nice, France, 2015.

[146] D. Carpenter, G. Kohse and L.W. Hu, "MITR Users' Guide," 2012.

[147] D. Carpenter, M. Ames, G. Zheng, G. Kohse and L.-w. Hu, "Tritium Production and Partioning from the Irradiation of Lithium-Beryllium Fluoride Salt," in *Proceedings of Tritium 2016,* Charleston, SC, 2016.

[148] R. B. Briggs, "Molten-Salt Reactor Program Semiannual Progress Report for Period Engind July 31, 1964," ORNL-3708, Oak Ridge National Laboratory, 1964.

[149] P. E. Warwick, D. Kim, I. W. Croudace and J. Oh, "Effective desorption of tritium from diverse solid matrices and its application to routine analysis of decommissioning materials," *Analytica Chimica Acta,* vol. 676, pp. 93-102, 2010.

[150] G. Buzzelli and A. W. Mosen, "Perchloric acid dissolution of graphite and pyrolytic carbon," *Talanta,* vol. 24, pp. 383-385, 1977.

[151] X. Liu, X. Huang, F. Xie, F. Jia, X. Feng and H. Li, "Source Term Analysis of the Irradiated Graphite in the Core of HTR-10," *Science and Technology of Nuclear Installations,* vol. 2017, 2017.

[152] G. F. Knoll, Radiation Detection and Measurement - 4th ed., Hoboken, NJ: John Wiley & Sons, Inc, 2010.

[153] ICRU report 31, "Average Energy Required to Produce an Ion Pair," Washington D.C., 1979.

[154] L. Rodrigo, J. M. Miller, S. R. Bokwa, R. E. Johnson, B. M. MacDonald and J. Senohrabek, "Tritium Measurenment and Monitoring in Experimental and Process Systems with Ionization Chambers," *Fusion Technology,* vol. 21, pp. 629-635, 1992.

[155] J. D. Hunn, M. P. Trammell and F. C. Montgomery, "Data Compilation for AGR-3/4 Matrix Ring Blank Lot RDKRS," 2011.

[156] H. E. Kissinger, "Variation of Peak Temperature with Heating Rate in Differential Thermal Analysis," *Journal of Research of the National Bureau of Standards,* vol. 57, no. 4, 1956.

[157] R. Wellen and E. L. Canedo, "On the Kissinger equation and the estimate of activation energies for non-isothermal cold crystallization of PET," *Polymer Testing,* vol. 40, pp. 33-38, 2014.

[158] K. Dolan, G. Zheng, D. Carpenter, S. Huang and L.W. Hu, "Tritium content and chemical form in nuclear graphite from molten fluoride salt irradiations," *Fusion Science and Technology,* vol. 76, pp. 398-403, 2020.

[159] H. Atsumi, T. Tanabe and T. Shikama, "Trapping state of hydrogen isotopes in carbon and graphite investigates by thermal desorption spectrometry," *Fusion Science and Technnology,* vol. 67, pp. 245-249, 2015.

[160] T. Tanabe and H. Atsumi, "Bulk hydrogen retention in graphite at elevated temperature," *Journal of Nuclear Materials,* vol. 209, pp. 109-112, 1994.

[161] T. Tanabe, N. Bekris, P. Coad, C. H. Skinner, M. Gluga and N. Miya, "Tritium retention of plasma facing components in tokamaks," *Journal of Nuclear Materials,* Vols. 313-316, pp. 478-490, 2003.

[162] T. Miner, *Private Communication*, Entegris, 2020.

[163] K. Morita and Y. Muto, "Isotopic effect in the thermal re-emission of hydrogen from graphite at elevated temperatures," *Journal of Nuclear Materials,* Vols. 196-198, pp. 963-966, 1992.

[164] M. I. Baskes, "DIFFUSE: A Code to Calculate One-Dimensional Diffusion and Trapping," Sandia National Laboratory, Livermore, CA, 1980.

[165] A. J. Robell and E. V. Ballou, "Surface Diffusion of Hydrogen on Carbon," *The Journal of Physical Chemistry,* vol. 68, no. 10, 1964.

[166] J. Crank, The Mathematics of Diffusion, Oxford: Clarendon Press, 1975.

[167] R. Delaporte-Mathurin, E. A. Hodille, J. Mougenot, Y. Charles and C. Grisolia, "Finite element analysis of hydrogen retention in ITER plasma facing components using FESTIM," *Nuclear Materials and Energy,* vol. 21, 2019.

[168] B. J. Marsden and G. N. Hall, "Graphite in Gas Cooled Reactors," in *Reference Module in Materials Science and Materials Engineering,* 2015.

[169] J. W. Anthony, R. A. Bideaux, K. W. Bladh and M. C. Nichols, Handbook of Mineralogy I (Elements, Sulfides, Sulfosalts), Chantilly, VA: Mineralogical Society of America, 1990.

[170] R. B. Briggs and C. W. Nestor, "A Method for Calculating the Steady-State Distribution of Tritium in a Molten-Salt Breeder Reactor Plant," Oak Ridge National Laboratory, ORNL-TM-4804, 1975.

[171] P. N. Haubenreich, "Tritium in the MSRE: Calculated Production Rates and Observed Amounts," Oak Ridge National Laboratory, ORNL CF-70-2-7, 1970.

[172] H. Qin, C. Wang, S. Qiu, D. Zhang, W. Tian and G. H. Su, "Study of tritium transport characteristics in a transportable fluoride-salt-cooled high-temperature reactor," *International Journal of Energy Research,* vol. 42, no. 4, 2017.

[173] Y. Zeng, W. Liu, W. Liu, G. Wang, Y. Qian, N. Qian, X. Wu, Y. Huang and S. Wu, "Tritium Transport Analysis in a 2-MW Liquid-Fueled Molten Salt Experimental Reactor with the Code TMSR-TTAC," *Nuclear Technology,* vol. 205, pp. 582-591, 2019.

[174] Kairos Power, "Private Communication".

[175] Kairos Power, "Technology - How it Works," 2020. [Online]. Available: https://kairospower.com/technology/.

[176] J. D. Gordon, J. K. Garner, W. G. Steele and W. D. Bjorndahl, "Nitrate-Salt-Cooled Blanket Concepts," *Fusion Technology,* vol. 8, 1985.

[177] M. G. Adamson, D. Calef and R. W. Moir, "Lithium Nitrate as a Fusion Reactor Coolant Fluid?: A Thermochemical Assessment," *Journal of Fusion Energy,* vol. 5, no. 3, 1986.

[178] A. T. Cisneros, "Pebble Bed Reactors Design Optimization Methods and their Application to the Pebble Bed Fluoride Salt Cooled High Temperature Reactor (PB-FHR)," University of California, Berkeley, PhD Thesis, 2013.

[179] R. Romatoski and L. Hu, "Fluoride salt coolant properties for nuclear reactor applications: A review," *Annals of Nuclear Energy,* vol. 109, pp. 635-647, 2017.

[180] National Institute of Standards and Technology, "NIST-JANAF Thermochemical Tables," NIST Standard Reference Database 13, 1998.

[181] S. Fukada, R. Anderl, Y. Hatano, S. Schuetz, R. Pawelko, D. Petti, G. Smolik, T. Terai, M. Nishikawa, S. Tanaka and A. Sagara, "Initial studies of tritium behavior in flibe and flibe-facing material," *Fusion Engineering and Design,* Vols. 61-62, pp. 783-788, 2002.

[182] Z. Xiangwen, L. Zhenming, Z. Jie, L. Bing, Z. Yanwen, T. Chunhe and T. Yaping, "Preparation of spherical fuel elements for HTR-PM in INET," *Nuclear Engineering and Design,* vol. 263, pp. 456-461, 2013.

[183] P. Harriot and R. M. Hamilton, "Solid-liquid mass transfer in turbulent pipe flow," *Chemical Engineering Science,* vol. 20, pp. 1073-1078, 1965.

[184] Y. Qin and J. M. S. Cabral, "Lumen Mass Transfer in Hollow-Fiber Membrane Processes with Constant External Resistances," *AIChE Journal,* vol. 43, no. 8, 1997.

[185] I. Hutchinson, A Student's Guide to Numerical Methods, Cambridge University Press, 2015.

[186] K. L. Wilson, "Hydron Recycling Properties of Stainless Steels," *Journal of Nuclear Materials,* vol. 103 & 104, pp. 453-464, 1981.

[187] A. Suzuki, T. Terai and S. Tanaka, "Tritium release behavior from Li2BeF4 molten salt by permeation through structural materials," *Fusion Engineering and Design,* Vols. 51-52, pp. 863-868, 2000.

[188] J. D. Rader, M. S. Greenwood and P. W. Humrickhouse, "Verification of Modelica-Based Models with Analytical Solutions for Tritium Diffusion," *Nuclear Technology,* vol. 203, pp. 58-65, 2018.

[189] T. Hayashi, T. Itoh, K. Kobayashi, K. Isobe and M. Nishi, "Safety handling characteristics of high-level tritiated water," *Fusion Engineering and Design,* vol. 81, pp. 1365-1369, 2006.

[190] S. Suppiah, D. Ryland, K. Marcinkowska, H. Boniface and A. Everatt, "Performance characterization of hydrogen isotope exchange and recombination catalysts for tritium processing," Chalk River Laboratories, CW-122300, Atomic Energy of Canada Limited.

[191] K. M. Song, S. H. Sohn, D. W. Kang and H. S. Chung, "Introduction to Wolsong Tritium Removal Facility (WTRF)," in *Transactions of the Korean Nuclear Society Autumn Meeting,* Busan, Korea, 2005.

[192] L. Frances, M. Douilly, M. Grivet, D. Ducret and M. Theobald, "Self-Radiolysis of Tritiated Water Stored in Zeolites 4A - Production and Behavior of H2 and O2," *Journal of Physical Chemistry,* 2015.

[193] Y. Grosu, O. Bondarchuk and A. Faik, "The effect of humidity, impurities and initial state on the corrosion of carbon and stainless steels in molten HitecXL salt for CSP application," *Solar Energy Materials and Solar Cells,* vol. 174, pp. 34-41, 2018.

[194] F. Sabathier, D. Brennan, N. Skinner and B. Patel, "Assessment of the performance of the JET exhaust detritiation system," *Fusion Engineering and Design,* vol. 54, pp. 547-553, 2001.

[195] Advanced Specialty Gas Equipment, "Moisture Conversion Table," [Online]. Available: http://www.asge-online.com/.

[196] Advanced Chemicals Supplier, "Materials Catalog - Molecular Sieves, 5A," [Online]. Available: https://www.acsmaterial.com/molecular-sieves-5a.html.

[197] W. T. Shmayda and P. Mayer, "Uranium Beds for Temporary Tritium Storage," *Journal of the Less-Common Metals,* vol. 104, pp. 239-250, 1984.

[198] R. M. Jebasty and R. Vidya, "Mechanical properites of multifunctional TiF4 from first-principles calculations," *ACS Biomaterials Science and Engineering,* vol. 5, pp. 2001-2012, 2019.

[199] Nation Institute of Standards and Technology, "JANAF Thermochemical Tables," 1998.

[200] General Electric, "General Electric Systems Technology Manual," Secondary Containment System, Chapter 4.2.

[201] R. J. Pearson, A. B. Antoniazzi and W. J. Nuttall, "Tritium supply and use: a key issue for the development of nuclear fusion energy," *Fusion Engineering and Design,* vol. 136, pp. 1140-1148, 2018.

[202] W. T. Shmayada, C. R. Shmayada and G. Torres, "Tritium Extraction from Water," *Fusion Science and Technology,* vol. 75, pp. 1030-1036, 2019.

[203] A. Pisarev, I. Tsvetkov and S. Yarko, "Hydrogen permeation through membranes with cracks in protection layer," *Fusion Engineering and Design,* vol. 82, pp. 2120-2125, 2007.

[204] C. Forsberg, G. Zheng, R. G. Ballinger and S. T. Lam, "Fusion Blankets and Fluoride-Salt-Cooled High-Temperature Reactors with Flibe Salt Coolant: Common Challenges, Tritium Control, and Opportunities for Synergistic Development Strategies Between Fission, Fusion, and Solar Salt Technologies," *Nuclear Technology,* 2019.

[205] V. D'Auria, S. Dulla, P. Ravetto, L. Savoldi, M. Utili and R. Zanino, "Tritium Extraction from Lithium-Lead in the EU DEMO Blank Using Permeator Against Vacuum," *Fusion Science and Technology,* vol. 71, pp. 537-543, 2017.

[206] P. W. Humrickhouse and B. K. Merrill, "Vacuum Permeator Analysis for Extraction of Tritium from DCLL Blankets," *Fusion Science and Technology,* vol. 68, 2015.

[207] J. McClure, "Fluid Configurations in a Random Sphere Packing," 4 April 2016. [Online]. Available: https://www.digitalrocksportal.org/projects/41.

[208] A. M. Ougouag and W. K. Terry, "A Preliminary Study of the Effect of Shifts in Packing Fraction on K-Effective in Pebble-Bed Reactors," Idaho National Engineering and Environmental Laboratory, INEEL/CON-01-00342, 2001.

[209] C. Kang, "Pressure Drop in a Pebble Bed Reactor," MS Thesis, Texas A&M University, 2010.

[210] G. Horhoianu, W. Vandermeulen and C. Janssen, "Helium Embrittlement in Type 316 Stainless Steel," Centre D'etude De L'energie Nucleaire, BLG 510, 1975.

[211] S. Nogami, A. Hasegawa, T. Tanno, K. Imasaki and K. Abe, "High-Temperature Helium Embrittlement of 316FR Steel," *Journal of Nuclear Science and Technology,* vol. 48, no. 1, pp. 130-134, 2011.

Appendix

A. Additional Details on MITR Fluoride Salt Irradiation Experiments

Further detail is provided here on the capsule designs and sample test matrix from each in-core Flibe irradiation at MITR. For the FS-1 experiment, the graphite crucible dimensions are displayed in Figure A.1. The samples and salt loading in each compartment are described in Table A.1. Desorption analysis was conducted with the crucible-third section containing compartments C and D, which are the two holes in the crucible without protruding metal wires. The metal hanging wires were used to suspend the 316SS and Hastelloy samples in the salt during the irradiation.

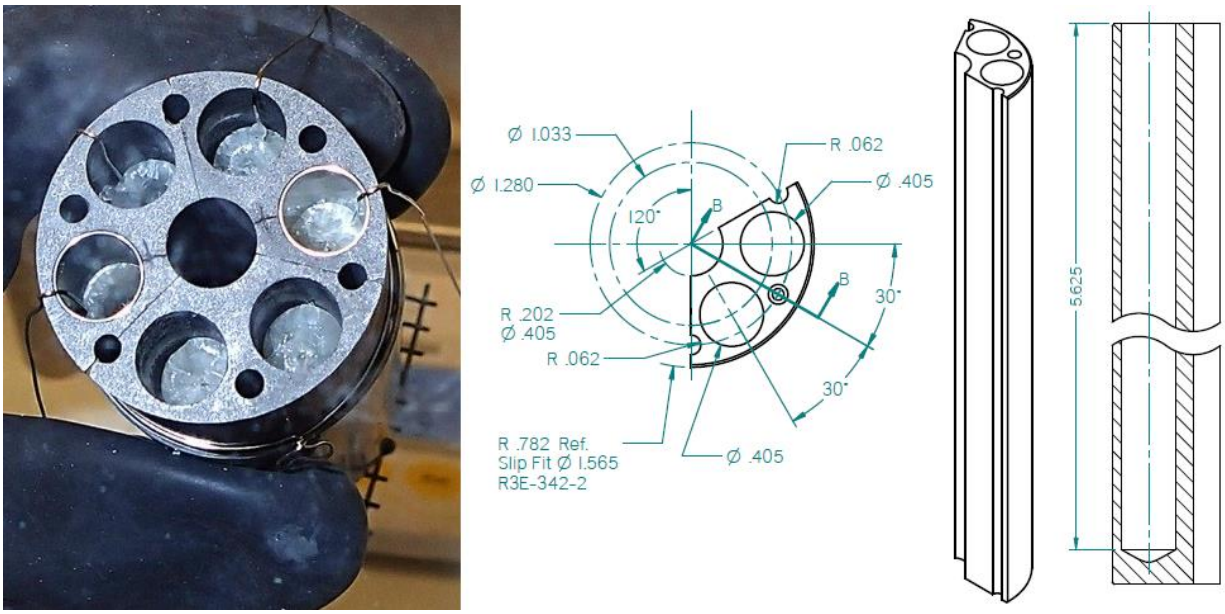

Figure A.1. FS-1 crucible before irradiation (left). The crucible was assembled from three sections (right) fabricated according to the drawing with dimensions in inches.

Table A.1. Salt and sample loading for the FS-1 irradiation. Additional descriptions in [17].

Compartment	Liner	Flibe Mass [g]	Samples
A	None	21.3	2 Hastelloy N Plates
B	None	21.2	2 316SS Plates
C	None	21.2	3 SiC/SiC, 1 SiC
D	None	21.2	~300 TRISO Surrogates
E	316SS	18.2	2 316SS Plates
F	Hastelloy N	18.1	2 Hastelloy N plates

Sample discs of IG-110U and ARB graphite from FS-2 were desorbed for tritium. The IG-110U and ARB samples were contained in the same crucible compartment during the irradiation.

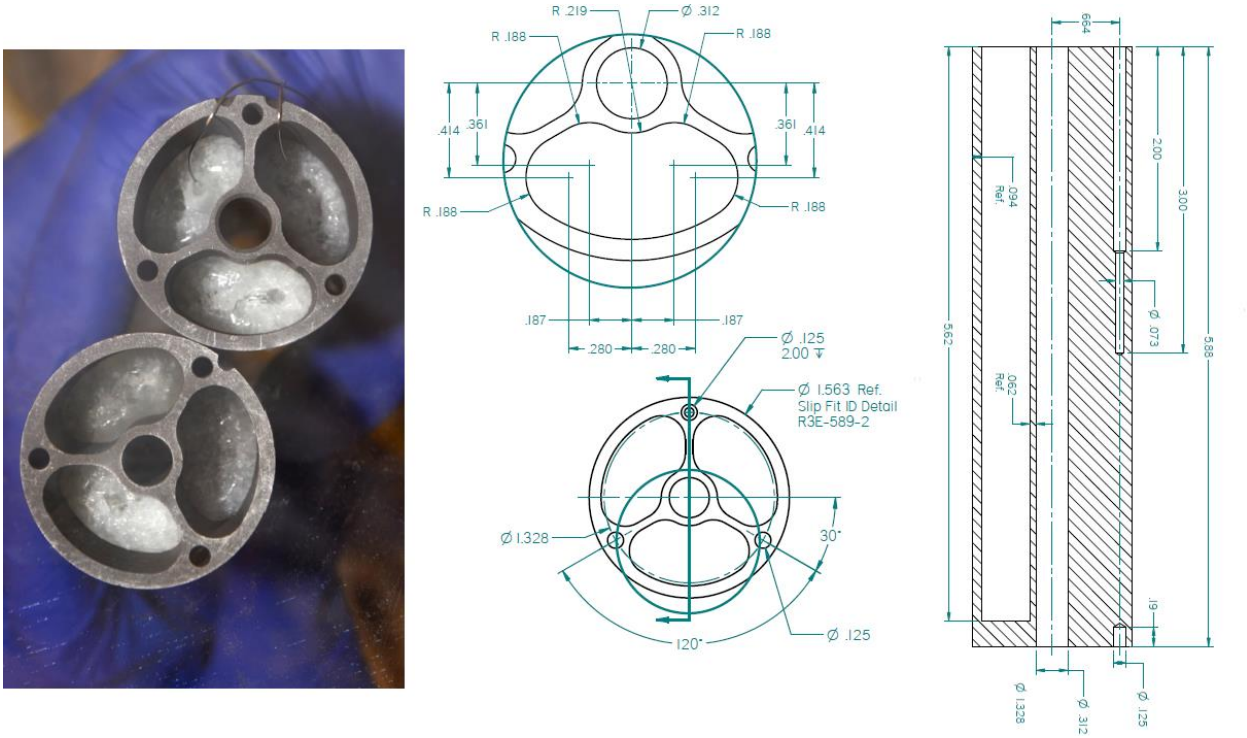

Figure A.2. FS-2 crucibles filled with salt before irradiation (left), crucible top view dimensions (center), and crucible axial cutaway (right).

Table A.2. Sample descriptions and dimensions (in mm) from FS-2. Additional details in [145].

Specimen	Description	Thickness	Width/Diameter	Height
IG110U-1	Disc	2.006	19.05	
IG110U-2	Disc	2.01	19.04	
ARB-1	Disc	1.978	19.04	
ARB-2	Disc	2.006	19.04	
CC-1	Rectangular	2.449	11.67	20.83
CC-2	Rectangular	2.388	11.99	20.34
316-1-1	Rectangular 1-hole	0.712	9.97	19.73
316-1-2	Rectangular 1-hole	0.641	9.86	19.74
316-1-3	Rectangular 1-hole	0.483	9.94	19.8
316-2-1	Rectangular 2-hole	0.516	9.96	19.84
SiC-1	Rectangular	1.835	7.55	20.15
SiC-2	Rectangular	1.871	7.62	20.07
SiC-3	Rectangular	1.894	7.55	21.42
SiC-4	Rectangular	1.865	7.62	20.10
TRISO	400 particles		0.916	

For the FS-3 experiment, samples from the upper and lower crucibles were tested. The samples were IG-110 from compartment FS-S-U4 and IG-110U from FS-3-3 listed in Table A.3. The FS-S-Ux crucible occupied the highest in core position, while FS-S-Lx was in the center, and FS-3-x was the lower crucible. Since no samples from FS-S-Lx were tested in this study, samples from the FS-3-x were referred to with the L designation, for simplicity.

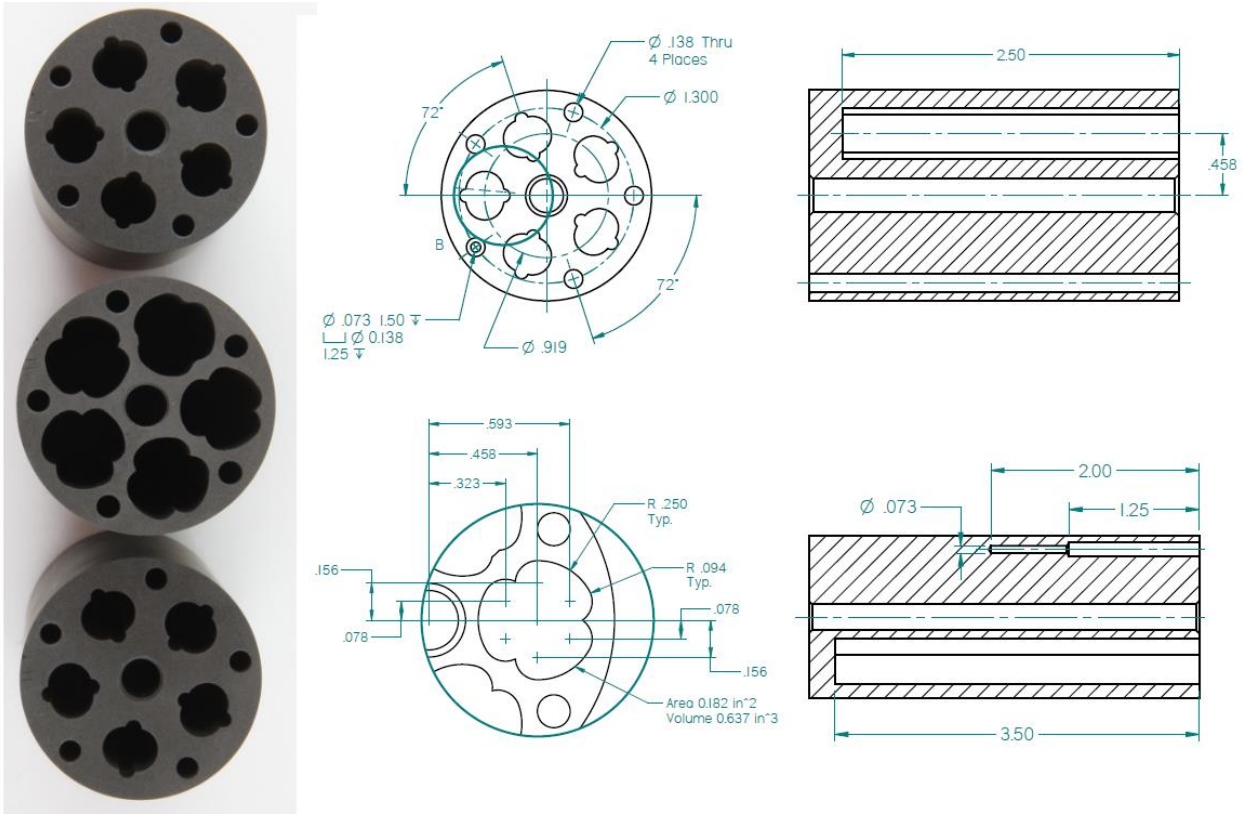

Figure A.3. FS-3 Crucibles after fabrication (left), top view drawings (center), and rotated axial cutaway drawings (right). Upper and lower crucibles have identical dimensions.

Table A.3. Sample matrix for FS-3 with dimensions and surface conditions.

Flibe salt	Sample name	Material name	Surface condition	Baking or not	Thickness [mm]	Diameter [mm]	Sample Mass [g]
5.2g	FS-S-U1-1	NG-CT-50			2.009	8.019	0.1773
	FS-S-U1-2	NG-CT-50			2.011	8.019	0.1768
	FS-S-U1-3	NG-CT-50			2.009	8.013	0.1774
	FS-S-U1-4	NG-CT-50			2.018	8.01	0.1771
	FS-S-U1-5	NG-CT-50	polished		2.0421	8.04	0.17244
	FS-S-U1-6	NG-CT-50	polished		2.0451	8.04	0.17359
	FS-S-U1-7	NG-CT-50			2.009	8.01	0.1775

5.2g	FS-S-U2-1	NG-CT-10		2.02	8.004	0.1871
	FS-S-U2-2	NG-CT-10		2.018	8.013	0.1889
	FS-S-U2-3	NG-CT-10		2.023	8.004	0.1864
	FS-S-U2-4	NG-CT-10		2.017	8.012	0.1909
	FS-S-U2-5	NG-CT-10	polished	2.0445	8.04	0.1803
	FS-S-U2-6	NG-CT-10	polished	2.0419	8.03	0.18385
	FS-S-U2-7	NG-CT-10		2.017	8.018	0.19
5.2g	FS-S-U3-1	TFX-10		2.038	8.013	0.1794
	FS-S-U3-2	TFX-10		2	8.025	0.176
	FS-S-U3-3	TFX-10		2.207	8.018	0.1881
	FS-S-U3-4	TFX-10		1.999	8.038	0.1769
	FS-S-U3-5	TFX-10	polished	2.0286	8.01	0.16519
	FS-S-U3-6	TFX-10	polished	2.0295	8.01	0.16564
	FS-S-U3-7	TFX-10		2.025	8.012	0.1746
5.2g	FS-S-U4-1	IG-110U		2.057	7.97	0.17829
	FS-S-U4-2	IG-110		2.022	8.005	0.1792
	FS-S-U4-3	IG-110		2.018	7.997	0.1787
	FS-S-U4-4	IG-110		2.007	8.00	0.1782
	FS-S-U4-5	IG-110	polished	2.0578	8.00	0.17701
	FS-S-U4-6	IG-110	polished	2.0568	8.01	0.17806
	FS-S-U4-7	IG-110		2.004	7.997	0.1757
5.2g	FS-S-U5-1	C/C		2.069	7.96	0.179
	FS-S-U5-2	C/C		2.075	7.985	0.1802
	FS-S-U5-3	C/C		2.058	7.959	0.1765
	FS-S-U5-4	C/C		2.067	7.958	0.1776
	FS-S-U5-5	C/C	polished	2.0566	7.99	0.17438
	FS-S-U5-6	C/C	polished	2.0587	8.04	0.17843
	FS-S-U5-7	C/C		2.068	7.978	0.1787
10.6g	FS-S-L1-1	NG-CT-50		15.997	8.018	1.4274
	FS-S-L1-2	NG-CT-50		15.998	8.00	1.4246
	FS-S-L1-3	NG-CT-50		16	7.948	1.4118
	FS-S-L1-4	NG-CT-50		16.003	8.02	1.428
	FS-S-L1-5	NG-CT-50		15.999	7.985	1.4174
10.6g	FS-S-L2-1	NG-CT-10		16.018	8.009	1.4991
	FS-S-L2-2	NG-CT-10		16.02	8.01	1.5013
	FS-S-L2-3	NG-CT-10		16.019	8.02	1.4981
	FS-S-L2-4	NG-CT-10		16.018	8.01	1.5282
	FS-S-L2-5	NG-CT-10		16.02	8.009	1.5141
10.6g	FS-S-L3-1	TFX-10		15.999	8.011	1.3836
	FS-S-L3-2	TFX-10		16.001	8.01	1.4036
	FS-S-L3-3	TFX-10		16	8.012	1.3849

	FS-S-L3-4	TFX-10			16.001	8.01	1.397
	FS-S-L3-5	TFX-10			15.99	8.01	1.399
10.6g	FS-S-L4-1	IG-110			16.019	8.00	1.4128
	FS-S-L4-2	IG-110			16.002	7.998	1.4193
	FS-S-L4-3	IG-110			16.019	8.001	1.4134
	FS-S-L4-4	IG-110			16.013	7.995	1.4123
	FS-S-L4-5	IG-110			16.018	7.998	1.4201
10.8g	FS-S-L5-1	C/C			10.108	10.03	1.4093
	FS-S-L5-2	C/C			10.111	10.05	1.4101
	FS-S-L5-3	C/C			10.109	10.049	1.4075
	FS-S-L5-4	C/C			10.122	10.024	1.4223
	FS-S-L5-5	C/C			10.12	10.016	1.4147
5.2g	FS-3-1-1	IG-110			2.018	7.995	0.179
	FS-3-1-2	IG-110U			2.0643	7.99	0.17929
	FS-3-1-3	IG-110U		baked	2.0658	7.99	0.18010
	FS-3-1-4	IG-110U			2.0672	7.98	0.17956
	FS-3-1-5	IG-110U	polished	baked	2.0717	7.98	0.18387
	FS-3-1-6	IG-110U	polished		2.0619	7.98	0.17929
	FS-3-1-7	IG-110U			2.0684	7.97	0.17875
5.2g	FS-3-2-1	A3-3			2.0583	7.98	0.16170
	FS-3-2-2	A3-3			2.0644	7.98	0.16271
	FS-3-2-3	A3-3		baked	2.0671	7.99	0.15901
	FS-3-2-4	A3-3		baked	2.0654	7.98	0.15808
	FS-3-2-5	A3-3	polished		2.0695	7.99	0.17520
	FS-3-2-6	A3-3	polished	baked	2.0866	7.99	0.17695
	FS-3-2-7	A3-3			2.0614	7.98	0.16244
5.2g	FS-3-3-1	IG-110U			2.0636	7.98	0.17896
	FS-3-3-2	IG-110U			2.0674	7.99	0.17932
	FS-3-3-3	IG-110U		baked	2.0710	7.98	0.18033
	FS-3-3-4	IG-110U		baked	2.0711	7.98	0.17928
	FS-3-3-5	IG-110U	polished		2.0758	7.98	0.18257
	FS-3-3-6	IG-110U	polished	baked	2.0658	7.98	0.18012
	FS-3-3-7	IG-110U			2.0726	7.98	0.18057
5.2g	FS-3-4-1	A3-3			2.0690	7.97	0.16124
	FS-3-4-2	A3-3			2.0640	7.97	0.16010
	FS-3-4-3	A3-3		baked	2.0644	7.97	0.15642
	FS-3-4-4	A3-3		baked	2.0683	7.98	0.15747
	FS-3-4-5	A3-3	polished		2.0307	7.99	0.16067
	FS-3-4-6	A3-3	polished	baked	2.0916	7.99	0.17887
	FS-3-4-7	A3-3			2.0680	7.98	0.15856
0g	FS-3-5-1	IG-110U	polished		2.0537	7.98	0.17862
	FS-3-5-2	A3-3	polished		2.0966	7.99	0.18288

FS-3-5-3	NG-CT-50	polished	2.0541	8.04	0.17411
FS-3-5-4	NG-CT-10	polished	2.0407	8.04	0.18199
FS-3-5-5	TFX-10	polished	2.0380	8.01	0.16662
FS-3-5-6	IG-110	polished	2.0562	8.02	0.17560
FS-3-5-7	C/C	polished	2.0568	8.00	0.17499

A. Calculations for Helium-3 Production with Exterior-Surface Coatings Applied

As discussed in Section 6.2.2, outer-surface coatings add permeation resistance by increasing the tritium concentration inside of metals, and thus raising the salt-metal tritium boundary condition. One undesirable feature of a higher tritium concentration is the buildup of helium-3 over time from tritium decay. Helium can cause embrittlement of stainless steels at high temperatures by concentrating into susceptible defects such as voids or grain boundaries [210]. In stainless steels, fast neutron reactions with Fe, Ni, Cr, and N can produce a source of helium inside metals under neutron irradiation [210]. Even at low concentrations, such as atomic parts per million (appm) levels, helium can create significant changes in the ductility of stainless steels at high temperatures [210]. For example, a transition from a ductile to fully intergranular fracture mechanism was observed during tensile tests at 750ºC with 316FR steel once loaded with 5 appm helium from an ion beam source [211]. The graphite reflector of a FHR will reduce the fast neutron flux near the reactor vessel, but the additional helium created from tritium decay could potentially cause a degradation of material properties if highly effective outer barriers are used.

The helium-3 concentration in structural metals can be calculated from TRIDENT Mod1 results with equation A.1, where λ is the decay constant for tritium and T_{RPV} is the inventory of tritium in the reactor vessel, for example, as a function of time. As shown in Figure A.4, the helium-3 concentration increases linearly once the reactor vessel reaches an equilibrium tritium concentration over roughly one year. An assumption in this analysis is that all helium-3 remains in the metal after production from tritium decay, and there is no losses of He-3 by diffusion out of the vessel. The steady state tritium inventories for the reactor vessel are shown in Table A.4 along with the time required to reach a helium-3 concentration of 1 appm, which is used only as a reference point. As the metal region with the second highest tritium inventory, the cold leg is also shown in Table A.4 for comparison.

Eq. A.1

$$^{3}He(t) = \lambda \int T_{RPV}(t)dt$$

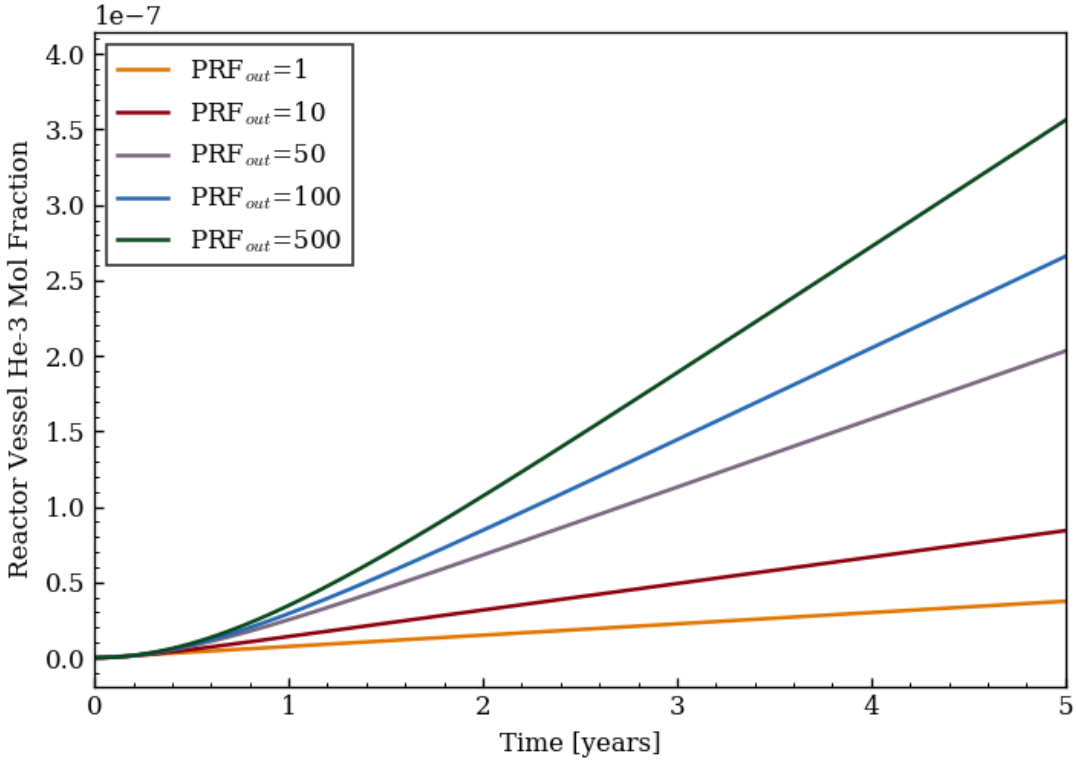

Figure A.4. Helium-3 buildup from tritium decay in the reactor vessel for various outer-coating permeation reduction factors assuming all helium-3 is immobile in the metal.

Table A.4. Equilibrium tritium inventories for the reactor vessel and cold leg under several outer-coating conditions along with the time at which each region reaches a helium-3 concentration of 1 atomic part per million in 316 stainless steel.

Region and PRF	Equilibrium H-3	Time to Reach 1 appm He-3
Vessel PRF_{out}=1	2136 Ci	113.5 yr
PRF_{out}=10	5004 Ci	57.20 yr
PRF_{out}=50	12860 Ci	22.67 yr
PRF_{out}=100	17350 Ci	17.07 yr
PRF_{out}=500	23930 Ci	12.67 yr
Cold Leg PRF_{out}=1	113.5 Ci	235.1 yr
PRF_{out}=10	124.8 Ci	213.8 yr
PRF_{out}=50	436.9 Ci	61.06 yr
PRF_{out}=100	678.0 Ci	39.35 yr
PRF_{out}=500	1102 Ci	24.21 yr